Advanced Structured Materials

Holm Altenbach
Frank Jablonski
Wolfgang H. Müller
Konstantin Naumenko
Patrick Schneider *Editors*

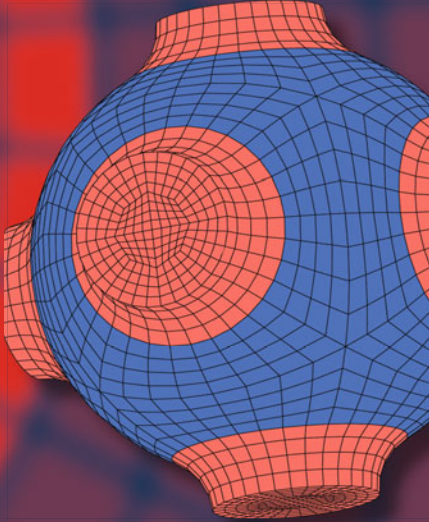

Advances in Mechanics of Materials and Structural Analysis

In Honor of Reinhold Kienzler

Springer

Advanced Structured Materials

Volume 80

Series editors

Andreas Öchsner, Southport Queensland, Australia
Lucas F. M. da Silva, Porto, Portugal
Holm Altenbach, Magdeburg, Germany

More information about this series at http://www.springer.com/series/8611

Holm Altenbach · Frank Jablonski
Wolfgang H. Müller · Konstantin Naumenko
Patrick Schneider
Editors

Advances in Mechanics of Materials and Structural Analysis

In Honor of Reinhold Kienzler

Springer

Editors
Holm Altenbach
Institute of Mechanics
Faculty of Mechanical Engineering
Otto-von-Guericke-University Magdeburg
Magdeburg, Sachsen-Anhalt
Germany

Frank Jablonski
Fakultät 5, Abt. 1
Hochschule Bremen
Bremen, Bremen
Germany

Wolfgang H. Müller
Institut für Mechanik
Technische Universität Berlin
Berlin
Germany

Konstantin Naumenko
Institute of Mechanics
Faculty of Mechanical Engineering
Otto-von-Guericke-University Magdeburg
Magdeburg, Sachsen-Anhalt
Germany

Patrick Schneider
Institute for Lightweight Construction
and Design (KLuB)
Technische Universität Darmstadt
Darmstadt
Germany

ISSN 1869-8433 ISSN 1869-8441 (electronic)
Advanced Structured Materials
ISBN 978-3-319-70562-0 ISBN 978-3-319-70563-7 (eBook)
https://doi.org/10.1007/978-3-319-70563-7

Library of Congress Control Number: 2017958632

© Springer International Publishing AG 2018
This work is subject to copyright. All rights are reserved by the Publisher, whether the whole or part of the material is concerned, specifically the rights of translation, reprinting, reuse of illustrations, recitation, broadcasting, reproduction on microfilms or in any other physical way, and transmission or information storage and retrieval, electronic adaptation, computer software, or by similar or dissimilar methodology now known or hereafter developed.
The use of general descriptive names, registered names, trademarks, service marks, etc. in this publication does not imply, even in the absence of a specific statement, that such names are exempt from the relevant protective laws and regulations and therefore free for general use.
The publisher, the authors and the editors are safe to assume that the advice and information in this book are believed to be true and accurate at the date of publication. Neither the publisher nor the authors or the editors give a warranty, express or implied, with respect to the material contained herein or for any errors or omissions that may have been made. The publisher remains neutral with regard to jurisdictional claims in published maps and institutional affiliations.

Printed on acid-free paper

This Springer imprint is published by Springer Nature
The registered company is Springer International Publishing AG
The registered company address is: Gewerbestrasse 11, 6330 Cham, Switzerland

Preface

It is time I stepped aside for a less experienced and less able man.

Scott Elledge, Goldwin Smith Professor of
English Literature at Cornell University on
the occasion of his retirement

The scientific papers compiled in this book are dedicated to Prof. Reinhold Kienzler on the occasion of his 66th birthday and retirement from Bremen University. From a topical point of view, they reflect the various scientific activities of Reinhold during his professional life. Therefore, it is only appropriate to dwell briefly on his achievements and to highlight the important steps in his career.

Reinhold Kienzler was born on 29th of August 1950 in Naumburg/Wolfhagen in Northern Hessia. He attended the local high school (Friedrichsgymnasium) in Kassel from 1961 to 1969 and obtained his high school diploma (Abitur) in 1969. After that, he went to the Technische Hochschule Darmstadt from 1970 to 1976 in order to study civil engineering and obtained his doctoral degree from the Department of Mechanics on December 17, 1980. His thesis entitled “Eine

Erweiterung der klassischen Schalentheorie; Der Einfluß von Dickenverzerrungen und Querschnittsverwölbungen" was supervised by Profs. Walter Schnell and Dietmar Gross. In fact, plate and shell theory has been an ongoing scientific topic of Reinhold ever since. In this context, it is fair to say that he always emphasized a straightforward, "rational" approach instead of intelligent patchwork as it is very common to this engineering discipline of linear elasticity.

After his dissertation, Reinhold went to Stanford University from 1981 to 1983 as a postdoc with Prof. George Herrmann from the Department of Applied Mechanics. Moreover, from 1983 to 1991, he worked as an engineer at the Fraunhofer Institut für Werkstoffmechanik in Freiburg/Breisgau. These activities sparked his interest in the fundamentals of fracture mechanics and in damage theory of materials. In this context, his monographs "Konzepte der Bruchmechanik: Integrale Bruchkriterien" (habilitation thesis) and "Mechanics in Material Space—With Applications to Defect and Fracture Mechanics" (co-authored with George Herrmann) are of particular, everlasting importance to our community.

In 1991, Reinhold received a call for the Professorship of Applied Mechanics at the University of Bremen, where he stayed until his retirement despite many other prestigious offers that were made to him after.

His principle of leadership is simple, effective, and unpretentious: His intention was never to aim for quantity but always for the highest quality instead. Therefore, the size of his group was always such that he had enough time to spend for intensive, individual discussions with every member. Nine dissertations and one habilitation are the fruits of his efforts, all within the fields of fracture and damage mechanics of materials and plate and shell theory. He is the author to more than 110 papers in peer-reviewed journals and eight books including four textbooks on Engineering Mechanics. Since 2004, he is the Editor-in-Chief of the journal Archive of Applied Mechanics—one of the oldest German journals in the field of mechanics.

For many years, he was (co)-organizer of the workshop series Mechanics of Materials at the Mathematisches Forschungsinstitut Oberwolfach, the German–Greek–Polish Symposium on Recent Advances in Mechanics, and the International Symposium on Defect and Material Mechanics. In 2002, he was Co-Chair of the EUROMECH Colloquium 444 "Critical Review of the Theories of Plates and Shells and New Applications." In 2004, the proceedings (co-edited with Holm Altenbach and Ingrid Ott) were published in the Springer's series "Lecture Notes in Applied and Computational Mechanics" as volume 16.

Reinhold was awarded the Berninghausen-Preis for excellence in teaching at the University of Bremen in 1996. He became an Honorary Member of the Polish Society of Theoretical and Applied Mechanics in 2011 and of the Hellenic Society of Theoretical and Applied Mechanics in 2013. He received a Distinguished Visiting Fellowship Award of the Royal Academy of Engineering, London, in 2013. In 2016, Reinhold was awarded an Honorary Doctor by the Ilia Vekua

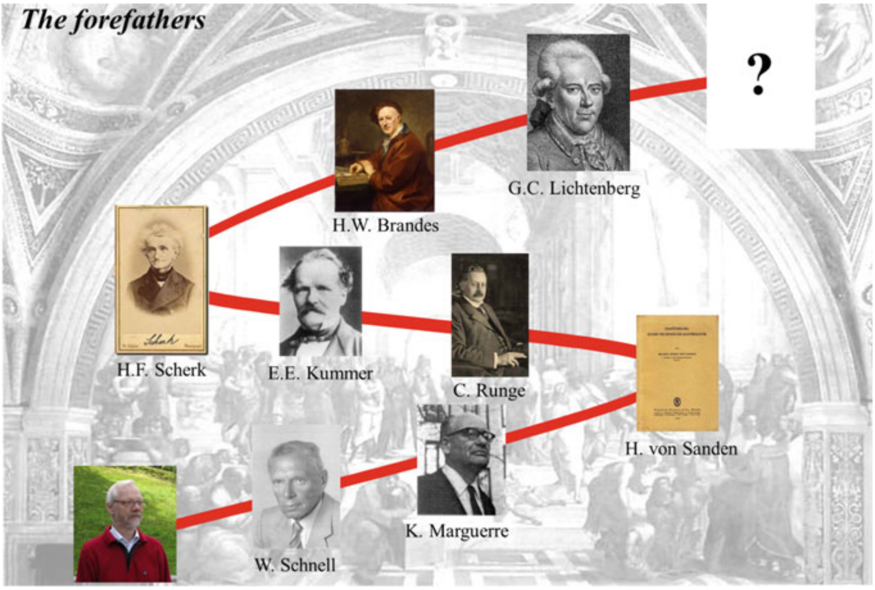

Institute of Applied Mathematics in Tbilisi, Georgia, for his engagement in the promotion of Georgian-German advancement in the sciences.

Now that we have explored Reinhold's scientific legacy, let us take a look at his scientific heritage (see picture). To be more precise, we shall explore who the doctor fathers of his doctor father were. It has been mentioned above that Reinhold graduated with a doctoral thesis under the supervision of Walter Schnell (1924–1999) who was one of the iconic figureheads at the Faculty of Mechanics at Darmstadt University right after the war. Schnell's supervisor at Darmstadt was Karl Marguerre (1906–1979), who is well known for his contributions to stability analysis and plate theory. He in turn was trained by Horst von Sanden (1883–1965), who worked in various fields of technical mathematics. The next in line is Carl Runge (1856–1927), whose name is immortal in numerical analysis, notably in the Runge–Kutta scheme. Runge in turn was educated by Ernst Eduard Kummer (1810–1893), who is famous for his work in the confluent hypergeometric function. The presence of the next doctor father, Heinrich Ferdinand Scherk (1798–1885), does not only explain Reinhold's passion for mathematic stringency (Scherk was a mathematics professor in Königsberg). He also connects Reinhold to Bremen, Reinhold's main place of activity, since he was born there. Now, we leave mathematics. The next supervisor of days passed was Heinrich Wilhelm Brandes (1777–1834) who worked in meteorology. Finally, the last one in Reinhold's scientific lineage is Georg Christoph Lichtenberg (1742–1799), who allegedly had no doctoral supervisor, was a physicist, and is known for his witty remarks. For example, "Es ist fast unmöglich, die Fackel der Wahrheit durch ein Gedränge zu tragen, ohne jemandem den Bart zu versengen." ("It is nearly impossible to carry the torch of truth through the crowds without scorching someone's beard.") Reinhold surely never minced his words when he had some truth to proclaim and in this sense is a worthy representative of his ancestor.

The editors would like to wish Reinhold and his family all the best for the future and many more years of active scientific life. We continue to need his presence and advice!

Magdeburg, Germany	Holm Altenbach
Bremen, Germany	Frank Jablonski
Berlin, Germany	Wolfgang H. Müller
Magdeburg, Germany	Konstantin Naumenko
Darmstadt, Germany	Patrick Schneider

Contents

On Constitutive Models for the Momentum Transfer to Particles in Fluid-Dominated Two-Phase Flows 1
Yan Cui, Jure Ravnik, Matjaž Hriberšek and Paul Steinmann

Flexible Beam-Like Structures - Experimental Investigation and Modeling of Cables 27
Vanessa Dörlich, Joachim Linn and Stefan Diebels

On Phase Transformation Induced Effects Controlling the Flow Behavior of Ferritic-Martensitic Dual-Phase Steels 47
A. Fillafer, E. Werner and C. Krempaszky

Hygro- and Thermo-Mechanical Modeling of Wood at Large Deformations: Application to Densification and Forming of Wooden Structures 59
Robert Fleischhauer and Michael Kaliske

Damage and Fracture of Ductile Sheet Metals: Experiments and Numerical Simulations with New Biaxial Specimens 99
S. Gerke, M. Schmidt, M. Dirian and M. Brünig

Influence of Shear Correction Factors on Eigenfrequencies of Layered Plates 117
Friedrich Gruttmann and Werner Wagner

Verification Examples for Strain and Strain-Rate Determination of Digital Image Correlation Systems 135
S. Hartmann and S. Rodriguez

Closed-Form Approximate Solutions for the Local Buckling Behavior of Composite Laminated Beams Based on Third-Order Shear Deformation Theory 175
Johannes Herrmann, Torsten Kühn, Tjorven Müllenstedt, Siham Mittelstedt and Christian Mittelstedt

Dislocation Dynamics as Gradient Descent in a Space of Currents 207
Thomas Hochrainer

Optimum Design of Thick Laminated Anisotropic Plates via Frequency Regulation. A BEM Approach 223
J. T. Katsikadelis and N. G. Babouskos

Application of Piezoelements in a Structured Thin-Walled Shaft Material to Active Control of Stability and Vibration 241
Włodzimierz Kurnik and Piotr Przybyłowicz

Remarks on a Fluid-Structure Interaction Scheme Based on the Least-Squares Finite Element Method at Small Strains 261
Carina Nisters, Alexander Schwarz, Solveigh Averweg and Jörg Schröder

Dynamic Analysis of Gradient Poroelastic Solids and Structures 281
Ioannis P. Pegios, Sofia Papargyri-Beskou and Dimitri E. Beskos

Microstructured Multiferroic Materials: Modelling Approaches Towards Efficiency and Durability 297
Andreas Ricoeur, Artjom Avakian and Stephan Lange

Biaxial Tensile Tests and Microstructure-Based Inverse Parameter Identification of Inhomogeneous SMC Composites 329
Malte Schemmann, Sebastian Gajek and Thomas Böhlke

Configurational Forces in a Phase Field Model for Dynamic Brittle Fracture 343
Alexander Schlüter, Charlotte Kuhn and Ralf Müller

A Multi-layer Piezocomposite Model and Application on Controlled Smart Structures 365
Georgios Tairidis, Georgia Foutsitzi and Georgios E. Stavroulakis

Optimal Design of Disks Under Large Creep Deformation 387
Aneta Ustrzycka, Krzysztof Szuwalski and Zbigniew L. Kowalewski

A J-Interaction Integral to Compute Force Stress and Couple Stress Intensity Factors for Cracks in Functionally Graded Micropolar Materials 419
Hongjun Yu and Meinhard Kuna

Analytical Modelling of the Tooth Translational Motions: Comparative Analysis for Different Shapes of Root 449
Kirill Yurkevich, Sergei Bosiakov and Holm Altenbach

On Constitutive Models for the Momentum Transfer to Particles in Fluid-Dominated Two-Phase Flows

Yan Cui, Jure Ravnik, Matjaž Hriberšek and Paul Steinmann

Abstract This contribution deals with fluid flow-particle interactions in fluid dominated two phase flows. Spherical as well as non-spherical particles in the form of are considered. In the case of ellipsoids, the hydrodynamic drag force model based on the Brenner-type resistance tensor is applied. As high shear flow regions are frequently encountered in complex flow patterns, special attention is devoted to the extension of established shear lift models, that are only valid for special cases of shear flows, to a general shear lift model based on permutations of the lift tensor, originally derived by Harper and Chang. A generalized lift vector, valid for ellipsoidal particles, is derived and implemented for the computation of the lift force in general shear flows. The derived generalized shear lift force model is validated against other numerical models for ellipsoids in Couette flow, and its influence on the translational motion of ellipsoidal particles in a three-dimensional lid-driven cavity flow is studied. The computational results confirm the correctness of the proposed generalized shear lift model.

Y. Cui (✉) · P. Steinmann
Chair of Applied Mechanics, University of Erlangen-Nuremberg,
Egerlandstr. 5, 91058 Erlangen, Germany
e-mail: yan.cui@fau.de

P. Steinmann
e-mail: paul.steinmann@fau.de

J. Ravnik · M. Hriberšek
Faculty of Mechanical Engineering, University of Maribor,
Smetanova 17, 2000 Maribor, Slovenia
e-mail: jure.ravnik@um.si

M. Hriberšek
e-mail: matjaz.hribersek@um.si

© Springer International Publishing AG 2018

H. Altenbach et al. (eds.), *Advances in Mechanics of Materials and Structural Analysis*, Advanced Structured Materials 80,
https://doi.org/10.1007/978-3-319-70563-7_1

1 Introduction

Fluid flows with dispersed solid particles are increasingly important in several fields of sciences, e.g. life sciences, natural sciences, medical sciences and engineering sciences. Processing of suspensions with fibres in the pulp industry [18], regulating heat transfer by use of particles with favorable thermal properties [15], magnetic separation of particles from the matrix fluid [21, 31], and waste water treatment [14] are only a few of many applications. Dispersed flows consist of particles (drops, bubbles, solids) that move in a continuous phase (air, water). Particles interact with the fluid flow, i.e. in general, they exchange mass, linear and angular momentum, and energy. Among the interactions that predominantly influence a particle trajectory, the linear momentum exchange is typically the most important one. However, in cases of high shear flow fields and/or rotating particles, angular momentum can also play an important role and can in general not be neglected.

The influence of the particles on the fluid flow and the collisions between particles cannot be ignored. However, in the case of dilute suspensions we may reasonably ignore particle-particle interactions and limit our considerations to the particle-fluid system. This leads to the fundamental theory of non-colloidal suspensions, which aims to provide reduced scale models for the two-way coupling between particles and the fluid flows [4]. Also, in cases of small particles (micro- and nano-sized) modelling of particle-fluid interactions is unavoidable, as one can not afford to fully resolve flow structures in the vicinity of the particles. In order to develop accurate computational tools for the particle-fluid interaction, one needs to implement the appropriate constitutive models for the interaction of the two phases.

2 Particle-Fluid Interaction in Fluid Dominated Flows

In the case of solid particles or micro-sized bubbles and drops the shape of a particle is not affected by the flow field, therefore the particles can be considered to be rigid particles, immersed in the fluid phase. As the flow field is typically described in the Eulerian frame of reference, the relative motion of the particulate phase with respect to the fluid phase favours the implementation of the Lagrangian frame of reference for the computation of the particle dynamics. In this case, the action of the fluid flow on the dispersed phase can be accounted for by the well established Lagrangian particle tracking method. Here the particle position is obtained by solving additional equations for the particle kinematics (relation between the configurational variables and their velocities) and the particle dynamics (balances of momenta) [20].

In the case of dilute suspensions, the effect of the dispersed phase on the fluid phase is weak, establishing conditions where only the influence of the fluid flow on the dispersed particles needs to be accounted for, i.e. the one-way coupling interaction is governing the motion of particles. In this case, the computational framework for the particle-fluid interaction can be split subsequently into the computation of the viscous fluid flow field, and the computation of the fluid flow's momentum exchange with the particles.

2.1 Viscous Fluid Flow

The computation of the numerical solution is predominantly performed in the Eulerian framework, where the flow field is typically described in terms of velocity and pressure fields. For fluid flow, the total change of a flow quantity in the control volume is due to the interaction with the surroundings of the control volume, i.e. due to surface and volumetric effects. Considering the net mass balance in a control volume leads to the continuity equation

$$\frac{\partial \rho_f}{\partial t} + \nabla \cdot [\rho_f \mathbf{u}] = 0, \tag{1}$$

where ρ_f is the fluid density and $\mathbf{u}$ is the fluid velocity. The continuity equation simplifies to $\nabla \cdot \mathbf{u} = 0$ for incompressible fluids.

Considering transport of momentum in an incompressible Newtonian fluid leads to the following momentum conservation equation

$$\frac{\partial \mathbf{u}}{\partial t} + [\mathbf{u} \cdot \nabla]\mathbf{u} = \mathbf{f}_f - \frac{1}{\rho_f}\nabla p + \nu \nabla^2 \mathbf{u}, \tag{2}$$

where ν is the fluid kinematic viscosity, p is the fluid pressure and $\mathbf{f}_f$ are volumetric source terms and fluid-particle interaction momentum exchange terms.

The evaluation of the translational momentum exchange between particles and fluid depends mainly on the data of the velocity field, whereas in the case of rotational momentum exchange (angular momentum, moment of momentum) it is essentially based on the vorticity field. As in the case of high shear flows there is also a strong influence of the vorticity field on the translational momentum exchange, the detailed information on the vorticity field,

$$\mathbf{w} = \nabla \times \mathbf{u} \tag{3}$$

being the curl of the velocity field, is also needed. The accuracy of the particle tracking scheme thus depends on the accurate calculation of velocity and vorticity fields. In the case of fluid dominated two-phase flows the contribution of the momentum exchange term $\mathbf{f}_f$ due to particle-fluid interactions is zero.

2.2 Particle Dynamics

The trajectory of a particle is a result of its interaction with the fluid flow, which in fluid dominated flows determines its translational and angular velocity. In the case of small particles, typically in the micro- and sub-micro range, the particles behave like rigid bodies, i.e. the deformation of a particle can be neglected. In order to determine the trajectory, particle transport is computed in the Lagrangian framework by particle tracking. Local values of velocity, vorticity and pressure in the fluid phase and their difference to the state of the particle determine transport phenomena between the dispersed and the fluid phase.

The particle linear momentum conservation equation is

$$\frac{d}{dt}(m_p\mathbf{v}) = m_p\frac{d\mathbf{v}}{dt} = m_p\mathbf{g} + \mathbf{F} \tag{4}$$

where m_p is the mass of the particle, $\mathbf{v}$ is the particle velocity, $\mathbf{g}$ is the gravity acceleration and $\mathbf{F}$ is the fluid force acting on the particle. The particle angular momentum conservation is

$$\frac{d}{dt}(\mathbf{I}_p \cdot \boldsymbol{\omega}) = \mathbf{I}_p \cdot \frac{d\boldsymbol{\omega}}{dt} + \boldsymbol{\omega} \times [\mathbf{I}_p \cdot \boldsymbol{\omega}] = \mathbf{T} \tag{5}$$

where $\mathbf{I}_p$ is the moment of inertia tensor of the particle, $\boldsymbol{\omega}$ is the particle angular velocity and $\mathbf{T}$ is the torque acting on the particle. Equations (4) and (5) enable determination of the change of velocities, which can then be applied to determine the new translational and angular positions of the particle by solving the kinematics equations. Translational kinematics is expressed using the particle barycentre position vector $\mathbf{r}$ as:

$$\frac{d\mathbf{r}}{dt} = \mathbf{v}. \tag{6}$$

In order to avoid singularity issues associated with the use of Euler angles rotational kinematics is usually expressed in terms of the time evolution of the Euler parameters $[e_0, e_1, e_2, e_3]$. The time evolution of the Euler parameters is connected to particle angular velocity expressed in the particle frame of reference.

2.3 Momentum Transfer in Particle-Fluid Interaction

The difference between particle velocity and fluid velocity in the vicinity of the particle gives rise to linear momentum exchange and in the case of angular velocity to angular momentum exchange. In fluid dominated flows, the fluid affects the trajectory of the particle but the particle doesn't influence the fluid flow, i.e. one-way coupling.

In the ideal case, the resolved stresses on the surface of the particle are the only information needed to determine the impact of the flow on the particle dynamics.

2.3.1 Direct Coupling

In fluid dominated flows, correct and accurate determination of the transfer of linear and angular momentum from the fluid to the rigid body presents the main modelling task. For direct coupling, one simultaneously integrates the Navier–Stokes equations, governing the fluid motion, and the equations of the rigid body motion, governing the motion of particles.

The linear momentum transfer from the fluid to the particle is encapsulated in the fluid force **F**, acting on the particle. It is the integral over the particle surface of the traction $\boldsymbol{\sigma} \cdot \mathbf{n}$ exerted by the fluid onto the particle surface Γ_p

$$\mathbf{F} = \int_{\Gamma_p} \boldsymbol{\sigma} \cdot \mathbf{n} d\Gamma_p = \int_{\Gamma_p} \left[-p\mathbf{n} + \rho_f \nu \left[\nabla \mathbf{u} + \nabla \mathbf{u}^T \right] \cdot \mathbf{n} \right] d\Gamma_p \tag{7}$$

with **n** the normal particle surface vector.

The angular momentum transfer from the fluid to the particle is encapsulated in the torque **T**, acting on the particle. The torque is the integral of the moment of the traction vector. As the particle is embedded in the fluid, at the surface of the particle no-slip conditions are applied, i.e. the fluid velocity is the same as the velocity at the particle surface,

$$\mathbf{u} = \mathbf{v} + \boldsymbol{\omega} \times \mathbf{r}_p, \tag{8}$$

where $\mathbf{r}_p$ is a vector originating at the particle barycentre and pointing towards particle surface. In the above equations, the body can have an arbitrary shape, discretized by a suitable surface mesh.

Although the direct coupling eliminates the need to introduce specific models for different phenomena in momentum transfer, it is extremely expensive in terms of computational cost, when particle sizes are very small or when there are large numbers of particles to be tracked. The flow domain in the vicinity of the particle, as well as the particle surface, need to be correctly discretized, and the movement of the particles requires changes to the computational grid to be made during computations. In order to avoid this problem dedicated interaction models are developed and predominantly used in numerical simulations.

2.3.2 Coupling by Dedicated Interaction Models

As already stated, in the case of small particles (micro- and nano-sized particles) a direct computation of fluid-particle interaction is practically not feasible, as flow and particle surface resolution demands would be computationally extremely expensive.

In order to overcome this problem, simplified models for the computation of the particle dynamics in fluid flow have to be implemented.

If particles are considered with diameters much smaller than the length scales of the smallest flow structures, there is no need to resolve the particle surface directly and the point particle approximation can be implemented. In this case, the flow domain does not include particles, the interaction with the particulate phase is merely included in the source term $\mathbf{f}_f$ in Eq. (2).

Since the particle is considered as a point particle, the physical models for the evaluation of forces (and torques) on the particle rely on the velocity and vorticity fields evaluated at the position of the particle. The overall action of the fluid flow on the particle, in direct coupling evaluated by solving Eq. (7), is now decomposed into specific phenomena described by different models. In the translational momentum balance of the dispersed phase this means that each specific phenomena is described by a force model, and all the forces are assumed to be linearly additive. In general, particles move due to the additive action of gravity, buoyancy, drag, pressure gradient and added mass forces.

In a shear flow, an additional force, the so-called Saffman lift force [5, 23, 24, 28], occurs, which acts perpendicular to the flow direction. Its magnitude and direction are related directly to the local value of the vorticity of the fluid, and it acts on both non-rotating and rotating particles. Moreover, particle rotation gives rise to additional forces, most notably the Magnus lift force, influencing the translational motion of a particle. When the particle is also rotating, the angular momentum equation must therefore additionally be solved in order to capture the effect of particle orientation and particle rotation.

In order to track the particle's translational and rotational motion the particle position, the particle velocity, the particle orientation and the angular velocity of the particle have to be advanced in time in each computational step.

Dynamics of translational motion

Maxey and Riley [19] considered the forces on a small rigid sphere in a nonuniform flow and derived a consistent approximation for the equation of motion. They treated forces in the undisturbed flow and the flow disturbance caused by the presence of the sphere, separately. Brenner [1] developed the drag expression for arbitrary particles. Neglecting the aerodynamic lift, time history effects, second-order terms and due to the small particle size, we may write

$$m_p \frac{d\mathbf{v}}{dt} = [m_p - m_f]\mathbf{g} + m_f \frac{D\mathbf{u}}{Dt} - \frac{1}{2} m_f \left[\frac{d\mathbf{v}}{dt} - \frac{d\mathbf{u}}{dt} \right] + \pi a \rho_f \nu \mathbf{K} \cdot [\mathbf{u} - \mathbf{v}] + \mathbf{F}. \tag{9}$$

where a is the semi-minor axis of ellipsoidal particles. The terms included in the equation are gravity, buoyancy, pressure gradient term, added mass term and drag (skin friction and form drag). Here, $d/dt = \partial/\partial t + [\mathbf{v} \cdot \nabla]$ stands for the time derivative following the particle, i.e. the material time derivative of the particle, and $D/Dt = \partial/\partial t + [\mathbf{u} \cdot \nabla]$ denotes the time derivative following the fluid element, i.e.

the material time derivative of the fluid. **K** is the resistance tensor in direct notation, its coefficients are typically expressed with respect to the Eulerian (inertial) frame of reference, and **F** now stands for additional forces, acting on a particle (e.g. lift force).

Let us now consider prolate ellipsoidal particles with semi-minor axis a and semi-major axis b. The aspect ratio of the ellipsoid is $\lambda = b/a$. The density of the particle is ρ_p and the mass of fluid occupying the same volume as the particle is denoted by m_f. The volume of the particle is $V_p = \frac{4}{3}\pi a^2 b = \frac{4}{3}\pi a^3 \lambda$ and its mass is related to its density as $m_p = \frac{4}{3}\pi a^3 \lambda \rho_p$.

Equation (9) is rewritten in non-dimensional form with u_0 and L being the characteristic fluid velocity scale and the characteristic problem length scale, respectively. With $\mathbf{u} \to \mathbf{u}/u_0$, $\mathbf{v} \to \mathbf{v}/u_0$ and $t \to tu_0/L$ this eventually leads to

$$\mathbf{a} = \frac{d\mathbf{v}}{dt} = \frac{A}{St}\left[\mathbf{v}_s + \frac{1}{6\lambda}\mathbf{K}\cdot[\mathbf{u}-\mathbf{v}]\right] + \frac{3}{2}R\frac{\partial \mathbf{u}}{\partial t} + R\left[[\mathbf{u} + \frac{1}{2}\mathbf{v}]\cdot\nabla\right]\mathbf{u} + \mathbf{f} \tag{10}$$

where $\mathbf{a}$ is the particle acceleration and the Stokes number St is defined as

$$St = \frac{2}{9}\frac{\rho_p}{\rho_f}\frac{a^2 u_0}{\nu L}, \tag{11}$$

the sedimentation velocity is

$$\mathbf{v}_s = \frac{2a^2}{9\nu u_0}\left[\frac{\rho_p}{\rho_f} - 1\right]\mathbf{g}, \tag{12}$$

and the parameters R and A are

$$R = \frac{\rho_f}{\rho_p + \frac{1}{2}\rho_f}, \qquad A = \frac{\rho_p}{\rho_p + \frac{1}{2}\rho_f}. \tag{13}$$

The ellipsoidal particle response time was introduced by Shapiro and Goldenberg [26] as

$$\tau_p = \frac{2}{9}\frac{\rho_p}{\rho_f}\frac{a^2}{\nu}\frac{\lambda \ln(\lambda + \sqrt{\lambda^2 - 1})}{\sqrt{\lambda^2 - 1}}, \tag{14}$$

Since the characteristic fluid time scale is $\tau_f = L/u_0$, we may write the ellipsoid particle Stokes number as

$$St_e = St\frac{\lambda \ln(\lambda + \sqrt{\lambda^2 - 1})}{\sqrt{\lambda^2 - 1}}. \tag{15}$$

The hydrodynamic drag force, i.e. the term $\pi a \rho_f \nu \mathbf{K}\cdot[\mathbf{u}-\mathbf{v}]$ in Eq. (9), acting on an ellipsoidal particle under Stokes flow conditions was derived by Brenner [2]. It introduces the resistance tensor, which may be evaluated in the particle frame of reference $[x', y', z']$. In the particle frame of reference, only diagonal components of the resistance tensor **K** are non-zero. They are a function of the particle aspect ratio and may be written as:

$$K'_{x'x'} = K'_{y'y'} = \frac{16[\lambda^2 - 1]^{3/2}}{[2\lambda^2 - 3]\ln(\lambda + \sqrt{\lambda^2 - 1}) + \lambda\sqrt{\lambda^2 - 1}} \tag{16}$$

$$K'_{z'z'} = \frac{8[\lambda^2 - 1]^{3/2}}{[2\lambda^2 - 1]\ln(\lambda + \sqrt{\lambda^2 - 1}) - \lambda\sqrt{\lambda^2 - 1}} \tag{17}$$

In the spherical particle limit $\lim_{\lambda\to 1}[\mathbf{K}]'$, one has $6[\mathbf{I}]$, where **I** is the identity tensor.

In order to express the coefficients of the resistance tensor in terms of the inertial reference frame, they must be rotated with respect to the current orientation of the particle. The rotation matrix, **V**, is used in the following way:

$$[\mathbf{K}] = [\mathbf{V}^T][\mathbf{K}]'[\mathbf{V}], \tag{18}$$

where $\mathbf{V}^T$ is the transpose (inverse) of the rotation matrix, and $[\mathbf{K}]$, $[\mathbf{K}]'$ denote the coefficients of **K** in the inertial and the particle rotational frames of reference.

Orientation in space may be parameterized by the Euler angles $[\varphi, \theta, \psi]$. However, when kinematic relations between the angles and angular velocity are set up, we observe (Fantoni [7]) that a singularity exists for $\theta = 0$ and $\theta = \pi$. To avoid this problem, we express the orientation and the kinematic relations in terms of the Euler parameters instead. The Euler parameters (Goldstein [11]) are linked by a constraint

$$e_0^2 + e_1^2 + e_2^2 + e_3^2 = 1. \tag{19}$$

In the inertia frame the rotation matrix written in terms of the Euler parameters reads

$$[\mathbf{V}] = \begin{bmatrix} e_0^2 + e_1^2 - e_2^2 - e_3^2 & 2[e_1e_2 + e_0e_3] & 2[e_1e_3 - e_0e_2] \\ 2[e_1e_2 - e_0e_3] & e_0^2 - e_1^2 + e_2^2 - e_3^2 & 2[e_2e_3 + e_0e_1] \\ 2[e_1e_3 + e_0e_2] & 2[e_2e_3 - e_0e_1] & e_0^2 - e_1^2 - e_2^2 + e_3^2 \end{bmatrix} \tag{20}$$

Subjecting spherical particles to high shear velocity the transverse lift force has to be accounted for [5, 23, 24, 28]

$$\mathbf{F}_{SL} = 6.46\rho_f a^2\sqrt{\nu}\frac{1}{\sqrt{|\mathbf{w}|}}\;[[\mathbf{u} - \mathbf{v}] \times \mathbf{w}] \tag{21}$$

Equation (21) is the well known Saffman-type lift force, and was further extended by Harper and Chang [12], Hogg [13] and Fan and Ahmadi [6] for non-spherical particles.

In a general shear flow, there exist six shear flows in the non-diagonal components of the velocity gradient tensor **G** with coefficients $\partial u_i/\partial j$ $(i, j \in \{x, y, z\}, i \neq j)$:

$$[\mathbf{G}] = \begin{bmatrix} \dfrac{\partial u_x}{\partial x} & \dfrac{\partial u_x}{\partial y} & \dfrac{\partial u_x}{\partial z} \\ \dfrac{\partial u_y}{\partial x} & \dfrac{\partial u_y}{\partial y} & \dfrac{\partial u_y}{\partial z} \\ \dfrac{\partial u_z}{\partial x} & \dfrac{\partial u_z}{\partial y} & \dfrac{\partial u_z}{\partial z} \end{bmatrix} \tag{22}$$

In the case of linear shear flow, only one non-diagonal component of the velocity gradient tensor has a non-zero value. Harper and Chang [12] derived a lift force for arbitrary three-dimensional rigid bodies moving in a linear shear flow $\partial u_x/\partial z$ at low Reynolds numbers as:

$$\mathbf{F}_{SL} = \frac{1}{\rho_f\ \nu^{3/2}} \frac{\partial u_x/\partial z}{|\partial u_x/\partial z|^{1/2}} \mathbf{D} \cdot \mathbf{L_{xz}} \cdot \mathbf{D} \cdot [\mathbf{u}^L - \mathbf{v}] \tag{23}$$

where $\mathbf{u}^L = [u_x,\ 0,\ 0]$ is the reference flow for the lift, and the Stokes drag $\mathbf{F}_{D,\,Stokes} = \mathbf{D} \cdot [\mathbf{u}^L - \mathbf{v}]$. The lift tensor, calculated by asymptotic methods, in a linear shear flow $\partial u_x/\partial z$ is found to be [12]

$$[\mathbf{L_{xz}}] = \begin{bmatrix} 0.0501 & 0 & 0.0329 \\ 0 & 0.0373 & 0 \\ 0.0182 & 0 & 0.0173 \end{bmatrix} \tag{24}$$

In the case of spherical particles $\mathbf{D} = 6\pi\rho_f \nu a\,\mathbf{I}$, Eq. (23) can be written as:

$$\mathbf{F}_{SL} = 36\pi^2\rho_f a^2\sqrt{\nu}\ \frac{\partial u_x/\partial z}{|\partial u_x/\partial z|^{1/2}} \mathbf{L_{xz}} \cdot [\mathbf{u}^L - \mathbf{v}] \tag{25}$$

In the case of ellipsoidal particles $\mathbf{D} = \pi a\rho_f \nu\mathbf{K}$, one can then write the shear lift force found by Harper and Chang [12] for an ellipsoidal particle in the linear shear flow $\partial u_x/\partial z$ as

$$\mathbf{F}_{SL} = \pi^2\rho_f a^2\sqrt{\nu}\ \frac{\partial u_x/\partial z}{|\partial u_x/\partial z|^{1/2}} \mathbf{K} \cdot \mathbf{L_{xz}} \cdot \mathbf{K} \cdot [\mathbf{u}^L - \mathbf{v}] \tag{26}$$

Fan and Ahmadi [6] proposed an expression for the lift force acting on an ellipsoid in a different linear shear flow $\partial u_x/\partial y$, which can be expressed as:

$$\mathbf{F}_{SL} = \pi^2\rho_f a^2\sqrt{\nu}\ \frac{\partial u_x/\partial y}{|\partial u_x/\partial y|^{1/2}} \mathbf{K} \cdot \mathbf{L_{xy}} \cdot \mathbf{K} \cdot [\mathbf{u}^L - \mathbf{v}] \tag{27}$$

where the lift tensor $\mathbf{L_{xy}}$, is a permuted version of $\mathbf{L_{xz}}$, is given by

$$[\mathbf{L_{xy}}] = \begin{bmatrix} 0.0501 & 0.0329 & 0 \\ 0.0182 & 0.0173 & 0 \\ 0 & 0 & 0.0373 \end{bmatrix} \tag{28}$$

However, the above models of shear lift force of non-spherical particles are only applicable to linear shear flows. In the following, we propose a new lift force model for arbitrary shear flow. This model was originally developed by Ravnik et al. [22] and is further extended on by the present study. A similar model has been presented by Feng and Kleinstreuer [8]. In case of arbitrary shear flow, six equations like (26) and (27) are needed to describe a general shear flow and six permutations of lift tensors exist as well,

$$[\mathbf{L_{xy}}] = \begin{bmatrix} A & B & 0 \\ D & E & 0 \\ 0 & 0 & C \end{bmatrix} \qquad [\mathbf{L_{xz}}] = \begin{bmatrix} A & 0 & B \\ 0 & C & 0 \\ D & 0 & E \end{bmatrix} \tag{29}$$

$$[\mathbf{L_{yx}}] = \begin{bmatrix} E & D & 0 \\ B & A & 0 \\ 0 & 0 & C \end{bmatrix} \qquad [\mathbf{L_{yz}}] = \begin{bmatrix} C & 0 & 0 \\ 0 & A & B \\ 0 & D & E \end{bmatrix} \tag{30}$$

$$[\mathbf{L_{zx}}] = \begin{bmatrix} E & 0 & D \\ 0 & C & 0 \\ B & 0 & A \end{bmatrix} \qquad [\mathbf{L_{zy}}] = \begin{bmatrix} C & 0 & 0 \\ 0 & E & D \\ 0 & B & A \end{bmatrix} \tag{31}$$

where

$$A = 0.0501,\ B = 0.0329,\ C = 0.0373,\ D = 0.0182,\ E = 0.0173. \tag{32}$$

In the following we propose a generalized lift vector **l**, defined as

$$\begin{aligned} [\mathbf{l}] = & \left[\frac{\partial u_x/\partial y}{|\partial u_x/\partial y|^{1/2}} \mathbf{K} \cdot \mathbf{L_{xy}} \cdot \mathbf{K} + \frac{\partial u_x/\partial z}{|\partial u_x/\partial z|^{1/2}} \mathbf{K} \cdot \mathbf{L_{xz}} \cdot \mathbf{K} \right] \cdot \begin{bmatrix} u_x - v_x \\ - v_y \\ - v_z \end{bmatrix} + \\ & \left[\frac{\partial u_y/\partial x}{|\partial u_y/\partial x|^{1/2}} \mathbf{K} \cdot \mathbf{L_{yx}} \cdot \mathbf{K} + \frac{\partial u_y/\partial z}{|\partial u_y/\partial z|^{1/2}} \mathbf{K} \cdot \mathbf{L_{yz}} \cdot \mathbf{K} \right] \cdot \begin{bmatrix} - v_x \\ u_y - v_y \\ - v_z \end{bmatrix} + \\ & \left[\frac{\partial u_z/\partial x}{|\partial u_z/\partial x|^{1/2}} \mathbf{K} \cdot \mathbf{L_{zx}} \cdot \mathbf{K} + \frac{\partial u_z/\partial y}{|\partial u_z/\partial y|^{1/2}} \mathbf{K} \cdot \mathbf{L_{zy}} \cdot \mathbf{K} \right] \cdot \begin{bmatrix} - v_x \\ - v_y \\ u_z - v_z \end{bmatrix} \end{aligned} \tag{33}$$

The lift force on a particle in a general shear flow can then be expressed by

$$\mathbf{F}_{SL} = \pi^2 \rho_f a^2 \sqrt{\nu}\, \mathbf{l} \tag{34}$$

The underlying idea is quite simple, i.e. sum of six shear lift forces. For the limiting case of a spherical particle with $\lambda \to 1$ one can obtain $\mathbf{K} \cdot \mathbf{L_{ij}} \cdot \mathbf{K} = 36\, \mathbf{L_{ij}}$. It should be noted that the j-component lift force induced by the velocity difference in the i-direction as evaluated from Eqs. (33) and (34) agrees with the result of Saffman

(Eq. 21), i.e. $36\pi^2 D = 6.46$, which corresponds to the finding of Harper and Chang [12] and Fan and Ahmadi [6]. In order to prevent numerical errors under the condition that $\partial u_i/\partial j = 0$, it is suggested adding a small value, e.g. $1.0e - -18$, to the root of the Eq. (33).

The lift tensor $\mathbf{L_{ij}}$ is applicable for any arbitrarily shaped 3D body [12] and is used to determine the shear lift force for an ellipsoidal particle by applying $\mathbf{K} \cdot \mathbf{L_{ij}} \cdot \mathbf{K}$. The orientation of the ellipsoid is taken into account by Eq. (18). Therefore, the generalized shear lift force is applicable for particles with ellipsoidal and fibre shapes at low Reynolds numbers.

Dynamics of rotational motion

The rotational motion of a nonspherical particle moving in a flow field is governed by

$$I_{x'}\frac{d\omega_{x'}}{dt} - \omega_{y'}\omega_{z'}[I_{y'} - I_{z'}] = T_{x'} \tag{35}$$

$$I_{y'}\frac{d\omega_{y'}}{dt} - \omega_{z'}\omega_{x'}[I_{z'} - I_{x'}] = T_{y'} \tag{36}$$

$$I_{z'}\frac{d\omega_{z'}}{dt} - \omega_{x'}\omega_{y'}[I_{x'} - I_{y'}] = T_{z'} \tag{37}$$

where $\omega_{x'}$, $\omega_{y'}$, $\omega_{z'}$ are the particle angular velocities with respect to the principal axes, $I_{x'}$, $I_{y'}$, $I_{z'}$ are the particle moments of inertia about the principal axes $[x', y', z']$, i.e. the principal components of the particle's inertia tensor, and $T_{x'}$, $T_{y'}$, $T_{z'}$ are the hydrodynamic torques acting on the particle with respect to the principal axes. The rotational motion of the particle in Eqs. (35)–(37) is stated in the particle reference frame.

The moments of inertia for an ellipsoid are

$$I_{x'} = I_{y'} = \frac{[1+\lambda^2]a^2}{5}m_p = \frac{4\pi}{15}\lambda[\lambda^2+1]a^5\rho_p \tag{38}$$

$$I_{z'} = \frac{2a^2}{5}m_p = \frac{8\pi}{15}\lambda a^5\rho_p \tag{39}$$

The flow near a small particle may be approximated as a linear shear flow. The hydrodynamic torque acting on an ellipsoidal particle suspended in a linear shear flow was derived by Jeffery [16]. In the particle reference frame, we have

$$T_{x'} = \frac{16\pi\rho_f\nu a^3\lambda}{3[\beta_0 + \lambda^2\gamma_0]}\left[[1-\lambda^2]f' + [1+\lambda^2][\xi' - \omega_{x'}]\right] \tag{40}$$

$$T_{y'} = \frac{16\pi\rho_f \nu a^3\lambda}{3[\alpha_0 + \lambda^2\gamma_0]}\left[[\lambda^2 - 1]g' + [1 + \lambda^2][\eta' - \omega_{y'}]\right] \tag{41}$$

$$T_{z'} = \frac{32\pi\rho_f \nu a^3\lambda}{3[\alpha_0 + \beta_0]}[\chi' - \omega_{z'}] \tag{42}$$

where f', g' are elements of the deformation rate tensor $\mathbf{D} := \mathbf{G}^{sym}$ and ξ', η' and χ' are elements of the spin tensor $\mathbf{W} := \mathbf{G}^{skw}$ with $\mathbf{w}$ the axial vector of $\mathbf{W}$, defined as

$$f' = \frac{1}{2}\left[\frac{\partial u_{z'}}{\partial y'} + \frac{\partial u_{y'}}{\partial z'}\right], \qquad g' = \frac{1}{2}\left[\frac{\partial u_{x'}}{\partial z'} + \frac{\partial u_{z'}}{\partial x'}\right] \tag{43}$$

$$\xi' = \frac{1}{2}\left[\frac{\partial u_{z'}}{\partial y'} - \frac{\partial u_{y'}}{\partial z'}\right], \quad \eta' = \frac{1}{2}\left[\frac{\partial u_{x'}}{\partial z'} - \frac{\partial u_{z'}}{\partial x'}\right], \quad \chi' = \frac{1}{2}\left[\frac{\partial u_{x'}}{\partial y'} - \frac{\partial u_{y'}}{\partial x'}\right] \tag{44}$$

In order to evaluate these terms, the velocity gradient tensor $\mathbf{G}$ must be rotated into the particle frame of reference using the rotation matrix as

$$[\mathbf{G}]' = [\mathbf{V}]\,[\mathbf{G}]\,[\mathbf{V}^T] \tag{45}$$

The nondimensional coefficients α_0, β_0 and γ_0 were defined by Gallily and Cohen [10] as

$$\alpha_0 = \beta_0 = \frac{\lambda^2}{\lambda^2 - 1} + \frac{\lambda}{2[\lambda^2 - 1]^{3/2}}\ \ln\left(\frac{\lambda - \sqrt{\lambda^2 - 1}}{\lambda + \sqrt{\lambda^2 - 1}}\right) \tag{46}$$

$$\lambda^2\gamma_0 = -\frac{2\lambda^2}{\lambda^2 - 1} - \frac{\lambda^3}{[\lambda^2 - 1]^{3/2}}\ \ln\left(\frac{\lambda - \sqrt{\lambda^2 - 1}}{\lambda + \sqrt{\lambda^2 - 1}}\right) \tag{47}$$

Inserting moments of inertia (38)–(39) and torques (40)–(42) into the equations of motion (35)–(37) and nondimensionalizing we obtain the governing equations for the rotational motion of ellipsoidal particles:

$$\frac{d\omega_{x'}}{dt} = \omega_{y'}\omega_{z'}\frac{\lambda^2 - 1}{1 + \lambda^2} + \frac{20\nu}{a^2[\beta_0 + \lambda^2\gamma_0]}\frac{\rho_f}{\rho_p}\frac{L}{u_0}\left[\frac{1 - \lambda^2}{1 + \lambda^2}f' + [\xi' - \omega_{x'}]\right] \tag{48}$$

$$\frac{d\omega_{y'}}{dt} = \omega_{z'}\omega_{x'}\frac{1 - \lambda^2}{1 + \lambda^2} + \frac{20\nu}{a^2[\alpha_0 + \lambda^2\gamma_0]}\frac{\rho_f}{\rho_p}\frac{L}{u_0}\left[\frac{\lambda^2 - 1}{1 + \lambda^2}g' + [\eta' - \omega_{y'}]\right] \tag{49}$$

$$\frac{d\omega_{z'}}{dt} = \frac{20\nu}{a^2[\alpha_0 + \beta_0]}\frac{\rho_f}{\rho_p}\frac{L}{u_0}[\chi' - \omega_{z'}] \tag{50}$$

Kinematics

The translational displacement of the particle is linked to its velocity,

$$\frac{d\mathbf{r}}{dt} = \mathbf{v}. \tag{51}$$

In the rotational part of the kinematics, the time evolution of the Euler parameters is related to the angular velocity of the particle in the particle frame of reference, $\omega_{i'}$, and is given by

$$\frac{de_0}{dt} = \frac{1}{2}[-e_1\omega_{x'} - e_2\omega_{y'} - e_3\omega_{z'}] \tag{52}$$

$$\frac{de_1}{dt} = \frac{1}{2}[e_0\omega_{x'} - e_3\omega_{y'} + e_2\omega_{z'}] \tag{53}$$

$$\frac{de_2}{dt} = \frac{1}{2}[e_3\omega_{x'} + e_0\omega_{y'} - e_1\omega_{z'}] \tag{54}$$

$$\frac{de_3}{dt} = \frac{1}{2}[-e_2\omega_{x'} + e_1\omega_{y'} + e_0\omega_{z'}] \tag{55}$$

Numerical solution of the momentum equations (9), (34), (48)–(50) and kinematics equations (51)–(55) is needed in order to obtain the time evolution of the particle trajectories, and the backward Euler method is applied for numerical integration of equations.

3 Validation - Particle Transport in Couette and Lid-Driven Cavity Flows

The developed Lagrangian particle tracking model is validated for two well-known fluid benchmark test cases in order to understand the reliability and accuracy of the above models for ellipsoidal particles. The first numerical validation is performed for the case of Couette flow by comparing the present model results with results for spheres as well as Harper and Chang's lift model [12] results. Moreover, in order to validate the developed models for the case of a complex fluid flow, the results are compared to the experimental results by Tsorng et al. [29], who studied particle motion in a lid-driven cavity flow.

3.1 Simulation Setup

All fluid flows in this numerical simulations are assumed to be stationary, and the particle influence on the fluid flow is neglected, leading to a one-way coupling of the fluid and particles. Due to low Reynolds number values the flow is considered laminar. The models considered for the kinematics and dynamics of the motion of ellipsoidal particles as summarized in Sect. 2.3.2 are also used for the case of a spherical particle by setting the aspect ratio to one. Additional numerical models for spherical particles used for the numerical validation are introduced later in this section.

As the fluid-particle coupling is considered as a one-way coupling, prior to the Lagrangian particle tracking, numerical computation of the stationary flow fields (see Fig. 1), i.e. Couette and lid-driven cavity flow, is conducted using the open-source code OpenFOAM® [30]. The cubic domains are identical for both flow conditions with the same edge length: $L = 0.1\,\text{m}$. For the lid-driven cavity case, the flow conditions are the same as used in the experimental study of Tsorng et al. [29]. The upper wall is moving with a constant velocity of $U_0 = 0.0813\,\text{m/s}$ in order to induce the shear flow in the cavity, with the resulting value of the Reynolds number $Re = \mu U_0/L = 470$. For lid-driven cavity flow at all other faces the non-slip boundary conditions are applied; for the Couette flow case, the zero gradient boundary conditions are assigned at the inlet and outlet boundaries whereas at the front and the back faces the symmetry boundary conditions are prescribed. For convenience, all boundary conditions are summarized in Table 1. The domain discretization consists of $40 \times 40 \times 40$ cells as shown in Fig. 2, and several prism layers are adapted in the near wall regions. The fluid flow regime in both cases is laminar, so no turbulence model is included in the computation. The specific fluid flow solver within

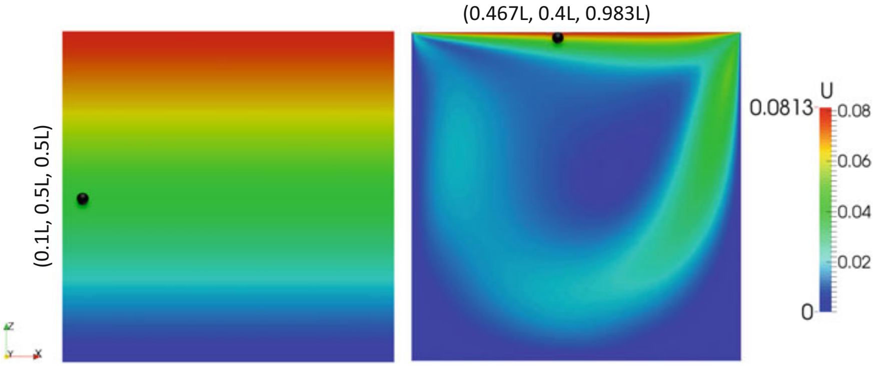

Fig. 1 Lagrangian particle tracking in Couette flow (left) and lid-driven cavity flow (right). Only one particle (black sphere) is placed in a predefined position: $x = 0.1L$, $y = 0.5L$, $z = 0.5L$ for Couette flow; $x = 0.467L$, $y = 0.4L$, $z = 0.983L$ for lid-driven cavity flow. For all cases: $Re = 470$, $D_{volume} = 3\,\text{mm}$, $[\rho_f - \rho_p]/\rho_f = 0.05\%$ or -0.07%, $St = 0.023$

Table 1 Boundary conditions for Couette and lid-driven cavity flows

Boundaries	Left & Right	Top & Bottom	Front & Back
Couette Flow	Zero Gradient	Non-slip	Full-slip
Lid-driven Cavity Flow	Non-slip	Non-slip	Non-slip

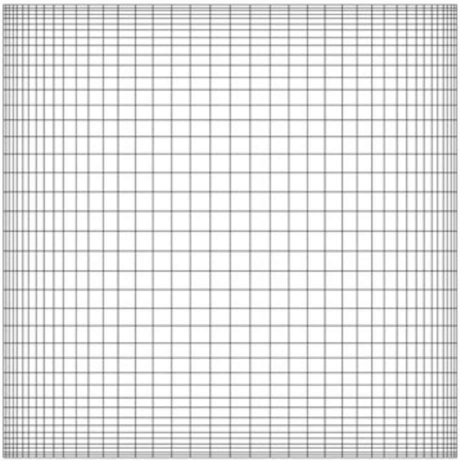

Fig. 2 Computational grid for the fluid domain; resolution: 40 × 40 × 40 grid cells

the OpenFOAM® distribution used is the icoFoam, which solves the incompressible laminar Navier–Stokes equations using the PISO (pressure implicit with splitting of the operator) algorithm (Ferziger and Peric [9]). The particle Stokes number considered in the present study is 0.023, and the kinematic viscosity of the fluid is $17.3\,\mathrm{mm}^2/\mathrm{s}$.

The spherical macro-particles used in Tsorng et al. [29] were plastic beads with a diameter $D_p = 3\,\mathrm{mm}$ and a density $\rho_p = 1210\,\mathrm{kg/m}^3$. For ellipsoidal particles, the volume equivalent diameter D_{volume} is considered. The relative density difference between the fluid and the particle, i.e. $[\rho_f - \rho_p]/\rho_f$, is very small, e.g. about 0.05% or $--0.07\%$, indicating slightly positive or negative buoyancy conditions. The relative density difference cannot be set too large, otherwise, a particle does not predominantly follow the flow and can easily hit the wall, thus creating an additional problem in specifying correct experimental data. In the numerical simulation, only a single particle is placed in the fluid domain with applied rotation of the major axis b in the direction perpendicular to the stream-wise direction. As illustrated in Fig. 1, the initial position of the particle in lid-driven cavity flow is at $[0.467L, 0.4L, 0.983L]$, and at $[0.1L, 0.5L, 0.5L]$ in the case of Couette flow.

To demonstrate the accuracy of the new shear lift model (Eq. 34), several models for spheres were chosen to compare with (Sommerfeld and Schmalfuss [27]). These models are widely used for Lagrangian particle tracking at higher particle Reynolds numbers including the drag force, the transverse lift force due to shear flow and particle rotation, as well as the particle rotation model, with more details in Sommerfeld and Schmalfuss [27]. Finally, all developed particle models are implemented into the Lagrangian solver icoUncoupledKinematicParcelFoam, a transient solver for the passive transport of a single kinematic particle cloud, included in the OpenFOAM®, which is finally used for Lagrangian particle tracking computations.

3.2 Couette Flow

The numerical accuracy of the proposed model for ellipsoidal particles is studied in this section by comparing them with other numerical models for spherical particles [27] as well as ellipsoidal particles [12]. In Couette flow a particle moves in the stream-wise direction by the drag force and is lifted by the linear shear $\partial u_x/\partial z$. In the following, we use Sommerfeld et al. to denote numerical models for spherical particles [27]. The effect of gravity was neglected in the simulation, while drag and shear lift force were calculated either jointly or separately.

The time evolution of a sphere, with its initial relative velocity between the fluid and the particle equal to zero, i.e. $\mathbf{u}_0 - \mathbf{v}_0 = \mathbf{0}\,\text{m/s}$, under the action of different drag forces indicated by black and red lines, are plotted in Fig. 3. It should be noted that the initial relative velocity in the stream-wise direction is not exactly zero due to numerical errors. Therefore a small drag force, about 2.66 nN, is observed at the beginning and is reduced afterwards as the particle velocity approaches to the velocity of the flow. After 0.2 s a quasi-steady state is reached since the particle is accelerated and decelerated by the flow due to the small density difference, i.e. $[\rho_f - \rho_p]/\rho_f = -0.07\%$. The overlapping of the results shows that Brenner's drag model demonstrates good agreement with the results of Sommerfeld et al. for the case of spherical particles. When the initial relative velocity is increased to match the velocity of the fluid (i.e. $\mathbf{v}_0 = \mathbf{0}\,\text{m/s}$), the difference in the results between the present work and Sommerfeld et al. (i.e. blue and magenta lines in Fig. 3) becomes evident. The reason for the difference in the results is due to the fact that in the case of larger relative velocities the Stokes flow conditions in the vicinity of the particle are no longer satisfied. Sommerfeld et al. [27] accounted for this effect by implementing an additional term solving the drag problem at high particle Reynolds numbers, where particles do not predominantly follow the fluid streamlines. Therefore, the simulations considering the influence of the drag force on ellipsoidal particles are only performed with small relative velocity.

The Couette flow considered here (i.e. linear shear flow, Fig. 1) with shear rate $\partial u_x/\partial z$ shares the same characteristics of the shear lift force of Harper and Chang (Eq. 26), so the new shear lift force (Eq. 34) can be compared to the results of Harper and Chang for different aspect ratios, as shown in Fig. 4. These simulations are only performed for test purposes by switching on the shear lift force and turning off the drag force, in order to eliminate the influence of the drag on the translational movement of the particle. Moreover, the initial velocity of the particle is set to zero for the purpose of increasing the shear lift force in the vertical direction. The ellipsoid

Fig. 3 Time evolution of the drag force on a spherical particle in Couette flow in comparison to alternative drag force models and initial relative velocities ($Time = 1\,\mathrm{s}$, $\lambda = 1$, $D_p = 3\,\mathrm{mm}$, $Re = 470$, $L = 0.1\,\mathrm{m}$, $[\rho_f - \rho_p]/\rho_f = -0.07\%$)

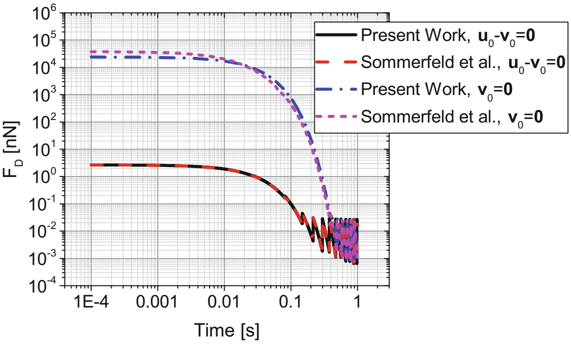

Fig. 4 Translational motion of an ellipsoidal particle in Couette flow for different aspect ratios; a comparison of various shear lift forces; the initial velocity of the particle is set to zero ($\mathbf{v}_0 = \mathbf{0}\,\mathrm{m/s}$, $Time = 1\,\mathrm{s}$, $\lambda = 1$, $D_p = 3\,\mathrm{mm}$, $Re = 470$, $L = 0.1\,\mathrm{m}$, $[\rho_f - \rho_p]/\rho_f = -0.07\%$)

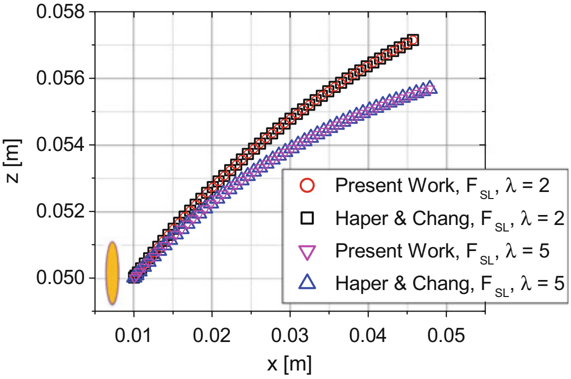

is initially placed with its major axis b perpendicular to the flow direction. The new model results are in good agreement with the results of Harper and Chang for all aspect ratios. This is obvious since the new model is identical to Harper and Chang's model in a linear shear flow (Eqs. 26 and 34). Furthermore, the particle travels a shorter distance in the vertical direction (z-direction) at larger aspect ratios, since the cross-sectional area of the minor axis a is reduced at the same volume equivalent diameter D_{volume}, which leads to a decrease of the shear lift force in the vertical direction.

After the validation of the new lift force, a parameter study is performed. In this study, both the drag and the generalized shear lift forces are incorporated in the simulation. The initial velocity of the particle relative to the fluid is set to zero. Figure 5a plots the time evolution of the drag force in the stream-line and vertical directions (i.e. x and z-directions) for different aspect ratio values. The component of the drag force in the stream-line direction at the beginning of the simulation is the largest, about 2.9–4.7 nN, and increases with increasing the aspect ratio λ from 2 to 10. Although the initial condition of zero relative velocity between the particle and the fluid (Eq. 33) was chosen, due to numerical errors in computing the x-component of the relative velocity, a non-zero drag force is computed. As a consequence of the

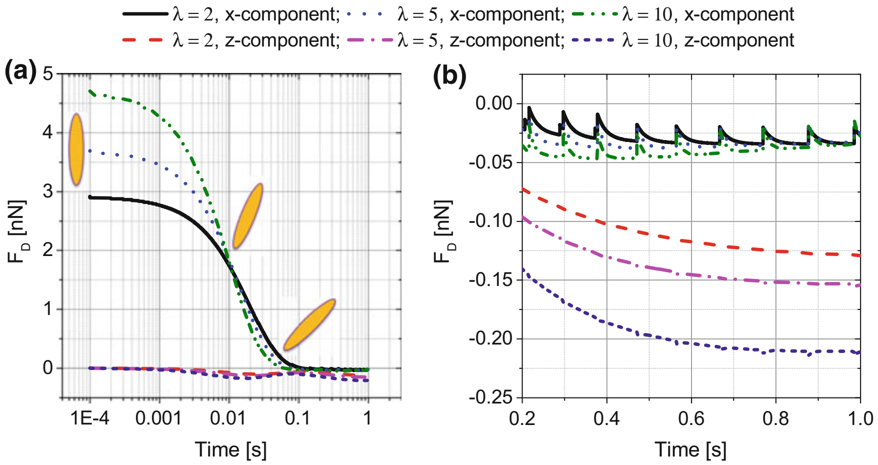

Fig. 5 Time evolution of x and z-components of the drag force acting on an ellipsoidal particle in Couette flow for different aspect ratios; simulation with drag and shear lift force for ellipsoidal particles; the initial velocity of the particle relative to the fluid is set to zero; **a** whole time period; **b** time period between 0.2 and 1 s ($\mathbf{u}_0 - \mathbf{v}_0 = \mathbf{0}\,\text{m/s}$, $Time = 1\,\text{s}$, $D_{volume} = 3\,\text{mm}$, $Re = 470$, $L = 0.1\,\text{m}$, $[\rho_f - \rho_p]/\rho_f = -0.07\%$)

decrease in relative velocity and the rotation of the particle, the drag force decreases significantly after only 0.1 s. The ellipsoidal particle tends to align its major axis b with the direction in which it is subject to a minimum torque, i.e. the mean flow direction in the linear shear flow, resulting in a decrease of the exposed cross-sectional area and hence reduction of the drag. Figure 5b shows a close-up of the drag force components in the time period from 0.2–1.0 s. The vertical component of the drag force assumes negative values, as the particle moves in the upward direction due to the shear lift, resulting in negative relative velocity in the z-direction and hence negative drag force. When the flow resistance is stabilized i.e. after 0.6 s, the x-component of the drag force fluctuates only slightly due to the creeping flow condition. The magnitude of the z-component of the drag increases with increasing aspect ratios since the exposed cross-sectional area of the ellipsoidal particle in the z direction becomes larger, which is a consequence of the geometry of the particle.

The corresponding generalized shear lift force in the stream-line and vertical directions are presented in Fig. 6. The largest shear lift force of the ellipsoid in the range of 1.0–2.7 nN is observed at the beginning of the simulation. Afterwards, the shear lift force decreases as the particle is accelerated or decelerated by the drag and more closely follows the flow. This leads to a decrease in relative velocity between the particle and the fluid. After 0.2 s, the x-components of the shear lift force for different aspect ratios become very small, in the range of 0.038–0.04 nN at 1.0 s, whereas the z-components are relatively large, in the range of 0.13–0.21 nN at 1.0 s, and increase with increasing aspect ratios. The difference between the x and z-components of the drag and shear lift forces are mainly as a consequence of the difference in relative

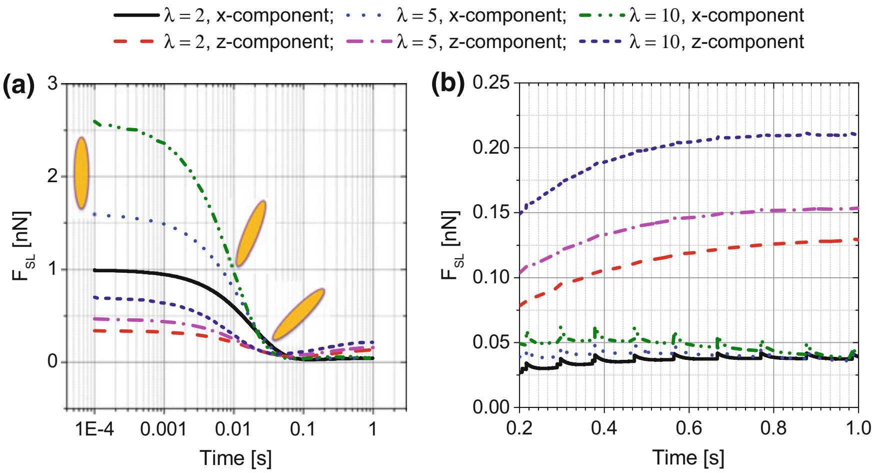

Fig. 6 Time evolution of x and z-components of the shear lift force on an ellipsoidal particle in Couette flow for different aspect ratios; simulation with drag and shear lift force for ellipsoidal particles; the initial velocity of the particle relative to the fluid is set to zero; **a** whole time period; **b** time period between 0.2 and 1 s ($\mathbf{u}_0 - \mathbf{v}_0 = \mathbf{0}$ m/s, $Time = 1$ s, $D_{volume} = 3$ mm, $Re = 470$, $L = 0.1$ m, $[\rho_f - \rho_p]/\rho_f = -0.07\%$)

velocity between the particle and the fluid. When the particle becomes more or less stable, i.e. after 0.6 s, the magnitude of the relative velocity in the stream-line direction becomes very small as the velocities in the flow direction are constant, while in the vertical direction it is much larger due to the existence of the shear rate $\partial u_x/\partial z$. Therefore, both the drag and the shear lift forces in the flow direction are smaller than force magnitudes observed in the vertical direction.

3.3 Lid-Driven Cavity Flow

The lid-driven cavity is a well-known benchmark problem for viscous incompressible fluid flows and has been studied extensively using analytical approaches (Shankar and Deshpande [25]), in laboratory experiments (Koseff and Street [17], Tsorng et al. [29]) and through numerical investigations (Chiang and Sheu [3]). However, research on the motion of particles in lid-driven cavity flows is relatively sparse. Tsorng et al. [29] investigated the behaviour of macroscopic rigid particles suspended in a fully three-dimensional viscous flow in a closed cubic cavity. The motion of macro-sized spherical particles in the approximate plane $y/L \approx 0.4$ near the upper downstream corner of the cavity was determined based on data from video images. The fluid streamlines computed from the numerical simulation are presented in Fig. 7. At $Re =$ 470, the flow pattern is driven by the moving top lid, generating a large primary eddy which occupies most of the cavity (Fig. 7a), and two secondary eddies form

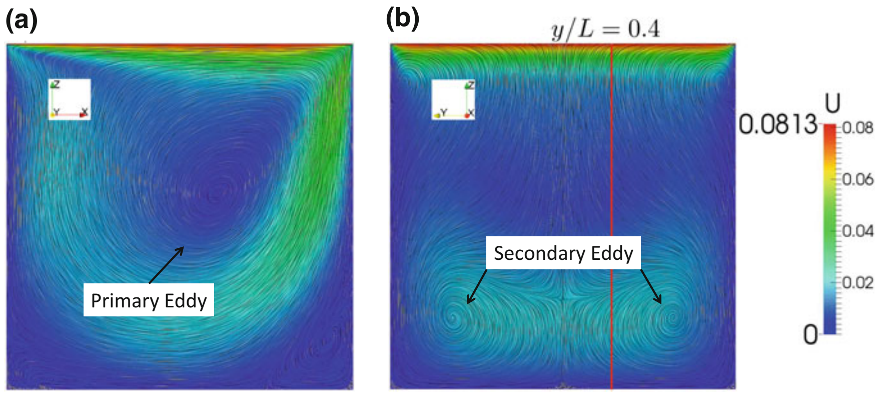

Fig. 7 Numerically calculated fluid streamlines in a lid-driven cavity flow; **a** the central longitudinal plane $y/L = 0.4$; **b** the central transverse plane $x/L = 0.5$; the red line indicate the plane of particle tracking $y/L = 0.4$; U is the magnitude of the fluid velocity ($\mathbf{u}_0 - \mathbf{v}_0 = \mathbf{0}$ m/s, $Time = 5$ s, $\lambda = 1$, $D_p = 3$ mm, $Re = 470$, $L = 0.1$ m, $[\rho_f - \rho_p]/\rho_f = 0.05\%$)

at the lower downstream corner in the transverse plane (Fig. 7b). The longitudinal plane $y/L \approx 0.4$ (red line in Fig. 7b) was chosen for the particle tracking because it features at its upper downstream corner an open pathway linking the primary eddy to the downstream secondary eddy [29].

The trajectories of the tracked spherical particle from experimental measurements (square symbols) and numerical calculations (colour lines) are presented in Fig. 8. The forces considered in the simulations are drag, gravity, lift force due to the shear flow and due to relative rotation. The Brenner's drag force is applicable to both spheres and ellipsoids whereas the generalized shear lift force is used for the calculation of ellipsoidal particles. Hence only the Brenner's drag is compared to other models for spheres [27]. As shown in Fig. 8, the results of different combinations of forces are nearly the same, which implies that the influence of the drag force is much larger than the lift force and dominates the translational motion of spherical particles. When the relative density difference increases, the sphere travels a shorter distance due to the change from negative to positive buoyancy conditions. Moreover, a slight difference is found between the present work and Sommerfeld et al. under the condition of $F_D + G$. The reason is that the Stokes flow condition is not satisfied in the upper downstream corner of the cavity since the particle changes its direction and moves downward. Additionally, the numerical results also show a good agreement with experimental data of Tsorng et al. [29], with a minor difference arising from the finite size effect of the macro-sized particles, i.e. 3 mm, whereas in our Lagrangian particle tracking the point particle assumption was adopted.

Figure 9a plots the trajectories of the tracked ellipsoidal particles over a period of 5 s under the condition of $F_D + G$. With increasing aspect ratios, the ellipsoidal particle tends to move away from the right side wall. This can be explained by Fig. 9b, which shows the time evolution of drag force for a period of 5 s at different aspect

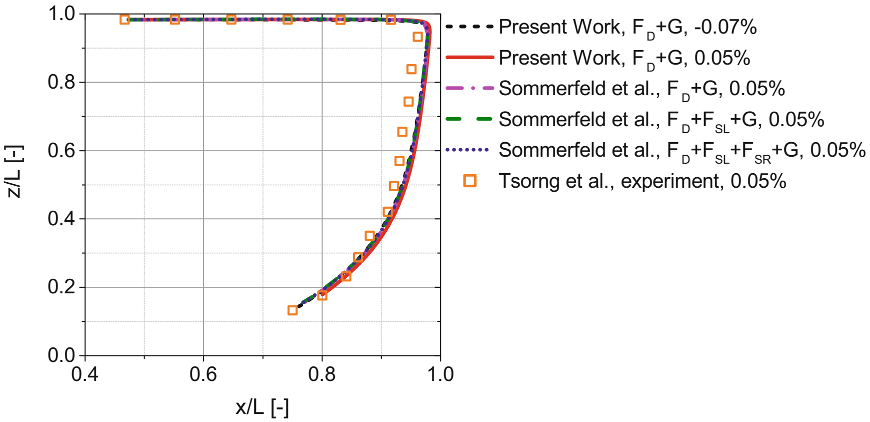

Fig. 8 Translational motion of a spherical particle in a lid-driven cavity flow obtained from both numerical and experimental studies ($\mathbf{u}_0 - \mathbf{v}_0 = \mathbf{0}$ m/s, $Time = 5$ s, $D_p = 3$ mm, $Re = 470$, $L = 0.1$ m, $[\rho_f - \rho_p]/\rho_f = 0.05\%$ or -0.07%)

ratios. The drag forces initially decrease since the particle tends to align its major axis b with the direction which subjects the particle to the minimum torque (i.e. mean flow direction before entering the upper downstream corner). Subsequently, the drag force increases significantly as the particle approaches the upper downstream corner where the ellipsoidal particle rotates and the relative velocity increases. After that, the particle aligns its major axis with the mean flow direction again, and hence the drag force is drastically reduced. At higher aspect ratios, e.g. $\lambda = 5$, the particle experiences smaller drag force after escaping from the upper downstream corner (see Fig. 9b time period 3.5–5.0 s), therefore the direction of the particle is slightly changed and as a result the particle moves away from the right side wall.

The existence of the shear lift force has a significant influence on the translational motion of ellipsoidal particles in cavity flows as illustrated in Fig. 10a. The shear flow near the top moving lid is the strongest. Therefore, the particle is lifted by the shear and moves closer to the top wall. Eventually, the particle enters the upper downstream region where the fluid vorticity is very large. The particle picks up spin due to higher vorticity of the fluid flow and becomes almost stationary. It remains in the upper right corner of the cavity for an extended duration of time. This phenomenon is also captured by the time evolution of the drag and lift forces as shown in Fig. 10b. In the beginning, i.e. 0–0.7 s, the drag force rises due to the increase in fluid velocity, as the particle is moving upwards due to the lift force. The lift force decreases because the cross-sectional area exposed to the fluid flow is smaller. After some time in the downstream region, due to the particle rotation, the particle eventually becomes increasingly unstable which results in higher drag and lift forces. After having found a new stable position at 3.9 s, the reorientation dynamics of the particle are reduced leading to a decrease in drag and shear lift forces. This is followed by a subsequent increase in drag and shear lift force due to the particle changing the spin direction

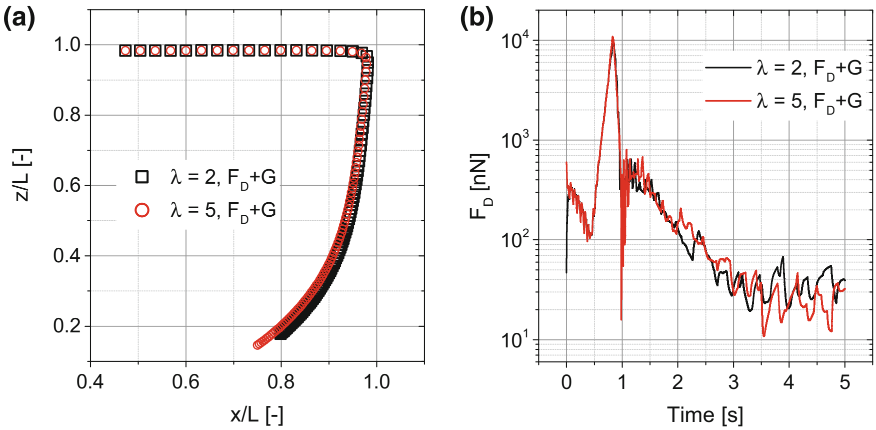

Fig. 9 The influence of the drag force on the translational motion of an ellipsoidal particle in a lid-driven cavity flow for different aspect ratios; **a** translational motion of the ellipsoid in the cavity; **b** time evolution of the drag force on the ellipsoid; for all cases only the drag force and the gravity were take into account ($\mathbf{u}_0 - \mathbf{v}_0 = \mathbf{0}\,\text{m/s}$, $Time = 5\,\text{s}$, $D_{volume} = 3\,\text{mm}$, $Re = 470$, $L = 0.1\,\text{m}$, $[\rho_f - \rho_p]/\rho_f = 0.05\%$)

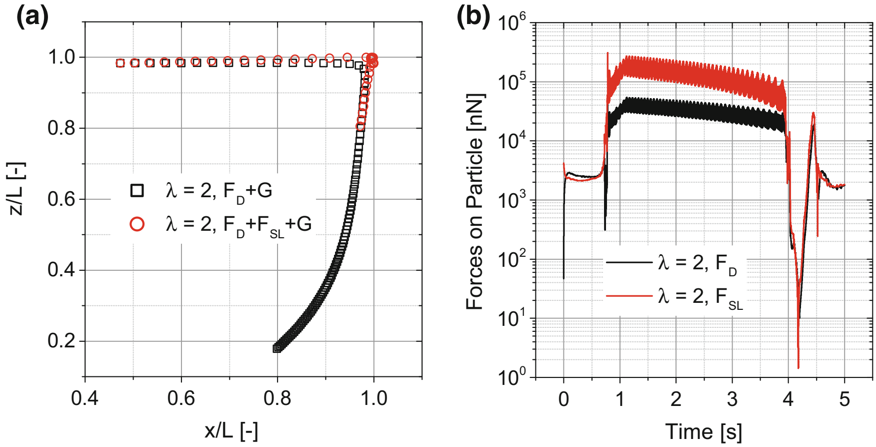

Fig. 10 The influence of the generalized shear lift force on the translational motion of an ellipsoidal particle in a lid-driven cavity flow; **a** translational motion of the ellipsoid in the cavity in comparison to two different force combinations, i.e. $F_D + G$ and $F_D + F_{SL} + G$; **b** time evolution of the drag force and generalized shear lift forces on the ellipsoid under the condition of $F_D + F_{SL} + G$; ($\mathbf{u}_0 - \mathbf{v}_0 = \mathbf{0}\,\text{m/s}$, $Time = 5\,\text{s}$, $\lambda = 2$, $D_{volume} = 3\,\text{mm}$, $Re = 470$, $L = 0.1\,\text{m}$, $[\rho_f - \rho_p]/\rho_f = 0.05\%$)

from clock-wise to counter clock-wise. Eventually, the ellipsoidal particle moves out of the top right corner and aligns its major axis *b* with the mean flow direction, hence reducing the drag force.

4 Conclusions

In the present paper, a Lagrangian particle tracking algorithm for simulating the motion of particles of ellipsoid shape was developed within the open-source code OpenFOAM®. The main objective of the present study is the evaluation of the drag and the lift forces with respect to the orientation of ellipsoidal particles. Instead of the Euler angles parametrization of the rotation tensor in Euler parameters/quaternions is used in order to avoid singularity issues. The rotation tensor provides the essential connection between the inertial frame and the particle rotational frame of reference. The time evolution of the Euler parameters is related to the orientation of ellipsoidal particles, resulting from rotational dynamics, whereas for the resistance to rotational motion the linear Jeffery torque [16] was adopted. In order to account for the effect of the particle shape, in modeling the drag force and the shear lift force exerted on an ellipsoidal particle the resistance tensor and the lift tensor, had to be implemented. The resistance tensor was used in the form developed by Brenner [1], who introduced a resistance tensor based on the aspect ratio of the ellipsoid and implemented it for computation of the hydrodynamic drag force acting on an ellipsoidal particle under Stokes flow conditions. The main achievement of the present paper is the derivation of a general lift vector, based on permutations of the linear shear lift tensor, that can be used in the computation of the shear lift force for a general shear flow.

In order to understand the accuracy and reliability of the overall model for Lagrangian tracking of ellipsoidal particles, numerical and experimental validations were performed for Couette and lid-driven cavity flows. First, the drag force was validated with numerical models for spheres (Sommerfeld et al. [27]) and the new shear lift forces was validated with a numerical model for ellipsoids (Harper and Chang [12]) in Couette flow, showing good agreement of the results under Stokes flow conditions. Secondly, the influence of drag and shear lift forces with respect to the particle orientation was studied for various ellipsoid aspect ratios. With the main axis perpendicular to the incoming flow direction, the ellipsoidal particle starts to rotate due to the shear and tends to align its major axis with the mean flow direction, resulting in a decrease of the drag and shear lift forces in the mean flow direction and an increase of both forces in the vertical direction. As a second test case, results of numerical models were compared with experimental investigations of particle transport in a lid-driven cavity flow (Tsorng et al. [29]). In general, the present model for ellipsoidal particles shows good agreement with the numerical and experimental results. In the case of an ellipsoidal particle, the shear lift force plays an important role in the translational motion of the particle. The ellipsoid moves closer to the lid and enters the upper downstream corner of the cavity, where its residence time is larger than in the case of the spherical particle.

The future work will be focused on the numerical tracking of micro-sized ellipsoidal particles moving in the Poiseuille flow at different initial circumferential locations.

Acknowledgements The authors thank the Deutsche Forschungsgemeinschaft for the financial support in the framework of the project STE 544/58.

References

1. Brenner, H.: The Stokes resistance of an arbitrary particle. Chem. Eng. Sci. **18**, 1–25 (1963)
2. Brenner, H.: The Stokes resistance of an arbitrary particle - IV. Arbitrary fields of flow. Chem. Eng. Sci. **19**, 703–727 (1964)
3. Chiang, T.P., Sheu, W.H.: Numerical prediction of eddy structure in a shear-driven cavity. Comput. Mech. **20**(4), 379–396 (1997)
4. Crowe, C.T., Sommerfeld, M., Tsuji, Y.: Multiphase Flows with Droplets and Particles. CRC press, Boca Raton (1998)
5. Derksen, J.J.: Numerical simulation of solids suspension in a stirred tank. AIChE J. **49**, 2700–2714 (2003)
6. Fan, F., Ahmadi, G.: A sublayer model for wall deposition of ellipsoidal particles in turbulent streams. J. Aerosol Sci. **26**, 813–840 (1995)
7. Fantoni, M.: Dynamics of ellipsiodal particles dispersed in channel flow turbulence. Ph.D. thesis, University of Udine (2008)
8. Feng, Y., Kleinstreuer, C.: Analysis of non-spherical particle transport in complex internal shear flows. Phys. Fluids **25**(9), 091904 (2013)
9. Ferziger, J.H., Peric, M.: Computational Methods for Fluid Dynamics, 3rd edn. Springer, Berlin (2002)
10. Gallily, I., Cohen, A.-H.: On the orderly nature of the motion of nonspherical aerosol particles II. Inertial collision between a spherical large droplet and axially symmetrical elongated particle. J. Colloid Interface Sci. **68**, 338–356 (1979)
11. Goldstein, H.: Classical Mechanics, 2nd edn. Addison Wesely, Reading (1980)
12. Harper, E.Y., Chang, I.D.: Maximum dissipation resulting from lift in a slow viscous shear flow. J. Fluid Mech. **33**(02), 209–225 (1968)
13. Hogg, A.J.: The inertial migration of non-neutrally buoyant spherical particles in two-dimensional shear flows. J. Fluid Mech. **212**, 285–318 (1994)
14. Hriberšek, M., Žajdela, B., Hribernik, A., Zadravec, M.: Experimental and numerical investigations of sedimentation of porous wastewater sludge flocs. Water Res. **45**(4), 1729–1735 (2011)
15. Jafari, A., Tynjälä, T., Mousavi, S.M., Sarkomaa, P.: Simulation of heat transfer in a ferrofluid using computational fluid dynamics technique. Int. J. Heat Fluid Flow **29**, 1197–1202 (2008)
16. Jeffery, G.B.: The motion of ellipsoidal particles immersed in a viscous fluid. Proc. R. Soc. A **102**, 161–179 (1922)
17. Koseff, J.R., Street, R.L.: The lid-driven cavity flow: a synthesis of qualitative and quantitative observations. J. Fluids Eng. **106**, 385–389 (1984)
18. Marchioli, C., Fantoni, M., Soldati, A.: Orientation, distribution and deposition of elongated, inertial fibers in turbulent channel flow. Phys. Fluids **49**, 33301 (2010)
19. Maxey, M.R.: Equation of motion for a small rigid sphere in a nonuniform flow. Phys. Fluids **26**(4), 883 (1983)
20. Sommerfeld, M.: Modellierung und numerische Berechnung von partikelbeladenen turbulenten Strömungen mit Hilfe des Euler/Lagrange- Verfahrens. Shaker Verlag, Aachen (1996)
21. Ravnik, J., Hriberšek, M.: High gradient magnetic particle separation in viscous flows by 3D BEM. Comput. Mech. **51**(4), 465–474 (2012)

22. Ravnik, J., Marchioli, C., Hriberšek, M., Soldati, A.: On shear lift force modelling for non-spherical particles in turbulent flows. In: Psihoyios, G., Simos, T.E., Tsitouras, Ch. (eds.) AIP Conference Proceedings, Rhodes, Greece, vol. 1558, pp. 1107–1110 (2013)
23. Saffman, P.G.: The lift on a small sphere in a slow shear flow. J. Fluid Mech. **22**, 385 (1965)
24. Saffman, P.G.: Corrigendum to: the lift on a small sphere in a slow shear flow. J. Fluid Mech. **31**, 624 (1968)
25. Shankar, P.N., Deshpande, M.D.: Fluid mechanics in the driven cavity. Annu. Rev. Fluid. Mech. **32**, 93–136 (2000)
26. Shapiro, M., Goldenberg, M.: Deposition of glass fiber particles from turbulent air flow in a pipe. J. Aerosol Sci. **24**, 65–87 (1993)
27. Sommerfeld, M., Schmalfuss, S.: Numerical analysis of carrier particle motion in a dry powder inhaler. ASME J. Fluids Eng. **138** (2015)
28. Stone, H.A.: Philip Saffman and viscous flow theory. J. Fluid Mech. **409**, 165–183 (2000)
29. Tsorng, S.J., Capart, H., Lo, D.C., Lai, J.S., Young, D.L.: Behaviour of macroscopic rigid spheres in lid-driven cavity flow. Int. J. Multiph. Flow **34**, 76–101 (2008)
30. Weller, H.G., Tabor, G., Jasak, H., Fureby, C.: A tensorial approach to computational continuum mechanics using object-oriented techniques. Comput. Phys. **12**(6), 620–631 (1998)
31. Zadravec, M., Hriberšek, M., Steinmann, P., Ravnik, J.: High gradient magnetic particle separation in a channel with bifurcations. Eng. Anal. Bound. Elem. **49**, 22–30 (2014)

Flexible Beam-Like Structures - Experimental Investigation and Modeling of Cables

Vanessa Dörlich, Joachim Linn and Stefan Diebels

1 Introduction

Flexible beam-like structures such as cables or hoses have various applications ranging from everyday to industrial use. Their main function is of course the conduction of electric current, gas, oil or other liquids. But the number of applications where cables and hoses move or have structural functions, e.g. in assembly robots or submarine cables, rises constantly [24, 25]. Therefore, their mechanical properties gain importance [4, 5, 13]. More precisely, the mechanical behavior determines the handling, operational lifetime and failure of cables and hoses [12, 19]. This contribution deals with the experimental investigation and modeling of slender, flexible structures using the example of cables.

We are looking for a model which is complex enough to cover the various effects that occur when cables are loaded mechanically. However, the model parameters have to be accessible in suitable experiments. The optimum in our case is the description of the mechanical behavior on the macroscopic scale, i.e. based on the sectional quantities of the beam. The effects are modeled by formulating the corresponding constitutive laws in the sectional quantities as well. The model parameters are then effective stiffness parameters, which can be obtained from well-known experiments for beam-like specimens. This procedure makes use of the classical framework of continuum mechanics [11] and the possibility to reduce slender objects such as cables to one-dimensional continua.

Section 2 deals with the experimental investigation and phenomena of cables under mechanical load. Three types of load cases are relevant in this context: uniaxial

V. Dörlich (✉) · J. Linn
Fraunhofer ITWM, Fraunhofer-Platz 1, 67663 Kaiserslautern, Germany
e-mail: vanessa.doerlich@itwm.fraunhofer.de

J. Linn
e-mail: joachim.linn@itwm.fraunhofer.de

S. Diebels
Universität des Saarlandes, Campus A4.2, 66123 Saarbrücken, Germany
e-mail: s.diebels@mx.uni-saarland.de

© Springer International Publishing AG 2018

H. Altenbach et al. (eds.), *Advances in Mechanics of Materials and Structural Analysis*, Advanced Structured Materials 80,
https://doi.org/10.1007/978-3-319-70563-7_2

tension, torsion and bending. Classical experiments representing these load cases are used to characterize the mechanical behavior of cables in a first step. Material effects resulting from the structure of cables will be observed.

In this work, we assume the cables' cross sections to be circular and isotropic. Furthermore, we model their mechanical behavior based on the sectional quantities with the Cosserat rod theory [1, 18, 20]. Its essential parts are geometrically exact kinematics, balance equations that govern the equilibrium of sectional forces and moments and constitutive laws that give the relations between objective deformation measures and sectional quantities. Section 3 will describe these more thoroughly.

2 Experiments for Flexible Beam-Like Structures

Executing suitable experiments is an important part of modeling the behavior of structural elements under mechanical load. Sections 2.1, 2.2 and 2.3 show characteristic results and phenomena of cables undergoing the three basic deformation modes uniaxial tension, torsion and bending [22]. The described experiments allow access to the elastic model parameters, i.e. the tensile, torsional and bending stiffnesses [7]. Furthermore, they already illustrate inelastic behavior when the experiments are executed cyclically.

2.1 Uniaxial Tensile Tests

The uniaxial tensile test is the most common experiment for beam-like specimens as well as the characterization of bulk materials. Its boundary conditions are shown in Fig. 1. It is widely used for determining elastic parameters like the Young's modulus E or plastic characteristics such as the yield strength or strain hardening. Usually, these characteristics are taken as material parameters from stress-strain curves, where normalization on the geometrical properties, i.e. the specimen's cross section area and length, is applied. This is reasonable for homogeneous, isotropic materials. In the case of cables and hoses, however, where properties strongly depend on the direction of load, we use force-displacement curves to calculate the tensile stiffness $(EA)_T$, where the cross section area A is still included. As the following results will show, it makes sense to characterize the cable's behavior with this parameter combining material and geometrical properties.

Despite its simplicity, the uniaxial tensile test yields a lot of information about the cable's deformation behavior, especially when executed cyclically. Figure 1 (right) shows the result of a cyclic uniaxial tensile test of a cable with a diameter of 2.8 mm and initial free length of 32 mm, where the uniaxial tensile force F_T is plotted over the measured machine displacement Δl. In order to illustratethe difference between

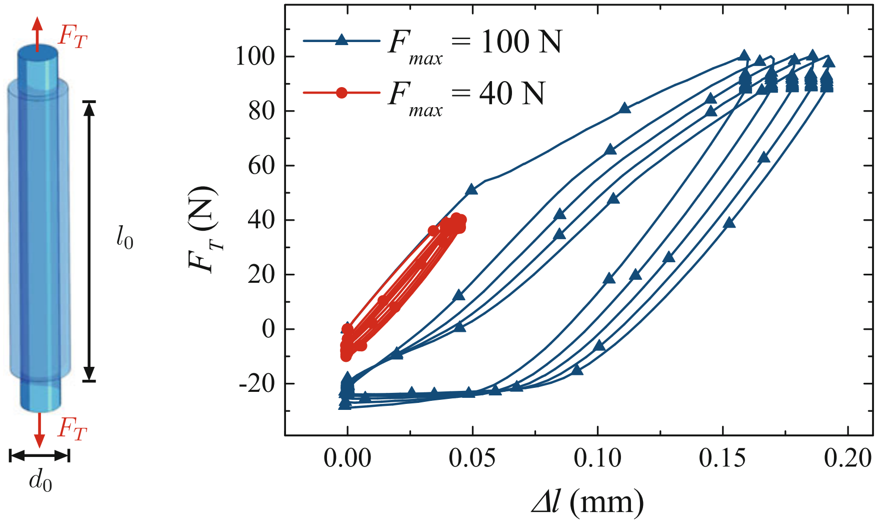

Fig. 1 Uniaxial tensile test: schematic drawing of the boundary conditions (**left**) and exemplary results of a cyclic experiment on a cable showing elastic behavior for $F_{max} = 40\,\text{N}$ and plastic behavior for $F_{max} = 100\,\text{N}$ (**right**)

elastic and inelastic behavior, two curves are shown. One results from a procedure with a maximum load of 40 N and the other one from loading up to 100 N. If the larger maximum force is applied, a bend in the first loading path, denoting the yield point at approximately 54 N and plastic hysteresis loops occur. For cyclic loading below the yield point, loading and unloading paths coincide and no bend occurs in the load-displacement diagram, i.e. the behavior is elastic in this range. The uniaxial tensile stiffness is calculated by applying a linear fit in the elastic range according to

$$F_T = (EA)_T \frac{\Delta l}{l_0}, \tag{1}$$

using the original length l_0 of the specimen.

2.2 Torsion Experiments

Similar to the uniaxial tensile test, the torsion test enables access to the torsional stiffness of a beam-like structure in the elastic range and information about plasticity effects from cyclic loading. The boundary conditions are shown in Fig. 2 (left) and the resulting diagram of torsional moment over torsional angle is shown in Fig. 2 (right) for a cable of 2.8 mm diameter and an initial free length of 33 mm. The result is strongly nonlinear and inelastic with a first load curve that differs from the following

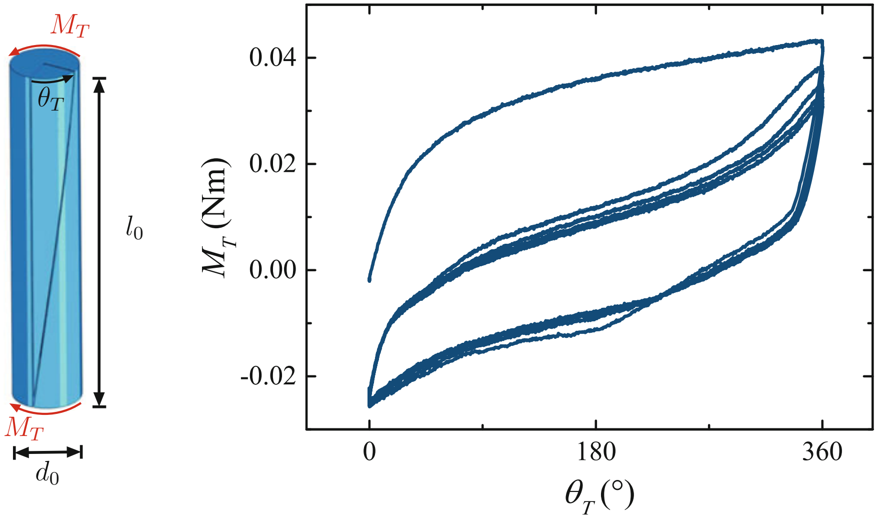

Fig. 2 Torsion test: schematic drawing of the boundary conditions (**left**) and exemplary results of a cyclic experiment on a cable showing plastic behavior for $\theta_{T,max} = 360°$ (**right**)

load paths. The first loading shows again a bend that can be interpreted as the yield point of the specimen. During unloading, a torsional moment in the opposite direction is necessary to reach the original position of 0° torsional angle. The torsional stiffness $(GJ)_T$ is estimated with the help of a linear fit in the elastic range according to

$$M_T = (GJ)_T \frac{\theta_T}{l_0}, \tag{2}$$

where G denotes the shear modulus and J the polar moment of inertia.

2.3 Bending Experiments

Three Point Bending Experiments

It is state of the art to use three point bending experiments [22] to investigate the behavior of cables undergoing bending deformation [7]. The theoretical boundary conditions are shown in Fig. 3 (left). In this experiment, the force F_B on the specimen, which is necessary to reach a certain deflection $w(z = {}^{l_0}/_2)$, is measured in the middle of the specimen. The evaluation of the bending stiffness $(EI)_B$ in this experiment is based on the Euler–Bernoulli assumptions stating that the beam's cross sections remain planar and normal to the beam's centerline after deformation. Furthermore, it is only valid for small deflections of sufficiently slender beams. Then, the bending stiffness can be evaluated from a linear fit according to

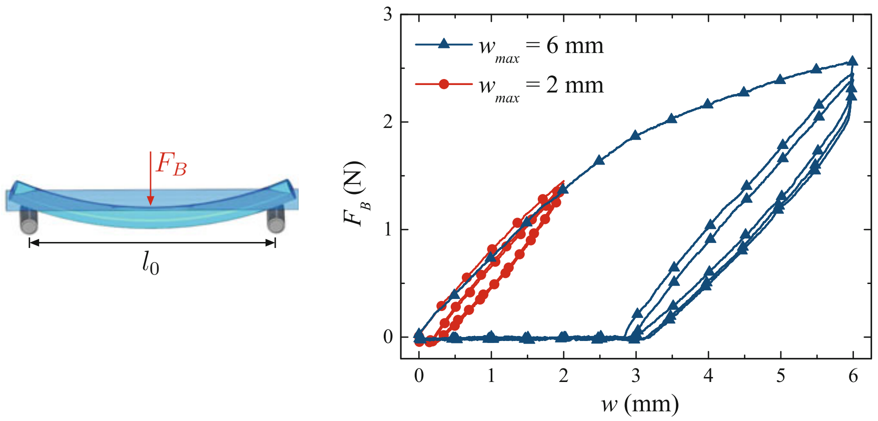

Fig. 3 Three point bending test: schematic drawing of the boundary conditions (**left**) and exemplary results of cyclic experiments on a cable showing elastic behavior for $w_{max} = 2\,\text{mm}$ and plastic behavior for $w_{max} = 6\,\text{mm}$ (**right**)

$$F_B(z = {}^{l_0}\!/_2) = 48\,(EI)_B \frac{w(z = {}^{l_0}\!/_2)}{l_0^3}. \tag{3}$$

Figure 3 (right) shows an exemplary result of three point bending of a cable with a diameter of 2.8 mm and a free length between the supports of 56 mm. Again, results of different load ranges are displayed in order to illustrate the difference between cyclic loading in the elastic and inelastic range. Applying a deflection of 6 mm results in plastic hysteresis loops, where a bend in the first load curve implies the beginning of the plastic region. Furthermore, the specimen stays deflected during unloading so that the punch loses contact and force equals zero before the punch reaches the original position. Bending the specimen only up to a maximum deflection of 2 mm yields in contrast a smaller hysteresis, which lacks the plastic region. Additionally, no bend can be observed in the force-displacement diagram for small deflections.

Although this experiment is well-known and easily implemented, it has its limitations. First of all, it is only valid for small deflections and should therefore not be used for the investigation of large deformation effects like plasticity. Secondly, it provides only integrated information about the curvature and bending moment along the axis of the specimen, not their local values, which are the quantities that are relevant for the constitutive law for bending in this context, see Sect. 3.4. In order to get information about the local curvature, e.g. corresponding to the measured yield point, additional measurements such as optical deformation measurements are necessary.

Pure Bending Experiments

We designed a device which enables pure bending [2, 3] of a cable and therefore overcomes these limitations. The symmetrical experimental setup is shown in Fig. 4. In the undeformed state, the cable ends are clamped and mounted on slides. Air bushings ensure friction-free gliding of these slides along the axis of the specimen.

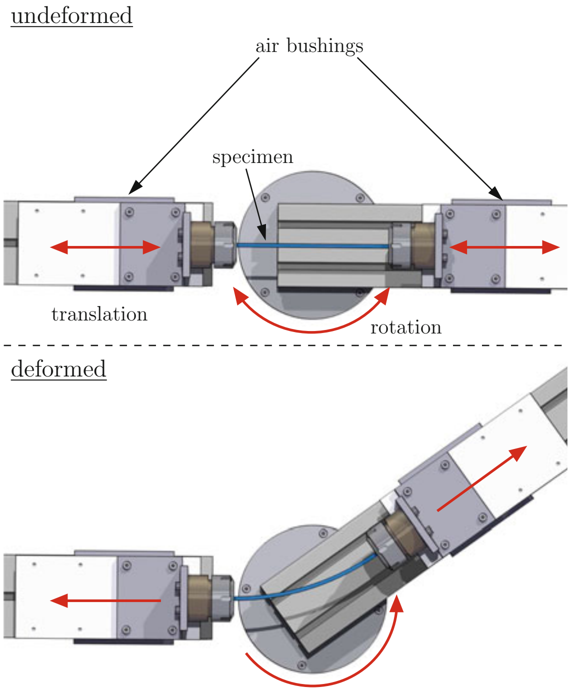

Fig. 4 Topview on the experimental setup for pure bending. The straight cable is clamped on slides which are mounted on friction-free air bushings. They allow for a translational motion of the specimen, while bending is realized by rotation of one cable end. Therefore, only a bending moment and no normal or shear forces act on the specimen

Thus, no normal forces act on the cable. Bending is realized by rotation of one of the cable ends. This setup guarantees that only a bending moment is applied on the specimen, i.e. no shear forces occur. The schematic boundary conditions are shown in Fig. 5 (left). These boundary conditions yield a configuration, where the bending moment M_B and the bending curvature K_B along the specimen are constant, i.e. the specimen's centerline is deformed to a circular arc. The specimen's bending curvature is then accessible as the inverse bending radius R of the specimen following basic geometry

$$K_B = \frac{1}{R}. \tag{4}$$

Calculating the stress distribution resulting from pure bending in the cross section of an Euler–Bernoulli beam under the assumptions of locally linear elastic material behavior, the bending moment can be derived as

$$M_B = (EI)_B \, K_B = \frac{EI}{R}. \tag{5}$$

Thus, the bending stiffness is in this experiment directly accessible as the slope of the elastic region of the bending moment over curvature diagram. An exemplary result of a cyclic pure bending experiment executed on a cable with a diameter of 2.8 mm and a

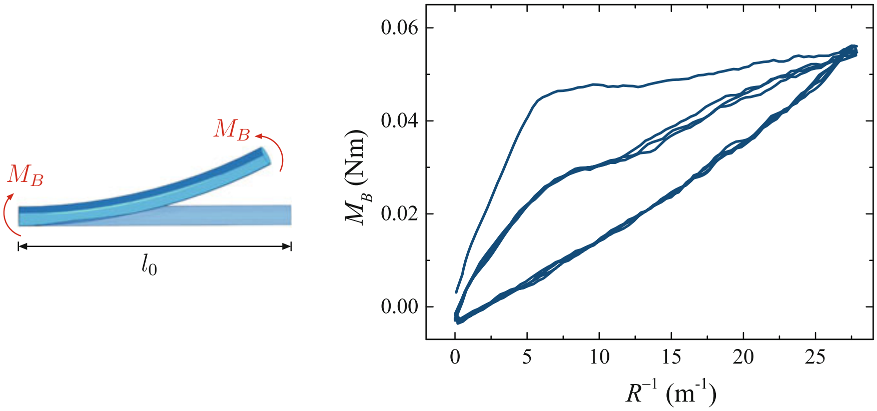

Fig. 5 Pure bending experiment: schematic drawing of the boundary conditions (**left**) and exemplary results of cyclic experiment on a cable showing plastic behavior for $\theta_{B,max} = 80°$ (**right**)

free length of 50 mm is shown in Fig. 5 (right). Comparing it to Fig. 3 (right), the same elastoplastic characteristics are observable as in the three point bending experiment. The advantage of the pure bending experiment is the fact that the observed yield point is given as bending moment and corresponding bending curvature, which are directly the quantities that enter the constitutive law for bending, see Sect. 3.4.

Varieties in Constitutive Bending Behavior

Figures 6 and 7 show experimental results of both types of bending experiments on different beam-like specimens with circular cross sections in order to illustrate the varieties of constitutive bending behavior.

The diagrams shown in Fig. 6 result from cyclic three point and pure bending experiments on comparatively stiff, but elastic carbon fiber reinforced polymer (CFRP) rods of a diameter of 3 mm. The specimen used in the three point bending experiment had an initial free length of 170 mm and in the case of pure bending it had a free length of 410 mm. It is noticeable, that the loading paths are linear and coincide perfectly with the unloading paths in both bending experiments.

The results displayed in Fig. 7 show almost elastic, but nonlinear constitutive bending behavior. In contrast to elastoplastic behavior shown in Figs. 3 and 5, loading and unloading paths coincide – except for some viscous effects – and are parallel, but the slope of the curves changes during loading and unloading. These characteristics are called piecewise linear elastic bending behavior in this work. These diagrams result from bending experiments on Bowden cables with a special structural setup. They typically consist of an inner wire rope and a hollow housing of composite structure, which is incompressible in the longitudinal direction. The inner wire rope of the Bowden cables used in the experiments has a diameter of 2.1 mm and the housing has a diameter of 7.8 mm. In the three point bending experiment, an initial free length of 300 mm was used and in the pure bending experiment, the specimen

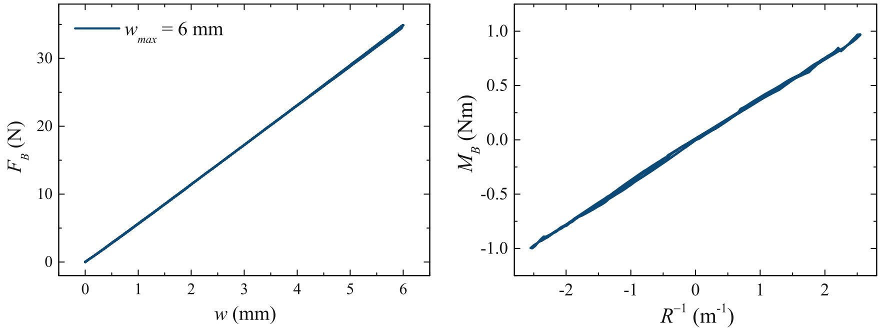

Fig. 6 Experimental results of cyclic bending experiments on elastic CFRP rods: three point bending with $w_{max} = 6\,\text{mm}$ (**left**) and pure bending with $\theta_{B,max} = \pm 60°$ (**right**)

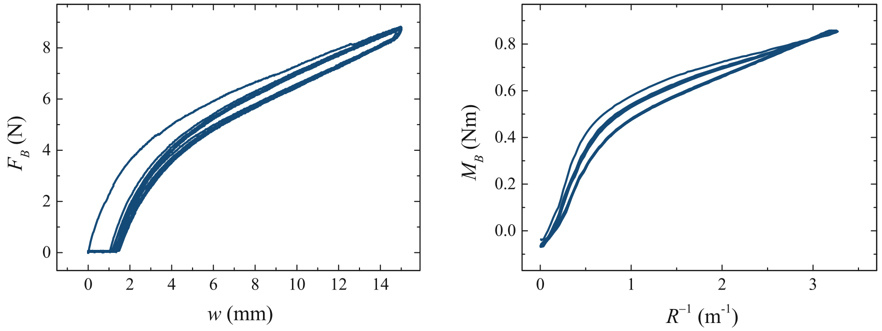

Fig. 7 Experimental results of cyclic bending experiments on Bowden cables showing nonlinear, approximately piecewise linear elastic behavior: three point bending with $w_{max} = 15\,\text{mm}$ (**left**) and pure bending with $\theta_{B,max} = 60°$ (**right**)

had a free length of 320 mm. Bowden cables are commonly used, e.g. in bicycle brakes or motorcycle clutches, to transmit a tensile force.

It can be noticed, that the three point bending experiment as well as the pure bending experiment show the characteristics of the respective constitutive behavior, e.g. yield points, linear or nonlinear, elastic or inelastic behavior. The pure bending experiment, however, directly depicts the constitutive bending model as it shows the bending moment over bending curvature.

2.4 Discussion of Experiments

It was shown that the classical experiments for beam-like specimens can be used to characterize the rate independent behavior of elastoplastic cables under mechanical load.

Table 1 Elastic stiffnesses and Young's moduli calculated from the different classic experiments on a simple cable with a diameter of 2.8 mm

$(EA)_T$	$(E)_{Ten}$	$(GJ)_{Tor}$	$(E)_{Tor}$	$(EI)_B$	$(E)_B$
$7.96 \cdot 10^4$ N	12900 MPa	$2.02 \cdot 10^{-3}$ Nm^2	1003.7 MPa	$1.37 \cdot 10^{-3}$ Nm^2	454.4 MPa

The elastic tensile, torsion and bending stiffnesses can be determined from linear fits to the elastic range of the corresponding experimental results. Table 1 shows the elastic stiffnesses that were determined from uniaxial tension, torsion and three point bending results given in the sections before. Under the assumptions of a circular, isotropic cross section and incompressible ($\nu = 0.5$) behavior, the Young's moduli were calculated from the respective stiffnesses by using

$$I = \frac{\pi}{4} R^4 = \frac{1}{2} J, \tag{6}$$

$$G = \frac{E}{2(1+\nu)} = \frac{E}{3}. \tag{7}$$

They are also given in Table 1 in addition to the corresponding stiffness. The comparison of the Young's moduli that were determined from the three different types of experiments yields that the tensile stiffness is considerably higher than the torsional and bending stiffnesses. That means, the cable behaves much stiffer under tension than under torsion or bending due to the anisotropic inner structure of the cable. Consequently, it is not sufficient to determine the Young's modulus as the elastic material parameter for one cable, but one has to investigate the three different load cases separately and to determine the stiffnesses as a combination of material and structural parameters.

Different phenomena in the constitutive behavior are illustrated by the described experiments, especially when they are executed in consecutive cycles. The tensile, torsion and bending experiments on cables show the characteristics of elastoplastic behavior resulting from the multi-component structure. They appear due to inner friction or delamination of the constituents and the metal plasticity of the inner wires.

Furthermore, experimental results for different kinds of beam-like specimens illustrating the variety of constitutive bending behavior were shown. CFRP rods showing linear elastic behavior and Bowden cables showing piecewise linear elastic behavior were investigated in bending experiments exemplarily and will be discussed in Sect. 3.4 in more detail.

It has to be mentioned, that the described experiments only cover the three basic deformation modes for beam-like structures and are mostly uniaxial. In applications, however, mostly multiaxial deformations combining the basic deformations occur. First approaches in the experimental investigation of multiaxial deformations of cables are executed in [7], but are beyond the scope of this work.

3 Modeling of Flexible Beam-Like Structures for Virtual Product Development

The variety of experimental effects and different kinds of behavior shown in Sect. 2 can be modeled in the framework of continuum mechanics [9, 23]. It provides physically correct models to simulate the deformation of parts with a complex microstructure such as cables without having to take the microstructural properties explicitly into account. These properties certainly influence the deformation behavior of the cables strongly, but it is computationally and experimentally too expensive to include them into the model. We consequently aim for a model which is complex enough to cover the measured phenomena of cables under load and at the same time simple enough in the sense that its parameters are accessible in experiments.

The long and slender shape of the flexible parts provides the possibility to reduce the continuum model analytically to one dimension. These models are based on the Cosserat rod theory [20], which basically consists of three main parts: Geometrically exact kinematics that relate configuration variables with objective strain measures, balance equations that govern the equilibrium of the sectional forces and moments and constitutive laws giving the sectional quantities in terms of the deformation measures. The following subsections will describe them in detail.

3.1 Kinematics of Geometrically Exact Rods

The geometrically exact kinematics of a Cosserat rod are based on its configuration variables, see Fig. 8. The centerline curve is described by a space curve

$$s \mapsto \mathbf{r}(s) \in \mathbb{R}^3, \tag{8}$$

and the orientation of the cross sections is given by a moving frame of orthonormal directors $\mathbf{a}^{(j)}(s)$

$$s \mapsto \mathsf{R}(s) = \mathbf{a}^{(j)}(s) \otimes \mathbf{e}_j \in SO(3), \tag{9}$$

both given as a function of the arc length parameter s [1]. The vectors $\mathbf{a}^{(1)}(s)$ and $\mathbf{a}^{(2)}(s)$ define the local cross section and $\mathbf{a}^{(3)} = \mathbf{a}^{(1)} \times \mathbf{a}^{(2)}$ is the cross section normal. The moving frame $\mathsf{R}(s)$ is called adapted to the curve if the tangent vector $\mathbf{t}(s) = \mathbf{r}'(s)$ equals $\mathbf{a}^{(3)}(s)$. This constraint is equivalent to the Euler–Bernoulli assumptions that cross sections remain orthogonal to the beam centerline and only a special case of the more general Cosserat curve which does not require this constraint.

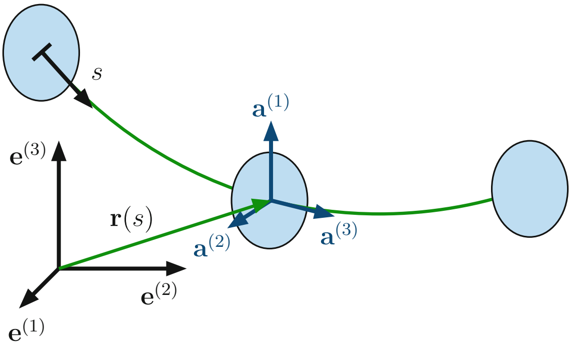

Fig. 8 The kinematics of Cosserat rods

3.2 Deformation Measures

Based on the geometrically exact kinematics given in the section before, objective deformation measures can be defined. The rotational deformations $\mathbf{K}$ and translational deformations $\boldsymbol{\Gamma}$ are given as vectors in the local coordinate system by

$$\begin{aligned} K^{(\alpha)} &:= \langle \mathbf{a}^{(\alpha)}, \mathbf{a}^{(3)} \times \partial_s \mathbf{a}^{(3)} \rangle; & \Gamma^{(\alpha)} &:= \langle \mathbf{a}^{(\alpha)}, \partial_s \mathbf{r} \rangle; \qquad \alpha = 1, 2 \\ K^{(3)} &:= \langle \mathbf{a}^{(2)}, \partial_s \mathbf{a}^{(1)} \rangle; & \Gamma^{(3)} &:= \langle \mathbf{a}^{(3)}, \partial_s \mathbf{r} \rangle - 1, \end{aligned} \tag{10}$$

where $\langle \bullet, \bullet \rangle$ is the scalar product. The components $K^{(\alpha)}$ give the curvatures for bending about the axes defined by $\mathbf{a}^{(\alpha)}$ and $K^{(3)}$ measures the torsional twist. The bending curvatures can be combined in the vector $\mathbf{K}_B = \left(K^{(1)}, K^{(2)}\right)^{\mathrm{T}}$ and its length

$$K_B = \|\mathbf{K}_B\| = \sqrt{(K^{(1)})^2 + (K^{(2)})^2} \tag{11}$$

is the absolute value of the bending curvature. The entries $\Gamma^{(\alpha)}$ measure the transverse shear strains and the longitudinal strain, relevant for uniaxial tension, is denoted by $\Gamma^{(3)}$.

3.3 Static Equilibrium Equations

In analogy to the deformation measures, the sectional quantities can be divided in translational sectional quantities, the sectional forces $\mathbf{F}$, and rotational sectional quantities, the sectional moments $\mathbf{M}$. The components $F^{(1,2)}$ of the sectional forces are in accordance with the translational deformation measures the transverse shear forces and $F^{(3)}$ is the longitudinal force which is equivalent to the force measured in the uniaxial tensile test. The moments resulting from bending about the bending axes are consequently $M^{(1,2)}$ and the torsional moment is given by $M^{(3)}$. Equivalently to the bending curvature given in (11), the bending moments can be summarized in the vector $\mathbf{M}_B = \left(M^{(1)}, M^{(2)}\right)^{\mathrm{T}}$ and the absolute value of the bending moment is given by the vector's length

$$M_B = \|\mathbf{M}_B\| = \sqrt{(M^{(1)})^2 + (M^{(2)})^2}. \tag{12}$$

Vectors denoted with a capital letter are material quantities, i.e. defined in the local coordinate system of the beam. The static equilibrium equations, however, can be formulated more neatly in the spatial sectional quantities, defined in the global coordinate system. They can be calculated from the material sectional quantities by using the moving frame according to

$$\mathbf{f} = \mathsf{R}(s) \cdot \mathbf{F}; \quad \mathbf{m} = \mathsf{R}(s) \cdot \mathbf{M}. \tag{13}$$

The system of static equilibrium equations for Cosserat rods is then given as

$$\begin{aligned} \partial_s \mathbf{f} + \mathbf{f}_{ext} &= \mathbf{0}, \\ \partial_s \mathbf{m} + \partial_s \mathbf{r} \times \mathbf{f} + \mathbf{m}_{ext} &= \mathbf{0}. \end{aligned} \tag{14}$$

The vectors $\mathbf{f}_{ext}$ and $\mathbf{m}_{ext}$ denote external forces and moments acting on the axis of the Cosserat rod.

3.4 Constitutive Laws

The continuum mechanical framework for the simulation of flexible, slender parts like cables is given in the previous sections, except for the constitutive equations. We will focus on these now since they provide the possibility to model different kinds of deformation behavior [14]. In contrast to a general three-dimensional formulation in tensor quantities, constitutive laws for Cosserat rods can be formulated in the vectors of the sectional quantities due to their slender geometry [10, 15, 17]. This is especially of advantage in regard of experiments. The sectional quantities are in most cases the measured quantities in the classical experiments for beams, which enables the investigation of the constitutive behavior directly in the experiments without the necessity for reverse engineering. In the following, the modeling of three types of rate independent constitutive behavior is described in more detail: linear elasticity, piecewise linear elasticity and elastoplasticity.

Linear Elasticity for Cosserat Rods

In the simplest case of linear elasticity the stress tensor σ is related linearly to the strain tensor E via the elastic stiffness tensor $\mathbb{C}$ in three dimensions

$$\sigma = \mathbb{C} : \mathsf{E}, \tag{15}$$

which is known as Hooke's law. It can be formulated equivalently for the material sectional quantities of the Cosserat rod as

$$\mathbf{F} = \mathbb{C}_{\mathbf{F}} \cdot \boldsymbol{\Gamma}_{el}; \qquad \mathbf{M} = \mathbb{C}_{\mathbf{M}} \cdot \mathbf{K}_{el}, \tag{16}$$

where the effective elastic stiffness matrices are given by

$$\mathbb{C}_{\mathbf{F}} = \begin{bmatrix} (GA)_1 & 0 & 0 \\ 0 & (GA)_2 & 0 \\ 0 & 0 & (EA)_T \end{bmatrix}; \qquad \mathbb{C}_{\mathbf{M}} = \begin{bmatrix} (EI)_1 & 0 & 0 \\ 0 & (EI)_2 & 0 \\ 0 & 0 & (GJ)_T \end{bmatrix}. \tag{17}$$

In case of isotropic circular cross sections, the bending stiffnesses are equal and denoted as $(EI)_1 = (EI)_2 = (EI)_B$. The same applies to the transverse shear stiffnesses, i.e. $(GA)_1 = (GA)_2 = (GA)_S$, which cannot be easily determined in experiments. It is, however, valid to calculate them from the other experimentally determined stiffnesses as the transverse shear is small in parts with a high aspect ratio.

An experimental result for linear elastic bending behavior is displayed in Fig. 6. The diagram resulting from pure bending on the right hand side directly illustrates the linear elastic constitutive law for bending of a specimen with a circular isotropic cross section in the plane,

$$M_B = (EI)_B \, K_B. \tag{18}$$

It is visible, that loading and unloading paths coincide, which means no energy is lost in this process and it is reversible. Only few beam-like specimens, such as the CFRP rods, behave linearly elastic at finite deformations. In most cases, linear elasticity is only observed at small deformations. Material nonlinearities, in contrast to the already introduced geometrical nonlinearities covered by the geometrically exact kinematics, have to be considered then.

Piecewise Linear Elasticity for Bending of Cosserat Rods

A different kind of reversible, rate independent, behavior is shown in Fig. 7: Piecewise linear elasticity in bending. This type of constitutive behavior has only been observed in bending experiments on Bowden cables, so far. It is still interesting to investigate in pure bending, since the constitutive behavior can be depicted directly in this experiment.

The characteristics of piecewise linear elastic bending behavior are portrayed schematically in Fig. 9 (left). The diagram of bending moment over bending curvature shows linear elastic bending with a bending stiffness $(EI)_{B,1}$ up to a certain threshold curvature $K_{B,t}$. At this point, the slope of the graph, i.e. the bending stiffness, changes to $(EI)_{B,2}$. The unloading path follows the same behavior and coincides with the loading path, no hysteresis occurs. The real results obtained in a pure bending experiment corresponding to this ideal behavior are shown in Fig. 7 (right). Obviously, the threshold curvature is not as clearly detectable as in theory and a small hysteresis, probably due to viscous material behavior or plastic structural

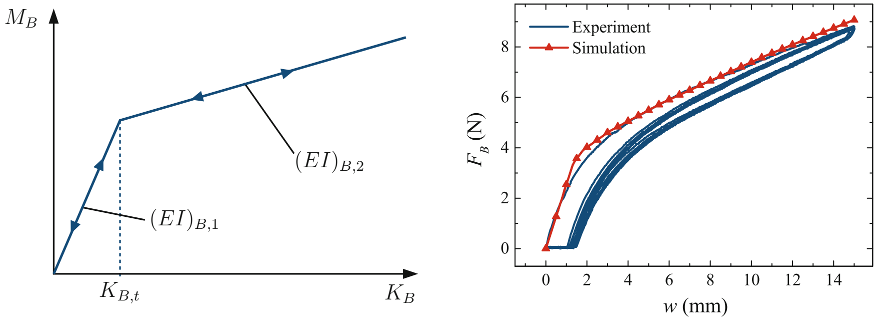

Fig. 9 Schematic drawing of piecewise linear elastic bending constitutive law (**left**) and comparison of experimental results of three point bending on a Bowden cable with simulation results using piecewise linear elastic bending (**right**)

Table 2 Experimentally determined model parameters for piecewise linear elastic bending model

Bending stiffness $(EI)_{B,1}$	Bending stiffness $(EI)_{B,2}$	Threshold curvature $K_{B,t}$
$1.40\,\mathrm{Nm}^2$	$0.19\,\mathrm{Nm}^2$	$0.18\,\mathrm{m}^{-1}$

effects, occurs. However, it is evident that the bending stiffness is higher at smaller curvatures and that the behavior is reversible.

This piecewise linear elasticity can simply be modeled by distinction of the cases

$$M_B = \begin{cases} (EI)_{B,1}\, K_B & \text{for } |K_B| < K_{B,t} \\ M_{B,t} + (EI)_{B,2}\left(K_B - K_{B,t}\right) & \text{for } |K_B| \geq K_{B,t}, \end{cases} \tag{19}$$

with the threshold bending moment $M_{B,t} = (EI)_{B,1}\, K_{B,t}$. The results of the simulation of a three point bending experiment with this kind of model are shown in Fig. 9 (right) in comparison with the experimental results of three point bending. The experimentally determined model parameters are given in Table 2. It has to be mentioned, that the curve resulting from simulation shows one complete cycle, i.e. loading and unloading. This is not visible, because the loading and unloading paths coincide. The experimental and simulated results show good agreement, except for a small hysteresis in the experiment which is probably caused by viscous or damage effects that are not covered in the model. The simple formulation of piecewise defined elastic bending stiffnesses at least models the loading behavior of Bowden cables in three point bending very well.

Elastoplasticity for Cosserat Rods

The results from cyclic experiments on simple cables given in Sects. 2.1, 2.2 and 2.3 illustrated strongly nonlinear and inelastic behavior under the three basic deformations. A rate independent elastoplastic constitutive law allows for the integration of the various underlying material and structural effects, such as metal plasticity,

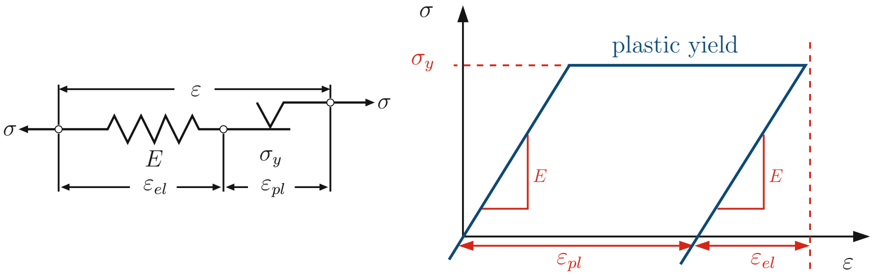

Fig. 10 Illustration of a one-dimensional rate independent elastoplastic rheological model, according to [21] (**left**) an d schematic stress-strain-diagram for one-dimensional perfect elastoplasticity (**right**)

friction between the constituents, delamination and damage without the necessity of investigating them on the microstructural level.

The rheological model shown in Fig. 10 illustrates the simplest case of one-dimensional elastoplasticity [21]. It consists of a linear elastic spring with Young's modulus E which is serially connected to a Coulomb friction element with yield point σ_y. The total strain ε can be split additively into an elastic part ε_{el} and a plastic part ε_{pl}, when the whole device is loaded with the stress σ. Starting at the linear elastic constitutive law,

$$\sigma = E\,\varepsilon_{el}, \tag{20}$$

and using the additive split of the total strain,

$$\varepsilon = \varepsilon_{el} + \varepsilon_{pl}, \tag{21}$$

the elastoplastic constitutive law can be formulated as

$$\sigma = E\left(\varepsilon - \varepsilon_{pl}\right). \tag{22}$$

The resulting stress-strain-curve is given schematically in Fig. 10 (right).

In our case of very slender objects, it is valid to transfer this simple concept to the deformation measures of the Cosserat rod, since the local deformations remain small, even if the global displacements and rotations are large. Otherwise, an additive split of the deformation measures would not suffice and a multiplicative split should be used. In analogy to (20), (21), (22), the deformation measures of the Cosserat rod are split into an elastic and a plastic part,

$$\boldsymbol{\Gamma} = \boldsymbol{\Gamma}_{el} + \boldsymbol{\Gamma}_{pl}; \quad \mathbf{K} = \mathbf{K}_{el} + \mathbf{K}_{pl}, \tag{23}$$

and the elastoplastic constitutive laws for the sectional forces and moments are

$$\begin{aligned} \mathbf{F} &= \mathbb{C}_{\mathbf{F}} \cdot \boldsymbol{\Gamma}_{el}; & \mathbf{M} &= \mathbb{C}_{\mathbf{M}} \cdot \mathbf{K}_{el}, \\ \mathbf{F} &= \mathbb{C}_{\mathbf{F}} \cdot \left(\boldsymbol{\Gamma} - \boldsymbol{\Gamma}_{pl}\right); & \mathbf{M} &= \mathbb{C}_{\mathbf{M}} \cdot \left(\mathbf{K} - \mathbf{K}_{pl}\right). \end{aligned} \tag{24}$$

In order to describe the onset of plastic yield, i.e. the limits of the elastic region, a yield criterion has to be defined. At first, we consider the case of perfect plasticity, where no hardening occurs. It is assumed, that the stress in the elastoplastic device cannot exceed the yield point σ_y and consequently, all admissible stress states have to be smaller than or equal to σ_y. In the most general case, the yield condition is then formulated as

$$f(\sigma) := |\sigma| - \sigma_y \le 0. \tag{25}$$

We can distinguish two cases in (25). As long as $f(\sigma) < 0$ is satisfied, the response of the device is instantaneous and elastic. The plastic strain does not change in this case, i.e. $\dot{\varepsilon}_{pl} = {}^{\partial \varepsilon_{pl}}/_{\partial t} = 0$. When $f(\sigma) = 0$ and a loading condition is fulfilled, the Coulomb friction element is active and plastic yield occurs. Consequently, the plastic strain changes and $\dot{\varepsilon}_{pl} \neq 0$. The change of the plastic strain is then described by an evolution equation called flow rule. If the flow rule is connected to the yield condition by

$$\dot{\varepsilon}_{pl} = \gamma \frac{\partial f}{\partial \sigma}, \tag{26}$$

i.e. the flow potential is equal to the yield condition, the flow rule is called associative. While the derivative ${}^{\partial f}/_{\partial \sigma}$ determines the direction of plastic flow, the proportionality factor γ gives the absolute value of the plastic strain rate. It can be calculated from the consistency condition

$$\gamma \dot{f}(\sigma) = 0, \text{ if } f(\sigma) = 0, \tag{27}$$

which states that if plastic flow occurs, the stress state has to remain on the yield surface, i.e. the value $f = 0$ does not change during yield. The necessary requirements for yielding can be summarized in the Kuhn–Tucker complementarity conditions, see e.g. [16],

$$\gamma \ge 0; \quad f(\sigma) \le 0; \quad \gamma f(\sigma) = 0. \tag{28}$$

In the following, we will focus on elastoplastic bending behavior, since this is the deformation mode most common regarding plasticity in applications of cables. The elastoplastic constitutive law for bending is formulated in analogy to (24), using the vectorial bending curvature and moment as

$$\mathbf{M}_B = (EI)_B \left(\mathbf{K}_B - \mathbf{K}_{B,pl}\right). \tag{29}$$

The experimental results in Sect. 2.3 showed elastoplastic behavior in three point bending, as well as in pure bending experiments on cables. If one compares the first load cycles in Figs. 3 and 5 to the illustration of perfect elastoplasticity in Fig. 10, it is evident, that perfect plasticity will not enable the modeling of the observed behavior.

During yield in the first load cycle, (strain) hardening occurs in the experiments, i.e. the bending moment increases after the yield point is reached.

In order to include hardening in the plasticity formulation, further internal variables in addition to the plastic strain have to be introduced. We will describe the simple case of linear isotropic strain hardening, since it seems to be sufficient to describe the first loading of the pure bending experiment shown in Fig. 5. The yield condition in one dimension is then given by

$$f(\sigma, \mathbf{q}) := |\sigma| - \left[\sigma_y + H\alpha\right] \leq 0, \;\; \alpha \geq 0, \tag{30}$$

with the internal hardening variable α, the hardening modulus H and the vector of internal variables $\mathbf{q}$. This yield condition describes isotropic hardening behavior, because the center of the elastic region does not change its position, but it expands isotropically. The evolution of α is given by the hardening law, which can be formulated as an associative evolution equation, as well,

$$\dot{\alpha} = \gamma \frac{\partial f(\sigma, \mathbf{q})}{\partial \mathbf{q}}. \tag{31}$$

The equivalent yield function for linear isotropic hardening for bending of a Cosserat rod can be formulated as

$$f(M_B, \mathbf{q}) := M_B - \left[M_{B,y} + (HI)_B\alpha\right] \leq 0, \;\; \alpha \geq 0, \tag{32}$$

using the effective bending moment given in (12). The yield point in bending is called $M_{B,y}$ and $(HI)_B$ is the hardening modulus for bending. In analogy to the bending stiffness $(EI)_B$, the area moment of inertia I is included into the definition of the hardening modulus. This yield function can be interpreted as a circle in the bending moment plane with a radius of $M_{B,y}$, which is suitable for homogeneous, isotropic and circular cable cross sections. It is shown in Fig. 11 (right). The resulting moment-curvature-diagram for pure bending is depicted in Fig. 11 (left). Comparing this theoretical diagram to the real experimental results of pure bending given in Fig. 5, it is evident that this formulation will enable the description of the first load path. The unloading in the experiment, however, deviates from the theoretical diagram, since it is not parallel to the elastic loading path. This indicates, that the inelastic effects in the experiment cannot be covered completely by an elastoplastic formulation. In [8], numerical experiments using the elastoplastic formulation with isotropic hardening given by (27)–(29), (31) and (32) are executed. For this purpose, a finite beam element based on Cosserat rod theory is derived and used for the simulation of three point bending and pure bending experiments of a cable. The comparison of the simulation results to the experimental results confirms the presumption that the elastoplastic formulation is not sufficient to model the unloading path in pure bending experiments. However, the change in stiffness during unloading can be modeled using an additional pseudo-damage formulation based on the sectional quantities of the Cosserat rod. This extension exceeds the scope of this work, but it is treated in detail in [8].

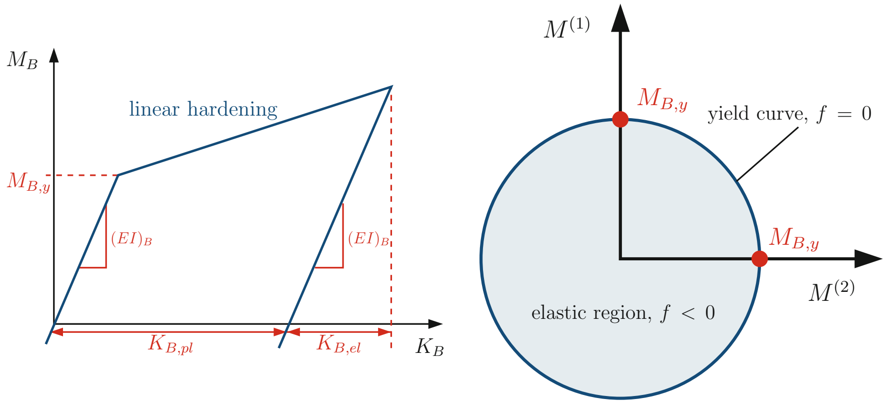

Fig. 11 Schematic illustration of elastoplastic bending behavior with linear hardening (**left**) and schematic drawing of a yield function in the bending moment plane (**right**)

It has to be noted that this formulation for elastoplastic bending does not account for coupling of the bending moment with the remaining sectional quantities of the Cosserat rod, i.e. tension and torsion. We assume that they stay in the elastic region and do not influence the bending plasticity, which is valid for the considered planar pure bending experiment. It is, however, only the first step towards describing the three-dimensional deformation behavior of cables showing inelastic behavior.

4 Conclusions

This chapter combines experimental work and theoretical considerations regarding the constitutive modeling of the deformation behavior of cables.

Since cables are slender and flexible, they can be characterized by means of classical experiments for beam-like structures. Section 2 treated experiments covering the three basic deformation modes of beams: tension, torsion and bending. In addition to the well-known uniaxial tension test, torsions test and three point bending experiment, a new device which enables the pure bending of cables, was introduced. It was shown, that the anisotropic and inhomogeneous structure of the cable demands for the use of stiffness parameters for the respective load cases in order to completely describe the elastic deformation behavior of the cable. It is not sufficient to determine only a material property, such as the Young's modulus E, to cover the behavior of a cable under load. Moreover, it was shown that the constitutive behavior, even of simple cables, exceeds linear elasticity. The multi-component structure of the cable causes inelastic effects, e.g. friction, damage or delamination, which is superposed by inelastic material effects such as metal plasticity of the conducting wires. Results of experiments executed on different kinds of beam-like specimens – CFRP rods and Bowden cables – illustrated the varieties in constitutive behavior with a focus on bending. The differences between linear elastic, piecewise linear elastic and elastoplastic bending behavior were depicted.

The slender geometry of cables allows for the reduction of the three-dimensional framework of continuum mechanics to one dimension. In Sect. 3, a brief summary of the Cosserat rod theory, which enables the constitutive modeling in terms of the sectional forces and moments of the beam, was given. This reduction not only simplifies the complexity of the model and therefore reduces the numerical effort, but it also corresponds very well to the experiments for beam-like structures. The sectional quantities of the Cosserat rod model correspond (most often) to the quantities measured in the experiments. Therefore, one may directly utilize experimental results as those given in Sect. 2 to deduce suitable constitutive models for Cosserat rods, as demonstrated in the particular examples describing linear elastic, piecewise linear elastic and elastoplastic bending behavior.

References

1. Antman, S.S.: Nonlinear Problems of Elasticity. Springer, Berlin (2005)
2. Balke, H.: Einführung in die Technische Mechanik. Springer, Berlin (2008)
3. Beer, F.P., Johnston, E.R.: Mechanics of Materials. McGraw-Hill, London (1992)
4. Costello, G.A., Phillips, J.W.: Effective modulus of twisted wire cables. J. Eng. Mech. Div. **102**(1), 171–181 (1976)
5. Costello, G.A., Sinha, S.K.: Torsional stiffness of twisted wire cables. J. Eng. Mech. Div. **103**(4), 766–770 (1977)
6. Dörlich, V., Diebels, S., Linn, J.: Investigation of elastoplastic effects of cables under large spatial deformation. Proc. Appl. Math. Mech. **15**, 185–186 (2015)
7. Dörlich, V., Linn, J., Scheffer, T., Diebels, S.: Towards viscoplastic constitutive models for cosserat rods. Arch. Mech. Eng. **63**, 215–230 (2016)
8. Dörlich, V., Česarek, P., Linn, J., Diebels, S.: Experimental investigation and numerical modeling of resultant-based bending plasticity in cables. In: Proceedings of 8th ECCOMAS Thematic Conference on Multibody Dynamics, Prague (2017)
9. Gurtin, M.E.: An Introduction to Continuum Mechanics. Academic Press, New York (1981)
10. Han, S., Bauchau, O.A.: Nonlinear, three-dimensional beam theory for dynamic analysis. In: Multibody System Dynamics, pp. 1–28 (2016)
11. Haupt, P.: Continuum Mechanics and Theory of Materials. Springer Science & Business Media (2013)
12. Hoeft, F., Stephan, T., Hermanns, O.: Eine neue Methode zur vergleichenden örtlichen Beanspruchungsanalyse für Kabel und Schläuche. SIMVEC Berechnung und Simulation im Fahrzeugbau, VDIBerichte **2107**, 297–309 (2010)
13. Knapp, R.H.: Derivation of a new stiffness matrix for helically armoured cables considering tension and torsion. Int. J. Numer. Meth. Eng. **14**(4), 515–529 (1979)
14. Lemaitre, J., Chaboche, J.L.: Mechanics of Solid Materials. Cambridge university press, Cambridge (1994)
15. Linn, J., Lang, H., Tuganov, A.: Geometrically exact Cosserat rods with Kelvin–Voigt type viscous damping. Mech. Sci. **4**(1), 79–96 (2013)
16. Luenberger, D.C.: Linear and Nonlinear Programming. Addison-Wesley Publishing Company, Reading (1984)
17. Mata, P., Oller, S., Barbat, A.H.: Static analysis of beam structures under nonlinear geometric and constitutive behavior. Comput. Methods Appl. Mech. Eng. **196**(45), 4458–4478 (2007)

18. Reissner, E.: On one-dimensional large-displacement finite-strain beam theory. Stud. Appl. Math. **52**, 87–95 (1973)
19. Schneider, F., Linn, J., Hermansson, T., Andersson, F.: Cable dynamics and fatigue analysis for digital mock-up in vehicle industry. In: Proceedings of 8th ECCOMAS Thematic Conference on Multibody Dynamics, Prague (2017)
20. Simo, J.C.: A finite strain beam formulation: the three dimensional dynamic problem - Part I. Comput. Meth. Appl. Mech. Eng. **49**(1), 55–70 (1985)
21. Simo, J.C., Hughes, T.J.R.: Computational Inelasticity. Springer, New York (1998)
22. Timoshenko, S.P., Gere, J.M.: Mechanics of Materials. Van Nostrand Reinhold Company, New York (1972)
23. Truesdell, C., Noll, W.: In: Antman, S.S. (ed.) The Non–linear Field Theories of Mechanics, 3rd edn. Springer, Berlin (2004)
24. Vaz, M.A., Aguiar, L.A.D., Estefen, S.F., Brack, M.: Experimental determination of axial, torsional and bending stiffness of umbilical cables. In: Proceedings of 17th International Conference on Offshore Mechanics and Arctic Engineering (1998)
25. Witz, J.A., Tan, Z.: Rotary bending of marine cables and umbilicals. Eng. Struct. **17**(4), 267–275 (1995)

On Phase Transformation Induced Effects Controlling the Flow Behavior of Ferritic-Martensitic Dual-Phase Steels

A. Fillafer, E. Werner and C. Krempaszky

Abstract In the present work, peculiarities of the macroscopic, initial flow behavior of ferritic-martensitic dual-phase steels and their causes are discussed. For this purpose, results of continuum-micromechanical finite-element simulations on model microstructures are presented. During production of dual-phase steels, a portion of their microstructure, i.e. austenite transforms to martensite and thereby expands. This causes 'transformation induced' residual stresses and plastic strains in their microstructure. These quantities are identified to govern the initial flow behavior of these steels.

1 Introduction

Dual-phase steels (DP-steels) are a group of high strength, low alloy steels well suited for sheet metal forming operations. Their most striking characteristics are continuous yielding behavior (i.e. the absence of a pronounced yield point), high (initial) strain hardening resulting in high strength after forming and appreciable ductility. DP-steels exhibit a coarse-grained microstructure consisting of ferrite and martensite. These microstructures are produced by annealing in the $\alpha + \gamma$-region of the iron-carbon phase diagram and subsequent quenching from the annealing temperature. With respect to mechanical properties they differ from ferritic-pearlitic microstructures in terms of the strong constituent's hardness. Typical pearlite hardness ranges up to roughly 350 HV [1], while in DP-steels, martensite hardness is between 400 and 850 HV [1].

The pioneering publications dealing with DP-steels date back to the end of the 1970s [2–5]. It took only until the end of the 1980s to find the DP-steels in the sheet metal product range of the major steel manufacturers.

A. Fillafer (✉) · E. Werner · C. Krempaszky
Institute of Materials Science and Mechanics of Materials,
Technische Universität München, Boltzmannstraße 15, 85748 Garching, Germany
e-mail: fillafer@wkm.mw.tum.de

© Springer International Publishing AG 2018

H. Altenbach et al. (eds.), *Advances in Mechanics of Materials and Structural Analysis*, Advanced Structured Materials 80,
https://doi.org/10.1007/978-3-319-70563-7_3

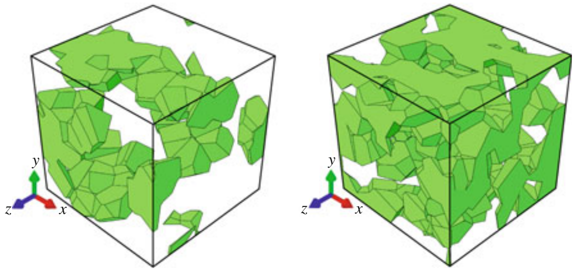

Fig. 1 Microstructures $\boxed{\mathfrak{A}}$ and $\boxed{\mathfrak{B}}$ in their undeformed configuration. Martensite: shaded; ferrite: transparent. The two microstructures exhibit equal phase specific constitutive behavior and differ only in martensite phase fraction P^{M} and consequently in martensite grain arrangement

$\boxed{\mathfrak{A}}$, $P^{\mathrm{M}} = 0.19$
'inclusion'-type martensite

$\boxed{\mathfrak{B}}$, $P^{\mathrm{M}} = 0.39$
'skeleton'-type martensite

The present publication intends to shed light on a few peculiarities of the DP-steel's macroscopic mechanical behavior, which emerge from microstructural effects. For this purpose, selected results of continuum-micromechanical simulations are discussed. The data originate from the two typical, yet artificial microstructures $\boxed{\mathfrak{A}}$ and $\boxed{\mathfrak{B}}$ in Fig. 1. These microstructures differ from each other only in martensite phase fraction and consequently also in martensite phase shape. They were generated by coloring periodically Voronoï-tessellated volume elements, for details see [6, 7].

One of the peculiarities discussed is related to the findings of Erdogan and Priestner [8]. They report on different flow stress in tension and compression of two dual-phase steels. Liedl [9] revisits this observation with the aid of a continuum-micromechanical simulation model, however, fails to explain this tension-compression asymmetry. The present work analyzes the reasons for this failure. It also highlights a requirement, which the study of microstructural field quantities in DP-steels puts on the geometric abstraction of their microstructures.

The employed simulation model [6] resolves field quantities on the grain level. The two phases both are modeled with isotropic elasticity and von Mises plasticity, see Table 1. Periodic boundary conditions are used when solving the field equations within a finite-element framework [10].

During quenching of DP-steels from the annealing temperature, part of their microstructure experiences a plastic transformation strain, as austenite transforms to martensite. It is the aim of the employed continuum-micromechanical simulation model to capture the consequences of this behavior. For this purpose, the martensitic transformation is taken into account via an initial 'transformation step'. This step represents cooling of the initial, stress free microstructures (as in Fig. 1) from 400 °C to 20 °C.[1] During cooling, martensite is assumed to expand isotropically[2] in accordance

---

[1] The martensite-start-temperature is assumed to be 400 °C.

[2] Deviatoric transformation strains are neglected here. Since each martensite grain most probably consists of several martensite variants, deviatoric strain of the grain most likely averages out.

Table 1 Phase specific properties used to model martensite and ferrite, respectively, on a continuum-micromechanical level. 'Strain per temperature' of ferrite conforms to the coefficient of thermal expansion (CTE) of ferritic steels. 'Strain per temperature' of martensite comprises the CTE of ferritic steel and a transformation strain

Property	Unit	Temp. dependence	Ferrite	Martensite
Elastic behavior	/	N/A	Isotropic	Isotropic
Poisson ratio, ν	–	Invariant	0.3	0.3
Young's modulus, E	GPa	Linear	Eq. (1)	Eq. (2)
Yield criterion	/	N/A	von Mises	von Mises
Hardening behavior	/	N/A	Isotropic	Isotropic
Flow rule	/	N/A	Normal to yield surface	Normal to yield surface
Flow stress, σ_f	MPa	Linear/invariant	Eq. (3)	Eq. (4)
Strain per temperature	$\frac{1}{\mathrm{K}}$	Invariant	$\alpha^{\mathrm{F}} = 1.20 \cdot 10^{-5}$	$\tilde{\alpha}^{\mathrm{M}} = -1.08 \cdot 10^{-5}$

with the parameter 'strain per temperature'[3] given in Table 1. This parameter is the sum of the isotropic expansion due to the austenite-martensite transformation and the coefficient of thermal expansion (CTE) of ferritic steels, leading to a negative value of martensite's 'strain per temperature'. Ferrite's 'strain per temperature' is equivalent to the CTE of ferritic steels, as indicated in the table.

The Young's moduli of ferrite and martensite are assumed to be linearly depending on temperature and behave according to

$$E^{\mathrm{F}} = \left(-\frac{8T}{95\,^{\circ}\mathrm{C}} + \frac{3870}{19}\right)\,\mathrm{GPa}, \tag{1}$$

and

$$E^{\mathrm{M}} = \left(-\frac{9T}{95\,^{\circ}\mathrm{C}} + \frac{3950}{19}\right)\,\mathrm{GPa}, \tag{2}$$

within the temperature range $20\,^{\circ}\mathrm{C} \leq T \leq 400\,^{\circ}\mathrm{C}$.

The employed flow stress functions of ferrite and martensite originate from an experimental campaign. Tensile tests on single phase ferritic and martensitic industrial steel grades were conducted at room temperature. The resulting stress-strain-relations were fitted with the generalized-Voce function and were used as input for 'master' flow stress functions (for details see [6]). The here employed ferrite and martensite flow stress functions were picked from the latter and are quite average in that case. Ferrite at 400 °C is assumed to exhibit half it's room temperature flow stress. With an assumed linear temperature dependence, its flow stress function is

---

[3] This parameter represents a volumetric expansion (transformation strain) of 1.23%, corresponding to the value used by Liedl [9, 11]. Another value representing an expansion of 3.05% delivers results qualitatively similar to those given in the present contribution [7].

$$\sigma_\mathrm{f}^\mathrm{F} = \left(\frac{39}{38} - \frac{T}{760\,°\mathrm{C}}\right) \cdot \left[228 + \left(145 + 430\,\varepsilon_\mathrm{eq}^\mathrm{pl}\right) \cdot \left(1 - e^{-24\,\varepsilon_\mathrm{eq}^\mathrm{pl}}\right)\right] \mathrm{MPa}, \tag{3}$$

for the temperature $20\,°\mathrm{C} \le T \le 400\,°\mathrm{C}$ and with $\varepsilon_\mathrm{eq}^\mathrm{pl}$ as the plastic equivalent strain.

The employed martensite flow stress function is assumed to be temperature invariant between 20 °C and 400 °C and is given by

$$\sigma_\mathrm{f}^\mathrm{M} = \left[966 + \left(346 + 7486\,\varepsilon_\mathrm{eq}^\mathrm{pl}\right) \cdot \left(1 - e^{-590\,\varepsilon_\mathrm{eq}^\mathrm{pl}}\right)\right] \mathrm{MPa}. \tag{4}$$

2 Phase Transformation-Induced Stresses and Strains

The austenite to martensite transformation, which happens only in a fraction of the DP-steels microstructure, causes local elastic strains (residual stresses), as well as local plastic strains. In the following, these quantities will be addressed with the prefix 'tr. induced' (transformation induced).

A graphical representation of microstructural, tr. induced plastic equivalent strains is depicted in Fig. 2. Two microstructures with 10 and 49% martensite phase fraction, respectively, are shown. The plastic strains $\varepsilon_\mathrm{eq}^\mathrm{pl}$ appear to be high in ferrite at regions close to the ferrite/martensite phase boundaries, as well as in narrow ligaments of ferrite. As discussed below, the magnitude of these strains is primarily governed by martensite phase fraction and its expansion and only secondarily by the arrangement of the martensite grains in the microstructure.

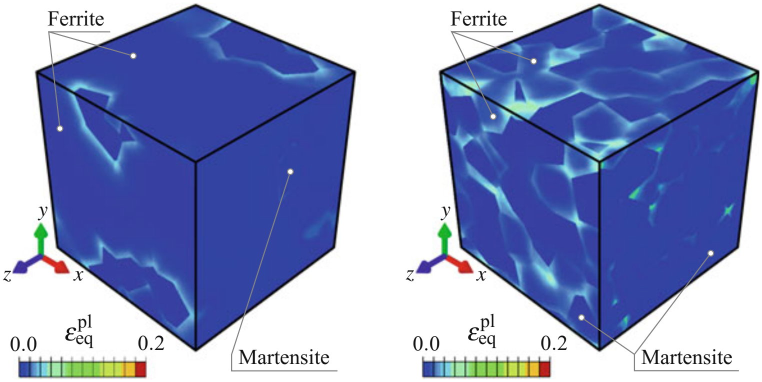
Ferrite
y
z
x
$\varepsilon_\mathrm{eq}^\mathrm{pl}$
0.0
0.2
Martensite
Ferrite
y
z
x
$\varepsilon_\mathrm{eq}^\mathrm{pl}$
0.0
0.2
Martensite

Fig. 2 Transformation induced plastic equivalent strain in microstructures with 10% (**left**, 'inclusion'-type) and 49% (**right**, 'skeleton'-type) martensite phase fraction (note: they are not the same as microstructures $\boxed{\mathfrak{A}}$ and $\boxed{\mathfrak{B}}$ in Fig. 1)

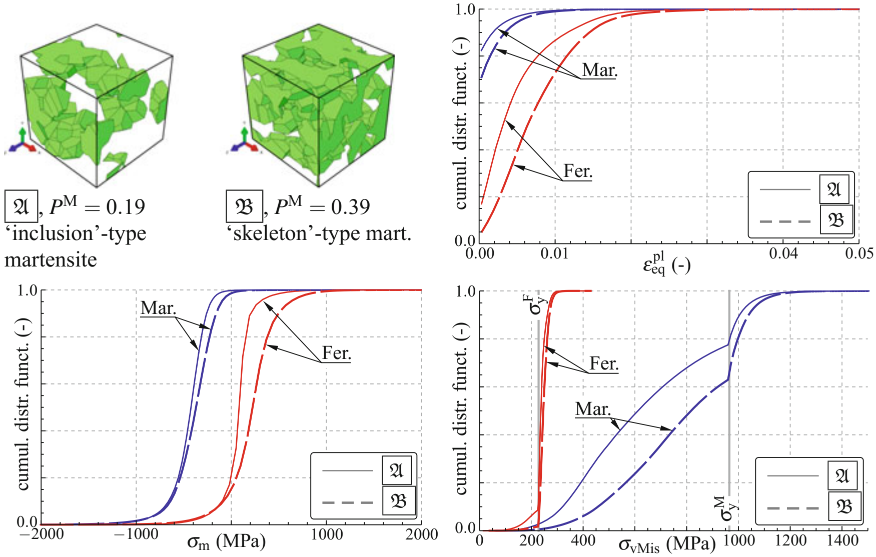
$\boxed{\mathfrak{A}}$, $P^{\mathrm{M}} = 0.19$ 'inclusion'-type martensite

$\boxed{\mathfrak{B}}$, $P^{\mathrm{M}} = 0.39$ 'skeleton'-type mart.

Fig. 3 Cumulative distribution functions of phase transformation induced field quantities in ferrite and martensite of microstructures $\boxed{\mathfrak{A}}$ and $\boxed{\mathfrak{B}}$. The individual graphs show plastic equivalent strain $\varepsilon_{\mathrm{eq}}^{\mathrm{pl}}$, hydrostatic stress σ_{m} and von Mises stress σ_{vMis}

Tr. induced plastic equivalent strains are depicted in Fig. 3 (upper right) in processed form. The diagram shows the phase specific cumulative distribution functions in microstructures $\boxed{\mathfrak{A}}$ and $\boxed{\mathfrak{B}}$. It can be seen that nearly all of ferrite (ca. 85–95%) experiences tr. induced plastic strains (of various amounts, roughly up to 2%). But this also applies to a significant fraction of martensite (ca. 20–30%, plastic strains up to roughly 1%). The tr. induced plastic equivalent strains averaged over the microstructure's volume is about 0.4% in case of microstructure $\boxed{\mathfrak{A}}$ and about 0.5% in case of microstructure $\boxed{\mathfrak{B}}$.

A field quantity important in the study of (microstructural) damage—although this is usually not encountered in the as-quenched condition—is the hydrostatic (tensile) stress component. It should be noted, that within the framework of the von Mises plasticity model employed here, hydrostatic stress does not lead to plastic deformation. The phase specific cumulative distribution functions of tr. induced hydrostatic stress σ_{m} in microstructures $\boxed{\mathfrak{A}}$ and $\boxed{\mathfrak{B}}$ are shown in Fig. 3 (lower left). As one expects, martensite is mostly subjected to hydrostatic compression (due to its expansion), whereas the opposite is true for ferrite. In the two microstructures, ferrite is on average loaded with roughly 80 and 220 MPa and martensite with roughly −430 and −380 MPa, respectively. The hydrostatic tension peaks in ferrite reach about 1 GPa. These only act on a very limited volume, but with such a high all-round tensile stress, formation of micro-voids—although hypothetical—seems logical. The hydrostatic stress averaged over the microstructure's volume equals zero in both cases, since up to this point no external loads are applied to the microstructures.

The field quantity driving plastic deformation is the deviatoric part of the stress tensor. This part shall be represented here in a simplified form by the scalar von Mises stress σ_{vMis}. The phase specific cumulative distribution functions of the tr. induced von Mises stress in microstructures $\boxed{\mathfrak{A}}$ and $\boxed{\mathfrak{B}}$ are shown in Fig. 3 (lower right). The vertical lines in the graph indicate the phase specific yield stress σ_{y}. The kinks in each distribution at these lines separate the yielded (and strain hardened) portion of each phase from the not yielded one. The von Mises stresses in the yielded portions reach about 400 MPa in ferrite and 1300 MPa in martensite. The von Mises stress averaged over the microstructure's volume is about 310 MPa in case of microstructure $\boxed{\mathfrak{A}}$ and 470 MPa in case of microstructure $\boxed{\mathfrak{B}}$.

The previously shown results are based on microstructures with polyhedral grains (Voronoï tessellated), as shown in Fig. 1. These geometries are—although quite simple—one step closer towards realistic grain shapes than primitive geometries such as cubes, spheres, etc.

To demonstrate the usefulness of polyhedral grains as used in our work, let us alternatively model martensite as spherical inclusions, isolated from each other, in a ferritic matrix. In the as-quenched condition (i.e. after the transformation step), martensite in such a microstructure would be subjected to hydrostatic compression only and the according cumulative distribution function would resemble a step-function. In such a martensite geometry, no deviatoric stresses, consequently no von Mises stress and no plastic strains would occur. This is clearly contradicted by the results in Fig. 3.

As another example, consider modeling a two-dimensional microstructure with circular martensite inclusions in a ferritic matrix. Regardless of the common boundary condition applied in the third direction, the hydrostatic stress in martensite will not resemble a step function. Although at a first glance, such a two-dimensional model might seem to be compatible with the first example, the field variables in the as-quenched condition will differ markedly.

Returning to the results in Fig. 3, it should be kept in mind that the distribution of field quantities is a direct result of the martensite formation and the results shown correspond to the as-quenched condition. In industrial practice, as-quenched DP-steels are sometimes subjected to an overaging treatment (tempering at roughly 250−300 °C). Tr. induced residual stresses might diminish or even vanish during this step due to recovery and/or diffusion controlled aging mechanisms (involving diffusion of C and N at this temperature [1]). Plastic strains (strain hardening) on the other hand are inherent to the microstructure and will most probably not be influenced at such low temperatures (diffusion of Fe is insignificant at these temperatures [1]).

3 Phase Transformation-Induced Macro-Scale Effects

Figure 4 shows results of virtual macroscopic uniaxial tension and compression tests (in x-direction) performed with microstructures $\boxed{\mathfrak{A}}$ and $\boxed{\mathfrak{B}}$. Each graph shows the stress-strain-relations with and without considering tr. induced stresses and strains. In the following, the according results are distinguished by the prefix 'tr. strained' (transformation strained) and 'unprestrained'.

The stress-strain-relations of unprestrained microstructures behave according to the theory of Fischmeister and Karlsson [3], which states that a microstructure, composed of a soft and a hard phase of equal elastic properties, yields when the softer phase's yield stress is reached. This theory applies to tension as well as to compression. Thus, martensite hardness and phase fraction do not influence the yield point of the two-phase composite. The results in the unprestrained case in Fig. 4 accurately reproduce this behavior.[4] According to Fischmeister's theory, in the unprestrained case the microstructural stress distribution is throughout homogeneous,[5] until ferrite starts to yield.

By comparing the stress-strain-relations of the unprestrained microstructures $\boxed{\mathfrak{A}}$ and $\boxed{\mathfrak{B}}$ in Fig. 4, it can be seen that martensite content influences strain hardening. This impacts $R_{\mathrm{p}0.2}$, which is in accordance with literature [12].

By comparing the individual stress-strain-relations in the tr. strained and unprestrained cases in Fig. 4, in the former case a gradual transition from the elastic to the plastic regime and no pronounced yield point can be observed. Also known as continuous yielding behavior, this is a desirable property in forming technology. Due to this behavior, $R_{\mathrm{p}0.2}$ is reduced. By comparing the stress-strain-relations of the tr. strained microstructures $\boxed{\mathfrak{A}}$ and $\boxed{\mathfrak{B}}$, it seems that the amount of martensite does not have a significant impact on the shape of the stress-strain-relations in the regime of continuous yielding. Continuous yielding vanishes at roughly 1% of macroscopic strain, in tension as well as in compression.

It has already been mentioned, that martensite expansion causes various levels of strain hardening (plastic strain) in DP-steel microstructures (mostly in ferrite). With this in mind, continuous yielding is easily comprehended. As the microstructure is mechanically loaded, the stress distribution is quite homogeneous (due to similar elastic properties of ferrite and martensite). The first zones to enter the plastic regime are the least strain hardened parts of ferrite. As these harden, the plastic zones gradually reach the stronger parts of ferrite and eventually also martensite. On a macroscopic scale, this manifests as a gradual transition from elastic to plastic deformation, also termed as micro-yielding [13].

---

[4] As given in Eq. (3), the employed ferrite yields at room temperature at 228 MPa. The unprestrained results in Fig. 4 show the yield point at approximately 215 MPa. This little mismatch is induced by a numerical artifact (coarse solver step-size).

[5] Except for small fluctuations due to the slightly differing Young's moduli chosen for ferrite and martensite.

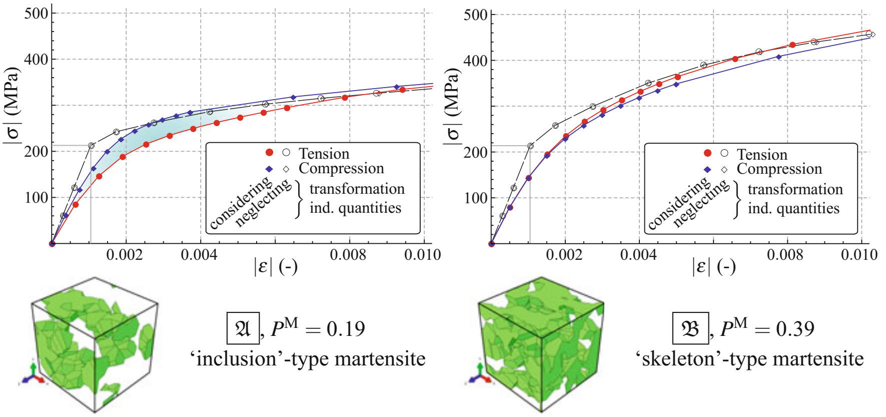

$\boxed{\mathfrak{A}}$, $P^{\mathrm{M}} = 0.19$
'inclusion'-type martensite

$\boxed{\mathfrak{B}}$, $P^{\mathrm{M}} = 0.39$
'skeleton'-type martensite

Fig. 4 Macroscopic tensile and compressive stress, respectively, of microstructures $\boxed{\mathfrak{A}}$ and $\boxed{\mathfrak{B}}$ as a function of macroscopic strain ε. Solid curves result when preceding, phase transformation induced stresses and strains are considered. Dashed curves result when the latter are neglected. The shaded zone in the left graph indicates higher initial flow stress in compression than in tension of the microstructure with 'inclusion'-type martensite

This explanation should, however, be refined at this point. From the results in Fig. 4, a primary and a secondary influence on continuous yielding may be deduced:

- Both tr. strained microstructures exhibit continuous yielding in tension as well as in compression. Hence, the quantity primarily causing it must be tr. induced, but cannot be signed. This points to the tr. induced plastic equivalent strain (strain hardening), a quantity which bears no sign per definition. This deduction is in accordance with the straightforward explanation given above.
- During yielding, microstructure $\boxed{\mathfrak{A}}$ behaves differently in tension and compression ('tension-compression-asymmetry', see the shaded zone in Fig. 4, left). Consequently, a secondary influence on continuous yielding exists. This influence shows by reversing the sign of the macroscopic stress. Thus, the secondary cause must be a signed quantity, which points to the tr. induced residual stresses. In the von Mises plasticity model employed here, plastic strain is solely influenced by deviatoric stresses, not by the hydrostatic stress component. Hence, tr. induced deviatoric stresses (here represented by the von Mises stress) exert the secondary influence on the continuous yielding behavior.

  In contrast to the primary influence, the secondary one might diminish or even fade away during aging if residual stresses are reduced.
- A detailed study [7] reveals why this tension-compression-asymmetry is not recognizable in the stress-strain relations of microstructure $\boxed{\mathfrak{B}}$. In a microstructure with a large martensite phase fraction, martensite must be distinguished into two types. As shown by Lee and Gurland [14], a phase can be separated into isolated and interconnected grains of that phase. While microstructure $\boxed{\mathfrak{A}}$ consists mainly of isolated grains of martensite embedded in ferrite, microstructure $\boxed{\mathfrak{B}}$ exhibits

martensite grains forming a skeleton. Obviously, in case of microstructures percolated by a martensite skeleton, the tension-compression-asymmetry vanishes. Furthermore, there is a gradual transition of this asymmetry as martensite changes its character from discontinuous (inclusion-type) to continuous (skeleton-type).

By comparing the elastic regimes of the individual stress-strain-relations in the tr. strained and unprestrained cases in Fig. 4, a lower Young's modulus in the tr. strained case is obvious. This effect was studied in detail by Liedl [9]. It can be explained by referring to Fig. 3, lower right. Nearly all of ferrite in both microstructures is subjected to tr. induced von Mises stress higher than ferrite's yield strength. Consequently, the yielded material is loaded with the local flow stress. Applying even a minimal macroscopic load,[6] these zones react with plastic, rather than with comparatively small elastic deformation. Hence, the microstructure is more compliant (less stiff) under a macroscopic load. Also this effect diminishes with aging the material. Liedl illustrates this with the aid of experiments studying the anelastic behavior of the material as a function of aging time [9].

The tension-compression-asymmetry of microstructure $\boxed{\mathfrak{A}}$ results in a higher initial flow stress in compression than in tension. Erdogan and Priestner [8] report such a behavior already in 1999 for dual-phase steels with 18 and 25% of martensite (most probably of inclusion-type). In 2002, Liedl [9] tries to capture this effect with continuum-micromechanical simulations in which a martensite grain is modeled as a Kelvin-Tetrakaidecahedron (a polyhedron of almost spherical shape). Liedl's simulation model fails to reproduce the tension-compression-asymmetry. The discussion in Sect. 2 highlights that the shape of the martensite regions/grains has a significant influence on the transformation induced stresses. In case of isolated, spherical martensite (as approximately assumed by Liedl), no tr. induced von Mises stresses occur. These, however, are responsible for the tension-compression-asymmetry.

4 Microscopic Effects of Macro-Deformation

In this section, the uniaxial tension and compression tests of the tr. strained microstructures $\boxed{\mathfrak{A}}$ and $\boxed{\mathfrak{B}}$ will be revisited. By analyzing **phase averaged** stresses throughout the deformation, the cause for the tension-compression-asymmetry will be explained in more detail.

The phase averaged hydrostatic and von Mises stresses during the transformation step and the subsequent tensile and compressive deformation are depicted in Fig. 5. The phase averaged von Mises stress of the individual microstructures shows a notable difference. This is highlighted as the shaded zone for microstructure $\boxed{\mathfrak{A}}$ (Fig. 5, center left). The highlighted zone shows that inclusion-type martensite experiences a stress reduction (i.e. 'springback') during the initial tensile deformation (until about 1% of macroscopic strain is reached). This stress reduction manifests as

---

[6] Unless the macroscopic load reduces the local von Mises stress.

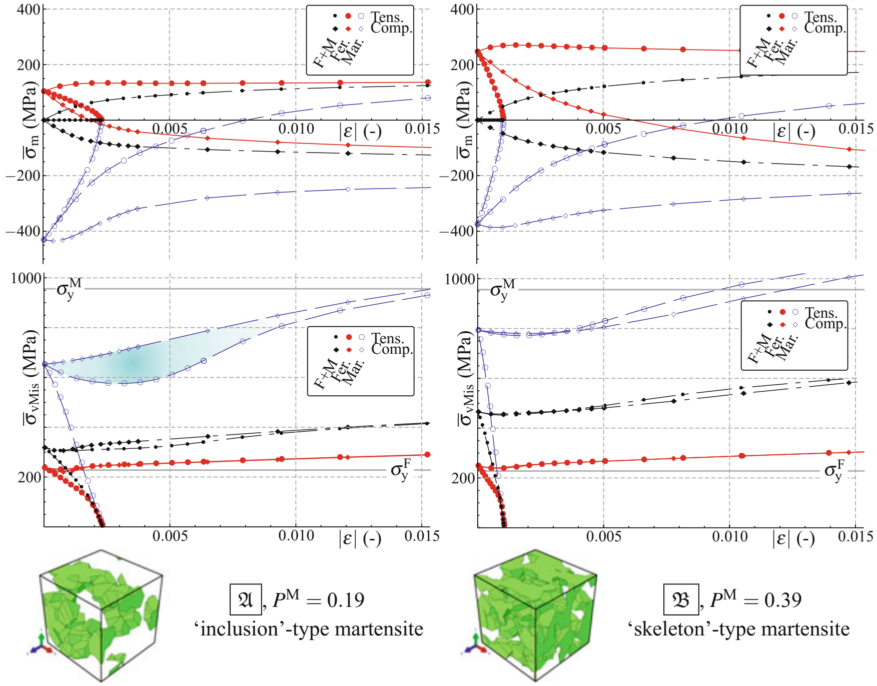

$\boxed{\mathfrak{A}}$, $P^{\mathrm{M}} = 0.19$
'inclusion'-type martensite

$\boxed{\mathfrak{B}}$, $P^{\mathrm{M}} = 0.39$
'skeleton'-type martensite

Fig. 5 Phase averaged hydrostatic stress $\overline{\sigma}_{\mathrm{m}}$ (**top**) and phase averaged von Mises stress $\overline{\sigma}_{\mathrm{vMis}}$ (**center**) in microstructures $\boxed{\mathfrak{A}}$ and $\boxed{\mathfrak{B}}$ as a function of macroscopic tensile and compressive strain ε, respectively. The curve-segments in the very left of the graphs result from martensite expansion ('transformation step'), the curve segments from left to right result from the macroscopic deformation. The shaded zone in the lower left graph indicates initial 'springback' of 'inclusion'-type martensite when the microstructure is subjected to tension

a lower flowstress in Fig. 4 in tension than in compression. There is no evidence of this springback in case of skeleton-type martensite (Fig. 5, center right). This effect is obviously provoked, if a direct load transfer from martensite grain to martensite grain is not possible and is interrupted by ferrite, as in case of inclusion-type martensite.

In contrast to the von Mises stress, the phase averaged hydrostatic stress (Fig. 5, top graph) shows no qualitative difference between both microstructures and hence martensite types. This again highlights that solely the deviatoric stress component is responsible for the tension-compression-asymmetry.

The phase averaged hydrostatic stress allows to derive approximately the macroscopic strain, at which tr. induced effects vanish. In the tensile test, this strain may be defined as the strain at which the sign of the phase averaged hydrostatic stress in martensite reverses. For both microstructures, this happens between 0.8 and 1% of macroscopic strain, which is in accordance with the observations discussed above.

5 Conclusions

Due to the special processing route of ferritic-martensitic dual phase steels, a fraction of the ferritic-austenitic microstructure transforms to martensite and thereby expands. This typically leads to microstructural **residual stresses and plastic strains** (transformation induced quantities). Due to the magnitude of martensite expansion, these quantities are not negligible and manifest themselves in form of macro-scale effects. Residual von Mises stresses have a magnitude of the individual phases' yield stress, while in average, plastic equivalent strains have a magnitude of roughly 0.5%.

Transformation induced quantities should be distinguished between diminishable and inherent ones. The former are stresses, which may be reduced by aging mechanisms (C and N diffusion) or macroscopic plastic deformation. The second category are plastic strains (strain hardening) which remain unchanged unless the microstructure is plastically deformed or subjected to elevated temperatures.

Macro-scale effects in DP-steels caused by transformation induced quantities may be summarized as follows

- **Continuous yielding behavior** is primarily caused by transformation induced plastic strains (local strain hardening in the microstructure). Secondarily, however, it is influenced by transformation induced stresses (see below).
- The **reduced Young's modulus** typically encountered with unaged DP-steels is caused by transformation induced stresses. These may be reduced by natural or artificial aging, restoring the Young's modulus to the steels' stress-free value.
- The **tension-compression-asymmetry** (i.e. higher initial flow stress in compression than in tension) of microstructures with 'inclusion'-type martensite is caused by a 'springback' of transformation induced deviatoric stresses in martensite. These may be reduced by natural or artificial aging. The asymmetry is governed by martensite (grain) shape and does not occur in microstructures with 'skeleton'-type martensite.
- Transformation induced effects may be observed on the macro-scale until they fade away at roughly 1% of macroscopic strain because of plastic deformation. In other words, transformation induced effects impact strongly the elastic, yield and initial flow behavior of DP-steels, but are negligible at higher plastic strains.

Acknowledgements The authors express their appreciation to *B. Regener*, *T. Taxer* and *R. Wesenjak*. Several code scripts they shared contributed to the results presented. *Y. Granbom* of *SSAB* and *A. Pichler* of *voestalpine* generously provided industrial steel samples for model input and validation.

The *Research Fund for Coal and Steel* supported part of this work through grant *RFSR-CT-2008-00027.*

References

1. Läpple, V.: Wärmebehandlung des Stahls. Verlag Europa-Lehrmittel, Haan-Gruiten (2006)
2. Rashid, M.S.: GM 980X-A unique high strength sheet steel with superior formability, SAE Technical Paper 760206. Society of Automotive Engineers Inc., Warrendale, PA (1976)
3. Fischmeister, H., Karlsson, B.: Plastizitätseigenschaften grob-zweiphasiger werkstoffe. Zeitschrift für Metallkunde **68**, 311–327 (1977)
4. Davies, R.G.: Influence of martensite composition and content on the properties of dual phase steels. Metall. Trans. A **9A**, 671–679 (1978)
5. Davies, R.G.: The deformation behavior of a vanadium-strengthened dual phase steel. Metall. Trans. A **9A**, 41–52 (1978)
6. Fillafer, A., Krempaszky, C., Werner, E.: On strain partitioning and micro-damage behavior of dual-phase steels. Mater. Sci. Eng. A **614**, 180–192 (2014)
7. Fillafer, A.: Fließ- und Mikroschädigungsverhalten ferritisch martensitischer Dualphasenstähle, Ph.D thesis, Technische Universität München (2015)
8. Erdogan, M., Priestner, R.: Effect of epitaxial ferrite on yielding and plastic flow in dual phase steel in tension and compression. Mater. Sci. Technol. **15**, 1273–1284 (1999)
9. Liedl, U.: Anfangsverformung- und Alterungsverhalten von Dual-Phasen Stahl, Ph.D thesis, Technische Universität München (2003)
10. Abaqus. Manuals, Version 6.10EF. Dassault Systèmes Simulia Corp. (2010)
11. Liedl, U., Traint, S., Werner, E.A.: An unexpected feature of the stress-strain diagram of dual-phase steel. Comput. Mater. Sci. **25**, 122–128 (2002)
12. Kim, N.J., Thomas, G.: Effects of morphology on the mechanical behavior of a dual phase fe/2si/0.1c steel. Metall. Trans. A **12A**, 483–489 (1981)
13. Daxner, T.: Finite element modelling of cellular materials. In: Altenbach, H., Öchsner, A. (eds.) Cellular and Porous Materials in Structures and Processes, pp. 47–106. Springer, Wien (2010)
14. Lee, H.C., Gurland, J.: Hardness and deformation of cemented tungsten carbide. Mater. Sci. Eng. **33**, 125–133 (1978)

Hygro- and Thermo-Mechanical Modeling of Wood at Large Deformations: Application to Densification and Forming of Wooden Structures

Robert Fleischhauer and Michael Kaliske

Abstract The contribution at hand provides a basis for modeling hygro- and thermo-mechanical processes, especially at large deformations. Therefore, hygro- and thermo-mechanical fundamentals of wood are introduced under consideration of moisture, temperature and displacement dependent processes. The influence of moisture on the density of wood is taken into account as well as a characterization of the interaction of temperature and moisture. Finite element formulations are derived,s together with constitutive laws, as a basis for the numerical solutions. A verification as well as a validation of the specific formulations for the hygro- and thermo-mechanical behavior of different wood species is presented. Finally, the applicability of the proposed finite element descriptions is demonstrated at the densification and forming process of wood.

1 Introduction

Wood and wooden structures are characterized by a complex micro-structure. The micro-structure can be identified by typical properties at the sub-microscopic, the microscopic and macroscopic length scale. The macroscopic properties are determined by the vessel structure, tree ring width as well as by heartwood and sapwood. Grain orientation, length of the grains, thickness of the grain walls, proportion of tissue and dimensions of tissue are the characteristic properties at the microscopic length scale. While the thickness of the cell walls and the proportion of lignin within the cell walls are influencing the sub-microscopic properties, see [40].

Due to grain orientation, wood is generally considered as an anisotropic material, see e.g. [2, 30]. Exemplarily, uniaxial test data are given in Figs. 1 and 2 for two different species, that undergo small to finite deformations, see e.g. [8, 11,

---

R. Fleischhauer · M. Kaliske (✉)
Institute for Structural Analysis, Technische Universität Dresden, Dresden, Germany
e-mail: michael.kaliske@tu-dresden.de

R. Fleischhauer
e-mail: robert.fleischhauer@tu-dresden.de

© Springer International Publishing AG 2018

H. Altenbach et al. (eds.), *Advances in Mechanics of Materials and Structural Analysis*, Advanced Structured Materials 80,
https://doi.org/10.1007/978-3-319-70563-7_4

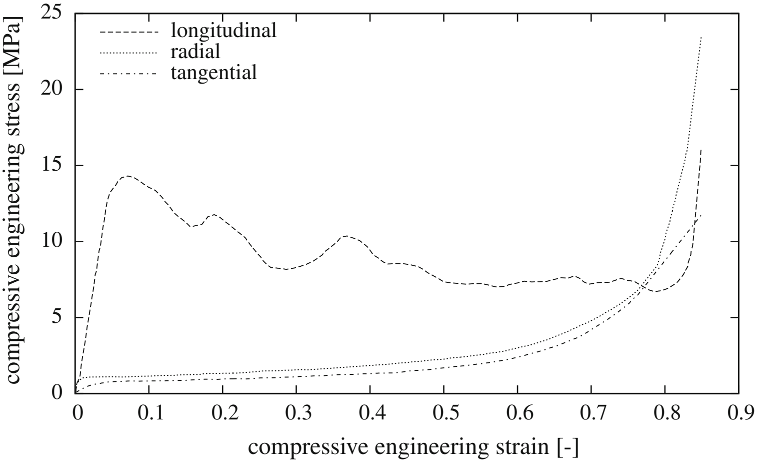

Fig. 1 Compression test results of balsa wood (*Ochroma Pyramidale*) at finite deformations (taken from [17]), depicting the grain orientation dependent material response

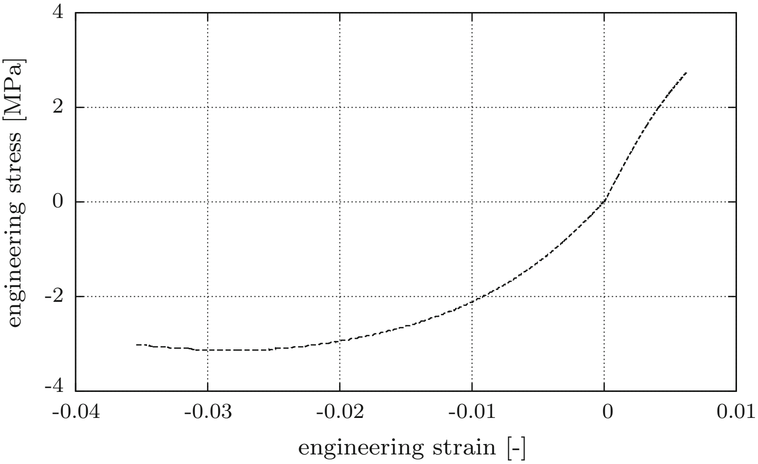

Fig. 2 Experimental result of spruce wood (*Picea Abies*) at small deformations (taken from [31]), depicting the tensile and compressive material response tangential to the grain

16, 17, 25, 31, 34]. Wood can also be considered to be a capillary porous media, compare [29], which is strongly influenced by its moisture content. Due to the micro-structure, moisture can be bound inside the cell walls and transported through the micro-structure by transport mechanisms, which influence the mechanical behavior of wooden structures, see e.g. [45, 46, 56].

Different approaches to model the inelastic effects of wood at small deformations are existing, see e.g. [28, 33, 41, 42]. These inelastic effects are e.g. viscosity and elasto-plasticity as time-dependent and rate-independent or rate-dependent processes. Further developments aim at a coupling between the mechanical field and the moisture content, see [4, 5, 22, 24, 27, 43, 44]. Multi-Fickian approaches are currently under development in order to capture moisture dependent phenomena in wood, see e.g. [14, 15]. An overview and discussion of moisture transport in wood is given in [13]. In [1, 55], the temperature field is taken into account for modeling of e.g. drying processes of wood. Different homogenization approaches are applied to wood, motivated by different structural properties at different length scales, see e.g. [3, 9, 10].

The proposed approach aims at modeling inelastic mechanical phenomena, neglecting the viscosity of wood but considering bound water and a change of the inner moisture content of wood. Additionally, temperature dependent finite deformation processes are accounted for within the proposed formulation, in order to capture a wide and general application range, such as densification, molding or forming of wood.

These transformation processes account for the improvement of the intrinsic wood properties with respect to form and functionality and are not restricted to small deformation ranges. Hygro-thermo-mechanical processing techniques enable wood to be competitive compared to other construction materials, see e.g. [47]. In contrast to existing models, the main aim of the theoretical and numerical approach at hand is to consider such a wide range of applications and to provide engineering tools to simulate hygro-thermo-mechanical processes of wood at finite deformations.

2 Hygro- and Thermo-Mechanical Fundamentals of Wood

This section introduces the basic governing system of partial differential equations, in order to numerically model the hygro-thermo-mechanical behavior of wood and wooden structures. The kinematics used as well as the balance principles of such deformation processes are introduced.

2.1 Kinematics at Finite Deformations, Temperature and Moisture Content

A continuum setting e.g. of a wooden structure B is assumed, where B is composed of material points $P \in B$, such that they are identically connected with the domain $\mathcal{B}$ in the Euclidean space $\mathbb{R}^3$. Observing a material point P while B moves, leads to the definition of the current position $\boldsymbol{x} = \boldsymbol{\chi}(P, t)$, where $\boldsymbol{\chi}$ is the configuration as a bijective mapping of $P \in B$ onto $\boldsymbol{x} \in \mathbb{R}^3$. The current configuration $\mathcal{B}_t = \boldsymbol{\chi}_t(B) \subset \mathbb{R}^3$ is a mapping of B onto the Euclidean space at current time t. At a fixed time t_0, B possesses a usually stress-free state with a homogeneous temperature and moisture distribution. The mapping $\mathcal{B}_0 = \boldsymbol{\chi}_0(B) \subset \mathbb{R}^3$ introduces the reference configuration

$\mathcal{B}_0$ at t_0, with the reference position $\boldsymbol{X} = \boldsymbol{\chi}(P, t_0)$. The displacement vector

$$\boldsymbol{u} := \boldsymbol{x} - \boldsymbol{X} \tag{1}$$

is expressed as the difference between the current and the reference position. Taking the derivative

$$\boldsymbol{F} := \operatorname{Grad} \boldsymbol{x} = \frac{\partial \boldsymbol{x}}{\partial \boldsymbol{X}}, \tag{2}$$

the deformation gradient $\boldsymbol{F}$ with a determinant $J = \det \boldsymbol{F}$ is defined. Subsequently, the right Cauchy Green deformation tensor

$$\boldsymbol{C} = \boldsymbol{F}^T \boldsymbol{g} \boldsymbol{F} \tag{3}$$

is introduced, where $\boldsymbol{g}$ denotes the current metric in its covariant representation.

The absolute temperature is expressed as θ. A measurement of θ in Kelvin [K] leads to the non-zero property $\theta > 0$ for the absolute temperature. Considering the reference configuration $\mathcal{B}_0$, usually characterized by a homogeneous temperature distribution, the absolute reference temperature θ_0 at t_0 for $\mathcal{B}_0$ is defined. Any change of temperature e.g. due to a change of the energy in the system under observation is subsequently depicted via

$$\vartheta := \theta - \theta_0, \tag{4}$$

where ϑ is the temperature change. Similarly, the absolute moisture content ϕ of e.g. a wooden structure is introduced for any point $\boldsymbol{x} \in \mathcal{B}_t$ and is measured as a relation of the mass of bound water versus the mass of the dry wood [kg/kg]. Considering $\mathcal{B}_0$ as the reference configuration with a unique distribution of moisture content ϕ_0 within B at t_0, any change of moisture content

$$\varphi := \phi - \phi_0 \tag{5}$$

at $\boldsymbol{x} \in \mathcal{B}_t$ can be formulated.

In the following descriptions, the logarithmic strain measure, compare [39],

$$\boldsymbol{\varepsilon} = \frac{1}{2} \ln \boldsymbol{C} \tag{6}$$

is used. The multiplicative split of the deformation gradient into

$$\boldsymbol{F} = \boldsymbol{F}^E \boldsymbol{F}^P \boldsymbol{F}^\vartheta \boldsymbol{F}^\varphi, \tag{7}$$

compare [35], introduces an elastic part ($\boldsymbol{F}^E$), a hygric part ($\boldsymbol{F}^\varphi$), a thermal part ($\boldsymbol{F}^\vartheta$), and a plastic part ($\boldsymbol{F}^P$) of deformation. The related intermediate configurations are schematically shown in Fig. 3. The hygric intermediate configuration can be obtained by applying a change of moisture at reference temperature and

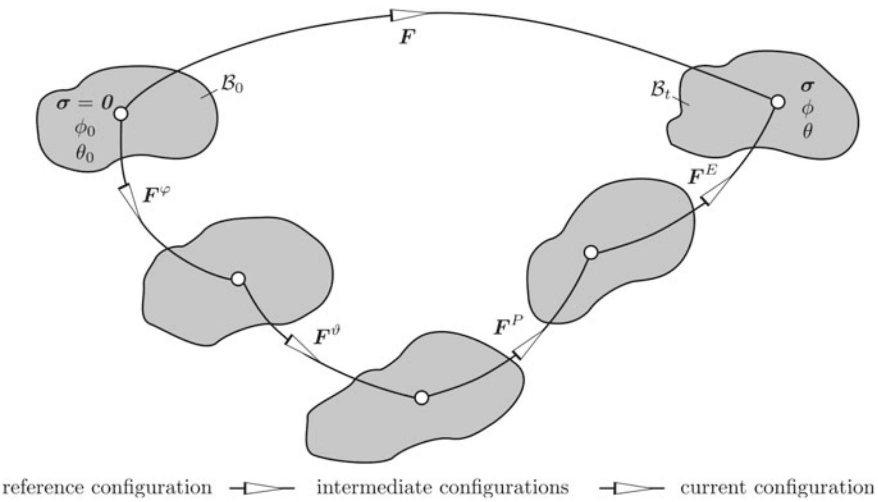
$\boldsymbol{F}$
$\boldsymbol{\sigma} = \boldsymbol{0}$
ϕ_0
θ_0
$\mathcal{B}_0$
$\mathcal{B}_t$
$\boldsymbol{\sigma}$
ϕ
θ
$\boldsymbol{F}^{\varphi}$
$\boldsymbol{F}^{\vartheta}$
$\boldsymbol{F}^{P}$
$\boldsymbol{F}^{E}$
reference configuration
intermediate configurations
current configuration

Fig. 3 Schematic representation of the multiplicative decomposition of the deformation gradient and the intermediate configurations introduced

de-stressing the current configuration to zero. The thermal intermediate configuration at a changed moisture content is achieved by a non-zero temperature change and a de-stressed current configuration. The plastic intermediate configuration is obtained by elastic de-stressing of the current configuration at a given change of moisture and temperature. The plastic intermediate configuration is not unique, since material rotations can change its shape but keeping it unstressed. Therefrom, $\boldsymbol{F}^E$ and $\boldsymbol{F}^P$ are not uniquely defined. For extensive discussions about elastic-plastic decomposition of the deformation gradient at finite deformations, the reader is referred to e.g. [20, 36, 48] and references therein. Now it is possible to express the total logarithmic deformation of P as

$$\frac{1}{2}\ln \boldsymbol{C} = \frac{1}{2}\ln \boldsymbol{F}^{\varphi^T}\boldsymbol{F}^{\vartheta^T}\boldsymbol{F}^{P^T}\boldsymbol{F}^{E^T}\boldsymbol{g}\boldsymbol{F}^{E}\boldsymbol{F}^{P}\boldsymbol{F}^{\vartheta}\boldsymbol{F}^{\varphi}, \tag{8}$$

$$\frac{1}{2}\ln \boldsymbol{C} \approx \boldsymbol{\varepsilon}^E + \boldsymbol{\varepsilon}^P + \boldsymbol{\varepsilon}^\vartheta + \boldsymbol{\varepsilon}^\varphi. \tag{9}$$

Due to the evaluation of the logarithm, using the spectral decomposition within the eigenspace of the appropriate quantity, Eq. (9) is not completely equal to Eq. (8), as detailed discussed in [39]. The additive structure of the split

$$\boldsymbol{\varepsilon}^E = \boldsymbol{\varepsilon} - \boldsymbol{\varepsilon}^P - \boldsymbol{\varepsilon}^\vartheta - \boldsymbol{\varepsilon}^\varphi \tag{10}$$

of the total deformation is further used as the basis for the constitutive formulations. $\boldsymbol{\varepsilon}^\vartheta$ depicts the part of the deformation, that arises from a change of temperature and $\boldsymbol{\varepsilon}^\varphi$ is the moisture induced deformation. $\boldsymbol{\varepsilon}^E$ and $\boldsymbol{\varepsilon}^P$ are the elastic and plastic logarithmic deformations, respectively. The advantage of this approach is a small strain like kinematic, which is able to account also for large deformations.

2.2 Stress Measures, Thermal and Hygric Quantities

Considering a stress vector $\boldsymbol{t}$ at the surface $\partial\mathcal{B}_t$ of the current configuration, the Cauchy stress theorem postulates an infinitesimal surface force $\boldsymbol{t}\mathrm{d}a$ according to

$$\boldsymbol{t}\mathrm{d}a := \boldsymbol{\sigma}\boldsymbol{n}\mathrm{d}a, \tag{11}$$

where $\boldsymbol{n}$ is the current normal at the material point $\boldsymbol{x} \in \partial\mathcal{B}_t$ directing outward from the surface. Since, the configuration $\mathcal{B}_t$ may be any subdomain of the body under observation, $\boldsymbol{\sigma}$ is defined for any point $\boldsymbol{x} \in \mathcal{B}_t$. The Cauchy stress $\boldsymbol{\sigma}$ denotes the true stress and is used here for further consideration.

The transport of thermal energy per time through a point $\boldsymbol{x} \in \partial\mathcal{B}_t$ is postulated via

$$q_\vartheta \mathrm{d}a = \boldsymbol{q}_\vartheta \cdot \boldsymbol{n}\mathrm{d}a, \tag{12}$$

introducing $\boldsymbol{q}_\vartheta$ as the spatial heat flux vector. Similarly, the moisture diffusion at a point $\boldsymbol{x} \in \partial\mathcal{B}_t$ is expressed as

$$q_\varphi \mathrm{d}a = \boldsymbol{q}_\varphi \cdot \boldsymbol{n}\mathrm{d}a, \tag{13}$$

where $\boldsymbol{q}_\varphi$ is the spatial moisture flux vector.

2.3 Hygro-Thermo-Mechanical Equilibrium Conditions

Any hygro-thermo-mechanical process is governed by balance laws, which have an axiomatic character and are given here with respect to $\mathcal{B}_t$ in local formulations, see e.g. [37, 38, 54]

2.3.1 Balance of Mass

The total mass of a body within a closed thermo-dynamic system is constant in time. The observed system at hand is a composition of a liquid or fluid phase and a solid phase. Having a look only at the solid phase, the balance of mass is assumed to be preserved. Since, the contribution at hand governs hygric processes and considers the moisture content ϕ at $\boldsymbol{x} \in \mathcal{B}_t$, compare Eq. (5), as a relation of bound water to the mass of the dry wood, the current total mass m of a hygro-thermo-mechanical system is assumed to be

$$m := \int_{\mathcal{B}_t} \rho_s \mathrm{d}v_s + \int_{\mathcal{B}_t} \rho_f \mathrm{d}v_f . \tag{14}$$

The subscript $\square_s$ denotes the solid phase and $\square_f$ characterizes the fluid phase within the domain $\mathcal{B}_t$. Thus, the current densities ρ_s and ρ_f are introduced accordingly. Knowing that the moisture content at $\boldsymbol{x} \in \mathcal{B}_t$ follows the relation

$$\phi = \frac{\rho_f \mathrm{d}v_f}{\rho_s \mathrm{d}v_s}, \tag{15}$$

a manipulation of Eq. (14) leads to the identity

$$m := \int_{\mathcal{B}_t} \rho_s \mathrm{d}v_s + \int_{\mathcal{B}_t} \rho_f \mathrm{d}v_f = \int_{\mathcal{B}_t} [1+\phi]\, \rho_s \mathrm{d}v_s . \tag{16}$$

The current volume of the solid phase $\mathrm{d}v_s = J\mathrm{d}V_s$ is depending on the state of deformation. This behavior follows from the transformation behavior of the deformation gradient from reference to current infinitesimal volume element. A further assumption is the equivalence of the solid volume and the total system volume, such that $\mathrm{d}v_s \approx \mathrm{d}v$. These assumptions lead to an averaged current density for a hygro-thermo-mechanical system according to

$$\rho = [1+\phi]\, \frac{1}{J} \rho_{0_s} . \tag{17}$$

Eq. (17) evolves the density of the observed system according to the moisture content at any $\boldsymbol{x} \in \mathcal{B}_t$. Generally, Eq. (17) is only valid below the fiber saturation point of the appropriate wood species.

2.3.2 Balance of Linear and Angular Momentum

The so-called Cauchy equation of motion states that the rate of linear momentum is equal to the sum of forces acting on the body and reads in its spatial local form

$$\mathbf{0} = \mathrm{div}(\boldsymbol{\sigma}). \tag{18}$$

The inertia and body force terms are neglected in Eq. (18), since the contribution at hand considers slow or quasi-static deformation processes with respect to the displacement field. Here, $\boldsymbol{\sigma}$ is the Cauchy stress tensor, compare Eq. (11). Equation (18) is the evolution equation for the unknown displacements. The time derivative of the linear momentum is enforced to be equal to the sum of moments of the forces acting on the body B with respect to a fixed point in space, which leads to the requirement

$$\boldsymbol{\sigma} = \boldsymbol{\sigma}^T \tag{19}$$

on the Cauchy stresses. This symmetry condition is the spatial local form of the balance of angular momentum.

2.3.3 Transient Heat Conduction Equation

The evolution equation of the unknown temperature within B can be derived from the balance of energy (first law of thermo-dynamics)

$$\rho\dot{e} = \boldsymbol{\sigma} : \boldsymbol{d} + \rho r - \mathrm{div}(\boldsymbol{q}_\vartheta) \tag{20}$$

and the balance of entropy (second law of thermo-dynamics)

$$\rho\gamma = \rho\dot{\eta} - \rho\frac{r}{\theta} + \mathrm{div}\left(\frac{\boldsymbol{q}_\vartheta}{\theta}\right) \geq 0, \tag{21}$$

see [12]. The balance of energy states that the rate of the mass specific internal energy density $\dot{e}$ is equal to the sum of the stress power, where $\boldsymbol{d} = \mathrm{sym}(\dot{\boldsymbol{F}}\boldsymbol{F}^{-1})$ and the thermal power $\rho r - \mathrm{div}(\boldsymbol{q}_\vartheta)$, containing the averaged density ρ and any heat source r. The balance of entropy postulates a state variable specific entropy η as an indicator of the reversibility and irreversibility in the direction of a thermo-dynamic process. Per definition, this law is an inequality and acts as a major restriction on constitutive equations. The specific rate of entropy production is equal to zero in case of a reversible process and larger than zero, when an irreversible process is encountered. Via a Legendre transformation of the Gibbs equation, the Helmholtz free energy $\psi := e - \theta\eta$ can be introduced and a certain dependency of $\psi = \psi(\boldsymbol{C}, \theta, \boldsymbol{\mathcal{I}})$ on the chosen state variables can be implied. Evaluating the Clausius-Planck inequality, the local part of dissipation is introduced by

$$\mathcal{D}_{loc} := -\rho\left(\partial_{\boldsymbol{\mathcal{I}}}\psi\right) : \dot{\boldsymbol{\mathcal{I}}} \geq 0, \tag{22}$$

where $\boldsymbol{\mathcal{I}}$ is a set of internal variables, such as plastic parts of deformation. The Fourier inequality

$$\mathcal{D}_{con} := -\frac{1}{\theta}\boldsymbol{q}_\vartheta \cdot \mathrm{grad}(\theta) \geq 0 \tag{23}$$

depicts a constraint for the description of the spatial heat flux vector $\boldsymbol{q}_\vartheta$. Further thermo-dynamic restrictions, see [6, 7], are defined by

$$2\rho\partial_{\boldsymbol{g}}\psi = \boldsymbol{\sigma}, \tag{24}$$

$$\eta = -\partial_\theta\psi, \tag{25}$$

$$\boldsymbol{0} = \partial_{\boldsymbol{G}}\psi, \tag{26}$$

in order to describe a consistent thermo-dynamic process with respect to Eqs. (20) and (21). The temperature gradient $\boldsymbol{\mathcal{G}} = \mathrm{grad}(\theta)$ is therefore introduced. Considering the specific heat capacity $c = -\theta\partial^2_{\theta\theta}\psi$, the spatial representation of the transient heat conduction equation reads

$$\rho c\dot{\theta} = -\mathrm{div}(\boldsymbol{q}_{\vartheta}) + \rho r + \underbrace{\left[\theta\partial_{\theta}\boldsymbol{\sigma} : \boldsymbol{d}\right]}_{w_{ext}} - \underbrace{\rho\left[\partial_{\boldsymbol{\mathcal{I}}}\psi - \theta\partial^2_{\boldsymbol{\mathcal{I}}\theta}\psi : \dot{\boldsymbol{\mathcal{I}}}\right]}_{w_{int}}. \tag{27}$$

The thermal work done by the Cauchy stresses w_{ext} as well as the rate of the dissipated energy w_{int} are therefore evaluated.

2.3.4 Modified Fick's Second Law

In order to account for the hygric effects of thermo-dynamic processes, Fick's second law is used and extended. The extension is carried out, such that a temperature and moisture dependent source term $r_{\varphi}(\varphi, \vartheta)$ are added and read

$$\rho\dot{\phi} = -\mathrm{div}(\boldsymbol{q}_{\varphi}) + \underbrace{\left[-\rho c_{\varphi}\cdot\varphi - \rho c_{\varphi\vartheta}\cdot\vartheta\right]}_{r_{\varphi}(\varphi,\vartheta)}. \tag{28}$$

The introduced constant c_{φ}, measured e.g. in [1/s], expresses the ability of wood to bind water inside of its cell walls per time. The interaction between moisture and temperature field is characterized by the material parameter $c_{\varphi\vartheta}$, measured e.g. in [1/Ks] and depicts the property of wood to unbound moisture while temperature increase. Equation (28) can only be applied to hygric processes below any saturation of the material with moisture.

3 Hygro- and Thermo-Mechanical Finite Element Formulations

The system of coupled partial differential equations in space and time introduced in Sect. 2.3, is now discretized in order to provide numerical solutions. The computational method proposed and used in this context is the finite element method (FEM). Starting point for deriving the finite element formulations is the Galerkin method. The boundary of body B in the reference configuration $\mathcal{B}_0$ is described by $\partial\mathcal{B}_0$ and in the current configuration by $\partial\mathcal{B}_t$. Both boundaries are sets of parts of prescribed displacements, temperatures, moisture changes. Additionally, forces, heat flows, moisture absorptive flows can be prescribed on the boundaries of B. Both sets read

$$\partial\mathcal{B}_0 \;:\; \left\{\partial\mathcal{B}_{0_{\boldsymbol{u}}}, \partial\mathcal{B}_{0_{\vartheta}}, \partial\mathcal{B}_{0_{\varphi}}, \partial\mathcal{B}_{0_{\boldsymbol{T}}}, \partial\mathcal{B}_{0_{\boldsymbol{Q}^{\vartheta}}}, \partial\mathcal{B}_{0_{\boldsymbol{Q}^{\varphi}}}\right\}, \tag{29}$$

$$\partial\mathcal{B}_t \;:\; \left\{\partial\mathcal{B}_{t_{\boldsymbol{u}}}, \partial\mathcal{B}_{t_{\vartheta}}, \partial\mathcal{B}_{t_{\varphi}}, \partial\mathcal{B}_{t_{\boldsymbol{t}}}, \partial\mathcal{B}_{t_{\boldsymbol{q}^{\vartheta}}}, \partial\mathcal{B}_{t_{\boldsymbol{q}^{\varphi}}}\right\}. \tag{30}$$

Additionally, the configuration $\mathcal{B}_t$ is subdivided into finite domains $\mathcal{B}_t^E$, for which

$$\mathcal{B}_t = \bigcup_{E=1}^{N} \mathcal{B}_t^E \tag{31}$$

holds.

3.1 Quasi-static Equilibrium

Equation (18) is the local form of the evolution equation of the unknown displacements. Applying the Galerkin method, a test function

$$\delta\boldsymbol{u} := \left\{\delta\boldsymbol{u}(\boldsymbol{x}) \in \mathcal{B}_t \;\mid\; \delta\boldsymbol{u} = \boldsymbol{0}\,\forall\,\boldsymbol{x} \in \partial\mathcal{B}_{t_{\boldsymbol{u}}}\right\}, \tag{32}$$

that is constant in time, is applied to Eq. (18) and the product is integrated over the domain $\mathcal{B}_t$, according to

$$\int_{\mathcal{B}_t} \delta\boldsymbol{u} \cdot \operatorname{div}(\boldsymbol{\sigma})\,\mathrm{d}v = 0. \tag{33}$$

A further manipulation leads to

$$\int_{\mathcal{B}_t} \boldsymbol{\sigma} : \operatorname{grad}(\delta\boldsymbol{u})\,\mathrm{d}v - \int_{\partial\mathcal{B}_{t_{\boldsymbol{t}}}} \delta\boldsymbol{u} \cdot \boldsymbol{t}\,\mathrm{d}a = 0, \tag{34}$$

where the symmetry condition of Eq. (19), the divergence theorem, the Cauchy theorem as well as the Gauss theorem are used. Subsequently, the observed body B has to be discretized by isoparametric finite elements with e.g. linear ansatz functions $\boldsymbol{N}(\boldsymbol{\xi})$ for describing the geometry of the finite elements. According to the isoparametric concept, $\boldsymbol{\xi}$ denote the local coordinates within a finite element, see e.g. [57]. The displacement field as well as the test function and their gradients are discretized accordingly, using

$$\boldsymbol{u}_i = \boldsymbol{N}^I(\boldsymbol{\xi})\boldsymbol{u}_i^I, \tag{35}$$

$$\delta\boldsymbol{u}_i = \boldsymbol{N}^I(\boldsymbol{\xi})\delta\boldsymbol{u}_i^I, \tag{36}$$

$$\mathrm{grad}(\boldsymbol{u})_{ij} = \frac{\partial \boldsymbol{N}^I(\boldsymbol{\xi})}{\partial \boldsymbol{x}_j}\boldsymbol{u}_i^I = \boldsymbol{B}_j^I\boldsymbol{u}_i^I, \tag{37}$$

$$\mathrm{grad}(\delta\boldsymbol{u})_{ij} = \frac{\partial \boldsymbol{N}^I(\boldsymbol{\xi})}{\partial \boldsymbol{x}_j}\delta\boldsymbol{u}_i^I = \boldsymbol{B}_j^I\delta\boldsymbol{u}_i^I, \tag{38}$$

where the subscripts $\square_i$ and $\square_j$ denoting the spatial directions and the superscript $\square^I$ the nodes of the finite element. Subsequently, the discretized residual force vector $\boldsymbol{R}_{\mathrm{mech}}$ of the mechanical field contribution reads

$$\boldsymbol{R}^I_{\mathrm{mech}_i} = \int\limits_{\mathcal{B}_t^E} \boldsymbol{B}_j^I\boldsymbol{\sigma}_{ij}\mathrm{d}v - \int\limits_{\partial\mathcal{B}_{t_t}^E} \boldsymbol{N}^I\boldsymbol{t}_i\mathrm{d}a, \tag{39}$$

representing the equilibrium between internal and external forces.

3.2 Thermal Equilibrium

In order to achieve thermal equilibrium, Eq. (27) has to be treated by Galerkin's method. Therefore, a thermal test function

$$\delta\vartheta := \left\{\delta\vartheta(\boldsymbol{x}) \in \mathcal{B}_t \;\mid\; \delta\vartheta = 0 \;\forall\; \boldsymbol{x} \in \partial\mathcal{B}_{t_\vartheta}\right\} \tag{40}$$

is introduced, that is constant in time. The multiplication of Eq. (27) with the thermal test function and the integration over the current domain yields

$$\int\limits_{\mathcal{B}_t} \delta\vartheta\left(\rho c\dot{\theta} + \mathrm{div}(\boldsymbol{q}_\vartheta) - w_{ext} + w_{int}\right)\mathrm{d}v = 0, \tag{41}$$

neglecting the internal heat sources. A further manipulation leads to

$$\int\limits_{\mathcal{B}_t} \delta\vartheta\left(\rho c\dot{\theta} - w_{ext} + w_{int}\right)\mathrm{d}v + \int\limits_{\partial\mathcal{B}_{t_{q^\vartheta}}} \delta\vartheta q_\vartheta\mathrm{d}a - \int\limits_{\mathcal{B}_t} \mathrm{grad}(\delta\vartheta)\cdot\boldsymbol{q}_\vartheta\mathrm{d}v = 0. \tag{42}$$

The temperature field and the thermal test function as well as their gradients are discretized according to the displacement field by

$$\vartheta = \boldsymbol{N}^I(\boldsymbol{\xi})\vartheta^I, \tag{43}$$

$$\delta\vartheta = \boldsymbol{N}^I(\boldsymbol{\xi})\delta\vartheta^I, \tag{44}$$

$$\text{grad}(\vartheta)_i = \frac{\partial \boldsymbol{N}^I(\boldsymbol{\xi})}{\partial \boldsymbol{x}_i}\vartheta^I = \boldsymbol{B}_i^I\vartheta^I, \tag{45}$$

$$\text{grad}(\delta\vartheta)_i = \frac{\partial \boldsymbol{N}^I(\boldsymbol{\xi})}{\partial \boldsymbol{x}_i}\delta\vartheta^I = \boldsymbol{B}_i^I\delta\vartheta^I, \tag{46}$$

using the isoparametric concept of the FEM. Subsequently, the discretized thermal residual $\boldsymbol{R}_{\text{ther}}$ reads

$$\boldsymbol{R}_{\text{ther}}^I = \int\limits_{\mathcal{B}_t^E} \boldsymbol{N}^I\left(\rho c\dot{\theta} - w_{ext} + w_{int}\right)\text{d}v + \int\limits_{\partial\mathcal{B}^E_{t_{q^\vartheta}}} \boldsymbol{N}^I q_\vartheta \text{d}a - \int\limits_{\mathcal{B}_t^E} \boldsymbol{B}_i^I \boldsymbol{q}_{\vartheta_i}\text{d}v \tag{47}$$

and represents the node specific rate of thermal and mechanical energy.

3.3 Hygric Equilibrium

Equation (28) represents the local evolution equation for the hygric field quantity. In order to achieve a finite element equation, Galerkin's method is applied after introducing a constant test function in time

$$\delta\varphi := \left\{\delta\varphi(\boldsymbol{x}) \in \mathcal{B}_t \;\mid\; \delta\varphi = 0 \,\forall\, \boldsymbol{x} \in \partial\mathcal{B}_{t_\varphi}\right\}. \tag{48}$$

The multiplied version of Eq. (28) with the test function and the integration over the domain leads to

$$\int\limits_{\mathcal{B}_t} \delta\varphi\left(\rho\dot{\phi} + \text{div}(\boldsymbol{q}_\varphi) - r_\varphi\right)\text{d}v = 0. \tag{49}$$

After the application of the product rule and the Gauss theorem, Eq. (49) takes the form

$$\int\limits_{\mathcal{B}_t} \delta\varphi\left(\rho\dot{\phi} - r_\varphi\right)\text{d}v + \int\limits_{\partial\mathcal{B}_{t_{q^\varphi}}} \delta\varphi q_\varphi \text{d}a - \int\limits_{\mathcal{B}_t} \text{grad}(\delta\varphi)\cdot\boldsymbol{q}_\varphi\text{d}v = 0. \tag{50}$$

The discretization of the hygric field and its test function as well as their gradients are carried out by the shape functions according to

$$\varphi = \boldsymbol{N}^I(\boldsymbol{\xi})\varphi^I, \tag{51}$$

$$\delta\varphi = \boldsymbol{N}^I(\boldsymbol{\xi})\delta\varphi^I, \tag{52}$$

$$\operatorname{grad}(\varphi)_i = \frac{\partial \boldsymbol{N}^I(\boldsymbol{\xi})}{\partial \boldsymbol{x}_i}\varphi^I = \boldsymbol{B}_i^I\varphi^I, \tag{53}$$

$$\operatorname{grad}(\delta\varphi)_i = \frac{\partial \boldsymbol{N}^I(\boldsymbol{\xi})}{\partial \boldsymbol{x}_i}\delta\varphi^I = \boldsymbol{B}_i^I\delta\varphi^I, \tag{54}$$

compare Sects. 3.1 and 3.2. Finally, the hygric residual expression $\boldsymbol{R}_{\text{hygr}}$ takes the form

$$\boldsymbol{R}_{\text{hygr}}^I = \int\limits_{\mathcal{B}_t^E} \boldsymbol{N}^I \left(\rho\dot{\phi} - r_\varphi\right) \mathrm{d}v + \int\limits_{\partial\mathcal{B}_{t_{q\varphi}}^E} \boldsymbol{N}^I q_\varphi \mathrm{d}a - \int\limits_{\mathcal{B}_t^E} \boldsymbol{B}_i^I \boldsymbol{q}_{\varphi_i} \mathrm{d}v \tag{55}$$

and represents the transport, the bounding and release of moisture per time. The extension of Fick's second law by the source term r_φ, see Eq. (28), together with the averaged density introduced in Eq. (17), yields in Eq. (55) the global change of mass of B per time.

4 Constitutive Formulations

The following section introduces the constitutive descriptions, which account for modeling the elastic, the inelastic, the temperature and moisture dependent material response of wood at small and finite deformations.

4.1 Helmholtz Free Energy, Cauchy Stresses and Hardening Response

The model makes use of the logarithmic strain measures, see Sect. 2.1, as well as stress measures related to the current configuration $\mathcal{B}_t$ at time t. The Cauchy stresses depend on ρ as the current averaged density, defined in Eq. (17) and $\psi = \psi(\boldsymbol{\varepsilon}^E, \boldsymbol{\mathcal{I}})$ as the free Helmholtz energy, compare Eq. (24). $\boldsymbol{\mathcal{I}}$ denotes a set of internal variables, that represents the state of inelasticity of the material at time t and is here defined as $\boldsymbol{\mathcal{I}} : \left\{\boldsymbol{\varepsilon}^P, \boldsymbol{\alpha}\right\}$. $\boldsymbol{\alpha}$ is a kinematic hardening strain. Recalling Eq. (6) and the consequence of Eq. (17), a rephrasing of Eq. (24)

$$\boldsymbol{\sigma} = \frac{\rho}{\rho_0}\frac{\partial \rho_0 \psi}{\partial \boldsymbol{\varepsilon}} : 2\frac{\partial \boldsymbol{\varepsilon}}{\partial \boldsymbol{g}} = \frac{\rho}{\rho_0}\hat{\boldsymbol{\sigma}} : 2\frac{\partial \boldsymbol{\varepsilon}}{\partial \boldsymbol{g}} \tag{56}$$

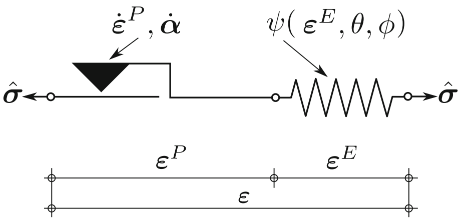
$\dot{\varepsilon}^P, \dot{\boldsymbol{\alpha}}$
$\psi(\varepsilon^E, \theta, \phi)$
$\hat{\boldsymbol{\sigma}}$
$\hat{\boldsymbol{\sigma}}$
ε^P
ε^E
ε

Fig. 4 Schematic rheological representation of the material model

introduces the logarithmic stress measures or Hencky stress $\hat{\boldsymbol{\sigma}}$. The derivative $2\partial_g \varepsilon$ can be obtained using the spectral representation of $\boldsymbol{C}$, see [18, 39].

The constitutive model has to consider the anisotropic elasticity of wood, where the initial state of stress depends on the angle between loading and grain. In the following, the direction of the grains will be labeled as longitudinal (L), both other directions perpendicular to the grains will be named tangential (T) and radial (R) with respect to the cut out of the trunk.

As can be seen in Fig. 1 and as explained in [17], irreversible yielding follows after elastic deformation due to collapse of the grain walls. The same phenomena can be observed under compression applied to e.g. spruce wood, see Fig. 2. The collapse coincides with the reduction of grain pore volume. Depending on the loading direction and amount of loading, this volume reduction continues until the wood is fully compressed. In case of longitudinal loading and due to the micro-structure of wood, softening with respect to the mechanical response accompanies this densification process. Having reached a fully densified and compressed state, wood is able to carry load as depicted in the large deformation domain of Fig. 1. At this deformation state, the hardening modulus is almost independent of the grain orientation. No hardening at finite deformations is visible in case of spruce wood due to brittle failure of the micro-structure, compare Fig. 2.

The rheology proposed in Fig. 4 is divided into two elements. First, energy is stored in an anisotropic spring according to

$$\begin{aligned} \rho_0 \psi(\varepsilon^E, \vartheta, \varphi) := {} & \frac{\lambda_{TR}}{2} (\mathrm{tr} \varepsilon^E)^2 + \mu_{TR} \varepsilon^E : \varepsilon^E + \frac{\lambda_L}{2} I_4^2 + \mu_L I_5 \\ & + \rho_0 c \left(\theta - \theta_0 - \theta \ln \left(\frac{\theta}{\theta_0} \right) \right) . \end{aligned} \tag{57}$$

Equation (57) and the terms therein are governing an underlying isotropic effect that is assumed to represent the loading situations with respect to T- and R-direction. Furthermore, the L-direction is considered by the superimposed terms containing the 4th and 5th invariant of ε^E, reading

$$I_4 = I_4(\varepsilon^E) := \boldsymbol{a} : (\varepsilon^E \boldsymbol{a}) = \boldsymbol{a} \otimes \boldsymbol{a} : \varepsilon^E , \tag{58}$$

$$I_5 = I_5(\varepsilon^E) := \boldsymbol{a} : (\varepsilon^E \varepsilon^E \boldsymbol{a}) = \boldsymbol{a} \otimes \boldsymbol{a} : (\varepsilon^E \varepsilon^E), \tag{59}$$

where $\boldsymbol{a}$ is the vector of grain direction in the global coordinate system. The 4 material constants introduced, compare [32], are the Lamé parameters of the appropriate material direction. Wood is here assumed to have minor differences in the mechanical properties of the tangential and radial direction, compare e.g. [19, 23, 26, 53]. Applying Eq. (56), one can express

$$\begin{aligned}\hat{\sigma}_{ij} &= \lambda_{TR}\mathrm{tr}\varepsilon^{E}\delta_{ij} + 2\mu_{TR}\varepsilon^{E}_{ij} \\ &\quad + \lambda_{L} I_4 \frac{1}{2}\left(a_i a_j + a_j a_i\right) + \mu_L \left(a_i \varepsilon^{E}_{jk} a_k + a_j \varepsilon^{E}_{ik} a_k\right). \end{aligned} \tag{60}$$

The second rheological element describes the inelasticity of wood. The frictional device is assumed to be governed by rate-independent, multi-surface yielding and an anisotropic hardening frictional device. Therefore, an internal variable, denoting a hardening strain-like tensor $\boldsymbol{\alpha}$, is introduced. The conjugated symmetric hardening stress tensor $\boldsymbol{q}$ can be derived from an anisotropic hardening potential

$$\phi(\boldsymbol{\alpha}) := \frac{h_{TR}}{2}\boldsymbol{\alpha} : \boldsymbol{\alpha} - 2h_L\left(\exp\left(-\frac{I_\alpha}{2}\right) - 1\right), \tag{61}$$

where $I_\alpha := \boldsymbol{a} : (\boldsymbol{\alpha}\boldsymbol{\alpha}\boldsymbol{a})$ is given, according to

$$q_{ij} := -\frac{\partial\phi(\boldsymbol{\alpha})}{\partial\alpha_{ij}} = -h_{TR}\alpha_{ij} - h_L \exp\left(-\frac{I_\alpha}{2}\right)\left(a_i\alpha_{jk}a_k + a_j\alpha_{ik}a_k\right). \tag{62}$$

In order to describe the micro-structural changes of wood, especially at finite deformations, Eq. (61) is chosen in a phenomenological manner. In order to evaluate Eq. (60), the evolution equations of the internal variables need to be defined according to the material behavior of wood. The set of internal variables is evolving with respect to

$$\dot{\boldsymbol{\varepsilon}}^P = \sum_{\alpha=1}^{12}\dot{\gamma}_\alpha \partial_{\hat{\boldsymbol{\sigma}}} f_\alpha(\hat{\boldsymbol{\sigma}}, \boldsymbol{q}), \tag{63}$$

$$\dot{\boldsymbol{\alpha}} = \sum_{\alpha=1}^{12}\dot{\gamma}_\alpha \partial_{\boldsymbol{q}} f_\alpha(\hat{\boldsymbol{\sigma}}, \boldsymbol{q}), \tag{64}$$

where the index $\square_\alpha$ denotes the yield surface $f_\alpha(\hat{\boldsymbol{\sigma}}, \boldsymbol{q})$. These surfaces are characterizing different yield levels at certain material directions with respect to the grain orientation (see e.g. Fig. 1). Equation (63) is an associated plastic flow rule and Eq. (64) is the hardening law, compare [51]. The 12 yield surfaces are described with respect to every logarithmic stress component, considering the symmetry of the logarithmic stress tensor, according to

$$
\begin{aligned}
f_1 &:= -\hat{\sigma}_{11} - \left(\sigma^Y_{c_{11}} - q_{11}\right), && (65)\\
f_2 &:= -\hat{\sigma}_{22} - \left(\sigma^Y_{c_{22}} - q_{22}\right), && (66)\\
f_3 &:= -\hat{\sigma}_{33} - \left(\sigma^Y_{c_{33}} - q_{33}\right), && (67)\\
f_4 &:= -\hat{\sigma}_{12} - \left(\sigma^Y_{c_{12}} - q_{12}\right), && (68)\\
f_5 &:= -\hat{\sigma}_{13} - \left(\sigma^Y_{c_{13}} - q_{13}\right), && (69)\\
f_6 &:= -\hat{\sigma}_{23} - \left(\sigma^Y_{c_{23}} - q_{21}\right), && (70)
\end{aligned}
$$

for the compressive loadings (negative stresses) and

$$
\begin{aligned}
f_7 &:= \hat{\sigma}_{11} - \sigma^Y_{t_{11}}, && (71)\\
f_8 &:= \hat{\sigma}_{22} - \sigma^Y_{t_{22}}, && (72)\\
f_9 &:= \hat{\sigma}_{33} - \sigma^Y_{t_{33}}, && (73)\\
f_{10} &:= \hat{\sigma}_{12} - \sigma^Y_{t_{12}}, && (74)\\
f_{11} &:= \hat{\sigma}_{13} - \sigma^Y_{t_{13}}, && (75)\\
f_{12} &:= \hat{\sigma}_{23} - \sigma^Y_{t_{23}}, && (76)
\end{aligned}
$$

in case of tensile loads (positive stresses). Eqs. (65)–(76) introduce the yield stress tensors $\boldsymbol{\sigma}^Y_c$ and $\boldsymbol{\sigma}^Y_t$ with regard to absolute values of the tensile t or compressive c yield stresses. Eqs. (65)–(76) have a linear form within the logarithmic stress space and provide the means to distinguish between tensile and compressive loadings. This set of equations defines the elastic domain $\mathbb{E} := \{(\hat{\boldsymbol{\sigma}}, \boldsymbol{q}) \in \mathbb{R}^6 \times \mathbb{R}^6 \mid f_\alpha < 0 \,\forall \alpha\}$ within the logarithmic stress space. The hardening stresses $\boldsymbol{q}$ are not considered within the tensile yield surfaces, since brittle failure around the yield stress is assumed. Thus, post-yield hardening behavior at tension is not governed by Eqs. (71)–(76). The composition of $\boldsymbol{\sigma}^Y_c$ and $\boldsymbol{\sigma}^Y_t$

$$
\sigma^Y_i := \begin{bmatrix} \sigma^i_{TR} & \sigma^s_{LTR} & \sigma^s_{LTR} \\ \sigma^s_{LTR} & \sigma^i_{TR} & \sigma^s_{LTR} \\ \sigma^s_{LTR} & \sigma^s_{LTR} & \sigma^i_{TR} \end{bmatrix} + \begin{bmatrix} a_1a_1 & a_1a_2 & a_1a_3 \\ a_2a_1 & a_2a_2 & a_2a_3 \\ a_3a_3 & a_3a_2 & a_3a_3 \end{bmatrix} \cdot \sigma^i_L \;\forall\, i \in c, t \qquad (77)
$$

is proposed and provides the means to account for the yield stress in grain direction and perpendicular to it. Again, L-direction is superimposed onto an underlying isotropic yield stress state, compare Eq. (57). This assumption is motivated by the orthotropic behavior of wood. The components of σ^Y_i are material constants, that have to be identified by appropriate experimental tests and are suggested as σ^c_{TR}, σ^t_{TR}, σ^c_L and σ^t_L, the main yield stresses as well as σ^s_{LTR} as the shear yield stress.

The inelastic consistency parameters $\dot{\gamma}_\alpha$ in Eqs. (63) and (64) have to satisfy the Kuhn-Tucker complementary conditions

$$\dot{\gamma}_\alpha \geq 0, \tag{78}$$

$$f_\alpha(\hat{\boldsymbol{\sigma}}, \boldsymbol{q}) \leq 0, \tag{79}$$

$$\dot{\gamma}_\alpha f_\alpha(\hat{\boldsymbol{\sigma}}, \boldsymbol{q}) = \dot{\gamma}_\alpha \dot{f}_\alpha(\hat{\boldsymbol{\sigma}}, \boldsymbol{q}) \equiv 0. \tag{80}$$

These conditions determine the active yield surfaces Eqs. (65)–(76). Active is meant in a sense that every $f_\alpha > 0$ is violated by a non-admissible logarithmic stress state outside of the $\mathbb{E}$. Generally, geometric interpretations of admissible and non-admissible logarithmic stress states in the logarithmic stress space are similar to the interpretations depicted in [51, 52]. The given logarithmic stress strain relations in Eq. (56) together with the definitions of Eqs. (6) and (9) as well as the evolution equations Eqs. (63) and (64) define a set of non-linear coupled partial differential equations in time. Regardless of the actual state of deformation, as outlined in [39], the chosen kinematic approach, see Sect. 2.1, preserves a solution strategy similar to small strain theory as depicted e.g. in [49].

4.1.1 Inelastic Loading and Closest Point Projection

After having introduced the kinematics and the essential mechanical constitutive formulations of the material characteristics of wood, the computation of the set of internal variables at time t for a point $\mathcal{P} \in \mathcal{B}_t$ needs to be carried out by a discretization in time. Therefore, a time step $\Delta t = t_{n+1} - t_n$ is introduced. Similar to [51], an implicit backward Euler scheme is used for the integration of the driving evolution equations, which leads to

$$\hat{\boldsymbol{\sigma}}_{n+1} = \partial_{\boldsymbol{\varepsilon}} \rho_0 \psi(\boldsymbol{\varepsilon}_{n+1} - \boldsymbol{\varepsilon}^P_{n+1}), \tag{81}$$

$$\boldsymbol{q}_{n+1} = -\,\partial_{\boldsymbol{\alpha}} \phi(\boldsymbol{\alpha}_{n+1}), \tag{82}$$

$$\boldsymbol{\varepsilon}^P_{n+1} = \boldsymbol{\varepsilon}^P_n + \sum_{\alpha=1}^{12} \Delta t \dot{\gamma}_{\alpha_{n+1}} \partial_{\hat{\boldsymbol{\sigma}}} f_\alpha(\hat{\boldsymbol{\sigma}}_{n+1}, \boldsymbol{q}_{n+1}), \tag{83}$$

$$\boldsymbol{\alpha}_{n+1} = \boldsymbol{\alpha}_n + \sum_{\alpha=1}^{12} \Delta t \dot{\gamma}_{\alpha_{n+1}} \partial_{\hat{\boldsymbol{q}}} f_\alpha(\hat{\boldsymbol{\sigma}}_{n+1}, \boldsymbol{q}_{n+1}), \tag{84}$$

for a given state of total logarithmic deformations $\boldsymbol{\varepsilon}_{n+1}$. The set of initial conditions $\{\boldsymbol{\varepsilon}_n, \boldsymbol{\varepsilon}^P_n, \boldsymbol{\alpha}_n\}$ at t_n is known. The discrete Kuhn-Tucker conditions read

$$f_\alpha(\hat{\boldsymbol{\sigma}}_{n+1}, \boldsymbol{q}_{n+1}) \leq 0, \tag{85}$$

$$\gamma_{\alpha_{n+1}} := \Delta t \dot{\gamma}_{\alpha_{n+1}} \geq 0, \tag{86}$$

$$\gamma_{\alpha_{n+1}} f_\alpha(\hat{\boldsymbol{\sigma}}_{n+1}, \boldsymbol{q}_{n+1}) = 0, \tag{87}$$

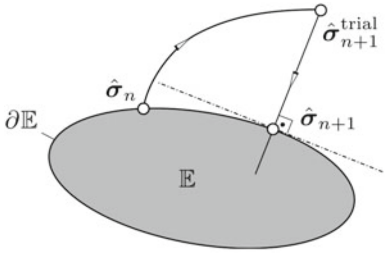
$\hat{\boldsymbol{\sigma}}_{n+1}^{\mathrm{trial}}$
$\hat{\boldsymbol{\sigma}}_n$
$\partial\mathbb{E}$
$\hat{\boldsymbol{\sigma}}_{n+1}$
$\mathbb{E}$

Fig. 5 Schematic representation of the closest point projection

and have to be solved by an elastic trial state and an inelastic correcter step, see [50] and Fig. 5 for a schematic representation. The elastic trial state is computed by the logarithmic elastic trial deformation

$$\boldsymbol{\varepsilon}_{n+1}^{E^{\mathrm{trial}}} = \boldsymbol{\varepsilon}_{n+1} - \boldsymbol{\varepsilon}_n^P \tag{88}$$

and the resulting logarithmic trial stresses

$$\hat{\boldsymbol{\sigma}}_{n+1}^{\mathrm{trial}} = \partial_{\boldsymbol{\varepsilon}} \rho_0 \psi(\boldsymbol{\varepsilon}_{n+1}^{E^{\mathrm{trial}}}). \tag{89}$$

An admissible trial stress state for all state variables is given, if the requirement $f_\alpha(\hat{\boldsymbol{\sigma}}_{n+1}^{\mathrm{trial}}, \boldsymbol{q}_n) \leq 0 \; \forall \; \alpha = 1 \ldots 12$ is met. Inelastic loading is encountered, if one or more yield surfaces are violated by

$$f_\alpha(\hat{\boldsymbol{\sigma}}_{n+1}^{\mathrm{trial}}, \boldsymbol{q}_n) > 0 \; \forall \; \alpha \in \boldsymbol{J}_{\mathrm{active}}, \tag{90}$$

where $\boldsymbol{J}_{\mathrm{active}} := \{\alpha \in \{1 \ldots 12\} \;|\; f_\alpha > 0\}$ denotes the set of active yield functions. Thus, an update for the set of internal variables $\{\boldsymbol{\varepsilon}^P, \boldsymbol{\alpha}\}$ has to be carried out.

The update, compare e.g. in [51], follows

$$\mathbf{R} := \begin{bmatrix} \mathbf{R}_1 \\ \mathbf{R}_2 \\ \mathbf{R}_3 \end{bmatrix} = \begin{bmatrix} -\boldsymbol{\varepsilon}_{n+1}^P + \boldsymbol{\varepsilon}_n^P + \sum\limits_{\beta \in \boldsymbol{J}_{\mathrm{active}}} \gamma_{\beta_{n+1}} \partial_{\hat{\boldsymbol{\sigma}}} f_\beta \\ -\boldsymbol{\alpha}_{n+1} + \boldsymbol{\alpha}_n + \sum\limits_{\beta \in \boldsymbol{J}_{\mathrm{active}}} \gamma_{\beta_{n+1}} \partial_{\boldsymbol{q}} f_\beta \\ f_\alpha \;|\; \alpha \in \boldsymbol{J}_{\mathrm{active}} \end{bmatrix}, \tag{91}$$

where $\mathbf{R}$ contains the residuals of Eqs. (63) and (64) after a time integration as well as the set of active yield functions. The unknowns $\mathbf{X}$ and their increments $\Delta\mathbf{X} = \mathbf{X}^{k+1} - \mathbf{X}^k$ during the iterative update are given by

$$\mathbf{X} := \begin{bmatrix} \boldsymbol{\varepsilon}_{n+1}^P \\ \boldsymbol{\alpha}_{n+1} \\ \gamma_{\alpha_{n+1}} \end{bmatrix}, \qquad \Delta\mathbf{X} := \begin{bmatrix} \Delta\boldsymbol{\varepsilon}^P \\ \Delta\boldsymbol{\alpha} \\ \Delta\gamma_\alpha \end{bmatrix}. \tag{92}$$

A linearization of the nonlinear set of equations of Eq. (91) leads to

$$\text{Lin}\mathbf{R} = \mathbf{R}|_{\mathbf{X}^k} + \left.\frac{\partial \mathbf{R}}{\partial \mathbf{X}}\right|_{\mathbf{X}^k} : \Delta\mathbf{X} = \mathbf{0}, \tag{93}$$

containing the local update moduli $\mathbf{A}$, reading

$$\mathbf{A} := \frac{\partial \mathbf{R}}{\partial \mathbf{X}} = \begin{bmatrix} \mathbf{A}_{11} & \mathbf{A}_{12} & \mathbf{A}_{13} \\ \mathbf{A}_{21} & \mathbf{A}_{22} & \mathbf{A}_{23} \\ \mathbf{A}_{31} & \mathbf{A}_{32} & \mathbf{0} \end{bmatrix} = \begin{bmatrix} \mathbf{B} & \mathbf{C} \\ \mathbf{D} & \mathbf{0} \end{bmatrix}. \tag{94}$$

The Schur complement $\mathbf{S}$ of the block $\mathbf{B}$ of $\mathbf{A}$ reads

$$\mathbf{S} = \mathbf{0} - \mathbf{D}\mathbf{B}^{-1}\mathbf{C}, \tag{95}$$

$$\mathbf{S} = -\left[\mathbf{A}_{31}, \mathbf{A}_{32}\right] : \begin{bmatrix} \mathbf{A}_{11} & \mathbf{A}_{12} \\ \mathbf{A}_{21} & \mathbf{A}_{22} \end{bmatrix}^{-1} : \begin{bmatrix} \mathbf{A}_{13} \\ \mathbf{A}_{23} \end{bmatrix}, \tag{96}$$

and has the dimensions $\{\mathbf{S}^{\alpha\beta} \mid \alpha, \beta \in \boldsymbol{J}_{\text{active}}\}$. Using the Schur complement $\mathbf{S}_B$ of $\mathbf{B}$ and collecting terms, $\mathbf{B}^{-1}$ can be explicitly expressed and Eq. (96) can be recast into

$$\begin{aligned} \mathbf{S} = &-\mathbf{A}_{31}\left[\mathbf{A}_{11}^{-1}\mathbf{A}_{13} + \mathbf{A}_{11}^{-1}\mathbf{A}_{12}\mathbf{S}_B^{-1}\mathbf{A}_{21}\mathbf{A}_{11}^{-1}\mathbf{A}_{13} - \mathbf{A}_{11}^{-1}\mathbf{A}_{12}\mathbf{S}_B^{-1}\mathbf{A}_{23}\right] \\ &- \mathbf{A}_{32}\mathbf{S}_B^{-1}\left[\mathbf{A}_{23} - \mathbf{A}_{21}\mathbf{A}_{11}^{-1}\mathbf{A}_{13}\right], \end{aligned} \tag{97}$$

where

$$\mathbf{S}_B = \mathbf{A}_{22} - \mathbf{A}_{21}\mathbf{A}_{11}^{-1}\mathbf{A}_{12}. \tag{98}$$

The utilization of the Schur complements within the iterative update and the solution of Eq. (93) avoids the full inversion of $\mathbf{A}$. Eq. (97) can now be evaluated using only the inversion of two tensors of fourth order. The update of $\{\gamma_\alpha \ \forall\, \alpha \in \boldsymbol{J}_{\text{active}}\}$ is given by

$$\Delta\mathbf{X}_3 = \Delta\gamma = \mathbf{S}^{-1} : \left(-\mathbf{R}_3 + \left[\mathbf{A}_{31}, \mathbf{A}_{32}\right] : \begin{bmatrix} \mathbf{A}_{11} & \mathbf{A}_{12} \\ \mathbf{A}_{21} & \mathbf{A}_{22} \end{bmatrix}^{-1} : \begin{bmatrix} \mathbf{R}_1 \\ \mathbf{R}_2 \end{bmatrix}\right). \tag{99}$$

The computed inelastic consistency parameters $\gamma_{\alpha_{n+1}}^{k+1} = \gamma_{\alpha_{n+1}}^{k} + \Delta\gamma_\alpha$ of the active constraints $\boldsymbol{J}_{\text{active}}$ have to be verified. A strict positiveness of the consistency parameters is required by the Kuhn-Tucker conditions, compare Eq. (78). Thus, only $\gamma_{\alpha_{n+1}}^{k+1} > 0$ are admissible in the context of the closest point projection. For a geometric representation of the multi-surface plasticity projection, see [51]. The update of the set of internal variables is carried out by solving

$$\begin{bmatrix} \Delta\mathbf{X}_1 \\ \Delta\mathbf{X}_2 \end{bmatrix} = \begin{bmatrix} \mathbf{A}_{11} & \mathbf{A}_{12} \\ \mathbf{A}_{21} & \mathbf{A}_{22} \end{bmatrix}^{-1} : \begin{bmatrix} -\mathbf{R}_1 - \mathbf{A}_{13}\Delta\mathbf{X}_3 \\ -\mathbf{R}_2 - \mathbf{A}_{23}\Delta\mathbf{X}_3 \end{bmatrix}. \tag{100}$$

The solution can be achieved by using the Schur complement of **B** given in Eq. (98). The iterative update of

$$\begin{bmatrix} \mathbf{X}_1^{k+1} \\ \mathbf{X}_2^{k+1} \end{bmatrix} = \begin{bmatrix} \mathbf{X}_1^{k} \\ \mathbf{X}_2^{k} \end{bmatrix} + \begin{bmatrix} \Delta\mathbf{X}_1 \\ \Delta\mathbf{X}_2 \end{bmatrix} \tag{101}$$

can be computed. The specific formulations of the derivatives in **A** have the form

$$\mathbf{A}_{11} = -\,\mathbb{I}^s - \left(\sum_{\beta\in\boldsymbol{J}_{\text{active}}} \gamma_{\beta_{n+1}} \frac{\partial^2 f_\beta}{\partial\hat{\boldsymbol{\sigma}}\partial\hat{\boldsymbol{\sigma}}} \right) : \hat{\mathbb{C}}, \tag{102}$$

$$\mathbf{A}_{12} = -\left(\sum_{\beta\in\boldsymbol{J}_{\text{active}}} \gamma_{\beta_{n+1}} \frac{\partial^2 f_\beta}{\partial\hat{\boldsymbol{\sigma}}\partial\boldsymbol{q}} \right) : \mathbb{K}, \tag{103}$$

$$\mathbf{A}_{13} = \frac{\partial f_\alpha}{\partial\hat{\boldsymbol{\sigma}}}, \tag{104}$$

$$\mathbf{A}_{21} = -\left(\sum_{\beta\in\boldsymbol{J}_{\text{active}}} \gamma_{\beta_{n+1}} \frac{\partial^2 f_\beta}{\partial\boldsymbol{q}\partial\hat{\boldsymbol{\sigma}}} \right) : \hat{\mathbb{C}}, \tag{105}$$

$$\mathbf{A}_{22} = -\,\mathbb{I}^s - \left(\sum_{\beta\in\boldsymbol{J}_{\text{active}}} \gamma_{\beta_{n+1}} \frac{\partial^2 f_\beta}{\partial\boldsymbol{q}\partial\boldsymbol{q}} \right) : \mathbb{K}, \tag{106}$$

$$\mathbf{A}_{23} = \frac{\partial f_\alpha}{\partial\boldsymbol{q}}, \tag{107}$$

$$\mathbf{A}_{31} = -\,\frac{\partial f_\alpha}{\partial\hat{\boldsymbol{\sigma}}} : \hat{\mathbb{C}}, \tag{108}$$

$$\mathbf{A}_{32} = -\,\frac{\partial f_\alpha}{\partial\boldsymbol{q}} : \mathbb{K}. \tag{109}$$

The fourth order symmetric identity tensor $\mathbb{I}^s_{ijkl} = 1/2(\delta_{ik}\delta_{jl} + \delta_{il}\delta_{jk})$, as well as the logarithmic elastic tangent and hardening tangent moduli

$$\hat{\mathbb{C}} = \frac{\partial \hat{\boldsymbol{\sigma}}}{\partial \boldsymbol{\varepsilon}} = -\frac{\partial \hat{\boldsymbol{\sigma}}}{\partial \boldsymbol{\varepsilon}^{P}}, \tag{110}$$

$$\mathbb{K} = -\frac{\partial \boldsymbol{q}}{\partial \boldsymbol{\alpha}} \tag{111}$$

of Eqs. (60) and (62) are introduced, having the specific form

$$\begin{aligned}\hat{\mathbb{C}}_{ijkl} &= \lambda_{TR}\delta_{ij}\delta_{kl} + 2\mu_{TR}\mathbb{I}^{s}_{ijkl} \\ &\quad + \lambda_L \left(a_i a_j a_k a_l\right) + \frac{\mu_L}{2}\left(a_i\delta_{jk}a_l + a_i\delta_{jl}a_k + a_k\delta_{il}a_j + a_l\delta_{ik}a_j\right),\end{aligned} \tag{112}$$

$$\begin{aligned}\mathbb{K}_{ijkl} &= h_{TR}\mathbb{I}^{s}_{ijkl} + h_L \exp\left(-\frac{I_\alpha}{2}\right) \\ &\quad \left(\frac{1}{2}\left(\left(a_i\alpha_{jm}a_m + a_j\alpha_{in}a_n\right)\left(a_k\alpha_{lo}a_o + a_l\alpha_{kp}a_p\right)\right)\right. \\ &\quad \left. - \left(a_i\delta_{jk}a_l + a_i\delta_{jl}a_k + a_k\delta_{il}a_j + a_l\delta_{ik}a_j\right)\right).\end{aligned} \tag{113}$$

4.2 Temperature and Moisture Dependent Constitutive Properties

The logarithmic thermal deformations $\boldsymbol{\varepsilon}^{\vartheta}$ are constitutively described by

$$\boldsymbol{\varepsilon}^{\vartheta} = \boldsymbol{\alpha}^{\vartheta}\vartheta, \tag{114}$$

introducing the anisotropic thermal expansion coefficients $\boldsymbol{\alpha}^{\vartheta}_{ij}$ for the appropriate coordinate direction. The logarithmic moisture dependent deformations $\boldsymbol{\varepsilon}^{\varphi}$ are introduced according to

$$\boldsymbol{\varepsilon}^{\varphi} = \boldsymbol{\alpha}^{\varphi}\varphi. \tag{115}$$

The moisture induced expansion effects for the different coordinate directions are captured by $\boldsymbol{\alpha}^{\varphi}_{ij}$.

In order to describe the spatial heat flux vector in Eq. (12), Fourier's law for isotropic materials is modified with respect to anisotropy and density dependency, according to

$$\boldsymbol{q}_{\vartheta} = -\frac{\rho}{\rho_0}\boldsymbol{K} : \mathrm{grad}(\vartheta). \tag{116}$$

The thermal conductivity coefficients $\boldsymbol{K}_{ij} > 0$, having a unit of e.g. [J/ms], are incorporated into the coefficient matrix $\boldsymbol{K}$. They describe the ability of transporting thermal energy per time and the appropriate global coordinate direction. The density dependency arises from the averaged density in Eq. (17), since the mass of a wooden structure is considered to be influenced by the amount of bounded moisture. Thus, the thermal conductivity of wood is also influenced by its moisture content. Similarly, the spatial moisture diffusion vector in Eq. (13) is specified as

$$\boldsymbol{q}_\varphi = -\frac{\rho}{\rho_0}\boldsymbol{D} : \operatorname{grad}(\varphi), \tag{117}$$

where $\boldsymbol{D}$ contains the moisture diffusion coefficients $\boldsymbol{D}_{ij} > 0$ in global coordinate directions. These coefficients are measured in e.g. [kg/ms] and describe therefore the ability of transporting a certain mass of moisture per time and the appropriate coordinate direction. The averaged density in Eq. (17) and the assumption that Eq. (28) is only valid below the wood specific fiber saturation point implies the phenomenological description in Eq. (117) of moisture transport mechanisms in wood. This description is based on Fick's first law.

5 Model Verification at Constant Moisture Content and Under Isothermal Conditions

The following section investigates the applicability of the proposed formulations to different experiments on spruce wood and balsa wood under isothermal conditions and at a fixed moisture content.

Spruce wood is generally much stiffer than balsa wood and does not undergo finite deformations, due to brittle fracture before reaching the large strain domain in tension as well as in compression. Balsa wood reaches a finite deformation yielding plateau under compression, see Figs. 1 and 2 and e.g. [8].

5.1 Mechanical Modeling of Spruce Wood (Picea Abies)

The validation of the mechanical part of the modeling approach presented, is carried out by simulations of spruce wood experiments from [31] at room temperature and at a reference density of $\rho_0 = 4 \cdot 10^{-7}$ kg/mm^3. The details of experimental setups and the specimen geometries are depicted in [31]. The set of parameters identified is documented in Table 1, where the value in round brackets is taken similar to data in literature, see [40]. Almost no hardening effect is assumed within the small strain regime, which means that h_L and h_{TR} are estimated values close to zero. The specific form of Eq. (61) in L-direction requires a negative value of the hardening parameter h_L in case of softening and a positive value in case of hardening. A positive value of the hardening parameter h_{TR} leads to hardening of the material response after yielding and a negative value softens the material after yielding.

Due to the intrinsic uncertainty of data, especially considering wooden materials, the experimental results are varying, see e.g. Figs. 6, 7, 8 and 9. The simulation result for tensile tests parallel to the grain direction are compared to experiments in

Table 1 Model parameters of spruce wood (*Picea Abies*)

λ_{TR} [N/mm^2]	μ_{TR} [N/mm^2]	λ_L [N/mm^2]	μ_L [N/mm^2]	h_L [N/mm^2]	h_{TR} [N/mm^2]
140	130	25000	600	10	3
σ^c_{TR} [N/mm^2]	σ^t_{TR} [N/mm^2]	σ^c_L [N/mm^2]	σ^t_L [N/mm^2]	σ^s_{LTR} [N/mm^2]	
3.2	3.5	(47)	110	±6	

Fig. 6. The simulation result fits within the range of the measured force displacement plots and captures the characteristic features of the tensile behavior of spruce wood. The simulation result in Fig. 7 captures the tensile experiments perpendicular to the fiber direction. Compression perpendicular to the grains is denoted by yielding and a hardening plateau subsequently. The experiments contain a transition between the elastic and inelastic material behavior, which is not as sudden as the simulation predicts. The evolution laws in Eqs. (63) and (64) lead to a fast increase in inelastic deformation, as soon as the logarithmic yield stress level is reached. The model captures the characteristics of the transition from elastic to inelastic material behavior and the simulation is in accordance with the experiments. The experiments of shear tests have a step-like shape, due to the time interval of the reaction forces measured. The experimental setup, see [31], causes a time delay in the measured reaction forces. This delay can be seen by the shift of the start of the plots at the abscissa. Thus, the simulation result is shifted by 0.5 mm at the displacement axis of Fig. 9. The model behavior is satisfying at shear parallel to grain, since the characteristics of the measured data are captured, see Fig. 9. Exemplarily, the Cauchy stress distribution and the inelastic logarithmic deformation are shown in Figs. 10. Figure 10a shows a homogeneous stress distribution within the parallel section of the specimen. The inelastic deformation in tensile direction is evolving within the appropriate stress domain. Fig. 10b shows the Cauchy stress distribution of the shear test simulation, which is ranging from low tensile stresses up to high compressive stresses due to the boundary conditions. From Fig. 10b can be seen, that only large stresses cause inelastic deformations. Concluding, it can be denoted, that the modeling approach successfully captures main characteristics of the mechanical behavior of stiff and brittle wood, such as spruce wood (see e.g. Fig. 8).

5.2 *Mechanical Modeling of Balsa Wood (Ochroma Pyramidale)*

The experiments modeled are taken from [8]. The simulations presented are carried out for room temperature and at a reference density of $\rho_0 = 1 \cdot 10^{-7}$ kg/mm^3. The uniaxial compression tests in T-, R- and L-direction lead to a homogenous stress distribution. The set of parameters identified is given in Table 2. Only the elastic con-

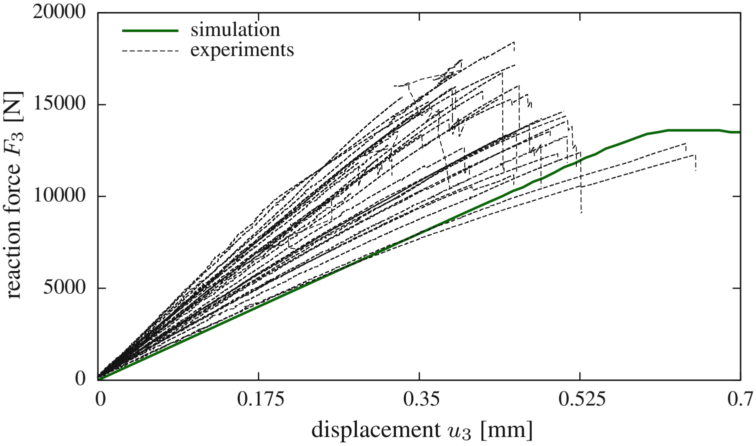

Fig. 6 Comparison of simulation and experiments at tensile tests parallel to the grains for spruce wood (*Picea Abies*)

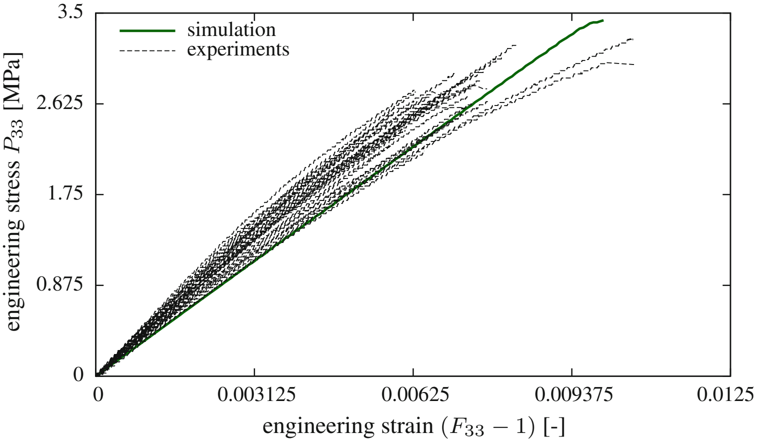

Fig. 7 Comparison of simulation and experiments at tensile tests perpendicular to the grains for spruce wood (*Picea Abies*)

stants, the hardening parameters and the compressive yield stresses are identified. The hardening modulus h_L has a negative value, compare Table 1, since at compression parallel to the grains, softening occurs. The simulation results are plotted in Fig. 11. Due to the above mentioned uncertainty of data and the fact, that only one

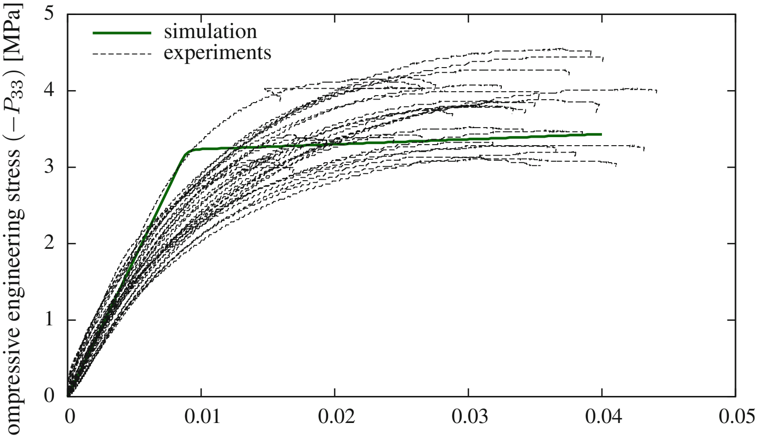

Fig. 8 Comparison of simulation and experiments at compressive tests perpendicular to the grains for spruce wood (*Picea Abies*)

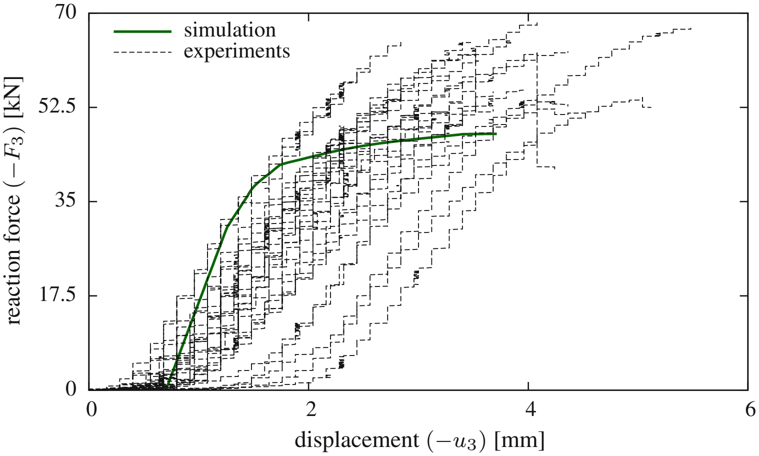

Fig. 9 Comparison of simulation and experiments at shear tests parallel to the grains for spruce wood (*Picea Abies*)

experimental stress-strain dependency is given per loading direction, the results in Fig. 11 are assumed to be satisfying. Concluding, the important characteristics of the mechanical compressive behavior of this species of wood is successfully captured by the model.

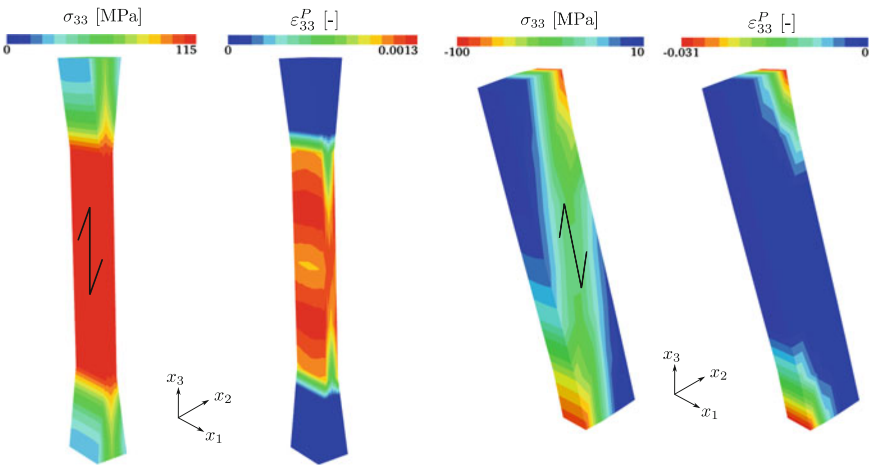
σ_{33} [MPa]
0
115
ε_{33}^P [-]
0
0.0013
x_3
x_2
x_1
σ_{33} [MPa]
-100
10
ε_{33}^P [-]
-0.031
0
x_3
x_2
x_1

(a) Tensile test simulation (b) Shear test simulation

Fig. 10 Cauchy stress distribution and inelastic logarithmic deformation according to two simulations of the experiments in [31]

Table 2 Model parameters of balsa wood at compressive finite deformation

λ_{TR} [N/mm^2]	μ_{TR} [N/mm^2]	λ_L [N/mm^2]	μ_L [N/mm^2]	h_L [N/mm^2]	h_{TR} [N/mm^2]
30	20	180	120	-10	0.3
σ_{TR}^c [N/mm^2]	σ_{TR}^t [N/mm^2]	σ_L^c [N/mm^2]	σ_L^t [N/mm^2]	σ_{LTR}^s [N/mm^2]	
1	-	13	-	-	

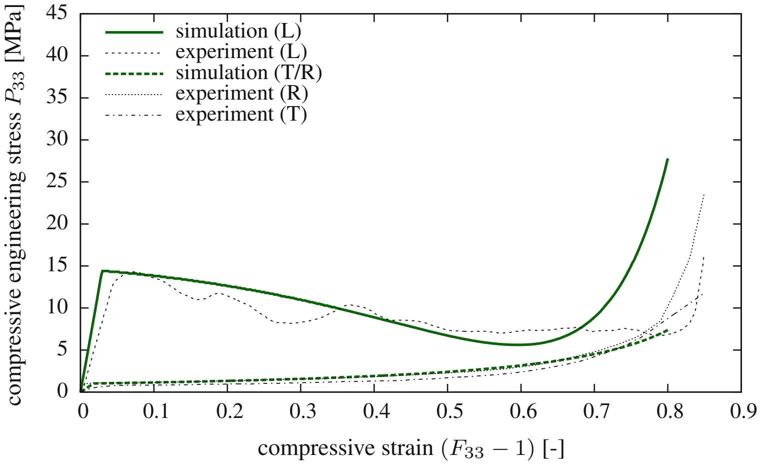

Fig. 11 Comparison of simulations and experiments at compressive tests for balsa wood

Table 3 Model parameters of beech wood (*Fagus Sylvatica*)

λ_{TR}	μ_{TR}	λ_L	μ_L	h_L	h_{TR}
[N/mm^2]	[N/mm^2]	[N/mm^2]	[N/mm^2]	[N/mm^2]	[N/mm^2]
43	51	1E+04	650	10	10.5
σ^c_{TR}	σ^t_{TR}	σ^c_L	σ^t_L	σ^s_{LTR}	ρ_0
[N/mm^2]	[N/mm^2]	[N/mm^2]	[N/mm^2]	[N/mm^2]	[kg/mm^3]
7	7	60	110	7	6.9E-07
c	α^L_ϑ	α^{TR}_ϑ	q^L_ϑ	q^{TR}_ϑ	
[Nmm/kg K]	[1/K]	[1/K]	[Nmm/mmKs]	[Nmm/mmKs]	
1.6E+06	3.5E-06	7E-06	0.16	0.17	
α^L_φ	α^{TR}_φ	q^L_φ	q^{TR}_φ	c_φ	$c_{\varphi\vartheta}$
[-]	[-]	kg/mm s]	[kg/mm s]	[1/s]	[1/Ks]
0.3	3.2	2E-09	3E-10	0	5.5E-08

6 Model Validation at Heating of a Beech Wood (*Fagus Sylvatica*) Board

This section presents a comparison between experimentally measured temperatures while heating a beech wood board up to 120°C for 45 minutes. The model parameters used are listed in Table 3. Figure 12 shows the geometry with the annual rings, the points inside the board, where the temperature evolution is measured, and the boundary conditions of the heating experiment. The surface of the board is discretized, using thermal convection and hygric absorption elements, respectively, as schematically depicted in Fig. 12c. The surface element formulation is based on the constitutive description of q_ϑ and q_φ, compare Eqs. (12) and (13) and the thermal residual as well as the hygric residuals in Eqs. (47) and (55). The thermal part of the surface element reads

$$\boldsymbol{R}^I_{\text{ther}} = \int\limits_{\partial\mathcal{B}^E_{t_{q^\vartheta}}} \boldsymbol{N}^I q_\vartheta \mathrm{d}a, \tag{118}$$

containing Newton's law of cooling, such that

$$q_\vartheta = h_\vartheta \left(\theta - \theta_\infty\right) \tag{119}$$

is specifically described. The hygric part of the surface element, responsible for capturing absorption or emission phenomena at the boundary of the appropriate body reads

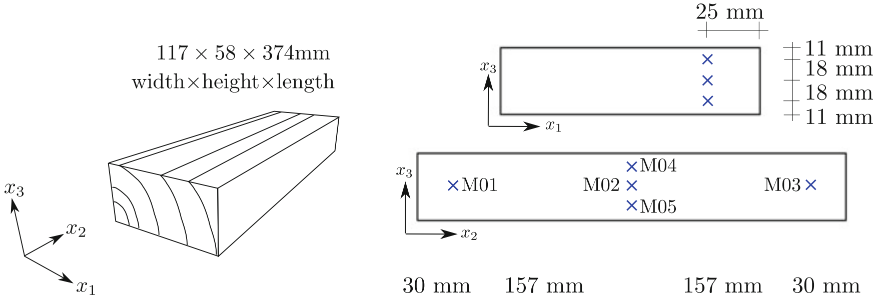
117 × 58 × 374mm
width×height×length
x_3
x_2
x_1
25 mm
11 mm
18 mm
18 mm
11 mm
x_3
x_1
×M04
×M01
M02 ×
M03 ×
×M05
x_3
x_2
30 mm
157 mm
157 mm
30 mm

(a) Geometry (b) Temperature measuring points

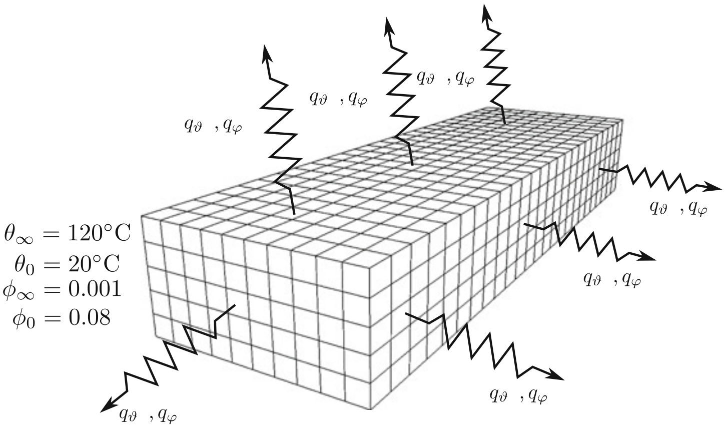
$\theta_\infty = 120°\text{C}$
$\theta_0 = 20°\text{C}$
$\phi_\infty = 0.001$
$\phi_0 = 0.08$
q_ϑ , q_φ

(c) Boundary conditions

Fig. 12 Geometry, boundary conditions and points of temperature measurements of heating experiment of beech wood

$$\boldsymbol{R}^{I}_{\text{hygr}} = \int\limits_{\partial \mathcal{B}^{E}_{t_{\boldsymbol{q}}\varphi}} \boldsymbol{N}^{I} q_\varphi \mathrm{d}a. \tag{120}$$

Similarly to Eq. (119), q_φ is constitutively formulated by

$$q_\varphi = h_\varphi \left(\phi - \phi_\infty\right) \tag{121}$$

in a phenomenological manner. The parameters h_ϑ in Eq. (119) and h_φ in Eq. (121) reflect the ability of exchanging thermal energy and moisture, respectively, per time via the surface area. In case of the beech wood board, they are identified to h_ϑ =1.5E-02 Nmm/sKmm^2 and h_φ =1.0E-10 kg/mm^{2}s. Having a look at Fig. 13, a satisfying agreement between the measured and simulated temperature evolution can be noted. The comparison between the deformed and the undeformed specimen

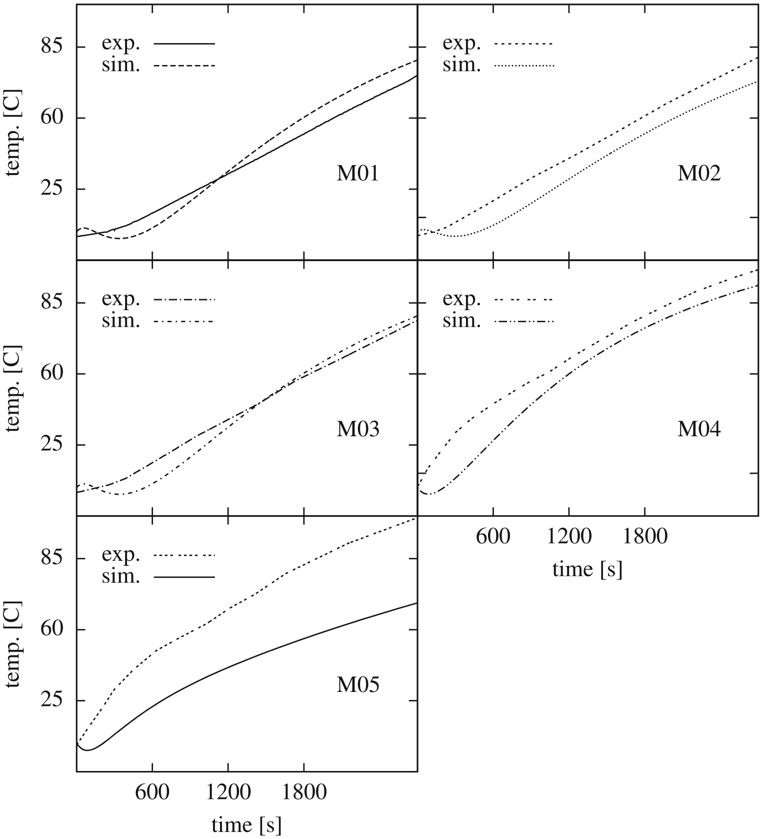

Fig. 13 Comparison of simulation and experiment at heating experiment of beech wood

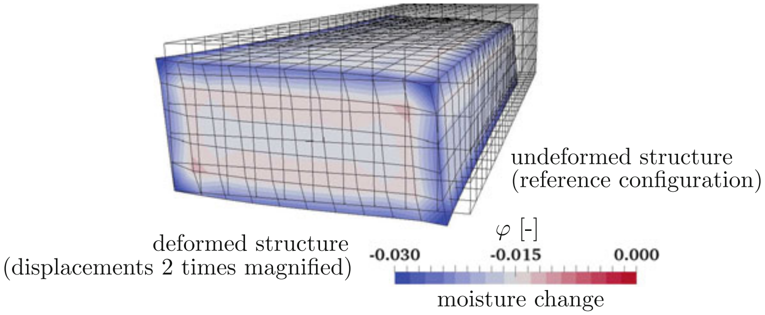
undeformed structure
(reference configuration)
deformed structure
(displacements 2 times magnified)
φ [-]
-0.030
-0.015
0.000
moisture change

Fig. 14 Deformed configuration and moisture distribution of heating experiment of beech wood

at $t = 45$ minutes is shown in Fig. 14 together with the moisture distribution. Due to the anisotropic model and the orientation of the annual rings, the deformation due to drying processes is irregular. Since no deformation is measured while heating the specimen, no comparison with the experimentally deformed board is shown. It can be concluded, that the modeling approach together with the surface discretization are able to capture the temperature evolution of wood successfully.

7 Modeling of Wood Densification and Forming Processes

Following [47], the main aim of wood densification and the forming processes is the tailored design of wooden structural elements with respect to form and functionality. In order to produce e.g. a wooden tube, densification and molding of wood has to be carried out. The final product and its production from a round piece of wood are shown in Fig. 15. This section depicts first a densification simulation, including a comparison to experimentally measured data (engineering strains and temperatures) and second a molding simulation of densified wood.

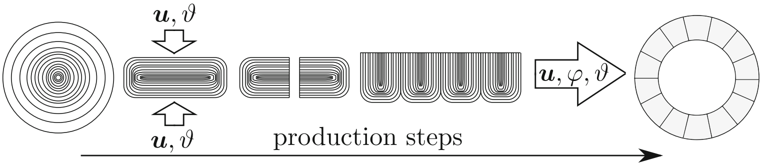
$\boldsymbol{u}, \vartheta$
$\boldsymbol{u}, \vartheta$
production steps
$\boldsymbol{u}, \varphi, \vartheta$

(a) production process

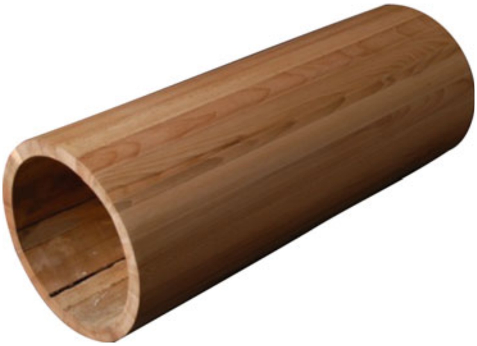

(b) wooden tube, taken from [21]

Fig. 15 Schematic steps of the production process of a tube and a final product in form of a structural tube made from wood

7.1 Densification of a Beech Wood (Fagus Sylvatica) Board

As shown in Fig. 15a, densification of boards is carried out, before they are glued together to a plate, which is afterwards molded. The simulation of such a densification process of one board is presented within this section, where additionally a comparison for strain and temperature quantities with respect to experimental data is carried out. Fig. 16a shows the initial geometry and the annual ring orientation of the specific board. The engineering strains are measured by photogrammetry at the front side surface of the board, as depicted in Fig. 16b. The white abscissa x_1, given in Fig. 16b, is the line of temperature measurements at the front side surface. The densification process is carried out by driving the top surface in a compression testing machine, with coincidentally heated top and bottom surfaces, as described in Fig. 16c. The specimen is discretized by the temperature-, moisture- and displacement-dependent solid finite elements, introduced in Sect. 3. The surface of the element is discretized by the convective and absorptive surface finite elements, as explained in Sect. 6. The top surface is driven up to 50% of the initial height within 14 minutes. The model parameters for beech wood, given in Table 3, are used for the solid finite elements. The model parameters for the description of moisture and temperature exchange with the environmental conditions are set to h_ϑ =1.5E-02 Nmm/sKmm^2 and h_φ =1.0E-10 kg/mm^{2}s. Having a look at Fig. 17, where the comparison between measured and simulated engineering strains transverse to the compression direction is shown, one can see a qualitatively satisfying agreement between simulation and experiment. Similarly, Fig. 18 shows the same qualitatively good agreement for the engineering strains in compression direction with respect to the front side surface of the specimen. The temperature of the front side surface along the white abscissa in Fig. 16b is measured at two distinct times: once at 25% of densification and at the final step of 50% densification. The comparison for both situations is given in Figs. 19 and 20, respectively. Both figures depict a good agreement between experiments and simulation. Additionally, the final density distribution for a transverse and a longitudinal cut through the board is given in Fig. 21. The density correlates with the stress distribution. In parts of high compressive Cauchy stresses, the density is increased, compared to the reference density. Concluding, it can be noted, that the given modeling approaches of volume and surface of the specimen are able to capture the main mechanical and thermal phenomena of wood densification processes.

7.2 Molding of Densified Beech Wood (Fagus Sylvatica)

After the densification and the assembling of densified boards into a plate, the molding process can be carried out. The reference density for the predictive molding simulation of a beech wood plate is taken from Fig. 21, having an averaged value of $\rho_0 = 1500$ kg/m^3. The initial and final configuration are shown in Fig. 22 as well as the discretized part of the specimen. The boundary conditions for the predic-

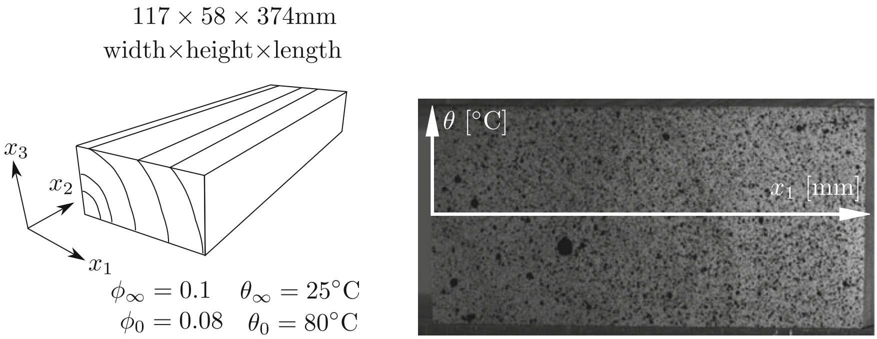
117 × 58 × 374mm
width×height×length
x_3
x_2
x_1
$\phi_\infty = 0.1$ $\theta_\infty = 25°$C
$\phi_0 = 0.08$ $\theta_0 = 80°$C
θ [°C]
x_1 [mm]

(a) Geometry (b) Measuring surface

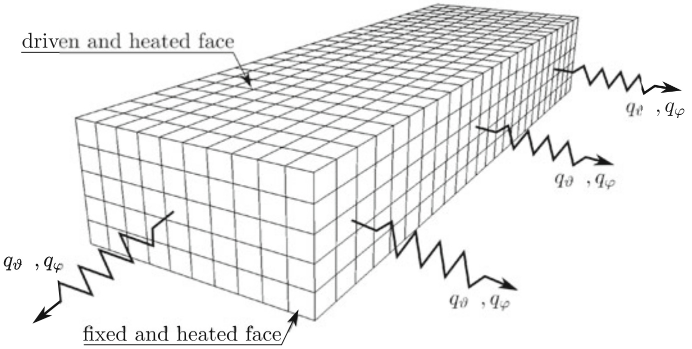
driven and heated face
q_ϑ , q_φ
q_ϑ , q_φ
q_ϑ , q_φ
q_ϑ , q_φ
fixed and heated face

(c) Boundary conditions

Fig. 16 Geometry, photogrammetric, thermographic measurement surface and boundary conditions of the densification experiment of beech wood

tive simulation are applied such that they meet approximately Fig. 15 in [47]. The spatial discretization of the driving mold by a partial linear approximation leads to a piecewise linearly deformed configuration, shown in Fig. 23. The stress results are additionally given in Fig. 23. The stress distribution of σ_{11} is symmetric and is denoted by tensile stresses at the lower surface, while compressive stresses at the top surface occur. The out of plane stresses σ_{22} are also symmetric and arise from the applied plane strain conditions of the simulation. Slight compressive stresses are present in the middle of the plate in the molding direction for σ_{33}, while the boundary parts of the specimen are stretched and therewith tensile stresses are computed. The only non-zero shear stress component is σ_{13}, where an antisymmetric distribution with respect to the symmetry axis is seen. The depicted stresses in Fig. 23 are of predictive character and need further validation by experimental investigations.

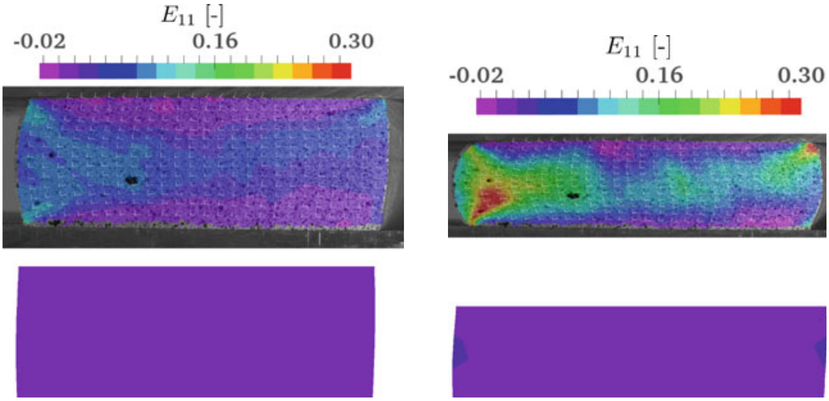

(a) Engineering strain E_{11} at 25% densification (b) Engineering strain E_{11} at 50% densification

Fig. 17 Comparison between simulation and experiment of engineering strain E_{11} distribution at surface of a beech board

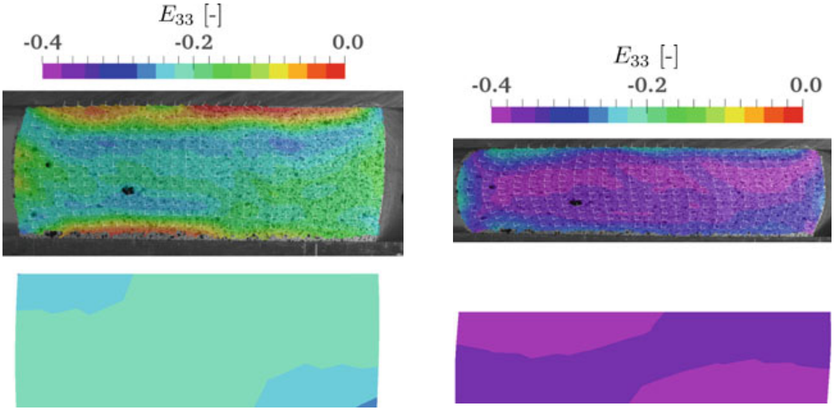

(a) Engineering strain E_{33} at 25% densification (b) Engineering strain E_{33} at 50% densification

Fig. 18 Comparison between simulation and experiment of engineering strain E_{33} distribution at surface of a beech board

8 Conclusions and Outlook

The following conclusions can be drawn. The contribution at hand provides hygro-thermo-mechanical fundamentals of wood, in order to govern equilibrium states under consideration of moisture, temperature and displacement dependent processes. Furthermore, the influence of moisture on the averaged density of wood is modeled by an extended mass balance. A modification of Fick's second law is carried out, in order to characterize the interacting field quantities of temperature and moisture.

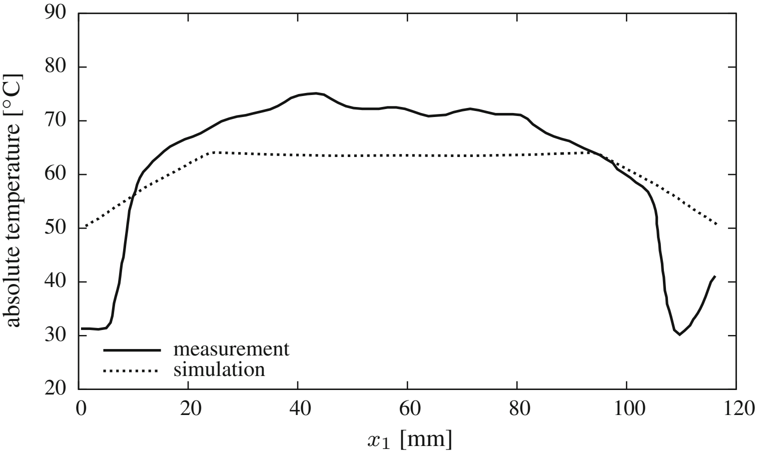

Fig. 19 Comparison of simulation and experiment of temperature at 25% densification of beech wood with respect to the abscissa in Fig. 16b

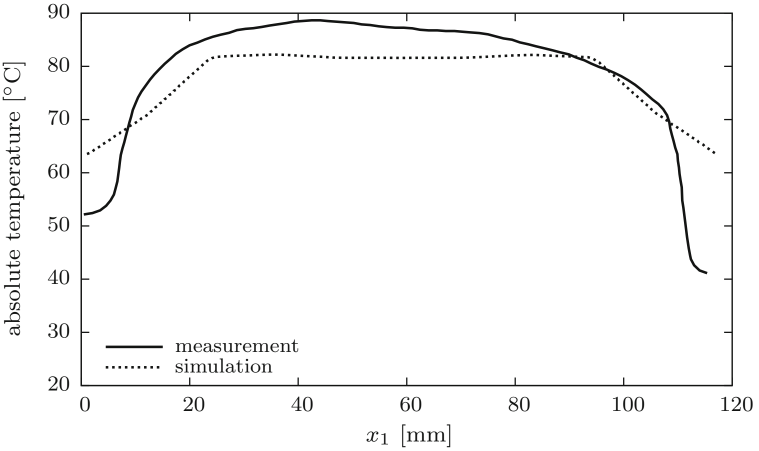

Fig. 20 Comparison of simulation and experiment of temperature at 50% densification of beech wood with respect to the abscissa in Fig. 16b

After providing local continuous balance principles, finite element formulations are derived, together with specific constitutive formulations. These specific formulations capture the hygro-, thermo-mechanical behavior of different wood species as validated for spruce, balsa and beech wood. The applicability of the derived finite element descriptions is demonstrated for modeling the densification and forming processes of beech wood.

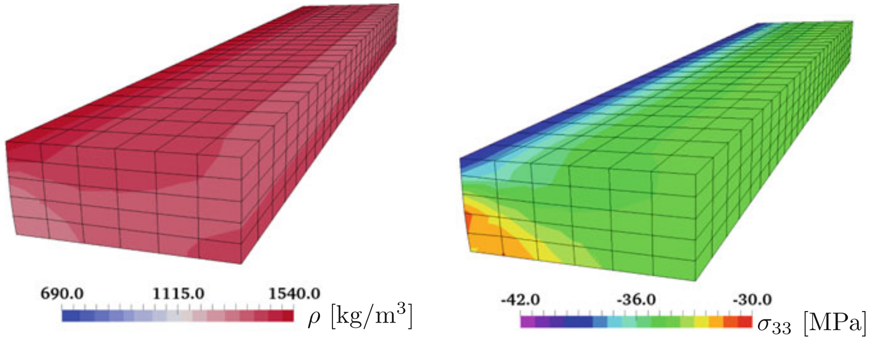
690.0
1115.0
1540.0
ρ [kg/m^3]
-42.0
-36.0
-30.0
σ_{33} [MPa]

(a) Longitudinal cut and density

(b) Longitudinal cut and stress

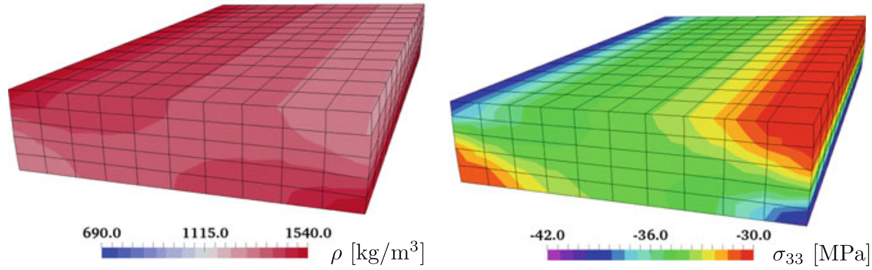
690.0
1115.0
1540.0
ρ [kg/m^3]
-42.0
-36.0
-30.0
σ_{33} [MPa]

(c) Transverse cut and density

(d) Transverse cut and stress

Fig. 21 Cauchy stress and density distribution at the final densification state in a transverse and a longitudinal cut through the specimen

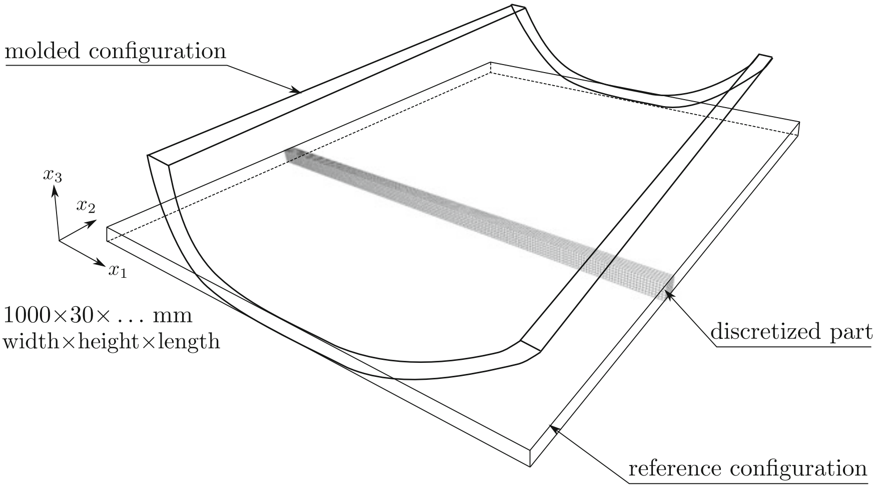
molded configuration
x_3
x_2
x_1
1000×30×… mm
width×height×length
discretized part
reference configuration

Fig. 22 Reference geometry, discretization and deformed configuration in a schematic representation

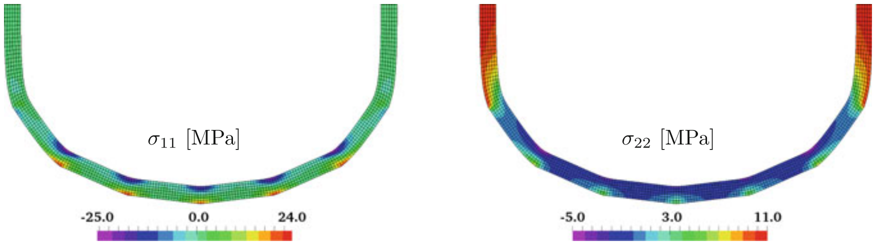

(a) Cauchy stress σ_{11} after molding (b) Cauchy stress σ_{22} after molding

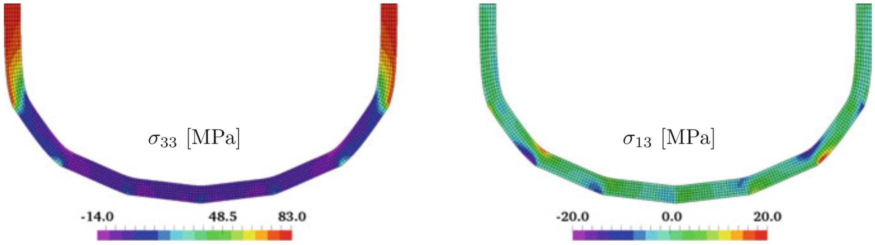

(c) Cauchy stress σ_{33} after molding (d) Cauchy stress σ_{13} after molding

Fig. 23 Cauchy stresses at the final deformation state for the front view of the discretized part of the densified beech wood plate

Material properties of wood are sensitive with respect to moisture content or temperature, e.g. a dried wooden structure is generally more stiff compared to a moister one. The consideration of temperature and moisture dependent material parameters (e.g. yield stresses or elastic properties) will be used in a next step. Therefore, thermal and hygric functions, describing this experimentally determined dependency, will be included into the proposed approach and consistently linearized with respect to the nodal temperature and nodal moisture content. This material characteristic has been neglected so far, due to a minor importance for the discussed application in Sects. 5–7. Additionally, further validation of the proposed modeling by experimental data is needed, especially for capturing the complex processes of producing wooden structural elements from densified wood.

Acknowledgements This research is financially supported by the Deutsche Forschungsgemeinschaft (DFG) under contract KA 1163/22, which is gratefully acknowledged by the authors. Furthermore, the authors would like to thank the Chair of Timber Engineering and Construction Design at Technische Universität Dresden for carrying out the experimental investigations of beech wood in Sects. 6 and 7.1.

References

1. Bazant, Z.P.: Constitutive equation of wood at variable humidity and temperature. Wood Sci. Technol. **19**, 159–177 (1985)
2. de Borst, K., Jenkel, C., Montero, C., Colmars, J., Gril, J., Kaliske, M., Eberhardsteiner, J.: Mechanical characterization of wood: An integrative approach ranging from nanoscale to structure. Comput. Struct. **127**, 53–67 (2013)
3. Carmeliet, J., Guyer, R., Derome, D.: Moisture and mechanical hysteretic behavior of wood: a two-scale approach. In: Proceedings of the Fourth European Conference on Computational Mechanics, Paris (2010)
4. Cave, I.: Modelling moisture-related mechanical properties of wood. Part I: Properties of the wood constituents. Wood Sci. Technol. **12**, 75–86 (1978a)
5. Cave, I.: Modelling moisture-related mechanical properties of wood. Part II: Computation of properties of a model of wood and comparison with experimental data. Wood Sci. Technol. **12**, 127–139 (1978b)
6. Coleman, B., Gurtin, M.E.: Thermodynamics with internal state variables. J. Chem. Phys. **47**, 597–613 (1967)
7. Coleman, B., Noll, W.: The thermodynamics of elastic materials with heat conduction and viscosity. Arch. Rational Mech. Anal. **13**, 167–178 (1963)
8. Easterling, K.E., Harryson, R., Gibson, L.J., Ashby, M.F.: On the mechanics of balsa and other woods. Proc. Royal Soc. Lond. A **383**, 31–41 (1982)
9. Eitelberger, J., Hofstetter, K.: Multiscale homogenization of wood transport properties: Diffusion coefficients for steady-state moisture transport. Wood Material Sci. Eng. **5**, 97–103 (2010)
10. Eitelberger, J., Hofstetter, K.: Prediction of transport properties of wood below the fiber saturation point - a multiscale homogenization approach and its experimental validation, Part II: Steady state moisture diffusion coefficient. Compos. Sci. Technol. **71**, 145–151 (2011)
11. Farruggia, F., Perré, P.: Microscopic tensile tests in the transverse plane of earlywood and latewood parts of spruce. Wood Sci. Technol. **34**, 65–82 (2000)
12. Fleischhauer, R.: A Boundary Value Driven Approach to Computational Homogenization. Dissertationsschrift, Technische Universität Dresden (2016)
13. Frandsen, H.L.: Modelling of Moisture Transport in Wood – State of the Art and Analytic Discussion. Report, Aalborg University (2005)
14. Frandsen, H.L., Svensson, S.: Implementation of sorption hysteresis in multi-fickian moisture transport. Holzforschung **61**, 693–701 (2007)
15. Frandsen, H.L., Damkilde, L., Svensson, S.: A revised multi-fickian moisture transport model to describe non-fickian effects in wood. Holzforschung **61**, 563–572 (2007)
16. Garab, J., Keunecke, D., Hering, S., Szalai, J., P N, : Measurement of standard and off-axis elastic moduli and poisson‘s ratios of spruce and yew wood in transverse plane. Wood Sci. Technol. **44**, 451–464 (2010)
17. Gibson, L.J., Ashby, M.F.: Cellular Solids - Structure and Properties. Cambridge University Press, Cambridge (2001)
18. Göktepe, S.: Micro-Macro Approaches to Rubbery and Glassy Polymers: Predictive Micromechanically-Based Models and Simulations. Dissertationsschrift, Universität Stuttgart (2007)
19. Goodman, J.R., Bodig, J.: Orthotropic elastic properties of wood. J. Struct. Div. Proc. Am. Soc. Civ. Eng. **96**, 2301–2319 (1970)
20. Green, A., Naghdi, P.: Some remarks on elastic-plastic deformation at finite strain. Int. J. Eng. Sci. **9**, 1219–1229 (1971)
21. Haller, P.: Personal Correspondance. Technische Universität Dresden, Chair of Timber Engineering and Construction Design (2010)
22. Hammoum, F., Audebert, P.: Modeling and simulation of (visco)-plastic behavior of wood under moisture change. Mech. Res. Commun. **26**, 203–208 (1999)

23. Hanhijärvi, A., Mackenzie-Helnwein, P.: Computational analysis of quality reduction during drying of lumber due to irrecoverable deformation. I: Orthotropic viscoelastic-mechanosorptive-plastic material model for the transverse plane of wood. J. Eng. Mech. **129**, 996–1005 (2003)
24. Hassani, M.M., Wittel, F.K., Hering, S., Herrmann, H.J.: Rheological model for wood. Comput. Methods Appl. Mech. Eng. **283**, 1032–1060 (2015)
25. Hauksson, J., Bergqvist, G., Bergsten, U., Sjöström, M., Edlund, U.: Prediction of basic wood properties for norway spruce intergretation of near infrared sprectroscopy data using partial least squares regression. Wood Sci. Technol. **35**, 475–485 (2001)
26. Helnwein, P., Eberhardsteiner, J., Mang, H.: Modeling of biaxially stressed wood under plane stress conditions as an orthotropic multi-surface elasto-plastic material. In: Mang, H.A., Rammerstorfer, F., Eberhardsteiner, J. (eds.) Proceedings of the Fifth World Congress on Computational Mechanics, Wien (2002)
27. Hering, S., Keunecke, D., Niemz, P.: Moisture-dependent orthotropic elasticity of beech wood. Wood Sci. Technol. **46**, 927–938 (2011)
28. Hering, S., Saft, S., Resch, E., Niemz, P., Kaliske, M.: Characterisation of moisture-dependent plasticity of beech wood and its application to a multi-surface plasticity model. Holzforschung **66**, 373–380 (2012)
29. Hozjan, T., Svensson, S.: Theoretical analysis of moisture transport in wood as an open porous hygroscopic material. Holzforschung **65**, 97–102 (2010)
30. Jenkel, C., Kaliske, M.: Finite element analysis of timber containing branches - an approach to model the grain course and the influence on the structural behaviour. Eng. Struct. **75**, 237–247 (2014)
31. Jenkel, C., Leichsenring, F., Graf, W., Kaliske, M.: Stochastic modelling of uncertainty in timber engineering. Eng. Struct. **99**, 296–310 (2015)
32. Kaliske, M.: A formulation of elasticity and viscoelasticity for fibre reinforced material at small and finite strains. Comput. Methods Appl. Mech. Eng. **185**, 225–243 (2000)
33. Kaliske, M., Jenkel, C., Saft, S., Resch, E.: Computational models for wooden structures. Comput. Technol. Rev. **2**, 145–176 (2010)
34. Keunecke, D., Hering, S., Niemz, P.: Three-dimensional elastic behaviour of common yew and norway spruce. Wood Sci. Technol. **42**, 633–647 (2008)
35. Lee, E.H.: Elastic-plastic deformation at finite strains. ASME J. Appl. Mech. **36**, 1–6 (1969)
36. Lubarda, V.A.: Constitutive theories based on the multiplicative decomposition of deformation gradient: Thermoelasticity, elastoplasticity, and biomechanics. Appl. Mech. Rev. **57**, 95–108 (2004)
37. Marsden, J., Hughes, T.: Mathematical Foundations of Elasticity. Prentice-Hall, Englewood Cliffs (1983)
38. Miehe, C.: Zur Behandlung Thermomechanischer Prozesse. Dissertationsschrift, Universität Hannover (1988)
39. Miehe, C., Apel, N., Lambrecht, M.: Anisotropic additive plasticity in the logarithmic strain space: modular kinematic formulation and implementation based on incremental minimization principles for standard materials. Comput. Methods Appl. Mech. Eng. **191**, 5383–5425 (2002)
40. Niemz, P.: Physik des Holzes und der Holzwerkstoffe. DRW-Verlag, Leinfelden-Echterdingen (1993)
41. Oudjene, M., Khelifa, M.: Elasto-plastic constitutive law for wood behaviour under compressive loadings. Constr. Building Mater. **23**, 3359–3366 (2009a)
42. Oudjene, M., Khelifa, M.: Finite element modelling of wooden structures at large deformations and brittle failure prediction. Mater. Design **30**, 4081–4087 (2009b)
43. Reichel, S., Kaliske, M.: Hygro-mechanically coupled modelling of creep in wooden structures, part i: Mechanics. Int. J. Solids Struct. **77**, 28–44 (2015a)
44. Reichel, S., Kaliske, M.: Hygro-mechanically coupled modelling of creep in wooden structures, part ii: Influence of moisture content. Int. J. Solids Struct. **77**, 45–64 (2015b)
45. Saft, S., Kaliske, M.: Numerical simulation of the ductile failure of mechanically and moisture loaded wooden structures. Comput. Struct. **89**, 2460–2470 (2011)

46. Saft, S., Kaliske, M.: A hybrid interface-element for the simulation of moisture-induced cracks in wood. Eng. Fract. Mech. **102**, 32–50 (2013)
47. Sandberg, D., Haller, P., Navi, P.: Thermo-hydro and thermo-hydro-mechanical wood processing: An opportunity for future environmentally friendly wood products. Wood Material Sci. Eng. **8**, 64–88 (2013)
48. Simo, J.: Algorithms for static and dynamic multiplicative plasticity that preserve the classical return mapping schemes of the infinitesimal theory. Comput. Methods Appl. Mech. Eng. **99**, 61–112 (1992)
49. Simo, J.C.: Numerical analysis and simulation of plasticity. In: Ciarlet, P.G., Lions, J.L. (eds.) Handbook of Numerical Analysis, vol. VI. Elsevier, Amsterdam (1998)
50. Simo, J.C., Ortiz, M.: A unified approach to finite deformation elastoplastic analysis based on the use of hyperelastic constitutive equations. Comput. Methods Appl. Mech. Eng. **49**, 221–245 (1985)
51. Simo, J.C., Kennedy, J.G., Govindjee, S.: Non-smooth multisurface plasticity and viscoplasticity. loading/unloading conditions and numerical algorithms. Int. J. Numer. Methods Eng. **26**, 2161–2185 (1988)
52. de Souza Neto, E.A., Perić, D., Owen, D.R.J.: Computational Methods for Plasticity - Theory and Applications. Wiley, Chichester (2008)
53. Tabiei, A., Wu, J.: Three-dimensional nonlinear orthotropic finite element material model for wood. Compos. Struct. **50**, 143–149 (2000)
54. Truesdell, C., Noll, W.: The Nonlinear Field Theories of Mechanics. Springer, Berlin (2004)
55. Zhu, Z., Kaliske, M.: Numerical simulation of coupled heat and mass transfer in wood dried at high temperature. Heat Mass Transf. **47**, 351–358 (2010)
56. Zhu, Z., Kaliske, M.: Modeling of coupled heat, moisture transfer and mechanical deformations of wood during drying process. Eng. Comput. **28**, 802–827 (2011)
57. Zienkiewicz, O., Taylor, R.: The Finite Element Method - Volume 1: The Basis, 5th edn. Butterworth-Heinemann, Oxford (2000)

Damage and Fracture of Ductile Sheet Metals: Experiments and Numerical Simulations with New Biaxial Specimens

S. Gerke, M. Schmidt, M. Dirian and M. Brünig

Abstract The paper deals with new experiments and corresponding numerical simulations to study the effect of stress state on damage and fracture behavior of ductile sheet metals. These stress-state-dependent processes are characterized by different mechanisms acting on the micro-level and, therefore, details of the stress state characterized by stress triaxiality and the Lode parameter in the critical parts of the specimens are of interest. Newly designed H-specimens are studied in a combined numerical-experimental procedure. Strain fields in critical regions of the specimens have been evaluated by digital image correlation (DIC) technique and compared with the results of finite element simulations. Considering different biaxial loading conditions it is possible to cover a wide range of stress triaxialities and Lode parameters in tension, shear and compression domains and consequently the newly proposed H-specimens facilitate a controlled study of damage and fracture at different stress states.

1 Introduction

Modeling and numerical simulation of inelastic behavior, damage and fracture of materials are important topics in engineering mechanics, for example, in analysis of complex structural components, in prediction of structural reliability, or in development and optimization of structural design. In particular, for sheet metals the

---

S. Gerke (✉) · M. Schmidt · M. Dirian · M. Brünig
Institut für Mechanik und Statik, Universität der Bundeswehr München,
Werner-Heisenberg-Weg 39, 85577 Neubiberg, Germany
e-mail: steffen.gerke@unibw.de

M. Schmidt
e-mail: m.schmidt@unibw.de

M. Dirian
e-mail: moritz.dirian@unibw.de

M. Brünig
e-mail: michael.bruenig@unibw.de

© Springer International Publishing AG 2018

H. Altenbach et al. (eds.), *Advances in Mechanics of Materials and Structural Analysis*, Advanced Structured Materials 80,
https://doi.org/10.1007/978-3-319-70563-7_5

simulation of complex forming processes is of interest. Based on many experimental and numerical studies it is nowadays evident that during loading of ductile metals inelastic deformations occur which are accompanied by damage and local failure mechanisms on micro- and meso-scales. The accumulation of these processes may lead to fracture of structural elements. The damage and failure mechanisms on the micro-level depend on stress state of the material sample. For example, under tension dominated stress conditions (high positive stress triaxialities) damage in ductile metals is mainly caused by nucleation, growth and coalescence of voids whereas under shear and compression dominated stress states (small positive or negative stress triaxialities) evolution of micro-shear-cracks is the predominant damage mechanism. Furthermore, combination of both basic mechanisms occurs for moderate positive stress triaxialities whereas no damage has been observed in ductile metals for finite negative stress states.

Therefore, to be able to develop phenomenological ductile material models it is important to analyze in detail and to understand these stress-state-dependent processes and mechanisms of damage and fracture acting on different scales.

These processes can be taken into account in a phenomenological way by continuum damage models and corresponding constitutive parameters can be identified by experiments with carefully designed specimens tested under a wide range of loading conditions. For example, elastic material properties, yield stress and coefficients characterizing plastic hardening are usually determined from one-dimensional tension tests with smooth cylindrical or flat rectangular specimens. To detect stress triaxiality dependence of the constitutive equations tension tests with differently pre-notched specimens and corresponding numerical simulations have been used, see for instance Becker et al. [4], Bao and Wierzbicki [2], Bonora et al. [5], Bai and Wierzbicki [1], Brünig et al. [7], Gao et al. [16], Driemeier et al. [13], Dunand and Mohr [14], Brünig et al. [8], Roth and Mohr [26]. These experiments with un-notched and differently notched flat specimens covered stress triaxialities (ratio of mean stress and von Mises equivalent stress: $\eta = \sigma_\mathrm{m}/\sigma_\mathrm{eq}$) between 0.33 and 0.6 which is only a small region in the positive triaxiality range. Larger values appear in tension tests with cylindrical (axis-symmetric) specimens but these can not be manufactured when the behavior of thin sheets is investigated. Therefore, it is necessary to develop new series of experiments with different geometries of flat specimens to analyze the effect of stress states over a wide range.

Specimens with new geometries have been proposed in the literature to analyze different stress states. In particular, specially designed shear specimens have been uniaxially loaded and nearly zero stress triaxialities have been achieved in their centers (Bao and Wierzbicki [2]; Brünig et al. [7]; Gao et al. [16]; Driemeier et al. [13]). Alternatively, shear-off-tests (punch tests) have been performed to axamine shear stress states (Xue et al.[29]). Furthermore, to take into account further ranges of stress states butterfly specimens have been developed (Mohr and Henn [24]; Bai and Wierzbicki [1]; Dunand and Mohr [14]) which can be tested in different directions using special experimental equipment. Corresponding numerical simulations showed stress triaxialities between -0.33 and 0.60 in the critical regions. Moreover, large values of stress triaxialities can be taken into account performing combined tension-torsion experiments on notched hollow cylinders, see e.g. Zheng et al. [30]; Barsoum and Faleskog [3]; Gao et al. [16]; Graham et al. [19]; Faleskog and Barsoum [15]; Haltom et al. [20]. However, these tests are only possible for structures with moderate thickness but not for thin sheets.

In the case of thin structures, it is necessary to develop series of alternative experiments with new flat specimens taken from thin sheets of ductile metals revealing information on inelastic behavior, damage and fracture for a wide range of stress states. For example, two-dimensional (2D) experiments and different geometries of cruciform specimens have been proposed (see, for example, Shiratori and Ikegami [27]; Makinde et al. [23]; Demmerle and Boehler [12]; Müller and Pöhland [25]; Kuwabara [22]; Kulawinski et al. [21]; Zillmann et al. [31]) to analyze the anisotropic plastic behavior or martensite formation of metal sheets under various loading paths. The specimens have been tested in biaxial machines under biaxial planar loading conditions and are characterized by an extended homogeneous central part where inelastic deformations are expected to occur. The main idea of these specimens is that in their centers almost homogeneous strain fields are generated, which can be measured by bonded strain gauges. In contrast, damage and failure processes are known to appear localized. However, on the experimental side strain fields of surfaces can nowadays be extracted by digital image correlation (DIC) systems, even in rather small regions of interest with sufficient resolution. Furthermore, detailed analysis of damage and failure behavior under different loading conditions should be based on more elevated and localized strains and therefore, new specimen geometries have to be developed.

In this context, Brünig et al. [10], Brünig et al. [11] presented a new biaxially loaded specimen where the damage and fracture behavior could be studied numerically as well as experimentally in a wide range of stress states. The specimen geometry studied here is characterized by a small notched region where localized strains and final fracture occur. But the geometry shows mainly two difficulties: Firstly, the specimen legs are pairwise coupled leading to transverse forces on the machine axis which should be avoided and, secondly, rotations of the central part of the non-symmetrc specimen occur during loading. Furthermore, Gerke et al. [18] presented a study of different new biaxially loaded specimens where the H-specimen has shown very promising results. Thus, the need of a detailed numerical-experimental study with this new H-specimen is evident and will be given in the present paper.

The paper is organized as follows: In the next section the main ideas of the phenomenological continuum damage model proposed by Brünig [6] are briefly discussed. In continuation, the numerical-experimental procedure is presented in detail and special focus is given to the experimental challenges. Then, a detailed numerical-experimental study of the H-specimen, covering shear, tension, shear/compression and shear/tension load cases leading to a large range of stress triaxialities is discussed. Finally, the main results are summarized and discussed and perspectives to future work are given.

2 Continuum Damage Model

The continuum framework presented in Brünig [6], Brünig et al. [10] facilitates the modeling of large inelastic deformations in ductile metals including the evolution of damage and is motivated by experiments and micro-mechanical simulations indicating different damage mechanisms caused by various loading conditions (Brünig et al. [9]). The phenomenological approach is briefly summarized here and takes into account damaged and fictitious undamaged configurations. The consistent framework is based on kinematic description of damage leading to definition of damage strain tensors. Here isotropic as well as anisotropic effects are taken into account and provide a realistic representation of ductile material degradation. In addition, the additive decomposition of the strain rate tensor into elastic, plastic and damage parts is takes into account by this kinematic approach.

Fictitiously undamaged configurations are introduced to characterize the elastic-plastic behavior of the undamaged matrix material. This leads to the effective Kirchhoff stress tensor

$$\bar{\boldsymbol{T}} = 2G\boldsymbol{A}^{\mathrm{el}} + \left(K - \frac{2}{3}G\right) \mathrm{tr}\boldsymbol{A}^{\mathrm{el}}\boldsymbol{1} \tag{1}$$

where G represent the shear, K the bulk modulus of the undamaged matrix material and $\boldsymbol{A}^{\mathrm{el}}$ the elastic part of the strain tensor. The plastic behavior is governed by the hydrostatic-stress-dependent yield criterion

$$f^{\mathrm{pl}}\left(\bar{I}_1, \bar{J}_2, c\right) = \sqrt{\bar{J}_2} - c\left(1 - \frac{a}{c}\bar{I}_1\right) = 0, \tag{2}$$

where $\bar{I}_1 = \mathrm{tr}\bar{\boldsymbol{T}}$ and $\bar{J}_2 = {}^1\!/_2\, \mathrm{dev}\bar{\boldsymbol{T}} \cdot \mathrm{dev}\bar{\boldsymbol{T}}$ represent the invariants of the effective stress tensor (1), c is the strength coefficient of the matrix material and a denotes the hydrostatic stress coefficient. In addition, the isochoric plastic strain rate

$$\dot{\bar{\boldsymbol{H}}}^{\mathrm{pl}} = \dot{\lambda}\, \frac{1}{2\sqrt{\bar{J}_2}} \mathrm{dev}\bar{\boldsymbol{T}} = \dot{\gamma}\bar{\boldsymbol{N}}. \tag{3}$$

is taken to describe the evolution of plastic deformations. In Eq. (3) $\bar{\boldsymbol{N}} = {}^1\!/\!\sqrt{2\bar{J}_2}\, \mathrm{dev}\bar{\boldsymbol{T}}$ denotes the normalized deviatoric stress tensor and $\dot{\gamma} = \bar{\boldsymbol{N}} \cdot \dot{\bar{\boldsymbol{H}}}^{\mathrm{pl}}$ represents the equivalent plastic strain rate measure used in the present continuum model.

Damaged configurations are introduced to characterize the behavior of anisotropically damaged samples. The Kirchhoff stress tensor of the damaged metal

$$\begin{aligned} \boldsymbol{T} = {} & 2\left(G + \eta_2\, \mathrm{tr}\boldsymbol{A}^{\mathrm{da}}\right)\boldsymbol{A}^{\mathrm{el}} + \left[\left(K - \frac{2}{3}G + 2\eta_1\, \mathrm{tr}\boldsymbol{A}^{\mathrm{da}}\right)\mathrm{tr}\boldsymbol{A}^{\mathrm{el}} + \eta_3\left(\boldsymbol{A}^{\mathrm{da}} \cdot \boldsymbol{A}^{\mathrm{el}}\right)\right]\boldsymbol{1} \\ & + \eta_3\, \mathrm{tr}\boldsymbol{A}^{\mathrm{el}}\boldsymbol{A}^{\mathrm{da}} + \eta_4\left(\boldsymbol{A}^{\mathrm{el}}\boldsymbol{A}^{\mathrm{da}} + \boldsymbol{A}^{\mathrm{da}}\boldsymbol{A}^{\mathrm{el}}\right) \end{aligned} \tag{4}$$

also takes into account the damage part of the strain tensor $\boldsymbol{A}^{\text{da}}$. Furthermore, the constitutive parameters $\eta_1 ... \eta_4$ describe the stress-state-dependent deteriorating effect of damage on the elastic material behavior and the damage criterion

$$f^{\text{da}} = \alpha I_1 + \beta \sqrt{J_2} - \sigma = 0 \tag{5}$$

describes onset and continuation of damage. Equation (5) is formulated in terms of the stress invariants $I_1 = \text{tr}\boldsymbol{T}$ and $J_2 = {}^1\!/\!_2\, \text{dev}\boldsymbol{T} \cdot \text{dev}\boldsymbol{T}$ of the Kirchhoff stress tensor (4) as well as in the damage threshold σ. The variables α and β represent damage mode parameters corresponding to different stress-state-dependent damage mechanisms on the micro-level as indicated before. For the current purpose the stress state is uniquely characterized by the stress intensity (von Mises equivalent stress) $\sigma_{\text{eq}} = \sqrt{3 J_2}$, the stress triaxiality

$$\eta = \frac{\sigma_{\text{m}}}{\sigma_{\text{eq}}} = \frac{I_1}{3\sqrt{3 J_2}} \tag{6}$$

with the mean stress $\sigma_{\text{m}} = {}^1\!/\!_3\, I_1$ and the Lode parameter

$$\omega = \frac{2\tilde{T}_2 - \tilde{T}_1 - \tilde{T}_3}{\tilde{T}_1 - \tilde{T}_3} \quad \text{with} \quad \tilde{T}_1 \geq \tilde{T}_2 \geq \tilde{T}_3 \tag{7}$$

expressed in terms of the principal Kirchhoff stress components $\tilde{T}_1$, $\tilde{T}_2$ and $\tilde{T}_3$. The damage strain rate tensor

$$\dot{\boldsymbol{H}}^{\text{da}} = \dot{\mu} \left(\bar{\alpha} \frac{1}{\sqrt{3}} \mathbf{1} + \bar{\beta} \boldsymbol{N} + \bar{\delta} \boldsymbol{M} \right) \tag{8}$$

reflects the evolution of macroscopic deformations of the material caused by stress-state-dependent damage processes acting on the micro-scale. For further information on the normalized tensors $\boldsymbol{N}$ and $\boldsymbol{M}$ see Brünig et al. [9].

The stress state dependent parameters $\bar{\alpha}$, $\bar{\beta}$ and $\bar{\delta}$ are kinematic variables describing the portion of volumetric and isochoric damage-based deformations and $\dot{\mu}$ represents the equivalent damage strain rate measure characterizing the amount of increase in damage. The damage rule (8) takes into account a volumetric part (first term in Eq. (8)) corresponding to isotropic growth of voids as well as deviatoric parts (second and third term in Eq. (8)) corresponding to anisotropic evolution of micro-shear-cracks and thus irreversible strains caused by damage mechanisms acting on the micro-level are modelled in an appropiate phaenomenological way by the proposed damage rule (8). It should be noted that various parameters appearing in the damage constitutive Eqs. (4), (5) and (8) depend on the stress state and their identification must be based on experiments. Consequently, it is desirable that corresponding experiments cover a wide range of stress triaxialities and Lode parameters. The newly developed H-specimen can facilitate this experimental data and the main focus of this paper is the presentation of the corresponding numerical-experimental procedure and results.

3 Geometry

Singh et al. [28] presented a symmetric specimen for shear-like failure under dynamic loading conditions. Gerke [17] modified this geometry and added notches in thickness direction to concentrate major deformations within this region. Furthermore, Roth and Mohr [26] presented a symmetric specimen with two shear fracture zones to be tested in a standard one-dimensional test machine under static loading conditions. The principal advantage of these specimens over standard one-dimensional shear specimens as presented for instance in Brünig et al. [7] and Driemeier et al. [13] is that rotations of the shear region leading to more tension-like behavior are as far as possible suppressed. But it is important to point out that symmetric behavior of the two regions with major deformations is assumed.

This concept is extended for biaxial loading resulting in the proposed H-specimen. This specimen (Fig. 1) is double-symmetric with four uniform notched regions allowing a direct relation between loading and stress states in this parts. Consequently, the specimen can be used under shear or tension loading as well as shear loading can be superimposed by tension or compression. Furthermore, as long as the specimen is loaded uniformly at opposite axis its center remains at the same place. This is an important aspect for the analysis of strain fields based on digital image correlation technique. Each notched region has a width of 6.0 mm and the depth of the notch is 1.0 mm on each side with a notch radius of 2.0 mm, see Fig. 2 for details.

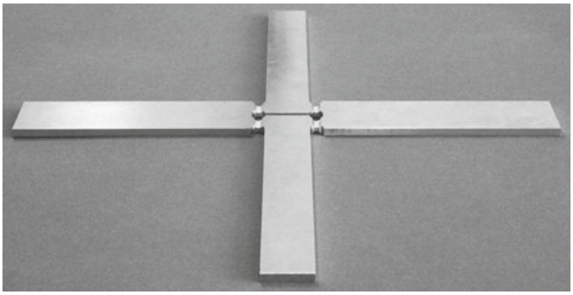

Fig. 1 Photo of H-specimen

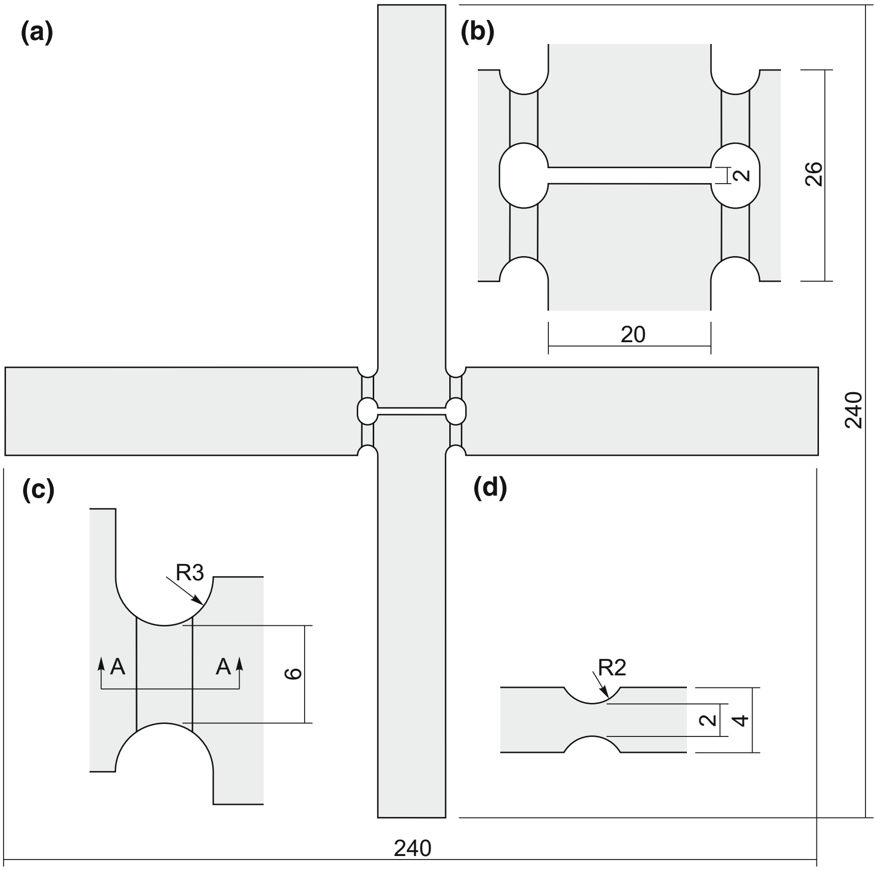

Fig. 2 Sketch of H-Specimen, all units in [mm]; **a** complete specimen; **b** central area; **c** upper right notch; **d** cross section A–A

4 Numerical-Experimental Approach

All experiments have been performed on the biaxial test machine LFM-BIAX 20 kN, produced by Walter & Bai, Switzerland. It contains four electro-mechanically, individually driven cylinders with load maxima of ±20 kN. During the experiments the specimens are clamped in the four heads of the cylinders and the machine reports the displacements $u^M_{i.j}$ $(i = 1, 2,\ j = 1, 2)$ as well as the applied forces $F_{i.j}$ of each cylinder, see Fig. 3. Within this notation the first index indicates the axis and the second index the direction.

The principal idea of the experimental technique is that the ratio between the forces $\zeta = {}^{F_2}/_{F_1}$ is kept constant during the tests and, consequently, the stress state within the notched region can be expected to vary only slightly. Non-symmetric behavior during the experiment can be caused by fabrication tolerances of the specimen, misalignment

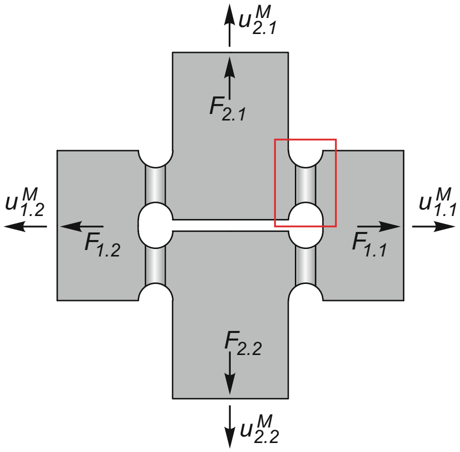

Fig. 3 Schematic sketch of experimental technique; red marked part is used to indicate results

of the machine and non-symmetric clamping and can not be avoided completely. To face this difficulties a mainly displacement-driven experimental procedure has been used: The leading machine displacement $u^M_{2.1}$ of cylinder 2.1 is continuously increased by 0.04 $^{\mathrm{mm}}/_{\mathrm{min}}$ while the same displacement is applied on the cylinder 2.2 on opposite side of the same axis, see Fig. 3. The generated force $F_{2.1}$ is now taken, divided by the factor ζ and applied on the cylinder 1.1 as $F_{1.1}$ causing the machine displacement $u^M_{1.1}$. In continuation the same displacement is applied as $u^M_{1.2}$ on the cylinder 1.2 on the opposite side of the same axis. This technique has been shown to be stable.

The full 3D displacement field on the specimen surface was measured with a Q-400 digital 3D image correlation (DIC) system provided by Dantec/Limess. The stereo setting consisted of two $6.0Mpx$ cameras equipped with 75 mm lenses. The evaluation was realized with the corresponding Istra 4D software provided with the system. One side of the specimen was firstly sprayed with a white acrylic lacquer and then the speckle pattern shown in Fig. 4 was sprayed on with a graphite-based coating. Specimen preparation was realized shortly before the experiment starts to avoid excessive curing and thus no exfoliation of the coating was observed during the experiments. Furthermore, the displacements $u^M_{i.j}$ as well as the applied forces $F_{i.j}$ were transferred and stored with the data sets of the image correlation system at a frequency of 1.0 Hz.

To compare numerical and experimental results the discrete data sets have to be matched. It is important to notice, that this can not be realized by the machine displacements $u^M_{i.j}$ since these include the machine stiffness as well as possible slipping at the clamping. Therefore, on the experimental side for all specimens two points have been chosen outside the notched region, see for example the red dots in Fig. 4, where the displacements in 2-direction $u_{2.1}$ and $u_{2.2}$ have been reported. The difference of these two displacements $\Delta u_{\mathrm{Ref}} = u_{2.1} - u_{2.2}$ reflects the relative movement of these two points in 2-direction.

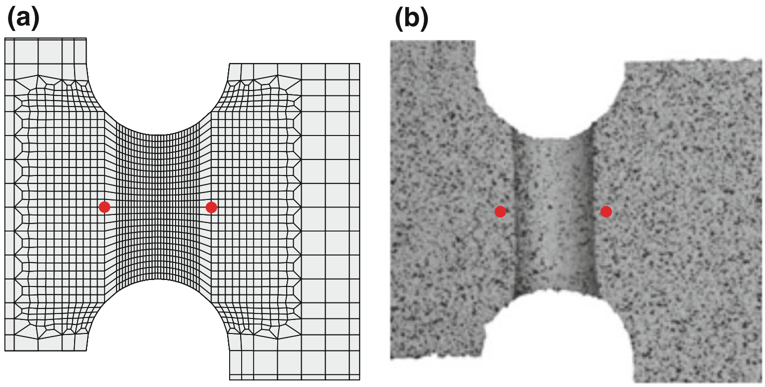

Fig. 4 Evaluation points for Δu_{ref}; **a** numerical at finite element node; **b** digital image correlation (DIC)

Corresponding elastic-plastic finite element (FE) simulations have been carried out with Ansys Classic. Elastic behavior of the investigated aluminum alloy 2017 is based on Young's modulus $E = 69000\,\mathrm{N/mm^2}$ and Poisson's ratio $\nu = 0.3$. Plastic behavior is modeled by nonlinear isotropic hardening (`nliso`) with the Voce hardening law

$$c = k + R_0 \epsilon^{\text{pl}} + R_\infty \left(1 - e^{-b\epsilon^{\text{pl}}}\right), \tag{9}$$

with the parameters $k = 320\,\mathrm{N/mm^2}$, $R_0 = 650\,\mathrm{N/mm^2}$, $R_\infty = 100\,\mathrm{N/mm^2}$ and $b = 30$. For all simulations the mesh shown in Fig. 5 with 79608 hexahedral elements was used with remarkable refinement in the region where localization of strains and stresses are expected to occur (Fig. 5). These `solid185`-elements were fully integrated and the B-bar option was active. To display strain fields on the specimen surfaces, the surface was overlaid with `shell181`-elements. For the shell elements `keyopt 1` was set to `2`, i.e. its stiffness was not included in the stiffness matrix and they are only used to display the numerical results on the specimen surface to be compared with available experimental data. For the numerical simulations the length of the specimen legs has been reduced from 120 to 26 mm in 1-direction and 23 mm in 2-direction and thus the numerical costs could be remarkably reduced.

The loading is applied similar to the experimental procedure discussed above. Firstly, the displacements of axis 1 in axis direction is kept constant while a displacement increment is applied on axis 2. At the end of this step the current force F_2 of axis 2 is reported. Secondly, in the next load step the force $F_1 = {}^1\!/_\zeta F_2$ is applied on axis 1 while the displacement of axis 2 is kept constant. By using this iterative procedure the force ratio ζ is maintained almost constant during the simulation which is an important aspect to analyze stress-state-dependent parameters. The relative displacement Δu_{ref} is taken on the numerical side by two corresponding nodes of the finite

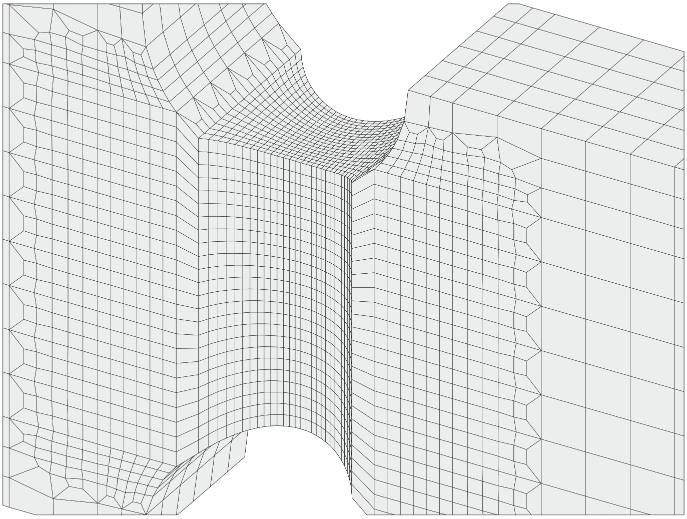

Fig. 5 Finite element mesh of notched region with remarkable refinement

element mesh located at the specimen surface, see Fig. 4. By matching the values on the numerical and on the experimental side, the corresponding load steps have been identified.

5 Experimental and Numerical Results

The major innovation of the H-specimens is the introduction of four individual notched regions. Evidently there may be disturbance of the assumed symmetry within experiments caused for example by non-symmetric manufacturing or non-symmetric clamping. Therefore, Fig. 6 compares Δu_{Ref} at all four notches of a H-specimen within the experiment with $F_1/F_2 = 0.5/1$. The curve progression is homogeneous

Fig. 6 DIC comparison of Δu_{ref} between different notches within one specimen, loading $F_1/F_2 = 0.5/1$

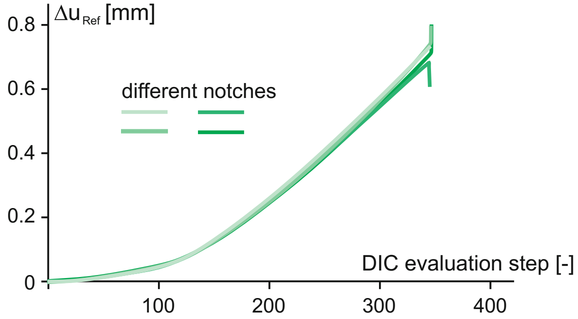

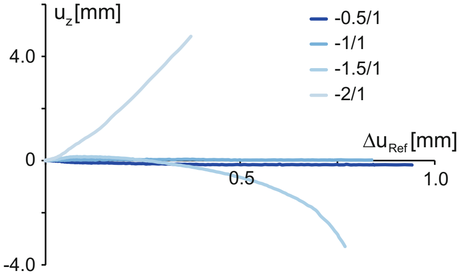

Fig. 7 Displacements u_z perpendicular to loading directions for different shear-compression loading conditions

and non-symmetric effects do not emerge significantly and finally, two (crosswise arranged) notches fracture.

The H-specimen can also be used under shear-tension and shear-compression loading. For compression-dominated loading out of plane movements or buckling of the specimen has to be controlled to avoid superimposed stresses caused by these additional deformation modes. Figure 7 indicates the experimentally measured displacement u_z perpendicular to the specimen for different shear-compression loading conditions. For $F_1/F_2 = -0.5/1$ and $F_1/F_2 = -1/1$ only negligible small out of plane movements can be observed while for $F_1/F_2 = -1.5/1$ with ongoing loading major out of plane movements occur and for $F_1/F_2 = -2/1$ the specimen indicated directly out of plane movements. Although the biaxial machine has been aligned carefully this out of plane movement is most likely due to slight differences in height of the clampings rather then buckling and for further experimental studies of compression-dominated loading an additional bearing has to be designed and installed. Consequently, the load cases $F_1/F_2 = -1.5/1$ and $F_1/F_2 = -2/1$ are not further investigated within this paper.

In Fig. 8 the experimental measured forces in axis 2 (responsible for shear loading) are indicated for different loading conditions F_1/F_2 with respect to Δu_{Ref}, see Fig. 4. By analyzing these results it is important to have in mind that the curves in Fig. 8

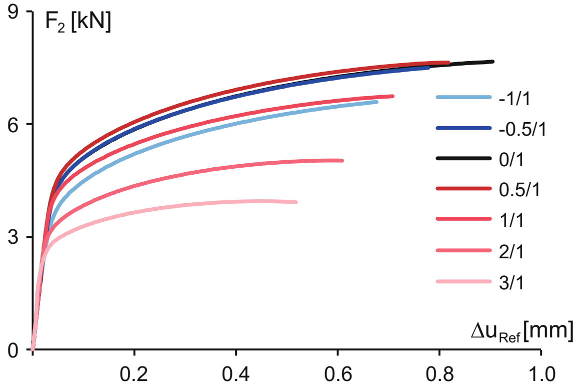

Fig. 8 Load-displacement curves for different loading conditions

Fig. 9 Load-displacement curve for uni-axial loading on axis 1

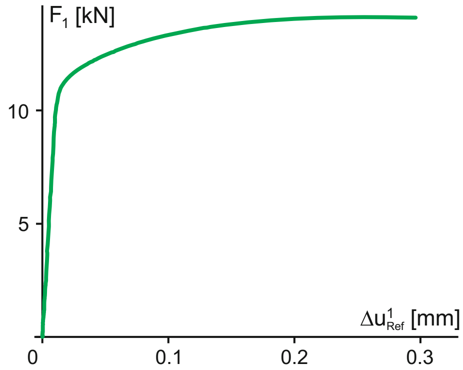

Fig. 10 Load $F_1^{\max}$ before fracture occurrence vs. load case F_2/F_1

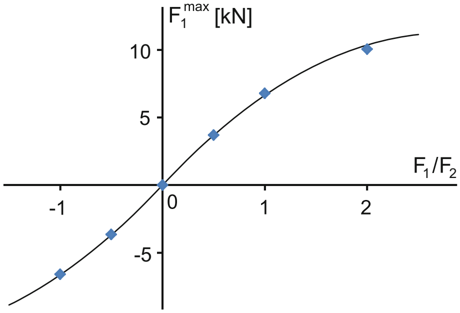

indicate only one axis, i.e. F_1 as well as $\Delta u_{\text{Ref}}^1 = u_{1.1} - u_{1.2}$ are not reflected. Although all curves show comparable behavior it can be noted that the curves of the experiments with superimposed compression ($F_1/F_2 = -0.5/1$ and $F_1/F_2 = -1/1$) increase more continuous than those with superimposed tension. In particular the curve of the experiment $F_1/F_2 = 3/1$ shows slight decreasing behavior before fracture.

The proposed H-specimen has the advantage that it can be loaded independently in both axis. For pure shear loading ($F_1/F_2 = 0/1$) the experimental curve is included in Figs. 8 and 9 indicates the behavior under pure loading in axis 1 ($F_1/F_2 = 1/0$), i.e. tension dominated. Due to the very concentrated zone of inelastic deformations the displacement Δu_{Ref}^1 reaches only approximately 3 mm. Furthermore, the curve is characterized by a sharp transition to inelastic behavior and unincisive hardening.

Figures 10, 11 and 12 refer to the loads at fracture $F_1^{\max}$ and $F_2^{\max}$ of the different tension or compression superimposed shear load cases. The blue dots reflect the discrete data points from the experiments and the thin black line gives a possible approximation. For superimposed tension the load $F_1^{\max}$ (tension component) indicates increasing values from the origin with decreasing slope, see Fig. 10. For superimposed compression the values are almost symmetric with respect to the origin whereas the absolute values are slightly smaller.

For the load $F_2^{\max}$ (shear component) the maximum load is given for the pure shear load case $F_1/F_2 = 0/1$. For superimposed tension and compression the values

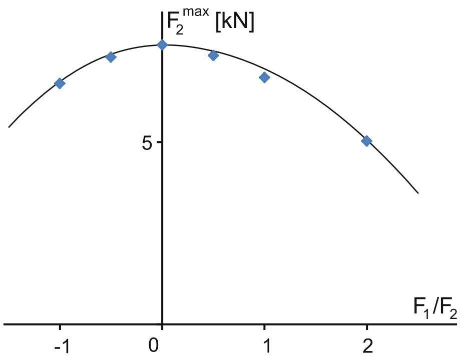

Fig. 11 Load $F_2^{\max}$ before fracture occurrence vs. load case F_2/F_1

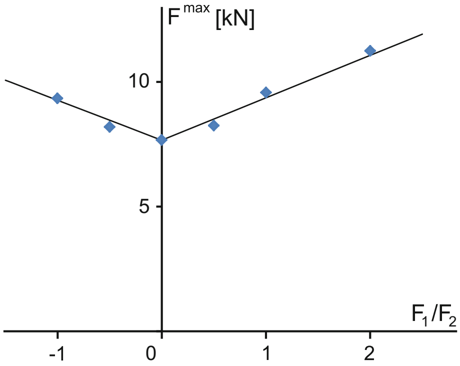

Fig. 12 Load $F^{\max}$ before fracture occurrence vs. load case F_2/F_1

decrease whereas for more significant tension or compression the decrease becomes more dominant. The behavior is almost symmetric while the reduction is slightly more significant for compression loading.

By defining the maximum load to

$$F^{\max} = \sqrt{\left(F_1^{\max}\right)^2 + \left(F_2^{\max}\right)^2} \tag{10}$$

i.e. as the absolute value of the vector sum a different picture is given: The minimum value of $F^{\max}$ is given for the pure shear case $F_1/F_2 = 0/1$. For superimposed tension as well as compression the values increase whereas a linear approximation seems to be most appropriate with a slightly smaller slope for superimposed compression, see Fig. 12.

Numerical simulations of the H-specimen have been realized for the experiments with different load cases. The respective stress triaxialities η and the Lode parameters ω are shown in Fig. 13 at $2/3$ of the maximum Δu_{ref}. The indicated distribution can be taken as representative and does not change significantly after plastic deformation has started which is caused by the central experimental idea of the constant load ratio F_2/F_1. For these load ratios the triaxialities are in the range of $-0.6 \leq \eta \leq 0.8$

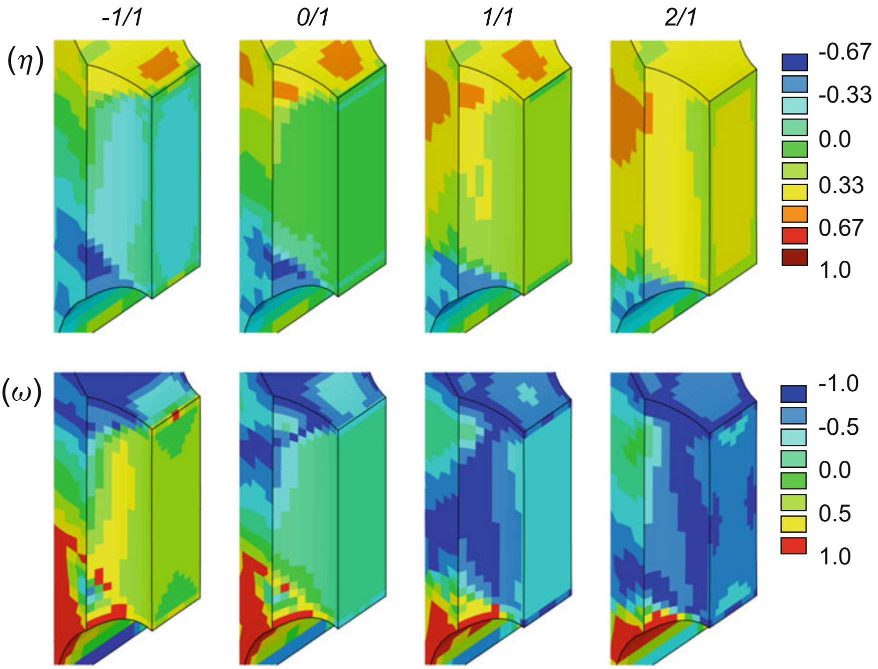

Fig. 13 Stress triaxiality η and Lode parameter ω under different loading conditions F_1/F_2

Fig. 14 Experimental and numerical load-displacement curves for $F_2/F_1 = 0/1$

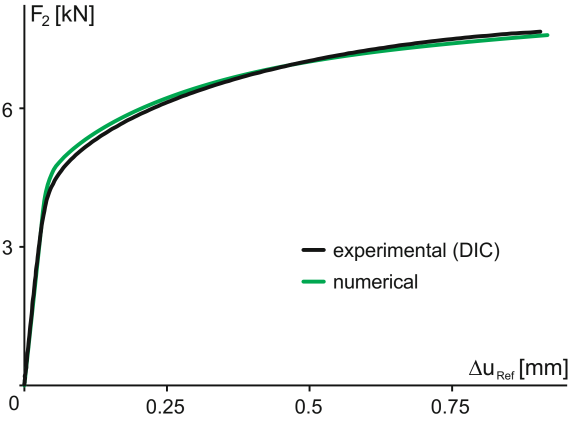

and the distribution of η and ω is very homogenous throughout the notch allowing a detailed study of the damage processes within this area. Therefore, biaxial tests with the H-specimen are excellently qualified for the development of stress-state-dependent functions in the damage constitutive Eqs. 4, 5 and 8.

Figure 14 indicates the experimental and numerically predicted load-displacement curves exemplarily of the pure shear load case ($F_2/F_1 = 0/1$). Both curves agree well

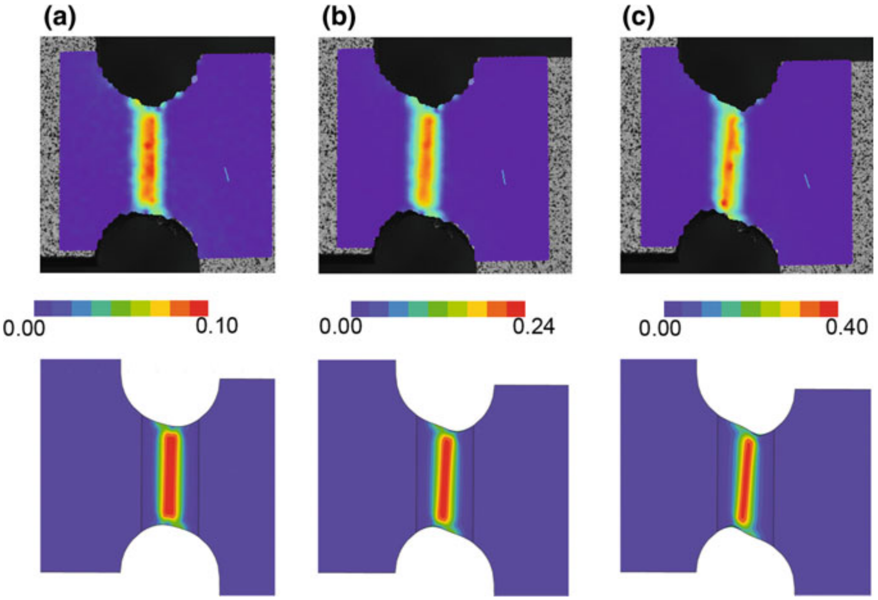

Fig. 15 Principal strain ε_1 at different loading stages for $F_1/F_2 = 0/1$; upper row experimental evaluation by DIC and lower row numerically predicted

while the numerically predicted curve has a sharper transition to inelastic material behavior.

In Fig. 15 the first principal strains ε_1 analyzed by the DIC technique are compared with the corresponding numerically predicted ones at different states throughout the experiment ((a) 1/3, (b) 2/3 of the maximum Δu_{ref} and (c) shortly before fracture) under shear loading conditions $F_1/F_2 = 0/1$. Good agreement can be observed at all three loading stages. Throughout the loading process the zone of more elevated deformations becomes more pronounced and tends to be inclined. The evolution of damage strains is modeled by Eq. (8) and, therefore, these experimental results can be used to propose functions for the stress-state-dependent parameters and to validate the damage rule (8).

Accumulation of damage leads to final fracture of the specimen as indicated for different loading ratios F_2/F_1 in Fig. 16. For the here presented load cases the specimen fractured in two (frequently crosswise) notches. Consequently fracture did not always occur in the in Fig. 3 marked part but for illustration purposes the pictures have been reflected. It can be seen that the inclination of the fracture depends on the loading condition and it is worthy to point out that for the load cases with superimposed shear loading a crack in notch direction is most likely under loading $F_1/F_2 = 0.5/1$ and not under $F_1/F_2 = 0/1$ as expected. Furthermore, for more elevated tension loading the inclination of the crack does not change significantly any more, which might be an effect of the notch length.

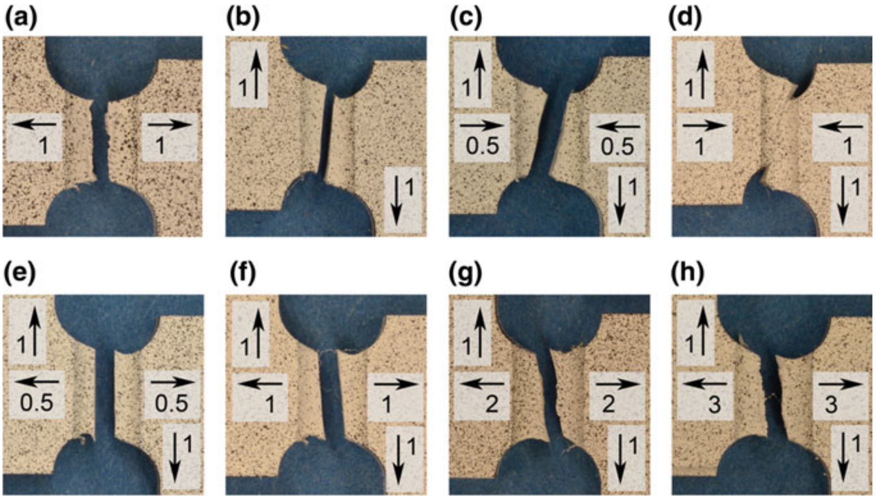

Fig. 16 Fractured specimens for different load cases

6 Conclusion

The paper has discussed a phenomenological continuum model taking into account the effect of stress state on damage and fracture mechanisms acting on different scales. Experiments are needed to validate this damage and failure model especially the stress-state-dependent constitutive laws. Consequently, a new specimen (H-specimen) has been developed and discussed in detail. The design of this new H-specimen is conducted by two ideas: Firstly, that strain localization can be achieved by reducing the material thickness in certain areas and secondly, that strain measurement at elevated levels can be analyzed by a digital image correlation (DIC) technique.

The H-specimen is characterized by four notched zones which are arranged in direction of the shear loading. By its geometry the coupling between loading and stress state within the notched part is easily accessible and the specimen can be used for a wide range of stress triaxialities. For elevated superimposed compression out of plane movements have been detected which need in the future further attention. In addition, investigations regarding the notch geometry are reasonable to study the effects of the notch radius and the notch length. These biaxially loaded H-specimen allows the study of damage and fracture processes under well controlled loading conditions and are an important improvement in this field of research.

Acknowledgements Financial support from Deutsche Forschungsgemeinschaft (German Research Foundation) though contract number BR1793/19-1. is gratefully acknowledged.

References

1. Bai, Y., Wierzbicki, T.: A new model of metal plasticity and fracture with pressure and Lode dependence. Int. J. Plast. **24**, 1071–1096 (2008)
2. Bao, Y., Wierzbicki, T.: On the fracture locus in the equivalent strain and stress triaxiality space. Int. J. Mech. Sci. **46**, 81–98 (2004)
3. Barsoum, I., Faleskog, J.: Rupture mechanisms in combined tension and shear - Experiments. Int. J. Solids Struct. **44**, 1768–1786 (2007)
4. Becker, R., Needleman, A., Richmond, O., Tvergaard, V.: Void growth and failure in notched bars. J. Mech. Phys. Solids **36**, 317–351 (1988)
5. Bonora, N., Gentile, D., Pirondi, A., Newaz, G.: Ductile damage evolution under triaxial state of stress: theory and experiments. Int. J. Plast. **21**, 981–1007 (2005)
6. Brünig, M.: An anisotropic ductile damage model based on irreversible thermodynamics. Int. J. Plast. **19**, 1679–1713 (2003)
7. Brünig, M., Chyra, O., Albrecht, D., Driemeier, L., Alves, M.: A ductile damage criterion at various stress triaxialities. Int. J. Plast. **24**, 1731–1755 (2008)
8. Brünig, M., Albrecht, D., Gerke, S.: Numerical analyses of stress-triaxiality-dependent inelastic deformation behavior of aluminum alloys. Int. J. Damage Mech. **20**, 299–317 (2011)
9. Brünig, M., Gerke, S., Hagenbrock, V.: Micro-mechanical studies on the effect of the stress triaxiality and the Lode parameter on ductile damage. Int. J. Plast. **50**, 49–65 (2013)
10. Brünig, M., Brenner, D., Gerke, S.: Stress state dependence of ductile damage and fracture behavior: Experiments and numerical simulations. Eng. Fract. Mech. **141**, 152–169 (2015)
11. Brünig, M., Gerke, S., Schmidt, M.: Biaxial experiments and phenomenological modeling of stress-state-dependent ductile damage and fracture. Int. J. Fract **200**, 63–76 (2016). https://doi.org/10.1007/s10704-016-0080-3
12. Demmerle, S., Boehler, J.: Optimal design of biaxial tensile cruciform specimens. J. Mech. Phys. Solids. **41**, 143–181 (1993)
13. Driemeier, L., Brünig, M., Micheli, G., Alves, M.: Experiments on stress-triaxiality dependence of material behavior of aluminum alloys. Mech. Mater. **42**, 207–217 (2010)
14. Dunand, M., Mohr, D.: On the predictive capabilities of the shear modified Gurson and the modified Mohr-Coulomb fracture models over a wide range of stress triaxialities and Lode angles. J. Mech. Phys. Solids. **59**, 1374–1394 (2011)
15. Faleskog, J., Barsoum, I.: Tension-torsion fracture experiments - Part I: experiments and a procedure to evaluate the equivalent plastic strain. Int. J. Solids. Struct. **50**, 4241–4257 (2013)
16. Gao, X., Zhang, G., Roe, C.: A study on the effect of the stress state on ductile fracture. Int. J. Damage Mech. **19**, 75–94 (2010)
17. Gerke, S.: Damage and fracture of ductile metals under dynamic loading conditions. Ph.D thesis, UniversitÃd't der Bundeswehr, MÃijnchen (2013)
18. Gerke, S., Adulyasak, P., Brünig, M.: New biaxially loaded specimens for the analysis of damage and fracture in sheet metals. Int. J. Solids Struct. (2017). https://doi.org/10.1016/j.ijsolstr.2017.01.027
19. Graham, S., Zhang, T., Gao, X., Hayden, M.: Development of a combined tension-torsion experiment for calibration of ductile fracture models under conditions of low triaxiality. Int. J. Mech. Sci. **54**, 172–181 (2012)
20. Haltom, S., Kyriakides, S., Ravi-Chandar, K.: Ductile failure under combined shear and tension. Int. J. Solids. Struct. **50**, 1507–1522 (2013)
21. Kulawinski, D., Nagel, K., Henkel, S., Hübner, P., Fischer, H., Kuna, M., Biermann, H.: Characterization of stress-strain behavior of a cast trip steel under different biaxial planar load ratios. Eng. Fract. Mech. **78**, 1684–1695 (2011)
22. Kuwabara, T.: Advances in experiments on metal sheet and tubes in support of constitutive modeling and forming simulations. Int. J. Plast. **23**, 385–419 (2007)
23. Makinde, A., Thibodeau, L., Neale, K.: Development of an apparatus for biaxial testing using cruciform specimens. Exp. Mech. **32**, 138–144 (1992)

24. Mohr, D., Henn, S.: Calibration of stress-triaxiality dependent crack formation criteria: A new hybrid experimental-numerical method. Exp. Mech. **47**, 805–820 (2007)
25. Müller, W., Pöhland, K.: New experiments for determining yield loci of sheet metal. Mater. Process. Technol. **60**, 643–648 (1996)
26. Roth, C.C., Mohr, D.: Ductile fracture experiments with locally proportional loading histories. Int. J. Plast. **79**, 328–354 (2016)
27. Shiratori, E., Ikegami, K.: Experimental study of the subsequent yield surface by using cross-shaped specimens. J. Mech. Phys. Solids. **16**, 373–394 (1968)
28. Singh, K.N., Clos, R., Schreppel, U., Veit, P., Hamann, A., Klingbeil, D., Sievert, R., KÃijnecke, G.: Versagenssimulation dynamisch belasteter Proben mit unterschiedlichen Mehrachsigkeit-szustÃd'nden unter Verwendung des Johnson-Cook-Versagensmodells fÃijr eine Nickelbasislegierung. Tec. Mech. **23**, 205–215 (2003)
29. Xue, Z., Pontin, M., Zok, F., Hutchinson, J.: Calibration procedures for a computational model of ductile fracture. Eng. Fract. Mech. **77**, 492–509 (2010)
30. Zheng, M., Hu, C., Luo, Z., Zheng, X.: Further study of the new damage model by negative stress triaxiality. Int. J. Fract. **63**, R15–R19 (1993)
31. Zillmann, B., Wagner, M.F.X., Schmaltz, S., Schmidl, E., Lampke, T., Willner, K., Halle, T.: In-plane biaxial compression and tension testing of thin sheet materials. Int. J. Solids. Struct. **66**, 111–120 (2015)

Influence of Shear Correction Factors on Eigenfrequencies of Layered Plates

Friedrich Gruttmann and Werner Wagner

1 Introduction

Finite plate elements which account for the layer sequence of a laminated structure are able to predict the deformation behaviour of the reference surface sufficiently accurate. This holds also for the layerwise linear shape of the in-plane stresses through the thickness, if the plate is not too thick. In contrast to that only averaged transverse shear strains through the thickness are obtained within the Reissner–Mindlin theory. As a consequence only the average of the transverse shear stresses is accurate. Neither the shape of the stresses is correct nor the boundary conditions at the outer surfaces are fulfilled. Within the Kirchhoff theory the transverse shear strains are set to zero. For this approach C^1–continuous shape functions are necessary, whereas Reissner–Mindlin elements require only C^0–continuity. On the other hand arrangements to avoid shear locking are necessary.

In several papers the equilibrium equations are exploited within a post-processing procedure to obtain the interlaminar stresses, e.g. [10, 24] for the transverse shear stresses. The essential restriction of the approach is the fact that these stresses are not embedded in the variational formulation and an immediate extension to geometrical and physical nonlinearity is not possible. Furthermore first and second derivatives of the in-plane stresses require bi-quadratic or bi-cubic shape functions.

F. Gruttmann (✉)
Fachgebiet Festkörpermechanik, Technische Universität Darmstadt,
Franziska-Braun-Str. 7, 64287 Darmstadt, Germany
e-mail: gruttmann@mechanik.tu-darmstadt.de

W. Wagner
Institut für Baustatik, Karlsruher Institut für Technologie, Kaiserstr. 12,
76131 Karlsruhe, Germany
e-mail: w.wagner@kit.edu

© Springer International Publishing AG 2018

H. Altenbach et al. (eds.), *Advances in Mechanics of Materials and Structural Analysis*, Advanced Structured Materials 80,
https://doi.org/10.1007/978-3-319-70563-7_6

The authors in [4, 5] present linear plate elements based on mixed-enhanced approaches. On basis of the first-order shear deformation theory enhanced incompatible modes are introduced.

Higher order plate formulations and layerwise approaches represent a wide class of advanced models, e.g. [3, 8, 9, 14, 19, 22]. These theories are characterized by a corresponding number of nodal degrees of freedom in the associated finite element formulation.

The use of brick elements or so-called solid shell elements, e.g. [16, 18] represents a computationally expensive approach. For a sufficient accurate evaluation of the interlaminar stresses each layer must be discretized with several elements ($\approx 4-10$) in thickness direction. Especially for non-linear practical problems with a multiplicity of load steps and several iterations in each load step this is not a feasible approach.

The notion of a shear correction factor was first introduced by Timoshenko [26]. For inhomogeneous plates shear factors have been computed e.g. in [1, 2, 4, 7, 15, 17, 20, 21, 25, 27, 28], and references therein. The factors are especially important for a frequency analysis of vibrating plates.

Present formulation is characterized by the following features.

- The displacements of the Reissner–Mindlin kinematics are enriched by out of plane warping displacements which are interpolated with layerwise cubic functions through the thickness. A constrained optimization problem is proposed, where the associated Euler–Lagrange equations include besides the equilibrium equations in terms of stress resultants the in-plane equilibrium in terms of stresses and a constraint which enforces the correct shape of warping through the thickness.
- The interpolation of the independent quantities is performed in representative volume elements in such a way that regular submatrices occur. This allows elimination of warping parameters and Lagrange parameters by static condensation. For linear elasticity and constant thickness the computation can be done once as a pre-processing, which reduces the computing time significantly. The condensation affects only the transverse shear stiffness. In this context shear correction factors for layered plates are defined.
- The resulting material matrix is used to compute the stiffness matrix of displacement based elements combined with the enhanced strain method or of mixed hybrid elements with the usual nodal degrees of freedom. This is an essential feature since standard geometrical boundary conditions can be applied.

2 Variational Formulation

2.1 Kinematics

The considered plates of thickness h are described using Cartesian coordinates $\{x, y\} = \{X^1, X^2\}$ for the middle surface Ω and a thickness coordinate $-h/2 \leq z = X^3 \leq h/2$. The coordinate on the boundary $\Gamma = \Gamma_u \bigcup \Gamma_\sigma$ of the plate is denoted by s. In the following the summation convention is used for repeated indices, where Latin indices range from 1 to 3 and Greek indices range from 1 to 2. Commas denote partial differentiation with respect to the coordinates X^i.

At first the position vector $\mathbf{X} = X^\alpha\,\mathbf{e}_\alpha$ and the normal vector $\mathbf{N} = \mathbf{e}_3 = \mathbf{e}_z$ of the undeformed middle surface Ω are introduced. The field of vectors $\mathbf{d}(X^1, X^2) = \mathbf{N} + \Delta\mathbf{d}(X^1, X^2)$ is not orthogonal to the deformed middle surface $\mathbf{x} = \mathbf{X} + \mathbf{u}$, which means transverse shear strains are accounted for. Within the vector field $\mathbf{v} := [\mathbf{u}, \boldsymbol{\varphi}]^T$ the displacements $\mathbf{u}(X^1, X^2) = u_i\,\mathbf{e}_i$ and the rotation vector $\boldsymbol{\varphi}(X^1, X^2) = \varphi_\alpha\,\mathbf{e}_\alpha$ are summarized. Here, $\Delta\mathbf{d} = \boldsymbol{\varphi} \times \mathbf{N}$ and φ_α denote rotations about $\mathbf{e}_\alpha$.

For inhomogeneous plates with certain layer sequences coupling of the membrane stiffness with the bending stiffness may occur. As a consequence, when applying pure transverse loading, besides curvatures $\kappa_{\alpha\beta}$ and transverse shear strains γ_α also membrane strains $\varepsilon_{\alpha\beta}$ appear. The strains and curvatures

$$\begin{aligned}\varepsilon_{\alpha\beta} &= \frac{1}{2}(\mathbf{u},_\alpha \cdot\mathbf{e}_\beta + \mathbf{u},_\beta \cdot\mathbf{e}_\alpha)\\ \kappa_{\alpha\beta} &= \frac{1}{2}(\Delta\mathbf{d},_\alpha \cdot\mathbf{e}_\beta + \Delta\mathbf{d},_\beta \cdot\mathbf{e}_\alpha)\\ \gamma_\alpha &= \mathbf{u},_\alpha \cdot\mathbf{N} + \Delta\mathbf{d}\cdot\mathbf{e}_\alpha\end{aligned} \tag{1}$$

with $\Delta\mathbf{d},_\alpha = \boldsymbol{\varphi},_\alpha \times\mathbf{N}$ are arranged in the vector

$$\boldsymbol{\varepsilon}(\mathbf{v}) = [\varepsilon_{11}, \varepsilon_{22}, 2\varepsilon_{12}, \kappa_{11}, \kappa_{22}, 2\kappa_{12}, \gamma_1, \gamma_2]^T\,. \tag{2}$$

In this paper out of plane warping displacements $\tilde{\mathbf{u}} = [\tilde{u}_x, \tilde{u}_y]^T$ are superposed on the linear shape of the Reissner–Mindlin kinematic. The shape of $\tilde{\mathbf{u}}$ through the thickness is chosen as in [13]

$$\tilde{\mathbf{u}}(z) = \boldsymbol{\Phi}(z)\,\boldsymbol{\alpha}\,. \tag{3}$$

The vector $\boldsymbol{\alpha}$ is constant throughout the representative volume element, as is defined in Sect. 3, and contains alternating discrete ordinates in x– and y–direction at nodes in thickness direction. The interpolation matrix contains cubic hierarchic functions

$$\begin{aligned}&\boldsymbol{\Phi}(z) = \left[\,\phi_1\,\mathbf{1}_2\;\phi_2\,\mathbf{1}_2\;\phi_3\,\mathbf{1}_2\;\phi_4\,\mathbf{1}_2\,\right]\mathbf{a}^i\\ &\phi_1 = \frac{1}{2}\,(1-\zeta) \qquad \phi_2 = 1-\zeta^2 \qquad \phi_3 = \frac{8}{3}\,\zeta\,(1-\zeta^2) \qquad \phi_4 = \frac{1}{2}\,(1+\zeta)\,,\end{aligned} \tag{4}$$

where $-1 \le \zeta \le 1$ is a normalized thickness coordinate of layer i. For N layers this leads to $M = 6\cdot N + 2$ components in $\boldsymbol{\alpha}$. Furthermore, $\mathbf{a}^i$ is an assembly matrix, which relates the 8 degrees of freedom of layer i to the M components of $\boldsymbol{\alpha}$ and $\mathbf{1}_n$ denotes a unit matrix of order n.

The layer strains $\mathbf{E} = [E_{11}, E_{22}, 2E_{12}, 2E_{13}, 2E_{23}]^T$ of a point with coordinate z are obtained with

$$\mathbf{E} = \mathbf{A}_1\,\boldsymbol{\varepsilon} + \mathbf{A}_2\,\boldsymbol{\alpha} \tag{5}$$

where

$$\begin{aligned}\mathbf{A}_1 &= \begin{bmatrix} \mathbf{1}_3 & z\,\mathbf{1}_3 & \mathbf{0} \\ \mathbf{0} & \mathbf{0} & \mathbf{1}_2 \end{bmatrix} & \mathbf{A}_2 &= \begin{bmatrix} \mathbf{0}_{3\times 8} \\ \mathbf{A}_{2s} \end{bmatrix} \mathbf{a}^i \\ \mathbf{A}_{2s} &= \frac{2}{h^i} \left[\phi_1' \mathbf{1}_2 \; \phi_2' \mathbf{1}_2 \; \phi_3' \mathbf{1}_2 \; \phi_4' \mathbf{1}_2 \right] & \phi_j' &= \frac{\mathrm{d}\phi_j}{\mathrm{d}\zeta} \, .\end{aligned} \tag{6}$$

The first part $\mathbf{A}_1\,\boldsymbol{\varepsilon}$ emanates from the Reissner–Mindlin kinematic, whereas the second part $\mathbf{A}_2\,\boldsymbol{\alpha}$ follows from the superposed warping displacements.

2.2 Constitutive Equations for the Stress Resultants

Assuming linear elastic orthotropic material behaviour the constitutive equations are introduced with $S^{33} = 0$ in the following standard manner

$$\begin{gathered}\begin{bmatrix} S^{11} \\ S^{22} \\ S^{12} \\ S^{13} \\ S^{23} \end{bmatrix} = \begin{bmatrix} C_{11} & C_{12} & C_{13} & 0 & 0 \\ C_{21} & C_{22} & C_{23} & 0 & 0 \\ C_{31} & C_{32} & C_{33} & 0 & 0 \\ 0 & 0 & 0 & C_{44} & C_{45} \\ 0 & 0 & 0 & C_{54} & C_{55} \end{bmatrix} \begin{bmatrix} E_{11} \\ E_{22} \\ 2E_{12} \\ 2E_{13} \\ 2E_{23} \end{bmatrix} \\ \mathbf{S} = \mathbf{C}\,\mathbf{E}\,.\end{gathered} \tag{7}$$

Due to the varying fibre orientation the material constants $C_{ij} = C_{ji}$ differ for each individual layer.

The relation of the stress resultants to $\mathbf{S}$ is defined by thickness integration of the specific internal virtual work and $\delta\mathbf{E} = \mathbf{A}_1\,\delta\boldsymbol{\varepsilon} + \mathbf{A}_2\,\delta\boldsymbol{\alpha}$. This yields

$$\int_{-h/2}^{+h/2} \delta\mathbf{E}^T\mathbf{S}\,\mathrm{d}z = \delta\boldsymbol{\varepsilon}^T\boldsymbol{\sigma}_1 + \delta\boldsymbol{\alpha}^T\boldsymbol{\sigma}_2 \quad \boldsymbol{\sigma}_1 := \int_{-h/2}^{+h/2} \mathbf{A}_1^T\mathbf{S}\,\mathrm{d}z \quad \boldsymbol{\sigma}_2 := \int_{-h/2}^{+h/2} \mathbf{A}_2^T\mathbf{S}\,\mathrm{d}z\,. \tag{8}$$

The components of

$$\boldsymbol{\sigma}_1 = [n^{11}, n^{22}, n^{12}, m^{11}, m^{22}, m^{12}, q^1, q^2]^T \tag{9}$$

are membrane forces $n^{\alpha\beta} = n^{\beta\alpha}$, bending moments $m^{\alpha\beta} = m^{\beta\alpha}$ and shear forces q^α. The components of $\boldsymbol{\sigma}_2$ are higher order stress resultants. They are work conjugate to the components of $\boldsymbol{\alpha}$.

Now, inserting (7) with (5) into $(8)_2$ and $(8)_3$ yields the constitutive law for the stress resultants

$$\begin{bmatrix} \boldsymbol{\sigma}_1 \\ \boldsymbol{\sigma}_2 \end{bmatrix} = \begin{bmatrix} \mathbf{D}_{11} & \mathbf{D}_{12} \\ \mathbf{D}_{21} & \mathbf{D}_{22} \end{bmatrix} \begin{bmatrix} \boldsymbol{\varepsilon} \\ \boldsymbol{\alpha} \end{bmatrix} \qquad \mathbf{D}_{\alpha\beta} = \int\limits_{-h/2}^{+h/2} \mathbf{A}_\alpha^T \, \mathbf{C} \, \mathbf{A}_\beta \, \mathrm{d}z = \mathbf{D}_{\beta\alpha}^T \, . \tag{10}$$

At first, $\mathbf{D}_{11}$ reads

$$\mathbf{D}_{11} = \int\limits_{-h/2}^{+h/2} \mathbf{A}_1^T \mathbf{C} \, \mathbf{A}_1 \, \mathrm{d}z = \begin{bmatrix} \mathbf{D}_m & \mathbf{D}_{mb} & \mathbf{0} \\ \mathbf{D}_{mb}^T & \mathbf{D}_b & \mathbf{0} \\ \mathbf{0} & \mathbf{0} & \mathbf{D}_s \end{bmatrix}_{(8\times 8)} . \tag{11}$$

The submatrices for membrane, bending and shear are obtained by summation over N layers and analytical integration in each layer leading to well-known expressions. In an analogous way the matrices $\mathbf{D}_{22}$ and $\mathbf{D}_{21}$ are assembled with the contributions of the layers using (6) and (7) in $(10)_2$. Since only powers of ζ occur analytical integration is possible. A numerical integration with three Gauss integration points also leads to exact results. Due to the interpolation functions with local layerwise support it follows that $\mathbf{D}_{22}$ is banded and thus is sparse. In $\mathbf{D}_{21}$ only the last two columns are populated.

2.3 Equilibrium Equations and a Constraint

Neglecting body forces the equilibrium equations for the in-plane directions read

$$\begin{bmatrix} S^{11}{}_{,1} + S^{12}{}_{,2} + S^{13}{}_{,3} \\ S^{12}{}_{,1} + S^{22}{}_{,2} + S^{23}{}_{,3} \end{bmatrix} := \mathbf{f} = \mathbf{0} \, . \tag{12}$$

In (12) the in-plane stresses $S^{\alpha\beta}$ as well as transverse shear stresses $S^{\alpha 3}$ enter. For the in-plane stresses holds with (5)–(7)

$$\begin{bmatrix} S^{11} \\ S^{22} \\ S^{12} \end{bmatrix} = \begin{bmatrix} C_{11} & C_{12} & C_{13} \\ C_{21} & C_{22} & C_{23} \\ C_{31} & C_{32} & C_{33} \end{bmatrix} \begin{bmatrix} \varepsilon_{11} + z \, \kappa_{11} \\ \varepsilon_{22} + z \, \kappa_{22} \\ 2\varepsilon_{12} + z \, 2\kappa_{12} \end{bmatrix} . \tag{13}$$

Introducing

$$\bar{\mathbf{C}}_{23} = \begin{bmatrix} C_{11} & C_{12} & C_{13} & C_{31} & C_{32} & C_{33} \\ C_{31} & C_{32} & C_{33} & C_{21} & C_{22} & C_{23} \end{bmatrix} \quad \boldsymbol{\lambda}_\varepsilon = \begin{bmatrix} \varepsilon_{11,1} \\ \varepsilon_{22,1} \\ 2\varepsilon_{12,1} \\ \varepsilon_{11,2} \\ \varepsilon_{22,2} \\ 2\varepsilon_{12,2} \end{bmatrix} \quad \boldsymbol{\lambda}_\kappa = \begin{bmatrix} \kappa_{11,1} \\ \kappa_{22,1} \\ 2\kappa_{12,1} \\ \kappa_{11,2} \\ \kappa_{22,2} \\ 2\kappa_{12,2} \end{bmatrix} \tag{14}$$

the derivatives of the in-plane stresses yield

$$\begin{bmatrix} S^{11}{}_{,1} + S^{12}{}_{,2} \\ S^{12}{}_{,1} + S^{22}{}_{,2} \end{bmatrix} = \begin{bmatrix} \bar{\mathbf{C}}_{23} & z\,\bar{\mathbf{C}}_{23} \end{bmatrix} \begin{bmatrix} \boldsymbol{\lambda}_{\varepsilon} \\ \boldsymbol{\lambda}_{\kappa} \end{bmatrix} \qquad \mathbf{f}_1 = \mathbf{C}_{23}\,\boldsymbol{\lambda}\,. \tag{15}$$

Furthermore we introduce

$$\boldsymbol{\sigma}_2 = -\int_{-h/2}^{+h/2} \boldsymbol{\Phi}^T \begin{bmatrix} S^{13}{}_{,3} \\ S^{23}{}_{,3} \end{bmatrix} \mathrm{d}z \qquad \mathbf{D}_{23} := -\int_{-h/2}^{+h/2} \boldsymbol{\Phi}^T \mathbf{C}_{23}\ \mathrm{d}z\,, \tag{16}$$

where the reformulation of $(8)_3$ to $(16)_1$ is obtained with integration by parts and consideration of stress boundary conditions $S^{\alpha 3}(-h/2) = S^{\alpha 3}(+h/2) = 0$. Again the integration for $\mathbf{D}_{23}$ can be performed by summation over layers and analytical integration or numerical Gauss integration with three integration points in each layer.

Now the integral form of $\mathbf{f} = \mathbf{0}$ according to (12) is formulated with $\delta\tilde{\mathbf{u}} = \boldsymbol{\Phi}\,\delta\boldsymbol{\alpha}$. Considering (15) and (16) it follows

$$\int_{-h/2}^{+h/2} \delta\tilde{\mathbf{u}}^T\,\mathbf{f}\,\mathrm{d}z = -\delta\boldsymbol{\alpha}^T(\boldsymbol{\sigma}_2 + \mathbf{D}_{23}\,\boldsymbol{\lambda}) = 0 \tag{17}$$

and one obtains with $\delta\boldsymbol{\alpha} \neq \mathbf{0}$

$$\boldsymbol{\sigma}_2 + \mathbf{D}_{23}\,\boldsymbol{\lambda} = \mathbf{0}\,, \tag{18}$$

which describes equilibrium of higher order stress resultants.

The warping displacements have to fulfill an orthogonality condition. To specify this constraint we introduce the equilibrium of virtual in-plane stresses considering (15)

$$\begin{bmatrix} \delta S^{11}{}_{,1} + \delta S^{12}{}_{,2} \\ \delta S^{12}{}_{,1} + \delta S^{22}{}_{,2} \end{bmatrix} = \mathbf{C}_{23}\,\delta\boldsymbol{\lambda} = \delta\mathbf{f}_1 = \mathbf{0}\,. \tag{19}$$

The integral form of $\delta\mathbf{f}_1 = \mathbf{0}$ yields with $\tilde{\mathbf{u}} = \boldsymbol{\Phi}\,\boldsymbol{\alpha}$

$$\int_{-h/2}^{+h/2} \delta\mathbf{f}_1^T\,\tilde{\mathbf{u}}\,\mathrm{d}z = \delta\boldsymbol{\lambda}^T \int_{-h/2}^{+h/2} \mathbf{C}_{23}^T\boldsymbol{\Phi}\ \mathrm{d}z\,\boldsymbol{\alpha} = 0\,. \tag{20}$$

Introducing $\mathbf{D}_{32} = -\int_{-h/2}^{+h/2} \mathbf{C}_{23}^T\,\boldsymbol{\Phi}\,\mathrm{d}z = \mathbf{D}_{23}^T$ Eq. (20) reads $-\delta\boldsymbol{\lambda}^T\mathbf{D}_{32}\,\boldsymbol{\alpha} = 0$, where $\delta\boldsymbol{\lambda} \neq \mathbf{0}$, and one obtains the constraint

$$\mathbf{g}(\boldsymbol{\alpha}) = \mathbf{D}_{32}\,\boldsymbol{\alpha} = \mathbf{0}\,. \tag{21}$$

This orthogonality condition enforces the correct shape of $\tilde{\mathbf{u}}$ through the thickness. It has the descriptive meaning that the superposed warping displacements must not lead to additional membrane forces and bending moments.

2.4 Constrained Optimization Problem

We introduce the constrained optimization problem

$$\Pi(\boldsymbol{\theta}) = \int_{\Omega} [W(\boldsymbol{\varepsilon}, \boldsymbol{\alpha}) + \boldsymbol{\lambda}^T \, \mathbf{g}(\boldsymbol{\alpha})] \, \mathrm{d}A + \Pi_{ext}(\mathbf{u}) \quad \rightarrow \quad \text{stat.} \tag{22}$$

with independent quantities $\boldsymbol{\theta} := [\mathbf{v}, \boldsymbol{\alpha}, \boldsymbol{\lambda}]^T$. The strain energy density $W(\boldsymbol{\varepsilon}, \boldsymbol{\alpha})$ per area element $\mathrm{d}A = \mathrm{d}X^1 \, \mathrm{d}X^2$ is obtained with thickness integration of $W(\mathbf{E}) = \frac{1}{2} \int_{-h/2}^{+h/2} \mathbf{E}^T \, \mathbf{C} \, \mathbf{E} \, \mathrm{d}z$ and leads with $\mathbf{E} = \mathbf{A}_1 \, \boldsymbol{\varepsilon} + \mathbf{A}_2 \, \boldsymbol{\alpha}$ and $(10)_2$ to the quadratic form

$$W(\boldsymbol{\varepsilon}, \boldsymbol{\alpha}) = \frac{1}{2} \begin{bmatrix} \boldsymbol{\varepsilon} \\ \boldsymbol{\alpha} \end{bmatrix}^T \begin{bmatrix} \mathbf{D}_{11} & \mathbf{D}_{12} \\ \mathbf{D}_{21} & \mathbf{D}_{22} \end{bmatrix} \begin{bmatrix} \boldsymbol{\varepsilon} \\ \boldsymbol{\alpha} \end{bmatrix} . \tag{23}$$

The Lagrange term $\boldsymbol{\lambda}^T \mathbf{g}$ is formulated with the vector of Lagrange multipliers $\boldsymbol{\lambda}$ to account for the constraint $\mathbf{g}(\boldsymbol{\alpha}) = \mathbf{0}$. The plate is loaded statically by surface loads $\bar{\mathbf{p}}$ in Ω and by boundary forces $\bar{\mathbf{t}}$ on the boundary Γ_σ. Hence, the potential of the external forces reads

$$\Pi_{ext}(\mathbf{u}) = -\int_{\Omega} \mathbf{u}^T \bar{\mathbf{p}} \, \mathrm{d}A - \int_{\Gamma_\sigma} \mathbf{u}^T \bar{\mathbf{t}} \, \mathrm{d}s \, . \tag{24}$$

With admissible variations $\delta\boldsymbol{\theta} = [\delta\mathbf{v}, \delta\boldsymbol{\alpha}, \delta\boldsymbol{\lambda}]^T$ and $\delta\mathbf{v} := [\delta\mathbf{u}, \delta\boldsymbol{\varphi}]^T$ the stationary condition for functional (22) yields

$$\begin{aligned} \delta\Pi(\boldsymbol{\theta}, \delta\boldsymbol{\theta}) &= \int_{\Omega} \begin{bmatrix} \delta\boldsymbol{\varepsilon} \\ \delta\boldsymbol{\alpha} \\ \delta\boldsymbol{\lambda} \end{bmatrix}^T \begin{bmatrix} \mathbf{D}_{11} & \mathbf{D}_{12} & \mathbf{0} \\ \mathbf{D}_{21} & \mathbf{D}_{22} & \mathbf{D}_{23} \\ \mathbf{0} & \mathbf{D}_{32} & \mathbf{0} \end{bmatrix} \begin{bmatrix} \boldsymbol{\varepsilon} \\ \boldsymbol{\alpha} \\ \boldsymbol{\lambda} \end{bmatrix} \mathrm{d}A + \delta\Pi_{ext} = 0 \\ \delta\Pi_{ext} &= -\int_{\Omega} \delta\mathbf{u}^T \bar{\mathbf{p}} \, \mathrm{d}A - \int_{\Gamma_\sigma} \delta\mathbf{u}^T \bar{\mathbf{t}} \, \mathrm{d}s \, , \end{aligned} \tag{25}$$

where the virtual strains $\delta\boldsymbol{\varepsilon} = [\delta\varepsilon_{11}, \delta\varepsilon_{22}, 2\delta\varepsilon_{12}, \delta\kappa_{11}, \delta\kappa_{22}, 2\delta\kappa_{12}, \delta\gamma_1, \delta\gamma_2]^T$ read

$$
\begin{aligned}
\delta\varepsilon_{\alpha\beta} &= \frac{1}{2}(\delta\mathbf{u},_{\alpha}\cdot\mathbf{e}_{\beta} + \delta\mathbf{u},_{\beta}\cdot\mathbf{e}_{\alpha}) \\
\delta\kappa_{\alpha\beta} &= \frac{1}{2}(\delta\mathbf{d},_{\alpha}\cdot\mathbf{e}_{\beta} + \delta\mathbf{d},_{\beta}\cdot\mathbf{e}_{\alpha}) \\
\delta\gamma_{\alpha} &= \delta\mathbf{u},_{\alpha}\cdot\mathbf{N} + \delta\mathbf{d}\cdot\mathbf{e}_{\alpha}
\end{aligned}
\tag{26}
$$

with $\delta\mathbf{d} = \delta\boldsymbol{\varphi}\times\mathbf{N}$ and $\delta\mathbf{d},_{\alpha} = \delta\boldsymbol{\varphi},_{\alpha}\times\mathbf{N}$.

Finally the Euler–Lagrange equations associated with the introduced functional are derived. For this purpose variational Eq. (25) is rewritten with $(10)_1$ and (21) as

$$
\delta\Pi(\boldsymbol{\theta},\delta\boldsymbol{\theta}) = \int_{\Omega} [\delta\boldsymbol{\varepsilon}^T\boldsymbol{\sigma}_1 + \delta\boldsymbol{\alpha}^T\left(\boldsymbol{\sigma}_2 + \mathbf{D}_{23}\,\boldsymbol{\lambda}\right) + \delta\boldsymbol{\lambda}^T\mathbf{g}]\,\mathrm{d}A + \delta\Pi_{ext} = 0\,. \tag{27}
$$

Integration by parts is applied to the first term in (27) using (9) and (26). Hence, applying standard arguments of variational calculus yields as Euler–Lagrange equations the equilibrium of stress resultants and stress couple resultants, the constraint $\mathbf{g} = \mathbf{0}$ in Ω (21) and with $\boldsymbol{\sigma}_2 + \mathbf{D}_{23}\,\boldsymbol{\lambda} = \mathbf{0}$ in Ω the equilibrium of higher order stress resultants (18). Furthermore one obtains the static boundary conditions on Γ_σ. The geometric boundary conditions $\mathbf{v} = \bar{\mathbf{v}}$ on Γ_u have to be fulfilled as constraints.

3 Representative Volume Element

The evaluation of the matrices defined in the last section is carried out in representative volume elements (RVEs) which are located at the integration points of the reference surface Ω, see Fig. 1. For linear elasticity and constant thickness h the computation can be done in advance for one RVE only. An orthonormal coordinate system is introduced in the center of the square reference surface Ω_i with edge length ℓ. An investigation on a proper choice of ℓ is performed in the examples section. Normalized coordinates $-1 \le \xi \le 1$ and $-1 \le \eta \le 1$ are defined with $\xi = \frac{2}{\ell}\,X^1$ and $\eta = \frac{2}{\ell}\,X^2$, which yields a constant Jacobian matrix

$$
\mathbf{J} = \begin{bmatrix} \frac{\partial X^1}{\partial\xi} & \frac{\partial X^2}{\partial\xi} \\ \frac{\partial X^1}{\partial\eta} & \frac{\partial X^2}{\partial\eta} \end{bmatrix} = \begin{bmatrix} \frac{\ell}{2} & 0 \\ 0 & \frac{\ell}{2} \end{bmatrix}. \tag{28}
$$

The approximation for $\boldsymbol{\theta}^h := [\boldsymbol{\varepsilon}^h, \boldsymbol{\alpha}^h, \boldsymbol{\lambda}^h]^T$ in Ω_i is chosen as

$$
\begin{aligned}
\begin{bmatrix} \boldsymbol{\varepsilon}^h \\ \boldsymbol{\alpha}^h \\ \boldsymbol{\lambda}^h \end{bmatrix} &= \begin{bmatrix} \mathbf{N}_\varepsilon^1 & \mathbf{N}_\varepsilon^2 & \mathbf{0} & \mathbf{0} & \mathbf{N}_\varepsilon^3 \\ \mathbf{0} & \mathbf{0} & \mathbf{0} & \mathbf{N}_\alpha & \mathbf{0} \\ \mathbf{0} & \mathbf{N}_\lambda^1 & \mathbf{N}_\lambda^2 & \mathbf{0} & \mathbf{N}_\lambda^3 \end{bmatrix} \begin{bmatrix} \hat{\boldsymbol{\varepsilon}} \\ \hat{\boldsymbol{\lambda}}_1 \\ \hat{\boldsymbol{\lambda}}_2 \\ \hat{\boldsymbol{\alpha}} \\ \hat{\boldsymbol{\lambda}}_3 \end{bmatrix} \\
\boldsymbol{\theta}^h &= \mathbf{N}_\theta\,\hat{\boldsymbol{\theta}}\,,
\end{aligned}
\tag{29}
$$

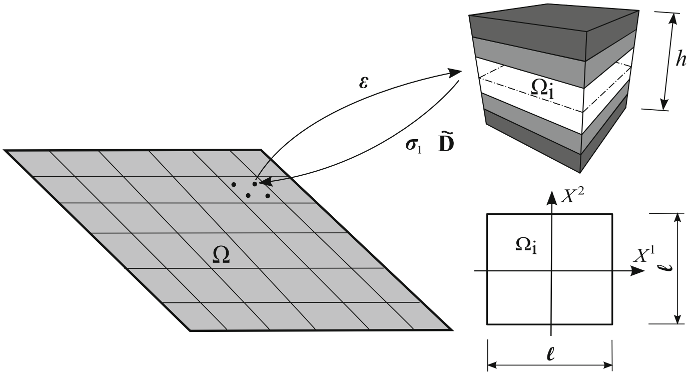
$\boldsymbol{\varepsilon}$
$\boldsymbol{\sigma}_1$ $\tilde{\mathbf{D}}$
Ω_i
h
Ω
X^2
Ω_i
X^1
ℓ
ℓ

Fig. 1 RVE at an integration point of a plate and reference surface of the RVE

where for the parameters $\hat{\boldsymbol{\varepsilon}} \in \mathbb{R}^8$, $\hat{\boldsymbol{\lambda}}_1 \in \mathbb{R}^6$, $\hat{\boldsymbol{\lambda}}_2 \in \mathbb{R}^4$, $\hat{\boldsymbol{\alpha}} \in \mathbb{R}^M$ and $\hat{\boldsymbol{\lambda}}_3 \in \mathbb{R}^8$ holds. The interpolation matrices $\mathbf{N}^1_\varepsilon = \mathbf{1}_8$, $\mathbf{N}^2_\varepsilon$ and $\mathbf{N}^3_\varepsilon$ are adapted from Ref. [12]

$$\begin{aligned}
\mathbf{N}^2_\varepsilon &= \begin{bmatrix} \mathbf{N}^{m2}_\varepsilon & \mathbf{0} & \mathbf{0} \\ \mathbf{0} & \mathbf{N}^{b2}_\varepsilon & \mathbf{0} \\ \mathbf{0} & \mathbf{0} & \mathbf{N}^{s2}_\varepsilon \end{bmatrix}_{8\times 6} \qquad \mathbf{N}^{m2}_\varepsilon = \mathbf{N}^{b2}_\varepsilon = \begin{bmatrix} \eta & 0 \\ 0 & \xi \\ 0 & 0 \end{bmatrix} \qquad \mathbf{N}^{s2}_\varepsilon = \begin{bmatrix} \eta & 0 \\ 0 & \xi \end{bmatrix} \\
\mathbf{N}^3_\varepsilon &= \begin{bmatrix} \mathbf{N}^{m3}_\varepsilon & \mathbf{0} \\ \mathbf{0} & \mathbf{N}^{b3}_\varepsilon \\ \mathbf{0} & \mathbf{0} \end{bmatrix}_{8\times 8} \qquad \mathbf{N}^{m3}_\varepsilon = \mathbf{N}^{b3}_\varepsilon = \begin{bmatrix} \xi & 0 & 0 & 0 \\ 0 & \eta & 0 & 0 \\ 0 & 0 & \xi & \eta \end{bmatrix} .
\end{aligned} \tag{30}$$

The coefficient matrices $\mathbf{T}^0_\varepsilon$, $(\mathbf{T}^0_\sigma)^{-1}$ and the quantities $\bar{\xi}$, $\bar{\eta}$, j_0/j, as are used in [12], can be discarded due to the rectangular shape of Ω_i.

With $\mathbf{N}_\alpha = \mathbf{1}_M$ the warping displacements $\boldsymbol{\alpha}^h$ are constant in Ω_i. This also holds for the derivatives of membrane strains and curvatures $\boldsymbol{\lambda}^h = [\boldsymbol{\lambda}^h_\varepsilon, \boldsymbol{\lambda}^h_\kappa]^T$ with

$$\begin{aligned}
\mathbf{N}^1_\lambda &= \begin{bmatrix} \mathbf{N}^{11}_\lambda & \mathbf{0} & \mathbf{0} \\ \mathbf{0} & \mathbf{N}^{11}_\lambda & \mathbf{0} \end{bmatrix} \qquad \mathbf{N}^{11}_\lambda = \frac{2}{\ell} \begin{bmatrix} 0 & 0 \\ 0 & 1 \\ 0 & 0 \\ 1 & 0 \\ 0 & 0 \\ 0 & 0 \end{bmatrix} \\
\mathbf{N}^2_\lambda &= \begin{bmatrix} \mathbf{N}^{21}_\lambda & \mathbf{0} \\ \mathbf{0} & \mathbf{N}^{21}_\lambda \end{bmatrix} \qquad \mathbf{N}^{21}_\lambda = \begin{bmatrix} 1 & 0 \\ 1 & 0 \\ 0 & 1 \\ 0 & 1 \\ 0 & 1 \\ 1 & 0 \end{bmatrix}
\end{aligned} \tag{31}$$

$$\mathbf{N}_\lambda^3 = \begin{bmatrix} \mathbf{N}_\lambda^{31} & \mathbf{0} \\ \mathbf{0} & \mathbf{N}_\lambda^{31} \end{bmatrix} \mathbf{N}_\lambda^{31} = \frac{2}{\ell} \begin{bmatrix} 1\,0\,0\,0 \\ 0\,0\,0\,0 \\ 0\,0\,1\,0 \\ 0\,0\,0\,0 \\ 0\,1\,0\,0 \\ 0\,0\,0\,1 \end{bmatrix}.$$

The components of $\mathbf{N}_\lambda^1$ and $\mathbf{N}_\lambda^3$ are obtained computing the derivatives of the membrane strains and curvatures in (29) with respect to X^α considering (28). When multiplying $\bar{\mathbf{C}}_{23}$ from (14) with $\mathbf{N}_\lambda^{21}$, one obtains a reduced form of $\bar{\mathbf{C}}_{23}$ as is used in [13] as approximation to avoid singular matrices. Here, $\mathbf{N}_\lambda^2\,\hat{\boldsymbol{\lambda}}_2$ describes an independent part of the interpolation.

Remark: In all computed examples the parameters associated with $\mathbf{N}_\varepsilon^{s2}$ in (30) are zero, such that this matrix and the associated parameters could be taken out. Furthermore, matrix $\mathbf{N}_\lambda^1$ in (29) has negligible influence on the results.

We insert $\boldsymbol{\theta}^h = \mathbf{N}_\theta\,\hat{\boldsymbol{\theta}}$ according to (29) and the corresponding equation for the virtual quantities $\delta\boldsymbol{\theta}^h = \mathbf{N}_\theta\,\delta\hat{\boldsymbol{\theta}}$ in variational Eq. (25), which now reads

$$\delta\Pi(\boldsymbol{\theta}^h, \delta\boldsymbol{\theta}^h) = \int\limits_{\Omega} \frac{1}{\ell^2} \int\limits_{\Omega_i} \delta\boldsymbol{\theta}^{hT}\mathbf{D}\,\boldsymbol{\theta}^h\,\mathrm{d}A_i\,\mathrm{d}A + \delta\Pi_{ext} = 0 \qquad \mathbf{D} = \begin{bmatrix} \mathbf{D}_{11} & \mathbf{D}_{12} & \mathbf{0} \\ \mathbf{D}_{21} & \mathbf{D}_{22} & \mathbf{D}_{23} \\ \mathbf{0} & \mathbf{D}_{32} & \mathbf{0} \end{bmatrix} \tag{32}$$

or

$$\delta\Pi(\boldsymbol{\theta}^h, \delta\boldsymbol{\theta}^h) = \int\limits_{\Omega} \delta\hat{\boldsymbol{\theta}}^T\,\mathbf{H}\,\hat{\boldsymbol{\theta}}\,\mathrm{d}A + \delta\Pi_{ext} = 0 \qquad \mathbf{H} = \frac{1}{\ell^2} \int\limits_{\Omega_i} \mathbf{N}_\theta^T\,\mathbf{D}\,\mathbf{N}_\theta\,\mathrm{d}A_i \tag{33}$$

with a constant and symmetric matrix $\mathbf{D}_{J\times J}$, where $J = 20+M$. Since only powers of ξ and η occur, the integration for $\mathbf{H}_{K\times K}$, where $K = 26+M$ and $\mathrm{d}A_i = \ell^2/4\ \mathrm{d}\xi\ \mathrm{d}\eta$, can be carried out analytically. A 2×2 Gauss integration also leads to correct results. It is important to note, that although $\mathbf{D}$ is singular, $\mathbf{H}$ is regular.

The parameters $\hat{\boldsymbol{\beta}} := [\hat{\boldsymbol{\lambda}}_1, \hat{\boldsymbol{\lambda}}_2, \hat{\boldsymbol{\alpha}}, \hat{\boldsymbol{\lambda}}_3]^T$ in $\hat{\boldsymbol{\theta}} = [\hat{\boldsymbol{\varepsilon}}, \hat{\boldsymbol{\beta}}]^T$ are independent quantities in the RVEs, and thus are not continuous in Ω. Furthermore $\delta\Pi_{ext}$ does not depend on $\hat{\boldsymbol{\beta}}$. For this reason static condensation of $\hat{\boldsymbol{\beta}}$ from the set of equations

$$\begin{bmatrix} \mathbf{H}_{11} & \mathbf{H}_{12} \\ \mathbf{H}_{21} & \mathbf{H}_{22} \end{bmatrix} \begin{bmatrix} \hat{\boldsymbol{\varepsilon}} \\ \hat{\boldsymbol{\beta}} \end{bmatrix} = \begin{bmatrix} \boldsymbol{\sigma}_1 \\ \mathbf{0} \end{bmatrix} \tag{34}$$

is possible. Here $\mathbf{H}_{\alpha\beta}$ are the submatrices of $\mathbf{H}$, where $\mathbf{H}_{11} = \mathbf{D}_{11}$ according to Eq. (11) holds. The right hand side of (34) contains the vector of stress resultants, since the lateral surfaces of the RVEs are not stress free. The elimination yields $\hat{\boldsymbol{\beta}} = -\mathbf{H}_{22}^{-1}\,\mathbf{H}_{21}\,\hat{\boldsymbol{\varepsilon}}$ and the material law for the stress resultants

$$\boldsymbol{\sigma}_1 = \tilde{\mathbf{D}}\,\hat{\boldsymbol{\varepsilon}} \qquad \tilde{\mathbf{D}} = \mathbf{H}_{11} - \mathbf{H}_{12}\,\mathbf{H}_{22}^{-1}\,\mathbf{H}_{21}\,. \tag{35}$$

Due to the interpolation in thickness direction with layerwise shape functions $\mathbf{H}_{22}$ is sparse. This means even for examples with many layers a comparatively limited effort for the elimination of $\hat{\boldsymbol{\beta}}$. The sequence of the sub-vectors in $\boldsymbol{\theta}^h$ and $\hat{\boldsymbol{\theta}}$ in Eq. (29) is interchanged. This causes a pivot change in $\mathbf{H}$ and only enables the static condensation.

The condensed matrix $\tilde{\mathbf{D}}_{8\times 8}$ possesses the same structure as $\mathbf{D}_{11}$, see Eq. (11).

$$\tilde{\mathbf{D}} = \begin{bmatrix} \tilde{\mathbf{D}}_m & \tilde{\mathbf{D}}_{mb} & \mathbf{0} \\ \tilde{\mathbf{D}}_{mb}^T & \tilde{\mathbf{D}}_b & \mathbf{0} \\ \mathbf{0} & \mathbf{0} & \tilde{\mathbf{D}}_s \end{bmatrix} \qquad \begin{aligned} \tilde{\mathbf{D}}_m &= \mathbf{D}_m \\ \tilde{\mathbf{D}}_b &= \mathbf{D}_b \\ \tilde{\mathbf{D}}_{mb} &= \mathbf{D}_{mb} \end{aligned} \qquad \tilde{\mathbf{D}}_s = \begin{bmatrix} \tilde{D}_{s11} & \tilde{D}_{s12} \\ \tilde{D}_{s12} & \tilde{D}_{s22} \end{bmatrix} \tag{36}$$

Only the shear stiffness $\mathbf{D}_s = \mathbf{D}_s^T$ with components $D_{s\alpha\beta}$ is affected by the static condensation. In this context shear correction factors are defined as

$$k_1 = \frac{\tilde{D}_{s11}}{D_{s11}} \qquad k_2 = \frac{\tilde{D}_{s22}}{D_{s22}} \qquad k_{12} = \frac{\tilde{D}_{s12}}{0.5\,(D_{s11} + D_{s22})}\,. \tag{37}$$

Since D_{s12} may take the value zero, the average of the diagonal terms is taken as reference value for k_{12}. For a homogeneous plate the well-known value $k_1 = k_2 = 5/6$, as is derived in [6, 23], is obtained with (37). Furthermore, $k_{12} = 0$ holds for a homogeneous and isotropic plate and for various anisotropic plates with certain stacking sequences. It is pointed out that $k_{12} = \sqrt{k_1\,k_2}$, as is assumed in several papers, does not hold here.

Identifying the parameters $\hat{\boldsymbol{\varepsilon}}$ in the RVEs with the plate strains $\boldsymbol{\varepsilon}$ according to (2), variational Eq. (33) yields with static condensation (35) the principle of virtual work as variational basis for elements based on the displacement method.

4 Examples

4.1 Comparison of Shear Correction Factors with Literature Results

In this section we compare shear correction factors according to Eq. (37) with results of Whitney [27, 28]. The material constants, chosen by Withney (here in SI units), are

$$\begin{aligned} E_1 &= 172369\ \text{N/mm}^2 & G_{12} &= 3447\ \text{N/mm}^2 & \nu_{12} &= 0.25 \\ E_2 &= 6895\ \ \ \ \text{N/mm}^2 & G_{23} &= 1379\ \text{N/mm}^2 & \nu_{23} &= 0.25\,. \end{aligned} \tag{38}$$

It is pointed out that due to the independent choice of G_{23} and ν_{23} these constants do not fulfill all conditions for transversal isotropy. According to Table 1 five different

Table 1 Shear correction factors for different layer sequences

Layer sequence [°]	Theory	k_1	k_2	k_{12}	Comments
[0/90]	[28]	0.8212	0.8212	–	Cylindrical bending
	Present	0.8212	0.8212	0	$C_{12} = C_{33} = 0$
	Present	0.8596	0.8596	0	
[0/90/90/0]	[28]	0.5952	0.7205	–	Cylindrical bending
	Present	0.5952	0.7205	0	$C_{12} = C_{33} = 0$
	Present	0.5936	0.7788	0	
[0/90/0/90/0/90/0/90/0]	[27]	0.6891	0.6112	–	Cylindrical bending
	Present	0.6891	0.6112	0	$C_{12} = C_{33} = 0$
	Present	0.6876	0.6188	0	
[30/−30]	[27]	0.8592	0.8592	–	Cylindrical bending
	Present	0.8750	0.7341	0	
[30/−30/−30/30]	[27]	0.7549	0.6730	–	Cylindrical bending
	Present	0.6773	0.6722	−0.0376	

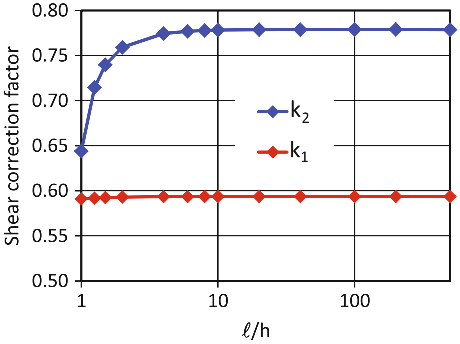

Fig. 2 Influence of ℓ/h on shear correction factors

layer sequences with equal layer thickness within a total thickness $h = 1$ mm are investigated. Only for the third example holds: each 0°-layer has a thickness $h/10$ and each 90°-layer has a thickness of $h/8$.

For the cross-ply laminate [0°/90°/90°/0°] the influence of the RVE-length ℓ on the shear correction factors is investigated. The values $k_1 = 0.5936$ and $k_2 = 0.7788$ according to Table 1 are obtained as ℓ/h exceeds certain values, see Fig. 2. Furthermore, in this range present factors are independent of the total thickness h. Similar results are obtained for other stacking sequences. Based on these investigations all further computations are performed with the ratio $\ell/h = 100$.

Present factors are slightly different from the literature results. When setting the elasticity parameters $C_{12} = C_{21}$ and C_{33} in $(14)_1$ to zero, we can verify the comparative results for cross-ply laminates. Thereby the simplifying assumption of cylindrical bending, as is used in [27, 28], is taken into account. Furthermore, the ansatz $\tilde{D}_{s12} = k_{12}\, D_{s12}$ with $k_{12} = \sqrt{k_1\, k_2}$ is used in [27]. From this equation

$\tilde{D}_{s12} = 0$ follows, since $D_{s12} = 0$ holds for all examples of Table 1. For the angle-ply laminates a transition to [27] can not be shown. Here, we verify present results for the last example via a frequency analysis of a vibrating plate in Sect. 4.2.

4.2 *Influence of Shear Correction Factors on Eigenfrequencies*

4.2.1 Simply Supported CFRP Plate

Eigenfrequencies of a simply supported square plate are computed in this section to verify the correctness of the computed shear factors. The plate length and the total thickness read $L = 1000\,\text{mm}$ and $h = 50\,\text{mm}$, respectively. Additional to the material data (38) a density $\rho = 1500\,\text{kg/m}^3$ is chosen. The last example of Table 1 with a $[30°/-30°/-30°/30°]$ stacking sequence is investigated. The plate results are obtained using a regular 80×80 mesh of 4-node elements. A 3D reference solution is computed using the 8-node solid shell element [16] and a regular $80 \times 80 \times (4 \times 4)$ mesh. The first 10 eigenfrequencies are listed in Table 2. Present results using the factors of Table 1 in a 4-node Reissner–Mindlin plate element with assumed transverse shear strains [11] show deviations of less than 0.4 % in comparison to the reference solution. In contrast to that the factors according to [27] lead with increasing frequency to increasing deviations. This becomes even more evident when using $k_1 = k_2 = 5/6$ for homogeneous plates. Plots of the normalized eigenvectors computed with present element are depicted in Fig. 3. Due to the chosen stacking sequence the eigenmodes are centrally symmetric.

Table 2 Eigenfrequencies of a layered plate

i	f_i (Hz)	Deviations (%)	Deviations (%)	Deviation (%)
	Solid shell [16]	Present	[27]	
		$k_1 = 0.6773$	$k_1 = 0.7459$	$k_1 = 0.8333$
	Reference	$k_2 = 0.6722$	$k_2 = 0.6730$	$k_2 = 0.8333$
	Solution	$k_{12} = -0.0376$		$k_{12} = 0$
1	253.20	0.22	1.05	2.38
2	444.31	0.16	1.02	2.86
3	669.01	0.31	2.32	4.66
4	710.02	−0.03	0.76	3.06
5	861.31	0.27	2.24	5.20
6	1020.29	−0.18	0.59	3.39
7	1148.31	−0.04	1.75	5.32
8	1187.15	0.21	3.24	6.56
9	1352.16	−0.34	0.51	3.85
10	1352.36	0.13	3.04	6.82

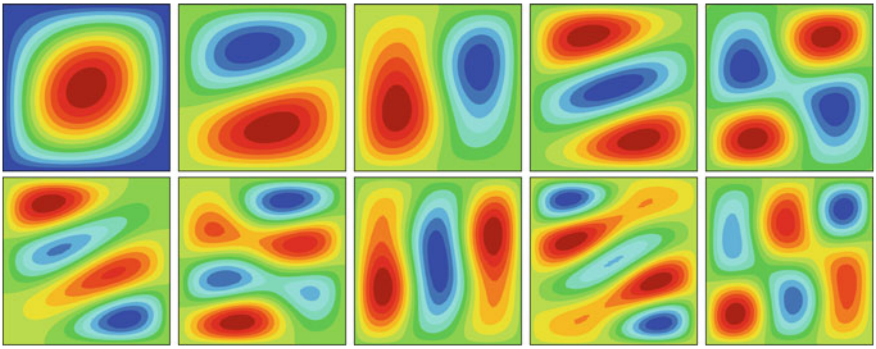

Fig. 3 Eigenvectors 1–5 and 6–10 using present element

Table 3 Eigenfrequencies of a layered plate

i	f_i [Hz]	Deviations [%]	Deviations [%]
	Solid shell [16]	Present	
		$k_1 = 0.3427$	$k_1 = 0.8333$
	Reference	$k_2 = 0.3427$	$k_2 = 0.8333$
	Solution	$k_{12} = 0$	$k_{12} = 0$
1	14.28	−0.15	3.22
2	31.32	−0.15	3.53
3	34.77	−0.14	4.34
4	52.23	−0.23	5.20
5	60.93	−0.18	5.23
6	63.09	−0.17	6.06
7	77.86	−0.28	6.46
8	85.82	−0.29	7.96
9	97.74	−0.26	7.41
10	98.99	−0.24	7.99

4.2.2 Simply Supported Timber Plate

The significance of the shear correction factors for a correct evaluation of eigenfrequencies is demonstrated with this example. Now a simply supported square plate with $L/h = 4800/120\,[\text{mm}]$ is considered. The plate consists of 8 layers of equal thickness and $[45°/-45°/45°/-45°/-45°/45°/-45°/45°]$ stacking sequence. The material parameters assuming transversal isotropic behaviour and the density for glued-laminated timber are chosen as

$$\begin{array}{lll} E_1 = 11600\ \text{N/mm}^2 & G_{12} = 720\ \text{N/mm}^2 & \nu_{12} = 0.03 \\ E_2 = 390\ \ \ \text{N/mm}^2 & G_{23} = 100\ \text{N/mm}^2 & \rho = 530\ \ \text{kg/m}^3\,. \end{array} \tag{39}$$

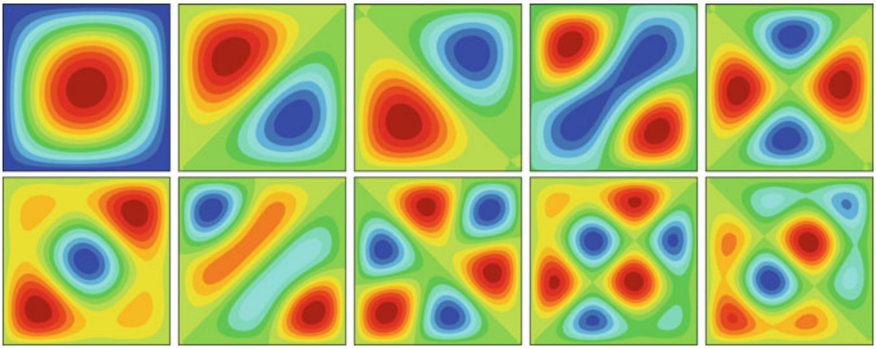

Fig. 4 Eigenvectors 1–5 and 6–10 using present element

Literature results for the shear factors are not available. Again a 3D reference solution is computed using solid shell [16] and a regular 80 × 80 × (8 × 4) mesh. For the plate solutions a mesh of 80 × 80 4-node elements is used.

For this example the computed factors $k_1 = k_2 = 0.3427$ deviate considerable from $k_1 = k_2 = 5/6$ for homogeneous plates, see Table 3. As consequence the deviations from the reference solution grow up to approximately 8% when computing the first 10 eigenfrequencies using $k_1 = k_2 = 5/6$. In contrast to that the deviations are less than 0.3% when using present factors. Plots of the normalized eigenvectors computed with present element are depicted in Fig. 4. The eigenmodes reflect the ±45° fibre orientation of the layers.

5 Conclusions

In this paper the kinematics of plates is extended as warping displacements are superposed on the linear shape of the Reissner–Mindlin theory. The variational formulation is based on a multi-field functional, where the associated Euler–Lagrange equations include besides the equilibrium equations formulated in stress resultants, the local in-plane equilibrium in terms of stresses and a constraint which enforces the correct shape of warping through the thickness. The material matrix for the stress resultants is computed in representative volume elements introducing appropriate interpolation matrices for the independent quantities. For linear elasticity and constant thickness this can be done once in advance. In doing so shear correction factors for layered shear elastic plates are obtained by static condensation of a set of parameters. Present factors are independent of the total thickness of the laminate. The importance of the factors for a correct evaluation of eigenfrequencies is shown.

References

1. Altenbach, H., Naumenko, K.: Shear correction factors in creep-damage analysis of beams, plates and shells. JSME Int. J. Ser. A **45**, 77–83 (2002)
2. Altenbach, H., Eremeyev, V.A., Naumenko, K.: On the use of the first order shear deformation plate theory for the analysis of three-layer plates with thin soft core layer. ZAMM **95**, 1004–1011 (2015)
3. Aßmus, M., Naumenko, K., Altenbach, H.: A multiscale projection approach for the coupled global-local structural analysis of photovoltaic modules. Compos. Struct. **158**, 340–358 (2016)
4. Auricchio, F., Sacco, E.: A mixed-enhanced finite-element for the analysis of laminated composite plates. Int. J. Numer. Methods Eng. **44**, 1481–1504 (1999)
5. Auricchio, F., Balduzzi, G., Khoshgoftar, M.J., Rahimi, G., Sacco, E.: Enhanced modeling approach for multilayer anisotropic plates based on dimension reduction method and Hellinger-Reissner principle. Compos. Struct. **118**, 622–633 (2014)
6. Bach, C., Baumann, R.: Elastizität und Festigkeit, 9th edn. Springer, Berlin (1924)
7. Birman, V., Bert, C.W.: On the choice of shear correction factor in sandwich structures. J. Sandw. Struct. Mater. **4**(1), 83–95 (2002)
8. Brank, B., Carrera, E.: Multilayered shell finite element with interlaminar continuous shear stresses: a refinement of the Reissner-Mindlin formulation. Int. J. Numer. Methods Eng. **48**, 843–874 (2000)
9. Carrera, E.: Theories and finite elements for multilayered plates and shells: a unified compact formulation with numerical assessment and benchmarking. Arch. Comput. Methods Eng. **10**, 215–296 (2003)
10. Chaudhuri, R.A.: An equilibrium method for prediction of transverse shear stresses in a thick laminated plate. Comput. Struct. **23**, 139–146 (1986)
11. Dvorkin, E., Bathe, K.J.: A continuum mechanics based four node shell element for general nonlinear analysis. Eng. Comput. **1**, 77–88 (1984)
12. Gruttmann, F., Wagner, W.: Structural analysis of composite laminates using a mixed hybrid shell element. Comput. Mech. **37**, 479–497 (2006)
13. Gruttmann, F., Wagner, W., Knust, G.: A coupled global-local shell model with continuous interlaminar shear stresses. Comput. Mech. **57**, 237–255 (2016)
14. Kienzler, R., Schneider, P.: Consistent theories of isotropic and anisotropic plates. J. Theor. Appl. Mech. **50**, 755–768 (2012)
15. Klarmann, R., Schweizerhof, K.: A Priori Verbesserung von Schubkorrekturfaktoren zur Berechnung von geschichteten anisotropen Schalentragwerken. Arch. Appl. Mech. **63**, 73–85 (1993)
16. Klinkel, S., Gruttmann, F., Wagner, W.: A continuum based 3D-shell element for laminated structures. Comput. Struct. **71**, 43–62 (1999)
17. Laitinen, M., Lahtinen, H., Sjölind, S.G.: Transverse shear correction factors for laminates in cylindrical bending. Commun. Numer. Methods Eng. **11**, 41–47 (1995)
18. Marimuthu, R., Sundaresan, M.K., Rao, G.V.: Estimation of interlaminar stresses in laminated plates subjected to transverse loading using three-dimensional mixed finite element formulation. Inst. Eng. (India) Tech. J. Aerosp. Eng. **84**, 1–8 (2003)
19. Naumenko, K., Eremeyev, V.A.: A layer-wise theory for laminated glass and photovoltaic panels. Compos. Struct. **112**, 283–291 (2014)
20. Noor, A.K., Peters, J.M.: A posteriori estimates for shear correction factors in multilayered composite cylinders. J. Eng. Mech. **115**, 1225–1244 (1989)
21. Pai, P.F.: A new look at shear correction factors and warping functions of anisotropic laminates. Int. J. Solids Struct. **32**, 2295–2313 (1995)
22. Reddy, J.N.: A simple high-order theory for laminated composite plates. J. Appl. Mech. **51**, 745–752 (1984)
23. Reissner, E.: On bending of elastic plates. Q. Appl. Math. **5**, 55–68 (1947)
24. Schürg, M., Wagner, W., Gruttmann, F.: An enhanced FSDT model for the calculation of interlaminar shear stresses in composite plate structures. Comput. Mech. **44**, 765–776 (2009)

25. Shariyat, M., Alipour, M.: Semi-analytical consistent zigzag-elasticity formulations with implicit layerwise shear correction factors for dynamic stress analysis of sandwich circular plates with FGM layers. Compos. Part B Eng. **49**, 43–64 (2013)
26. Timoshenko, S.P.: On the correction for shear of the differential equation for transverse vibrations of prismatic bars. Philos. Mag. Ser. 6 **41**(245), 744–746 (1921)
27. Whitney, J.M.: Stress analysis of thick laminated composite and sandwich plates. J. Compos. Mater. **6**, 426–440 (1972)
28. Whitney, J.M.: Shear correction factors for orthotropic laminates under static load. J. Appl. Mech. **40**, 302–304 (1973)

Verification Examples for Strain and Strain-Rate Determination of Digital Image Correlation Systems

S. Hartmann and S. Rodriguez

Abstract Digital Image Correlation techniques (DIC) constitute a growing field of experimental measurement tools to determine the displacement and strain distribution on the surface of a specimen under external mechanical loads. In this article, the aspect of strain computation in surfaces is recapped in a first step. Here, two different approaches are compared. One method is related to the basic ideas emerging in finite elements, while the other approach is frequently applied in commercial DIC-systems. Unfortunately, there are no adequate measures to investigate the accuracy of the strain calculations. This article provides analytical examples concerning strain determination, stretches in arbitrary surface directions, and shear angles. The provided verification examples can be used either to study existing DIC-codes or can be applied by code developers working on new systems. In this regard, the focus will first be on determining strains and strain-rates within a surface. Second, particular surface descriptions are used to investigate examples of homogeneous and inhomogeneous deformations such as simple shear, combined tension-torsion of a cylindrical bar, bending of a thin sheet and a deep-drawing process. It will be shown that some situations show accurate results, while other problems demand special care concerning the interpretation of the final strain field distribution. Thus, the article does not focus on assessing image patterns, but addresses strain determination on point clouds.

Keywords Large strains · Surface strains · Digital image correlation · Verification

1 Introduction

Today, Digital Image Correlation (DIC) can provide the information concerning displacements at discrete points within a certain region on the surface of a deformed material body. As a result, the strain distribution is calculated based on the assumption

---

S. Hartmann (✉) · S. Rodriguez
Institute of Applied Mechanics, Clausthal University of Technology,
Adolph-Roemer-Str. 2a, 38678 Clausthal-Zellerfeld, Germany
e-mail: stefan.hartmann@tu-clausthal.de

© Springer International Publishing AG 2018

H. Altenbach et al. (eds.), *Advances in Mechanics of Materials and Structural Analysis*, Advanced Structured Materials 80,
https://doi.org/10.1007/978-3-319-70563-7_7

of a continuous deformation field. In this growing field of Experimental Mechanics there are different objectives. A first approach is to evaluate the pictures in view of accuracy, see, for example, Lava et al. [27, 28], Bornert et al. [4]. For dynamical problems, see, Moulart et al. [32] and the literature cited therein, where the main interest is how fast the systems are able to track the surface pattern. For an overview of those problems, we refer to Grédiac [10], Hild and Roux [20], Le Cam [29]. Third, the systems are applied to specific applications. Either the experimental results are used to interpret the behavior of a specific solid material under different loading conditions, or the measurements can be compared to numerical results. Here, we can distinguish between a pure comparison to finite element results – or other numerical methods to compute boundary-value problems called *validation* – and the possibility to use the experimental full-field information for purposes of material parameter identification (*calibration*). In other words, there are three main purposes of strain computation. First, process monitoring can provide information about the stressed product during the manufacturing of parts. Second, the results of finite element programs can be compared with the experimental (optical) measurement. This process – which is called validation, Babuska and Oden [2], Roache [36] – is of particular interest concerning strongly and inhomogeneously deformed parts, see Le Cam [29], Schmaltz and Willner [39]. Finally, the constitutive models embedded in finite element programs contain material parameters which must be calibrated to experimental results. Here, non-linear optimization tools are applied to the entire finite element program to find a minimum of the residual between the simulation and the experimental data, see, for example, Andresen et al. [1], Mahnken and Stein [30], Hartmann et al. [16, 17], Kreissing et al. [26], Miehe et al. [31]. A first critical remark on the deviation of finite elements and a DIC-system is given in an abstract by Stier and Reese [42]. For considerably less information provided by imaging data drawing on only contour data of the specimen and a few discrete points on the surface, we refer to Hartmann et al. [16], Gilbert et al. [8]. Bio-medical applications are, for instance, shown in Sutton et al. [43], Badel et al. [3].

Apart from the displacements of the discrete points, which are based on the difference of coordinates in the reference and the current configuration, strain determination is an especially challenging aspect. This is due to the fact that strains are based on the derivatives of a function. Thus it is necessary to provide a surface description that is based on the coordinate information of the images. There are a couple of methods to determine the strains drawing on DIC-systems. First, using either spray paint or regular patterns, small dots are applied to the surface so that they can be tracked by means of the DIC-system during the deformation of the surface. Second, the camera system (here, we study only 3D-systems, but the basic principle works for 2D-systems as well) has to be adjusted so that (relative) coordinates can be determined for both the initial configuration as well as any other configuration to a specific time. Third, the evaluation of the pattern, either regular or irregular dot conglomerations, leads to a surface description with various possibilities. The simplest one is a local plane obtained by least square fits, see, for instance, GOM [9], Sutton et al. [44], or in more complex situations, by surface descriptions using complex spline functions, see, for example, Rogers [37], de Falco et al. [6]. Finally, the comparison between the surface description in the reference and the current configuration must be exploited to obtain local (surface) strains. Unfortunately, the theory manuals of the DIC-systems either circumvent a consistent theory of strain computation or show misleading results. Thus, a clear description of a strain measure within a surface in the scope of DIC was provided in Hartmann and Sguazzo [15]. Moreover, there is the classical gap between the knowledge in Continuum Mechanics and the methods used in practice – such as the statement that strains in uniaxial tensile tests are defined by change of length divided by initial length, $\varepsilon = \Delta L/L_0$, and not the derivative of the displacement field $u(x)$, $\varepsilon(x) = \mathrm{d}u(x)/\mathrm{d}x$. Thus, a clear description of the deformation of surfaces is required. Since the description of strains in Hartmann and Sguazzo [15] and those proposed in GOM [9], Sutton et al. [44] appear to differ, we provide a unified framework. Thus, in a first step, we recap the fundamentals from Hartmann and Sguazzo [15], which is mainly based on the more abstract description in Gurtin and Murdoch [11], Papastavrou et al. [35], Javili et al. [24] and extended to curvilinear coordinates. Of course, similarities can be found in shell kinematics, see, for example, [47, pp. 320]. The investigations are also extended to strain-rate computations.

All numerical codes have to verified, either by code-to-code verification or by analytical solutions. Regarding the aspect of *verification*, we refer to Babuska and Oden [2], Roache [36] and The American Society of Mechanical Engineers [45]. Thus, a major aspect of our contribution is that we also provide examples for code verification.

Finally, some simple verification examples are evaluated and discussed – namely simple shear, combined tension-torsion of a cylindrical specimen, bending of a surface, and a deep-drawing example – to address the problems of different basis systems and to estimate the accuracy we can expect from DIC-systems.

The paper has the following structure: first, the kinematic of surfaces is recapped and a general description of the deformation of surfaces is provided. This includes in-plane strain tensors, stretches, angles between prescribed line elements, thickness determination and stretch rates. Moreover, two approaches are compared, and it will be shown how the classical formulation fits into the general surface strain calculation in curvilinear form. Afterwards, various analytical examples are provided: simple shear (homogeneous, plane deformation), tension-torsion of a cylinder (curvilinear problem), bending of a sheet and an analytical deep-drawing process. In these examples, the surface description using the concept in finite elements is chosen.

2 Kinematics of Surfaces

In order to obtain different strain measures at the surface of a material body, we study the kinematics of surfaces. Initially, the geometrical description of a spatially fixed surface is introduced. Based on this description, the deformation of the surface is explained in the context of finite strains. Subsequently, we provide solutions for both stretches (or strains) in an arbitrary direction as well as a shear angle between

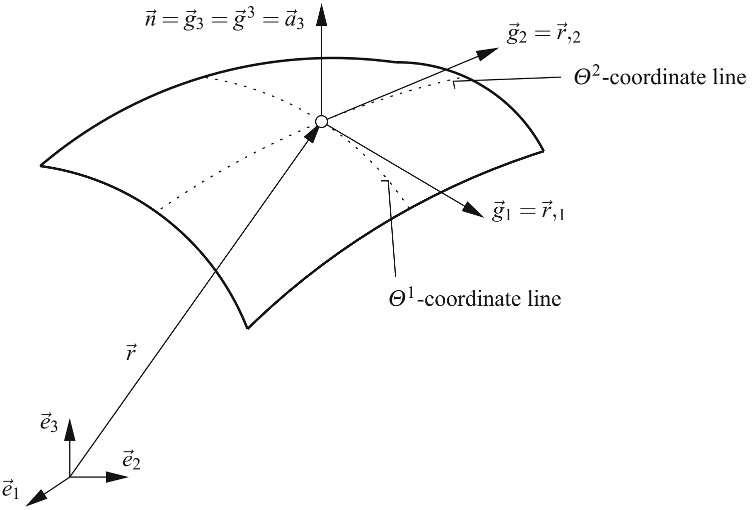
$\vec{n} = \vec{g}_3 = \vec{g}^3 = \vec{a}_3$
$\vec{g}_2 = \vec{r}_{,2}$
Θ^2-coordinate line
$\vec{g}_1 = \vec{r}_{,1}$
Θ^1-coordinate line
$\vec{r}$
$\vec{e}_3$
$\vec{e}_2$
$\vec{e}_1$

Fig. 1 Geometry of a surface

two prescribed directions. Since the specimens changes in thickness are of particular interest under the assumption of incompressibility, this aspect is discussed in the context of small and large strains. Finally, the polynomial description of surfaces is introduced, and different aspects regarding the strain rates are investigated.

2.1 Geometrical Description of Surfaces

A surface $\mathscr{S}$ is described by the position vector $\vec{r} = \hat{\vec{r}}(\Theta^1, \Theta^2)$ depending on the surface coordinates Θ^1 and Θ^2, which are called Gaussian surface parameters, see Fig. 1. For more details see Itskov [23]. According to Klingbeil [25] we introduce an auxiliary point

$$\vec{R}(\Theta^1, \Theta^2, \Theta^3) = \vec{r}(\Theta^1, \Theta^2) + \Theta^3 \vec{a}_3(\Theta^1, \Theta^2) \tag{1}$$

which is outside the surface. The surface itself is formulated for $\Theta^3 = 0$. The tangent vectors to the coordinate lines are given by

$$\vec{g}_\alpha = \frac{\partial \vec{R}}{\partial \Theta^\alpha} = \frac{\partial \vec{r}}{\partial \Theta^\alpha} + \Theta^3 \frac{\partial \vec{a}_3}{\partial \Theta^\alpha} = \vec{a}_\alpha + \Theta^3 \vec{a}_{3,\alpha}, \qquad \alpha = 1, 2, \tag{2}$$

$$\vec{g}_3 = \vec{a}_3. \tag{3}$$

As is common practice, the Greek indices take the values 1 and 2, whereas the Latin letters run from 1 to 3. The tangential vectors inside the plane are abbreviated by

$$\vec{a}_\alpha := \vec{g}_\alpha|_{\Theta^3=0} = \vec{r}_{,\alpha}\,, \quad \alpha = 1, 2. \tag{4}$$

We define $\vec{a}_3$ to be a unit vector which is perpendicular to the tangential plane spanned by the tangential vectors,

$$\vec{a}_3 \cdot \vec{a}_\alpha = 0, \quad \vec{a}_3 \cdot \vec{a}_3 = 1 \;\Rightarrow \vec{a}_3 \cdot \vec{a}_{3,\alpha} = 0, \tag{5}$$

or

$$\vec{a}_3 = \frac{\vec{a}_1 \times \vec{a}_2}{\left|\vec{a}_1 \times \vec{a}_2\right|}. \tag{6}$$

Thus, the covariant metric coefficients are

$$a_{\alpha\beta} := g_{\alpha\beta}|_{\Theta^3=0} = \left|\vec{g}_\alpha \cdot \vec{g}_\beta\right|_{\Theta^3=0} = \vec{a}_\alpha \cdot \vec{a}_\beta, \tag{7}$$

$$a_{\alpha 3} = 0, \qquad a_{33} = 1, \tag{8}$$

i.e. in matrix representation

$$\left[g_{\alpha\beta}\right]_{\Theta^3=0} = \begin{bmatrix} \vec{a}_1 \cdot \vec{a}_1 & \vec{a}_1 \cdot \vec{a}_2 & 0 \\ \vec{a}_1 \cdot \vec{a}_2 & \vec{a}_2 \cdot \vec{a}_2 & 0 \\ 0 & 0 & 1 \end{bmatrix} \tag{9}$$

The contravariant metric coefficient can be calculated by the inverse of the matrix of the covariant metric coefficients (9),

$$a_{\alpha\gamma} a^{\gamma\beta} = \delta_\alpha^{\,\beta}, \qquad [a^{\alpha\beta}] = [a_{\alpha\beta}]^{-1}, \tag{10}$$

where $\delta_\alpha^{\,\beta}$ defines the Kronecker-symbol. The contravariant basis vectors (gradient vectors) can be obtained by

$$\vec{a}^{\,\alpha} = a^{\alpha\beta}\vec{a}_\beta, \tag{11}$$

where

$$\vec{a}^{\,3} = \vec{g}^{\,3} = \frac{\vec{a}_1 \times \vec{a}_2}{\vec{a}_1 \cdot (\vec{a}_2 \times \vec{a}_3)} = g^{3j}\vec{g}_j = g^{33}\vec{g}_3 = \vec{g}_3 = \vec{a}_3. \tag{12}$$

Using the calculation of gradient vectors and inserting Eq. (6) into Eq. $(12)_3$ yields

$$\frac{\vec{a}_1 \times \vec{a}_2}{\vec{a}_1 \cdot (\vec{a}_2 \times \vec{a}_3)} = \frac{\vec{a}_1 \times \vec{a}_2}{\vec{a}_3 \cdot (\vec{a}_1 \times \vec{a}_2)} = \frac{(\vec{a}_1 \times \vec{a}_2)\left|\vec{a}_1 \times \vec{a}_2\right|}{(\vec{a}_1 \times \vec{a}_2) \cdot (\vec{a}_1 \times \vec{a}_2)} = \frac{\vec{a}_1 \times \vec{a}_2}{\left|\vec{a}_1 \times \vec{a}_2\right|},$$

i.e. $\vec{a}^{\,3}$ is a unit vector as well, $\left|\vec{a}^{\,3}\right| = 1$.

Accordingly, all information of the surface is provided and the deformation of the surface can be treated.

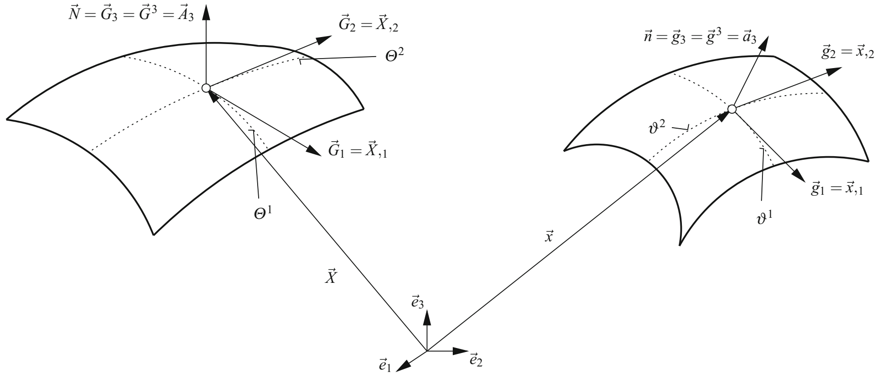
$\vec{N} = \vec{G}_3 = \vec{G}^3 = \vec{A}_3$
$\vec{G}_2 = \vec{X}_{,2}$
Θ^2
$\vec{G}_1 = \vec{X}_{,1}$
Θ^1
$\vec{X}$
$\vec{x}$
$\vec{e}_3$
$\vec{e}_1$
$\vec{e}_2$
$\vec{n} = \vec{g}_3 = \vec{g}^3 = \vec{a}_3$
$\vec{g}_2 = \vec{x}_{,2}$
ϑ^2
$\vec{g}_1 = \vec{x}_{,1}$
ϑ^1

Fig. 2 Surface deformation and its geometrical quantities

2.2 Definition of Deformation

Concerning the deformation of a surface, we look at Fig. 2. The relation between the parameters in the reference and in the current configuration Θ^1, Θ^2, and ϑ^1, ϑ^2, respectively, is given by the motion $\vartheta^\alpha = \theta^\alpha_{\rm R}(\Theta^\beta) = \theta^\alpha_{\rm R}(\Theta^1, \Theta^2)$, i.e. ϑ^α, $\alpha = 1, 2$, are the surface parameters in the current configuration. The surface in the reference configuration is described by $\vec{X} = \hat{\vec{X}}(\Theta^1, \Theta^2)$ and in the current configuration $\vec{x} = \hat{\vec{x}}(\vartheta^1, \vartheta^2)$ with the tangent vectors $\vec{A}_\alpha = \partial \hat{\vec{X}}/\partial \Theta^\alpha$ and $\vec{a}_\alpha = \partial \hat{\vec{x}}/\partial \vartheta^\alpha$.

The material line element in the tangential plane of the current configuration draws on the differential

$$\mathrm{d}\vartheta^\alpha = \frac{\partial \theta^\alpha_{\rm R}}{\partial \Theta^\beta} \mathrm{d}\Theta^\beta, \tag{13}$$

if we multiply expression (13) with the spatial tangent vector $\vec{a}_\alpha = \partial$,

$$\mathrm{d}\hat{\vec{x}} = \mathrm{d}\vartheta^\alpha \vec{a}_\alpha = \frac{\partial \theta^\alpha_{\rm R}}{\partial \Theta^\beta} \mathrm{d}\Theta^\beta \vec{a}_\alpha = \frac{\partial \theta^\alpha_{\rm R}}{\partial \Theta^\beta} \mathrm{d}\Theta^\gamma \underbrace{\delta^\beta_\gamma}_{\vec{A}_\gamma \cdot \vec{A}^\beta} \vec{a}_\alpha = \frac{\partial \theta^\alpha_{\rm R}}{\partial \Theta^\beta} (\vec{a}_\alpha \otimes \vec{A}^\beta) \underbrace{\mathrm{d}\Theta^\gamma \vec{A}_\gamma}_{\mathrm{d}\vec{X}} = \hat{\mathbf{F}} \mathrm{d}\hat{\vec{X}}. \tag{14}$$

The tensor

$$\hat{\mathbf{F}} = \frac{\partial \theta^\alpha_{\rm R}}{\partial \Theta^\beta} (\vec{a}_\alpha \otimes \vec{A}^\beta) = \theta^\alpha_{\rm R},_\beta \, (\vec{a}_\alpha \otimes \vec{A}^\beta) \tag{15}$$

is interpreted as the in-plane deformation gradient, which is singular. It describes the change of the material line element in the tangential surface of the reference configuration $\mathrm{d}\hat{\vec{X}} = \mathrm{d}\Theta^\gamma \vec{A}_\gamma$

$$\mathrm{d}\hat{\vec{x}} = \hat{\mathbf{F}} \mathrm{d}\hat{\vec{X}}. \tag{16}$$

In the case of convective coordinates, where both coordinates are identical, we have $\vartheta^\alpha = \Theta^\alpha$, meaning that representation (15) reduces to

$$\hat{\mathbf{F}} = \vec{a}_\alpha \otimes \vec{A}^\alpha \tag{17}$$

because of the property $\partial\theta^\alpha_{\mathrm{R}}/\partial\Theta^\beta = \delta^\alpha_{\ \beta}$.

Before we continue, some further properties are discussed. In Gurtin and Murdoch [11], Papastavrou et al. [35], Javili et al. [24], the projector

$$\hat{\mathbf{I}} = \mathbf{I} - \vec{A}_3 \otimes \vec{A}^3 \tag{18}$$

is introduced, which is equivalent to $\hat{\mathbf{I}} = \mathbf{I} - \vec{N} \otimes \vec{N}$, where $\vec{N} = \vec{A}_3 = \vec{A}^3$ is the normal vector onto the material surface element in the reference configuration, see Eq. (12). Obviously,

$$\hat{\mathbf{F}} = \mathbf{F}\hat{\mathbf{I}} \tag{19}$$

holds and is called the "material surface identity tensor", see Appendix 6. In DIC-systems $\mathbf{F}$ cannot be provided, i.e. we only obtain $\hat{\mathbf{F}}$.

We start with the in-plane right Cauchy–Green tensor

$$\hat{\mathbf{C}} = \hat{\mathbf{F}}^T\hat{\mathbf{F}} = \theta^\gamma_{\mathrm{R}},_\alpha\,\theta^\delta_{\mathrm{R}},_\beta\,(\vec{A}^\alpha \otimes \vec{a}_\gamma)(\vec{a}_\delta \otimes \vec{A}^\beta) = \underbrace{\theta^\gamma_{\mathrm{R}},_\alpha\,\theta^\delta_{\mathrm{R}},_\beta\,a_{\gamma\delta}}_{\hat{C}_{\alpha\beta}}\,\vec{A}^\alpha \otimes \vec{A}^\beta = \hat{C}_{\alpha\beta}\vec{A}^\alpha \otimes \vec{A}^\beta \tag{20}$$

to develop various kinds of strain tensors and further strain measures, e.g. principal stretches to represent the strain state in the surface. In the case of convective coordinates, the coefficients of the right Cauchy–Green tensor relative to the gradient vectors (contravariant basis) are identical to the metric coefficients of the tangent vectors in the current configuration, $\hat{C}_{\alpha\beta} = a_{\alpha\beta}$. $\hat{\mathbf{C}}$ is a singular tensor, i.e. one eigenvalue is zero, which is a priorily evaluated in the following. Of course, we can use $\hat{\mathbf{C}}$ to determine the in-plane stretch tensor $\hat{\mathbf{U}}$ under the assumption that one eigenvalue is zero. However, we circumvent this by the following idea. The basis vectors $\vec{A}_\alpha \in \mathbb{V}^3$ and $\vec{A}^\beta \in \mathbb{V}^3$ are elements of the three-dimensional vector space. Since both vectors, which are oblique-angled in the general case and span the tangential space, represent a two-dimensional space (embedded in the three-dimensional space), the new basis vectors $\vec{\mathsf{A}}_\alpha \in \mathbb{V}^2$ have the same norm and the same direction, $\vec{\mathsf{A}}_\alpha \mathrel{\hat{=}} \vec{A}_\alpha$. However, $\vec{\mathsf{A}}_\alpha$ contains only two components. This should hold for the contravariant basis as well: $\vec{\mathsf{A}}^\beta \in \mathbb{V}^2$, $\vec{\mathsf{A}}^\beta \mathrel{\hat{=}} \vec{A}^\beta$. Accordingly, the in-plane right Cauchy–Green tensor is represented by

$$\hat{\mathsf{C}} = \hat{C}_{\alpha\beta}\vec{\mathsf{A}}^\alpha \otimes \vec{\mathsf{A}}^\beta. \tag{21}$$

Using the contravariant metric coefficients $A^{\alpha\beta} = \vec{\mathsf{A}}^\alpha \cdot \vec{\mathsf{A}}^\beta = \vec{A}^\alpha \cdot \vec{A}^\beta$, the mixed-variant representation, $\hat{C}^\gamma_{\ \beta} = A^{\alpha\gamma}\hat{C}_{\alpha\beta}$, of the in-plane right Cauchy–Green tensor is obtained, $\hat{\mathsf{C}} = \hat{C}^\gamma_{\ \beta}\vec{\mathsf{A}}_\gamma \otimes \vec{\mathsf{A}}^\beta$, which is necessary to calculate the in-plane right stretch tensor $\hat{\mathsf{U}}$. This is achieved by determining the spectral representation of the tensor $\hat{\mathsf{C}}$. The mixed variant representation is needed to calculate the eigenvalue problem

$$[\hat{\mathsf{C}} - \mu \mathsf{I}]\vec{\mathsf{q}} = \vec{\mathsf{0}}, \tag{22}$$

i.e. in component representation ($\mathsf{I} = \delta^{\alpha}{}_{\gamma} \vec{\mathsf{A}}_\alpha \otimes \vec{\mathsf{A}}^\gamma$)

$$\left((\hat{C}^{\alpha}{}_{\gamma} - \mu\delta^{\alpha}{}_{\gamma})\vec{\mathsf{A}}_\alpha \otimes \vec{\mathsf{A}}^\gamma\right)(q^\beta \vec{\mathsf{A}}_\beta) = [\hat{C}^{\alpha}{}_{\beta} - \mu\delta^{\alpha}{}_{\beta}]q^\beta \vec{\mathsf{A}}_\alpha = \vec{\mathsf{0}}. \tag{23}$$

This holds, due to the linear independence of the vectors $\vec{\mathsf{A}}_1$ and $\vec{\mathsf{A}}_2$, for the classical symmetric eigenvalue problem

$$\begin{aligned} \det[\hat{C}^{\alpha}{}_{\beta} - \mu\delta^{\alpha}{}_{\beta}] &= \begin{vmatrix} \hat{C}^1_{\ 1} - \mu & \hat{C}^1_{\ 2} \\ \hat{C}^2_{\ 1} & \hat{C}^2_{\ 2} - \mu \end{vmatrix} = \\ &= \mu^2 - (\hat{C}^1{}_1 + \hat{C}^2{}_2)\mu + (\hat{C}^1{}_1\hat{C}^2{}_2 - \hat{C}^1{}_2\hat{C}^2{}_1) = 0, \end{aligned} \tag{24}$$

where the principal invariants read

$$\mathrm{I}_{\hat{\mathbf{C}}} = \operatorname{tr}\hat{\mathbf{C}} = \hat{\mathbf{C}} \cdot \mathbf{I} = \hat{\mathsf{C}} \cdot \mathsf{I} = \hat{C}^1{}_1 + \hat{C}^2{}_2 \tag{25}$$

$$\mathrm{II}_{\hat{\mathbf{C}}} = \frac{1}{2}\left((\operatorname{tr}\hat{\mathbf{C}})^2 - \operatorname{tr}\hat{\mathbf{C}}^2\right) = \frac{1}{2}\left((\operatorname{tr}\hat{\mathsf{C}})^2 - \operatorname{tr}\hat{\mathsf{C}}^2\right) = \det[\hat{C}^{\alpha}{}_{\beta}] = \hat{C}^1{}_1\hat{C}^2{}_2 - \hat{C}^1{}_2\hat{C}^2{}_1, \tag{26}$$

but $\mathrm{III}_{\hat{\mathbf{C}}} = \det\hat{\mathbf{C}} = 0$. The solution of Eq. (24) is given by

$$\mu_{1,2} = \frac{\mathrm{I}_{\hat{\mathbf{C}}}}{2} \pm \sqrt{\frac{\mathrm{I}^2_{\hat{\mathbf{C}}}}{4} - \mathrm{II}_{\hat{\mathbf{C}}}}. \tag{27}$$

Here, we apply a numerical eigenvalue and eigenvector computation, see, for a discussion, Hartmann [14]. The eigensolver provides the coefficients of the eigenvectors,

$$\mathbf{q}_1 = \begin{Bmatrix} q^1{}_1 \\ q^2{}_1 \end{Bmatrix}, \qquad \mathbf{q}_2 = \begin{Bmatrix} q^1{}_2 \\ q^2{}_2 \end{Bmatrix}, \tag{28}$$

i.e. the eigenvectors $\vec{\mathsf{q}}$ relative to the oblique-angled tangent basis read

$$\vec{\mathsf{q}}_1 = q^{\alpha}{}_1 \vec{\mathsf{A}}_\alpha \quad \text{and} \quad \vec{\mathsf{q}}_2 = q^{\alpha}{}_2 \vec{\mathsf{A}}_\alpha, \tag{29}$$

where the eigenvectors are orthogonal, $\vec{\mathsf{q}}_1 \cdot \vec{\mathsf{q}}_2 = 0$, but $\vec{\mathsf{A}}_\alpha$ and $\vec{\mathsf{A}}_\beta$ are not in general orthogonal, $\vec{\mathsf{A}}_\alpha \cdot \vec{\mathsf{A}}_\beta = A_{\alpha\beta}$. In the following, the eigenvectors are chosen to be normalized, $\vec{\mathsf{n}}_\alpha = \vec{\mathsf{q}}_\alpha / |\vec{\mathsf{q}}_\alpha|$, and orthonormal, $\vec{\mathsf{n}}_\alpha \cdot \vec{\mathsf{n}}_\beta = \delta_{\alpha\beta}$, so that the spectral representation of the right Cauchy–Green tensor reads

$$\hat{\mathsf{C}} = \sum_{\alpha=1}^{2} \mu_\alpha \vec{\mathsf{n}}_\alpha \otimes \vec{\mathsf{n}}_\alpha . \tag{30}$$

In order to define arbitrary strain tensors, the polar decomposition of the deformation gradient

$$\hat{\mathbf{F}} = \hat{\mathbf{R}}\hat{\mathbf{U}} \qquad \text{or} \qquad \hat{\mathsf{F}} = \hat{\mathsf{R}}\hat{\mathsf{U}} \tag{31}$$

is applied. $\hat{\mathsf{R}}^{-1} = \hat{\mathsf{R}}^{T}$, with $\det \hat{\mathsf{R}} = +1$, is a pure rotation within the tangential space, and $\hat{\mathsf{U}} = \hat{\mathsf{U}}^{T}$ is a positive definite and symmetric tensor, which is not true for $\hat{\mathbf{U}}$. $\hat{\mathbf{U}}$ represents the in-plane right stretch tensor describing the stretch of the material line elements $\mathrm{d}\hat{\vec{X}}$ in the tangential surface. The stretch tensor can be calculated by

$$\hat{\mathsf{U}} = \hat{\mathsf{C}}^{1/2} = \sum_{\alpha=1}^{2} \mu_\alpha^{1/2} \vec{\mathsf{n}}_\alpha \otimes \vec{\mathsf{n}}_\alpha = \sum_{\alpha=1}^{2} \lambda_\alpha \vec{\mathsf{n}}_\alpha \otimes \vec{\mathsf{n}}_\alpha \tag{32}$$

expressing the spectral representation. $\lambda_\alpha = \mu_\alpha^{1/2}$ are the eigenvalues (stretches) and $\vec{\mathsf{n}}_\alpha \in \mathbb{V}^2$ the eigenvectors of $\hat{\mathsf{U}}$. Relative to the original basis we have, with $\vec{\mathsf{n}}_\alpha = \vec{\mathsf{q}}_\alpha / |\vec{\mathsf{q}}_\alpha|$ using Eq. (29),

$$\hat{\mathsf{U}} = \sum_{\alpha=1}^{2} \lambda_\alpha \vec{\mathsf{n}}_\alpha \otimes \vec{\mathsf{n}}_\alpha = \underbrace{\sum_{\alpha=1}^{2} \frac{\lambda_\alpha}{|\vec{\mathsf{q}}_\alpha|^2} q^{\beta}{}_{\alpha} q^{\gamma}{}_{\alpha}}_{\hat{U}^{\beta\gamma}} \vec{\mathsf{A}}_\beta \otimes \vec{\mathsf{A}}_\gamma \tag{33}$$

with

$$|\vec{\mathsf{q}}_\alpha| = \sqrt{q^{\beta}{}_{\alpha} \vec{\mathsf{A}}_\beta \cdot q^{\gamma}{}_{\alpha} \vec{\mathsf{A}}_\gamma} = \sqrt{q^{\beta}{}_{\alpha} q^{\gamma}{}_{\alpha} A_{\beta\gamma}}, \qquad \not\Sigma\, \alpha . \tag{34}$$

The tangent vectors $\vec{\mathsf{A}}_\alpha$ are commonly oblique-angled vectors containing only the information of the direction and the norm. Thus, the vectors are not explicitly provided with numbers (such as a column vector in linear algebra). Accordingly, the matrix representation of the in-plane right stretch tensor $\hat{\mathsf{U}}$ has only the meaning relative to the basis $\vec{\mathsf{A}}_1$ and $\vec{\mathsf{A}}_2$, which is not helpful in the case of curvilinear coordinates. The only case in which the coefficients in $\hat{\mathsf{U}}$ can be directly interpreted with stretches in the global coordinate system, is that of Cartesian coordinates in the reference configuration. If there is an out-of-plane component in the tangent vectors $\vec{A}_\alpha$ this does not hold anymore. Moreover, $\hat{U}^{\beta\gamma}$ are no physical coordinates because the basis vectors $\vec{\mathsf{A}}_\beta$ are not necessarily unit vectors. Now, we go back to the real space. Here, Eq. (33) reads

$$\hat{\mathbf{U}} = \sum_{\alpha=1}^{2} \frac{\lambda_\alpha}{|\vec{\mathsf{q}}_\alpha|^2} q^{\beta}{}_{\alpha} q^{\gamma}{}_{\alpha} \vec{A}_\beta \otimes \vec{A}_\gamma , \tag{35}$$

i.e. we have

$$\hat{\mathbf{C}} = \sum_{\alpha=1}^{2} \frac{\mu_\alpha}{|\vec{\mathsf{q}}_\alpha|^2} q^\beta{}_\alpha q^\gamma{}_\alpha \vec{A}_\beta \otimes \vec{A}_\gamma, \tag{36}$$

Having determined the surface stretch tensor $\hat{\mathsf{U}}$, one can also calculate the in-plane rotation tensor

$$\hat{\mathsf{R}} = \hat{\mathsf{F}}\hat{\mathsf{U}}^{-1}, \tag{37}$$

with $\hat{\mathsf{U}}^{-1} = \sum_{\alpha=1}^{2} \mu_\alpha^{-1/2} \vec{\mathsf{n}}_\alpha \otimes \vec{\mathsf{n}}_\alpha$. Of course, $\hat{\mathsf{F}}$ has the representation $\hat{\mathsf{F}} = \hat{F}^\alpha{}_\beta \vec{\mathsf{a}}_\alpha \otimes \vec{\mathsf{A}}^\beta$ and we obtain

$$\hat{\mathsf{R}} = \left(\hat{F}^\delta{}_\varepsilon \vec{\mathsf{a}}_\delta \otimes \vec{\mathsf{A}}^\varepsilon\right)\left(\sum_{\alpha=1}^{2} \frac{\lambda_\alpha^{-1}}{|\vec{\mathsf{q}}_\alpha|^2} q^\beta{}_\alpha q^\gamma{}_\alpha \vec{\mathsf{A}}_\beta \otimes \vec{\mathsf{A}}_\gamma\right) = \sum_{\alpha=1}^{2} \frac{\lambda_\alpha^{-1}}{|\vec{\mathsf{q}}_\alpha|^2} \hat{F}^\delta{}_\beta q^\beta{}_\alpha q^\gamma{}_\alpha \vec{\mathsf{a}}_\delta \otimes \vec{\mathsf{A}}_\gamma, \tag{38}$$

or in convective coordinates relative to the real tangent basis

$$\hat{\mathbf{R}} = \sum_{\alpha=1}^{2} \frac{\lambda_\alpha^{-1}}{|\vec{\mathsf{q}}_\alpha|^2} q^\beta{}_\alpha q^\gamma{}_\alpha \vec{a}_\beta \otimes \vec{A}_\gamma. \tag{39}$$

2.3 Strain Measures

There exists an infinite number of strain tensors, some of which are of practical and others of theoretical interest. In the following, general strain tensors in the tangential space can be defined by Seth-Hill strain measures, see Ogden [33], Haupt and Tsakmakis [19]. To this end, we define the principal strains by

$$\varepsilon_\alpha^{(\mathrm{m})} = \begin{cases} \dfrac{1}{m}(\lambda_\alpha^m - 1) & \text{if } m \neq 0 \\ \ln \lambda_\alpha & \text{if } m = 0 \end{cases} \tag{40}$$

As is well-known, these strains have the property of vanishing in the undeformed state $\varepsilon_\alpha^{(\mathrm{m})}|_{\lambda_\alpha=1} = 0$ and to be monotonous increasing, $\partial\varepsilon_\alpha^{(\mathrm{m})}/\partial\lambda_\alpha > 0$ for $\lambda_\alpha > 0$. Moreover, all principal strains coincide in the undeformed state, $\partial\varepsilon_\alpha^{(\mathrm{m})}/\partial\lambda_\alpha|_{\lambda_\alpha=1} = 1$. Accordingly, we obtain the representation of generalized strain tensors

$$\hat{\mathsf{E}}^{(\mathrm{m})} = \sum_{\alpha=1}^{2} \varepsilon_\alpha^{(\mathrm{m})} \vec{\mathsf{n}}_\alpha \otimes \vec{\mathsf{n}}_\alpha, \tag{41}$$

see, for example, Ogden [33], Haupt and Tsakmakis [19]. In order to re-calculate other strain tensors for a given particular strain tensor, we draw on Eq. (40) and obtain

$$\lambda_\alpha = \begin{cases} \left(m\varepsilon_\alpha^{(\mathrm{m})} + 1\right)^{(1/m)} & \text{if} \quad m \neq 0 \\ \exp \varepsilon_\alpha^{(0)} & \text{if} \quad m = 0 \end{cases} \tag{42}$$

and, accordingly,

$$\varepsilon_\alpha^{(l)} = \begin{cases} \frac{1}{l}\left(\left(m\varepsilon_\alpha^{(\mathrm{m})} + 1\right)^{(l/m)} - 1\right) & \text{if} \quad m \neq 0 \text{ and } l \neq 0 \\ \frac{1}{l}\left(\exp(l\varepsilon_\alpha^{(0)}) - 1\right) & \text{if} \quad m = 0 \text{ and } l \neq 0 \\ \frac{1}{m}\ln\left(m\varepsilon_\alpha^{(\mathrm{m})} + 1\right) & \text{if} \quad m \neq 0 \text{ and } l = 0 \\ \varepsilon_\alpha^{(\mathrm{m})} = \varepsilon_\alpha^{(0)} & \text{if} \quad m = 0 \text{ and } l = 0 \end{cases} \tag{43}$$

Thus, the tensor representations read

$$\hat{\mathsf{U}} = \begin{cases} (m\hat{\mathsf{E}}^{(\mathrm{m})} + \hat{\mathsf{I}})^{1/m} & \text{if } m \neq 0 \\ \exp \hat{\mathsf{E}}^{(0)} & \text{if } m = 0 \end{cases} \tag{44}$$

and

$$\hat{\mathsf{E}}^{(l)} = \begin{cases} \frac{1}{l}\left(\left(m\hat{\mathsf{E}}^{(\mathrm{m})} + \hat{\mathsf{I}}\right)^{(l/m)} - \hat{\mathsf{I}}\right) & \text{if} \quad m \neq 0 \text{ and } l \neq 0 \\ \frac{1}{l}\left((\exp \hat{\mathsf{E}}^{(0)})^l - \hat{\mathsf{I}}\right) & \text{if} \quad m = 0 \text{ and } l \neq 0 \\ \frac{1}{m}\ln\left(m\hat{\mathsf{E}}^{(\mathrm{m})} + \hat{\mathsf{I}}\right) & \text{if} \quad m \neq 0 \text{ and } l = 0 \\ \hat{\mathsf{E}}^{(\mathrm{m})} = \hat{\mathsf{E}}^{(0)} & \text{if} \quad m = 0 \text{ and } l = 0 \end{cases} \tag{45}$$

Commonly, only the values $m = 0, 1, 2$ are chosen, i.e. for the tensors in the tangential surface we have

$$\hat{\mathsf{E}}^{(0)} = \ln \hat{\mathsf{U}}, \qquad \hat{\mathsf{E}}^{(1)} = \hat{\mathsf{U}} - \hat{\mathsf{I}}, \qquad \hat{\mathsf{E}}^{(2)} = \frac{1}{2}(\hat{\mathsf{C}} - \hat{\mathsf{I}}). \tag{46}$$

The first tensor is called Hencky-strain tensor and the third one defines the Green (-Lagrange) strain tensor – here relative to the tangential space. The component representation is relative to the tangential space

$$\hat{\mathsf{E}}^{(m)} = \sum_{\alpha=1}^{2} \frac{\varepsilon_\alpha^{(m)}}{|\vec{\mathsf{q}}_\alpha|^2} q^\beta{}_\alpha q^\gamma{}_\alpha \vec{\mathsf{A}}_\beta \otimes \vec{\mathsf{A}}_\gamma \tag{47}$$

or relative to the three-dimensional space

$$\hat{\mathbf{E}}^{(m)} = \sum_{\alpha=1}^{2} \frac{\varepsilon_\alpha^{(m)}}{|\vec{\mathsf{q}}_\alpha|^2} q^\beta{}_\alpha q^\gamma{}_\alpha \vec{A}_\beta \otimes \vec{A}_\gamma. \tag{48}$$

2.4 Strains in Arbitrary Directions and Shear Angles

There are two pieces of information that are of practical interest. First, the stretch of a material line element in an arbitrary in-plane direction in the reference state is of particular importance. Secondly, the shear angle in the tangential surface must be provided. The stretch is defined as the ratio of the length of material line elements in current and reference configuration $\hat{\lambda} = |\mathrm{d}\hat{\vec{x}}|/|\mathrm{d}\hat{\vec{X}}|$. In order to obtain this quantity, we calculate its square

$$\hat{\lambda}^2 = \frac{\mathrm{d}\hat{\vec{x}} \cdot \mathrm{d}\hat{\vec{x}}}{\mathrm{d}\hat{\vec{X}} \cdot \mathrm{d}\hat{\vec{X}}} = \frac{\mathrm{d}\hat{\vec{X}} \cdot \hat{\mathbf{F}}^T \hat{\mathbf{F}} \mathrm{d}\hat{\vec{X}}}{\mathrm{d}\hat{\vec{X}} \cdot \mathrm{d}\hat{\vec{X}}} = \hat{\vec{e}} \cdot \hat{\mathbf{C}} \hat{\vec{e}} \quad \Rightarrow \quad \hat{\lambda} = \sqrt{\hat{\vec{e}} \cdot \hat{\mathbf{C}} \hat{\vec{e}}} \tag{49}$$

with

$$\hat{\vec{e}} = \mathrm{d}\hat{\vec{X}}/|\mathrm{d}\hat{\vec{X}}|. \tag{50}$$

In the case of a homogeneous deformation, $\hat{\vec{e}}$ can be prescribed by a user and the stretch $\hat{\lambda}$ can be determined in the direction of $\hat{\vec{e}}$. This can be evaluated in any DIC-system.

The second aspect treats the shear angle γ, see Fig. 3, which can be interpreted as the deviation of orthogonal material line elements during the deformation, $\gamma = 90° - \alpha$, see, for instance, Haupt [18]. If we apply the scalar product

$$\mathrm{d}\hat{\vec{x}}_1 \cdot \mathrm{d}\hat{\vec{x}}_2 = |\mathrm{d}\hat{\vec{x}}_1||\mathrm{d}\hat{\vec{x}}_2| \cos\alpha = |\mathrm{d}\hat{\vec{x}}_1||\mathrm{d}\hat{\vec{x}}_2| \sin\gamma$$

i.e.

$$\mathrm{d}\hat{\vec{X}}_1 \cdot \hat{\mathbf{C}} \mathrm{d}\hat{\vec{X}}_2 = \hat{\lambda}_1 |\mathrm{d}\hat{\vec{X}}_1| \hat{\lambda}_2 |\mathrm{d}\hat{\vec{X}}_2| \sin\gamma,$$

and draw on both a division by $|\mathrm{d}\hat{\vec{X}}_1|$ and $|\mathrm{d}\hat{\vec{X}}_2|$ as well as exploiting relations (49) and (50), i.e.

$$\hat{\lambda}_1 = \sqrt{\hat{\vec{e}}_1 \cdot \hat{\mathbf{C}} \hat{\vec{e}}_1} \quad \text{and} \quad \hat{\lambda}_2 = \sqrt{\hat{\vec{e}}_2 \cdot \hat{\mathbf{C}} \hat{\vec{e}}_2}, \tag{51}$$

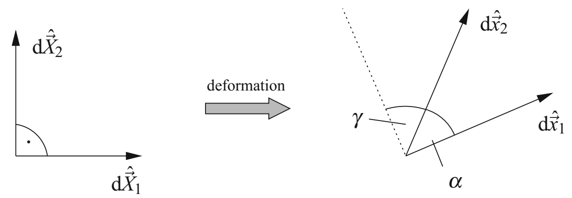
$\mathrm{d}\hat{\vec{X}}_2$
$\mathrm{d}\hat{\vec{X}}_1$
deformation
$\mathrm{d}\hat{\vec{x}}_2$
γ
$\mathrm{d}\hat{\vec{x}}_1$
α

Fig. 3 Explanation of shear angle

we obtain

$$\sin\gamma = \frac{\hat{\vec{e}}_1 \cdot \hat{\mathbf{C}}\hat{\vec{e}}_2}{\sqrt{\hat{\vec{e}}_1 \cdot \hat{\mathbf{C}}\hat{\vec{e}}_1}\sqrt{\hat{\vec{e}}_2 \cdot \hat{\mathbf{C}}\hat{\vec{e}}_2}}. \tag{52}$$

Accordingly, the stretches and the shear angle in the tangential plane can be obtained. In a real application, $\hat{\vec{e}}_1 \in \mathbb{V}^3$ and $\hat{\vec{e}}_2 \in \mathbb{V}^3$, $\hat{\vec{e}}_\alpha \cdot \hat{\vec{e}}_\beta = \delta_{\alpha\beta}$ have to be prescribed by the user, either relative to the global Cartesian coordinate system or relative to some tangential vectors $\hat{\vec{A}}_\beta$, $\hat{\vec{e}}_\alpha = m_\alpha{}^\beta \hat{\vec{A}}_\beta$ in the tangent plane, where $m_\alpha{}^\beta$ must be known.

2.5 Thickness Strain Determination

The determination of the thickness strains is another important issue if one is interested in both the volumetric behavior as well as in the isotropy of the material. Experimentally, this is done in De Almeida et al. [5], Röhrig [38] using a DIC-system, where, apart from the original surface, the surface in thickness direction is considered as well. However, specific assumptions regarding the strain distribution of the uniaxial tensile case are introduced.

With regard to metal forming of steel plates, the assumption of incompressibility serves as a basis to estimate the change of the metal sheet's change in thickness. The DIC-systems are able to provide this information as well. Here, the related equations are developed and estimations of the error of the assumption are discussed.

Again, we start with the assumption of the motion, see Eq. (1), which now reads

$$\vec{R}(\Theta^1, \Theta^2, \Theta^3) = \vec{r}(\Theta^1, \Theta^2) + f(\Theta^3)\vec{a}_3(\Theta^1, \Theta^2). \tag{53}$$

Again, $\vec{a}_3$ should have the same properties as given by Eqs. (5) and (6), i.e. it should be orthogonal to the tangential space which is spanned by the tangential vectors $\vec{a}_1$ and $\vec{a}_2$. The function $f(\Theta^3)$ is assumed to have the form

$$f(\Theta^3) = \overline{\lambda}\Theta^3, \tag{54}$$

with $f'(\Theta^3) = \overline{\lambda}$ and the properties

$$f(0) = 0 \quad \text{and} \quad f'(0) = \overline{\lambda}. \tag{55}$$

This leads to the covariant metric coefficients,

$$\left[g_{\alpha\beta}\right]_{\Theta^3=0} = \begin{bmatrix} \vec{a}_1 \cdot \vec{a}_1 & \vec{a}_1 \cdot \vec{a}_2 & 0 \\ \vec{a}_1 \cdot \vec{a}_2 & \vec{a}_2 \cdot \vec{a}_2 & 0 \\ 0 & 0 & \overline{\lambda}^2 \end{bmatrix}. \tag{56}$$

For the case of convective coordinates, the right Cauchy–Green tensor reads at Θ^3

$$\mathbf{C} = g_{ij}\vec{G}^i \otimes \vec{G}^j = a_{\alpha\beta}\vec{A}^\alpha \otimes \vec{A}^\beta + g_{33}\vec{A}^3 \otimes \vec{A}^3. \tag{57}$$

Since there is a decoupling of the in-plane deformation and the $\vec{A}^3$-direction, the entire scheme of Sect. 2.2 can be applied, i.e. the resulting stretch tensor reads

$$\mathbf{U} = \hat{\mathbf{U}} + \bar{\lambda}\vec{A}^3 \otimes \vec{A}^3 = \sum_{\alpha=1}^{2} \lambda_\alpha \vec{n}_\alpha \otimes \vec{n}_\alpha + \bar{\lambda}\vec{A}^3 \otimes \vec{A}^3, \tag{58}$$

where λ_1 and λ_2 are the maximum and minimum in-plane stretches and $\bar{\lambda}$ the thickness stretch. The volumetric behavior at a material point is given by

$$\det \mathbf{F} = \det \mathbf{U} = \lambda_1\lambda_2\bar{\lambda}. \tag{59}$$

For the given stretches λ_1 and λ_2, the assumption of incompressibility, $\det \mathbf{F} = 1$, leads to

$$\bar{\lambda}_{\text{inc}} = (\lambda_1\lambda_2)^{-1}. \tag{60}$$

If there is no incompressible material under consideration, we have $\det \mathbf{F} = 1 + d$. The parameter d describes the deviation to incompressibility, i.e. using Eq. (59) we have

$$\bar{\lambda}_{\text{comp}} = \frac{1+d}{\lambda_1\lambda_2}. \tag{61}$$

If we assume that $T = \bar{\lambda}T_0$ is the current thickness and T_0 the thickness in the reference state, the ratio between the thicknesses with and without the assumption of incompressibility reads

$$\frac{T_{\text{comp}}}{T_{\text{inc}}} = \frac{\bar{\lambda}_{\text{comp}}}{\bar{\lambda}_{\text{inc}}} = 1 + d. \tag{62}$$

In other words, the difference between the case of incompressibility and the compressible case is linearly dependent on the parameter d.

3 Classical Strain Determination

Strain computation in connection with DIC-systems can be seen as a standard procedure. However, a closed look at the development of the underlying equations reveals some drawbacks. In [44] most of the algorithmic steps are described by words, and not based on unique equations. Thus, specific aspects are left to the interpretation of the reader. Even the description in [9] does not offer a clear explanation how to

Fig. 4 Surface description in [44]

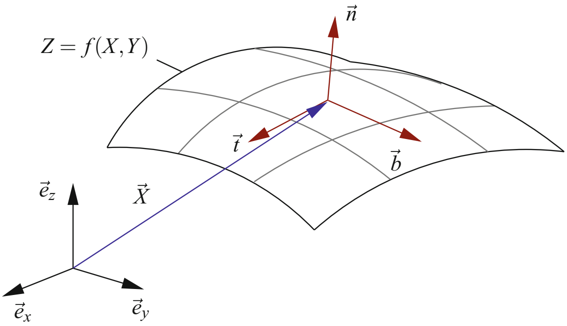

determine the strains. In the following, we will try to interpret the steps of Sutton et al. [44] with the notation used here.

The surface description is different from the presentation here, since a more or less pure Cartesian description is applied. In the reference configuration, the coordinates, $\vec{X}_i \in \mathbb{R}^3$, $i = 1, \ldots, n_\mathrm{p}$, which are fitted by a function

$$Z = f(X, Y) = \sum_{i=1}^{n_\mathrm{LS}} N_i(X, Y) C_i, \tag{63}$$

where $N_i(X, Y)$ are the monomials $(1, X, X^2, \ldots, Y, Y^2, \ldots, XY, \ldots)$ and C_i the coefficients, which are obtained by a least-square fit, see Fig. 4, $(n_\mathrm{p} \geq n_\mathrm{LS})$. The position vector describing the surface reads

$$\vec{X} = X_k \vec{e}_k = X\vec{e}_x + Y\vec{e}_y + f(X, Y)\vec{e}_z, \tag{64}$$

$(\vec{e}_x = \vec{e}_1, \vec{e}_y = \vec{e}_2, \vec{e}_z = \vec{e}_3)$. The tangent vectors are calculated in the direction of the coordinates X and Y,

$$\vec{G}_1 := \vec{G}_X = \frac{\partial \vec{X}}{\partial X} = \vec{e}_x + f,_X \vec{e}_z, \quad \vec{G}_2 := \vec{G}_Y = \frac{\partial \vec{X}}{\partial Y} = \vec{e}_y + f,_y \vec{e}_z, \tag{65}$$

and are used to determine the unit vectors

$$\hat{\vec{E}}_1 := \vec{t} = \frac{\vec{G}_1}{|\vec{G}_1|}, \quad \hat{\vec{E}}_2 := \vec{b} = \frac{\vec{G}_2}{|\vec{G}_2|}, \tag{66}$$

with

$$|\vec{G}_1| = \sqrt{1 + f,_X^2}, \quad |\vec{G}_2| = \sqrt{1 + f,_Y^2}, \tag{67}$$

and the normal vector

$$\hat{\vec{E}}_3 := \vec{G}_3 = \vec{n} = \frac{\vec{G}_1 \times \vec{G}_2}{|\vec{G}_1 \times \vec{G}_2|} = \frac{1}{|\vec{G}_1 \times \vec{G}_2|} \left(\vec{e}_x + f,_X \vec{e}_z\right) \times \left(\vec{e}_y + f,_Y \vec{e}_z\right) = \tag{68}$$

$$= \frac{1}{|\vec{G}_1 \times \vec{G}_2|} \left(-f,_X \vec{e}_x - f,_Y \vec{e}_y + \vec{e}_z\right) = \frac{1}{\sqrt{1 + f,_X^2 + f,_Y^2}} \left(-f,_X \vec{e}_x - f,_Y \vec{e}_y + \vec{e}_z\right) \tag{69}$$

with

$$|\vec{G}_1 \times \vec{G}_2| = \sqrt{1 + f,_X^2 + f,_Y^2}. \tag{70}$$

The normalized tangent basis $\hat{\vec{E}}_1 := \vec{t}$, $\hat{\vec{E}}_2 := \vec{b}$ and $\hat{\vec{E}}_3 := \vec{n}$ is evaluated in a "center-point" of the surface.

In the next step, the DIC-system determines new coordinates of the deformed configuration, $\vec{x}_i$, $i = 1, \ldots, n_\text{p}$, so that displacements of the n_p points can be calculated relative to the original basis, $\vec{u}_i = \vec{x}_i - \vec{X}_i = u_{ik}\vec{e}_k$, $i = 1, \ldots, n_\text{p}$. For each point i, $i = 1, \ldots, n_\text{p}$, three displacement components relative to the original basis are assigned, u_{ik}, $k = 1, 2, 3$. Next, each displacement vector is expressed relative to the basis $\hat{\vec{E}}_k$, $\vec{u}_i = u_{ik}\vec{e}_k = \hat{u}_{ik}\hat{\vec{E}}_k$, leading to

$$\hat{u}_{ik} = Q_{lk} u_{il} \tag{71}$$

with

$$\hat{\vec{e}}_k = Q_{lk}\vec{e}_l, \quad \text{with} \quad Q_{lk} = \vec{e}_l \cdot \hat{\vec{E}}_k. \tag{72}$$

In concrete terms, we have

$$\mathbf{Q}(X, Y) = [Q_{ij}] = \begin{bmatrix} \dfrac{1}{\sqrt{1 + f,_X^2}} & 0 & \dfrac{-f,_X}{\sqrt{1 + f,_X^2 + f,_Y^2}} \\ 0 & \dfrac{1}{\sqrt{1 + f,_Y^2}} & \dfrac{-f,_Y}{\sqrt{1 + f,_X^2 + f,_Y^2}} \\ \dfrac{f,_X}{\sqrt{1 + f,_X^2}} & \dfrac{f,_Y}{\sqrt{1 + f,_Y^2}} & \dfrac{1}{\sqrt{1 + f,_X^2 + f,_Y^2}} \end{bmatrix} \tag{73}$$

In other words, we need n_p transformations. A further least-square method is applied to the displacement components $\hat{u}_{ik}$ of the n_p points

$$\begin{Bmatrix} \hat{u}_1(X, Y) \\ \hat{u}_2(X, Y) \\ \hat{u}_3(X, Y) \end{Bmatrix} = \begin{Bmatrix} \displaystyle\sum_{i=1}^{m_\text{LS}} \hat{N}_i(X, Y) d_{i1} \\ \displaystyle\sum_{i=1}^{m_\text{LS}} \hat{N}_i(X, Y) d_{i2} \\ \displaystyle\sum_{i=1}^{m_\text{LS}} \hat{N}_i(X, Y) d_{i3} \end{Bmatrix} = \hat{\mathbf{N}}(X, Y)\mathbf{d}, \tag{74}$$

i.e. m_{LS} unknowns have to be determined. m_{LS} can be different to n_{LS}, i.e. a different interpolation is chosen for the displacement components and the original surface $f(X, Y)$. The displacement field now reads

$$\vec{u}(X, Y, f(X, Y)) = \hat{u}_k(X, Y)\ \hat{\vec{E}}_k(X, Y) = \hat{u}_k(X, Y)\ Q_{lk}(X, Y)\vec{e}_l. \tag{75}$$

The strains are determined at the middle point $\vec{X}_C$ using the components $\hat{u}_1(X_C, Y_C, f(X_C, Y_C))$ and $\hat{u}_2(X_C, Y_C, f(X_C, Y_C))$. Unfortunately, it is not clear whether the spatial dependence of the basis $\hat{\vec{E}}_k$ in the calculation of the displacement gradient is considered as well.

In order to demonstrate how the "classical" approach can be embedded into the more general description explained before, we proceed as follows: let $\Theta^1 = X$ and $\Theta^2 = Y$, then the tangent vectors in the reference configuration read $\vec{A}_1 = \vec{G}_1$ and $\vec{A}_2 = \vec{G}_2$, see Eq. (65). The contravariant basis $\vec{A}^\alpha = A^{\alpha\beta}\vec{A}_\beta$ requires the inverse covariant metric coefficient matrix

$$\begin{aligned}[A^{\alpha\beta}] = [A_{\alpha\beta}]^{-1} &= \begin{bmatrix} 1 + f,_X^2 & f,_X\, f,_Y \\ f,_X\, f,_Y & 1 + f,_Y^2 \end{bmatrix}^{-1} \\ &= \frac{1}{(1 + f,_X^2)(1 + f,_Y^2) - (f,_X\, f,_Y)^2} \begin{bmatrix} 1 + f,_Y^2 & -f,_X\, f,_Y \\ -f,_X\, f,_Y & 1 + f,_X^2 \end{bmatrix}. \end{aligned} \tag{76}$$

In view of Eq. (17), the tangent vectors in the current configuration are calculated with $\vec{x} = \vec{X} + \vec{u}$ by

$$\vec{a}_\alpha = \vec{x},_\alpha = \vec{X},_\alpha + \vec{u},_\alpha = \vec{A}_\alpha + \vec{u},_\alpha, \tag{77}$$

using $\vec{u}$ of Eq. (75). This leads to

$$\vec{u},_\alpha = \left(\left(\sum_{i=1}^{m_{\mathrm{LS}}} \hat{N}_i(X, Y) d_{i1}\right)\hat{\vec{E}}_k\right)_{,\alpha} = \left(\sum_{i=1}^{m_{\mathrm{LS}}} \hat{N}_{i,\alpha}(X, Y) d_{i1}\right)\hat{\vec{E}}_k + \left(\sum_{i=1}^{m_{\mathrm{LS}}} \hat{N}_i(X, Y) d_{i1}\right)\hat{\vec{E}}_{k,\alpha} \tag{78}$$

with $\hat{\vec{E}}_{k,\alpha} = Q_{lk,\alpha}\vec{e}_l$. The basis $\hat{\vec{E}}_{k,\alpha}$ is not dependent on the coordinates if $\mathbf{Q}$ is constant. This holds for a plane $f(X, Y) = C_0 + C_1 X + C_2 Y$, see Eq. (73). However, this is not the case in general.

3.1 Polynomial Description of Surfaces

The tangent planes have to be described by a given pattern, or – more precisely – by coordinates measured using the DIC-system, see, for example, Fig. 5a. We assume that a basic pattern is given by n_{en} points $\mathbf{X}_k$ in the reference configuration,

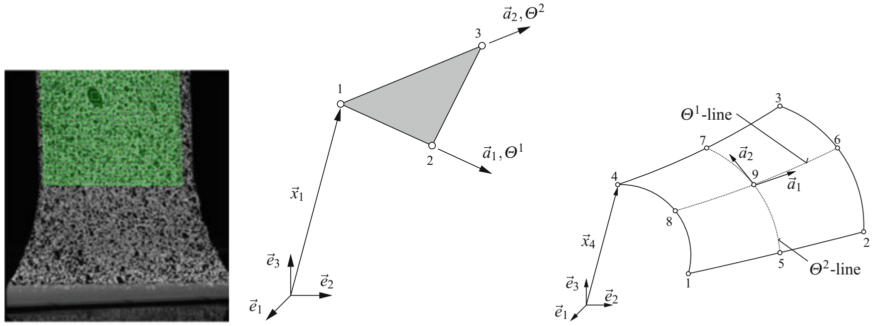

(a) Pattern of facets on a specimen (here, the GOM-system is chosen)

(b) Numbering of the triangular surface

(c) Numbering of the bi-quadratic description of the surface

Fig. 5 Pattern on surfaces for strain determination

$k = 1, \ldots, n_{\text{en}}$, with $\mathbf{X}_k \in \mathbb{R}^3$, which must not necessarily be in a plane and which are not necessarily given by a rectangular pattern in the reference (undeformed) configuration. We define the components $\mathbf{X}_k = \{X_{k1}, X_{k2}, X_{k3}\}$ in a Cartesian coordinate system, where $\vec{X}_k = X_{kj}\vec{e}_j$ is the vector representation of point k relative to the orthonormal basis $\vec{e}_j$, $j = 1, 2, 3$, see Fig. 5b or c for the numbering of a triangle or a nine-noded pattern. There are several possibilities to define a surface by given coordinates. The simplest possibility is a triangulation in a given cloud of points. A more sophisticated approach is to use arbitrary functions for which the parameters are determined by a least-square method. Other possible concepts can be taken from the finite element literature. Even here, the simplest scheme is to be seen in a triangulation of the pattern (if one does not follow the unknown implementation (black-box) of the DIC-provider). An alternative might be a bi-quadratic formulation. Both cases are related to finite elements, see, for example, Hughes [22], for shape functions of three-noded or nine-noded elements. The coordinate representation reads

$$\mathbf{X}(\Theta^1, \Theta^2) = \sum_{k=1}^{n_{\text{en}}} N_k(\Theta^1, \Theta^2)\mathbf{X}_k \quad \Rightarrow \quad \vec{X}(\Theta^1, \Theta^2) = \left(\sum_{k=1}^{n_{\text{en}}} N_k(\Theta^1, \Theta^2) X_{kj}\right)\vec{e}_j \tag{79}$$

with the shape functions $N_k(\Theta^1, \Theta^2)$, $k = 1, \ldots, n_{\text{en}}$, see Appendix 7. These functions have the property of partition of unity, i.e. the sum of all functions is 1 at all points (Θ^1, Θ^2). Moreover, we have $-1 \leq \Theta^\alpha \leq 1$ for the case of a rectangular region in the parameter space.

Choosing the same ansatz for the coordinates in the current configuration

$$\mathbf{x}(\Theta^1, \Theta^2, t) = \sum_{k=1}^{n_{\text{en}}} N_k(\Theta^1, \Theta^2)\mathbf{x}_k(t), \quad \Rightarrow \quad \vec{x}(\Theta^1, \Theta^2, t) = \left(\sum_{k=1}^{n_{\text{en}}} N_k(\Theta^1, \Theta^2) x_{kj}(t)\right)\vec{e}_j \tag{80}$$

leads to the case of convective coordinates. Here, $\mathbf{x}_k$, $k = 1, \ldots, n_{\text{en}}$, define the coordinates of the measured points in the current state, i.e. at time t. Thus, the formulas discussed in Sect. 2.2 can be used to calculate the strains at every point of the pattern. Another possibility would be to apply smoothing techniques such as the mean-value determination at each node, drawing on the connecting pattern information. For a given unknown and an irregular cloud of points a triangulation can be chosen, see, for example, Shewchuk [40, 41]. In a triangle, see Hsu et al. [21], Orteu [34] for a similar approach, a constant stretch occurs, see Appendix 7. Here, we have to decide at each node which stretch has to be chosen – or whether to compute the mean value of the patterns connected to that node. Our examples are based on the latter. The nine-noded approach focuses – quite naturally – on a curvilinear surface description, whereas the triangulation is, a priori, in the tangential space. In conclusion, the stretch, and, accordingly, also the strains can be evaluated at each point of the pattern. Here, we have to ask how accurate the results can be – which can only be determined for given analytical examples.

Regarding the computation of the tangent vectors in the reference and in the current configuration, see Eq. (4), we have

$$\vec{A}_\alpha = \vec{X}_{,\alpha} = \left(\sum_{k=1}^{n_{\text{en}}} N_{k,\alpha} X_{kj} \right) \vec{e}_j, \quad \vec{a}_\alpha = \vec{x}_{,\alpha} = \left(\sum_{k=1}^{n_{\text{en}}} N_{k,\alpha} x_{kj}(t) \right) \vec{e}_j, \tag{81}$$

and the contravariant basis vectors $\vec{A}^\alpha = A^{\alpha\beta} \vec{A}_\beta$ with $[A^{\alpha\beta}] = [A_{\alpha\beta}]^{-1} = [\vec{A}_\alpha \cdot \vec{A}_\beta]^{-1}$, which is required for the deformation gradient (17).

3.2 Strain-Rate Calculation

The strain-rate computation drawing on DIC-systems largely focuses on two main goals. First, in the case of constitutive models of rate-type (viscoelasticity or viscoplasticity), it is either helpful to identify the material parameters or to validate the model under consideration. Second, high local strain rates are an indicator for strain localization in a material, where a crack, or shear band might start. Thus, some helpful relations must be provided. However, the strain-rate computation is much more complex. We restrict ourselves to the stretch-rate determination.

The time derivative of the deformation gradient (17) reads

$$\dot{\hat{\mathbf{F}}} = \dot{\vec{a}}_\alpha \otimes \vec{A}^\alpha, \tag{82}$$

with

$$\dot{\vec{a}}_\alpha = \frac{\partial}{\partial t} \frac{\partial \vec{x}}{\partial \Theta^\alpha} = \sum_{k=1}^{n_{\text{en}}} N_{k,\alpha}(\Theta^1, \Theta^2) \dot{\vec{x}}_k(t) = \left(\sum_{k=1}^{n_{\text{en}}} N_{k,\alpha}(\Theta^1, \Theta^2) \dot{x}_{kj}(t) \right) \vec{e}_j \tag{83}$$

for the interpolation concept proposed by Eq. (80), or

$$\dot{\vec{a}}_\alpha = \frac{\partial}{\partial t}\vec{u}_{,\alpha} = \dot{\hat{u}}_{k,\alpha}\vec{\hat{E}}_k \tag{84}$$

with $\hat{u}_k$ given in Eq. (74) for the classical approach. Here, we remember that $\vec{x}_k(t) = x_{kj}(t)\vec{e}_j$ are given coordinates.

The coordinates $\dot{\vec{x}}_k(t)$ are given by discrete points in time, $\dot{\vec{x}}_k(t_n), n = 0, \ldots, N$, so that an interpolation in the time domain is required as well. The simplest interpolation is linear,

$$\dot{\vec{x}}_k(t_n) \approx \frac{\vec{x}_k(t_{n+1}) - \vec{x}_k(t_n)}{t_{n+1} - t_n}, \quad n = 0, \ldots, N-1. \tag{85}$$

Using $\hat{\mathbf{C}} = \hat{\mathbf{F}}^T\hat{\mathbf{F}}$, the time derivative reads

$$\dot{\hat{\mathbf{C}}} = \dot{\hat{\mathbf{F}}}^T\hat{\mathbf{F}} + \hat{\mathbf{F}}^T\dot{\hat{\mathbf{F}}} = (\dot{\vec{a}}_\alpha \cdot \vec{a}_\beta + \vec{a}_\alpha \cdot \dot{\vec{a}}_\beta)\vec{A}^\alpha \otimes \vec{A}^\beta. \tag{86}$$

For practical purposes, we are only interested in the stretch rate, i.e. the time derivative of $\lambda_k = \mu_k^{1/2}$,

$$\dot{\lambda}_k = \frac{1}{2}\mu_k^{1/2}\dot{\mu}_k = \frac{1}{2}\frac{\dot{\mu}_k}{\lambda_k}, \tag{87}$$

using Eq. (27). With $\mu_{1,2} = \hat{\mu}_{1,2}(\mathrm{I}_{\hat{\mathbf{C}}}(\hat{\mathbf{C}}), \mathrm{II}_{\hat{\mathbf{C}}}(\hat{\mathbf{C}}))$, we obtain by applying the chain-rule

$$\dot{\mu}_{1,2} = \left(\frac{\partial\hat{\mu}_{1,2}}{\partial\mathrm{I}_{\hat{\mathbf{C}}}}\frac{\mathrm{dI}_{\hat{\mathbf{C}}}}{\mathrm{d}\hat{\mathbf{C}}} + \frac{\partial\hat{\mu}_{1,2}}{\partial\mathrm{II}_{\hat{\mathbf{C}}}}\frac{\mathrm{dII}_{\hat{\mathbf{C}}}}{\mathrm{d}\hat{\mathbf{C}}}\right) \cdot \dot{\hat{\mathbf{C}}}, \tag{88}$$

where the derivatives are determinable by

$$\frac{\partial\hat{\mu}_{1,2}}{\partial\mathrm{I}_{\hat{\mathbf{C}}}} = \frac{1}{2}\left(1 \pm \left(\mathrm{I}_{\hat{\mathbf{C}}}^2 - 4\mathrm{II}_{\hat{\mathbf{C}}}\right)^{-1/2}\right), \quad \frac{\partial\hat{\mu}_{1,2}}{\partial\mathrm{II}_{\hat{\mathbf{C}}}} = \pm(-1)\left(\mathrm{I}_{\hat{\mathbf{C}}}^2 - 4\mathrm{II}_{\hat{\mathbf{C}}}\right)^{-1/2}, \tag{89}$$

and

$$\frac{\mathrm{dI}_{\hat{\mathbf{C}}}}{\mathrm{d}\hat{\mathbf{C}}} = \mathbf{I}, \qquad \frac{\mathrm{dII}_{\hat{\mathbf{C}}}}{\mathrm{d}\hat{\mathbf{C}}} = \mathrm{I}_{\hat{\mathbf{C}}}\mathbf{I} - \hat{\mathbf{C}}. \tag{90}$$

4 Verification Examples

In order to investigate the aforementioned theoretical aspects of Sect. 2, we propose four examples, for which the deformation is prescribed analytically, while the procedure for strain determination is based on the surface description of Sects. 2.1 and 2.2. A full investigation of the method in Sect. 3 would go beyond the scope of this presentation. The verification examples are simple shear, combined tension-torsion, bending of a thin sheet (metal sheet or polymer foil), and a deep-drawing process. Of course, other verification examples – such as rigid body motions (pure translation or pure rotation), simple tension or compression as well as (rigid) rotations of the examples mentioned before are possible and should be guaranteed by the algorithms as well.

4.1 Simple Shear

We start with the homogeneous deformation of simple shear, for which analytical solutions are available. This can be used to investigate any kind of geometrical description – for example that of Sect. 3.1 – using the surface description (79). Thus, the simple shear test might be suitable as a verification or benchmark example for strain measuring procedures in 2D and 3D DIC-systems.

4.1.1 Analytical Solution

The case of simple shear is given by the motion

$$\vec{x} = \vec{\chi}_{\mathrm{R}}(\vec{X}, t) = (X + \kappa Y)\vec{e}_1 + Y\vec{e}_2 + Z\vec{e}_3 \tag{91}$$

yielding the deformation gradient relative to a Cartesian basis

$$\mathbf{F} = \mathbf{I} + \kappa \vec{e}_1 \otimes \vec{e}_2, \tag{92}$$

where κ is geometrically shown in Fig. 6.

This leads to the right Cauchy–Green tensor

$$\mathbf{C} = \mathbf{F}^T\mathbf{F} = \mathbf{U}^2 = \begin{bmatrix} 1 & \kappa & 0 \\ \kappa & 1+\kappa^2 & 0 \\ 0 & 0 & 1 \end{bmatrix} \vec{e}_i \otimes \vec{e}_j \tag{93}$$

Fig. 6 Geometrical sketch of the simple shear case

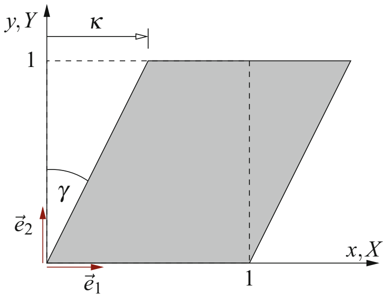

with the eigenvalues

$$\mu_{1,2} = \frac{1}{2}(2 + \kappa^2 \pm \kappa\sqrt{4 + \kappa^2}), \quad \mu_3 = 1 \tag{94}$$

and the normed eigenvectors

$$\begin{aligned} \vec{n}_1 &= \big(2\vec{e}_1 + (\kappa + \sqrt{4 + \kappa^2})\vec{e}_2\big)/\sqrt{4 + (\kappa + \sqrt{4 + \kappa^2})^2} \\ \vec{n}_2 &= \big(2\vec{e}_1 + (\kappa - \sqrt{4 + \kappa^2})\vec{e}_2\big)/\sqrt{4 + (\kappa - \sqrt{4 + \kappa^2})^2} \\ \vec{n}_3 &= \vec{e}_3 \end{aligned} \tag{95}$$

Accordingly, the right stretch tensor $\mathbf{U} = \sum_{k=1}^{3} \mu_k^{1/2} \vec{n}_k \otimes \vec{n}_k$ and all depending strain measures can be determined. Moreover, analytical expressions, see the exercise in [33], yield the right stretch and the rotation tensors

$$\mathbf{U} = \frac{1}{\sqrt{4+\kappa^2}} \begin{bmatrix} 2 & \kappa & 0 \\ \kappa & 2+\kappa^2 & 0 \\ 0 & 0 & \sqrt{4+\kappa^2} \end{bmatrix} \vec{e}_i \otimes \vec{e}_j, \quad \mathbf{R} = \frac{1}{\sqrt{4+\kappa^2}} \begin{bmatrix} 2 & \kappa & 0 \\ -\kappa & 2 & 0 \\ 0 & 0 & \sqrt{4+\kappa^2} \end{bmatrix} \vec{e}_i \otimes \vec{e}_j. \tag{96}$$

4.1.2 Numerical Example

In the first example, the pattern matches the plate exactly (we assume $Z = 0$), i.e. we assume in Eq. (79) the shape functions (130). In other words, $\vec{X}_k$, $k = 1, \ldots, 9$, have the coordinates shown in Fig. 7a. The point coordinates of the deformed state,

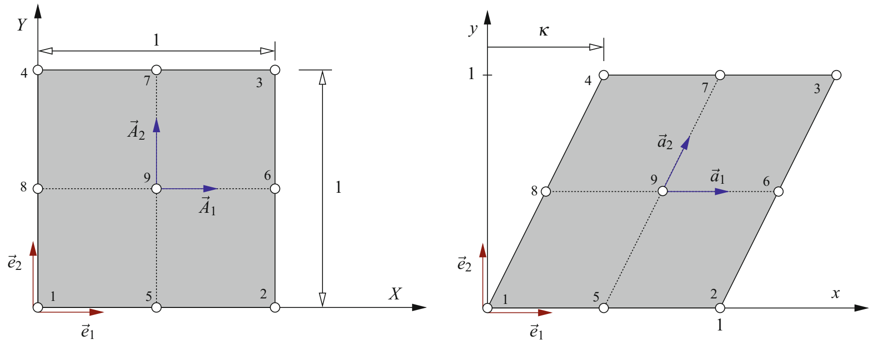

(a) Reference configuration (b) Current configuration

Fig. 7 Regular pattern on simple shear specimen (tangential vectors in reference configuration are parallel to the coordinate axes)

$\vec{x}_k$, $k = 1, \ldots, 9$, are given in Fig. 7b. Thus, the tangent vectors $\vec{A}_1$ and $\vec{A}_2$ coincide with the direction of the original basis vectors, $\vec{A}_1 = 0.5\vec{e}_1$ and $\vec{A}_2 = 0.5\vec{e}_2$, see Fig. 7a. We assume $\kappa = 1/2$ yielding the deformed pattern in Fig. 7b. In this case the tangent vectors in the current configuration $\vec{a}_1 = 0.5\vec{e}_1$ and $\vec{a}_2 = 0.25\vec{e}_1 + 0.5\vec{e}_2$ are obtained. The deformation gradient at point 9, see Fig. 5c, reads

$$\hat{\mathbf{F}} = \vec{a}_\alpha \otimes \vec{A}^\alpha = \begin{bmatrix} 1 & 0.5 & 0 \\ 0 & 1 & 0 \\ 0 & 0 & 0 \end{bmatrix} \vec{e}_i \otimes \vec{e}_j$$

with $\vec{A}^1 = 2\vec{e}_1$ and $\vec{A}^2 = 2\vec{e}_2$, see Eq. (11). The right Cauchy–Green tensor (21) in tangential space or relative to the global Cartesian system, see Eq. (20), is given by

$$\hat{\mathsf{C}} = \begin{bmatrix} 1 & 0.5 \\ 0.5 & 1.25 \end{bmatrix} \vec{\mathsf{A}}^\alpha \otimes \vec{\mathsf{A}}^\beta, \qquad \hat{\mathbf{C}} = \begin{bmatrix} 1 & 0.5 & 0 \\ 0.5 & 1.25 & 0 \\ 0 & 0 & 0 \end{bmatrix} \vec{e}_i \otimes \vec{e}_j. \tag{97}$$

The eigenvalues of the right Cauchy–Green tensor are

$$\mu_1 \approx 0.6096, \qquad \mu_2 \approx 1.6404 \tag{98}$$

and the related eigenvectors

$$\vec{n}_1 \approx -0.788\vec{e}_1 + 0.615\vec{e}_2, \qquad \vec{n}_2 \approx -0.615\vec{e}_1 - 0.788\vec{e}_2, \tag{99}$$

which are calculated by $\vec{n}_\alpha = (q^\beta{}_\alpha / |\vec{\mathsf{q}}_\alpha|)\vec{A}_\beta$, $\not\Sigma\,\alpha$. For the homogeneous deformation even the curvilinear formulation yields exact results.

Of course, the pattern in a verification example should not only be aligned to the original coordinate system. In Fig. 8a, the pattern is assumed to be rotated by 45°. In this case we obtain $\vec{A}_1 = 0.25\vec{e}_1 + 0.25\vec{e}_2$, $\vec{A}_2 = -0.25\vec{e}_1 + 0.25\vec{e}_2$, $\vec{A}^1 = 2\vec{e}_1 + 2\vec{e}_2$ and $\vec{A}^2 = -2\vec{e}_1 + 2\vec{e}_2$ as well as the spatial tangent vectors $\vec{a}_1 = 0.375\vec{e}_1 + 0.25\vec{e}_2$ and $\vec{a}_2 = -0.125\vec{e}_1 + 0.25\vec{e}_2$, see Fig. 8b. The eigenvalues and the eigenvectors of the right Cauchy–Green tensor are equivalent to Eqs. (98) and (99), and are, of course, unchanged by another pattern. In this case, however, we obtain the right Cauchy–Green tensor in the tangential space

$$\hat{\mathsf{C}} = \begin{bmatrix} 1.625 & 0.125 \\ 0.125 & 0.625 \end{bmatrix} \vec{\mathsf{A}}^\alpha \otimes \vec{\mathsf{A}}^\beta, \quad \hat{\mathbf{C}} = \begin{bmatrix} 1 & 0.5 & 0 \\ 0.5 & 1.25 & 0 \\ 0 & 0 & 0 \end{bmatrix} \vec{e}_i \otimes \vec{e}_j,$$

i.e. the coefficients differ to Eq. (97) since we have different contravariant basis vectors.

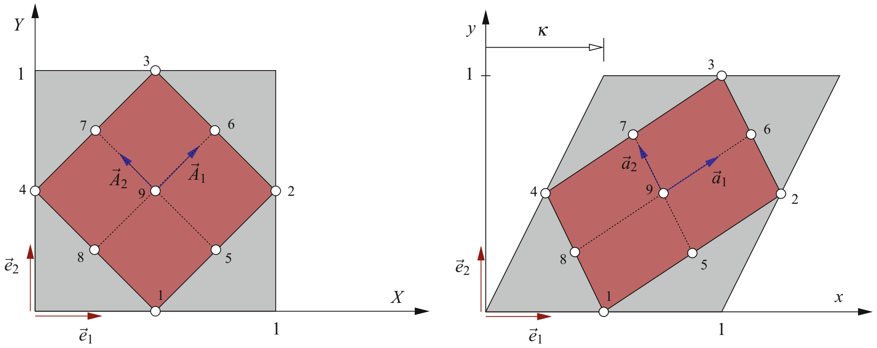

(a) Reference configuration (b) Current configuration

Fig. 8 Rotated pattern on simple shear specimen

4.1.3 Simple Shear Rotated

Of course, the simple shear example can be extended to a rotation in the (X, Z)-plane by an angle φ. This can be chosen to investigate the influence of the changing accuracy due to misaligned camera angles. This, however, is left to the reader. Moreover, as we are again dealing with a plane (homogeneous) motion, not all inaccuracies of the approaches by interpolation schemes become evident. Thus, the following example is of particular interest.

4.2 Combined Tension and Torsion

In the second example, which is more sophisticated than simple shear since a curvilinear problem is provided, we consider combined tension and torsion of a cylinder under the assumption of incompressibility. First, the analytical solution is recapped. After that, the numerical strain and stretch computation are compared.

4.2.1 Analytical Solution

The motion of combined stretch and torsion of a cylinder is given by $\vec{x} = \vec{\chi}_R(\vec{X}, t) = r\vec{e}_r + z\vec{e}_z$ with

$$r = \lambda^{-1/2} R, \quad \vartheta = \Theta + DZ, \quad z = \lambda Z,$$

where (R, Θ, Z) are cylindrical coordinates in the reference configuration, (r, ϑ, z) the coordinates of the material point in the current configuration, and (D, λ) denotes the twist ($D = \alpha/L_0$, where α represents the torsion angle and L_0 the initial length of the specimen) and the axial stretch, see Fig. 9. Here, $Z \in [0, L_0]$ and $\Theta \in [0, 2\pi]$

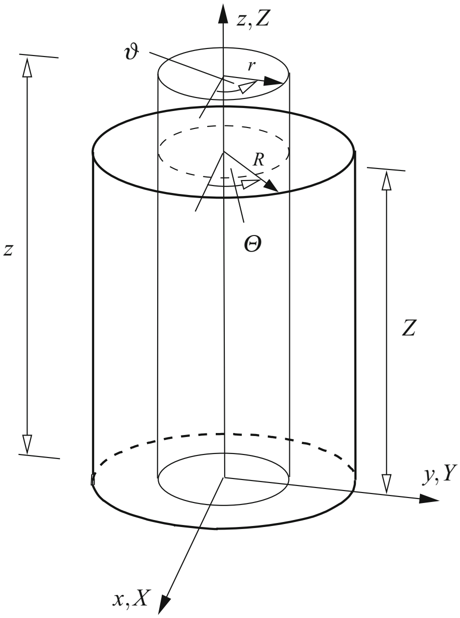

Fig. 9 Cylindrical coordinates in reference and current configuration

hold. For the geometrical description of combined tension and torsion, see Truesdell and Noll [46], Fosdick [7], Ogden [33] or, for the material parameter identification under torsion, Hartmann [12, 13]. The vectors $\vec{e}_r$, $\vec{e}_\vartheta$ and $\vec{e}_z$ represent normalized tangent vectors relative to the current configuration in radial, circumferential and axial direction with

$$\vec{e}_r = \cos\vartheta\,\vec{e}_1 + \sin\vartheta\,\vec{e}_2, \quad \vec{e}_\vartheta = -\sin\vartheta\,\vec{e}_1 + \cos\vartheta\,\vec{e}_2, \quad \vec{e}_z = \vec{e}_3. \tag{100}$$

Analogously,

$$\vec{E}_R = \cos\Theta\,\vec{e}_1 + \sin\Theta\,\vec{e}_2, \quad \vec{E}_\Theta = -\sin\Theta\,\vec{e}_1 + \cos\Theta\,\vec{e}_2, \quad \vec{E}_Z = \vec{e}_3 \tag{101}$$

hold in the reference state. The deformation gradient results in

$$\mathbf{F} = \operatorname{Grad}\vec{\chi}_{\mathrm{R}}(\vec{X},t) = \frac{\partial \chi_R^k}{\partial X^L}\vec{g}_k \otimes \vec{G}^L = \begin{bmatrix} \lambda^{-1/2} & 0 & 0 \\ 0 & \lambda^{-1/2} & Dr \\ 0 & 0 & \lambda \end{bmatrix} \vec{e}_k \otimes \vec{E}_L, \tag{102}$$

$k = r, \vartheta, z$ and $L = R, \Theta, Z$. Accordingly, the right Cauchy–Green tensor

$$\mathbf{C} = \mathbf{F}^T\mathbf{F} = \begin{bmatrix} \lambda^{-1} & 0 & 0 \\ 0 & \lambda^{-1} & DR \\ 0 & DR & \lambda^2 + (DR\lambda^{-1/2})^2 \end{bmatrix} \vec{E}_I \otimes \vec{E}_J, \tag{103}$$

$(I, J = R, \Theta, Z)$ is obtained. Locally, the deformation represents a simple shear state for $\lambda = 1$ (no axial stretch). The eigenvalues are

$$\mu_1 = \lambda^{-1}, \quad \mu_{2,3} = \left(1 + \lambda^3 + (DR)^2 \pm \sqrt{(1 + \lambda^3 + (DR)^2)^2 - 4\lambda^3}\right)/(2\lambda). \tag{104}$$

The first eigenvalue μ_1 is related to the square of the stretch in radial direction, while the others symbolize the squares of the stretches in the circumferential/axial tangential plane.

4.2.2 Numerical Example

Let us assume $R = 10\text{mm}$, $\lambda = 1.2$, and $D = \alpha/L_0 = 45°\pi/180°/60\text{mm} \approx 0.0131\text{mm}^{-1}$ with $L_0 = 60\text{mm}$ leading to

$$\mathbf{C} \approx \begin{bmatrix} 0.833 & 0 & 0 \\ 0 & 0.833 & 0.109 \\ 0 & 0.109 & 1.454 \end{bmatrix} \vec{E}_I \otimes \vec{E}_J, \tag{105}$$

with $\mu_1 \approx 0.833$, $\mu_2 \approx 1.473$ and $\mu_3 \approx 0.815$. This leads to the eigenvectors $\vec{n}_1 = \vec{E}_R, \vec{n}_2 \approx 0.168\vec{E}_\Theta + 0.986\vec{E}_Z$, and $\vec{n}_3 \approx -0.986\vec{E}_\Theta + 0.168\vec{E}_Z$. We place the (3×3)-pattern of the size $b = h$ (b is the width in circumferential direction and h the height in z-direction) in the center of the specimen, see Fig. 10, and vary the width b. By defining the relative error

$$\varepsilon_{\text{err}}^{(\text{m})} = \frac{|\varepsilon_{\text{meas}}^{(\text{m})} - \varepsilon_{\text{ex}}^{(\text{m})}|}{\varepsilon_{\text{ex}}^{(\text{m})}} \times 100, \qquad \lambda_{\text{err}}^{(\text{m})} = \frac{|\lambda_{\text{meas}}^{(\text{m})} - \lambda_{\text{ex}}^{(\text{m})}|}{\lambda_{\text{ex}}^{(\text{m})}} \times 100, \tag{106}$$

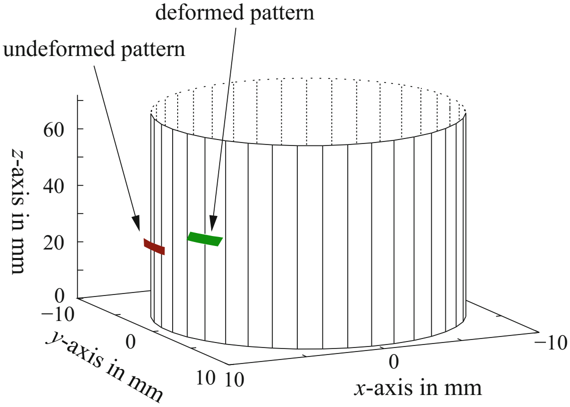

Fig. 10 Deformed and undeformed pattern on the surface of the cylindrical specimen. Here, only the deformed cylinder is shown

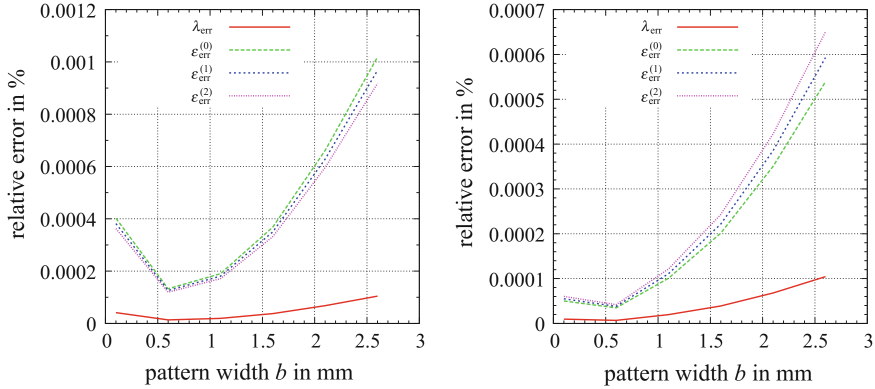

(a) 2nd principal stretch/strains (b) 3rd principal stretch/strains

Fig. 11 Error in principal stretch and principal strains versus the width of the pattern

of the strain measures (40) for $m = 0, 1, 2$ (and of the stretch itself), where the indices "meas" and "ex" indicate measured and exact values, we obtain very small errors for the small, nine-noded pattern-size, see Fig. 11.However, it becomes obvious that increasing pattern sizes lead to an increasing error. Thus, the pattern size must be chosen carefully.

This example can be extended for verifying results at the left or the right "border" of the cylinder (not too close to the visual border, or some points of the pattern will vanish during torsion), where the camera systems yield more inaccurate results. This is left to the reader.

4.3 Bending

For the scope of metal forming technology, there is no access to the deformation during the process – so it can only be studied before and after applying the load. As an example, Fig. 15 shows the reference configuration and the final shape of a deep-drawing (bending) process, where the motion of a mesh of points is followed. According to such applications, we investigate the bending of a thin sheet, i.e. we assume that a plane specimen, see Fig. 12a, is deformed to a bend of 90° (bracket), see Fig. 12b. Apart from the bending, we assume that the surface is homogeneously stretched from L_0 to L so that the entire specimen shows a stretch of $\lambda = L/L_0$. A lateral view serves to describe the deformation, based on the three points ①-③, see Fig. 13. The three dots ①-③ represent, for instance, the combinations (4, 8, 1), (7, 9, 5) or (3, 6, 2) for a nine-noded pattern. We assume that there are two dots inside the curved region, see Fig. 13b. In this case we have the geometrical constraints

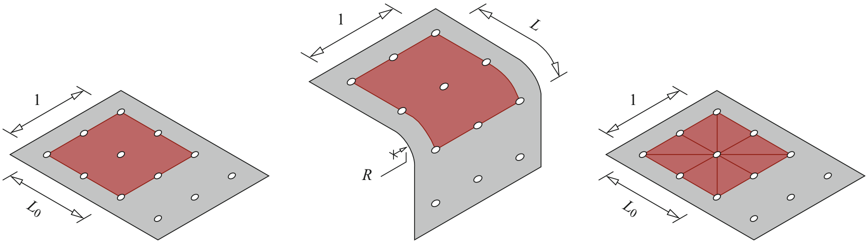

(a) 9-noded pattern on a sheet in the undeformed state (b) 9-noded pattern on a sheet in the deformed state (c) 3-noded pattern on a sheet in the undeformed state

Fig. 12 Bended sheet

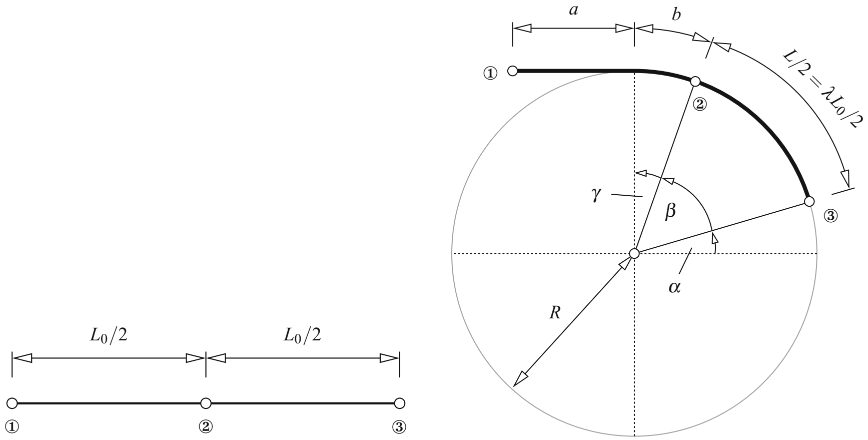

(a) Cross section of the sheet in the reference configuration (b) Cross section of the sheet in the reference configuration

Fig. 13 Geometrical description of cross-section

$$\frac{L}{2} = \frac{\lambda L_0}{2} = 2\pi R \frac{\beta}{360^\circ}, \quad a = \frac{L}{2} - b = \frac{L}{2} - 2\pi R \frac{\gamma}{360^\circ}$$

For given λ, R, L_0, and γ we determine β and a. For our example we assume $L_0 = 4\,\text{mm}$, $R = 4\,\text{mm}$, and a stretch of $\lambda = 1.5$.

We are interested in the deviation of the stretch and strain measures if we vary the angle γ, $0 \leq \gamma \leq \gamma_{\max}$ with $\gamma_{\max} = 42.9718^\circ$ (here, the point ① reaches the upper point on the circle). If we choose the relative errors of Eq. (106), the varying angle γ leads to the behavior in Fig. 14.In this difficult region, the stretch is adequately computed (less than 10% deviation). However, the strains are more sensitive. It is especially the Green–Lagrange principal strain that behaves worse, which becomes clear in view of definition (40). The comparison of the 9-noded pattern and the mean value in the middle of the triangle pattern of Fig. 12c shows that the mean value computation leads to better results, although the quadratic approach is better than the linear approximation.

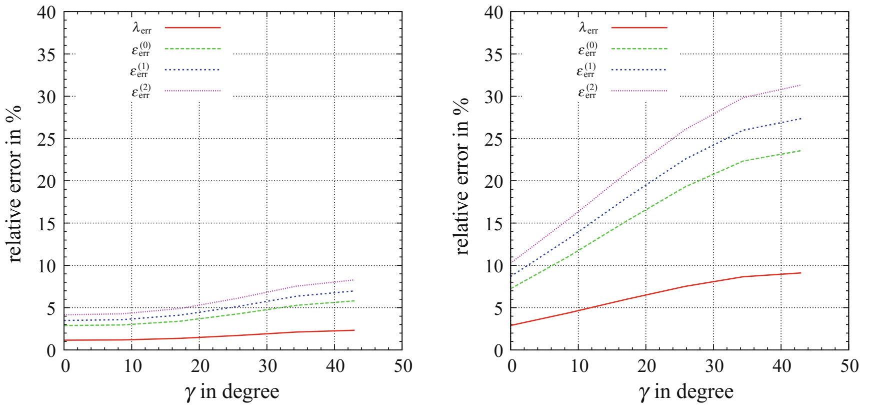

(a) Mean value of the middle node of the triangle pattern in Fig. 12(c)

(b) 9-noded pattern in Fig. 12(a), evaluated at the middle node

Fig. 14 Relative error of Eq. (106) versus angle γ

4.4 Deep Drawing

A more realistic deformation is represented by a deep drawing process, which is analytically generated to investigate the entire strain measurement, see Fig. 15. To this end, we introduce cylindrical coordinates, based on the assumption of axisymmetry, see Fig. 16a. We decompose the region of a flat circle in the reference configuration $0 = R_1 \leq R \leq R_6$ into five subintervals with the coordinates $R_k, k = 1, \ldots, 6$. After the deformation, the circular sheet has the form of a cup, and each subregion is stretched with its own stretch measure $\lambda_k, k = 1, \ldots, 5$. We assume circular regions in the two edges, $R_2 \leq R \leq R_3$ and $R_4 \leq R \leq R_5$, see Fig. 16b.

The motion is given by

$$\vec{x} = \vec{\chi}_{\mathrm{R}}(\vec{X}, t) = \hat{r}(R)\vec{e}_r + \tilde{z}(\hat{r}(R))\vec{e}_z = \hat{r}(R)\vec{e}_r + \hat{z}(R)\vec{e}_z, \tag{107}$$

with the angles $\varphi = \Phi$ in the reference and in the current configuration of each subregion. We are interested in determining the deformation gradient $\hat{\mathbf{F}} = \partial\theta^i(\Theta^1, \Theta^2, \Theta^3)/\partial\Theta^K \vec{g}_i \otimes \vec{G}^K$ and the resulting stretches. The curvilinear coordinates $\theta^i = \{r, \varphi, z\}$ in the current and $\Theta^K = \{R, \Phi, Z\}$ in the reference configuration are cylindrical coordinates. The tangent vectors in the current configuration read $\vec{g}_1 = \vec{e}_r$, $\vec{g}_2 = r\vec{e}_\varphi$, $\vec{g}_3 = \vec{e}_z$, whereas the gradient vectors obtain the representation $\vec{G}^1 = \vec{e}_r$, $\vec{G}^2 = (1/R)\vec{e}_\varphi$, $\vec{G}^3 = \vec{e}_z$. Accordingly, the deformation gradient is given by

$$\hat{\mathbf{F}} = \begin{bmatrix} \hat{r}'(R) & 0 & 0 \\ 0 & 1 & 0 \\ \hat{z}'(R) & 0 & 0 \end{bmatrix} \vec{g}_i \otimes \vec{G}^K = \begin{bmatrix} \hat{r}'(R) & 0 & 0 \\ 0 & \hat{r}(R)/R & 0 \\ \hat{z}'(R) & 0 & 0 \end{bmatrix} \vec{e}_i \otimes \vec{e}_k, \quad i, k = r, \varphi, z, \tag{108}$$

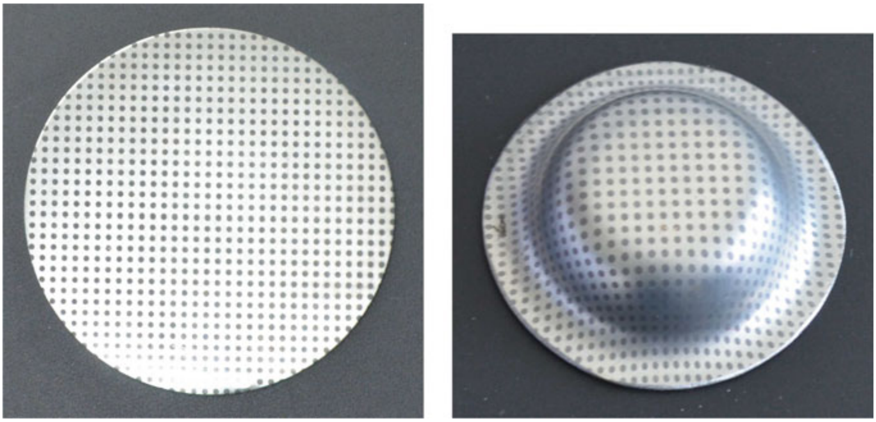

(a) Initial configuration (b) Deformed configuration

Fig. 15 Overall pattern of deep-drawing metal sheet before and after deforming the specimen

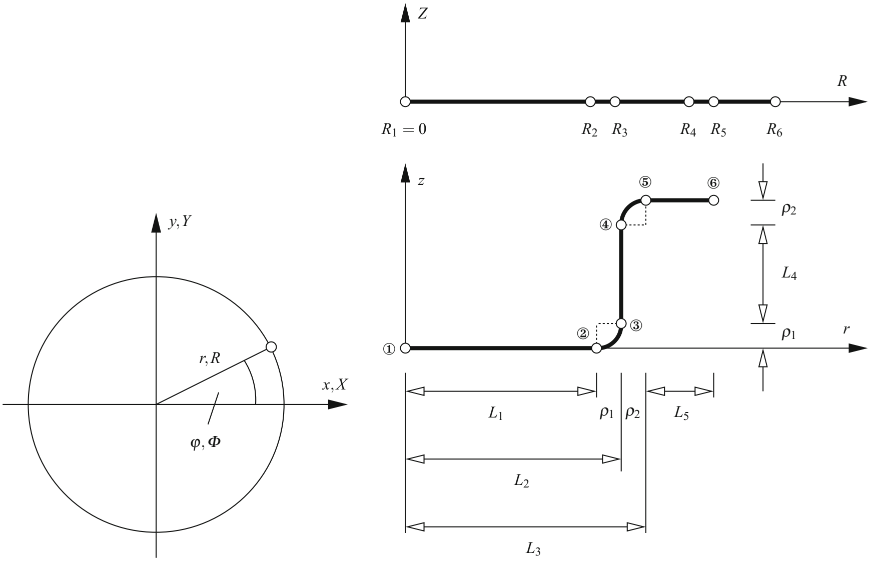
Z
R
$R_1 = 0$
R_2
R_3
R_4
R_5
R_6
z
⑤
⑥
④
③
②
①
ρ_2
L_4
ρ_1
r
L_1
ρ_1
ρ_2
L_5
L_2
L_3
y, Y
r, R
x, X
φ, Φ

(a) Cylindrical coordinates (b) Geometry in reference and current configuration

Fig. 16 Coordinates and deformation in analytical deep drawing process

(and/or $\hat{z}'(R) = \tilde{z}'(r)\hat{r}'(R)$). The prime symbolizes the derivative with respect to the argument, e.g. $\hat{r}'(R) = \mathrm{d}\hat{r}(R)/\mathrm{d}R$. With the help of the deformation gradient (108), the right Cauchy–Green tensor reads

$$\hat{\mathbf{C}}^T = \hat{\mathbf{F}}^T\hat{\mathbf{F}} = \begin{bmatrix} (\hat{r}'(R))^2 + (\hat{z}'(R))^2 & 0 & 0 \\ 0 & (\hat{r}(R)/R)^2 & 0 \\ 0 & 0 & 0 \end{bmatrix} \vec{e}_i \otimes \vec{e}_k, \quad i, k = r, \varphi, z. \tag{109}$$

This leads to the right stretch tensor

$$\hat{\mathbf{U}} = \begin{bmatrix} \sqrt{(\hat{r}'(R))^2 + (\hat{z}'(R))^2} & 0 & 0 \\ 0 & \hat{r}(R)/R & 0 \\ 0 & 0 & 0 \end{bmatrix} \vec{e}_i \otimes \vec{e}_k, \quad i, k = r, \varphi, z. \tag{110}$$

Thus, the stretches in radial and circumferential directions are known

$$\lambda_r = \vec{e}_r \cdot \hat{\mathbf{U}}\vec{e}_r = \sqrt{(\hat{r}'(R))^2 + (\hat{z}'(R))^2} \quad \text{and} \quad \lambda_\varphi = \vec{e}_\varphi \cdot \hat{\mathbf{U}}\vec{e}_\varphi = \frac{\hat{r}(R)}{R}. \tag{111}$$

For the representation $\tilde{z}(\hat{r}(R))$ we have $\lambda_r = \sqrt{1 + \left(\frac{\mathrm{d}\hat{z}(r)}{\mathrm{d}r}\right)^2} \frac{\mathrm{d}\hat{r}(R)}{\mathrm{d}R}$ and we expect that λ_r is equivalent to the prescribed stretches $\lambda_k, k = 1, \ldots, 5$, in each subinterval.

Subinterval $0 = R_1 \leq R \leq R_2$:

In the first subinterval (bottom of the deep drawing cup), a radial stretch λ_1 is assumed,

$$\vec{x}_1 = \lambda_1 R \vec{e}_r \qquad \Rightarrow \qquad \hat{r}(R) = \lambda_1 R, \quad \hat{z}(R) = 0, \tag{112}$$

leading to the stretches in radial and circumferential direction

$$\lambda_r = \lambda_1 \quad \text{and} \quad \lambda_\varphi = \lambda_1 \tag{113}$$

see Eq. (111).

Subinterval $R_2 \leq R \leq R_3$:

In this subinterval a stretch of λ_2 is assumed, i.e. the arc has a length of $b = \lambda_2(R_3 - R_2)$, see Fig. 16b, or Fig. 17a.Thus, the radius is

$$\rho_1 = \frac{b}{\pi/2} = \frac{2\lambda_2(R_3 - R_2)}{\pi}. \tag{114}$$

Accordingly, the motion is given by

$$\vec{x}_2 = \vec{\chi}_\mathrm{R}(\vec{X}, t) = \underbrace{(L_1 + \rho_1 \sin\vartheta)}_{\hat{r}(R)} \vec{e}_r + \underbrace{(\rho_1(1 - \cos\vartheta))}_{\hat{z}((R)} \vec{e}_\varphi \tag{115}$$

with

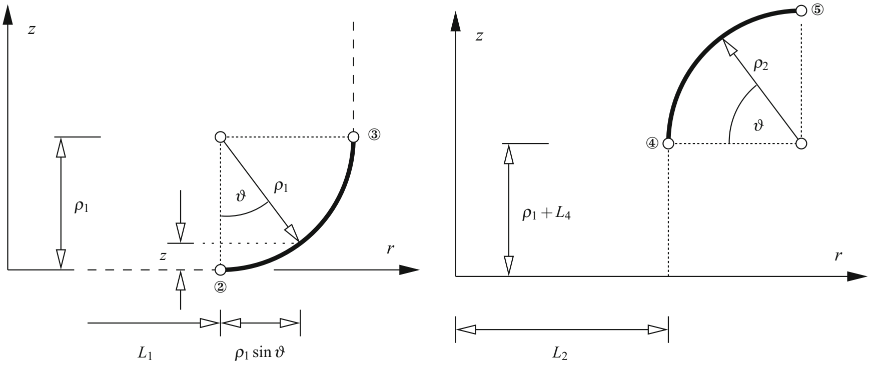

(a) Curved region between points ② and ③

(b) Curved region between points ④ and ⑤

Fig. 17 Geometry in curved regions

$$\vartheta = \hat{\vartheta}(R) = \frac{\pi}{2}\frac{R - R_2}{R_3 - R_2}. \tag{116}$$

and

$$\hat{r}'(R) = \rho_1(\cos\hat{\vartheta}(R))\frac{\pi}{2(R_3 - R_2)} = \lambda_2 \cos\hat{\vartheta}(R), \quad \hat{z}'(R) = \lambda_2 \sin\hat{\vartheta}(R). \tag{117}$$

This results in the deformation gradient

$$\hat{\mathbf{F}} = \begin{bmatrix} \lambda_2 \cos\vartheta & 0 & 0 \\ 0 & \dfrac{L_1 + \rho_1 \sin\vartheta}{R} & 0 \\ \lambda_2 \sin\vartheta & 0 & 0 \end{bmatrix} \vec{e}_i \otimes \vec{e}_k, \quad i, k = r, \varphi, z \tag{118}$$

with $L_1 = \lambda_1(R_2 - R_1) = \lambda_1 R_2$. This leads to

$$\lambda_r = \lambda_2 \quad \text{and} \quad \lambda_\varphi(R) = \frac{L_1 + \rho_1 \sin\hat{\vartheta}(R)}{R}. \tag{119}$$

Subinterval $R_3 \le R \le R_4$:

The motion in the sidewall

$$\vec{x}_3 = \vec{\chi}_{\mathrm{R}}(\vec{X}, t) = L_2 \vec{e}_r + (\lambda_3(R - R_3) + \rho_1)\vec{e}_z \tag{120}$$

is described by a stretch λ_3 yielding the deformation gradient

$$\hat{\mathbf{F}} = \begin{bmatrix} 0 & 0 & 0 \\ 0 & \frac{L_3}{R} & 0 \\ \lambda_3 & 0 & 0 \end{bmatrix} \vec{e}_i \otimes \vec{e}_k, \quad i, k = r, \varphi, z \tag{121}$$

with $L_2 = L_1 + \rho_1$. The stretches are, see Eq. (111),

$$\lambda_r = \lambda_3 \quad \text{and} \quad \lambda_\varphi = \frac{L_2}{R}, \tag{122}$$

i.e. $\lambda_\varphi(R_3) = L_2/R_3$ and $\lambda_\varphi(R_4) = L_2/R_4$.
Subinterval $R_4 \leq R \leq R_5$:

Analogously to the second subinterval, the arc is $b = \lambda_4(R_5 - R_4) = \rho_2\pi/2$, i.e. $\rho_2 = 2\lambda_4(R_5 - R_4)/\pi$, and the angle is given by $\vartheta = (R - R_4)/(R_5 - R_4)(\pi/2)$, see Fig. 17b. Thus, the motion

$$\vec{x}_4 = \vec{\chi}_\mathrm{R}(\vec{X}, t) = \underbrace{(L_2 + \rho_2(1 - \cos\vartheta))}_{\hat{r}(R)}\,\vec{e}_r + \underbrace{\rho_1 + L_4 + \rho_2 \sin\vartheta}_{\hat{z}(R)}\,\vec{e}_z \tag{123}$$

with $L_4 = \lambda_3(R_4 - R_3)$ is given. The derivatives

$$\hat{r}'(R) = \frac{\rho_2(\sin\vartheta)\pi}{2(R_5 - R_4)} = \lambda_4 \sin\vartheta, \quad \hat{z}'(R) = \lambda_4 \cos\vartheta \tag{124}$$

lead to the stretches

$$\lambda_r = \lambda_4 \quad \text{and} \quad \lambda_\varphi = \frac{L_2 + \rho_2(1 - \cos\hat{\vartheta}(R))}{R} \tag{125}$$

which yields the values $\lambda_\varphi(R_4) = L_2/R_4$ and $\lambda_\varphi(R_5) = L_3/R_5$ with $L_3 = L_2 + \rho_2$.
Subinterval $R_5 \leq R \leq R_6$:

In the final subinterval, the motion

$$\vec{x}_5 = \vec{\chi}_\mathrm{R}(\vec{X}, t) = (L_3 + \lambda_5(R - R_5))\vec{e}_r + (\rho_1 + L_4 + \rho_2)\vec{e}_z \tag{126}$$

is given, leading to the stretches

$$\lambda_r = \lambda_5 \quad \text{and} \quad \lambda_\varphi = \frac{L_3 + \lambda_5(R - R_5)}{R}. \tag{127}$$

The circumferential stretches obtain the values at the interval's bounds $\lambda_\varphi(R_5) = L_3/R_5$ and $\lambda_\varphi(R_6) = (L_3 + \lambda_5(R_6 - R_5))/R_5$.

For our example, we choose $R_1 = 0\,\mathrm{mm}$, $R_2 = 30\,\mathrm{mm}$, $R_3 = 34\,\mathrm{mm}$, $R_4 = 46\,\mathrm{mm}$, $R_5 = 50\,\mathrm{mm}$, $R_6 = 60\,\mathrm{mm}$, $\lambda_1 = 1.01$, $\lambda_2 = 1.5$, $\lambda_3 = 1.3$, $\lambda_4 = 1.5$, and $\lambda_5 = 1.05$. Figure 18 shows the results of the stretch distributions $\lambda_r(R)$ and $\lambda_\varphi(R)$. Apparently, there are jumps in the stretches, which, of course, cannot be observed in realistic situations. However, strain localization might occur just before crack initiation occurs.

We generate a grid of points in the reference and the current configuration, see Fig. 19a and apply the triangulation using the algorithm published in Shewchuk [40], see Fig. 19b. By employing the proposed triangular surface representation and

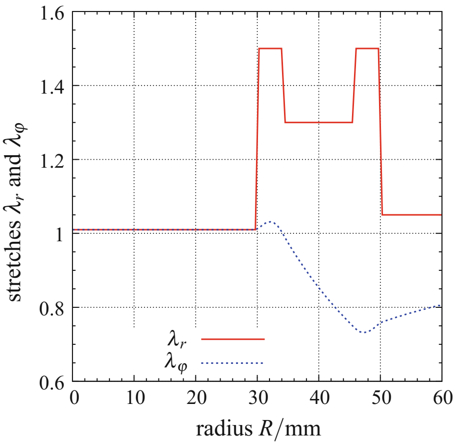

Fig. 18 Radial and circumferential stretches in the deep drawing example

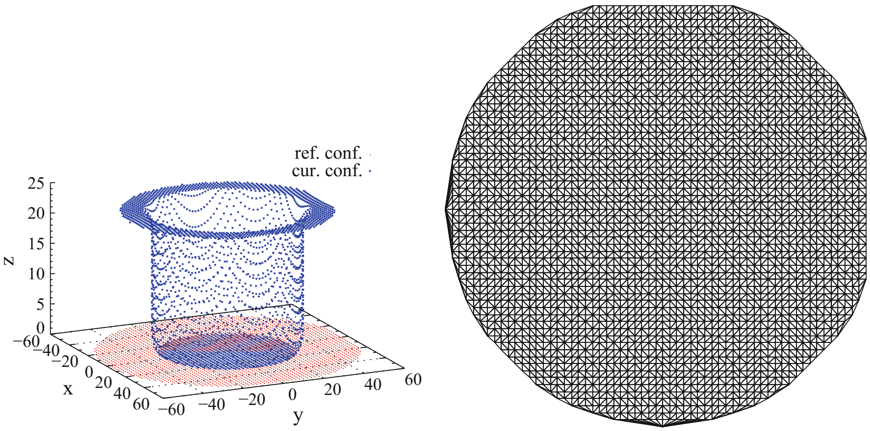

(a) Generated points in reference and current configuration

(b) Triangles generated by a Delaunay triangulation in the reference state

Fig. 19 Point generation and triangulation of a deep-drawing process

computing the mean values of the maximum principal stretch, we obtain the relative error of definition (106), as shown in Fig. 20. We intentionally introduce two points at $(0, -60, 0)$ and $(-60, 0, 0)$ to study the behavior of a more serious problem. These points lead to extremely flat triangles in the triangulation and to errors up 10, 000% (these points are omitted in the figure). The main errors occur in the curved regions, as we expected. The magnitude of the error in all other patterns goes up to 30% for the maximum principal stretch. Thus, special care is required to evaluate principal strains in such regions, which is a common task in the scope of metal forming technology.

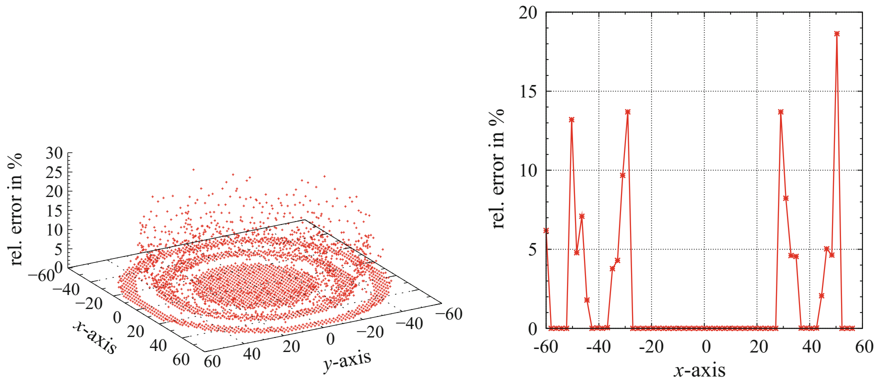

(a) Relative error

(b) Relative error for $y = 0$

Fig. 20 Relative error of maximum principal stretch using triangulation based on mean-value computation

5 Conclusions

One of the main goals of the paper is to provide the basic equations for surface strains given by any kind of surface description. Thus, curvilinear coordinates need to be considered. As demonstration examples, a triangular and a bi-quadratic surface description are chosen for a first instance. There is a clear discrepancy between the general theory and the information provided in the theory manuals of DIC-systems, which is due to the state of knowledge in differential geometry and the kinematics of arbitrary deformations. This article tries to fill this gap. One example is related to orthonormal coordinate systems, as commonly assumed, which are only applicable for real plane problems or for the tangential plane itself (here, however, the orientation is user-dependent). However, the latter changes from point to point and is, accordingly, questionable for real applications if only one Cartesian system is assumed. Here, the basic conditions for the classical approach are provided.

Often, the points of the pattern are very close (speckle pattern) to each other if tension, shear or combined tension-torsion problems are used. In these cases, the error of the strain determination is small. In the case of a point pattern, such as in metal forming processes where bending or deep-drawing of thin metal sheets are investigated, it turns out that we can obtain drastic errors of more than 30%. Thus, it is necessary to either choose smaller patterns or to provide new surface descriptions – especially for problems related to metal forming processes. Furthermore, the provided analytical test examples can help to improve digital imaging systems if they are used for evaluating the systems themselves.

Acknowledgements The author would like to thank the German Research Foundation DFG (grant no. HA2024-12-1) for funding the present investigations.

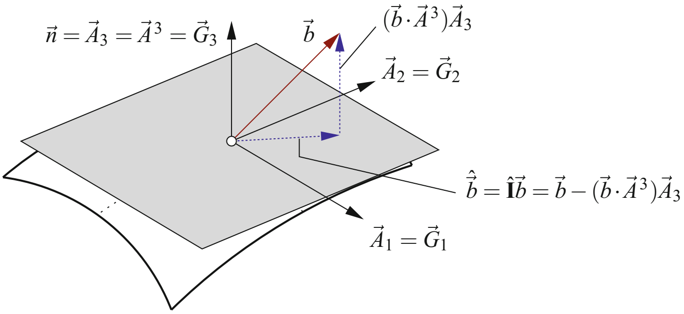
$\vec{n}=\vec{A}_3=\vec{A}^3=\vec{G}_3$
$\vec{b}$
$(\vec{b}\cdot\vec{A}^3)\vec{A}_3$
$\vec{A}_2=\vec{G}_2$
$\hat{\vec{b}}=\hat{\mathbf{I}}\vec{b}=\vec{b}-(\vec{b}\cdot\vec{A}^3)\vec{A}_3$
$\vec{A}_1=\vec{G}_1$

Fig. 21 Projection of a vector $\vec{b}$ into the tangential space

Appendix

6 Projection to Tangential Plane

The projector (18) maps (projects) an arbitrary vector $\vec{b}$ into the tangential surface, see Fig. 21. This can be seen by applying

$$\begin{aligned}\hat{\vec{b}} = \hat{\mathbf{I}}\vec{b} = (\mathbf{I} - \vec{A}_3 \otimes \vec{A}^3)\vec{b} = (\delta^i{}_j \vec{A}_i \otimes \vec{A}^j - \vec{A}_3 \otimes \vec{A}^3) b^k \vec{A}_k = \\ = b^k \vec{A}_k - \delta^3{}_k b^k \vec{A}_3 = b^1 \vec{A}_1 + b^2 \vec{A}_2\end{aligned}$$

or more compact

$$\hat{\mathbf{I}}\vec{b} = \vec{b} - (\vec{b} \cdot \vec{A}^3)\vec{A}_3.$$

7 Shape Functions

For the representation of the surface the shape functions of a triangle and a 9-noded pattern are required. The triangle, see Fig. 22a, in the parameter space has the shape functions

$$N_1(\Theta^1, \Theta^2) = 1 - \Theta^1 - \Theta^2, \quad N_2(\Theta^1, \Theta^2) = \Theta^1, \quad N_3(\Theta^1, \Theta^2) = \Theta^2. \tag{128}$$

These functions lead to constant tangent vectors in the reference and the current configuration. As an example, we consider those in the reference configuration

$$\mathbf{\mathsf{A}}_1 = \frac{\partial \mathbf{\mathsf{X}}}{\partial \Theta^1} = \mathbf{\mathsf{X}}_2 - \mathbf{\mathsf{X}}_1, \qquad \mathbf{\mathsf{A}}_2 = \frac{\partial \mathbf{\mathsf{X}}}{\partial \Theta^2} = \mathbf{\mathsf{X}}_3 - \mathbf{\mathsf{X}}_1. \tag{129}$$

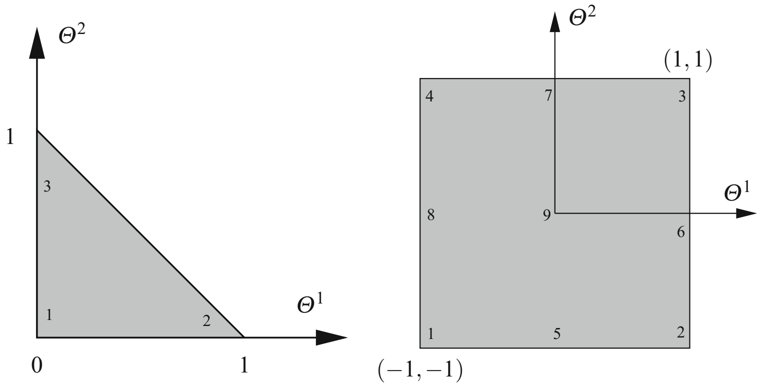

(a) 3-noded pattern (b) 9-noded pattern

Fig. 22 Parameter space of 3- and 9-noded pattern

All resulting vectors are constant within the triangular pattern, and, accordingly, only constant stretches and strains occur. This is known in finite elements as well.

The 9-noded pattern, see Fig. 22b, has the following shape-functions:

$$\begin{aligned}
N_1(\Theta^1,\Theta^2) &= \frac{\Theta^1\Theta^2}{4}(1-\Theta^1)(1-\Theta^2),\\
N_2(\Theta^1,\Theta^2) &= -\frac{\Theta^1\Theta^2}{4}(1+\Theta^1)(1-\Theta^2)\\
N_3(\Theta^1,\Theta^2) &= \frac{\Theta^1\Theta^2}{4}(1+\Theta^1)(1+\Theta^2)\\
N_4(\Theta^1,\Theta^2) &= -\frac{\Theta^1\Theta^2}{4}(1-\Theta^1)(1+\Theta^2)\\
N_5(\Theta^1,\Theta^2) &= -\frac{\Theta^2}{2}(1-(\Theta^1)^2)(1-\Theta^2)\\
N_6(\Theta^1,\Theta^2) &= \frac{\Theta^1}{2}(1+\Theta^1)(1-(\Theta^2)^2)\\
N_7(\Theta^1,\Theta^2) &= \frac{\Theta^2}{2}(1-(\Theta^1)^2)(1+\Theta^2)\\
N_8(\Theta^1,\Theta^2) &= -\frac{\Theta^1}{2}(1-\Theta^1)(1-(\Theta^2)^2)\\
N_9(\Theta^1,\Theta^2) &= (1-(\Theta^1)^2)(1-(\Theta^2)^2)
\end{aligned} \tag{130}$$

where $-1 \le \Theta^\alpha \le +1]$ holds.

References

1. Andresen, K., Dannemeyer, S., Friebe, H., Mahnken, R., Ritter, R., Stein, E.: Parameteridentifikation für ein plastisches Stoffgesetz mit FE-Methoden und Rasterverfahren. Bauingenieur **71**, 21–31 (1996)
2. Babuska, I., Oden, J.T.: Verification and validation in computational engineering and science: basic concepts. Comput. Methods Appl. Mech. Eng. **193**, 4057–4066 (2004)
3. Badel, P., Genovese, K., Avril, S.: 3D residual stress field in arteries: novel inverse method based on optical full-field measurements. Strain **48**, 528–538 (2012)
4. Bornert, M., Brèmand, F., Doumalin, P., Dupré, J.-C., Fazzini, M., Grèdiac, M., Hild, F., Mistou, S., Molimard, J., Orteu, J.-J., Robert, L., Surrel, Y., Vacher, P., Wattrisse, B.: Assessment of digital image correlation measurements errors: methodolody and results. Exp. Mech. **49**, 353–370 (2009)
5. De Almeida, O., Lagattu, F., Brillaud, J.: Analysis by a 3D DIC technique of volumetric deformation gradients: application to polypropylene/EPR/talc composites. Compos. Part A Appl. Sci. Manuf. **39**, 1210–1217 (2008)
6. de Falco, C., Reali, A., Vázquez, R.: GeoPDSs: a research tool for isogeometric analysis of PDEs. Adv. Eng. Softw. **42**, 1020–1034 (2011)
7. Fosdick, R.L.: Dynamically possible motions of incompressible, isotropic, simple materials. Arch. Ration. Mech. Anal. **29**, 272–288 (1968)
8. Gilbert, R.R., Hartmann, S., Kudela, L., Rank, E., Sahar, G., Yosibash, Z., Yossef, O.: Parameter identification of the passive response in arteries. Technical Report Series Fac3-16-01, Faculty of Mathematics/Computer Science and Mechanical Engineering, Clausthal University of Technology (Germany) (2016)
9. GOM: Aramis - User manual: the basics of strain. GOM - Gesellschaft für optische Messtechnik, Braunschweig, Germany (2011)
10. Grédiac, M.: The use of full-field measurement methods in composite material characterization: interest and limitations. Compos. Part A **35**, 751–761 (2004)
11. Gurtin, M.E., Murdoch, A.I.: A continuum theory of elastic material surfaces. Arch. Ration. Mech. Anal. **57**, 291–323 (1975)
12. Hartmann, S.: Numerical studies on the identification of the material parameters of Rivlin's hyperelasticity using tension-torsion tests. Acta Mech. **148**, 129–155 (2001)
13. Hartmann, S.: Parameter estimation of hyperelasticity relations of generalized polynomial-type with constraint conditions. Int. J. Solids Struct. **38**(44–45), 7999–8018 (2001)
14. Hartmann, S.: Computational aspects of the symmetric eigenvalue problem of second order tensors. Technische Mechanik **23**(2–4), 283–294 (2003)
15. Hartmann, S., Sguazzo, C.: Strain analysis in sandwich structures using digital image correlation. Fortschrittsberichte der Materialforschung und Werkstofftechnik / Bulletin of Materials Research and Engineering, vol. 1, pp. 61–71. Clausthaler Zentrum für Materialtechnik, Shaker Verlag, Aachen (2015)
16. Hartmann, S., Tschöpe, T., Schreiber, L., Haupt, P.: Large deformations of a carbon black-filled rubber. Experiment, optical measurement and parameter identification using finite elements. Eur. J. Mech. Ser. A Solids **22**, 309–324 (2003)
17. Hartmann, S., Gibmeier, J., Scholtes, B.: Experiments and material parameter identification using finite elements. Uniaxial tests and validation using instrumented indentation tests. Exp. Mech. **46**(1), 5–18 (2006)
18. Haupt, P.: Continuum Mechanics and Theory of Materials, 2nd edn. Springer, Berlin (2002)
19. Haupt, P., Tsakmakis, C.: Stress tensors associated with deformation tensors via duality. Arch. Mech. **48**, 347–384 (1996)
20. Hild, F., Roux, S.: Digital image correlation: from displacement measurements ot identification of elastic properties - a review. Strain **42**, 69–80 (2006)
21. Hsu, F.P.K., Schwab, C., Rigamonti, D., Humphrey, J.D.: Identification of response functions from axisymmetric membrane inflation tests: implications for biomechanics. Int. J. Solids Struct. **31**, 3375–3386 (1994)

22. Hughes, T.J.R.: The Finite Element Method, 1st edn. Prentice-Hall, Engelwood Cliffs (1987)
23. Itskov, M.: Tensor Algebra and Tensor Analysis for Engineers. Springer, Berlin (2007)
24. Javili, A., McBride, A., Steinmann, P.: Thermomechanics of solids with lower-dimensional energetics: on the importance of surface, interface and curve structures at the nanoscale. A unifying review. App. Mech. Rev. **65**(1), 1–31 (2013)
25. Klingbeil, E.: Tensorrechnung für Ingenieure, 1st edn. BI - Wissenschaftsverlag, Mannheim (1966)
26. Kreissig, R., Benedix, U., Goerke, U.-J.: Statistical aspects of the identification of material parameters for elasto-plastic models. Arch. Appl. Mech. **71**, 123–134 (2001)
27. Lava, P., Cooreman, S., Coppieters, S., De Strycker, M., Debruyne, D.: Assessment of measuring errors in DIC using deformation fields generated by plastic FEA. Opt. Lasers Eng. **47**, 747–753 (2009)
28. Lava, P., Coppieters, S., Wang, Y., Van Houtte, P., Debruyne, D.: Error estimation in measuring strain fields with DIC on planar sheet metal specimens with non-perpendicular camera alignment. Opt. Lasers Eng. **49**, 57–65 (2011)
29. Le Cam, J.-B.: A review of the challenges and limitations of full-field measurements applied to large heterogeneous deformations of rubber. Strain **48**, 174–188 (2012)
30. Mahnken, R., Stein, E.: A unified approach for parameter identification of inelastic material models in the frame of the finite element method. Comput. Methods Appl. Mech. Eng. **136**, 225–258 (1996)
31. Miehe, C., Göktepe, S., Diez, J.M.: Finite viscoplasticity of amorphous glassy polymers in the logarithmic strain space. Int. J. Solids Struct. **46**, 181–202 (2009)
32. Moulart, R., Pierron, F., Hallett, S.R., Wisnom, M.R.: Full-field strain measurement and identification of composite moduli at high strain rate wit hthe virtual fields method. Exp. Mech. **51**, 509–536 (2011)
33. Ogden, R.W.: Non-Linear Elastic Deformations. Ellis Horwood, Chichester (1984)
34. Orteu, J.-J.: 3-D computer vision in experimental mechanics. Opt. Lasers Eng. **47**, 282–291 (2009)
35. Papastavrou, A., Steinmann, P., Kuhl, E.: In the mechanics of continua with boundary energies and growing surfaces. J. Mech. Phys. Solids **61**, 1446–1463 (2013)
36. Roache, P.J.: Verification and Validation in Computational Science and Engineering. Hermosa Publisher, Albuquerque (1998)
37. Rogers, D.F.: An Introduction to NURBS with Historical Perspective. Academic Press, San Diego (2001)
38. Röhrig, C., Scheffer, T., Diebels, S.: Mechanical characterization of a short fiber-reinforced polymer at room temperature. Experimental setups evaluated by an optical measurement system. Continuum Mechanics and Thermodynamics (in print) (2017)
39. Schmaltz, S., Willner, K.: Comparison of different biaxial tests for the inverse identification of sheet steel material parameters. Strain (2014)
40. Shewchuk, J.R.: Triangle: engineering a 2D quality mesh generator and delaunay triangulator. In: Lin, M.C., Manocha, D. (eds.) Applied Computational Geometry: Towards Geometric Engineering. Lecture Notes in Computer Science, vol. 1148, pp. 203–222. Springer, Berlin (1996). From the First ACM Workshop on Applied Computational Geometry
41. Shewchuk, J.R.: Delaunay refinement algorithms for triangular mesh generation. Comput. Geom. Theory Appl. **22**(1–3), 21–74 (2002)
42. Stier, B., Reese, S.: Verification of an optical metrology system (ARAMIS) by comparing experimental data with FE calculations and continuum approaches. PAMM Proc. Appl. Math. Mech. **11**, 289–290 (2011)
43. Sutton, M.A., Ke, X., Lessner, S.M., Goldbach, M., Yost, M., Zhao, F., Schreier, H.W.: Strain field measurements on mouse carotid arteries using microscopic three-dimensional digital image correlation. J. Biomed. Mater. Res. Part A **84A**(1), 178–190 (2008)
44. Sutton, M.A., Orteu, J.-J., Schreier, H.-W.: Image Correlation for Shape, Motion and Deformation Measurements, 1st edn. Springer, New York (2009)

45. The American Society of Mechanical Engineers: Guide for Verification and Validation in Computational Solid Mechanics, vol. ASME V&V 10-2006, New York (2006)
46. Truesdell, C., Noll, W.: The Non-Linear Field Theories of Mechanics. Handbuch der Physik III/3. Springer, Berlin (1965)
47. Truesdell, C., Toupin, R.: The classical field theories. Principles of classical mechanics and field theory. Encyclopedia of Physics, vol. III/1, pp. 226–793. Springer, Berlin (1960)

Closed-Form Approximate Solutions for the Local Buckling Behavior of Composite Laminated Beams Based on Third-Order Shear Deformation Theory

Johannes Herrmann, Torsten Kühn, Tjorven Müllenstedt, Siham Mittelstedt and Christian Mittelstedt

1 Introduction

Composite structures, especially in the form of thin-walled laminates with layers made of fiber-reinforced plastics have found an increasing use in all engineering branches where the weight of a structure is a crucial design aspect. Naturally, this prominently holds for aeronautics and astronautics, but also for industry branches such as automotive or civil engineering.

The most elementary structural elements in almost every engineering branch are prismatic beams with arbitrary cross-sections, subjected to axial, bending and/or torsion load. When designing laminated composite beams according to their stability behaviour, we distinguish between global and local buckling behaviour. Therein, global buckling pertains to such stability cases where the beam exhibits buckling modes where the cross-section remains underformed and where the beam buckles as a whole (i.e. Euler-type column buckling, but also lateral buckling or torsional-flexural buckling). Barbero and Tomblin [2] investigated the Euler-type buckling and also the torsional buckling of thin-walled composite beams and presented rather simple analysis equations as well as experimental data. A related work has been presented by Barbero and Raftoyiannis [3] which included analysis equations for Euler buckling of laminated composite beams under axial compression and where the tran-

J. Herrmann · T. Müllenstedt
Helmut-Schmidt-Universität Hamburg, Hamburg, Germany

T. Kühn
Elbe Flugzeugwerke, Dresden, Germany

S. Mittelstedt
Sogeti Deutschland GmbH, Hamburg, Germany

C. Mittelstedt (✉)
Technische Universität Darmstadt, Darmstadt, Germany
e-mail: christian.mittelstedt@klub.tu-darmstadt.de

© Springer International Publishing AG 2018

H. Altenbach et al. (eds.), *Advances in Mechanics of Materials and Structural Analysis*, Advanced Structured Materials 80,
https://doi.org/10.1007/978-3-319-70563-7_8

sition between global and local buckling for beams with variable length has been investigated in detail. A follow-up paper has been published with [4]. Barbero and Raftoyiannis [5] determined the lateral buckling behaviour of pultruded beams under single moments and point loads and used adequate displacement formulations for the analysis of global and local stability modes. Davalos and Qiao [6] investigated the lateral and torsional buckling behaviour and the interaction of these buckling modes of wide-flange composite beams and presented simple analysis equations for critical loads as well as experimental data. Davalos et al. [7] reported analytical and experimental results for the flexural-torsional buckling behaviour of pultruded beams made of composite materials. The finite element method has been employed by Gan et al. [8] for the analysis of critical buckling loads of pultruded composite beams. Analytical models for Euler-type buckling as well as the torsional and flexural-torsional buckling of composite laminated beams under axial compression have been presented by Lee and Kim [9]. Based on these considerations, a one-dimensional finite element has been developed for according buckling analyses. Kollár [10] employed Vlassov's beam theory for the development of an analysis model for the determination of the buckling behaviour of thin-walled orthotropic beams under uniaxial compression. Qiao et al. [11] employed adequate representations for displacements and rotations for the analytical treatment of the torsional-flexural buckling behaviour of cantilever beams with I-cross-sections and also presented experimental data. Shan and Qiao [12] determined the flexural-torsional buckling behaviour of open-profile composite beams and used adequate displacement representations in conjunction with a variational principle. Further, [12] includes some experimental results. The Ritz-method has been employed by De Lorenzis and La Tegola [13] for the analysis of the global buckling behaviour of thin-walled composite beams. Teter and Kolakowski [14] investigated the interactive global-local behaviour of thin-walled beams strengthened by local stiffeners using the finite element method. Kolakowski and Kubiak [15] considered the post-critical behaviour and ultimate load-carrying capacity of thin-walled beams by performing nonlinear finite elements analyses. Vo and Lee [16] developed an analytical method for the analysis of Euler-type as well as torsional and flexural-torsional buckling of composite box beams under axial compression and derived a one-dimensional finite element for according numerical analyses. The coupled vibration and flexural-torsional buckling behaviour of thin-walled composite beams considering transverse shear deformations and arbitrary laminate lay-ups has been investigated by Vo and Lee [17] using a purely numerical approach. Naderian et al. [18] used the finite strip method for the assessment of the torsional and flexural-torsional buckling behaviour of composite beams under axial compressive load. The boundary element method has been employed by Sapountzakis and Dourakopoulos [19] for the analysis of the flexural-torsional behaviour of thin-walled composite beams.

Given the fact that the segments of the beam cross-sections (i.e. webs and flanges) are generally rather thin-walled when compared to the length of the beam, besides the global buckling behaviour naturally the local buckling behaviour is a further deciding factor during the analysis and design phase as well that needs to be tackled by adequate means of analysis. If closed-form analytical methods are to be used, in most

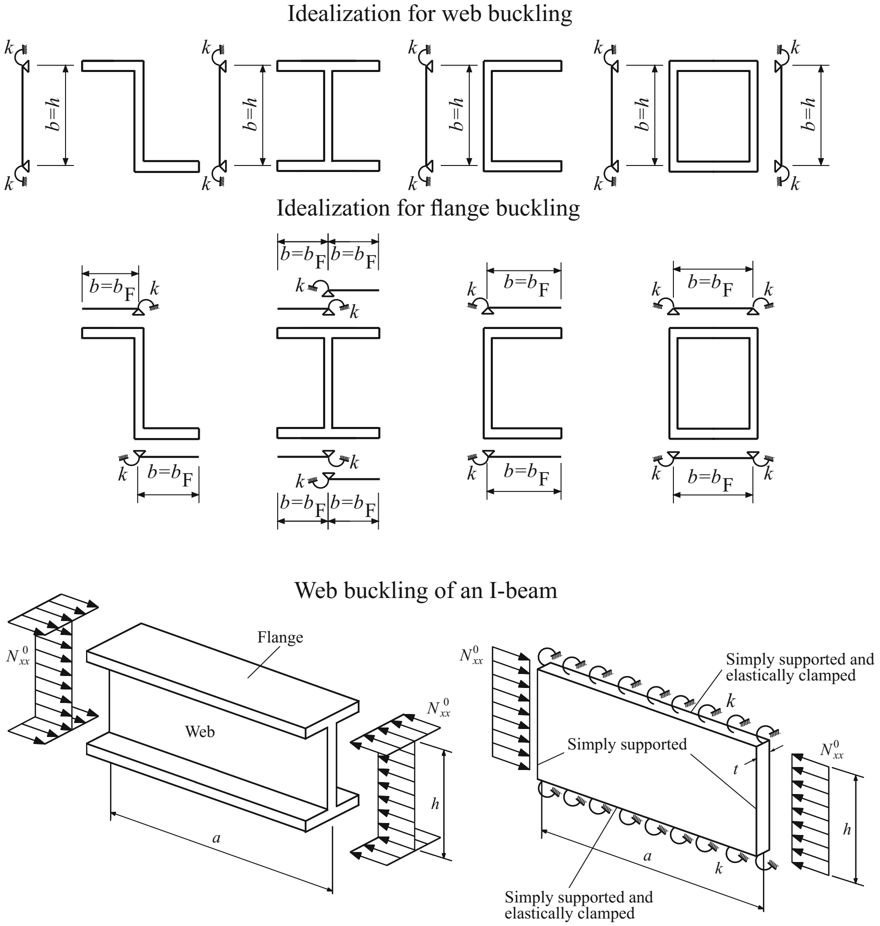
Idealization for web buckling
k
b=h
k
Idealization for flange buckling
b=b_F
k
Web buckling of an I-beam
N_xx^0
Flange
Web
a
h
Simply supported and elastically clamped
Simply supported
t

Fig. 1 The discrete plate approach for local buckling analysis

cases such local buckling analyses employ rather simplified idealization concepts that enable the development of closed-form analysis formulas. A typical approach is the so-called discrete plate approach (Fig. 1) during which the segment of interest (web or flange) is separated from the cross-section and elastic rotational restraints (restraint stiffness k) are employed at the cutting edges as indicated for several typical cross-sections. The buckling analysis is then performed for this separated segment with elastic restraints. The length of the considered beam is a, and the width b is taken as h (for web buckling) or b_F (for flange buckling). Figure 1, lower part, shows the idealization approach for the local web buckling of an I-beam. All four edges of the web plate are taken to be simply supported, while in addition the longitudinal unloaded edges are elastically clamped (restraint stiffness k). The restraints stiffness values can be determined from the properties of the adjacent beam segments, and according analysis rules are given for instance in Qiao and Shan [20] which we recommend for further reading in this regard. Analysis approaches within the framework of discrete plate analysis have been presented e.g. by Qiao and Shan [20], Bank and Yin [21], Kollár [22, 23], Qiao et al. [24], Qiao and Zou [25], Zureick and Shih [26], wherein all of the cited references operate with the framework of CLPT and only consider orthotropic plates and laminates, respectively, under uniaxial compressive load. Mittelstedt [27, 28] considered the local flange buckling of thin-walled composite beams taking bending-twisting coupling into account. Mittelstedt and Beerhorst [29] used discrete plate models for the local buckling analysis of stiffened composite panels. The combination of compressive and shear load has been considered by Beerhorst et al. [30]. An extension of existing CLPT models for the local buckling analysis of webs and flanges of composite laminated beams to FSDT has been presented by Kühn et al. [31].

In this paper we present a novel discrete plate analysis approach for the local buckling behaviour of composite laminated beams based on TSDT. For this, we will employ adequate and rather simple shape functions for the out-of-plane buckling deflections as well as for the rotational angles of the web and flange cross-sections and use the principle of minimum elastic potential of the buckled discrete plate under the assumption of symmetric and purely orthotropic laminates. The shape functions are required to fulfill the given geometric boundary conditions, and the employed methodology allows for closed-form approximate solutions of the buckling loads according to TSDT that can be used with ease in a practical engineering environment. Comparison to reference results shows that the current analysis approach delivers quite reliable and reasonable results and can thus be recommended for use in engineering practice.

2 Third Order Shear Deformation Theory

In this paper, an analysis method for the local buckling of composite laminated beams under uniaxial compression, based on third order shear deformation theory (TSDT) according to Reddy, will be derived. In this section we briefly summarize this specific theory. The interested reader is referred to [1] for further details.

Unlike classical laminated plate theory (CLPT) that is based on the hypotheses of Kirchhoff's classical plate theory (i.e. normal hypothesis, cross-sections remain unwarped during plate deformations), TSDT does not use these assumptions and explicitly allows for non-normal and warped plate cross-sections. However, the requirement that the transverse normal stress σ_{zz} vanishes and that no changes in plate thickness h occur are also maintained within TSDT. A comparison between CLPT, first order shear deformation theory (FSDT) and TSDT is given in Fig. 2. The global coordinate system is denoted as x, y, z, wherein x and y generate the laminate middle plane and z denotes the thickness direction. The laminate thickness is denoted as t. TSDT employs the following displacement field:

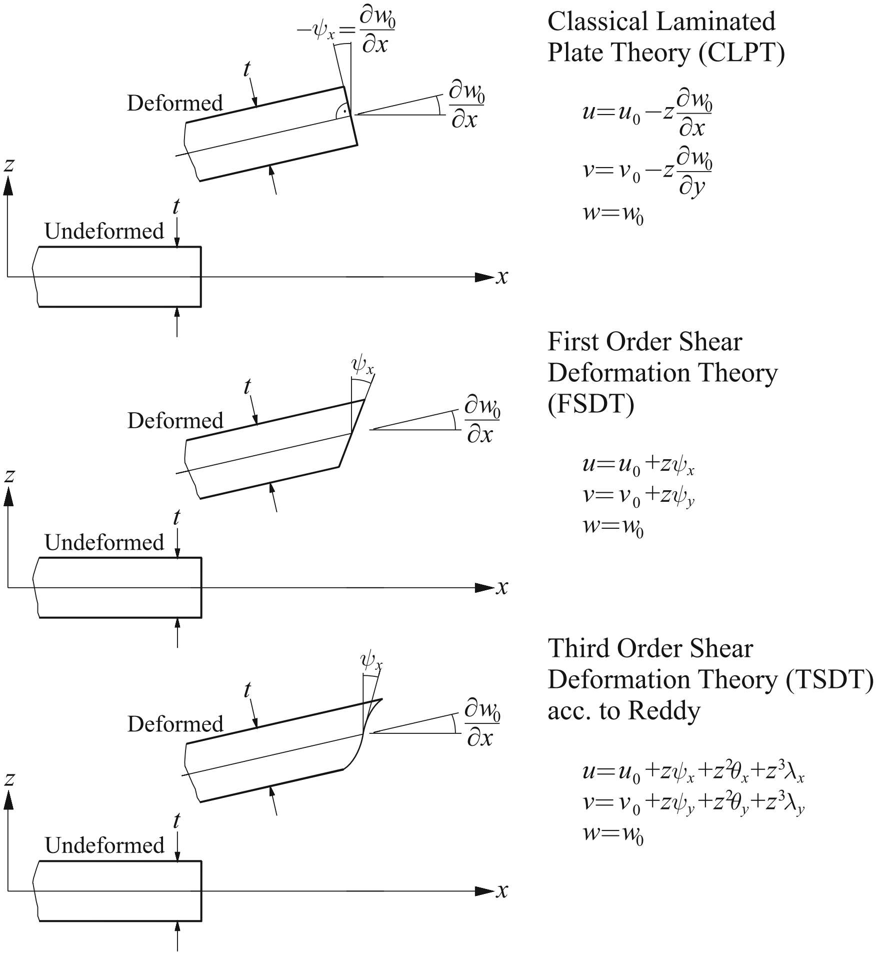
$-\psi_x = \frac{\partial w_0}{\partial x}$
t
Deformed
$\frac{\partial w_0}{\partial x}$
z
t
Undeformed
x
Classical Laminated Plate Theory (CLPT)
$u = u_0 - z\frac{\partial w_0}{\partial x}$
$v = v_0 - z\frac{\partial w_0}{\partial y}$
$w = w_0$
ψ_x
t
Deformed
$\frac{\partial w_0}{\partial x}$
z
t
Undeformed
x
First Order Shear Deformation Theory (FSDT)
$u = u_0 + z\psi_x$
$v = v_0 + z\psi_y$
$w = w_0$
ψ_x
t
Deformed
$\frac{\partial w_0}{\partial x}$
z
t
Undeformed
x
Third Order Shear Deformation Theory (TSDT) acc. to Reddy
$u = u_0 + z\psi_x + z^2\theta_x + z^3\lambda_x$
$v = v_0 + z\psi_y + z^2\theta_y + z^3\lambda_y$
$w = w_0$

Fig. 2 Comparison between CLPT (upper part), FSDT (middle) and TSDT (lower part)

$$\begin{aligned} u(x, y, z) &= u_0(x, y) + z\psi_x(x, y) + z^2\theta_x(x, y) + z^3\lambda_x(x, y), \\ v(x, y, z) &= v_0(x, y) + z\psi_y(x, y) + z^2\theta_y(x, y) + z^3\lambda_y(x, y), \\ w(x, y) &= w_0(x, y). \end{aligned} \tag{1}$$

Therein, the quantities ψ_x, ψ_y, θ_x, θ_y, λ_x, λ_y are a priori unknown functions that characterize the deformation behaviour of the laminate cross-section. Hence, as a starting point there are nine unknown displacement functions that need to be determined. The quantities u_0, v_0, w_0 are the displacements of the laminate middle plane (indicated by the index 0), and ψ_x, ψ_y are the rotation angles of the cross-section on the laminate middle plane at $z = 0$:

$$\psi_x = \left.\frac{\partial u}{\partial z}\right|_{z=0}, \quad \psi_y = \left.\frac{\partial v}{\partial z}\right|_{z=0}. \tag{2}$$

The remaining quantities $\theta_x, \theta_y, \lambda_x, \lambda_y$ can be interpreted as:

$$2\theta_x = \left.\frac{\partial^2 u}{\partial z^2}\right|_{z=0}, \quad 2\theta_y = \left.\frac{\partial^2 v}{\partial z^2}\right|_{z=0}, \quad 6\lambda_x = \left.\frac{\partial^3 u}{\partial z^3}\right|_{z=0}, \quad 6\lambda_y = \left.\frac{\partial^3 v}{\partial z^3}\right|_{z=0}. \tag{3}$$

The requirement that the transverse shear stresses τ_{yz} and τ_{xz} vanish at the free laminate surfaces at $z = -\frac{t}{2}$ and $z = +\frac{t}{2}$ eventually leads to:

$$\begin{aligned}
&\frac{\partial w_0}{\partial y} + \psi_y - t\theta_y + \frac{3t^2}{4}\lambda_y = 0,\\
&\frac{\partial w_0}{\partial y} + \psi_y + t\theta_y + \frac{3t^2}{4}\lambda_y = 0,\\
&\frac{\partial w_0}{\partial x} + \psi_x - t\theta_x + \frac{3t^2}{4}\lambda_x = 0,\\
&\frac{\partial w_0}{\partial x} + \psi_x + t\theta_x + \frac{3t^2}{4}\lambda_x = 0,
\end{aligned} \tag{4}$$

meaning that for $\theta_x, \theta_y, \lambda_x, \lambda_y$ we achieve:

$$\theta_x = 0, \quad \theta_y = 0, \quad \lambda_x = -\frac{4}{3t^2}\left(\psi_x + \frac{\partial w_0}{\partial x}\right), \quad \lambda_y = -\frac{4}{3t^2}\left(\psi_y + \frac{\partial w_0}{\partial y}\right). \tag{5}$$

The displacement field (1) then assumes the following form:

$$\begin{aligned}
u(x, y, z) &= u_0(x, y) + z\psi_x(x, y) - \frac{4z^3}{3t^2}\left(\psi_x(x, y) + \frac{\partial w_0(x, y)}{\partial x}\right),\\
v(x, y, z) &= v_0(x, y) + z\psi_y(x, y) - \frac{4z^3}{3t^2}\left(\psi_y(x, y) + \frac{\partial w_0(x, y)}{\partial y}\right),\\
w(x, y) &= w_0(x, y).
\end{aligned} \tag{6}$$

Like FSDT, TSDT thus uses five degress of freedom, namely the three middle plane displacements u_0, v_0, w_0 and the two rotation angles ψ_x, ψ_y.

The strain field according to TSDT can be written as follows:

$$\begin{aligned}
\varepsilon_{xx} &= \frac{\partial u}{\partial x} = \frac{\partial u_0}{\partial x} + z\frac{\partial \psi_x}{\partial x} - \frac{4z^3}{3t^2}\left(\frac{\partial \psi_x}{\partial x} + \frac{\partial^2 w_0}{\partial x^2}\right),\\
\varepsilon_{yy} &= \frac{\partial v}{\partial y} = \frac{\partial v_0}{\partial y} + z\frac{\partial \psi_y}{\partial y} - \frac{4z^3}{3t^2}\left(\frac{\partial \psi_y}{\partial y} + \frac{\partial^2 w_0}{\partial y^2}\right),
\end{aligned}$$

$$\begin{aligned}
\varepsilon_{zz} &= \frac{\partial w}{\partial z} = 0, \quad \gamma_{yz} = \frac{\partial v}{\partial z} + \frac{\partial w}{\partial y} = \psi_y - \frac{4z^2}{t^2}\left(\psi_y + \frac{\partial w_0}{\partial y}\right) + \frac{\partial w_0}{\partial y},\\
\gamma_{xz} &= \frac{\partial u}{\partial z} + \frac{\partial w}{\partial x} = \psi_x - \frac{4z^2}{t^2}\left(\psi_x + \frac{\partial w_0}{\partial x}\right) + \frac{\partial w_0}{\partial x},\\
\gamma_{xy} &= \frac{\partial u}{\partial y} + \frac{\partial v}{\partial x} = \frac{\partial u_0}{\partial y} + \frac{\partial v_0}{\partial x} + z\left(\frac{\partial \psi_x}{\partial y} + \frac{\partial \psi_y}{\partial x}\right) - \frac{4z^3}{3t^2}\left(\frac{\partial \psi_x}{\partial y} + \frac{\partial \psi_y}{\partial x} + 2\frac{\partial^2 w_0}{\partial x \partial y}\right).
\end{aligned} \tag{7}$$

Using a vector-matrix notation we have:

$$\begin{aligned}
&\underline{\varepsilon}^{(0)} = \begin{pmatrix} \varepsilon_{xx}^{(0)} \\ \varepsilon_{yy}^{(0)} \\ \gamma_{xy}^{(0)} \end{pmatrix} = \begin{pmatrix} \frac{\partial u_0}{\partial x} \\ \frac{\partial v_0}{\partial x} \\ \frac{\partial u_0}{\partial y} + \frac{\partial v_0}{\partial x} \end{pmatrix}, \quad \underline{\varepsilon}^{(1)} = \begin{pmatrix} \varepsilon_{xx}^{(1)} \\ \varepsilon_{yy}^{(1)} \\ \gamma_{xy}^{(1)} \end{pmatrix} = \begin{pmatrix} \frac{\partial \psi_x}{\partial x} \\ \frac{\partial \psi_y}{\partial y} \\ \frac{\partial \psi_x}{\partial y} + \frac{\partial \psi_y}{\partial x} \end{pmatrix},\\
&\underline{\varepsilon}^{(3)} = \begin{pmatrix} \varepsilon_{xx}^{(3)} \\ \varepsilon_{yy}^{(3)} \\ \gamma_{xy}^{(3)} \end{pmatrix} = \begin{pmatrix} -\frac{4}{3t^2}\left(\frac{\partial \psi_x}{\partial x} + \frac{\partial^2 w_0}{\partial x^2}\right) \\ -\frac{4}{3t^2}\left(\frac{\partial \psi_y}{\partial y} + \frac{\partial^2 w_0}{\partial y^2}\right) \\ -\frac{4}{3t^2}\left(\frac{\partial \psi_x}{\partial y} + \frac{\partial \psi_y}{\partial x} + 2\frac{\partial^2 w_0}{\partial x \partial y}\right) \end{pmatrix},\\
&\underline{\gamma}^{(0)} = \begin{pmatrix} \gamma_{yz}^{(0)} \\ \gamma_{xz}^{(0)} \end{pmatrix} = \begin{pmatrix} \psi_y + \frac{\partial w_0}{\partial y} \\ \psi_x + \frac{\partial w_0}{\partial x} \end{pmatrix}, \quad \underline{\gamma}^{(2)} = \begin{pmatrix} \gamma_{yz}^{(2)} \\ \gamma_{xz}^{(2)} \end{pmatrix} = \begin{pmatrix} -\frac{4}{t^2}\left(\psi_y + \frac{\partial w_0}{\partial y}\right) \\ -\frac{4}{t^2}\left(\psi_x + \frac{\partial w_0}{\partial x}\right) \end{pmatrix}.
\end{aligned} \tag{8}$$

Hence:

$$\underline{\varepsilon} = \underline{\varepsilon}^{(0)} + z\underline{\varepsilon}^{(1)} + z^3\underline{\varepsilon}^{(3)}, \quad \underline{\gamma} = \underline{\gamma}^{(0)} + z^2\underline{\gamma}^{(2)}. \tag{9}$$

Here and in all that follows, a superimposed index 0 indicates quantities that are related to the laminate middle plane.

We now introduce the inplane force fluxes N_{xx}^0, N_{yy}^0, N_{xy}^0, the moment fluxes M_{xx}^0, M_{yy}^0, M_{xy}^0 and the transverse shear force fluxes Q_y, Q_x as resultants of the inplane stresses σ_{xx}, σ_{yy}, τ_{xy} and the transverse shear stresses τ_{yz}, τ_{xz} as:

$$\begin{aligned}
\underline{N}^0 &= \begin{pmatrix} N_{xx}^0 \\ N_{yy}^0 \\ N_{xy}^0 \end{pmatrix} = \int_{-\frac{t}{2}}^{+\frac{t}{2}} \begin{pmatrix} \sigma_{xx} \\ \sigma_{yy} \\ \tau_{xy} \end{pmatrix} \mathrm{d}z,\\
\underline{M}^0 &= \begin{pmatrix} M_{xx}^0 \\ M_{yy}^0 \\ M_{xy}^0 \end{pmatrix} = \int_{-\frac{t}{2}}^{+\frac{t}{2}} \begin{pmatrix} \sigma_{xx} \\ \sigma_{yy} \\ \tau_{xy} \end{pmatrix} z\mathrm{d}z,
\end{aligned}$$

$$\underline{Q} = \begin{pmatrix} Q_y \\ Q_x \end{pmatrix} = \int_{-\frac{t}{2}}^{+\frac{t}{2}} \begin{pmatrix} \tau_{yz} \\ \tau_{xz} \end{pmatrix} \mathrm{d}z. \tag{10}$$

TSDT further requires the definition of warping moments as:

$$\underline{P} = \begin{pmatrix} P_{xx} \\ P_{yy} \\ P_{xy} \end{pmatrix} = \int_{-\frac{t}{2}}^{+\frac{t}{2}} \begin{pmatrix} \sigma_{xx} \\ \sigma_{yy} \\ \tau_{xy} \end{pmatrix} z^3 \mathrm{d}z,$$

$$\underline{R} = \begin{pmatrix} R_y \\ R_x \end{pmatrix} = \int_{-\frac{t}{2}}^{+\frac{t}{2}} \begin{pmatrix} \tau_{yz} \\ \tau_{xz} \end{pmatrix} z^2 \mathrm{d}z. \tag{11}$$

At this point Hooke's generalized law for monoclinic laminate layer according to a plane state of stress is employed:

$$\begin{pmatrix} \sigma_{xx} \\ \sigma_{yy} \\ \tau_{xy} \end{pmatrix} = \begin{bmatrix} \bar{Q}_{11} & \bar{Q}_{12} & \bar{Q}_{16} \\ \bar{Q}_{12} & \bar{Q}_{22} & \bar{Q}_{26} \\ \bar{Q}_{16} & \bar{Q}_{26} & \bar{Q}_{66} \end{bmatrix} \begin{pmatrix} \varepsilon_{xx} \\ \varepsilon_{yy} \\ \gamma_{xy} \end{pmatrix}. \tag{12}$$

Therein the quantities $\bar{Q}_{ij}$ $(i, j = 1, 2, 6)$ are the so-called transformed reduced stiffness components of a laminate layer that can be determined from a transformation of the reduced stiffnesses Q_{ij} from the local layer coordinate system x_1, x_2, x_3 into the global system x, y, z:

$$\begin{aligned}
\bar{Q}_{11} &= Q_{11}\cos^4\theta + 2\left(Q_{12} + 2Q_{66}\right)\cos^2\theta\sin^2\theta + Q_{22}\sin^4\theta, \\
\bar{Q}_{22} &= Q_{11}\sin^4\theta + 2\left(Q_{12} + 2Q_{66}\right)\cos^2\theta\sin^2\theta + Q_{22}\cos^4\theta, \\
\bar{Q}_{12} &= \left(Q_{11} + Q_{22} - 4Q_{66}\right)\cos^2\theta\sin^2\theta + Q_{12}\left(\cos^4\theta + \sin^4\theta\right), \\
\bar{Q}_{66} &= \left(Q_{11} + Q_{22} - 2Q_{12} - 2Q_{66}\right)\cos^2\theta\sin^2\theta + Q_{66}\left(\cos^4\theta + \sin^4\theta\right), \\
\bar{Q}_{16} &= \left(Q_{11} - Q_{12} - 2Q_{66}\right)\cos^3\theta\sin\theta + \left(Q_{12} - Q_{22} + 2Q_{66}\right)\cos\theta\sin^3\theta, \\
\bar{Q}_{26} &= \left(Q_{11} - Q_{12} - 2Q_{66}\right)\cos\theta\sin^3\theta + \left(Q_{12} - Q_{22} + 2Q_{66}\right)\cos^3\theta\sin\theta.
\end{aligned} \tag{13}$$

Herein, θ is the orientation angle of an orthotropic laminate layer with respect to the global coordinate system. The reduced stiffnesses can be computed for each laminate layer as:

$$Q_{11} = \frac{E_{11}}{1 - \nu_{12}\nu_{21}}, \quad Q_{22} = \frac{E_{22}}{1 - \nu_{12}\nu_{21}}, \quad Q_{12} = \frac{\nu_{12}E_{22}}{1 - \nu_{12}\nu_{21}}, \quad Q_{66} = G_{12}, \tag{14}$$

wherein E_{11}, E_{22}, G_{12}, ν_{12} and ν_{21} are the elastic properties of the considered orthotropic laminate layer.

Inserting (12) with (7) into (10) and (11) yields the constitutive law for a composite laminate in the framework of TSDT:

$$\begin{pmatrix} N^0_{xx} \\ N^0_{yy} \\ N^0_{xy} \\ M^0_{xx} \\ M^0_{yy} \\ M^0_{xy} \\ P_{xx} \\ P_{yy} \\ P_{xy} \\ Q_y \\ Q_x \\ R_y \\ R_x \end{pmatrix} = \begin{bmatrix} \underline{\underline{A}} & \underline{\underline{B}} & \underline{\underline{E}} & \underline{\underline{0}} & \underline{\underline{0}} \\ \underline{\underline{B}} & \underline{\underline{D}} & \underline{\underline{F}} & \underline{\underline{0}} & \underline{\underline{0}} \\ \underline{\underline{E}} & \underline{\underline{F}} & \underline{\underline{H}} & \underline{\underline{0}} & \underline{\underline{0}} \\ \underline{\underline{0}} & \underline{\underline{0}} & \underline{\underline{0}} & \underline{\underline{A}}_S & \underline{\underline{D}}_S \\ \underline{\underline{0}} & \underline{\underline{0}} & \underline{\underline{0}} & \underline{\underline{D}}_S & \underline{\underline{F}}_S \end{bmatrix} \begin{pmatrix} \frac{\partial u_0}{\partial x} \\ \frac{\partial v_0}{\partial x} \\ \frac{\partial u_0}{\partial y} + \frac{\partial v_0}{\partial x} \\ \frac{\partial \psi_x}{\partial x} \\ \frac{\partial \psi_y}{\partial y} \\ \frac{\partial \psi_x}{\partial y} + \frac{\partial \psi_y}{\partial x} \\ -\frac{4}{3t^2}\left(\frac{\partial \psi_x}{\partial x} + \frac{\partial^2 w_0}{\partial x^2}\right) \\ -\frac{4}{3t^2}\left(\frac{\partial \psi_y}{\partial y} + \frac{\partial^2 w_0}{\partial y^2}\right) \\ -\frac{4}{3t^2}\left(\frac{\partial \psi_x}{\partial y} + \frac{\partial \psi_y}{\partial x} + 2\frac{\partial^2 w_0}{\partial x \partial y}\right) \\ \psi_y + \frac{\partial w_0}{\partial y} \\ \psi_x + \frac{\partial w_0}{\partial x} \\ -\frac{4}{t^2}\left(\psi_y + \frac{\partial w_0}{\partial y}\right) \\ -\frac{4}{t^2}\left(\psi_x + \frac{\partial w_0}{\partial x}\right) \end{pmatrix}. \qquad (15)$$

In symbolic form we have:

$$\begin{pmatrix} \underline{N}^0 \\ \underline{M}^0 \\ \underline{P} \\ \underline{Q} \\ \underline{R} \end{pmatrix} = \begin{bmatrix} \underline{\underline{A}} & \underline{\underline{B}} & \underline{\underline{E}} & \underline{\underline{0}} & \underline{\underline{0}} \\ \underline{\underline{B}} & \underline{\underline{D}} & \underline{\underline{F}} & \underline{\underline{0}} & \underline{\underline{0}} \\ \underline{\underline{E}} & \underline{\underline{F}} & \underline{\underline{H}} & \underline{\underline{0}} & \underline{\underline{0}} \\ \underline{\underline{0}} & \underline{\underline{0}} & \underline{\underline{0}} & \underline{\underline{A}}_S & \underline{\underline{D}}_S \\ \underline{\underline{0}} & \underline{\underline{0}} & \underline{\underline{0}} & \underline{\underline{D}}_S & \underline{\underline{F}}_S \end{bmatrix} \begin{pmatrix} \underline{\varepsilon}^{(0)} \\ \underline{\varepsilon}^{(1)} \\ \underline{\varepsilon}^{(3)} \\ \underline{\gamma}^{(0)} \\ \underline{\gamma}^{(3)} \end{pmatrix}, \qquad (16)$$

with the laminate stiffness matrix as:

$$\begin{bmatrix} \underline{\underline{A}} & \underline{\underline{B}} & \underline{\underline{E}} & \underline{\underline{0}} & \underline{\underline{0}} \\ \underline{\underline{B}} & \underline{\underline{D}} & \underline{\underline{F}} & \underline{\underline{0}} & \underline{\underline{0}} \\ \underline{\underline{E}} & \underline{\underline{F}} & \underline{\underline{H}} & \underline{\underline{0}} & \underline{\underline{0}} \\ \underline{\underline{0}} & \underline{\underline{0}} & \underline{\underline{0}} & \underline{\underline{A}}_S & \underline{\underline{D}}_S \\ \underline{\underline{0}} & \underline{\underline{0}} & \underline{\underline{0}} & \underline{\underline{D}}_S & \underline{\underline{F}}_S \end{bmatrix} = \begin{bmatrix} A_{11} & A_{12} & A_{16} & B_{11} & B_{12} & B_{16} & E_{11} & E_{12} & E_{16} & 0 & 0 & 0 & 0 \\ A_{12} & A_{22} & A_{26} & B_{12} & B_{22} & B_{26} & E_{12} & E_{22} & E_{26} & 0 & 0 & 0 & 0 \\ A_{16} & A_{26} & A_{66} & B_{16} & B_{26} & B_{66} & E_{16} & E_{26} & E_{66} & 0 & 0 & 0 & 0 \\ B_{11} & B_{12} & B_{16} & D_{11} & D_{12} & D_{16} & F_{11} & F_{12} & F_{16} & 0 & 0 & 0 & 0 \\ B_{12} & B_{22} & B_{26} & D_{12} & D_{22} & D_{26} & F_{12} & F_{22} & F_{26} & 0 & 0 & 0 & 0 \\ B_{16} & B_{26} & B_{66} & D_{16} & D_{26} & D_{66} & F_{16} & F_{26} & F_{66} & 0 & 0 & 0 & 0 \\ E_{11} & E_{12} & E_{16} & F_{11} & F_{12} & F_{16} & H_{11} & H_{12} & H_{16} & 0 & 0 & 0 & 0 \\ E_{12} & E_{22} & E_{26} & F_{12} & F_{22} & F_{26} & H_{12} & H_{22} & H_{26} & 0 & 0 & 0 & 0 \\ E_{16} & E_{26} & E_{66} & F_{16} & F_{26} & F_{66} & H_{16} & H_{26} & H_{66} & 0 & 0 & 0 & 0 \\ 0 & 0 & 0 & 0 & 0 & 0 & 0 & 0 & 0 & A_{44} & A_{45} & D_{44} & D_{45} \\ 0 & 0 & 0 & 0 & 0 & 0 & 0 & 0 & 0 & A_{45} & A_{55} & D_{45} & D_{55} \\ 0 & 0 & 0 & 0 & 0 & 0 & 0 & 0 & 0 & D_{44} & D_{45} & F_{44} & F_{45} \\ 0 & 0 & 0 & 0 & 0 & 0 & 0 & 0 & 0 & D_{45} & D_{55} & F_{45} & F_{55} \end{bmatrix}. \qquad (17)$$

The quantities $\underline{\underline{A}}$, $\underline{\underline{B}}$, $\underline{\underline{D}}$ are the well-known matrices including the membrane, coupling and plate stiffness components of a laminate according to CLPT (cf. [1]).

$$A_{ij} = \int_{-\frac{t}{2}}^{\frac{t}{2}} \bar{Q}_{ij} \mathrm{d}z, \quad B_{ij} = \int_{-\frac{t}{2}}^{\frac{t}{2}} \bar{Q}_{ij} z \mathrm{d}z, \quad D_{ij} = \int_{-\frac{t}{2}}^{\frac{t}{2}} \bar{Q}_{ij} z^2 \mathrm{d}z. \tag{18}$$

Further, in (17) we also find the matrix of the transverse shear stiffness components $\underline{\underline{A}}_S$ that arises when dealing with a laminate analysis according to FSDT. Its components read:

$$A_{44} = \int_{-\frac{t}{2}}^{+\frac{t}{2}} \bar{C}_{44} \mathrm{d}z, \quad A_{55} = \int_{-\frac{t}{2}}^{+\frac{t}{2}} \bar{C}_{55} \mathrm{d}z, \quad A_{45} = \int_{-\frac{t}{2}}^{+\frac{t}{2}} \bar{C}_{45} \mathrm{d}z, \tag{19}$$

with the stiffness parameters according to Hooke's generalized law for a three-dimensional monoclinic continuum (see [1]). Note that the shear correction factor K that is typically (and oftentimes in a somewhat random fashion) used at this stage in the framework of FSDT is not required when TSDT is employed.

In (17) we also find the additional submatrices $\underline{\underline{E}}$, $\underline{\underline{F}}$, $\underline{\underline{H}}$, $\underline{\underline{D}}_S$ and $\underline{\underline{F}}_S$ that are unique features of TSDT and which can be interpreted as transverse shear stiffnesses. The additional force vectors $\underline{P}$ and $\underline{R}$ can be interpreted as warping moments. In detail, we have for the additional quantities in the framework of TSDT:

$$\begin{aligned}
\underline{\underline{E}} &= \begin{bmatrix} E_{11} & E_{12} & E_{16} \\ E_{12} & E_{22} & E_{26} \\ E_{16} & E_{26} & E_{66} \end{bmatrix} = \int_{-\frac{t}{2}}^{\frac{t}{2}} \begin{bmatrix} \bar{Q}_{11} & \bar{Q}_{12} & \bar{Q}_{16} \\ \bar{Q}_{12} & \bar{Q}_{22} & \bar{Q}_{26} \\ \bar{Q}_{16} & \bar{Q}_{26} & \bar{Q}_{66} \end{bmatrix} z^3 \mathrm{d}z, \\
\underline{\underline{F}} &= \begin{bmatrix} F_{11} & F_{12} & F_{16} \\ F_{12} & F_{22} & F_{26} \\ F_{16} & F_{26} & F_{66} \end{bmatrix} = \int_{-\frac{t}{2}}^{\frac{t}{2}} \begin{bmatrix} \bar{Q}_{11} & \bar{Q}_{12} & \bar{Q}_{16} \\ \bar{Q}_{12} & \bar{Q}_{22} & \bar{Q}_{26} \\ \bar{Q}_{16} & \bar{Q}_{26} & \bar{Q}_{66} \end{bmatrix} z^4 \mathrm{d}z, \\
\underline{\underline{H}} &= \begin{bmatrix} H_{11} & H_{12} & H_{16} \\ H_{12} & H_{22} & H_{26} \\ H_{16} & H_{26} & H_{66} \end{bmatrix} = \int_{-\frac{t}{2}}^{\frac{t}{2}} \begin{bmatrix} \bar{Q}_{11} & \bar{Q}_{12} & \bar{Q}_{16} \\ \bar{Q}_{12} & \bar{Q}_{22} & \bar{Q}_{26} \\ \bar{Q}_{16} & \bar{Q}_{26} & \bar{Q}_{66} \end{bmatrix} z^6 \mathrm{d}z,
\end{aligned} \tag{20}$$

and

$$\begin{aligned}
\underline{\underline{D}}_S &= \begin{bmatrix} D_{44} & D_{45} \\ D_{45} & D_{55} \end{bmatrix} = \int_{-\frac{t}{2}}^{\frac{t}{2}} \begin{bmatrix} \bar{C}_{44} & \bar{C}_{45} \\ \bar{C}_{45} & \bar{C}_{55} \end{bmatrix} z^2 \mathrm{d}z, \\
\underline{\underline{F}}_S &= \begin{bmatrix} F_{44} & F_{45} \\ F_{45} & F_{55} \end{bmatrix} = \int_{-\frac{t}{2}}^{\frac{t}{2}} \begin{bmatrix} \bar{C}_{44} & \bar{C}_{45} \\ \bar{C}_{45} & \bar{C}_{55} \end{bmatrix} z^4 \mathrm{d}z.
\end{aligned} \tag{21}$$

Note that these quantities contain z of higher powers so that it can be concluded that these quantities will start influencing the buckling results in such cases where the thickness of the considered laminate cannot be classified strictly as thin anymore. We will study this in detail later on.

3 Structural Situation and Energy Formulation for Buckling Analysis

We consider the local buckling of composite laminated beams under uniaxial compression using the discrete plate approach (cf. Fig. 1). Hence, we treat the two separate buckling problems as depicted in Fig. 3. In both cases we consider a composite laminated plate with the global coordinate system x, y, z, length a and width $b = h$ (web buckling) respectively $b = b_\mathrm{F}$ (flange buckling) as indicated. In order to develop a generally applicable analysis method we will refer to the width of the web and flange plates as b, keeping in mind that b needs to be substituted with h or b_F as required. Both situations consider a constant uniaxial load N_{xx}^0 that acts in the laminate middle plane. In the case of local web buckling, all four edges are simply supported, while in addition the longitudinal edges at $y = 0$ and $y = b$ are elastically clamped (restraint stiffness k). The analysis approach for local flange buckling considers the same structural situation with the exception of the longitudinal edge at $y = b$ which is supposed to be free of any support or restraints.

The total elastic potential Π of the buckled laminate consist of the inner potential Π_i (i.e. the strain energy), the outer potential Π_a and the energy stored in the elastic restraints at the longitudinal edges (see Fig. 1):

$$\Pi = \Pi_i + \Pi_a + \Pi_s. \tag{22}$$

Consistent with the assumptions of TSDT we have for Π_i:

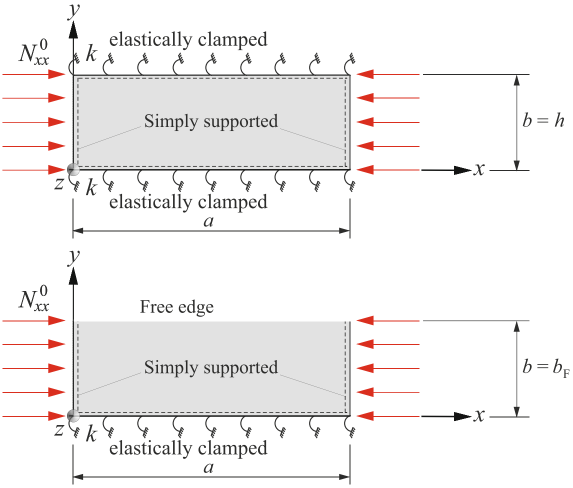

Fig. 3 Local web buckling (upper part) and flange buckling (lower part) using the discrete plate approach

$$\begin{aligned}\Pi_i &= \frac{1}{2}\int_V \sigma_{ij}\varepsilon_{ij}\mathrm{d}V \\ &= \frac{1}{2}\int_V (\sigma_{xx}\varepsilon_{xx} + \sigma_{yy}\varepsilon_{yy} + \tau_{xy}\gamma_{xy} + \tau_{xz}\gamma_{xz} + \tau_{yz}\gamma_{yz})\mathrm{d}V. \end{aligned} \tag{23}$$

Inserting the strain field (7) according to TSDT we get:

$$\begin{aligned}\Pi_i = \frac{1}{2}\int_{-\frac{t}{2}}^{\frac{t}{2}}\int_0^b\int_0^a \Bigg\{ & \sigma_{xx}\left[\frac{\partial u_0}{\partial x} + z\frac{\partial \psi_x}{\partial x} - \frac{4z^3}{3t^2}\left(\frac{\partial \psi_x}{\partial x} + \frac{\partial^2 w_0}{\partial x^2}\right)\right] \\ & + \sigma_{xx}\left[\frac{\partial u_0}{\partial x} + z\frac{\partial \psi_x}{\partial x} - \frac{4z^3}{3t^2}\left(\frac{\partial \psi_x}{\partial x} + \frac{\partial^2 w_0}{\partial x^2}\right)\right] \\ & + \tau_{xy}\left[\frac{\partial u_0}{\partial y} + \frac{\partial v_0}{\partial x} + z\left(\frac{\partial \psi_x}{\partial y} - \frac{\partial \psi_y}{\partial x}\right) - \frac{4z^3}{3t^2}\left(\frac{\partial \psi_x}{\partial y} - \frac{\partial \psi_y}{\partial x} + 2\frac{\partial^2 w_0}{\partial x \partial y}\right)\right] \\ & + \tau_{xz}\left[\psi_x - \frac{4z^2}{3t^2}\left(\psi_x + \frac{\partial w_0}{\partial x}\right) + \frac{\partial w_0}{\partial x}\right] \\ & + \tau_{yz}\left[\psi_y - \frac{4z^2}{3t^2}\left(\psi_y + \frac{\partial w_0}{\partial y}\right) + \frac{\partial w_0}{\partial y}\right]\Bigg\}\mathrm{d}x\mathrm{d}y\mathrm{d}z. \end{aligned} \tag{24}$$

Performing the integration with respect to the thickness coordinate z leads to:

$$\begin{aligned}\Pi_i = \frac{1}{2}\int_0^b\int_0^a \Bigg[& N_{xx}^0\frac{\partial u_0}{\partial x} + N_{yy}^0\frac{\partial v_0}{\partial y} + N_{xy}^0\left(\frac{\partial u_0}{\partial y} + \frac{\partial v_0}{\partial x}\right) + M_{xx}^0\frac{\partial \psi_x}{\partial x} + M_{yy}^0\frac{\partial \psi_y}{\partial y} \\ & + M_{xy}^0\left(\frac{\partial \psi_x}{\partial y} + \frac{\partial \psi_y}{\partial x}\right) - \frac{4}{3t^2}P_{xx}^0\left(\frac{\partial \psi_x}{\partial x} + \frac{\partial^2 w_0}{\partial x^2}\right) - \frac{4}{3t^2}P_{yy}^0\left(\frac{\partial \psi_y}{\partial y} + \frac{\partial^2 w_0}{\partial y^2}\right) \\ & - \frac{4}{3t^2}P_{xy}^0\left(\frac{\partial \psi_x}{\partial y} + \frac{\partial \psi_y}{\partial x} + 2\frac{\partial^2 w_0}{\partial x \partial y}\right) + Q_y\left(\psi_y + \frac{\partial w_0}{\partial y}\right) + Q_x\left(\psi_x + \frac{\partial w_0}{\partial x}\right) \\ & - \frac{4}{t^2}R_y\left(\psi_y + \frac{\partial w_0}{\partial y}\right) - \frac{4}{t^2}R_x\left(\psi_x + \frac{\partial w_0}{\partial x}\right)\Bigg]\mathrm{d}x\mathrm{d}y. \end{aligned} \tag{25}$$

We now consider the constitutive law (15) with (17). Considering that in this work we investigate symmetric and orthotropic laminates exclusively we have $B_{ij} = 0$ and $E_{ij} = 0$ and also $\bar{C}_{45} = 0$. Furthermore, for such laminates we have:

$$\begin{aligned} & A_{16} = A_{26} = B_{ij} = D_{16} = D_{26} = E_{ij} = F_{16} \\ & = F_{26} = H_{16} = H_{26} = A_{45} = D_{45} = F_{45} = 0. \end{aligned} \tag{26}$$

Further taking into account that for symmetric laminates no displacements u_0 and v_0 occur when the laminate buckles, we finally achieve the following representation for the inner potential Π_i:

$$
\begin{aligned}
\Pi_i = \frac{1}{2}\int_0^b\int_0^a \Bigg[& D_{11}\left(\frac{\partial\psi_x}{\partial x}\right)^2 + 2D_{12}\frac{\partial\psi_x}{\partial x}\frac{\partial\psi_y}{\partial y} + D_{22}\left(\frac{\partial\psi_y}{\partial y}\right)^2 + D_{66}\left(\frac{\partial\psi_x}{\partial y}\right)^2 \\
& + 2D_{66}\frac{\partial\psi_x}{\partial y}\frac{\partial\psi_y}{\partial x} + D_{66}\left(\frac{\partial\psi_y}{\partial x}\right)^2 - \frac{8}{3t^2}F_{11}\left(\frac{\partial\psi_x}{\partial x}\right)^2 \\
& - \frac{8}{3t^2}F_{11}\frac{\partial^2 w_0}{\partial x^2}\frac{\partial\psi_x}{\partial x} - \frac{16}{3t^2}F_{12}\frac{\partial\psi_x}{\partial x}\frac{\partial\psi_y}{\partial y} - \frac{8}{3t^2}F_{12}\frac{\partial^2 w_0}{\partial y^2}\frac{\partial\psi_x}{\partial x} \\
& - \frac{8}{3t^2}F_{12}\frac{\partial^2 w_0}{\partial x^2}\frac{\partial\psi_y}{\partial y} - \frac{8}{3t^2}F_{22}\left(\frac{\partial\psi_y}{\partial y}\right)^2 - \frac{8}{3t^2}F_{22}\frac{\partial^2 w_0}{\partial y^2}\frac{\partial\psi_y}{\partial y} \\
& - \frac{8}{3t^2}F_{66}\left(\frac{\partial\psi_x}{\partial y}\right)^2 - \frac{16}{3t^2}F_{66}\frac{\partial\psi_x}{\partial y}\frac{\partial\psi_y}{\partial x} - \frac{8}{3t^2}F_{66}\left(\frac{\partial\psi_y}{\partial x}\right)^2 \\
& - \frac{16}{3t^2}F_{66}\frac{\partial^2 w_0}{\partial x\partial y}\frac{\partial\psi_x}{\partial y} - \frac{16}{3t^2}F_{66}\frac{\partial^2 w_0}{\partial x\partial y}\frac{\partial\psi_y}{\partial x} + \frac{16}{9t^4}H_{11}\left(\frac{\partial\psi_x}{\partial x}\right)^2 \\
& + \frac{32}{9t^4}H_{11}\frac{\partial^2 w_0}{\partial x^2}\frac{\partial\psi_x}{\partial x} + \frac{16}{3t^2}H_{11}\left(\frac{\partial^2 w_0}{\partial x^2}\right)^2 + \frac{32}{9t^4}H_{12}\frac{\partial\psi_x}{\partial x}\frac{\partial\psi_y}{\partial y} \\
& + \frac{32}{9t^4}H_{12}\frac{\partial^2 w_0}{\partial y^2}\frac{\partial\psi_x}{\partial x} + \frac{32}{9t^4}H_{12}\frac{\partial^2 w_0}{\partial x^2}\frac{\partial\psi_y}{\partial y} + \frac{32}{9t^4}H_{12}\frac{\partial^2 w_0}{\partial x^2}\frac{\partial^2 w_0}{\partial y^2} \\
& + \frac{16}{9t^4}H_{22}\left(\frac{\partial\psi_y}{\partial y}\right)^2 + \frac{32}{9t^4}H_{22}\frac{\partial^2 w_0}{\partial y^2}\frac{\partial\psi_y}{\partial y} + \frac{16}{9t^4}H_{22}\left(\frac{\partial^2 w_0}{\partial y^2}\right)^2 \\
& + \frac{16}{9t^4}H_{66}\left(\frac{\partial\psi_x}{\partial y}\right)^2 + \frac{32}{9t^4}H_{66}\frac{\partial\psi_x}{\partial y}\frac{\partial\psi_y}{\partial x} + \frac{64}{9t^4}H_{66}\frac{\partial^2 w_0}{\partial x\partial y}\frac{\partial\psi_x}{\partial y} \\
& + \frac{16}{9t^4}H_{66}\left(\frac{\partial\psi_y}{\partial x}\right)^2 + \frac{64}{9t^4}H_{66}\frac{\partial^2 w_0}{\partial x\partial y}\frac{\partial\psi_y}{\partial x} + \frac{64}{9t^4}H_{66}\left(\frac{\partial^2 w_0}{\partial x\partial y}\right)^2 \\
& + A_{44}\psi_y^2 + 2A_{44}\frac{\partial w_0}{\partial y}\psi_y + A_{44}\left(\frac{\partial w_0}{\partial y}\right)^2 + A_{55}\psi_x^2 + 2A_{55}\frac{\partial w_0}{\partial x}\psi_x \\
& + A_{55}\left(\frac{\partial w_0}{\partial x}\right)^2 - \frac{8}{t^2}D_{44}\psi_y^2 - \frac{16}{t^2}D_{44}\frac{\partial w_0}{\partial y}\psi_y - \frac{8}{t^2}D_{44}\left(\frac{\partial w_0}{\partial y}\right)^2 \\
& - \frac{8}{t^2}D_{55}\psi_x^2 - \frac{16}{t^2}D_{55}\frac{\partial w_0}{\partial x}\psi_x - \frac{8}{t^2}D_{55}\left(\frac{\partial w_0}{\partial x}\right)^2 + \frac{16}{t^4}F_{44}\psi_y^2 \\
& + \frac{32}{t^4}F_{44}\frac{\partial w_0}{\partial y}\psi_y + \frac{16}{t^4}F_{44}\left(\frac{\partial w_0}{\partial y}\right)^2 + \frac{16}{t^4}F_{55}\psi_x^2 + \frac{32}{t^4}F_{55}\frac{\partial w_0}{\partial x}\psi_x \\
& + \frac{16}{t^4}F_{55}\left(\frac{\partial w_0}{\partial x}\right)^2 \Bigg]\mathrm{d}x\mathrm{d}y.
\end{aligned}
\tag{27}
$$

For the outer potential we have (see e.g. [31]):

$$
\Pi_a = -\frac{1}{2}N_{xx}^0\int_0^b\int_0^a\left(\frac{\partial w_0}{\partial x}\right)^2\mathrm{d}x\mathrm{d}y. \tag{28}
$$

The energy that is stored within the elastic restraints (restraint stiffness k) at the longitudinal edges amount to

$$\Pi_s = \frac{1}{2}k\int_0^a [\psi_y^2(y=0) + \psi_y^2(y=b)]\mathrm{d}x \tag{29}$$

in the case of local web buckling, and

$$\Pi_s = \frac{1}{2}k\int_0^a [\psi_y^2(y=0)]\mathrm{d}x \tag{30}$$

when local flange buckling is considered.

4 Governing Equations and Boundary Conditions

We now derive the underlying differential equations and boundary conditions that constitute the current local buckling problems. The geometric boundary conditions impose requirements on the displacement quantities u_0, v_0, w_0, ψ_x, ψ_y while the dynamic boundary conditions state requirements for the force quantities N^0_{xx}, N^0_{yy}, N^0_{xy}, M^0_{xx}, M^0_{yy}, M^0_{xy}, P_{xx}, P_{yy}, P_{xy}, Q_y, Q_x, R_y, R_x. We can derive the desired equations from the principle of minimum total elastic potential of the buckled plate, i.e. the requirement of a vanishing first variation $\delta\Pi$ of Π:

$$\delta\Pi = \delta\Pi_i + \delta\Pi_a + \delta\Pi_s = 0. \tag{31}$$

Performing the variation as indicated in (31), integrating by parts and collecting terms of the same order we arrive at the following expression:

$$\begin{aligned}
&-\frac{1}{2}\int_0^b\int_0^a \Bigg\{(N^0_{xx,x} + N^0_{xy,y})\delta u_0 + (N^0_{yy,y} + N^0_{xy,x})\delta v_0 + \bigg(\frac{4}{3t^2}P_{xx,xx} + \frac{4}{3t^2}P_{yy,yy}\\
&+\ \frac{4}{3t^2}P_{xy,xy} + Q_{y,y} + Q_{x,x} - \frac{4}{t^2}R_{y,y} - \frac{4}{t^2}R_{x,x} - 2N^0_{xx}w_{0,xx}\bigg)\delta w_0\\
&+\bigg(M^0_{xx,x} + M^0_{xy,y} - \frac{4}{3t^2}P_{xx,x} - \frac{4}{3t^2}P_{xy,y} - Q_x + R_x\bigg)\delta\psi_x + \bigg(M^0_{yy,y}\\
&+\ M^0_{xy,x} - \frac{4}{3t^2}P_{yy,y} - \frac{4}{3t^2}P_{xy,x} - Q_y + R_y\bigg)\delta\psi_y\Bigg\}\,\mathrm{d}x\mathrm{d}y\\
&+\frac{1}{2}\int_0^a \Bigg\{\bigg[N^0_{xy}\delta u_0 + N^0_{yy}\delta v_0 + \bigg(\frac{4}{3t^2}P_{yy,y} + \frac{8}{3t^2}P_{xy,x} + Q_y - \frac{4}{t^2}R_y\bigg)\delta w_0\\
&+\ \bigg(M^0_{xy} - \frac{4}{3t^2}P_{xy}\bigg)\delta\psi_x + \bigg(M^0_{yy} - \frac{4}{3t^2}P_{yy}\bigg)\delta\psi_y - \frac{4}{3t^2}P_{yy}\delta w_{0,y}\bigg]\bigg|_0^b\\
&+\ k\psi_y(y=0)\delta\psi_y(y=0) + k\psi_y(y=b)\delta\psi_y(y=b)\Bigg\}\,\mathrm{d}x
\end{aligned}$$

$$+\frac{1}{2}\int_0^b\left\{\left[N_{xx}^0\delta u_0+N_{xy}^0\delta v_0+\left(\frac{4}{3t^2}P_{xx,x}+\frac{8}{3t^2}P_{xy,y}+Q_x-\frac{4}{t^2}R_x\right.\right.\right.$$
$$\left.-\ 2N_{xx}^0w_{0,x}\right)\delta w_0+\left(M_{xx}^0-\frac{4}{3t^2}P_{xx}\right)\delta\psi_x+\left(M_{xy}^0-\frac{4}{3t^2}P_{xy}\right)\delta\psi_y$$
$$\left.\left.-\ \frac{4}{3t^2}P_{xx}\delta w_{o,x}\right]\Bigg|_0^a\right\}\mathrm{d}y-\frac{1}{2}\left(\frac{8}{3t^2}P_{xy}\delta w_0\right)\Bigg|_0^a\Bigg|_0^b=0. \tag{32}$$

Since the variations that appear within (32) are independent and arbitrary we can solve this equation only if we take the variations of the displacement quantities to be vanishing independently, i.e. by requiring that either $\delta u_o=0$, $\delta v_0=0$, $\delta w_0=0$, $\delta w_{o,x}=0$, $\delta w_{0,y}=0$, $\delta\psi_x=0$, $\delta\psi_y=0$ or the associated terms become zero. Since in this contribution we do not make use of the governing differential equations but will use an energetic approach later on, we will not discuss the buckling differential equations at this point but focus on the underlying boundary conditions instead. In the case of local web buckling ($b=h$), we have:

$$\begin{aligned}
&w_0(x=0)=0,\quad w_0(x=a)=0,\quad w_0(y=0)=0,\quad w_0(y=b)=0,\\
&\psi_x(y=0)=0,\quad \psi_x(y=b)=0,\quad \psi_y(x=0)=0,\quad \psi_y(x=a)=0,\\
&P_{xx}(x=0)=0,\quad P_{xx}(x=a)=0,\quad P_{yy}(y=0)=0,\quad P_{yy}(y=b)=0,\\
&\left(M_{xx}^0-\frac{4}{3t^2}P_{xx}\right)(x=0)=0,\quad \left(M_{xx}^0-\frac{4}{3t^2}P_{xx}\right)(x=a)=0,\\
&\left(M_{yy}^0-\frac{4}{3t^2}P_{yy}\right)(y=0)=k\psi_y(y=0),\\
&\left(M_{yy}^0-\frac{4}{3t^2}P_{yy}\right)(y=b)=-k\psi_y(y=b).
\end{aligned} \tag{33}$$

For local flange buckling ($b=b_{\mathrm{F}}$) where a free edge exists at $y=b$ and only the longitudinal edge at $y=0$ is elastically clamped, we achieve:

$$\begin{aligned}
&w_0(x=0)=0,\quad w_0(x=a)=a,\quad w_0(y=0)=0,\\
&\psi_x(y=0)=0,\quad \psi_y(x=0)=0,\quad \psi_y(x=a)=0,\\
&P_{xx}(x=0)=0,\quad P_{xx}(x=a)=0,\quad P_{yy}(y=0)=0,\qquad P_{yy}(y=b)=0,\\
&\left(\frac{4}{3t^2}P_{yy,y}+\frac{8}{3t^2}P_{xy,x}+Q_y-\frac{4}{t^2}R_y\right)(y=b)=0,\\
&\left(M_{xy}^0-\frac{4}{3t^2}P_{xy}\right)(y=b)=0,\\
&\left(M_{xx}^0-\frac{4}{3t^2}P_{xx}\right)(x=0)=0,\quad \left(M_{xx}^0-\frac{4}{3t^2}P_{xx}\right)(x=a)=0,\\
&\left(M_{yy}^0-\frac{4}{3t^2}P_{yy}\right)(y=0)=k\psi_y(y=0),\qquad \left(M_{yy}^0-\frac{4}{3t^2}P_{yy}\right)(y=b)=0.
\end{aligned} \tag{34}$$

It is interesting to note that the geometric boundary conditions that arise by the use of TSDT are identical to those that need to be considered when dealing with analysis approaches within the framework of FSDT (see Kühn et al. [31] where similar buckling problems are treated).

5 Closed-Form Approximate Solution

For the approximate analysis of the buckling loads N^0_{xx} for the local buckling problems outlined in Fig. 3 we use rather simple shape functions for the buckling modes, characterized by w_0, ψ_x and ψ_y. A general formulation would be:

$$w_0 = W w_1(x) w_2(y), \qquad \psi_x = X\psi_{x1}(x)\psi_{x2}(y), \qquad \psi_y = Y\psi_{y1}(x)\psi_{y2}(y), \quad (35)$$

with the constants W, X, Y and the shape functions $w_1(x)$, $w_2(y)$, $\psi_{x1}(x)$, $\psi_{x2}(y)$, $\psi_{y1}(x)$, $\psi_{y2}(y)$ that will be defined in detail later on. The shape functions are required to fulfill the geometric boundary conditions outlined in (33) and (34). Inserting the formulations (35) into the energy formulations (27)–(29) (respectively (30) when flange buckling is considered) and introducing the abbreviations

$$\begin{aligned}
I_1 &= \int_0^a \left(\frac{\mathrm{d}\psi_{x1}}{\mathrm{d}x}\right)^2 \mathrm{d}x, \qquad I_2 = \int_0^a \frac{\mathrm{d}\psi_{x1}}{\mathrm{d}x}\psi_{y1}\mathrm{d}x, \qquad I_3 = \int_0^a \psi_{y1}^2\mathrm{d}x,\\
I_4 &= \int_0^a \psi_{x1}^2\mathrm{d}x, \qquad I_5 = \int_0^a \psi_{x1}\frac{\mathrm{d}\psi_{y1}}{\mathrm{d}x}\mathrm{d}x, \qquad I_6 = \int_0^a \left(\frac{\mathrm{d}\psi_{y1}}{\mathrm{d}x}\right)^2 \mathrm{d}x,\\
I_7 &= \int_0^a \frac{\mathrm{d}^2 w_1}{\mathrm{d}x^2}\frac{\mathrm{d}\psi_{x1}}{\mathrm{d}x}\mathrm{d}x, \qquad I_8 = \int_0^a w_1\frac{\mathrm{d}\psi_{x1}}{\mathrm{d}x}\mathrm{d}x, \qquad I_9 = \int_0^a \frac{\mathrm{d}^2 w_1}{\mathrm{d}x^2}\psi_{y1}\mathrm{d}x,\\
I_{10} &= \int_0^a w_1\psi_{y1}\mathrm{d}x, \qquad I_{11} = \int_0^a \frac{\mathrm{d}w_1}{\mathrm{d}x}\psi_{x1}\mathrm{d}x, \qquad I_{12} = \int_0^a \frac{\mathrm{d}w_1}{\mathrm{d}x}\frac{\mathrm{d}\psi_{y1}}{\mathrm{d}x}\mathrm{d}x,\\
I_{13} &= \int_0^a \left(\frac{\mathrm{d}^2 w_1}{\mathrm{d}x^2}\right)^2 \mathrm{d}x, \qquad I_{14} = \int_0^a \frac{\mathrm{d}^2 w_1}{\mathrm{d}x^2}w_1\mathrm{d}x, \qquad I_{15} = \int_0^a w_1^2\mathrm{d}x,\\
I_{16} &= \int_0^a \left(\frac{\mathrm{d}w1}{\mathrm{d}x}\right)^2 \mathrm{d}x,\\
J_1 &= \int_0^b \psi_{x2}^2\mathrm{d}y, \qquad J_2 = \int_0^b \psi_{x2}\frac{\mathrm{d}\psi_{y2}}{\mathrm{d}y}\mathrm{d}y, \qquad J_3 = \int_0^b \left(\frac{\mathrm{d}\psi_{y2}}{\mathrm{d}y}\right)^2 \mathrm{d}y,\\
J_4 &= \int_0^b \left(\frac{\mathrm{d}\psi_{x2}}{\mathrm{d}y}\right)^2 \mathrm{d}y, \qquad J_5 = \int_0^b \frac{\mathrm{d}\psi_{x2}}{\mathrm{d}y}\psi_{y2}\mathrm{d}y, \qquad J_6 = \int_0^b \psi_{y2}^2\mathrm{d}y,\\
J_7 &= \int_0^b w_2\psi_{x2}\mathrm{d}y, \qquad J_8 = \int_0^b \frac{\mathrm{d}^2 w_2}{\mathrm{d}y^2}\psi_{x2}\mathrm{d}y, \qquad J_9 = \int_0^b w_2\frac{\mathrm{d}\psi_{y2}}{\mathrm{d}y}\mathrm{d}y,\\
J_{10} &= \int_0^b \frac{\mathrm{d}^2 w_2}{\mathrm{d}y^2}\frac{\mathrm{d}\psi_{y2}}{\mathrm{d}y}\mathrm{d}y, \qquad J_{11} = \int_0^b \frac{\mathrm{d}w_2}{\mathrm{d}y}\frac{\mathrm{d}\psi_{x2}}{\mathrm{d}y}\mathrm{d}y,
\end{aligned}$$

$$
\begin{aligned}
&J_{12}=\int_0^b \frac{\mathrm{d}w_2}{\mathrm{d}y}\psi_{y2}\mathrm{d}y,\\
&J_{13}=\int_0^b w_2^2\mathrm{d}y,\qquad J_{14}=\int_0^b w_2\frac{\mathrm{d}^2w_2}{\mathrm{d}y^2}\mathrm{d}y,\qquad J_{15}=\int_0^b\left(\frac{\mathrm{d}^2w_2}{\mathrm{d}y^2}\right)^2\mathrm{d}y,\\
&J_{16}=\int_0^b\left(\frac{\mathrm{d}w_2}{\mathrm{d}y}\right)^2,\qquad C_{1rot}=\psi_{y2}^2(y=0),\qquad C_{2rot}=\psi_{y2}^2(y=b)
\end{aligned}
\tag{36}
$$

while taking $C_{2rot}=0$ when flange buckling is considered, we eventually arrive at the following formulation for the total elastic potential Π:

$$
\begin{aligned}
\Pi=\ &\frac{1}{2}D_{11}X^2I_1J_1+D_{12}XYI_2J_2+\frac{1}{2}D_{22}Y^2I_3J_3+\frac{1}{2}D_{66}X^2I_4J_4+D_{66}XYI_5J_5\\
&+\frac{1}{2}D_{66}Y^2I_6J_6-\frac{4}{3t^2}F_{11}X^2I_1J_1-\frac{4}{3t^2}F_{11}WXI_7J_7-\frac{8}{3t^2}F_{12}XYI_2J_2\\
&-\frac{4}{3t^2}F_{12}WXI_8J_8-\frac{4}{3t^2}F_{12}WYI_9J_9-\frac{4}{3t^2}F_{22}Y^2I_3J_3-\frac{4}{3t^2}F_{22}WYI_{10}J_{10}\\
&-\frac{4}{3t^2}F_{66}X^2I_4J_4-\frac{8}{3t^2}F_{66}XYI_5J_5-\frac{4}{3t^2}F_{66}Y^2I_6J_6-\frac{8}{3t^2}F_{66}WXI_{11}J_{11}\\
&-\frac{8}{3t^2}F_{66}WYI_{12}J_{12}+\frac{8}{9t^4}H_{11}X^2I_1J_1+\frac{16}{9t^4}H_{11}WXI_7J_7+\frac{8}{9t^4}H_{11}W^2I_{13}J_{13}\\
&+\frac{16}{9t^4}H_{12}XYI_2J_2+\frac{16}{9t^4}H_{12}WXI_8J_8+\frac{16}{9t^4}H_{12}WYI_9J_9\\
&+\frac{16}{9t^4}H_{12}W^2I_{14}J_{14}+\frac{8}{9t^4}H_{22}Y^2I_3J_3+\frac{16}{9t^4}H_{22}WYI_{10}J_{10}+\frac{8}{9t^4}H_{22}W^2I_{15}J_{15}\\
&+\frac{8}{9t^4}H_{66}X^2I_4J_4+\frac{16}{9t^4}H_{66}XYI_5J_5+\frac{32}{9t^4}H_{66}WXI_{11}J_{11}\\
&+\frac{8}{9t^4}H_{66}Y^2I_6J_6+\frac{32}{9t^4}H_{66}WYI_{12}J_{12}+\frac{32}{9t^4}H_{66}W^2I_{16}J_{16}+\frac{1}{2}A_{44}Y^2I_3J_6\\
&+A_{44}WYI_{10}J_{12}+\frac{1}{2}A_{44}W^2I_{15}J_{16}+\frac{1}{2}A_{55}X^2I_4J_1+A_{55}WXI_{11}J_7\\
&+\frac{1}{2}A_{55}W^2I_{16}J_{13}-\frac{4}{t^2}D_{44}Y^2I_3J_6-\frac{8}{t^2}D_{44}WYI_{10}J_{12}-\frac{4}{t^2}D_{44}W^2I_{15}J_{16}\\
&-\frac{4}{t^2}D_{55}X^2I_4J_1-\frac{8}{t^2}D_{55}WXI_{11}J_7-\frac{4}{t^2}D_{55}W^2I_{16}J_{13}+\frac{8}{t^4}F_{44}Y^2I_3J_6\\
&+\frac{16}{t^4}F_{44}WYI_{10}J_{12}+\frac{8}{t^4}F_{44}W^2I_{15}J_{16}+\frac{8}{t^4}F_{55}X^2I_4J_1+\frac{16}{t^4}F_{55}WXI_{11}J_7\\
&+\frac{8}{t^4}F_{55}W^2I_{16}J_{13}-\frac{1}{2}N_{xx}^0W^2I_{16}J_{13}+\frac{1}{2}kY^2I_3(C_{1rot}+C_{2rot}).
\end{aligned}
\tag{37}
$$

Equilibrium is established when the first variation $\delta\Pi$ vanishes which, given the shape functions (35), reduces to the Ritz equations as follows:

$$\frac{\partial \Pi}{\partial W} = 0, \quad \frac{\partial \Pi}{\partial X} = 0, \quad \frac{\partial \Pi}{\partial Y} = 0. \tag{38}$$

Using the abbreviations

$$\begin{aligned}
\lambda_{11} &= \frac{16}{9t^4} H_{11} I_{13} J_{13} + \frac{32}{9t^4} H_{12} I_{14} J_{14} + \frac{16}{9t^4} H_{22} I_{15} J_{15} + \frac{64}{9t^4} H_{66} I_{16} J_{16} + A_{44} I_{15} J_{16} \\
&\quad + A_{55} I_{16} J_{13} - \frac{8}{t^2} D_{44} I_{15} J_{16} - \frac{8}{t^2} D_{55} I_{16} J_{13} + \frac{16}{t^4} F_{44} I_{15} J_{16} + \frac{16}{t^4} F_{55} I_{16} J_{13}, \\
\bar{\lambda}_{11} &= I_{16} J_{13}, \\
\lambda_{12} &= -\frac{4}{3t^2} F_{11} I_7 J_7 - \frac{4}{3t^2} F_{12} I_8 J_8 - \frac{8}{3t^2} F_{66} I_{11} J_{11} + \frac{16}{9t^4} H_{11} I_7 J_7 \\
&\quad + \frac{16}{9t^4} H_{12} I_8 J_8 + \frac{32}{9t^4} H_{66} I_{11} J_{11} + A_{55} I_{11} J_7 - \frac{8}{t^2} D_{55} I_{11} J_7 + \frac{16}{t^4} F_{55} I_{11} J_7, \\
\lambda_{13} &= -\frac{4}{3t^2} F_{12} I_9 J_9 - \frac{4}{3t^2} F_{22} I_{10} J_{10} - \frac{8}{3t^2} F_{66} I_{12} J_{12} + \frac{16}{9t^4} H_{12} I_9 J_9 \\
&\quad + \frac{16}{9t^4} H_{22} I_{10} J_{10} + \frac{32}{9t^4} H_{66} I_{12} J_{12} + A_{44} I_{10} J_{12} - \frac{8}{t^2} D_{44} I_{10} J_{12} + \frac{16}{t^4} F_{44} I_{10} J_{12}, \\
\lambda_{22} &= D_{11} I_1 J_1 + D_{66} I_4 J_4 - \frac{8}{3t^2} F_{11} I_1 J_1 - \frac{8}{3t^2} F_{66} I_4 J_4 + \frac{16}{9t^4} H_{11} I_1 J_1 \\
&\quad + \frac{16}{9t^4} H_{66} I_4 J_4 + A_{55} I_4 J_1 - \frac{8}{t^2} D_{55} I_4 J_1 + \frac{16}{t^4} F_{55} I_4 J_1, \\
\lambda_{23} &= D_{12} I_2 J_2 + D_{66} I_5 J_5 - \frac{8}{3t^2} F_{12} I_2 J_2 - \frac{8}{3t^2} F_{66} I_5 J_5 + \frac{16}{9t^4} H_{12} I_2 J_2 \\
&\quad + \frac{16}{9t^4} H_{66} I_5 J_5, \\
\lambda_{33} &= D_{22} I_3 J_3 + D_{66} I_6 J_6 - \frac{8}{3t^2} F_{22} I_3 J_3 - \frac{8}{3t^2} F_{66} I_6 J_6 + \frac{16}{9t^4} H_{22} I_3 J_3 \\
&\quad + \frac{16}{9t^4} H_{66} I_6 J_6 + A_{44} I_3 J_6 - \frac{8}{t^2} D_{44} I_3 J_6 + \frac{16}{t^4} F_{44} I_3 J_6 + k I_3 (C_{1rot} + C_{2rot}),
\end{aligned} \tag{39}$$

we can write the equation system resulting from (38) as follows:

$$\begin{bmatrix} \lambda_{11} - N_{xx}^0 \bar{\lambda}_{11} & \lambda_{12} & \lambda_{13} \\ \lambda_{12} & \lambda_{22} & \lambda_{23} \\ \lambda_{13} & \lambda_{23} & \lambda_{33} \end{bmatrix} \begin{pmatrix} W \\ X \\ Y \end{pmatrix} = \begin{pmatrix} 0 \\ 0 \\ 0 \end{pmatrix}. \tag{40}$$

In order to avoid the trivial solution $W = 0$, $X = 0$, $Y = 0$ we require a vanishing coefficient determinant and arrive at the following closed-form approximate solution for the buckling load N_{xx}^0:

$$N_{xx}^0 = \frac{\lambda_{11}(\lambda_{22}\lambda_{33} - \lambda_{23}\lambda_{23}) - \lambda_{12}(\lambda_{12}\lambda_{33} - \lambda_{23}\lambda_{13}) + \lambda_{13}(\lambda_{12}\lambda_{23} - \lambda_{22}\lambda_{13})}{\bar{\lambda}_{11}(\lambda_{22}\lambda_{33} - \lambda_{23}\lambda_{23})}. \tag{41}$$

6 Shape Functions

In order to evaluate the buckling solution derived with (41) we need to determine adequate shape functions $w_1(x)$, $w_2(y)$, $\psi_{x1}(x)$, $\psi_{x2}(y)$, $\psi_{y1}(x)$, $\psi_{y2}(y)$. Given the fact that both FSDT and TSDT use the same degrees of freedom and that further the current geometric boundary conditions are identical to those as they arise in the framework of FSDT (see Kühn et al. [31]) we use identical shape functions as employed in [31]. Hence, for local web buckling we use the following formulations:

$$\begin{aligned} w_0 &= W w_1(x) w_2(y) \\ &= W \sin\left(\frac{m\pi x}{a}\right)\left[(1-\beta)\sin\left(\frac{\pi y}{b}\right)+\frac{1}{2}\beta\left(1-\cos\left(\frac{2\pi y}{b}\right)\right)\right], \\ \psi_x &= X\psi_{x1}(x)\psi_{x2}(y) \\ &= X\cos\left(\frac{m\pi x}{a}\right)\left[(1-\beta)\sin\left(\frac{\pi y}{b}\right)+\frac{1}{2}\beta\left(1-\cos\left(\frac{2\pi y}{b}\right)\right)\right], \\ \psi_y &= Y\psi_{y1}(x)\psi_{y2}(y) \\ &= Y\sin\left(\frac{m\pi x}{a}\right)\left[(1-\beta)\sin\left(\frac{\pi y}{b}\right)+\beta\sin\left(\frac{2\pi y}{b}\right)\right]. \end{aligned} \tag{42}$$

While the shape functions $w_1(x)$, $\psi_{x1}(x)$, $\psi_{y1}(x)$ fulfill all boundary conditions at the loaded edges $x = 0$ and $x = a$, the shape functions with respect to the y-coordinate $w_2(y)$, $\psi_{x2}(y)$, $\psi_{y2}(y)$ are chosen strictly due to engineering intuition and are basically composed of two limit states. The first limit state is the case of simply supported longitudinal edges $y = 0$ and $y = b$, and the second state consists of fully clamped longitudinal edges. The quantity β as given in (42) is an interpolation factor that interpolates between these two limit states (i.e. $\beta = 0$ for simply supported longitudinal edges and thus $k = 0$, and $\beta = 1$ for fully clamped longitudinal edges and thus $k \to \infty$) and the determination of which will be discussed at a later stage. With the set of shape functions (42) we have for the abbreviations (36):

$$\begin{aligned} &I_1 = I_6 = -I_9 = I_{12} = -I_{14} = I_{16} = \frac{m^2\pi^2}{2a}, \quad -I_2 = I_5 = -I_8 = I_{11} = \frac{m\pi}{2}, \\ &I_3 = I_4 = I_{10} = I_{15} = \frac{a}{2}, \quad I_7 = \frac{m^3\pi^3}{2a^2}, \quad I_{13} = \frac{m^4\pi^4}{2a^3}, \\ &J_1 = J_7 = J_{13} = \frac{b(64\beta - 64\beta^2 + 12\pi - 24\pi\beta + 21\pi\beta^2)}{24\pi}, \\ &J_2 = -J_5 = J_9 = -J_{12} = -\frac{8}{3}\beta + \frac{8}{3}\beta^2 - \frac{1}{2}\pi + \pi\beta - \pi\beta^2, \\ &J_3 = \frac{\pi(16\beta - 16\beta^2 + 3\pi - 6\pi\beta + 15\pi\beta^2)}{6b}, \\ &J_4 = -J_8 = J_{11} = -J_{14} = J_{16} = \frac{\pi(16\beta - 16\beta^2 + 3\pi - 6\pi\beta + 6\pi\beta^2)}{6b}, \end{aligned}$$

$$
\begin{aligned}
J_6 &= \frac{b(16\beta - 16\beta^2 + 3\pi - 6\pi\beta + 6\pi\beta^2)}{6\pi}, \\
J_{10} &= \frac{\pi^2(16\beta - 16\beta^2 + 3\pi - 6\pi\beta + 15\pi\beta^2)}{6b^2}, \\
J_{15} &= \frac{\pi^3(16\beta - 16\beta^2 + 3\pi - 6\pi\beta + 15\pi\beta^2)}{6b^3}, \quad C_{1rot} = C_{2rot} = (1-\beta)^2. \qquad (43)
\end{aligned}
$$

In the case of local flange buckling the following shape functions can be employed:

$$
\begin{aligned}
w_0 &= W w_1(x) w_2(y) \\
&= W \sin\left(\frac{m\pi x}{a}\right)\left[(1-\beta)\frac{y}{b} + \beta\left(1 - \cos\left(\frac{\pi y}{2b}\right)\right)\right], \\
\psi_x &= X \psi_{x1}(x) \psi_{x2}(y) \\
&= X \cos\left(\frac{m\pi x}{a}\right)\left[(1-\beta)\frac{y}{b} + \beta\left(1 - \cos\left(\frac{\pi y}{2b}\right)\right)\right], \\
\psi_y &= Y \psi_{y1}(x) \psi_{y2}(y) \\
&= Y \sin\left(\frac{m\pi x}{a}\right)\left[(1-\beta)\frac{1}{2} + \beta \sin\left(\frac{\pi y}{2b}\right)\right], \qquad (44)
\end{aligned}
$$

and thus:

$$
\begin{aligned}
&I_1 = I_6 = -I_9 = I_{12} = -I_{14} = I_{16} = \frac{m^2\pi^2}{2a}, \quad -I_2 = I_5 = -I_8 = I_{11} = \frac{m\pi}{2}, \\
&I_3 = I_4 = I_{10} = I_{15} = \frac{a}{2}, \quad I_7 = \frac{m^3\pi^3}{2a^2}, \quad I_{13} = \frac{m^4\pi^4}{2a^3}, \\
&J_1 = J_7 = J_{13} = \frac{1}{6} b \left(\frac{48\beta - 48\beta^2 + 5\pi^2\beta^2 + 2\pi^2\beta + 2\pi^2 - 24\pi\beta}{\pi^2}\right), \\
&J_2 = J_9 = -\frac{1}{4}\beta\left(\frac{8 - 8\beta + \pi^2\beta - 4\pi}{\pi}\right), \quad J_3 = \frac{1}{8}\left(\frac{\pi^2\beta^2}{b}\right), \\
&J_4 = J_{11} = J_{16} = \frac{1}{8}\left(\frac{-8\beta^2 + 8 + \pi^2\beta^2}{b}\right), \\
&J_5 = J_{12} = \frac{1}{4}\left(\frac{8\beta - 8\beta^2 + 2\pi - 2\pi\beta + \pi^2\beta^2}{\pi}\right), \\
&J_6 = \frac{1}{4} b \left(\frac{8\beta - 8\beta^2 + \pi + 3\pi\beta^2 - 2\pi\beta}{\pi}\right), \\
&J_8 = J_{14} = -\frac{1}{8}\beta\left(\frac{8 - 8\beta + \pi^2\beta - 4\pi}{b}\right), \\
&J_{10} = \frac{1}{16}\left(\frac{\pi^3\beta^2}{b^2}\right), \quad J_{15} = \frac{1}{32}\left(\frac{\pi^4\beta^2}{b^3}\right), \quad C_{1rot} = \frac{1}{4}(1-\beta)^2. \qquad (45)
\end{aligned}
$$

The factor β is chosen according to the analysis approach outlined in [31] and reads:

$$\beta = \frac{kb}{2D_{22}\pi + kb}. \tag{46}$$

This formulation holds for both local web and flange buckling. It can readily be shown that β can attain values between $\beta = 0$ and $\beta = 1$, depending on the restraint stiffness k.

7 Results and Discussion

As first examples we consider three different I-beam configurations taken from a civil engineering application [32]. The employed elastic laminate layer properties for a typical carbon fiber reinforced plastic are given in Table 1. The three different I-beam configurations are described in detail in Table 2. Therein, N is the total number of laminate layers. Note that for all three considered beams, the web properties remain unchanged. The web and flange laminates can be classified as moderately thick so that the application of shear deformation theories is justified. Note that the laminate layups considered here do not exactly fulfill the requirement for orthotropic laminates. In order to facilitate the computations, we have set the according stiffness parameters in the laminate stiffness matrix (17) to zero. The determination of the restraint stiffness k for both web and flange buckling has been determined according to an approach outlined by Qiao and Shan in [20]. We will not go into deeper details at this point, the interested reader is referred to [20] and the references cited therein for detailed information. It is important to note, however, that the determination of k showed that for all beam configurations considered in Table 2 web buckling is the relevant case. Figures 6, 7 and 8 contain buckling curves for N_{xx}^0 (with N_{xx}^0 given in the unit N/mm) using the present methodology wherein the length a is varied between $a = 0$ and $a = 4000$ mm. For verification, we have also included results using CLPT (see [28, 29]) as well as using FSDT (see [31]) where it is important to note that the reference results have all been extensively verified using comparative

Table 1 Material properties [32]

Parameter	Value	Unit
E_{11}	1,21,000	MPa
E_{22}	8600	MPa
E_{33}	8600	MPa
G_{12}	4700	MPa
G_{13}	4700	MPa
G_{23}	3100	MPa
ν_{12}	0.27	–
ν_{13}	0.27	–
ν_{23}	0.4	–

Table 2 I-beam configurations 1–3 [32]

		N	Thickness t [mm]	Width b [mm]	Laminate layup
I-beam 1	Web	176	22	444	$[\pm 45_8/90_3/0_3]_{4S}$
	Flange	224	28	100	$[0_{20}/\pm 45_2/90_4]_{4S}$
I-beam 2	Web	176	22	500	$[\pm 45_8/90_3/0_3]_{4S}$
	Flange	200	25	105	$[0_{17}/\pm 45_2/90_4]_{4S}$
I-beam 3	Web	176	22	554	$[\pm 45_8/90_3/0_3]_{4S}$
	Flange	200	25	110	$[0_{15}/\pm 45_2/90_4]_{4S}$

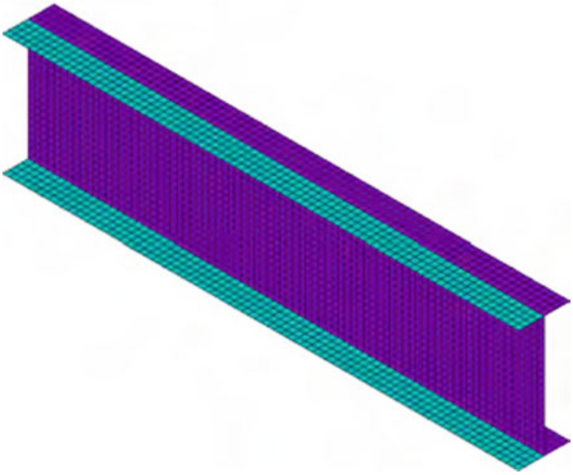

Fig. 4 Exemplary mesh of a full beam model

finite element computations. These FEM computations that we will not discuss in full detail due to reasons of brevity have been performed using full beam models (see [31, 32] for more details) based on shell models accounting for transverse shear deformations. An exemplary mesh the density of which has been determined by convergence studies is given in Fig. 4. The employed boundary conditions and load introduction by using multi-point constraints is shown in Fig. 5 where here the mesh density is depicted in a much coarser way so as to facilitate the representation of boundary conditions.

Note that while even the web laminate is the same for all three considered I-beams, the local web buckling problem also depends significantly on the restraint stiffness values k which in turn depend on the properties of the flange laminates. The results contained in Figs. 6, 7 and 8 can thus be interpreted as a study of the influence of the variation of k. Apparently, the results reflect buckling curves as they are typical when investigating the critical buckling loads of laminates with variable length. All curves tend to infinite values for N_{xx}^0 when very short laminates are considered. On the other hand the curves $N_{xx}^0(a)$ tend to an asymptotic limit value when a takes on sufficiently high values. In between, the buckling curves reach several local maxima

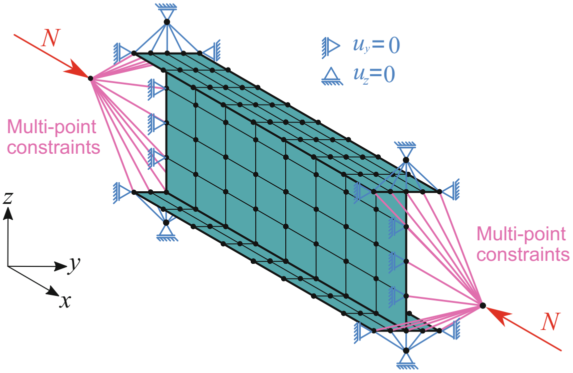
N
$u_y = 0$
$u_z = 0$
Multi-point constraints
z
y
x
Multi-point constraints
N

Fig. 5 Boundary conditions and load introduction in the framework of the numerical model

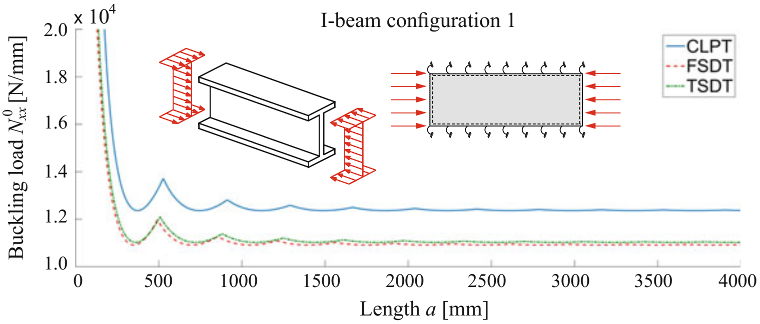

Fig. 6 Local web buckling of I-beam 1

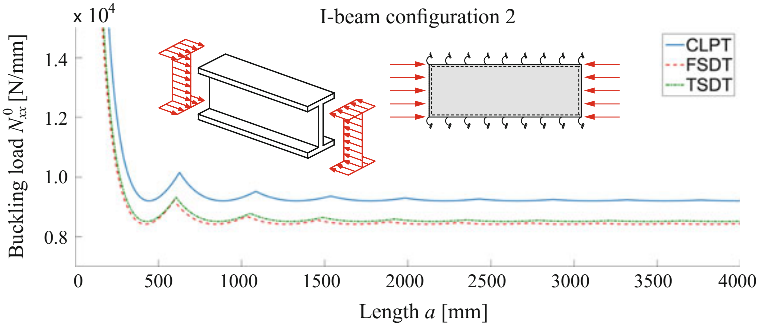

Fig. 7 Local web buckling of I-beam 2

that correspond to changes in the buckling modes. It furthermore becomes quite obvious that the results by CLPT are significantly higher than those by FSDT and TSDT, where the latter ones are quite close to each other. On the one hand this verifies the current TSDT approach as rather accurate since the FSDT results are matched

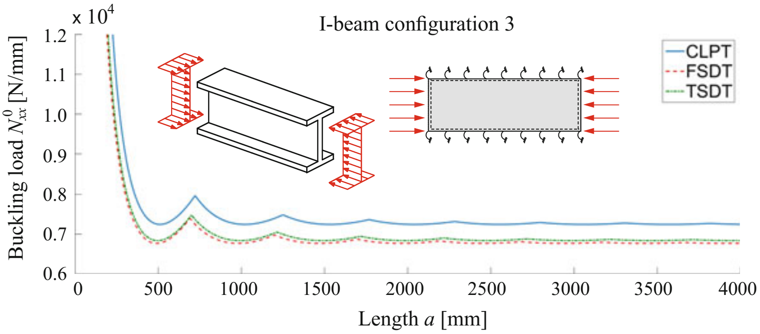

Fig. 8 Local web buckling of I-beam 3

Table 3 Material properties [31]

Parameter	Value	Unit
E_{11}	1,55,000	MPa
E_{22}	10,000	MPa
E_{33}	10,000	MPa
G_{12}	4500	MPa
G_{13}	4500	MPa
G_{23}	4500	MPa
ν_{12}	0.3	–
ν_{13}	0.3	–
ν_{23}	0.3	–

quite closely, and on the other hand due to the usage of TSDT the necessity of a shear correction factor can be discarded which is very beneficial for practical application. In the light of these results the local web buckling approach can be considered to be verified.

For further verification we consider some I-beam configurations taken from Kühn et al. [31] which we will denote as I-beams 4–6. The assumed material properties are given in Table 3. All I-beam configurations as described in Table 4 are assumed to consist of purely orthotropic, symmetric and moderately thick composite laminate layups. The determination of the restraint stiffness values k for web and flanges showed that in this case flange buckling is the relevant local stability case. The following study thus serves as a verification of the developed local flange buckling analysis method. Note that in this case, both webs and flanges show the same laminate layups. Buckling curves similar to those already discussed before are given in Figs. 9, 10 and 11.

Again we are comparing our results with those obtained with closed-form approximate solutions based on CLPT and FSDT. We have varied the length a [mm] in the range between $a = 0$ mm and $a = 1200$ mm respectively $a = 1440$ mm and plotted the resultant buckling load N_{xx}^0 in N/mm as a function of a. The results contained in

Table 4 I-beam configurations 4–6 [31]

		N	Thickness t [mm]	Width b [mm]	Laminat layup
I-beam 4	Web	73	9.125	100	$[(90/0)_{18}/90/(0/90)_{18}]$
	Flange	73	9.125	40	$[(90/0)_{18}/90/(0/90)_{18}]$
I-beam 5	Web	98	12.25	100	$[(90/0)_{24}/90]_S$
	Flange	98	12.25	40	$[(90/0)_{24}/90]_S$
I-beam 6	Web	130	16.25	100	$[(90/0)_{32}/90]_S$
	Flange	130	16.25	80	$[(90/0)_{32}/90]_S$

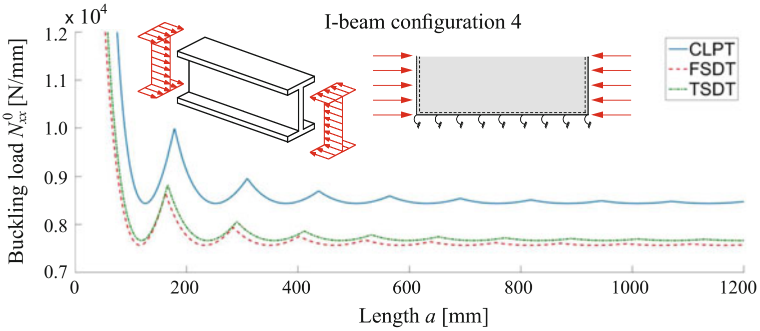

Fig. 9 Local flange buckling of I-beam 4

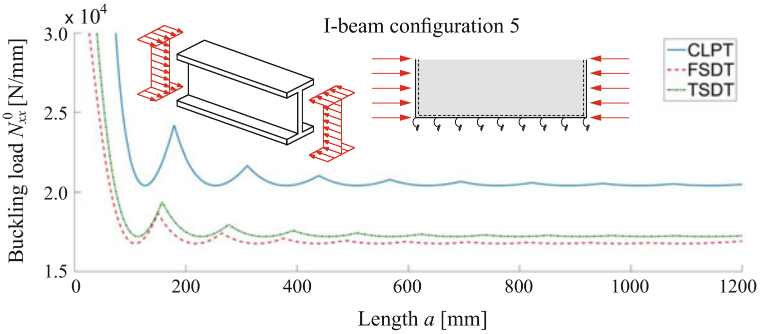

Fig. 10 Local flange buckling of I-beam 5

Figs. 9, 10 and 11 show similar characteristics as already observed for the local web buckling presented in Figs. 6, 7 and 8 so that a renewed discussion can be omitted at this point. It is important to note at this point that again, the results based on FSDT and TSDT are significantly lower than the CLPT results, and that both FSDT and TSDT deliver quite similar results. In conclusion the present TSDT approach can be assumed to deliver very reliable results also in the case of local flange buckling.

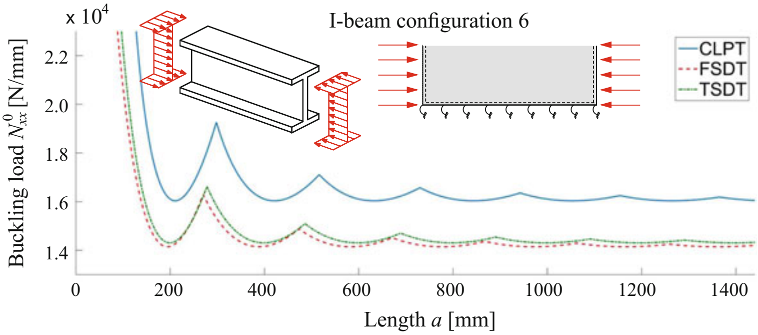

Fig. 11 Local flange buckling of I-beam 6

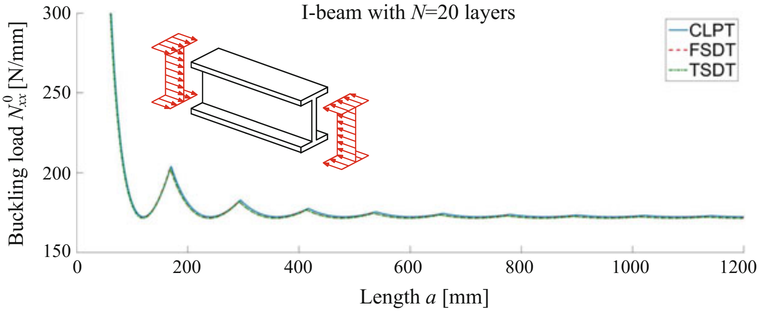

Fig. 12 Buckling curves of an I-beam with $N = 20$ laminate layers

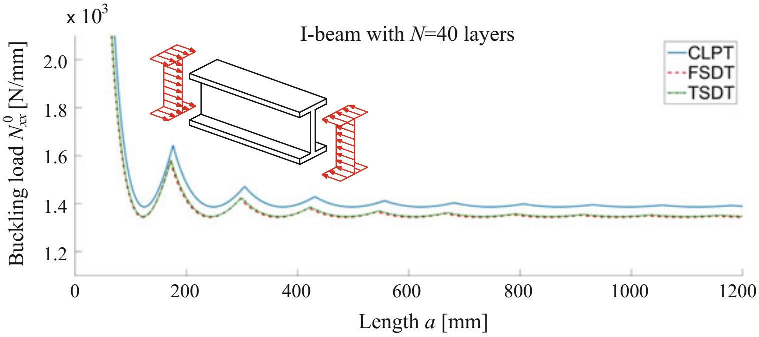

Fig. 13 Buckling curves of an I-beam with $N = 40$ laminate layers

The following Figs. 12, 13, 14, 15, 16 and 17 show a study of the influence of the laminate thickness t on the resultant buckling curves according to CLPT, FSDT and TSDT. For this purpose we consider an I-beam with a web height of 100 mm and a flange width of 40 mm. We employ the material properties as given in Table 3 and assume that all laminate layups are strictly orthotropic and symmetric. We are now

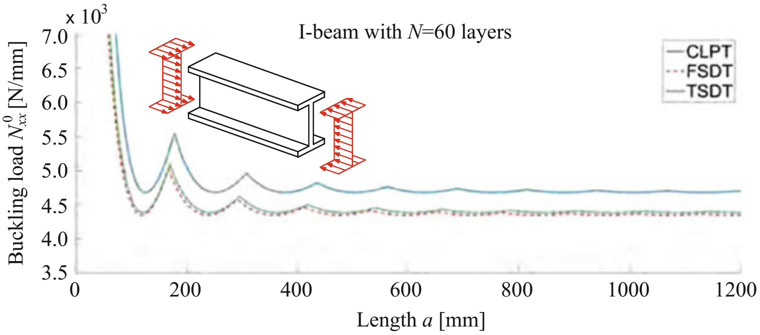

Fig. 14 Buckling curves of an I-beam with $N = 60$ laminate layers

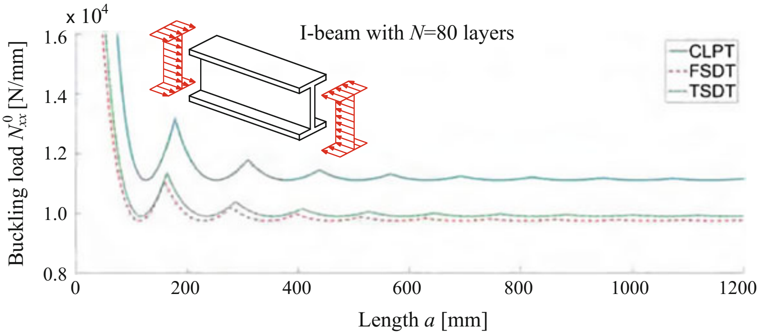

Fig. 15 Buckling curves of an I-beam with $N = 80$ laminate layers

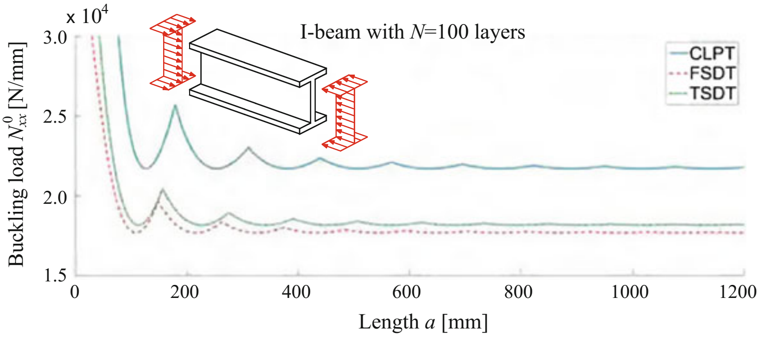

Fig. 16 Buckling curves of an I-beam with $N = 100$ laminate layers

varying the number N of laminate layers between $N = 20$ and $N = 120$ in steps of 20 while assuming a layer thickness of 0.125 mm. The resultant buckling curves for the currently considered elastically restrained composite laminates, contained in Figs. 12, 13, 14, 15, 16 and 17, show a behaviour of the buckling curves as it is

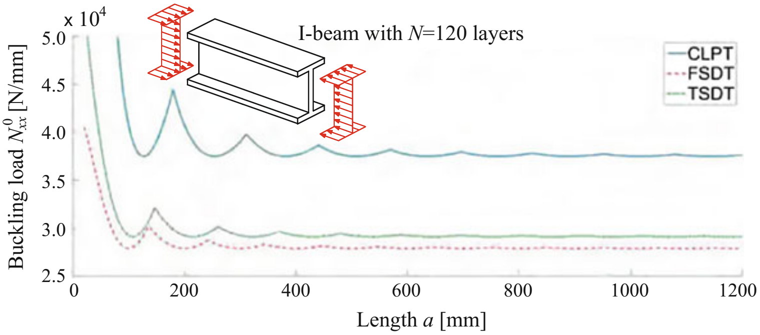

Fig. 17 Buckling curves of an I-beam with $N = 120$ laminate layers

common for laminated composite materials where transverse shear deformations play a role in the structural response. Apparently, for $N = 20$ laminate layers (Fig. 12) the three considered laminate theories deliver identical results. For such a rather thin laminate, a higher order theory beyond CLPT with the computational effort that comes along with improved theories is apparently not necessary. With an increasing number of layers, however, the three laminate theories deliver increasingly different results. The difference between the CLPT results and the results according to FSDT and TSDT increases as N increases, and the results generated by FSDT and TSDT also begin to exhibit increasing differences between each other. The reason can be found in the fact that the higher-order terms that appear in the constitutive matrix (17) and which are not present in CLPT and FSDT begin to play a more dominant role in the structural response of the composite laminates and thus lead to more pronounced differences between the results of all three considered laminate theories.

8 Summary and Conclusions

This paper presents a new energy-based approach for the approximate determination of the local buckling loads (i.e. web and flange buckling) of composite laminated beams made of symmetric and orthotropic laminates under uniaxial compressive load. The analysis is based on Reddy's third-order shear deformation theory and works with rather simple shape functions for the unknown displacement quantities that arise during the onset of buckling. A closed-form approximate solution for the local buckling loads is derived from the principle of minimum elastic potential of the buckled web and flange plates. The new buckling method has been verified by comparison with similar results according to CLPT and FSDT, taken from literature references that in turn were verified by comparison with extensive finite element computations. The obtained results were shown to be very plausible and reliable when compared to the reference results. While for rather thin laminates all laminate theories deliver identical results, the deviations become more and more pronounced the higher the laminate thickness becomes which is a unique feature when dealing with different laminate theories. In all, the presented novel approach has been proven to deliver very plausible and reliable results.

It is worth noting that a formulation using TSDT yields somewhat more complicated expressions when compared to methods based on CLPT and FSDT. However, especially when dealing with thick laminates, an analysis using CLPT is not an option due to the very pronounced transverse shear deformations which have a detrimental effect on the buckling resistance of such composite laminates and where CLPT not only delivers false, but also non-conservative results in each and every case. Since the number of degrees of freedom is the same within FSDT and TSDT, the computational effort itself is identical for both these two theoretical frameworks so that there is no reason to favor FSDT over TSDT from a purely computational point of view. However, as a major advantage, TSDT does not require the (sometimes tedious) determination of shear correction factors which makes it less prone to a potentially erroneous determination and interpretation of results where it is well-known that the choice of shear correction factors does have a significant impact (see [1]) on static and dynamic results for laminated plates which, in the case of inadequate values, can lead to not only false but also non-conservative and thus dangerous results.

The present methodology is applicable only for prismatic composite laminated beams under uniform uniaxial compression. However, there is considerable practical interest in analysis methods that are able to capture more complicated load cases such as non-uniform compression, shear, bending, and combinations thereof. Further, the present approach only holds for purely orthotropic laminate layups and does not account for important coupling effects such as bending-twisting-coupling (see [1] for deeper details). Both these issues can be solved by using more extensive buckling shape functions as presented in e.g. [27, 28] in the framework of CLPT. The extension of this methodology to FSDT and TSDT is the topic of currently ongoing research and will be documented in future reports. Furthermore it will be of interest to extend the current analysis method to more complicated beam geometries, for instance non-prismatic beams as they occur when dedicated weight optimization routines are applied. This can be tackled by using series expansions for the degrees of freedom and according energy formulations of the buckled beams.

As a closure it is important to note that the present model only accounts for strictly local buckling modes. However, an actual engineering analysis of thin-walled composite beams, especially for long and slender beams, must also consider global modes such as Euler-type buckling, torsional buckling, flexural-torsional buckling under compressive load or lateral buckling under bending load as well. This is, however, beyond the scope of the present paper, but can be done using the analysis approaches as given in [2–19] or in many textbooks on structural stability (see e.g. [33]). The lowest possible global or local buckling load then indicates which buckling mode is relevant for the given application.

Acknowledgements Parts of the research contained in this paper have been financially supported by the Bundesinstitut für Bau-, Stadt- und Raumforschung under grant no. SWD-10.08.18.7-15.62 which the authors gratefully acknowledge.

References

1. Reddy, J.N.: Mechanics of Laminated Composite Plates and Shells, 2nd edn. CRC Press, Boca Raton (2004)
2. Barbero, E., Tomblin, J.: Euler buckling of thin-walled composite columns. Thin-Walled Struct. **17**, 237–258 (1993)
3. Barbero, E., Raftoyiannis, I.G.: Euler buckling of pultruded composite columns. Compos. Struct. **24**, 139–147 (1993)
4. Barbero, E., Tomblin, J.: A phenomenological design equation for FRP columns with interaction between local and global buckling. Thin-Walled Struct. **18**, 117–131 (1994)
5. Barbero, E., Raftoyiannis, I.G.: Lateral and distortional buckling of pultruded I-beams. Compos. Struct. **27**, 261–268 (1994)
6. Davalos, J., Qiao, P.: Analytical and experimental study of lateral and distortional buckling of FRP wide-flange beams. J. Compos. Constr. **1**, 150–159 (1997)
7. Davalos, J., Qiao, P., Salim, H.A.: Flexural-torsional buckling of pultruded fiber reinforced plastic composite I-beams: experimental and analytical evaluations. Compos. Struct. **38**, 241–250 (1997)
8. Gan, L.H., Ye, L., Mai, Y.W.: Simulations of mechanical performance of pultruded I-beams with various ange-web conjunctions. Compos. B **30**, 423–429 (1999)
9. Lee, J., Kim, S.E.: Flexural torsional buckling of thin-walled I-section composites. Comput. Struct. **79**, 987–995 (2001)
10. Kollár, L.P.: Flexural-torsional buckling of open section composite columns with shear deformation. Int. J. Solids Struct. **38**, 7525–7541 (2001)
11. Qiao, P., Zou, G., Davalos, J.F.: Flexural-torsional buckling of fiber-reinforced plastic composite cantilever I-beams. Compos. Struct. **60**, 205–217 (2003)
12. Shan, L., Qiao, P.: Flexural-torsional buckling of fiber-reinforced plastic composite open channel beams. Compos. Struct. **68**, 211–224 (2005)
13. De Lorenzis, L., La Tegola, A.: Effect of the actual distribution of applied stresses on global buckling of isotropic and transversely isotropic thin-walled members: theoretical analysis. Compos. Struct. **68**, 339–348 (2005)
14. Teter, A., Kolakowski, Z.: Buckling of thin-walled composite structures with intermediate stiffeners. Compos. Struct. **69**, 421–428 (2005)
15. Kolakowski, Z., Kubiak, T.: Load-carrying capacity of thin-walled composite structures. Compos. Struct. **67**, 417–426 (2005)
16. Vo, T.P., Lee, J.: Flexural-torsional buckling of thin-walled composite box beams. Thin-Walled Struct. **45**, 790–798 (2007)
17. Vo, T.P., Lee, J.: Flexural-torsional coupled vibration and buckling of thin-walled open section composite beams using shear-deformable beam theory. Int. J. Mech. Sci. **51**, 631–641 (2009)
18. Naderian, H.R., Ronagh, H.R., Azharic, M.: Torsional and flexural buckling of composite FRP columns with cruciform sections considering local instabilities. Compos. Struct. **93**, 2575–2586 (2011)
19. Sapountzakis, E.J., Dourakopoulos, J.A.: Flexural-torsional buckling analysis of composite beams by BEM including shear deformation effect. Mech. Res. Commun. **35**, 497–516 (2008)
20. Qiao, P., Shan, L.: Explicit local buckling analysis and design of fiber-reinforced plastic composite structural shapes. Compos. Struct. **70**, 468–483 (2005)
21. Bank, L.C., Yin, J.: Buckling of orthotropic plates with free and rotationally restrained edges. Thin-Walled Struct. **24**, 83–96 (1996)

22. Kollár, L.: Buckling of unidirectionally loaded composite plates with one free and one rotationally restrained unloaded edge. J. Struct. Eng. **128**, 1202–1211 (2002)
23. Kollár, L.: Local buckling of fiber reinforced plastic composite structural members with open and closed cross sections. J. Struct. Eng. **129**, 1503–1513 (2003)
24. Qiao, P., Davalos, J.F., Wang, J.: Local buckling of composite FRP shapes by discrete plate analysis. J. Struct. Eng. **127**, 245–255 (2001)
25. Qiao, P., Zou, G.: Local buckling of elastically restrained fiber-reinforced plastic plates and its application to box sections. J. Eng. Mech. **128**, 1324–1330 (2002)
26. Zureick, A., Shih, B.: Local buckling of fiber-reinforced polymeric structural members under linearly-varying edge loading - part 1. Compos. Struct. **41**, 79–86 (1998)
27. Mittelstedt, C.: Stability behaviour of arbitrarily laminated composite plates with free and elastically restrained unloaded edges. Int. J. Mech. Sci. **49**, 819–833 (2007)
28. Mittelstedt, C.: Local buckling of wide-flange thin-walled anisotropic composite beams. Arch. Appl. Mech. **77**, 439–452 (2007)
29. Mittelstedt, C., Beerhorst, M.: Closed-form buckling analysis of compressively loaded composite plates braced by omega-stringers. Compos. Struct. **88**, 424–435 (2009)
30. Beerhorst, M., Seibel, M., Mittelstedt, C.: Buckling behavior of an orthotropic plate strip under combined compression and shear. J. Aircr. **48**, 1360–1367 (2011)
31. Kühn, T., Pasternak, H., Mittelstedt, C.: Local buckling of shear-deformable laminated composite beams with arbitrary cross-sections using discrete plate analysis. Compos. Struct. **113**, 236–248 (2014)
32. Mittelstedt, S., Schürg, M., Mittelstedt, C.: Globale Stabilität schubweicher anisotroper hochbelasteter Laminat- und Sandwich-Träger unter kombinierter Belastung im Brücken- und allgemeinen Ingenieurhochbau (in German). Research report, Sogeti Deutschland GmbH, Hamburg, Germany (2017)
33. Timoshenko, S., Gere, J.: Theory of Elastic Stability. McGraw-Hill Inc, New York (1961)

Dislocation Dynamics as Gradient Descent in a Space of Currents

Thomas Hochrainer

Abstract Recent progress in continuum dislocation dynamics (CDD) has been achieved through the construction of a local density approximation for the dislocation energy and the derivation of constitutive laws for the average dislocation velocity by means of variational methods from irreversible thermodynamics. Individual dislocations are driven by the Peach–Koehler-force which is likewise derived from a variational principle. This poses the question if we may expect that the averaged dislocation state expressed through the CDD density variables is driven by a variational gradient of the average energy, as is assumed in irreversible thermodynamics. In the current contribution we do not answer this questions, but rather present the mathematical framework within which the evolution of discrete dislocations is literally understood as a gradient descent. The suggested framework is that of de Rham currents and differential forms. We briefly sketch why we believe the results to be useful for formulating CDD theory as a gradient flow.

1 Introduction

During the last two decades crystal plasticity revealed itself as an area which poses great challenges in the discrete to continuum transition from individual dislocations to continuum dislocation formulations. One important line among others in this field is the program of continuum dislocation dynamics (CDD) pursued by the author and co-workers [12]. The original problem solved by CDD is the definition of sufficiently rich dislocation density measures capable of describing the evolution of a dislocation system in a kinematically closed form [14]. At least for single glide situations we regard this problem as solved since the introduction of a hierarchy of dislocation alignment tensors and their evolution equations [10] – even though the latter require closure assumptions in order to arrive at useful crystal plasticity theories [23]. But

---

T. Hochrainer (✉)
Institut für Festigkeitslehre, Technische Universität Graz, Kopernikusgasse 24,
8010 Graz, Austria
e-mail: hochrainer@tugraz.at

© Springer International Publishing AG 2018

H. Altenbach et al. (eds.), *Advances in Mechanics of Materials and Structural Analysis*, Advanced Structured Materials 80,
https://doi.org/10.1007/978-3-319-70563-7_9

the achieved kinematic consistency has to be accompanied by a kinetic theory in order turn CDD into a crystal plasticity materials law.

Regarding a kinetic closure we currently regard energetic approaches as most promising. The energetic approach assumes that the energy of a dislocation system may be expressed by an energy functional depending on the CDD density variables. The evolution of the density variables, which are naturally formulated in terms of an average dislocation speed, are then derived in the spirit of irreversible thermodynamics from a variational derivative of the energy with respect to the evolution of the CDD variables [11]. This reasoning has been substantiated by the derivation of a local density approximation for the dislocation energy in terms of CDD variables, which (the derivation) bears strong analogies to quantum mechanics [26]. In the current contribution we are interested in the complementary question to energetic modelling in CDD, namely how the single dislocation evolution presents itself as a gradient descent.

Dislocations are well known to move in response to the so-called Peach–Koehler force. The Peach–Koehler force on dislocations is a prototypical configurational force *ante verbum*. In the original paper, Peach and Koehler [25] derived the force as the negative variational derivative of the 'interaction energy with [the] stress field'. The dislocation mobility turns this force per length into a dislocation (segment) velocity. This means that discrete dislocation simulations, which employ the Peach–Koehler force, perform a gradient descent in energy space of some form. With regard to constitutive modeling in CDD this raises two questions: (*i*) What is a proper mathematical space in which the motion due to the Peach–Koehler force on single dislocations may actually be viewed as a 'gradient descent'? – Where we expect the (variational) gradient to be obtained from a Gâteaux differential. (*ii*) Can we expect the gradient structure of the evolution equation to be conserved upon (ensemble) averaging? In the current contribution we focus on the first question (*i*) and only briefly discuss how the answer to the first question may affect reasoning on the second one.

The paper is structured as follows: in Sect. 2 we introduce the notions of (vector valued) differential forms and currents. In Sect. 3 we describe the differential calculus on currents from the perspective of variational theory. Subsequently, we briefly discuss the energetics of dislocations in Sect. 4. The key result is obtained in Sect. 5 where we introduce a metric structure which turns the equation of overdamped dislocation motion into a gradient descent in a space of one-dimensional vector valued currents. Finally we briefly summarize the results and give a cursory outlook on challenges in kinetic modeling of CDD in Sect. 6.

2 Mathematical Preliminaries

We focus on the case of interacting dislocation lines in an infinite crystal and employ the assumptions of small deformations and linear elasticity. Despite our restriction to small deformations, we will distinguish upper and lower indices in the sequel.

Consequently, we usually employ the original Einstein summation convention, where automatic contraction is restricted to pairs of like upper and lower indices. We think it is important to distinguish vector spaces and their dual spaces in the current context both locally and globally – even if the standard metric is available for mutual identification. As will be discussed in Sect. 5, we regard the viscous drag of dislocation motion as the origin of a *physical* metric of dislocation theory, which supersedes the standard metric.

In the current Section we introduce differential forms, vector valued differential forms, currents, and vector valued currents in a very condensed way, which, hopefully allows the reader to follow the subsequent theory. For thorough introductions to differential forms we refer to standard text books, e.g. [5, 21]. More details on vector valued differential forms may be found in [9, 15]. For the notion of currents we recommend [2], for their application to dislocations and the vector valued case we refer to [9, 13]. Note that we leave out all functional analytic or measure theoretic complexities.

Basic notation and differential forms

As we deal with small deformation theory, we regard the crystal as a Euclidean manifold with standard coordinates x^1, x^2, x^3. The according basis vectors of the tangent space are denoted with ∂_i and the dual basis one-forms of the co-tangent space are denoted with $\mathrm{d}x^i$. Differential forms are purely covariant and fully antisymmetric tensors, which are non-trivial in the three-dimensional case only for degrees 0,1,2, and 3. The wedge-product $\wedge$ is used to combine two differential forms of order p and q to a differential form of order $p + q$. For details on the calculus of differential forms see [5, 21] and many other introductory book in differential geometry. We just recall a few salient features of and operators defined on differential forms. One important feature is that differential p-forms may be integrated over p-dimensional oriented submanifolds S^p,

$$\int_{S^p} \alpha^p, \tag{1}$$

without assigning a standard 'volume (surface or line) element' to the submanifold. Furthermore, the exterior derivative d is defined independent of both Riemannian metrics and connections and maps differential p-forms to differential $p + 1$-forms. The generalized Stokes theorem on differential forms reads

$$\int_{S^{p+1}} \mathrm{d}\alpha^p = \int_{\partial S^{p+1}} \alpha^p. \tag{2}$$

The interior multiplication $\iota_X \alpha^p$ with a vector field X turns a differential p-form into a differential $(p - 1)$-form. The Lie-derivative $\mathscr{L}_X$ along a vector field X, which keeps the degree of a differential form fixed, is defined by Cartan's *magic formula*,

$$\mathscr{L}_X \alpha = \iota_X \mathrm{d}\alpha + \mathrm{d}\iota_X \alpha. \tag{3}$$

Vector valued differential forms

In general, vector valued differential forms take values in some vector bundle (which includes, e.g., tensor bundles) over the crystal manifold [17]. In the current paper this will be either the tangent bundle or the co-tangent bundle (see [9, 15] for more detailed introductions of this special case). In the sequel we will reserve the term vector valued differential form usually for those taking values in the tangent bundle while we speak of one-form valued differential forms in the latter case. In local coordinates a vector valued p-form is of the form

$$P = \frac{1}{p!} P_{i_1 \cdots i_p}{}^{j} \mathrm{d}x^{i_1} \wedge \cdots \wedge \mathrm{d}x^{i_p} \otimes \partial_j, \tag{4}$$

while a one-form valued p-form appears as

$$Q = \frac{1}{p!} Q_{i_1 \cdots i_p j} \mathrm{d}x^{i_1} \wedge \cdots \wedge \mathrm{d}x^{i_p} \otimes \mathrm{d}x^{j}. \tag{5}$$

Vector valued differential forms (in the general sense) only allow for an integral calculus if the vector bundle is a trivial bundle and a trivialization is fixed. However, we do not explicitly integrate vector valued differential forms in the sequel, but restrict integration to differential forms arising from a generalized *dotted* wedge product $\dot{\wedge}$, taking a vector valued and a one-form valued form (or vice versa) to a usual differential form through[1]

$$P^p \dot{\wedge} Q^q := \frac{1}{p!q!} P_{i_1 \cdots i_p}{}^{j} Q_{i_{p+1} \cdots i_{p+q} j} \mathrm{d}x^{i_1} \wedge \cdots \wedge \mathrm{d}x^{i_p} \wedge \mathrm{d}x^{i_{p+1}} \wedge \cdots \wedge \mathrm{d}x^{i_{p+q}} \tag{6}$$

$$Q^q \dot{\wedge} P^p := (-1)^{pq} \, P^p \dot{\wedge} Q^q. \tag{7}$$

The generalization of the exterior derivative to vector valued differential forms requires the consideration of a connection ∇ on the vector bundle and is denoted with d^{∇}. In the Euclidean case, the connection is of course the standard connection with vanishing connection coefficients. The generalized exterior derivative of vector valued and one-form valued differential forms satisfies the product rule

$$\mathrm{d}\left(P^p \dot{\wedge} Q\right) = \mathrm{d}^{\nabla} P^p \dot{\wedge} Q + (-1)^p \, P^p \dot{\wedge} \mathrm{d}^{\nabla} Q. \tag{8}$$

The interior multiplication ι_X applies in the usual fashion to the differential form part of the vector and one-form valued differential forms. We define a generalized Lie-derivative on vector and one-form valued differential forms through [9]

$$\mathscr{L}_X^{\nabla} = \iota_X \mathrm{d}^{\nabla} \alpha + \mathrm{d}^{\nabla} \iota_X \alpha. \tag{9}$$

---

[1] Note that in [9] there is a mistake in the anti-symmetry condition below, where the exponent of -1 is erroneously given as p and not pq.

Currents

Currents are defined as linear functional on spaces of differential forms. In this work we deal with the basic definition according to de Rham [2], where the arguments of currents are C^{∞} differential forms with compact support. De Rham developed the notion of currents from electrodynamics at the prototype of a current carrying wire. Such wire may be described as an electrical current (singularly) concentrated on a one-dimensional manifold. Even though such objects are often described by integrals over Dirac delta distributions, it is advantageous to regard singularities along submanifolds as objects of their own right. Currents which are non-trivial only for differential forms of a given degree p are called p-dimensional currents. This obviously includes p-dimensional submanifolds S^p which map smooth differential p-forms α^p onto their integral over the submanifold. We denote the current induced by such submanifold with γ_{S^p}, which is defined by

$$\gamma_{S^p}\left[\alpha^p\right] := \int_{S^p} \alpha^p. \tag{10}$$

Note that we mark the application of a functional to differential forms with brackets $[\cdot]$. Delta distributions at a point r are in this sense 0-dimensional currents assigning to a function f its value at r, i.e.,

$$\gamma_r\left[f\right] := f\left(r\right). \tag{11}$$

If the underlying space M is n-dimensional, p-dimensional currents are likewise said to be of degree $n-p$. The rational for this notion is that $n-p$-dimensional differential forms β^{n-p} define linear functionals on differential p forms as follows,

$$\gamma_{\beta^{n-p}}\left[\alpha^p\right] := \int_M \beta^{n-p} \wedge \alpha^p. \tag{12}$$

The above examples of currents motivate the following transfer of operations from manifolds or differential forms to currents. Stokes' theorem (2) immediately yields the notion of the boundary of a current ∂, which is defined through

$$\partial\gamma\left[\alpha\right] := \gamma\left[\mathrm{d}\alpha\right]. \tag{13}$$

The product rule of the exterior differential derivative yields the closely connected definition

$$\mathrm{d}\gamma\left[\alpha^p\right] := (-1)^{p+1}\,\gamma\left[\mathrm{d}\alpha^p\right]. \tag{14}$$

The interior multiplication with a vector field X is defined as

$$\iota_X\gamma\left[\alpha^p\right] := (-1)^{p+1}\,\gamma\left[\iota_X\alpha^p\right]. \tag{15}$$

Finally, the Lie derivative of a current in the direction of a vector field is

$$\mathscr{L}_X\gamma\left[\alpha^p\right] := -\gamma\left[\mathscr{L}_X\alpha^p\right]. \tag{16}$$

Currents from moving submanifolds

The Lie derivative of currents plays a special role for currents derived from moving submanifolds. It seems that the following transport theorem (e.g. found in [5, 21]) lacks a common denomination and is occasionally 'rediscovered' [4]. It may be viewed as a generalization of the Reynolds transport theorem to differential forms. We directly introduce it in the language of currents. Let $N(t)$ be a moving submanifold, where the motion of every point is described by a vector field $v(t)$ along the manifold. Let moreover $\gamma_{N(t)}$ denote the induced current on smooth differential forms, then the time derivative of the current is given by

$$\partial_t\gamma_{N(t)} = -\mathscr{L}_{v(t)}\gamma_{N(t)}. \tag{17}$$

Vector valued currents

We regard vector valued currents as linear functionals acting on one-form valued differential forms and vice versa. For example, a dislocation line c defines a vector valued (because of the Burgers vector b) one-dimensional current γ_{c^b} acting on one-form-valued one-forms $L = L_{ji}\mathrm{d}x^j \otimes \mathrm{d}x^i$ through

$$\gamma_{c^b}\left[L\right] = \int_c L_{ij}b^j\mathrm{d}x^i. \tag{18}$$

The generalized operations on vector valued differential forms transfer to vector valued currents in full analogy to their original definition on currents, when replacing the exterior derivative with the connection dependent exterior derivative, that is

$$\mathrm{d}^\nabla\gamma\left[P^p\right] := (-1)^{p+1}\,\gamma\left[\mathrm{d}^\nabla P^p\right], \tag{19}$$

$$\iota_X\gamma\left[P^p\right] := (-1)^{p+1}\,\gamma\left[\iota_X P^p\right], \tag{20}$$

$$\mathscr{L}_X^\nabla\gamma\left[\alpha^p\right] := -\gamma\left[\mathscr{L}_X^\nabla\alpha^p\right]. \tag{21}$$

Vector valued currents from moving submanifolds

As a generalization of the second last paragraph imagine a moving submanifold to which a vector field is appended. A motion of such a current consists additionally to the spatial vector field v, which moves the base manifold, also of a variation $\dot{X}$ of the vector field X. The latter variation may be split in the sense of a co-variant time derivative, $\dot{X} = X_t + \nabla_v X$, where X_t is the variation of the vector field keeping N fixed, while $\nabla_v X$ is understood as the covariant derivative of X along the motion path of each point moving with the flow of v. The according time derivative of the induced current was found in [9] as

$$\partial_t \gamma_{N^b} = -\mathscr{L}_v^{\nabla} \gamma_{N^x} + \gamma_{N^{\dot{x}}} \tag{22}$$

Double forms

In order to deal with interacting dislocations we work with the interaction energy of two dislocations. The interaction energy will be discussed in detail below. At this point we only note for motivational purposes, that the interaction energy is obtained as a double integral over the two dislocation lines. In the terminology employed here, the kernel of the double integral is a one-form valued double differential form on the product space of the crystal manifold with itself. When dealing with double forms on $M \times M$ we distinguish the coordinates on the first and second copy of M as x^i and $\bar{x}^i$. For the first manifold we use the notations introduced above, while for the latter we employ the vector basis $\bar{\partial}_i$ and the co-vector basis $\mathrm{d}\bar{x}^i$. In local coordinates a double (p, q)-form reads

$$\mathscr{D}^{p,q} = \frac{1}{p!q!} D_{i_1 \cdots i_p | j_1 \cdots j_q} \mathrm{d}x^{i_1} \wedge \cdots \wedge \mathrm{d}x^{i_p} \mathrm{d}\bar{x}^{j_1} \wedge \cdots \wedge \mathrm{d}\bar{x}^{j_q}. \tag{23}$$

Vector and one-form valued double forms are defined accordingly.

Double currents

Double currents are linear functionals on spaces of double differential forms. Of specific importance are products of single currents. Note that the double form $\mathscr{D}^{p,q}$ may (with interchangeable perspective) be viewed as a differential p-form on M taking values in the vector space (consequently a trivial vector bundle) of q-forms on M. If a fixed q-dimensional current γ^q is applied to the resulting q-form at every x this yields a real number, and henceforth this composition defines a (real-valued) differential p-form D^p. For this operation we introduce the following notation

$$D^p \left(\gamma^q\right) := \gamma^q \left[\mathscr{D}^{p,q}\right]. \tag{24}$$

Likewise a p-dimensional current produces a q-form, which we write as

$$D^q \left(\gamma^p\right) := \gamma^p \left[\mathscr{D}^{p,q}\right]. \tag{25}$$

The resulting differential p- or q-form, respectively, may again be used as argument for a p- or q-dimensional current. We define this composition of two currents as their product

$$\gamma^q \gamma^p \left[\mathscr{D}^{p,q}\right] := \gamma^q \left[D^q \left(\gamma^p\right)\right] = \gamma^p \left[D^p \left(\gamma^q\right)\right]. \tag{26}$$

The product is commutative, that is $\gamma^p \gamma^q = \gamma^q \gamma^p$ and it defines a double current on M. The generalization to vector and one-form valued double currents is obvious.

3 Variational Methods and the Lie-Derivative of Currents

We discuss the case that a current γ_N is induced by a submanifold N of the crystal manifold M. A variation of the submanifold N is assumed to be given by a (variational) vector field $\tilde{v}$ along the manifold. This likewise induces a variation of the induced current, which is according to the transport theorem (17) given by

$$\tilde{\gamma}_N = -\mathscr{L}_{\tilde{v}}\gamma_N. \tag{27}$$

It seems worth noting that $\tilde{\gamma}_N$ is a tangent vector at γ_N to the space of currents. We now regard a functional $F^\phi\left[\gamma_N\right]$ on currents which is induced by a differential form ϕ whose degree equals the dimension of N, such that

$$F^\phi\left[\gamma_N\right] = \int_N \phi = \gamma_N[\phi]. \tag{28}$$

The Gâteaux differential $\mathrm{d}F^\phi$ (at 'point' N) is a linear operator mapping tangent vectors $\tilde{\gamma}_N$ to scalars. It is defined by

$$\mathrm{d}F^\phi\left[\tilde{\gamma}_N\right] = \lim_{t\to 0}\frac{F^\phi\left[\gamma_{N_t(\tilde{v})}\right] - F^\phi\left[\gamma_N\right]}{t}, \tag{29}$$

where $N_t\left(\tilde{v}\right)$ is the manifold which results from letting each point of N move with the flow of $\tilde{v}$ for time t. In other words the variational derivative was already given in the transport theorem (17), such that

$$\mathrm{d}F^\phi\left[\tilde{\gamma}_N\right] = -\mathscr{L}_{\tilde{v}}\gamma_N\left[\phi\right] = \gamma_N\left[\mathscr{L}_{\tilde{v}}\phi\right]. \tag{30}$$

For the vector valued case we work with the induced current γ_{N^X} of a submanifold N with an appended vector field X. The functional F^P shall be induced by an according differential form P which takes values in the dual space to the vector bundle of X, such that

$$F^P\left[\gamma_{N^X}\right] = \gamma_{N^X}[P] = \int_N P\dot{\wedge}X. \tag{31}$$

From the transport theorem for vector valued currents we obtain

$$\mathrm{d}F^P\left[\tilde{\gamma}_{N^X}\right] = -\mathscr{L}^{\nabla}_{\tilde{v}}\gamma_{N^X}\left[P\right] + \gamma_{N^{\tilde{X}}}\left[P\right] \tag{32}$$

where the variational current $\tilde{\gamma}_{N^X}$ is induced by the spatial variation $\tilde{v}$ and the variation of the vector field $\tilde{X} = \tilde{X}_t + \nabla_{\tilde{v}}X$.

4 Energetics of Dislocation

As we work consistently with vector valued differential forms, we adopt the understanding of [15, 18] that the stress tensor σ is most naturally viewed as a one-form valued two form

$$\sigma = \frac{1}{2}\sigma_{ijk}\,\mathrm{d}x^i \wedge \mathrm{d}x^j \otimes \mathrm{d}x^k. \tag{33}$$

The components of the usual (fully covariant) stress tensor may be obtained (for once employing the modified Einstein summation convention) through $\sigma_{ij} = \frac{1}{2}\varepsilon_{ikl}\sigma_{klj}$. The latter relation may be reversed to $\sigma_{ijk} = \varepsilon_{ijl}\sigma_{lk}$. We disregard the possibility of body forces in the sequel, such that the stress tensor is solenoidal, which means it is closed in differential form formalism, that is $\mathrm{d}^\nabla\sigma = 0$.

The interaction energy $E^{\mathrm{cr}}\left[\gamma_{c^b}\right]$ is considered as a functional on vector valued currents in the sense of the last Section. The interaction energy of a dislocation with a stress field is usually given in terms of the work done to create the according loop within the stress field. Let S denote a surface swept by the dislocation to create the loop $c = \partial S$. The work done in creating the loop is then taken to be given by the integral of the scalar product of the stress vector on the surface with the Burgers vector b. In the language of currents this is the application of the vector valued current induced by the swept surface combined with the Burgers vector S^b to the stress form, i.e.,

$$E^{\mathrm{cr}}\left[\gamma_{c^b}\right] = \gamma_{S^b}\left[\sigma\right] = \int_S \frac{1}{2}\sigma_{ijk}\,b^k \mathrm{d}x^i \wedge \mathrm{d}x^j. \tag{34}$$

Obviously, this definition only makes sense if this integral does not depended on the specific surface S whose boundary is the dislocation line c. We will briefly discuss this independence in Sect. 5.

Interaction energy

In this Section we define the interaction energy of two dislocations via a double integral over the dislocation lines. The integral kernel in this is in the current terminology a (each time) one-form valued (1, 1) form

$$\mathscr{E} = E_{ik|jl}\mathrm{d}x^k \otimes \mathrm{d}x^i \mathrm{d}\bar{x}^l \otimes \mathrm{d}\bar{x}^j. \tag{35}$$

The total interaction energy $E\left[\gamma_{c_1^b}, \gamma_{c_2^b}\right]$ of two dislocations c_1^b and c_2^b may then be defined in terms of a double current as

$$E\left[\gamma_{c_1^b}, \gamma_{c_2^b}\right] := \gamma_{c_1^b}\gamma_{c_2^b}\left[\mathscr{E}\right] = \int_{c_1}\int_{c_2} E_{ik|jl}\,b_1^k b_2^l \mathrm{d}x^i \mathrm{d}\bar{x}^j. \tag{36}$$

Explicit expressions for the interaction kernel are known since decades for isotropic elasticity in an infinite medium, e.g. [3, 6, 8]. But only recently, Lazar and Kirchner [19] presented a closed form expression for the case of anisotropic elasticity, which reads (once again applying the modified Einstein convention)

$$E_{ik|jl} = \varepsilon_{jmn} C_{lnpq} \varepsilon_{qri} C_{stkr} F^0_{tmps}, \tag{37}$$

where the fourth rank tensor F^0_{tmps} derives as a convolution of the elastic greens function tensor $G^0_{ps,tm}$ and the Greens function of the Laplace operator G^Δ as

$$F^0_{tmps} = -G^0_{ps,tm} * G^\Delta. \tag{38}$$

Very recently Lazar and co-workers [20] were able to derive an analogous formula for gradient elasticity, where only the Green functions have to be exchanged for those of the underlying gradient elasticity theory. This is possibly the most elegant way of dealing with the problem of self-energies which are not defined in the classical case where the integrand is singular on the dislocation line. With this in mind we will not go in any detail about the modeling of self energies and shall keep the double integral formulation also for a single dislocation, such that we formally write

$$E^{\text{self}}\left[\gamma_{c^b}\right] = \frac{1}{2} E\left[\gamma_{c^b}, \gamma_{c^b}\right], \tag{39}$$

where the factor $1/2$ corrects for double counting.

5 Variational Calculus Applied to Dislocation Energies

As a first application of the general variational formulas presented above we check the independence of the energy of creation $E^{\text{cr}}\left[\gamma_{c^b}\right]$ from the chosen surface S with $\partial S = c$. Locally, the value of the energy of creation is independent of the surface S, if the Gâteaux differential vanishes for any variational vector field $\tilde{v}_0$, which vanishes along the boundary line, $\tilde{v}_0 \circ c = 0$, thus maintaining $\partial S = c$. We denote the according tangent vector in the space of currents with $\tilde{\gamma}^0_{S^b}$. The independence of the energy from the specific surface is a consequence of the solenoidality of the stress tensor, as we find

$$\mathrm{d}_{S^b} E^{\text{cr}}\left[\tilde{\gamma}^0_{S^b}\right] = \int_S \mathscr{L}^{\nabla}_{\tilde{v}_0} \sigma \dot{\wedge} b \tag{40}$$

$$= \int_S \mathrm{d}^{\nabla} \iota_{\tilde{v}_0} \sigma \dot{\wedge} b + \iota_{\tilde{v}_0} \mathrm{d}^{\nabla} \sigma \dot{\wedge} b \tag{41}$$

$$= \int_S \mathrm{d}\left(\iota_{\tilde{v}_0} \sigma \dot{\wedge} b\right) \tag{42}$$

$$= \int_c \iota_{\tilde{v}_0} \sigma \dot{\wedge} b = 0. \tag{43}$$

In the above calculation we employed the product rule (8), the constancy of the Burgers vector ($\dot{b} = 0$), and the boundary condition $\tilde{v}_0 \circ c = 0$. All neighboring surfaces to S thus yield the same result for the creation energy and this consequently applies to all surfaces with the same boundary line which may be obtained from S by a continuous deformation *within* the crystal. Two surface with the same boundary line may for example *not* be continuously (without tearing) transformed into each other if the volume surrounded by them contains holes or inclusions. If we exclude the possibility of holes in the matrix[2] there is a potential one-form valued one-form (called the stress function tensor of first kind [19]) $\phi = \phi_{ij} \mathrm{d}x^i \otimes \mathrm{d}x^j$ available such that $\sigma = \mathrm{d}^\nabla \phi$. The exterior differential turns into a curl-relation in classical vector calculus. Using this potential we may directly turn the surface integral for the creation energy into a line integral along the dislocation by Stokes theorem (using $\nabla b = 0$)

$$E^{\mathrm{cr}} \left[\gamma_{c^b}\right] = \int_S \mathrm{d}^\nabla \phi \dot{\wedge} b = \int_{\partial S} \phi \dot{\wedge} b = \gamma_{c^b} \left[\phi\right]. \tag{44}$$

This formulation is well suited to inspect the result of varying the position of the dislocation c, as opposed to varying the position of the surface S. In this case we obtain the Gâteaux differential with regard to a vector field $\tilde{v}$ *along the curve*, and find

$$\mathrm{d}_{c^b} E^{\mathrm{cr}} \left[\tilde{\gamma}_{c^b}\right] = \int_c \mathscr{L}_{\tilde{v}}^\nabla \phi \dot{\wedge} b \tag{45}$$

$$= \int_c \mathrm{d}^\nabla \iota_{\tilde{v}} \phi \dot{\wedge} b + \iota_{\tilde{v}} \mathrm{d}^\nabla \phi \dot{\wedge} b \tag{46}$$

$$= \int_c \iota_{\tilde{v}} \sigma \dot{\wedge} b. \tag{47}$$

We expect this differential to be related to the Peach-Koheler force. To see this we write the one-form in the last integral in index notation and express it through the classical stress tensor $\tilde{v}^i \sigma_{\underset{\smile}{ijk}} b^k \mathrm{d}x^j = \tilde{v}^i \varepsilon_{ijl} \sigma_{lk} b^k \mathrm{d}x^j$. When the curve is parametrized by arc length s and if t denotes the unit tangent to the curve we easily find that

$$\mathrm{d}_{c^b} E^{\mathrm{cr}} \left[\tilde{\gamma}_{c^b}\right] = \int_c \tilde{v}^i \varepsilon_{ijl} \sigma_{lk} b^k t^j \mathrm{d}s = - \int_c \tilde{v}^i F_i \left(t, b\right) \mathrm{d}s, \tag{48}$$

---

[2] Regions without holes are called non-periphractic by Gurtin [7], a term which goes back to Maxwell [22]. In terms of modern topology this means that the second Betti number is zero, such that all closed two-forms are exact, saying that they may be obtained from some one-form (a potential) by exterior differentiation.

with the well-known Peach–Koehler force $F_i\,(t, b) = \epsilon_{ilj}\sigma_{lk}b^k t^j$. We thus found the Peach–Koehler force as a representation of the negative Gâteaux differential on the space of currents. This comes of courses at no surprise, because the Peach–Koehler force has been derived as a variational derivative of the interaction energy with the stress field from the outset [25].

However, the abstract Gâteaux differential is essential to understand how, and with regard to which Riemannian metric on the space of currents, classical equations of motion for dislocations actually define a gradient descent. We note that a gradient is a tangent vector as opposed to the differential which is a co-tangent vector. A Riemannian metric defines a linear way of mapping tangent vectors to co-vectors and vice versa. The gradient of a function, as opposed to its differential, will thus depend on the given Riemannian metric. The appropriate metric will as usual in the theory of gradient flow in dissipative systems be defined from the viscosity.[3] In linear overdamped dislocation theory (as usually assumed in discrete dislocation simulations) the dislocation velocity v is obtained from the Peach–Koehler force by a mobility tensor M^{ij} as $v = M^{ij} F_j \partial_i$. Note that the mobility tensor dependents on the Burgers vector, $M = M\,(b)$, though we will usually not state this explicitly. The velocity field then defines a tangent vector $-\mathscr{L}_v\gamma_{c^b}$ to the space of currents at γ_{c^b}, such that altogether we map the Gâteaux differential $\mathrm{d}_{c^b}E^{\mathrm{cr}}$ to a tangent (velocity) vector to the space of currents. Note that such a map would be defined through any non-linear mobility law as well. However, in the linear case, and if M is additionally positive definite, the so obtained evolution law may be understood as a gradient descent in the space of currents.[4] The Riemannian metric is defined by the viscosity tensor B_{ij}, which is the inverse of the mobility tensor M_{ij}, i.e., $B_{ik}M^{kj} = \delta_i{}^k$ and $M^{ik}B_{kj} = \delta^k{}_i$. We note that this implies $F_i = B_{ij}v^j$ for the velocity defined by the linear mobility law. The viscosity tensor defines a Riemannian metric on the tangent space of dislocations with Burgers vector b as follows

$$g_B\left(-\mathscr{L}_v\gamma_{c^b}, -\mathscr{L}_w\gamma_{c^b}\right) = \int_c v^i B_{ij}\,(b)\,w^j \mathrm{d}s. \tag{49}$$

With regard to the viscosity metric the gradient of the creation energy $\mathrm{grad}^B_{c^b}\,E^{\mathrm{cr}}$ at γ_{c^b} is defined as the tangent vector satisfying

$$g_B\left(\mathrm{grad}^B_{c^b}\,E^{\mathrm{cr}}, -\mathscr{L}_w\gamma_{c^b}\right) = \mathrm{d}_{c^b}E^{\mathrm{cr}}\left[-\mathscr{L}_w\gamma_{c^b}\right]. \tag{50}$$

---

[3] Compare [24], where Felix Otto puts it as follows: 'The merit of the right gradient flow formulation of a dissipative evolution equation is that it separates energetics and kinetics. The energetics endow the state space M with a functional E, the kinetics endow the state space with a Riemannian geometry via the metric tensor g.'

[4] If the mobility is for instance taken to be zero in the climb-direction, M^{ij} is not positive definite. In this case the tangent space to dislocations is restricted to variations within the glide plane, such that only the in-plane component of the Peach–Koehler force matters. If one then assumes M to be positive definite for vectors in the glide plane, all the following ideas remain valid.

By inserting $v^i = M^{ij} F_j$ into (49) we immediately verify that

$$-\operatorname{grad}^B_{c^b} E^{\mathrm{cr}} = -\mathscr{L}_{M^{ij} F_j \partial_i} \gamma_{c^b}, \tag{51}$$

and consequently

$$\partial_t \gamma_{c^b} = -\operatorname{grad}^B_{c^b} E^{\mathrm{cr}}. \tag{52}$$

From the fact that dislocations evolve by a gradient descent with respect to the metric g_B we also obtain the usual interpretation of the evolution of the energy. The energy will never increase, the decrease in energy is entirely dissipative, and it is quadratic in (dislocation) velocity and force,

$$\begin{aligned} \partial_t E^{\mathrm{cr}} \left[\gamma_{c^b}\right] &= -g_B \left(\operatorname{grad}^B_{c^b} E^{\mathrm{cr}}, \operatorname{grad}^B_{c^b} E^{\mathrm{cr}}\right) && (53) \\ &= -\int_c v^i B_{ij} v^j \mathrm{d}s && (54) \\ &= -\int_c v^i F_i \mathrm{d}s. && (55) \end{aligned}$$

Dislocation ensembles as interacting particle systems

The derivation of the Peach–Koehler force and the understanding of the usual equation of motion of dislocation lines as a steepest gradient descend in a space of currents is naturally transferred to the case of dislocations interacting by the interaction energy $E\left[c_1^b, c_2^b\right]$, if the Lie-derivative operation is applied to the according coordinates. That is, for two interacting dislocations, we obtain their evolution as

$$\partial_t \gamma_{c_i^b} = -\operatorname{grad}^B_{c_i^b} E\left[\gamma_{c_1^b}, \gamma_{c_2^b}\right], \quad \text{for } i = 1, 2. \tag{56}$$

We see that in this abstract form we may view a dislocation ensemble of N dislocations with total energy

$$E^{\mathrm{tot}} = \sum_{i=1}^{N} E^{\mathrm{cr}}\left[\gamma_{c_i^b}\right] + \frac{1}{2} \sum_{i=1}^{N} \sum_{j=1}^{N} E\left[\gamma_{c_i^b}, \gamma_{c_j^b}\right], \tag{57}$$

as an interacting 'particle' system, where each particle follows a steepest descent with regard to the viscosity metric g_B,

$$\partial_t \gamma_{c_i^b} = -\operatorname{grad}^B_{c_i^b} E^{\mathrm{tot}} = -\operatorname{grad}^B_{c_i^b} E^{\mathrm{cr}} - \sum_{j=1}^{N} \operatorname{grad}^B_{c_i^b} E\left[\gamma_{c_i^b}, \gamma_{c_j^b}\right]. \tag{58}$$

6 Summary and Outlook

In the current work we took an abstract approach to dislocation systems, which is designed for averaging static and dynamic dislocation systems. We consider dislocations as linear functionals on spaces of differential forms, i.e., as vector valued de Rham currents. A transport theorem for moving manifolds provided us with descriptions of tangent vectors to the space of currents and differentials of functions on the space of currents. Tangent vectors at a current are induced Lie-derivatives of the current in the direction of vector fields along the dislocation line. We showed that the Peach–Koehler force is a representation of the negative Gâteaux differential of the energy function on the space of currents. Moreover, the overdamped linear viscous drag law for dislocations as employed in discrete dislocation dynamics simulations was identified as a gradient flow on the space of currents with regard to a Riemannian metric induced by the viscosity tensor.

The interpretation of the dislocation evolution in terms of a gradient descent may not be very surprising. We motivated the current investigation from the underlying question, if the variational methods applied to a recently derived local density approximation for continuous dislocation systems may be justified from averaging the discrete case. This question is still open and far beyond the scope of this paper. But we may sketch in which sense we think the results of the current work will help understanding the variational approach to constitutive modeling in CDD as a gradient flow on spaces of differential forms. Like in the discrete case, the salient question in the continuum case is the definition of the right Riemannian metric on the density spaces [24]. For particle systems underlying porous media equations, the distance induced by the appropriate Riemannian metric is known as the Wasserstein distance (which actually goes back to Kantorovich [16]). The Wasserstein distance between two (normed) densities may be interpreted as the minimum energy needed to shift either of the density distributions into the other. The Wasserstein distance is closely related to the conservation law for densities ρ of point particles, i.e., for evolution equations of the form $\partial_t \rho = -\,\mathrm{div}\,(\rho v)$ [1]. If the densities are considered as differential three-forms $\omega = \rho dV$, where dV is the standard volume element, this evolution equation has the form of a Lie-derivative $\partial_t \omega = -\mathscr{L}_v \omega$. We note that the general theory of currents developed in this paper yields that tangent vectors to point particles interpreted as zero-dimensional currents γ_p are likewise of the form $-\mathscr{L}_v \gamma_p$, in full analogy to the finding for moving dislocations. We may therefore hope to generalized the concept of viscous Riemannian metrics and the Wasserstein distance to the evolution equations of the CDD density variables which have the structure of generalized conservation laws [10] deriving from Lie-derivatives in the discrete case.

Acknowledgements This paper is dedicated to Professor Reinhold Kienzler, who was a mentor for me during my time as 'Juniorprofessor' the Universtät Bremen, on the occasion of his official retirement.

I moreover gratefully acknowledge funding by the German Science Foundation DFG within the DFG Research Unit 'Dislocation based plasticity' FOR 1650 under project HO 4227/5-1.

References

1. Benamou, J.D., Brenier, Y.: A computational fluid mechanics solution to the Monge-Kantorovich mass transfer problem. Numer. Math. **84**(3), 375–393 (2000)
2. de Rham, G.: Differentiable Manifolds. Springer, Berlin (1984)
3. de Wit, R.: The continuum theory of stationary dislocations. Solid State Phys. **10**, 249–292 (1960)
4. Falach, L., Segev, R.: Reynolds transport theorem for smooth deformations of currents on manifolds. Math. Mech. Solids **20**(6), 770–786 (2015)
5. Frankel, T.: The Geometry of Physics: An Introduction, 3 edn. Cambridge University Press (2011)
6. Ghoniem, N.M., Sun, L.Z.: Fast-sum method for the elastic field of three-dimensional dislocation ensembles. Phys. Rev. B **60**(1), 128–140 (1999)
7. Gurtin, M.E.: A generalization of the Beltrami stress functions in continuum mechanics. Arch. Ration. Mech. Anal. **13**(1), 321–329 (1963)
8. Hirth, J.P., Lothe, J.: Theory of Dislocations. McGraw-Hill, New York (1968)
9. Hochrainer, T.: Moving dislocations in finite plasticity: a topological approach. ZAMM - J. Appl. Math. Mech. / Zeitschrift für Angewandte Mathematik und Mechanik. **93**(4) (2013)
10. Hochrainer, T.: Multipole expansion of continuum dislocations dynamics in terms of alignment tensors. Philos. Mag. **95**(12), 1321–1367 (2015)
11. Hochrainer, T.: Thermodynamically consistent continuum dislocation dynamics. J. Mech. Phys. Solids **88**, 12–22 (2016)
12. Hochrainer, T., Sandfeld, S., Zaiser, M., Gumbsch, P.: Continuum dislocation dynamics: towards a physically theory of plasticity. J. Mech. Phys. Solids **63**, 167–178 (2014)
13. Hochrainer, T., Zaiser, M.: Fundamentals of a Continuum Theory of Dislocations. PoS(SMPRI2005)002 (2006)
14. Hochrainer, T., Zaiser, M., Gumbsch, P.: A three-dimensional continuum theory of dislocations: kinematics and mean field formulation. Philos. Mag. **87**(8–9), 1261–1282 (2007)
15. Kanso, E., Arroyo, M., Tong, Y., Yavari, A., Marsden, J.E., Desbrun, M.: On the geometric character of stress in continuum mechanics. J. Appl. Math. Phys. (ZAMP) **58**, 1–14 (2007)
16. Kantorovitch, L.: On the translocation of masses. Manag. Sci. **5**(1), 1–4 (1958)
17. Kobayashi, S., Nomizu, K.: Foundations of Differential Geometry, vol. 1. Interscience Publishers, New York (1963)
18. Lazar, M.: On the fundamentals of the three-dimensional translation gauge theory of dislocations. Math. Mech. Solids **16**, 253–264 (2011)
19. Lazar, M., Kirchner, H.O.: Dislocation loops in anisotropic elasticity: displacement field, stress function tensor and interaction energy. Philos. Mag. **93**(1–3), 174–185 (2013)
20. Lazar, M., Po, G.: A Non-singular Theory of Dislocations in Anisotropic Crystals. ArXiv e-prints (2017)
21. Marsden, J.E., Hughes, T.J.R.: Mathematical Foundations of Elasticity. Dover Publications Inc., New York (1983)
22. Maxwell, J.C.: I.–On reciprocal figures, frames, and diagrams of forces. Trans. Royal Soc. Edinb. **26**(1), 140 (1870)
23. Monavari, M., Sandfeld, S., Zaiser, M.: Continuum representation of systems of dislocation lines: a general method for deriving closed-form evolution equations, J. Mech. Phys. Solids **95**, 575–601 (2016)
24. Otto, F.: The geometry of dissipative evolution equations: The porous medium equation. Commun. Partial Differ. Equ. **26**(1–2), 101–174 (2001)
25. Peach, M., Koehler, J.S.: The forces exerted on dislocations and stress fields produced by them. Phys. Rev. **80**(3), 436–439 (1950)
26. Zaiser, M.: Local density approximation for the energy functional of three-dimensional dislocation systems. Phys. Rev. B **92**, 120–174 (2015)

Optimum Design of Thick Laminated Anisotropic Plates via Frequency Regulation. A BEM Approach

J. T. Katsikadelis and N. G. Babouskos

Abstract The optimum design of a thick laminated anisotropic plate in order to regulate its dynamic response is studied. The optimization problem consists in establishing the ply orientation of each layer for which the fundamental frequency is maximized, minimized or forced to reach a prescribed value. The evaluation of the objective function requires the solution of the dynamic bending problem of a thick laminated plate which is solved using the Analog Equation Method (AEM) in conjunction with the Boundary Element Method (BEM). A nonlinear optimization problem is formulated and the optimum solution is obtained through the sequential quadratic programming algorithm. Several plate optimization problems have been studied giving realistic and meaningful optimum designs.

1 Introduction

Laminated plates made of various layers of anisotropic materials exhibit certain significant advantages over singled layer plates. For this reason they are extensively used in various engineering structures, like buildings, ship, aircrafts and space structures. Laminated plates give the designers the opportunity to optimize their response according to structural requirements. By changing the material principal directions of each layer, the number of the layers, their thickness or their sequence we can minimize the weight of the structure, maximize the buckling load, regulate natural frequencies or minimize the deflection of the plate.

J. T. Katsikadelis (✉) · N. G. Babouskos
School of Civil Engineering, National Technical University of Athens
Zografou Campus, Athens 15773, Greece
e-mail: jkats@central.ntua.gr

© Springer International Publishing AG 2018

H. Altenbach et al. (eds.), *Advances in Mechanics of Materials and Structural Analysis*, Advanced Structured Materials 80,
https://doi.org/10.1007/978-3-319-70563-7_10

Frequency regulation is of great importance in structures under dynamic excitation. By regulating (minimizing, maximizing or specifying) the fundamental or higher order natural frequencies, we can avoid the destructive consequences of various dynamic phenomena, like resonance and flutter instability.

The frequency optimization of thin and thick laminated plates has been studied by many researchers. Most of them investigate frequency optimization by maximizing the fundamental frequency using as design variables the fiber orientation and the thickness of each layer. Narita [1, 2], Apalak et al. [3] and Ghashochi [4] study frequency maximization of thin laminated plates using the Finite Element Method (FEM). Houmat [5] study frequency maximization assuming that fiber orientation may be position dependent within a layer of a thin plate.

Many researchers have shown that shear effects cannot be neglected even in thin laminated anisotropic plates, which are made of modern materials with increased ratio of Young to shear modulus [6]. Fares et al. [7] investigate optimal design of laminated plates using various plate theories. They optimize the dynamic response of the plate using as design variables the fiber orientation and the thickness of the layers. They concluded that Mindlin plate theory give results close to higher order theories in case of moderate thick laminated plates. Frequency optimization of Mindlin laminated plates has been studied by many researchers using FEM and gradient optimization methods [8–10]. Some researchers minimize the weight of the plate under a frequency constraint using as design variables the fiber orientation of each layer [11–13]. Modern evolutionary optimization methods have been also used in frequency optimization of thick laminated plates [14–16].

In this paper we consider the problem of frequency regulation of a thick laminated plate made of various orthotropic layers. The plate may have arbitrary geometry and is subjected to any type of boundary conditions. The optimization problem consists in determining the angle of the material principal direction of each layer (ply orientation) for which the plate fundamental frequency is optimized, i.e., it becomes minimum, maximum or reaches certain specified value between the extrema. The optimization problem is subjected to upper and lower bounds on ply orientation. The evaluation of the objective function (fundamental frequency) requires the solution of the free vibration problem of an anisotropic thick plate, which is described by a system of three coupled hyperbolic partial differential equations (PDE) of second order. Following the principle of the analog equation [17], the original system of equations is substituted by three uncoupled quasi-static Poisson's equation under fictitious loads. The Poisson's equations are solved using the conventional BEM [18] with constant boundary elements and linear triangular elements for domain discretization. The optimization problem is solved using sequential quadratic programming algorithm by a ready to use Matlab function. Several optimization problems for plates of various shapes and boundary conditions have been analyzed, yielding thus realistic and meaningful optimum designs.

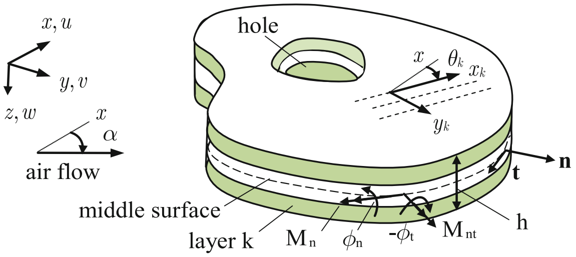

Fig. 1 Laminated thick plate

2 Statement of the Problem

2.1 Optimization Problem

We consider a thick elastic plate made of L orthotropic layers of uniform thickness occupying the two-dimensional multiply connected domain Ω in the xy-plane with the boundary $\Gamma = \cup_{i=0}^{i=K} \Gamma_i$ (Fig. 1). The nonintersecting curves $\Gamma_i \quad (i = 0, 1, 2, \ldots, K)$ may be piecewise smooth. The principal axes $(x_k y_k) \quad (k = 1, 2, \ldots, L)$ of the k-lamina may be inclined at an angle θ_k with respect to global coordinate system (Fig. 1). The plate may be simply supported, clamped or free along the boundary. The objective function of the problem is the fundamental frequency, which is obtained from the solution of the free vibration problem in absence of damping.

The optimization problem consists in determining the angles $\theta_k \quad (k = 1, 2, \ldots, L)$ for which the fundamental frequency becomes maximum or minimum or takes a certain specified value between them. Thus, the evaluation of the objective function requires the solution of the dynamic bending problem of an anisotropic thick plate.

2.2 The Equation of Motion of a Thick Laminated Anisotropic Plate

The Mindlin plate theory [19] is adopted to approximate the response of the thick plate. According to this theory the displacement field is given as

$$u(x, y, z) = z\phi_x(x, y), v(x, y, z) = z\phi_y(x, y), \quad w(x, y, z) = w(x, y) \tag{1a, b, c}$$

where w is the transverse deflection of the middle surface of the plate and ϕ_x, ϕ_y its rotations about y and x axis, respectively.

The constitutive equations of the $k = 1, 2, \ldots, L$ layer, which is made of an orthotropic material, are given as

$$\begin{Bmatrix} \sigma_x \\ \sigma_y \\ \tau_{xy} \end{Bmatrix}^k = \begin{bmatrix} C_{11} & C_{12} & C_{16} \\ C_{12} & C_{22} & C_{26} \\ C_{16} & C_{26} & C_{66} \end{bmatrix}^k \begin{Bmatrix} z\phi_{x,x} \\ z\phi_{y,y} \\ z(\phi_{x,y} + \phi_{y,x}) \end{Bmatrix} \tag{2}$$

$$\begin{Bmatrix} \tau_{xz} \\ \tau_{yz} \end{Bmatrix}^k = \begin{bmatrix} C_{55} & C_{45} \\ C_{45} & C_{44} \end{bmatrix}^k \begin{Bmatrix} \phi_x + w,_x \\ \phi_y + w,_y \end{Bmatrix} \tag{3}$$

where C_{ij} are the elastic constants of the orthotropic material as transformed from the material axes (x_k, y_k) to the global axes (x, y) [17, 20]. Thus, the stress resultants are

$$\begin{Bmatrix} M_x \\ M_y \\ M_{yx} \end{Bmatrix} = \sum_{k=1}^{L} \int_{z_k}^{z_{k+1}} \begin{Bmatrix} \sigma_x \\ \sigma_y \\ \tau_{xy} \end{Bmatrix}^k z dz = \begin{bmatrix} D_{11} & D_{12} & D_{16} \\ D_{12} & D_{22} & D_{26} \\ D_{16} & D_{26} & D_{66} \end{bmatrix} \begin{Bmatrix} \phi_{x,x} \\ \phi_{y,y} \\ \phi_{x,y} + \phi_{y,x} \end{Bmatrix} \tag{4}$$

$$\begin{Bmatrix} Q_x \\ Q_y \end{Bmatrix} = K_s \sum_{k=1}^{L} \int_{z_k}^{z_{k+1}} \begin{Bmatrix} \tau_{xz} \\ \tau_{yz} \end{Bmatrix}^k dz = \begin{bmatrix} A_{55} & A_{45} \\ A_{45} & A_{44} \end{bmatrix} \begin{Bmatrix} \phi_x + w,_x \\ \phi_y + w,_y \end{Bmatrix} \tag{5}$$

where K_s is the shear correction factor.

By taking the first variation of the total potential of the plate [17], we obtain the equations of motion of the plate in terms of the stress resultants

$$\frac{\partial M_x}{\partial x} - \frac{\partial M_{xy}}{\partial y} - Q_x = I_2 \ddot{\phi}_x \tag{6a}$$

$$\frac{\partial M_{yx}}{\partial x} + \frac{\partial M_y}{\partial y} - Q_y = I_2 \ddot{\phi}_y \tag{6b}$$

$$\frac{\partial Q_x}{\partial x} + \frac{\partial Q_y}{\partial y} = I_1 \ddot{w} \tag{6c}$$

where I_1, I_2

$$I_1 = \int_{-h/2}^{h/2} \rho(z) dz, \quad I_2 = \int_{-h/2}^{h/2} z^2 \rho(z) dz \tag{7a,b}$$

with $\rho(z)$ being the density variation through the thickness. Note that the twisting moments M_{xy}, M_{yx} are positive when they have the direction of the outward normal to the cross section [17].

The associated boundary and initial conditions are:

$$\alpha_1 w + \alpha_2 Q_n = \alpha_3 \tag{8a}$$

$$\beta_1 \phi_n + \beta_2 M_n = \beta_3 \tag{8b}$$

$$\gamma_1\phi_t + \gamma_2 M_{nt} = \gamma_3 \tag{8c}$$

$$w(x, y, 0) = g_1^{(1)}(x, y), \quad \dot{w}(x, y, 0) = g_2^{(1)}(x, y) \tag{8d}$$

$$\phi_x(x, y, 0) = g_1^{(2)}(x, y), \quad \dot{\phi}_x(x, y, 0) = g_2^{(2)}(x, y) \tag{8e}$$

$$\phi_y(x, y, 0) = g_1^{(3)}(x, y), \quad \dot{\phi}_y(x, y, 0) = g_2^{(3)}(x, y) \tag{8f}$$

where

$$Q_n = Q_x n_x + Q_y n_y, \quad M_n = M_x n_x^2 + M_y n_y^2 + 2n_x n_y M_{yx} \tag{9a,b}$$

$$M_{nt} = M_{xy}(n_x^2 - n_y^2) + n_x n_y (M_x - M_y) \tag{9c}$$

$$\phi_n = n_x\phi_x + n_y\phi_y, \quad \phi_t = -n_y\phi_x + n_x\phi_y \tag{9d,e}$$

with n_x and n_y being the direction cosines of the normal to the boundary (Fig. 1). It is not necessary to specify the functions $g_1^{(i)}(x, y)$, $g_2^{(i)}(x, y)$, $(i = 1, 2, 3)$ of the initial conditions Eq. (8d), (8e), (8f), since we are interested on the evaluation of the natural frequencies of the plate.

All types of boundary conditions can be derived from Eqs. (8a), (8b), (8c) by appropriate selection of the parameters $\alpha_i, \beta_i, \gamma_i$ $(i = 1, 2, 3)$. Thus an edge is:

(i) clamped for $\alpha_1 = \beta_1 = \gamma_1 = 1$ and $\alpha_2 = \beta_2 = \gamma_2 = 0$, $\alpha_3 = \beta_3 = \gamma_3 = 0$
(ii) simply supported of type I (hard) for $\alpha_1 = \beta_2 = \gamma_1 = 1$ and $\alpha_2 = \beta_1 = \gamma_2 = \alpha_3 = \beta_3 = \gamma_3 = 0$,
(iii) simply supported of type II (soft) for $\alpha_1 = \beta_2 = \gamma_2 = 1$ and $\alpha_2 = \beta_1 = \gamma_1 = \alpha_3 = \beta_3 = \gamma_3 = 0$
(iv) free for $\alpha_2 = \beta_2 = \gamma_2 = 1$ and $\alpha_1 = \beta_1 = \gamma_1 = \alpha_3 = \beta_3 = \gamma_3 = 0$.

Substituting Eqs. (4) and (5) in Eq. (6) we obtain the equations of motion in terms of the displacements

$$\begin{aligned} &D_{11}\phi_{x,xx} + 2D_{16}\phi_{x,xy} + D_{66}\phi_{x,yy} + D_{16}\phi_{y,xx} + (D_{12} + D_{66})\phi_{y,xy} \\ &\qquad + D_{26}\phi_{y,yy} - A_{55}(\phi_x + w,_x) - A_{45}(\phi_y + w,_y) = I_2\ddot{\phi}_x \end{aligned} \tag{10a}$$

$$\begin{aligned} &D_{66}\phi_{y,xx} + 2D_{26}\phi_{y,xy} + D_{22}\phi_{y,yy} + D_{16}\phi_{x,xx} + (D_{12} + D_{66})\phi_{x,xy} \\ &\qquad + D_{26}\phi_{x,yy} - A_{45}(\phi_x + w,_x) - A_{44}(\phi_y + w,_y) = I_2\ddot{\phi}_y \end{aligned} \tag{10b}$$

$$A_{55}(\phi_{x,x} + w_{xx}) + A_{45}(\phi_{x,y} + \phi_{y,x} + 2w_{xy}) - A_{44}(\phi_{y,y} + w,_{yy}) = I_1\ddot{w} \tag{10c}$$

2.3 Evaluation of the Objective Function

The initial-boundary value problem of Eqs. (8) and (10) is solved using the AEM [17]. Since the governing Eq. (11) represents a system of three coupled second order PDEs with respect to spatial coordinates, the analog equations are:

$$\nabla^2 w = b_1(x, y, t), \quad \nabla^2 \phi_x = b_2(x, y, t), \quad \nabla^2 \phi_y = b_3(x, y, t) \qquad (11a, b, c)$$

where b_1, b_2 and b_3 are time dependent fictitious sources, unknown in the first instance. Equations (11a,b,c) are quasi-static equations, that is the time appears as a parameter, or in other words the equations are instantaneous elliptic. Their solution is given in integral form as [18]

$$\varepsilon w(\mathbf{x}, t) = \int_\Omega u^* b_1(\mathbf{y}) d\Omega_\mathbf{y} - \int_\Gamma (u^* w,_n - u,_n^* w) ds_\xi \qquad (12a)$$

$$\varepsilon \phi_x(\mathbf{x}, t) = \int_\Omega u^* b_2(\mathbf{y}) d\Omega_\mathbf{y} - \int_\Gamma (u^* \phi_x,_n - u,_n^* \phi_x) ds_\xi \qquad (12b)$$

$$\varepsilon \phi_y(\mathbf{x}, t) = \int_\Omega u^* b_3(\mathbf{y}) d\Omega_\mathbf{y} - \int_\Gamma (u^* \phi_y,_n - u,_n^* \phi_y) ds_\xi \qquad (12c)$$

in which $\mathbf{x} \in \Omega \cup \Gamma$, $\mathbf{y} \in \Omega$, $\xi \in \Gamma$; $u^* = \ln r / 2\pi$ is the fundamental solution of the Poisson's equation, i.e., Eq. (11a); $r = \|\mathbf{y} - \mathbf{x}\|$ in domain integrals and $r = \|\xi - \mathbf{x}\|$ in boundary integrals; ε is the free term coefficient ($\varepsilon = 1$ if $\mathbf{x} \in \Omega, \varepsilon = a/2\pi$ if $\mathbf{x} \in \Gamma$and $\varepsilon = 0$ if $\mathbf{x} \notin \Omega \cup \Gamma$; a is the interior angle between the tangents of boundary at point $\mathbf{x}$; $\varepsilon = 1/2$ for points where the boundary is smooth (Fig. 2a)). The subscript in the differentials, i.e., $d\Omega_\mathbf{y}$ and ds_ξ, denotes the point with respect to which the integration is performed. Eq. (12) are solved numerically using the BEM. The boundary integrals are approximated using N constant boundary elements, whereas the domain integrals are approximated using linear triangular elements resulting in total M domain nodal points (Fig. 2b). The domain discretization is performed automatically using the Delaunay triangulation. Since the fictitious source is not defined on the boundary, the nodal points of the triangles adjacent to the boundary are not placed on the vertices of the tringle but on their sides (Fig. 2c). A detailed description of integration procedure is found in [17].

Thus, after discretization and application of Eqs. (12a)–(12c) at the N boundary nodal points we obtain

$$\mathbf{H} \begin{Bmatrix} \mathbf{w} \\ \phi_x \\ \phi_y \end{Bmatrix} + \mathbf{A} \begin{Bmatrix} \mathbf{b_1} \\ \mathbf{b_2} \\ \mathbf{b_3} \end{Bmatrix} = \mathbf{G} \begin{Bmatrix} \mathbf{w_{,n}} \\ \phi_{\mathbf{x,n}} \\ \phi_{\mathbf{y,n}} \end{Bmatrix} \qquad (13)$$

where $\mathbf{H}, \mathbf{G}$ are $3N \times 3N$ known matrices originating from the integration of the kernel functions on the boundary elements and $\mathbf{A}$ is an $3N \times 3M$ coefficient matrix

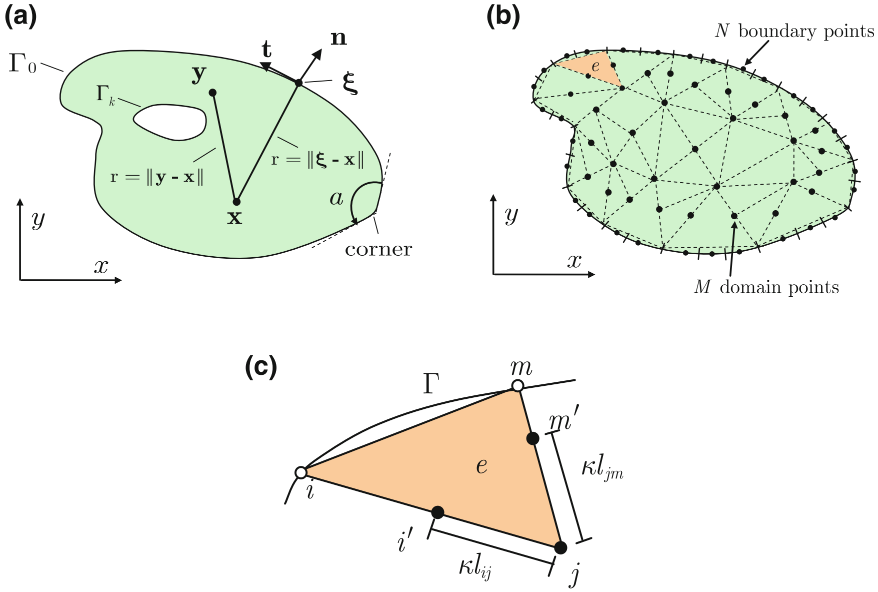

Fig. 2 **a** BEM notation; **b** boundary and domain discretization; **c** triangle adjacent to the boundary (l_{jm}, l_{im} side lengths, $0 < \kappa < 1$)

originating from the integration of the kernel function on the domain elements; $\mathbf{b}_1(t)$, $\mathbf{b}_2(t)$, $\mathbf{b}_3(t)$ are vectors containing the values of the fictitious loads at the M domain points at instant t. Applying the boundary conditions, Eqs. (8a), (8b), (8c), at the N boundary nodal points and using Eqs. (9d,e) we obtain

$$\bar{\mathbf{H}} \begin{Bmatrix} \mathbf{w} \\ \phi_x \\ \phi_y \end{Bmatrix} + \bar{\mathbf{G}} \begin{Bmatrix} \mathbf{w}_{,\mathbf{n}} \\ \phi_{\mathbf{x},\mathbf{n}} \\ \phi_{\mathbf{y},\mathbf{n}} \end{Bmatrix} = \begin{Bmatrix} \alpha_3 \\ \beta_3 \\ \gamma_3 \end{Bmatrix} \tag{14}$$

The tangential derivatives of $\phi_{x,t}$, $\phi_{y,t}$, which appear in the boundary conditions, are expressed in terms of ϕ_x, ϕ_y using a finite difference scheme. Equations (13) and (14) constitute a system of $6N$ algebraic equations which can be solved for the boundary quantities w, ϕ_x, ϕ_y, $w_{,n}$, $\phi_{x,n}$, $\phi_{y,n}$. Substituting the boundary quantities in the discretized counterpart of Eqs. (12) we obtain the displacements w, ϕ_x, ϕ_y and their derivatives at the M domain nodal points in terms of the fictitious loads

$$\mathbf{w}_{,pq}(t) = \mathbf{W}^{(1)}_{,pq}\mathbf{b}_1(t) + \mathbf{W}^{(2)}_{,pq}\mathbf{b}_2(t) + \mathbf{W}^{(3)}_{,pq}\mathbf{b}_3(t) \tag{15a}$$

$$\phi_{x,pq}(t) = \mathbf{S}^{(1)}_{,pq}\mathbf{b}_1(t) + \mathbf{S}^{(2)}_{,pq}\mathbf{b}_2(t) + \mathbf{S}^{(3)}_{,pq}\mathbf{b}_3(t) \tag{15b}$$

$$\phi_{y,pq}(t) = \mathbf{V}^{(1)}_{,pq}\mathbf{b}_1(t) + \mathbf{V}^{(2)}_{,pq}\mathbf{b}_2(t) + \mathbf{V}^{(3)}_{,pq}\mathbf{b}_3(t) \tag{15c}$$

where $p, q = 0, x, y$ and $\mathbf{W}^{(i)}_{,pq}, \mathbf{S}^{(i)}_{,pq}, \mathbf{V}^{(i)}_{,pq}$ $(i = 1, 2, 3)$ are $M \times M$ known matrices. Finally, collocating the governing Eqs. (10a), (10b), (10c) at the M domain nodal points and substituting the displacements and their derivatives from Eqs. (15), we obtain the equations of motion in terms of the fictitious loads $\mathbf{b}_1, \mathbf{b}_2, \mathbf{b}_3$

$$\mathbf{M}\ddot{\mathbf{a}} + \mathbf{K}\mathbf{a} = \mathbf{0} \tag{16}$$

where $\mathbf{M}, \mathbf{K}$ are the $3M \times 3M$ mass matrix and stiffness matrix, respectively; $\mathbf{a} = \left\{ \mathbf{b}_1 \ \mathbf{b}_2 \ \mathbf{b}_3 \right\}^T$ is a $3M \times 1$ vector with the values of the fictitious loads at instant t.

In order to evaluate the natural frequencies of the plate we assume a time harmonic solution

$$\mathbf{a}(t) = \beta e^{i\omega t} \tag{17}$$

where β is a vector of time independent parameters and ω the frequency of the vibration. Substituting Eq. (17) in (16) we obtain

$$\left(-\omega^2 \mathbf{M} + \mathbf{K}\right) \ \beta = 0 \tag{18}$$

Equation (18) is an eigenvalue problem which is solved numerically by ready to use program (Matlab function). The first eigenfrequency is the objective function of the optimization problem.

2.4 The Optimization Procedure

The frequency optimization problem reads:

$$\text{maximize } \omega_1 \text{ or minimize } \omega_1 \text{ or minimize } (1 - \omega_1/\omega_{pr})^2 \tag{19}$$

under the constraints of lower θ_l and upper θ_u bounds

$$\theta_l < \theta_k < \theta_u \tag{20}$$

where $\omega_1 = \omega_1(\theta_1, \theta_2, ..., \theta_k)$ is the fundamental frequency of the plate and ω_{pr} a prescribed value between the bounds.

The optimization problem is solved with the sequential quadratic programming (SQP) algorithm using Matlab function *fmincon*. This method belongs to the classical gradient based methods. The optimum solution is regarded as a local optimum. The global optimum can be obtained by exhaustive search of the design space starting the optimization procedure from various initial solutions.

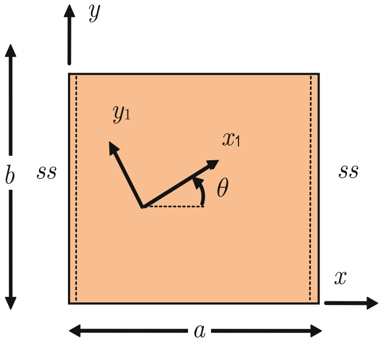

Fig. 3 Rectangular laminated plate of Example 1

3 Examples

Example 1 As a first example we optimize a rectangular $a \times b$ laminated plate with thickness $h = 0.1a$ made of two layers of orthotropic material with stacking sequence $(\theta, -\theta)$. The material parameters are: $E_1 = 132.38$GPa, $E_2 = 10.76$GPa, $G_{12} = G_{13} = 5.65$GPa, $G_{23} = 3.61$GPa, $\nu_{12} = 0.25$. The plate is simply supported (type I) along the sides $x = 0, a$ while various types of boundary conditions are considered for the sides $y = 0, b$, more specifically (Fig. 3):

(i) simply supported at $y = 0, b$;
(ii) clamped at $y = 0$ and simply supported at $y = b$
(iii) clamped at $y = 0, b$
(iv) free at $y = 0$ and simply supported at $y = b$
(v) free at $y = 0$ and clamped at $y = b$

The results were obtained using $N = 200$ boundary elements and $M = 181$ domain points resulting from 300 triangular elements (Fig. 4). Figure 5 presents the non-dimensional fundamental frequency $\bar{\omega}_1 = \omega_1 a\sqrt{\rho/E_2h^2}$ versus angle θ for the different boundary conditions of the analyzed square plate. The results are compared with those obtained by Levy-type solution [20] for three angles, i.e., $\theta = 30, 45, 60$. Table 1 presents the optimum value of angle θ for maximum fundamental frequency for the considered types of boundary conditions of the square plate. Finally, Fig. 6 presents optimum angle θ for maximum fundamental frequency versus aspect ratio a/b for three different boundary conditions. It is observed that the optimum ply orientation of each lamina tends to be parallel to one of the plate sides as the aspect ratio increases. Note the notation for the opposite sides: ss = both simply supported; cc = both clamped; cs = clamped-simply supported; fs = free-simply supported; fc = free-clamped.

Example 2 A rectangular thick laminated plate $a \times b$ consisting of four layers of equal thickness made of orthotropic material is optimized. The elastic parameters are: $E_1 = 40E_2$, $G_{12} = G_{13} = 0.6E_2$, $G_{23} = 0.5E_2$, $\nu_{12} = 0.25$, $E_2 = 1$GPa. The plate is simply supported (type I) along the boundary. The total thickness

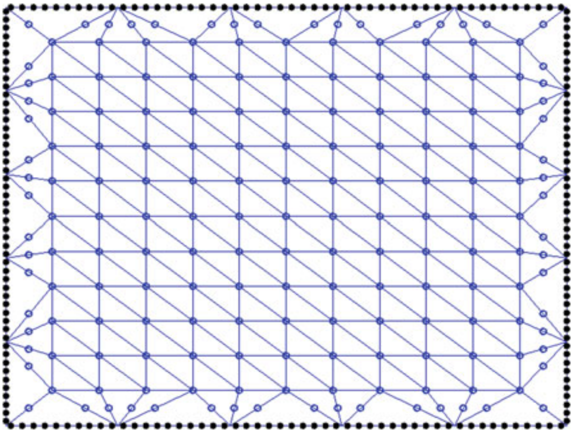

Fig. 4 Boundary and domain discretization of rectangular plate in Example 1

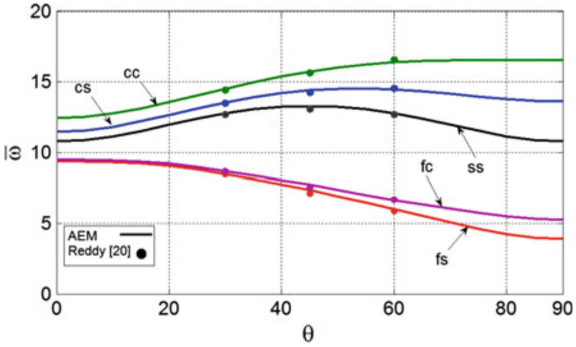

Fig. 5 Frequency $\bar{\omega}_1$ versus angle θ ($0 \leq \theta \leq 90$) for the various cases of the boundary conditions in Example 1

Table 1 Optimum angle θ for maximum fundamental frequency in Example 1

Boundary condition	ss	cs	cc	fs	fc
$\theta_{optimum}$	45	55	75	0	0
$\bar{\omega}_{1max}$	13.27	14.53	16.54	9.35	9.46

of the plate is $h = 0.1a$. Two cases of stacking sequence are studied: symmetric $(\theta_1, \theta_2, \theta_2, \theta_1)$ and antisymmetric $(\theta_1, \theta_2, -\theta_2, -\theta_1)$. The results were obtained using $N = 200$ boundary elements and $M = 133$ domain points resulting from 212 triangular elements. Figures 7 and 8 present the non-dimensional fundamental frequency $\bar{\omega}_1 = \omega_a\sqrt{\rho/E_2h^2}$ versus angles θ_1 and θ_2 for symmetric and antisymmetric laminates for the square ($a = b$) and a rectangular plate ($b = a/2$), respectively. It is observed that there are various local optimum solutions for a maximum or minimum fundamental frequency. Tables 2 and 3 present the optimum angles θ_1 and θ_2 for maximum fundamental frequency, starting from different initial values of the

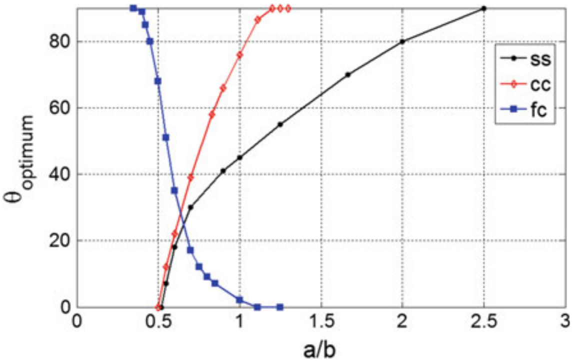

Fig. 6 Optimum angle θ versus aspect ratio a/b for three different boundary conditions in Example 1

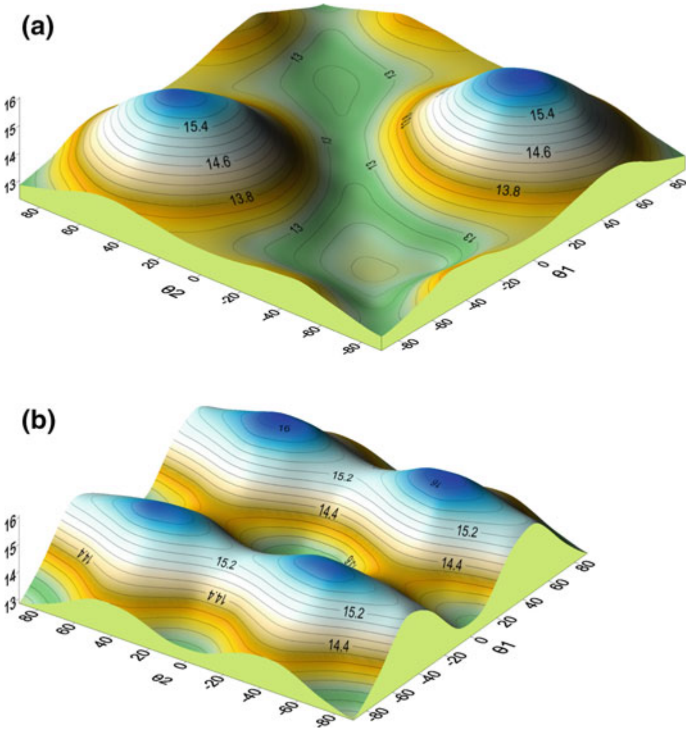

Fig. 7 Frequency $\bar{\omega}_1$ versus angle θ_1 and θ_2 for **a** symmetric and **b** antisymmetric square plate in Example 2

design variables. Finally, Tables 4 and 5 present local optimum sets of θ_1 and θ_2 for minimum fundamental frequency.

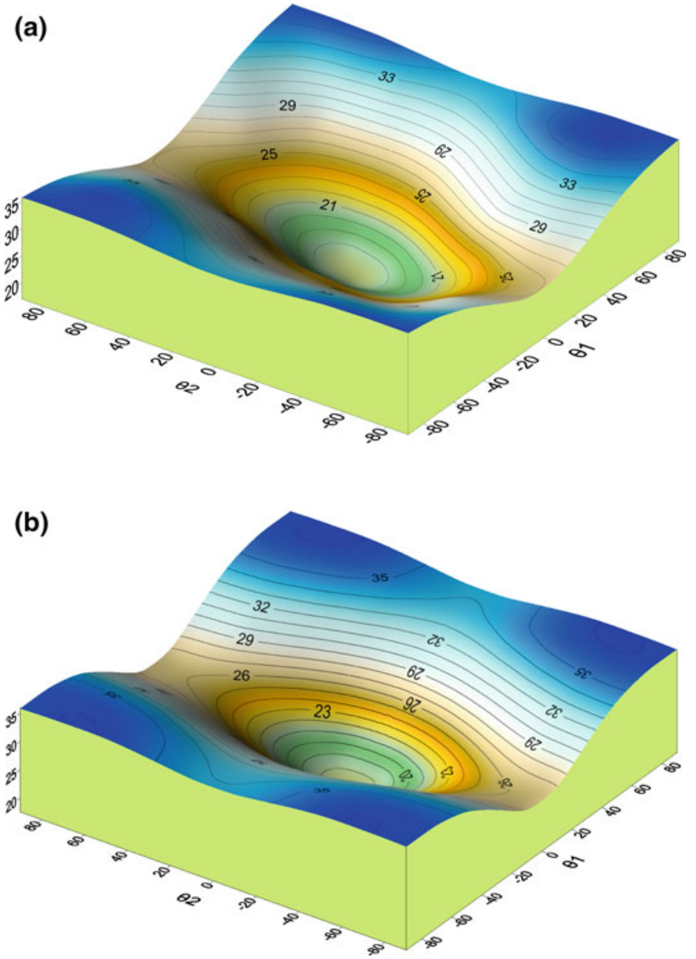

Fig. 8 Frequency $\bar{\omega}_1$ versus angles θ_1 and θ_2 for **a** symmetric and **b** antisymmetric rectangular plate $a \times (a/2)$ in Example 2

Example 3 The laminated cantilever plate of Fig. 9a simulating an airplane wing is optimized. The plate consists of 5 layers with total thickness $h = 0.2\,\text{m}$ (Fig. 9b). The face sheets (layers 1 and 5) are made of isotropic material with elastic parameters $E = 70\,\text{GPa}$, $\nu = 0.333$, mass density $\rho = 2.7\,\text{kNs}^2/\text{m}^{-4}$ and thickness $h_s = 0.01\,\text{m}$. The core with thickness $h_c = 0.18\,\text{m}$ consists of three layers of equal thickness made of orthotropic material in sequence $(\theta_1, \theta_2, \theta_3)$ with elastic parameters $E_1 = 25E_2$, $G_{12} = G_{13} = 0.5E_2$, $G_{23} = 0.2E_2$, $E_2 = 10\,\text{GPa}$, $\nu_{12} = 0.25$ and mass density $\rho = 1.55\,\text{kNs}^2/\text{m}^{-4}$. The results were obtained with $N = 310$ boundary elements and $M = 215$ internal nodal points resulting from 350 linear triangular elements (Fig. 9c). Tables 6 and 7 present the initial and the optimum set of the design variables for the

Table 2 Optimum angles θ_1 and θ_2 for maximum fundamental frequency $\bar{\omega}_1$ of a square plate in Example 2

	Initial		Optimum		max $\bar{\omega}_1$
	θ_1	θ_2	θ_1	θ_2	
Symmetric	−20	20	−45.19	45.10	16.24
	20	−20	44.74	−44.99	16.39
	20	20	90	45.12	14.01
	−20	−20	−90	−45.58	13.90
Antisymmetric	20	20	44.85	44.96	16.39
	−20	−20	−45.15	−45.10	16.24
	20	−20	44.80	−44.95	16.39
	−20	20	−45.15	45.10	16.24

Table 3 Optimum angles θ_1 and θ_2 for maximum fundamental frequency $\bar{\omega}_1$ of a rectangular plate $a \times a/2$ in Example 2

	Initial		Optimum		max $\bar{\omega}_1$
	θ_1	θ_2	θ_1	θ_2	
Symmetric	60	−60	79.01	−64.08	36.31
	60	60	90.00	68.93	36.03
	−60	60	−80.40	63.72	36.45
Antisymmetric	60	60	84.21	62.74	36.37
	60	−40	84.21	62.74	36.37
	−40	−40	84.20	62.74	36.37

Table 4 Optimum angles θ_1 and θ_2 for minimum fundamental frequency $\bar{\omega}_1$ of a square plate in Example 2

	Initial		Optimum		min $\bar{\omega}_1$
	θ_1	θ_2	θ_1	θ_2	
Symmetric	10	10	−1.01	0.01	13.11
	−60	20	−88.72	0.01	13.54
	−60	−60	−88.85	−90.00	13.11
Antisymmetric	−60	−60	−58.62	−58.35	12.98
	60	60	58.51	58.37	12.86
	60	−60	90.00	−88.89	13.11

maximum, minimum as well as for a specified value of the fundamental frequency. Figures 10 and 11 present the fundamental frequency versus θ_1, θ_2 and θ_3 (Table 8).

Table 5 Optimum angles θ_1 and θ_2 for minimum fundamental frequency $\bar{\omega}_1$ of rectangular plate $a \times a/2$ in Example 2

	Initial		Optimum		min $\bar{\omega}_1$
	θ_1	θ_2	θ_1	θ_2	
Symmetric	20	20	−1.90	−1.90	17.18
	−60	60	−1.89	−1.90	17.18
	60	−60	−1.91	−1.92	17.18
Antisymmetric	40	40	−0.56	0.012	17.43
	40	−40	−0.56	0.012	17.43
	−60	60	−0.56	0.012	17.43

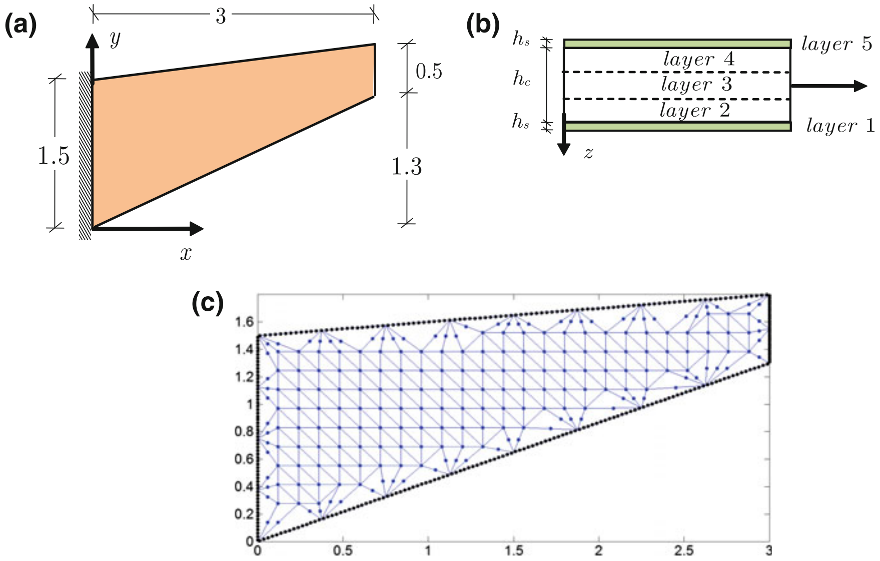
(a)
3
y
0.5
1.5
1.3
x
(b)
h_s
h_c
h_s
layer 5
layer 4
layer 3
layer 2
layer 1
z
(c)
1.6
1.4
1.2
1
0.8
0.6
0.4
0.2
0
0
0.5
1
1.5
2
2.5
3

Fig. 9 **a** Geometry of cantilever plate, **b** stacking sequence and **c** boundary and domain discretization in Example 3

Table 6 Initial and optimum angles θ_1, θ_2 and θ_3 for maximum fundamental frequency ω_1 of the cantilever plate in Example 3

Initial			Optimum			max ω_1
θ_1	θ_2	θ_3	θ_1	θ_2	θ_3	
0	0	0	11.87	11.06	11.76	317.91
60	60	60	11.91	10.84	11.76	317.91
−10	−20	−10	11.93	10.81	11.74	317.91

Table 7 Initial and optimum angles θ_1, θ_2 and θ_3 for minimum fundamental frequency ω_1 of the cantilever plate in Example 3

Initial			Optimum			min ω_1
θ_1	θ_2	θ_3	θ_1	θ_2	θ_3	
0	0	0	−89.24	90	−89.94	109.92
0	−30	0	84.47	−67.64	−90.00	108.10
70	70	−20	−90	−69.63	−490	108.48

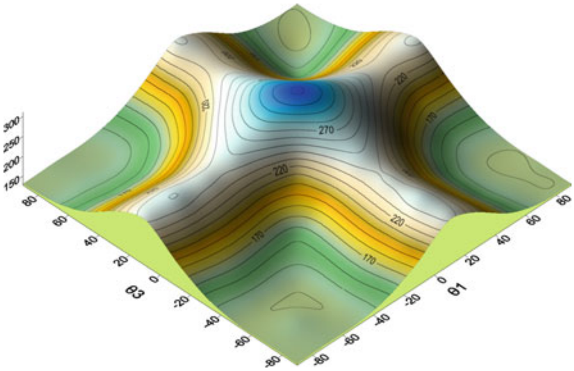

Fig. 10 Fundamental frequency versus angle θ_1 and θ_3 for $\theta_2 = 11.06^0$ in Example 3

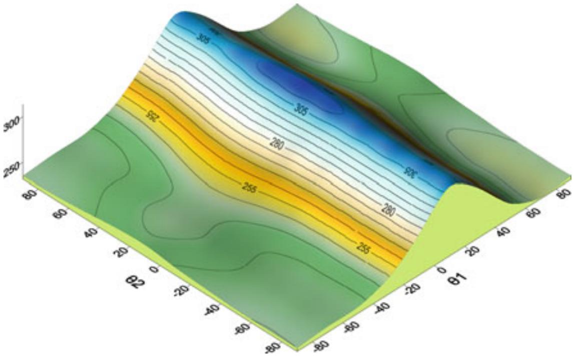

Fig. 11 Fundamental frequency versus angle θ_1 and θ_2 for $\theta_3 = 11.76^0$ in Example 3

Table 8 Initial and optimum angles θ_1, θ_2 and θ_3 for specified fundamental frequency $\omega_1 = 250$ of the cantilever plate in Example 3

Initial			Optimum			
θ_1	θ_2	θ_3	θ_1	θ_2	θ_3	
0	0	0	−9.73	4.87	−9.88	w_1=250
20	20	0	31.50	21.25	−25.52	
20	0	20	29.54	0.90	29.54	

4 Conclusions

The problem of frequency regulation of a thick laminated plate made of various orthotropic layers is studied. The plate may have arbitrary geometry and is subjected to any type of boundary conditions. The optimization problem consists in determining the angle of the material principal direction of each layer (ply orientation) for which the plate fundamental frequency is optimized, i.e., it becomes minimum, maximum or reaches certain specified value between the extrema. The optimization problem is subjected to upper and lower bounds on ply orientation. The fundamental frequency (objective function) is evaluated by the solution of the free vibration problem of a thick anisotropic plate. This problem is described by a system of three coupled hyperbolic partial differential equations (PDE) of second order. Using the AEM the coupled PDEs are converted into three uncoupled quasi-static Poisson's equations, which are solved by the conventional BEM with constant boundary elements and linear triangular elements for domain discretization. The optimization problem is solved using sequential quadratic programming algorithm by a ready-to-use Matlab function.

Several optimization problems for plates of various shapes and boundary conditions have been analyzed, yielding realistic and meaningful optimum designs. The main conclusions of the presented investigation are:

(a) The fundamental frequency of a thick laminated plate can change considerably (more than 100%) by optimizing the ply orientation of its layers.
(b) The design space includes many local optima and requires exhaustive search, starting the optimization procedure from various initial points. Otherwise modern evolutionary methods should be included in the optimization procedure.
(c) In rectangular plates the optimum ply-orientation for maximum fundamental frequency tends to be parallel to one of its sides as the aspect ratio increases.

References

1. Narita, Y.: Layerwise optimization for the maximum fundamental frequency of laminated composite plates. J. Sound Vib. **263**, 1005–1016 (2003)
2. Yoshihiro, Narita: Maximum frequency design of laminated plates with mixed boundary conditions. Int. J. Solids Struct. **43**, 4342–4356 (2006)
3. Apalak, K.M., Yildirim, M., Ekici, R.: Layer optimization for maximum fundamental frequency of laminated composite plates for different edge conditions. Compos.Sci. Technol. **68**, 537–550 (2008)
4. Ghashochi, B.H., Sadr, M.H.: Stacking sequence optimization of composite plates for maximum fundamental frequency using particle swarm optimization algorithm. Meccanica **47**, 719–730 (2012)
5. Houmat, A.: Optimal lay-up design of variable stiffness laminated composite plates by a layerwise optimization technique. Eng. Optim. (2017). https://doi.org/10.1080/0305215X.2017.1307978
6. Pai, P.: A new look at shear correction factors and warping functions of anisotropic laminates. Int. J. Solids Struct. **32**(16), 2295–2313 (1995)

7. Fares, M.E., Youssif, Y.G., Alamir, A.E.: Optimal design and control of composite laminated plates with various boundary conditions using various plate theories. Compos. Struct. **56**, 1–12 (2002)
8. Kam, T.Y., Chang, R.R.: Design of laminated composite plates for maximum buckling load and vibration frequency. Comput. Methods Appl. Mech. Eng. **106**, 65–81 (1993)
9. Kam, T.Y., Lai, F.M.: Design of laminated composite plates for optimal dynamic characteristics using a constrained global optimization technique. Comput. Methods Appl. Mech. Eng. **120**, 389–402 (1995)
10. Topal, U., Uzman, U.: Frequency optimization of laminated folded composite plates. Mater. Design **30**, 494–501 (2009)
11. Huang, C., Kröplin, B.: On the optimization of composite laminated plates. Eng. Comput. **12**, 403–414 (1995)
12. Vo-Duy, T., Ho-Huu, V., Do-Thi, T.D., Dang-Trung, H., Nguyen-Thoi, T.: A global numerical approach for lightweight design optimization of laminated composite plates subjected to frequency constraints. Compos. Struct. **159**, 646–655 (2017)
13. Assie, A.E., Kabeel, A.M., Mahmoud, F.F.: Optimum design of laminates composite plates under dynamic excitation. Appl. Math. Modell. **36**, 668–682 (2012)
14. Vosoughi, A.R., Nikoo, M.R.: Maximum fundamental frequency and thermal buckling temperature of laminated composite plates by a new hybrid multi-objective optimization technique. Thin-Walled Struct. **95**, 408–415 (2015)
15. Vosoughi, A.R., Dehghani Forkhorji, H., Roohbakhsh, H.: Maximum fundamental frequency of thick laminated composite plates by a hybrid optimization method. Compos. Part B **86**, 254–260 (2016)
16. Topal, U., Dede, T., Tahsin Ozturk, H.: Stacking sequence optimization for maximum fundamental frequency of simply supported antisymmetric laminated composite plates using teaching-learning-based optimization. KSCE Journal of Civil Engineering **18**, 1–8 (2017)
17. Katsikadelis, J.T.: The Boundary Element Method for Plate Analysis. Academic Press, Elsevier (2014)
18. Katsikadelis, J.T.: The Boundary Element method for Engineer and Scientists. Academic Press, Elsevier (2016)
19. Mindlin, R.D.: Influence of rotary inertia and shear on flexural motions of isotropic, elastic plates, ASME. J. Appl. Mech. **18**, 31–38 (1951)
20. Reddy, J.N.: Mechanics of Laminated Composite Plates and Shells Theory and Analysis. CRC Press, Florida (2003)

Application of Piezoelements in a Structured Thin-Walled Shaft Material to Active Control of Stability and Vibration

Włodzimierz Kurnik and Piotr Przybyłowicz

Abstract The paper is concerned with damping of beam and shaft vibrations using piezoelements with external shunting circuits. Usually, distributed piezoactuators are applied to beams or plates to contract curvature occurring during transverse vibrations. Here, an alternative concept of vibration control is explored consisting in utilising additional dissipation in shunting circuits of piezoelements bonded to a beam or shaft surface. Attention is focused on a cantilever beam subject to tip-concentrated follower load (Beck's column) and/or to kinematic excitation by clamped edge motion. Efficiency of piezodamping is studied in both stabilising the equilibrium and reduction of resonance. On the other hand, the effect of shunting is examined in case of ring-like piezotransducers controlling torsional vibrations of a shaft under harmonic excitation. A shift of resonance zone and reduction of top vibration amplitudes are shown as functions of shunting parameters. Application of piezoelements in vibration control of shafts is developed into a concept of a structural piezoactive material controlled by external voltage coupled with the current state of the shaft. Making use of smart technology combining passive composites with active fibers permanently embedded into their structure is discussed. Fundamentals of active reduction of torsional vibration of a shaft entirely made of the smart piezoceramic composite are proposed and analysed. It is proved that this method may occur advantageous both because of increased strength-to-weight properties as well as enhanced ability to damp torsional vibrations of the system.

W. Kurnik (✉) · P. Przybyłowicz
Warsaw University of Technology, Narbutta 84 St., 02-524 Warsaw, Poland
e-mail: wku@simr.pw.edu.pl

P. Przybyłowicz
e-mail: piotr.przybylowicz@simr.pw.edu.pl

© Springer International Publishing AG 2018

H. Altenbach et al. (eds.), *Advances in Mechanics of Materials and Structural Analysis*, Advanced Structured Materials 80,
https://doi.org/10.1007/978-3-319-70563-7_11

1 Introduction

The piezoelectric effect consists in coupling of mechanical and electrical fields that a piezoelectric body is subject to. Known for more than hundred years (see [10] for detailed physical properties), it has found many applications in mechatronic systems, including flexural and torsional vibration control [1, 3, 12, 17]. It was shown by Kurnik and Przybyłowicz [7] that PZT transducers appropriately located and working in closed-loop control can prevent beams subject to follower loads from flatter instability. The basic concept of using piezoelements in mechanical vibration control is sensing and contracting deformations. However, piezoelements following deformations of a controlled system at their location, generate electric charge and produce additional stiffness of electromechanical nature, dependent on the electric capacitance of a transducer natural or possibly shunted. On the other hand, a shunting circuit supplied by induced piezo-voltage can introduce electric dissipation resulting in what is called electronic damping in the considered structure (see [5, 8] for exemplary applications). Tuneable electronic damping can be important especially in fine vibrating systems in which external and internal dissipation is not sufficient.

In the linear approximation constitutive equations of a piezoelectric are as follows

$$\varepsilon_i = \sum_{j=1}^{6} S_{ij}\sigma_j + \sum_{k=1}^{3} d_{ki}E_k \quad (i = 1, \ldots, 6) \tag{1}$$

$$D_l = \sum_{j=1}^{6} d_{jl}\sigma_j + \sum_{k=1}^{3} e_{kl}E_l \qquad (l = 1, 2, 3) \tag{2}$$

where the notations are: $\varepsilon_i (i = 1, \ldots, 6)$ - strains components, $\sigma_i (i = 1, \ldots, 6)$ - stresses, S_{ij} - mechanical compliances, d_{ki} $(k = 1, 2, 3)$- elements of an electromechanical coupling matrix, $e_{kl} (k, l = 1, 2, 3)$ - dielectric constants, D_k, E_k - electric induction and electric field components, respectively.

Since the 1960s commercial piezoelectrics like PZT or PVDF have been available and applied for various purposes [5, 17]. Massive PZTs are used for actuators and light PVDFs for sensors. From the point of view of the present applications the crucial role is played by the electromechanical coupling coefficients, d_{31} and d_{15}. For a PZT composed of $PbZrO_3$ and $PbTiO_3$ in proportion one-to-one coupling coefficients are of order 10^{-10} [m/V]. Electromechanical coupling in shear is three times stronger than in longitudinal deformation.

Recently, much attention has been paid to piezoelectric energy harvesters that have become a very promising alternative to electric batteries for low-power electronics, especially for MEMS (see overview papers [13, 16] and a quite new publication [18] including numerous references).

In the following we are going to examine the piezoelectric damping when applied to flexural vibrations of a beam and to torsional vibrations of a shaft. Both external and internal dissipation will be neglected for the purpose of this study.

2 Piezoelectric Beam Transducer with Shunting Circuit

Consider a strip-like piezoelement to be bonded to the beam surface, as shown in Fig. 1 If bonding is perfect the transducer will follow strains of the beam surface with no regard to the reason of the beam deflection. Longitudinal stress resulting from deformation will produce electric polarisation and voltage between lower and upper transducer surfaces. One equation of (1) and one of (2) are constitutive for the considered problem of generating electric voltage between the parallel surfaces of the transducer. They can be expressed are as follows

$$\sigma_1 = E_p \left(\varepsilon_1 - \frac{d_{31}}{h_p} U \right) \tag{3}$$

$$D_3 = d_{31} E_p \varepsilon_1 + \frac{e_3}{h_p} U \left(1 - \frac{d_{31}^2 E_p}{e_3} \right) \tag{4}$$

where $U = E_3 h_p$ denotes electric voltage, h_p - transducer thickness, $E_p = 1/S_{11}$ - Young's modulus. The electric voltage, U can be either externally supplied to induce desired transducer and beam stress or internally generated and possibly shunted to additionally dissipate energy of the system. The first technique was shown by Kurnik and Przybyowicz [7] to stabilize the Leipholz column. Here we want to examine the latter effect and its influence on stability and excited transverse vibration of a cantilever beam with tip-concentrated follower load (compare [8]).

The electric charge, Q on the surface of transducer of length, a surface is expressed as

$$Q = b d_{31} E_p \int_0^a \varepsilon_1(x) \mathrm{d}x + \frac{e_3}{h_p} abU \left(1 - \frac{d_{31}^2 E_p}{e_3} \right) \tag{5}$$

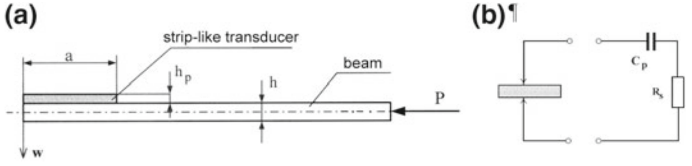

Fig. 1 Piezoelement bonded to the beam surface: **a** configuration, **b** shunting circuit

Thus, the electric charge occurs as a results of deformation and externally applied voltage.

The external shunting circuit is described by the following equation (R_s denotes shunting resistance)

$$R_s \frac{\mathrm{d}Q}{\mathrm{d}t} = -U \tag{6}$$

which will constitute a source of energy dissipation.

3 Dynamics of Beck's Column with Shunted Piezotransducer

Consider a cantilever beam of rectangular cross-section subject to a tip-concentrated follower load as shown in Fig. 1 If the clamped end is immovable we are faced with the Beck's problem. The Beck's column shows flutter instability under increasing follower load. More general is the problem with kinematic excitation by a damped edge motion $s(t)$.

The beam is subject to the tangential transducer force q, which appears as a result of deformation and applied electric field. In case of kinematically undisturbed system a dynamic equation of transverse beam motion with perfectly bonded transducer interaction can be derived in the following linear form

$$\begin{gathered} \rho A \frac{\partial^2 w}{\partial t^2} = -EJ \frac{\partial^4 w}{\partial x^4} - P \frac{\partial^2 w}{\partial x^2} + \\ -\frac{1}{2} h_b E_p A_p \frac{\partial^2}{\partial x^2} \left\{ \left(\frac{h_b}{2} \frac{\partial^2 w}{\partial x^2} - \frac{d_{31}}{h_p} U \right) [H(x) - H(x-a)] \right\} \end{gathered} \tag{7}$$

where$H(\cdot)$denotes Heaviside's function, P is a tip-concentrated follower force, ρ, A are beam density and cross-section area and EJ denotes beam flexural rigidity. Equation (6) of the shunting circuit can be transformed to the following form

$$\frac{\mathrm{d}U}{\mathrm{d}t} + \frac{1}{R_s C_p} U = -\frac{1}{2} d_{31} E_p b h_b \frac{\partial \dot{w}}{\partial x}(a, t) \tag{8}$$

where C_p denotes total transducer electric capacitance and U is resulting transducer voltage.

Thus, Eqs. (7) and (8) constitute a system of coupled electromechanical equations of the beam with shunted piezoelectric transducer.

In case of kinematic excitation $s = s(t)$ as shown in Fig. 3, equation of transverse vibration with reference to the damped edge has the form (7) supplemented with right-hand side term expressing excitation $p(x, t) = -\rho A \ddot{s}$.

It is well known from the theory of columns under follower forces (see [6]) that analysis of stability and eigenvalues needs at least two lowest eigenmodes. Thus, the beam deflection must be expressed as a combination of two shape functions. First, dimensionless variables and constants are introduced as follows

$$W = \frac{w}{h} \qquad X = \frac{x}{l} \qquad \tau = \frac{t}{k_t} \qquad k_t^2 = l^4 \frac{\rho A}{EJ}$$
$$p = \frac{Pl^2}{EJ} \qquad \lambda = \frac{1}{2}\frac{E_p A_p l^2}{EJ} u = \frac{U}{U_0 h_p} \qquad S(t) = \frac{s(t)}{h_b}$$

where U_0 denotes piezoelectric break down voltage measured in V/m. After two-mode Galerkin's discretisation

$$W(X, \tau) = y_1(\tau)F_1(X) + y_2(\tau)F_2(X) \tag{9}$$

coupled electromechanical equations become

$$\begin{cases} \ddot{y}_1 + (e_{11} + pe_{13} + \lambda\lambda_1 e_{15})y_1 + (pe_{14} + \lambda\lambda_1 e_{16})y_2 - \lambda\lambda_2 e_{17} u = -e_{18}\ddot{S} \\ (pe_{23} + \lambda\lambda_1 e_{25})y_1 + \ddot{y}_2 + (e_{22} + pe_{24} + \lambda\lambda_1 e_{26})y_2 - \lambda\lambda_2 e_{27} u = -e_{28}\ddot{S} \\ \alpha_2 e_{31}\dot{y}_1 + \alpha_2 e_{32}\dot{y}_2 + \dot{u}\alpha_1 u = 0 \end{cases} \tag{10}$$

where $\lambda_1 = \frac{h_b^2}{2l^2}$, $\lambda_2 = d_{31}U_0$, $\alpha_1 = \frac{k_t}{R_s}$, $\alpha_2 = \frac{h_b^2 b d_{31} E_p}{2h_p l U_0 C_p}$ and e_{ij} are discretisation constants.

Equations (10) can be studied either as autonomous ($S \equiv 0$) for flutter instability threshold or as externally excited ($S(t)$ - harmonic) for resonant behaviour. It should be noted that in the latter case analysis makes sense in the stable region of equilibrium only. The trivial equilibrium $[y_1, y_2, u] = [0, 0, 0]$ in autonomous case is stable if all the eigenvalues of the system matrix have non-positive real parts. In terms of the non-dimensional follower load, p the stability domain is a set

$$\Phi = \left\{ p : \max_{\mathrm{k}} \ \mathrm{Re}\,[r_k(p)] \leq 0 \right\} \tag{11}$$

where r_k denotes k-th eigenvalue ($k = 1, \ldots, 5$). Stability threshold $p = p_{cr}$ depends on the parameters of the shunting circuit that can be represented by a dimensionless parameter, $\gamma = R_s C_p / k_t$. Thus, $\gamma = 0$ corresponds to the short shunting circuit, while $\gamma \to \infty$ means open-circuit conditions.

It is known from analyses of flutter instability of slender columns under follower loads (see [6]) that internal friction can produce instability. Therefore, it is interesting to examine the resistive piezoelectric shunting effect in Beck's column. Exemplary results are shown in Fig. 2. where the critical compressive follower load is presented as function of the resistive parameter, γ.

Assume $p < p_{cr}$ and consider harmonic kinematic excitation in the form

$$S(t) = S_O \cos \omega t = S_O \ \mathrm{Re}\,\{\exp(i\omega t)\} \tag{12}$$

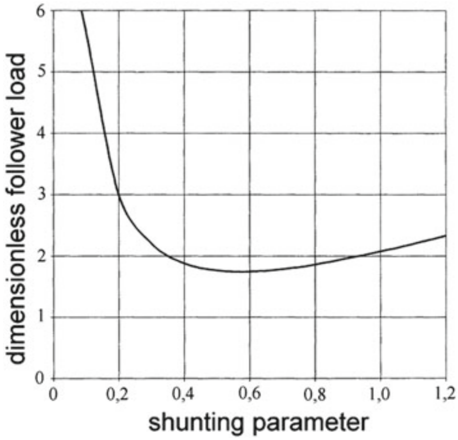

Fig. 2 Critical follower load versa resistive shunting parameter

To examine the effect of piezoelectric shunting we shall concentrate on the first mode only reducing Eq. (10) to the following

$$\begin{cases} \ddot{y}_1 + c_1 y_1 - a_1 u = s_O \gamma^2 \cos \omega t \\ a_2 y_1 + \dot{u} + \alpha_1 u = 0 \end{cases} \tag{13}$$

In the numerical calculations we shall assume $c_1 = 1$ ($p = 0$, passive stiffening neglected).

A steady-state harmonic solution has the form

$$\begin{bmatrix} y_1 \\ u \end{bmatrix} = \begin{bmatrix} \tilde{B}_1 \\ \tilde{B}_u \end{bmatrix} \exp(i\omega t) \tag{14}$$

where i denotes imaginary unit and $\tilde{B}_1$, $\tilde{B}_u$ are complex amplitudes, that are functions of excitation frequency, ω

$$\tilde{B}_1(i\omega) = \frac{s_O \omega^2(\alpha_1 + i\omega)}{D(i\omega)}, \tilde{B}_u(i\omega) = -\frac{i s_O \omega^3 a_2}{D(i\omega)} \tag{15}$$

where $D(i\omega) = (1 - \omega^2)(\alpha_1 + i\omega) + i a_1 a_2 \omega$. The resonant curves $\left|\tilde{B}_1\right|$ and $\left|\tilde{B}_u\right|$ are shown in Fig. 3.

If the passive stiffening by piezoelement is neglected, the original elastic system is identified with the case of short-circuit conditions. The beam with an open-circuit piezotransducer is slightly stiffer than the original one and the reason consists in an electric charge displacement in the transducer. It results in shifting the resonance zone, but the resonant amplitudes are unlimited (see Fig. 3(2)). In case of resistive shunting with additional electrical capacitance supplemented that of the piezotrans-

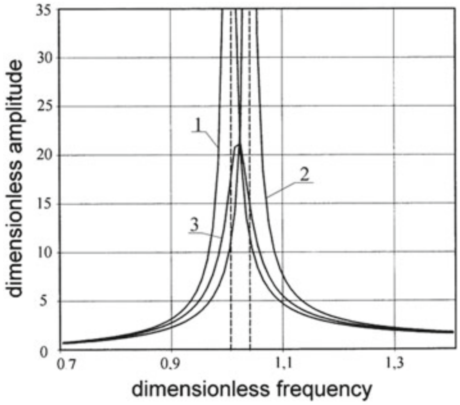

Fig. 3 Resonant curves: (1) - short circuit, (1) - open circuit, (3) - resistive shunting

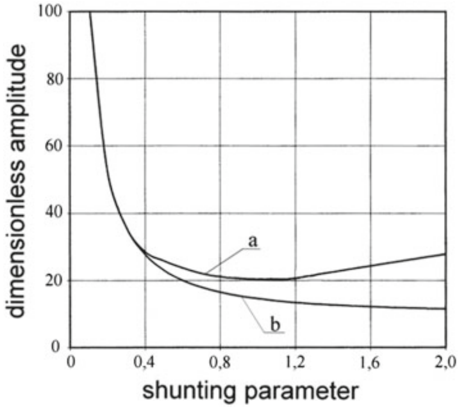

Fig. 4 Excited vibration amplitude $\left|\tilde{B}_1\right|$as function of the shunting parameter γ: **a** - at the original resonance $\omega = 1$, **b** - at the actual resonance

ducer, a kind of internal system dissipation occurs which results in limited vibration amplitudes for all excitation frequencies.

The resulting resonance curve is shown in Fig. 3(3). The effect of resistive shunting is shown in Fig. 4. where the amplitude of vibration at the original resonance frequency ($\omega = 1$) as well as maximum resonance vibration amplitude are presented as functions of the resistive parameter, γ.

4 Torsional Resonance of a Shaft with Shunted Piezotransducer

The considered torsionally vibrating system is a continuous shaft of circular cross-selection, clamped on one end and subject to harmonic moment excitation on the other. A ring-like PZT transducer of length l_p is assumed to be perfectly bonded to the shaft surface at a certain position x_1, as shown in Fig. 5. Unlike in beams, the

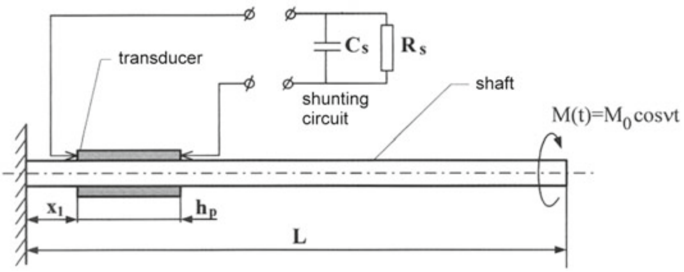

Fig. 5 Shaft with piezotransducer and shunting circuit

electric field in a transducer controlling shaft torsion is directed along the shaft axis (see [1]).

Upon Eqs. (1) and (2), applying engineering notations of shear stress and strain, i.e. $\varepsilon_5 = 0.5\gamma_p, \delta_5 = \tau_p$, one obtains equations of the piezoelectric transducer expressing the direct and converse piezoelectric effects, respectively

$$D_1 = d_{15} G_p \gamma_p + \frac{e_1}{l_p} U \left(1 - \frac{2d_{15}^2 G_p}{e_1}\right) \qquad \tau_p = G_p \gamma_p - \frac{2d_{15} G_p U}{l_p} \tag{16}$$

where $U = E_1 \cdot l_p$ is electric voltage between transducer electrodes and l_p denotes transducer length. The electric charge, Q induced on the edge surfaces of the transducer is

$$Q = D_1^* \cdot 2\pi R \cdot h_p \tag{17}$$

where R, h_p denote shaft radius and transducer thickness, respectively and D_1^* is charge displacement averaged along the transducer. Thus, the electric charge occurs as a result o shear deformation, γ_p and interelectrode voltage, U, as follows

$$Q = \frac{2\pi R h_p d_{15} G_p}{l_p} \cdot \int\limits_{x_1}^{x_1 + l_p} \gamma_p \mathrm{d}x + 2\pi R h_p \frac{e_1}{l_p} U \left(1 - \frac{2d_{15}^2 G_p}{e_1}\right) \tag{18}$$

The shunting electrical circuit is described by Eq. (6).

Assume perfect transducer bonding, what means that shear deformations of the transducer and shaft on its surface are equal to each other. Moreover, we shall neglect shear stress changes across the transducer thickness. Thus, the radial shear stress distribution in the shaft and in the transducer are as follows

$$\tau(r) = Gr \frac{\partial \phi}{\partial x} \qquad \tau_p = G_p R \frac{\partial \phi}{\partial x} - 2G_p d_{15} \frac{U}{l_p} \tag{19}$$

where $\phi(x,t)$ denotes angle of shaft torsion. The torque as a shear stress resultant can be expressed as follows

$$M = \left\{ GI_O + \frac{2}{3}\pi G_p R\left[(R+h_p)^3 - R^3\right]\right\}\frac{\partial \phi}{\partial x} - \frac{2}{3}\pi G_p\left[(R+h_p)^3 - R^3\right] d_{15}\frac{U}{l_p} \tag{20}$$

Neglecting slight increase of torsional stiffness corresponding to the transducer itself, we obtain the following expression for torque, valid for any $x \in < O, l >$.

$$M = GI_O\frac{\partial \phi}{\partial x} - \lambda^* U\left[H(x) - H(x-l_p)\right] \tag{21}$$

where $\lambda^* = \frac{2}{3}\pi G_p\left[(R+h_p)^3 - R^3\right]\frac{d_{15}}{l_p}$. Dynamic equation of the shaft with perfectly bonded piezotransducer is as follows

$$\rho I_O\frac{\partial^2 \phi}{\partial t^2} - GI_O\frac{\partial^2 \phi}{\partial x^2} = \frac{-\lambda^*}{l}U\left[\delta(x) - \delta(x-l_p)\right] + \frac{M_O}{l}\cos\gamma t\cdot\delta(x-l) \tag{22}$$

where ρ is shaft density and $\delta(\cdot)$ denotes Dirac's distribution. Shaft equation (22) is coupled with transducer equation (6) which can be rewritten in the form

$$\frac{\mathrm{d}U}{\mathrm{d}t} + \frac{1}{R_s C_p}U = -\frac{2\pi R^2 h_p d_{15} G_p}{l_p C_p}\dot{\phi}(l_p, t) \tag{23}$$

where

$$C_p = 2\pi R h_p\frac{e_1}{l_p}\left(1 - \frac{2d_{15}G_p}{e_1}\right) + C_s$$

where in turn C_x denotes additional capacitance in the shunting circuit.

Introducing dimensionless variables and constants

$$\tau = \frac{t}{k_t} \qquad X = \frac{x}{l} \qquad k_t = l\sqrt{\frac{G}{\rho}} \qquad \lambda = \frac{\lambda * k_t^2 U_O l_p}{\rho I_O \cdot l}$$

$$\Omega = \gamma k_t \qquad m_O = M_O\frac{k_t^2}{l\rho I_O} \qquad u = \frac{U}{U_O l_p} \qquad a = \frac{l_p}{l}$$

$$\alpha_1 = \frac{k_t}{C_p R_s} \qquad \alpha_2 = \frac{2\pi R^2 h_p d_{15} G_p}{l_p^2 C_p U_O}$$

and performing discretisation based on the eigenfunctions corresponding to unloaded shaft

$$\Phi_n(X) = \sin k_n X \tag{24}$$

we can analyse n-th projection of Eqs. (22) and (23) in the form

$$\begin{cases} \ddot{y}_1 + k_n^2 y_n = \lambda a_n u + m_O b_n \cos\omega t \\ \dot{u} + \alpha_1 u = -\alpha_2 c_n \dot{y}_n \end{cases} \tag{25}$$

Fig. 6 Resonant curves of torsional vibration: (1) - original undamped system, (2) - open circuit, (3) - resistive shunting

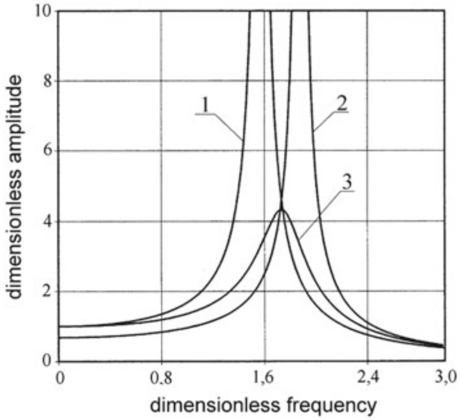

where a_n, b_n and c_n are discretisation constants. To examine the effect of piezoelectric shunting we shall concentrate on the first mode only, substituting $n = 1$ in Eq. (20). The steady-state solution of Eq. (21) has the form

$$\begin{bmatrix} y_1 \\ u \end{bmatrix} = \mathrm{Re}\begin{bmatrix} \tilde{B}_1 \\ \tilde{B}_u \end{bmatrix}\exp(i\omega t) = \begin{bmatrix} \left|\tilde{B}_1\right|\cos(\omega t + \psi_1) \\ \left|\tilde{B}_u\right|\cos(\omega t + \psi_u) \end{bmatrix} \tag{26}$$

where $i$denotes imaginary limit and $\tilde{B}_1$, $\tilde{B}_u$ are complex amplitudes

$$\tilde{B}_1(i\omega) = \frac{m_O(\alpha_1 + i\omega)}{D(i\omega)} \qquad \tilde{B}_u(i\omega) = -\frac{i m_O c_1 \alpha_2 \omega}{D(i\omega)} \tag{27}$$

$$D(i\omega) = \left(k_1^2 - \omega^2\right)(\alpha_1 + i\omega) + i\lambda a_1 c_1 \alpha_2 \omega \tag{28}$$

The resonant curves of the system are $\left|\tilde{B}_1\right|$ and $\left|\tilde{B}_u\right|$. The original undamped shaft has dimensionless natural frequency of the first mode equal to k_1. Thus, unlimited amplitude $\left|\tilde{B}_1\right|$ is expected in the system for $\omega = k_1$. The corresponding resonant curves are shown in Fig. 6.

5 Active Damping of Torsional Vibration in Shafts Made of Piezoelectric Composites

Despite good electromechanical properties of piezoelectric ceramics, the surface-bonded actuators are brittle, heavy, non-flexible and non-conformable elements. Their alternatives, PVDF copolymers are, admittedly, flexible and conformable to any shape but they have high electrical losses, are difficult to pole and their properties are sensitive to temperature variations. Instead of looking for an entirely new class of piezoelectric materials without the above-mentioned drawbacks, a concept of piezoelectric composites has come into being. First patterns of diphasic materials and several different piezocomposites were fabricated at Pennsylvania State University. Properties of ceramic/polymer composites can be tailored by changing connectivity of the phases, volume fraction of the active component and spatial distribution of the ceramic phase. Piezocomposites exhibit excellent electromechanical properties and limit detrimental characteristics of monoliths at the same time [2].

In literature, one can come across various techniques used to form a variety of novel piezoceramic/polymer composites. Among them Solid Freeform Fabrication (SFF) containing Fused Deposition of Ceramics (FDC) and Sanders Prototype (SP) are most popular. The FDC or the lost mould endows piezocomposites with particularly good electromechanical properties. That way, Volume Fraction Gradients (VGFs), staggered rods, radial tubes, curved transducers and many other composite structures are fabricated [14].

The integration of piezoceramic (PZT) fibers within composite materials represents a new type of material evolution. Tiny PZT fibers of 30 μm in diameter can be aligned in an array, electrodized with interdigital electrodes and then integrated into planar architectures. Such architectures are embedded within glass or graphite fiber-reinforced polymers and become piezoelectric after being poled [15]. The idea of combining piezoceramics with polymers occurred in the 1980s [9] and several years later it evolved towards smart composite materials, see Fig. 7.

Piezoelectric Fiber Composites (PFCs) have a large potential for controlling. Matrix and ceramic combinations, volume fractions, and ply angles contribute to the tailorability of PFCs, which make them applicable to structures requiring highly distributed actuation and sensing. Manufacturing technologies of PFCs have been adopted from graphite/epoxy manufacturing methods. Today, PFCs are being equipped with an interdigitated electrode pattern (the so-called IDEPFCs), see Fig. 8. Regardless of the electrode arrangement, the piezoelectric composites now create a class of active materials which may be used for manufacturing of entire structures and curved elements such as shafts, tubes or shells.

In this paper, the making use of active piezocomposites is focused on their capability of reducing torsional vibration in axi-symmetric shafts made of such materials. Different arrangements of lamination are considered in terms of the efficiency in

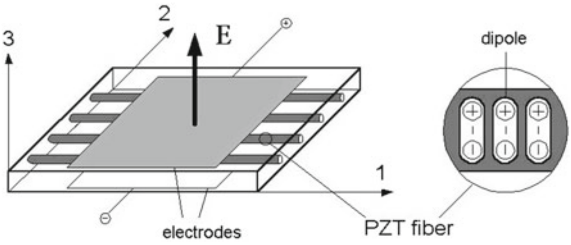

Fig. 7 Active piezoelectric lamina - geometric configuration of active fibers and the poling direction

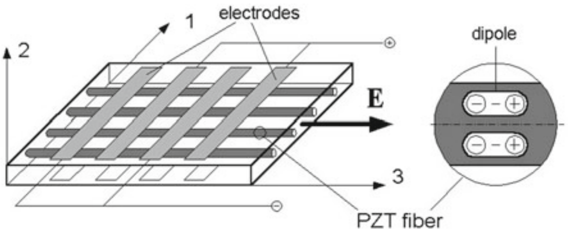

Fig. 8 Interdigitated electrode pattern and the poling of an IDEPFC lamina

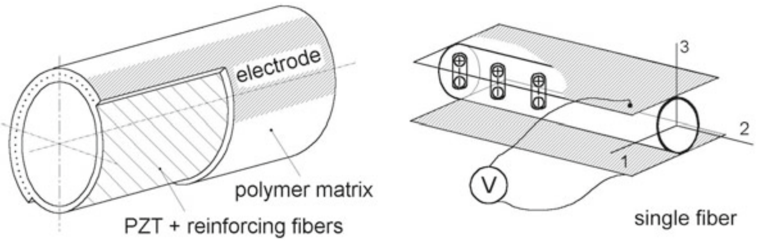

Fig. 9 Shaft made of a composite with acitve piezoceramic fibers (left) and a single fiber subject to an electric field

damping the amplitude of torque-excited vibration. To this aim, concentrate now on pure torsion of a PFC laminated shaft modelled as a closed cylindrical shell with a regular structure (symmetric or anti-symmetric, cross- or angle-plied). The active piezocomposite fixed-free shaft is subject to a tip-concentrated torque at the free end. Its fragment together with a single fiber is shown in Fig. 9.

The equation of torsional vibration of a cylindrical shaft has the following well known form:

$$\rho J_0 \frac{\partial^2 \varphi}{\partial t^2} = \frac{\partial M_T}{\partial x} \tag{29}$$

where ρ is the averaged mass density of the composite, J_0 axi-symmetric cross-sectional moment of inertia, φ angular displacement of the shaft, x axial coordinate, t time. In the analyzed case, the moment (torque) M_T contains both mechanical and electromechanical components:

$$M_T = J_0 \left(G_0 \frac{\partial \varphi}{\partial x} - \frac{1}{r} \Xi_T \, E \left[H(x) - H(x-l) \right] \right) \tag{30}$$

where r is the mean radius of the shaft, E denotes intensity of the applied electric field, $H(.)$ is Heaviside's function (the electrodes cover entire length l of the shaft, i.e. $0 < x < l$). The effective shear modulus G_0 depends on the lamination angle and has correspondingly the following form in symmetric and antisymmetric laminates:

$$G_0 = \bar{Q}_{66} \quad \text{(sym.)} \qquad G_0 = \bar{Q}_{66} - \frac{\bar{Q}_{16}}{N^2 \bar{Q}_{11}} \quad \text{(antisym.)} \tag{31}$$

where N denotes the number of composite layers and

$$\begin{aligned} \bar{Q}_{11} &= Q_{11}\cos^4\theta + (Q_{12} + 2Q_{66})\sin^2 2\theta + Q_{22}\sin^4\theta \\ \bar{Q}_{16} &= (Q_{11} - Q_{12} - 2Q_{66})\sin\theta\cos^3\theta + (Q_{12} - Q_{22} + 2Q_{66})\sin^3\theta\cos\theta \\ \bar{Q}_{66} &= (Q_{11} + Q_{22} - 4Q_{12} - 2Q_{66})\sin^2\theta\cos^2 + Q_{66}(\sin^4\theta + \cos^4\theta) \end{aligned} \tag{32}$$

and:

$$Q_{11} = \frac{Y_1}{1 - {\nu_{12}}^2 \frac{Y_2}{Y_1}} \quad Q_{22} = \frac{Y_2}{1 - {\nu_{12}}^2 \frac{Y_2}{Y_1}} \quad Q_{12} = \frac{\nu_{12} Y_2}{1 - {\nu_{12}}^2 \frac{Y_2}{Y_1}} \quad Q_{66} = 2G_{12} \tag{33}$$

In the above formulas, Y_1, Y_2, G_{12}, ν_{21} denote Young's moduli with respect to principal directions of the lamina (along the fibers and perpendicularly), Kirchhoff's modulus and Poisson's ratio, respectively. The constant Ξ_T in (30) corresponds to the electric part of the system and describes the averaged piezoelectric effect brought about by piezoceramic fibers upon the action of the electric field. An explicit form of this constant is presented in Table 1.

In Table 1, the particular terms denote:

$$\begin{aligned} \bar{\Xi}_{11} &= \Xi_{11}\cos^2\theta + \Xi_{21}\sin^2\theta \qquad & \bar{\Xi}_{13} &= \Xi_{13}\cos^2\theta + \Xi_{23}\sin^2\theta \\ \bar{\Xi}_{31} &= (\Xi_{21} - \Xi_{11})\sin\theta\cos\theta \qquad & \bar{\Xi}_{33} &= (\Xi_{23} - \Xi_{13})\sin\theta\cos\theta \\ \bar{\Xi}_{11}^{(S)} &= \Xi_{11}\cos^3\theta + (\Xi_{21} + 2\Xi_{32})\sin\theta\cos^2\theta && \\ \bar{\Xi}_{31}^{(S)} &= [(\Xi_{21} - \Xi_{11})\cos^2\theta + \Xi_{32}\cos 2\theta]\sin\theta && \end{aligned} \tag{34}$$

in which:

$$\begin{aligned} &\Xi_{11} = Q_{11}d_{33}^* + Q_{12}d_{31}^* \quad \Xi_{21} = Q_{12}d_{33}^* + Q_{22}d_{31}^* \quad \Xi_{13} = d_{31}^* Q_{11} + d_{32}^* Q_{12} \\ &\Xi_{23} = d_{31}^* Q_{12} + d_{32}^* Q_{22} \quad \Xi_{32} = Q_{66}d_{15}^* \end{aligned} \tag{35}$$

Table 1 Expressions for Ξ_T in different configurations of the electrode pattern and type of lamination

	PFC	IDEPFC	S-IDEPFC
symmetric lamination	$\Xi_T = \frac{1}{N}\left(\bar{\Xi}_{33} - \frac{\bar{Q}_{16}}{\bar{Q}_{11}}\bar{\Xi}_{13}\right)$	$\Xi_T = \frac{1}{N}\left(\bar{\Xi}_{31} - \frac{\bar{Q}_{16}}{\bar{Q}_{11}}\bar{\Xi}_{11}\right)$	$\Xi_T = \frac{1}{N}\left(\bar{\Xi}_{31}^{(S)} - \frac{\bar{Q}_{16}}{\bar{Q}_{11}}\bar{\Xi}_{11}^{(S)}\right)$
antisymmetric lamination	$\Xi_T = \frac{1}{2}\bar{\Xi}_{13}\frac{\bar{Q}_{66}}{\bar{Q}_{11}}$	$\Xi_T = \frac{1}{2}\bar{\Xi}_{11}\frac{\bar{Q}_{66}}{\bar{Q}_{11}}$	$\Xi_T = \frac{1}{2}\bar{\Xi}_{11}^{(S)}\frac{\bar{Q}_{66}}{\bar{Q}_{11}}$

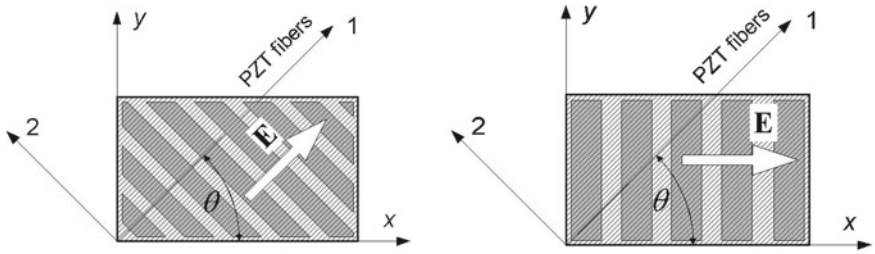

Fig. 10 Two types of interdigitated electrode patterns IDEPFC (left) and S-IDEPFC (right). The principal 1–2 directions and a rotated coordinate system Oxy

where d^*_{ij} are effective (averaged) electromechanical coupling constants of the piezoelectric lamina. The meaning of abbreviations IDEPFC and S-IDEPFC used in Table 1 is concerned with the way of supplying an electric field to the piezoelectric layer and is explained in Fig. 10. The PFC arrangement is shown in Fig. 7.

Now get back to equation of motion (29) assuming the presence of a harmonic excitation torque $m(x,t) = m_0 \sin \nu t$ applied to the free end of the shaft. In that case:

$$\frac{\partial^2 \varphi}{\partial t^2} - \frac{G_0}{\rho}\frac{\partial^2 \phi}{\partial x^2} + \frac{1}{\rho r}\Xi_T E[\delta(x) - \delta(x-l)] = m(x,t)\delta(x-l) \tag{36}$$

$\delta(\,.\,)$ is Dirac's delta function. Introducing a simple control strategy based on the velocity feedback:

$$U_A = c_d \frac{\mathrm{d}U_S}{\mathrm{d}t} \quad \text{and} \quad E = \frac{U_A}{h_e} \tag{37}$$

where U_A is the voltage applied through the electrodes to the active fibers, c_d - gain factor, h_e - distance between the electrodes (in PFCs $h_e = h/N$ with h being thickness of the shaft). The voltage U_S produced by the sensor is

$$U_S = \frac{Y_S\,(d_{S32} - d_{S31})\sin 4\theta}{4(1 + \nu_{S12})}\,\frac{h_S r}{\varepsilon_S}\,\frac{\partial \varphi(x_S)}{\partial x} \tag{38}$$

where Y_S is Young's modulus of the sensor material in the principal direction, ν_{S12} - its Poisson's ratio, h_S - thickness, θ - angle of orientation of the principal axis of the sensor with respect to the shaft axis, ε_S - dielectric permittivity of the sensor, x_S - location coordinate of the sensor along the shaft axis, d_{S32} , d_{S31} - electromechanical coupling constants [11]. Substituting (37) and (38) into (36), the equation of motion becomes:

$$\frac{\partial^2 \varphi}{\partial t^2} - a^2 \frac{\partial^2 \varphi}{\partial x^2} + \beta \frac{\partial^2 \varphi(x_S, t)}{\partial x\, \partial t}[\delta(x) - \delta(x-l)] = m(t)\delta(x-l) \tag{39}$$

where:

$$a^2 = \frac{G_0}{\rho} \quad \beta = c_d \frac{h\, \varXi_T}{h_e\, \varepsilon_S\, \rho} \frac{Y_S\, (d_{S32} - d_{S31}) \sin 4\theta}{4(1 + \nu_{S12})} \tag{40}$$

Solution to the equation of motion can be predicted in form of an infinite series expressed in terms of the eigenfunctions corresponding to the given fixed-free boundary conditions

$$\phi(x,t) = \sum_{i=1}^{\infty} \varPhi_i(x) T_i(t) \tag{41}$$

where $\varPhi_i(x)$ is the i-th eigenfunction and $T_i(t)$ - arbitrary time function. Expressing the right-hand side of (39) by an analogous infinite series, i.e.:

$$m(x,t) = \sum_{i=1}^{\infty} \varPhi_i(x) \mu_i(t) \tag{42}$$

one obtains:

$$\mu_i = m_0 \sin \nu t \frac{\int_0^l \varPhi_i(x)\delta(x-l)\,\mathrm{d}x}{\int_0^l {\varPhi_i}^2(x)\mathrm{d}x} = m_0 \frac{\varPhi_i(l)}{\int_0^l {\varPhi_i}^2(x)\mathrm{d}x} \sin \nu t = m_0\, \varGamma_i(l) \sin \nu t \tag{43}$$

Now, the active term in (39) is to be expanded into $\varPhi_i$-series as well:

$$\beta \frac{\partial^2 \varphi(x_S, t)}{\partial x\, \partial t} [\delta(x) - \delta(x-l)] = \sum_{i=1}^{\infty} \varPhi_i(x) \beta_i(t) \tag{44}$$

To this end, multiply (44) by $\varPhi_j(x)$ and integrate over the entire length of the shaft:

$$\sum_{i=1}^{\infty} \beta_i(t) \int_0^l \varPhi_i(x)\, \varPhi_j(x)\, \mathrm{d}x = \beta \sum_{i=1}^{\infty} \dot{T}_i(t) \frac{\mathrm{d}\varPhi_i(x_S)}{\mathrm{d}x} \int_0^l \varPhi_j(x)\, [\delta(x) - \delta(x-l)]\, \mathrm{d}x \tag{45}$$

which, keeping in mind that $\forall j \in \mathrm{N}\ \varPhi_j(0) = 0$, yields:

$$\beta_n(t) = -\beta\, \varGamma_n(l) \sum_{i=1}^{\infty} \dot{T}_i(t) \frac{\mathrm{d}\varPhi_i(x_S)}{\mathrm{d}x} \tag{46}$$

Substituting the above expressions into the equation of motion, one gets:

$$\sum_{i=1}^{\infty} \Phi_i(x)\ddot{T}_i(t) - a^2 \sum_{i=1}^{\infty} \frac{\mathrm{d}^2\Phi_i(x_S)}{\mathrm{d}x^2} T_i(t) + \sum_{i=1}^{\infty} \Phi_i(x)\beta_i(t) = \sum_{i=1}^{\infty} \Phi_i(x)\mu_i(t) \quad (47)$$

Taking into account that:

$$\frac{\mathrm{d}^2\Phi_i(x)}{\mathrm{d}x^2} = -\frac{{\omega_i}^2}{a^2}\Phi_i(x) \quad (48)$$

where ω_i is the i-th eigenfrequency of the fixed-free shaft, and knowing that the eigenforms $\Phi_i(x)$ are linearly independent, one writes down:

$$\ddot{T}_i(t) + {\omega_i}^2 T_i(t) + \beta_i(t) = \mu_i(t) \quad (49)$$

for every $i \in N$. The term $\beta_i(t)$ is related to $\dot{T}_i$ as follows:

$$\beta_i(t) = -\beta\, \Gamma_i(l) \sum_{j=1}^{\infty} \dot{T}_j(t) \frac{\mathrm{d}\Phi_j(x_s)}{\mathrm{d}x} = \sum_{j=1}^{\infty} \dot{T}_j(t)\, \beta_{ij}(x_s) \quad (50)$$

where $\beta_{ij} = -\beta\, \Gamma_i\,(l)\mathrm{d}\Phi_j(x_s)/dx$. Finally, one gets an infinite system of simultaneous linear ordinary differential equations of the second order:

$$\ddot{T}_i + \sum_{j=1}^{\infty} \beta_{ij}\dot{T}_i + {\omega_i}^2 T_i = \mu_i \;, \qquad i = 1\,,\; \ldots\,,\; n\,,\; \ldots \infty \quad (51)$$

or:

$$\begin{cases} \ddot{T}_1 + \beta_{11}\dot{T}_1 + \beta_{12}\dot{T}_2 + \ldots + \beta_{1n}\dot{T}_n + \ldots + {\omega_1}^2 T_1 = \mu_1 \\ \ddot{T}_2 + \beta_{21}\dot{T}_1 + \beta_{22}\dot{T}_2 + \ldots + \beta_{2n}\dot{T}_n + \ldots + {\omega_2}^2 T_2 = \mu_2 \\ \qquad\qquad\qquad \ldots \\ \ddot{T}_n + \beta_{1n}\dot{T}_1 + \;\beta_{2n}\dot{T}_2 + \ldots + \beta_{nn}\dot{T}_n + \ldots + {\omega_n}^2 T_n = \mu_n \\ \qquad\qquad\qquad \ldots \end{cases} \quad (52)$$

The infinite set of non-homogeneous ordinary differential equations (52) can be easily transformed into a set of corresponding algebraic equations (complex ones) by making use of the substitution:

$$\mu_j(t) = m_0\, \Gamma_j(l)\mathrm{e}^{\mathrm{i}\nu t} \quad T_j(t) = \tilde{A}_j(\nu)\, \mathrm{e}^{\mathrm{i}\nu t} \quad (53)$$

where $\tilde{A}_j(\nu)$ is a complex amplitude of the j-th eigenform, ν - excitation frequency. The amplitudes can be found from the following infinite set of equations:

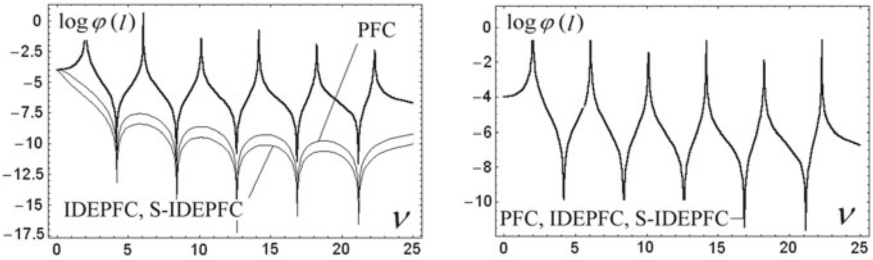

Fig. 11 Resonant curves for $\theta = 0^0$. Symmetric (left) and antisymmetric (right) lamination

$$\begin{bmatrix} \omega_1^2 - \nu^2 + i\nu\beta_{11} & i\nu\beta_{12} & \dots & i\nu\beta_{1n} & \dots \\ i\nu\beta_{21} & \omega_2^2 - \nu^2 + i\nu\beta_{22} & \dots & i\nu\beta_{2n} & \dots \\ \dots & \dots & \dots & \dots & \dots \\ i\nu\beta_{n1} & i\nu\beta_{n2} & \dots & \omega_n^2 - \nu^2 + i\nu\beta_{nn} & \dots \\ \dots & \dots & \dots & \dots & \dots \end{bmatrix} \begin{bmatrix} \tilde{A}_1(\nu) \\ \tilde{A}_2(\nu) \\ \dots \\ \tilde{A}_n(\nu) \\ \dots \end{bmatrix} = \begin{bmatrix} \mu_1(t) \\ \mu_2(t) \\ \dots \\ \mu_n(t) \\ \dots \end{bmatrix} \tag{54}$$

Having found all the amplitudes $\tilde{A}_j(\nu)$ up to a certain numerical limit N, one can determine the amplitude of torsional vibration at the end of the shaft:

$$A(\nu) = \left| \sum_{j=1}^{N} \Phi_j(l) \tilde{A}_j(\nu) \right| \tag{55}$$

The results of numerical simulations in form of amplitude frequency characteristics are shown in figures below. The thick lines correspond to characteristics without active control. The thin lines present drops in the vibration amplitude due to the applied electronic damping for three the patterns of electrodes supplying the shaft with the electric field (transversely poled PFCs, longitudinally IDEPFCs and S-IDEPFCs) (see left Fig. 11).

As can be seen, in some cases all curves cover one another (see e.g. right Fig. 11), which means inability to damp the vibration for the given geometric arrangement of the laminate. Sometimes, only some of the curves are in line (e.g. right Fig. 15). In Fig. 14, the resonant characteristics are shown for the lamination angles denoted by $\theta_{\max ef}$, i.e. θ at which the efficiency of piezoelectric actuation is the greatest. For antisymmetric laminates $\theta_{\max ef}$ is about 80° and 70° for symmetric ones (Fig. 14).

6 Conclusions

Resistive shunting of distributed piezotransducers bonded to the surface of a beam or a shaft generates internal dissipation of electric nature supplementing natural damping of the structure. Short shunting circuit does not affect original resonant

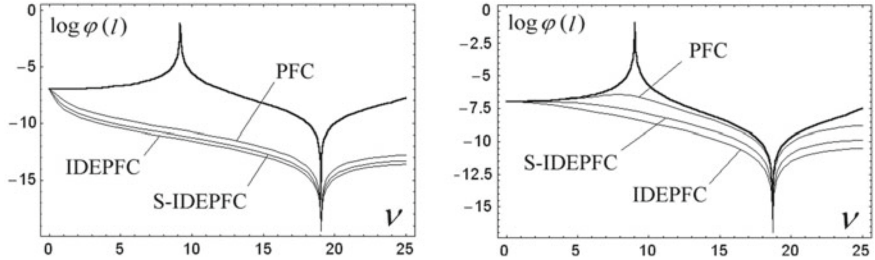

Fig. 12 Resonant curves for $\theta = 45^0$. Symmetric (left) and antisymmetric (right) lamination

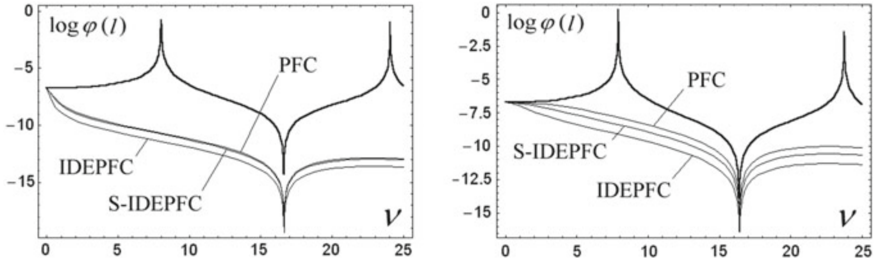

Fig. 13 Resonant curves for $\theta = 60^0$. Symmetric (left) and antisymmetric (right) lamination

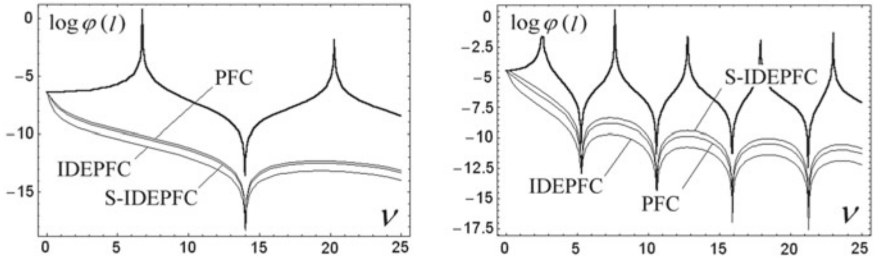

Fig. 14 Resonant curves for $\theta = \theta_{\max ef}$. Symmetric (left) and antisymmetric (right) lamination

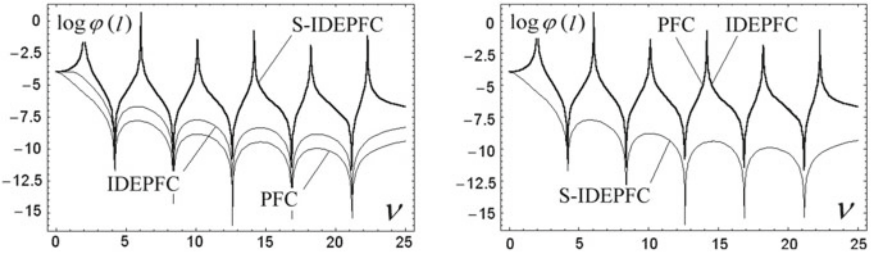

Fig. 15 Resonant curves for $\theta = 90^0$. Symmetric (left) and antisymmetric (right) lamination

properties of a beam or a Shaft. Open-circuit conditions mean an increase in stiffness without dissipation and produce shifted resonance curves with unlimited maximum amplitudes. The top amplitude in the case of closed shunting circuit depends on both shunting resistance and additional transducer capacitance. The efficiency of resistive shunting shows maximum as a function of circuit resistance. The resistive shunting effect is limited by the electric breakdown in the transducer.

Smart composites containing piezoelectric fibers may constitute an alternative to active reduction of torsional vibration in thin-walled shafts and similar structures. They are integrated structural elements endowed with some attractive electromechanical capabilities from the point of view of intelligent technology. Simulations prove that the making use of piezocomposites leads to a considerable drop in the amplitude of torsional vibration. At the same time, it is possible to find an optimum lamination angle corresponding to the best compromise between strength of the piezocomposite structure and its ability to reduce torsional vibration.

Acknowledgements The paper is dedicated to Professor Reinhold Kienzler on the occasion of his 70-th birthday, in recognition of his outstanding achievements in applied mechanics and extraordinary efforts as the Co-chairman of the two-decade long series of German-Greek-Polish Symposia on *Recent Advances in Mechanics*.

References

1. Chia-Chi, S., Vasundara, V.V., Xiao-Qi, B., Vijay, K.V.: Active Control of Torsional Vibration Using Piezoceramic Sensors and Actuators, AIAA/ASME/ASCE/ AHS/ASC 31-st Structures, Structural Dynamics and Materials Conference, AIAA-90-1130-CP Paper, pp. 2317–2322, 1990
2. Cheng, J., Li, G.: Stress analyses of a smart composite pipe joint integrated with piezoelectric composite layers under torsion loading. Int. J. Solids Struct. **45**(5), 1153–1178 (2008)
3. Crawley, E.F., de Luis, J.: Use of piezoelectric actuators as elements of intelligent structures. AIAA J. **25**, 1373–1385 (1987)
4. Damjanovic, D., Newnham, R.E.: Electrostrictive and piezoelectric materials for actuator applications. J. Intell. Mater. Struct. Syst. **3**(4), 190–208 (1992)
5. Davis, C.L., Lesieutre, G.A., Dosch, J.: A Tunable Electrically Shunted Piezoceramic Vibration Absorber. In: Davis, L.P. (ed.) Proceedings of SPIE Smart Structures and Materials, vol. 3045, pp. 51–59 (1997)
6. Kurnik, W., Pekalak, M.: Stability and bifurcation analysis of the non-Linear damped leipholz column. J. Sound Vib. **152**, 285–294 (1992)
7. Kurnik, W., Przybyłowicz, P.M.: Non-Linear Behaviour of the Leipholz Column Actively Stabilised by Piezoelements, Active 95, Newport Beach, pp. 139–150. CA, USA (1995)
8. Kurnik, W.: Piezoelectric stabilisation of leipholz columns. Mach. Dyn. Probl. **24**(1), 121–129 (2000)
9. Newnham, R.E., Bowen, K.A., Klicker, K.A., Cross, L.E.: Composite piezoelectric transducers. Mater. Eng. **2**, 93–106 (1980)
10. Nye, J.F.: Physical Properties of Crystals. Clarendon, Oxford (1985)
11. Odegard, G.M.: Constitutive modeling of piezoelectric polymer composites. Acta Materialia **52**(18), 53155330 (2004)
12. Przybyłowicz, P.M.: Piezoelectric Vibration Control of Rotating Structures, Scientific works of the Warsaw University of Technology, Mechanics, vol 197, Publishing House of WUT, (2002)

13. Saadon, S., Sidek, O.: A review of vibration-based MEMS piezoelectric energy harvesters. Energy Convers. Manag. **52**, 500–504 (2011)
14. Safari, A.: Novel piezoelectric ceramics and composites for sensor and actuator applications. Mater. Res. Innov. **2**, 263–269 (1999)
15. Sporn, D., Schoencker, A.: Composites with piezoelectric thin fibers first evidence of piezoelectric behaviour. Mater. Res. Innov. **2**, 303–308 (1999)
16. Toprak, A., Tigli, O.: Piezoelectric energy harvesting: state-of-the-art and challenges. Appl. Phys. Rev. **1**(3), (2014). https://doi.org/10.1063/1.4896166
17. Tylikowski, A.: Control of circular plate vibrations via piezoelectric actuators shunted with a capacitive circuit. Thin-Walled Struct. **39**, 83–94 (2001)
18. Yang, Y., Wang, S., Stein, P., Xu, B.-X., Yang, T.: Vibration-based energy harvesting with a clamped piezoelectric circular diaphragm: analysis and identification of optimal structural parameters. Smart Mater. Struct. **26**(4), (2017). https://doi.org/10.1088/1361-665X/aa5fda

Remarks on a Fluid-Structure Interaction Scheme Based on the Least-Squares Finite Element Method at Small Strains

Carina Nisters, Alexander Schwarz, Solveigh Averweg and Jörg Schröder

Abstract The present contribution introduces a least-squares finite element method (LSFEM) based fluid-structure interaction (FSI) approach. The proposed method is based on the formulation of mixed finite elements in terms of stresses and velocities for both the fluid and the solid regime. The LSFEM offers the advantage of a flexibility to construct functionals with sophisticated physical quantities as e.g. stresses, velocities and displacements. The approximation of the stresses and velocities in suitable spaces, namely in the spaces $H(\text{div})$ and H^1, respectively, leads to the inherent fulfillment of the coupling conditions of a FSI method. A numerical example considering an incompressible, linear elastic material behavior at small deformations and the incompressible Navier–Stokes equations demonstrates the applicability of the LSFEM-FSI method.

1 Introduction to Fluid-Structure Interaction

The simulation of fluid-structure interaction (FSI) problems gained increasingly attention in the framework of computer-based mechanical and mathematical research in the last decades. Recent findings in FSI simulations were established in the framework of a continuum mechanical suitable description, mathematical treatment and several algorithmic approaches. Fundamental research effort can be attributed to the work of many research groups, an overview on that can be found in e.g. [10, 35].

C. Nisters (✉) · A. Schwarz · S. Averweg · J. Schröder
University of Duisburg-Essen, Universitätsstraße 15, 45141 Essen, Germany
e-mail: carina.nisters@uni-due.de

A. Schwarz
e-mail: alexander.schwarz@uni-due.de

S. Averweg
e-mail: solveigh.averweg@uni-due.de

J. Schröder
e-mail: j.schroeder@uni-due.de

© Springer International Publishing AG 2018

H. Altenbach et al. (eds.), *Advances in Mechanics of Materials and Structural Analysis*, Advanced Structured Materials 80,
https://doi.org/10.1007/978-3-319-70563-7_12

Numerous FSI models are based on finite element formulations of the mixed Galerkin method in the framework of fluid and solid mechanics. The approaches of this kind are successfully applied and improved continuously in recent years. A second essential and popular method is the finite volume method. The following publications and the references therein are exemplarily for research on FSI methods [15–17, 24, 25, 42, 44].

In case of partial differential equations with not self-adjoint operators (e.g. in case of fluid flow and transport problems) the mixed Galerkin method leads to unsymmetric and in case of incompressible materials or fluids to indefinite systems of equations. In order to guarantee solvability and stability of such saddle point problems the finite element methods have to satisfy ellipticity as well as the Ladyzhenskaya–Babuška–Brezzi (LBB) condition (also inf-sup condition), see e.g. [8]. A summarizing overview on stabilized FE formulations for fluid mechanics is given in [14], for instance. Furthermore, the following publications and the references herein furnish detailed explanations on the different stabilization schemes as for example the penalty-method [32, 33], the SUPG-method [9, 18] and the Galerkin/least-squares method [19]. In the framework of stable and robust finite element methods in solid mechanics a considerable effort was pursued in the past. Especially, research on quasi-incompressible materials as can be found in biological tissues was encouraged. Different approaches were developed as for example mixed or hybrid formulations, see e.g. [29, 39, 45]. We can conclude, there exist robust, stable and efficient (mixed) finite element formulations in the regime of fluid and solid mechanics, which cover a wide range of application scenarios and requirement profiles.

Next to the demand for performant FE-formulations special attention has to be paid to the interface description in fluid-structure interaction problems. The coupling conditions need to be fulfilled on the interface, which are the equilibrium of the traction vectors of the fluid and the solid domain and the equality of the velocities of both domains. In order to guarantee these conditions there exist *monolithic* and *staggered* or *segregated* approaches in the established FSI applications, see e.g. the list of publications above and especially the overviews in [10, 35]. Anyways the known methods can lead to issues regarding convergence and stability. Additionally, the employed solvers, which are developed independently for the fluid and the solid part, can be inadequate, see e.g. [47] and the references herein.

Todays research in FSI focusses therefore on the performance of utilized solvers (e.g. [41]), the stability and robustness of modern time integration schemes (e.g. [12, 43]) and the extension to complex 3D applications (e.g. [3] or [2]). Furthermore, the effect of turbulent flows in fluid-structure-interaction, see [1] for instance, is investigated. Modern FSI applications can be found in structural design or biomechanics, see e.g. [6, 24], which give detailed overviews on established FSI solution procedures in biomechanics.

In this contribution a least-squares FEM based fluid-structure interaction approach is introduced. The idea is based on a certain choice of the approximated values and discretization spaces. Therefore, both the fluid and the solid domain are described by mixed least-squares finite element formulations in terms of stresses and velocities discretized in $H(\text{div})$ and H^1, respectively. This leads to the simulation of a FSI problem within one triangulation, which fulfills the coupling conditions intrinsically.

2 The Least-Squares Finite Element Method

The least-squares finite element method (LSFEM) is an alternative variational approach compared to the well-known mixed Galerkin method. It provides some theoretical benefits, which make its application favorable in certain cases: Firstly, the method is not restricted to the LBB-condition, hence a free choice of the polynomial degree of the interpolating functions is possible. Secondly, the least-squares FEM offers a wide range of mixed approaches based on different solution variables such as stresses, pressure, displacements or velocities, since they can be included in the variational formulation inherently and at free choice. Furthermore, the LSFEM results in general in stable formulations for first-order systems and is applied successfully especially in fluid mechanics. The construction of the finite elements leads to positive definite and symmetric system matrices, also for differential equations with not self-adjoint operators, see e.g. [5], which describes its success in the framework of computational fluid dynamics. Furthermore, the resulting systems offer a robust convergence behavior for a certain choice of iterative solvers, compare to [36] for instance. A further convenient benefit is the availability of an a posteriori error estimator without additional costs, which can be used in adaptive meshing strategies. This conception is applicable to nonlinear theories, too, see e.g. [28, 40].

The least-squares finite element formulation is based on the construction of a functional $\mathscr{F}$ in terms of the L^2-norm of certain residuals $\mathscr{R}_i$ defining the problem to be solved. With the residuals

$$||\mathscr{R}_i||_{L^2(\Omega)} = \left\{ \int\limits_{\Omega} |\mathscr{R}_i(x)|^2 \mathrm{d}x \right\}^{\frac{1}{2}}, \tag{1}$$

the functional is defined with

$$\mathscr{F} = \frac{1}{2}\left(\sum_{i=1}^{r} ||\omega_i \mathscr{R}_i||^2_{L^2(\Omega)} \right), \tag{2}$$

where r denotes the number of residuals of the system and ω_i weighting factors. This can be displayed by the bilinear form of the residual $\mathscr{R} = \boldsymbol{L} \cdot \boldsymbol{u} - \boldsymbol{f}$, such that

$$\mathscr{F} = \frac{1}{2}\omega^2 ||\boldsymbol{L} \cdot \boldsymbol{u} - \boldsymbol{f}||^2_{L^2(\Omega)} = \frac{1}{2}\omega^2 (\boldsymbol{L} \cdot \boldsymbol{u} - \boldsymbol{f}, \boldsymbol{L} \cdot \boldsymbol{u} - \boldsymbol{f}) \rightarrow \text{minimal}, \tag{3}$$

with (•, •) denoting the inner product. The problem can be identified to be solved for the minimization of the constructed functional $\mathscr{F}$. The condition for minimization is fulfilled for the first variation of the problem equals to zero, such that

$$\delta\mathscr{F} = \frac{\partial\mathscr{F}}{\partial \boldsymbol{u}} \cdot \delta\boldsymbol{u} = \lim_{\varepsilon\to 0} \frac{\mathscr{F}(\boldsymbol{u} + \varepsilon\,\delta\boldsymbol{u}) - \mathscr{F}(\boldsymbol{u})}{\varepsilon} := \omega^2(\boldsymbol{L}\cdot\boldsymbol{u} - \boldsymbol{f}, \boldsymbol{L}\cdot\delta\boldsymbol{u}) = 0\,, \tag{4}$$

see e.g. [20]. The finite element formulations considered in the following are of mixed form and suitable approximation spaces have to be chosen. As mentioned before the LSFEM is not restricted to the LBB condition. Anyways the choice of the approximation spaces and related interpolation functions is essential regarding approximation quality and efficiency. Both aspects are self-evident to be presupposed: The formulations have to guarantee the correctness of the results compared to given reference solutions. Secondly, the formulations have to satisfy the requirements of complex boundary value problems.

The experiences of previous work and the state of art in research indicate, that the usage of vector-valued Raviart–Thomas interpolation spaces for the stress approximation with $W \subset H(\text{div}, \Omega)$ and Lagrangian interpolation spaces for the velocity approximation with $V \subset H^1(\Omega)$ are suitable in appropriate combinations. The approximation spaces for the stresses and velocities of the finite elements are chosen with

$$\boldsymbol{W}_m^h = \{\boldsymbol{\sigma} \in H(\text{div}, \Omega)^2 : \boldsymbol{\sigma}|_{\Omega_e} \in RT_m(\Omega_e)^2\, \forall\, \Omega_e\} \subseteq \boldsymbol{W}\,, \tag{5}$$

$$\boldsymbol{V}_k^h = \{\boldsymbol{v} \in H^1(\Omega)^2 : \boldsymbol{v}|_{\Omega_e} \in P_k(\Omega_e)^2\, \forall\, \Omega_e\} \subseteq \boldsymbol{V}\,. \tag{6}$$

The finite element is then denoted with $RT_m P_k$ in the following. In detail two interpolation combinations are investigated in the numerical examples, namely elements of order $RT_1 P_2$ and $RT_3 P_4$. For more details on the approximation with vector-valued Raviart–Thomas interpolation functions, the reader is referred to [7, 31, 34]. The chosen finite element spaces fulfill inherently the essential boundary conditions both

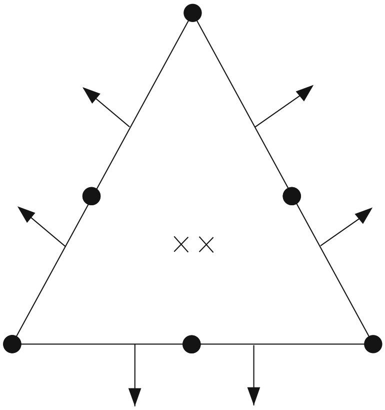

Fig. 1 Interpolation sites of $RT_1 P_2$ with arrows and crosses denoting the interpolation sites of the Raviart–Thomas interpolation and bullets denoting the interpolation sites of the Lagrange interpolation

for the velocities and for the stresses, as well as the interaction conditions as described in Sect. 3.1. Exemplarily the interpolation sites of an RT_1P_2 are given in Fig. 1, with the arrows and crosses marking the interpolation sites of the vector-valued Raviart–Thomas functions on the edges of the element, and inside the element, respectively. The filled dots denote the quadratic Lagrange interpolation sites.

3 A Least-Squares Finite Element Based Fluid-Structure Interaction Scheme

In this Section the general idea on the least-squares FEM based fluid-structure interaction scheme is introduced. Therefore, advanced least-squares formulations both for the solid and the fluid regime are used and investigated regarding efficiency and interpolation order as well as time integration.

3.1 Governing Equations for the FSI Scheme

In both frameworks the governing differential equations are given by the balance of momentum and the constitutive equations for the solid and the fluid phase. In case of the fluid domain the physical behavior is described by the incompressible stationary Navier–Stokes equations given by the balance of momentum

$$-\rho\nabla\boldsymbol{v}\cdot\boldsymbol{v}+2\mu\,\mathrm{div}(\nabla^s\boldsymbol{v})-\nabla p=\mathbf{0}, \tag{7}$$

and the continuity equation

$$\mathrm{div}\,\boldsymbol{v}=0. \tag{8}$$

In here, $\boldsymbol{v}$ denotes the velocity vector, p the pressure, ρ the density and μ the dynamic viscosity of a medium flowing through a domain Ω. The symmetric gradient of the velocity field is given by

$$\nabla^s\boldsymbol{v}=\frac{1}{2}(\nabla\boldsymbol{v}+(\nabla\boldsymbol{v})^T). \tag{9}$$

For applications of the proposed fluid-structure interaction scheme with an intrinsic fulfillment of the coupling conditions the Cauchy stresses $\boldsymbol{\sigma}$ are used in the following. Then Eq. (7) can be rewritten as

$$-\rho\nabla\boldsymbol{v}\cdot\boldsymbol{v}+\mathrm{div}\,\boldsymbol{\sigma}=\mathbf{0}\qquad\text{and}\qquad\boldsymbol{\sigma}=2\mu\nabla^s\boldsymbol{v}-p\mathbf{1}. \tag{10}$$

In case of the solid domain the finite element formulation is based on the balance of momentum

Fig. 2 Coupling conditions on the interface Γ_{if} of a fluid and a solid finite element

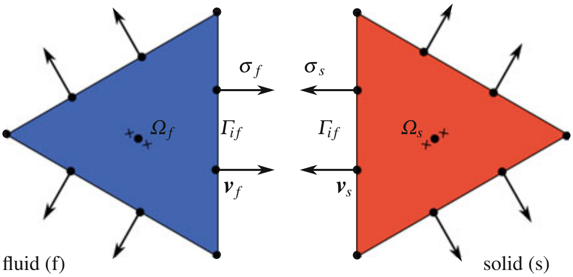

$$\operatorname{div}\boldsymbol{\sigma} + \mathbf{f} - \rho\,\boldsymbol{a} = \mathbf{0}, \tag{11}$$

with $\mathbf{f}$ denoting a body force, $\boldsymbol{a} = \dfrac{\partial^2 \boldsymbol{u}}{\partial t^2}$ denoting the acceleration, $\boldsymbol{u}$ denoting the displacements, and the constitutive law for small deformations and linear elasticity

$$\boldsymbol{\sigma} = \mathbb{C}_{ijkl} : \nabla^s \boldsymbol{u}, \tag{12}$$

with the elasticity tensor $\mathbb{C}_{ijkl} = \kappa\,\delta_{ij}\delta_{kl} + 2\mu\,(\delta_{ik}\delta_{jl} - \frac{1}{3}\delta_{ij}\delta_{kl})$ where κ and μ denote Lamé constants.

The central idea is the introduction of least-squares finite element formulations with both the stresses $\boldsymbol{\sigma}$ and the velocities $\boldsymbol{v}$ as independent degrees of freedom, which then intrinsically fulfill the coupling conditions of a fluid-structure interaction scheme. These coupling conditions are given by $\boldsymbol{\sigma}_f \cdot \boldsymbol{n} = \boldsymbol{\sigma}_s \cdot \boldsymbol{n}$ on the interface between the fluid domain Ω_f and the solid domain Ω_s domain denoted with Γ_{if} and $\boldsymbol{v}_f = \boldsymbol{v}_s$ on Γ_{if}, respectively. This coupling is illustrated in Fig. 2. The least-squares finite element formulations regarding the introduced equations are presented in the following two subsections.

3.2 *Least-Squares Finite Element Formulation for the Fluid Part*

The least-squares finite element formulation used in this contribution regarding the fluid domain bases on the incompressible stationary Navier–Stokes equations as given in (7) and (8). In the following a stress-velocity (SV) formulation is introduced, which is based on the findings in [11, 37]. Within the formulation a redundant residual is added to the functional without additional variables in order to strengthen specific physical relations, see e.g. [38]. Both the SV formulation as well as the SV formulation with additional residual are based on the three-field stress-velocity-pressure (SVP) formulation, see [4, 11]. For the derivation of the three-field SVP approach the Cauchy stress tensor $\boldsymbol{\sigma}$ is introduced as an additional variable to the system of equations in (7) and (8), compare to (10), such that the three residual forms of the well-known stress-velocity-pressure formulation are achieved with

$$\mathscr{R}_1^F := \operatorname{div} \boldsymbol{\sigma} - \rho \nabla \boldsymbol{v} \cdot \boldsymbol{v}, \quad \mathscr{R}_2^F := \boldsymbol{\sigma} - 2\mu \, \nabla^s \boldsymbol{v} + p\mathbf{1}, \quad \mathscr{R}_3^F := \operatorname{div} \boldsymbol{v}. \tag{13}$$

Then, taking the trace of the second equation in (13) and inserting the continuity equation given in (8) yields the governing equation for the pressure p, such that

$$p = -\frac{1}{3}\operatorname{tr}(\boldsymbol{\sigma}). \tag{14}$$

We can reduce the system of equations by inserting this definition of the pressure into $(13)_2$. Furthermore, assuming the definition of the deviatoric part of the Cauchy stresses, which is

$$\operatorname{dev} \boldsymbol{\sigma} = \boldsymbol{\sigma} - \frac{1}{3}\operatorname{tr}(\boldsymbol{\sigma}) \, \mathbf{1}, \tag{15}$$

we obtain the remaining residuals of the stress-velocity two-field formulation, see e.g. [11].

Previous investigations have shown, that this formulation has the drawback of a poor approximation quality especially with respect to mass conservation. These findings lead to the extension of the given formulation by [37]. They proposed to take a further residual into account. Analogous deliberations were made by [26] for the Stokes equations. Anyways the authors do not give a detailed study on the influence on the numerical results of the extended system in contrast to the basic SV formulation at that point. A detailed investigation of the SV formulation with the third residual can be found in [27].

In the before mentioned contributions the continuity equation is introduced as an additional condition, such that the residuals of the system are given by

$$\mathscr{R}_1^F := \operatorname{div} \boldsymbol{\sigma} - \rho \nabla \boldsymbol{v} \cdot \boldsymbol{v}, \quad \mathscr{R}_2^F := \operatorname{dev} \boldsymbol{\sigma} - 2\mu \, \nabla^s \boldsymbol{v} \quad \text{and} \quad \mathscr{R}_3^F := \operatorname{div} \boldsymbol{v}. \tag{16}$$

The related extended two-field functional reads then

$$\begin{aligned} \mathscr{F}_{SV\ fluid}(\boldsymbol{\sigma}, \boldsymbol{v}) = \frac{1}{2}\Bigg(& \left\| \frac{1}{\sqrt{\rho}}(\operatorname{div} \boldsymbol{\sigma} - \rho \nabla \boldsymbol{v} \cdot \boldsymbol{v}) \right\|^2_{L^2(\Omega)} \\ & + \left\| \frac{1}{\sqrt{\mu}}(\operatorname{dev} \boldsymbol{\sigma} - 2\mu \, \nabla^s \boldsymbol{v}) \right\|^2_{L^2(\Omega)} + \left\| \operatorname{div} \boldsymbol{v} \right\|^2_{L^2(\Omega)} \Bigg), \end{aligned} \tag{17}$$

with appropriate weightings. For further details on weighted least-squares FEM see e.g. [13, 30]. The first variation of the functional $\mathscr{F}_{SV\ fluid}$ with respect to each variable is given by

$$\delta_{\boldsymbol{\sigma}}\mathscr{F}_{SV\ fluid}(\boldsymbol{\sigma},\boldsymbol{v};\delta\boldsymbol{\sigma}) = \int\limits_{\Omega} \frac{1}{\rho}\text{div}\ \delta\boldsymbol{\sigma}\cdot(\text{div}\ \boldsymbol{\sigma} - \rho\nabla\boldsymbol{v}\cdot\boldsymbol{v})\text{d}V + \int\limits_{\Omega} \frac{1}{\mu}\text{dev}\ \delta\boldsymbol{\sigma} : (\text{dev}\ \boldsymbol{\sigma} - 2\mu\nabla^{s}\boldsymbol{v})\text{d}V, \tag{18}$$

$$\begin{aligned}\delta_{\boldsymbol{v}}\mathscr{F}_{SV\ fluid}(\boldsymbol{\sigma},\boldsymbol{v};\delta\boldsymbol{v}) = &-\int\limits_{\Omega} 1(\nabla\delta\boldsymbol{v}\cdot\boldsymbol{v} + \nabla\boldsymbol{v}\cdot\delta\boldsymbol{v})\cdot(\text{div}\ \boldsymbol{\sigma} - \rho\nabla\boldsymbol{v}\cdot\boldsymbol{v})\text{d}V\\ &-\int\limits_{\Omega} 2\nabla^{s}\delta\boldsymbol{v} : (\text{dev}\ \boldsymbol{\sigma} - 2\mu\nabla^{s}\boldsymbol{v})\text{d}V\\ &+\int\limits_{\Omega} \text{div}\ \delta\boldsymbol{v}\cdot\text{div}\ \boldsymbol{v}\,\text{d}V.\end{aligned} \tag{19}$$

Implementation aspects on the finite element within the fluid part are given in Sect. 3.4 and in the Appendix in Table 1.

3.3 Least-Squares Finite Element Formulation for the Solid Part

Based on the deliberations in the beginning of this Section the two residuals of the considered linear elasticity LSFEM formulation are given by

$$\mathscr{R}_1^S := \text{div}\ \boldsymbol{\sigma} + \mathbf{f} - \rho\,\boldsymbol{a} \quad \text{and} \quad \mathscr{R}_2^S := \mathbb{C}^{-1} : \boldsymbol{\sigma} - \nabla^{s}\boldsymbol{u}. \tag{20}$$

Thus the least-squares functional in terms of stress and velocity is given by

$$\mathscr{F}_{SV\ solid}(\boldsymbol{\sigma},\boldsymbol{v}) = \frac{1}{2}\left(\left|\left|\omega_1(\text{div}\ \boldsymbol{\sigma} + \mathbf{f} - \rho\,\boldsymbol{a})\right|\right|^2_{L^2(\Omega)} + \left|\left|\omega_2(\mathbb{C}^{-1} : \boldsymbol{\sigma} - \nabla^{s}\boldsymbol{u})\right|\right|^2_{L^2(\Omega)}\right), \tag{21}$$

with the weighting factors ω_1 and ω_2. Hence, the first variation of the time-discretized functional $\mathscr{F}_{SV\ solid}$ with respect to each unknown is given by

$$\delta_{\boldsymbol{\sigma}}\mathscr{F}_{SV\ solid}(\boldsymbol{\sigma},\boldsymbol{v};\delta\boldsymbol{\sigma}) = \int\limits_{\Omega} \left[\omega_1^2\,\text{div}\ \delta\boldsymbol{\sigma}\cdot(\text{div}\ \boldsymbol{\sigma} + \mathbf{f} - \rho\boldsymbol{a}) + \omega_2^2\,\mathbb{C}^{-1} : \delta\boldsymbol{\sigma} : \left(\mathbb{C}^{-1} : \boldsymbol{\sigma} - \nabla^{s}\boldsymbol{u}\right)\right]\text{d}V \tag{22}$$

and

$$\delta_{\boldsymbol{v}} \mathscr{F}_{SV\ solid}(\boldsymbol{\sigma}, \boldsymbol{v}; \delta \boldsymbol{v}) = \int_{\Omega} \left[\delta \tilde{\boldsymbol{a}} \cdot (\operatorname{div} \boldsymbol{\sigma} + \mathbf{f} - \rho \boldsymbol{a}) + \nabla^s \delta \tilde{\boldsymbol{u}} : \left(\mathbb{C}^{-1} : \boldsymbol{\sigma} - \nabla^s \boldsymbol{u}\right)\right] \mathrm{d}V \tag{23}$$

with the abbreviations $\delta \tilde{\boldsymbol{a}}$ and $\nabla^s \delta \tilde{\boldsymbol{u}}$

$$\delta \tilde{\boldsymbol{a}} = \delta \boldsymbol{v}(-\omega_1^2 \rho \alpha_1) \quad \text{and} \quad \nabla^s \delta \tilde{\boldsymbol{u}} = \nabla^s \delta \boldsymbol{v}(-\omega_2^2 \alpha_2), \tag{24}$$

with α_1 and α_2 are depending on the choice of the time discretization scheme and defined in the following as well as the weighting factors ω_1 and ω_2.

In this contribution the time discretization is described by the Houbolt method. We achieve a discretization scheme in time that interpolates the displacements and the accelerations from the actual velocities and the history variables of the last time steps. The Houbolt method is based on a third-order interpolation of the displacements and the multistep implicit formulas are obtained by using a backward difference scheme in general. The reformulation with respect to the velocities leads to an approximation scheme for the displacements and accelerations, given with

$$\boldsymbol{u}_{n+1} = \frac{6}{11} \boldsymbol{v}_{n+1} \Delta t + \frac{18}{11} \boldsymbol{u}_n - \frac{9}{11} \boldsymbol{u}_{n-1} + \frac{2}{11} \boldsymbol{u}_{n-2}, \tag{25}$$

and

$$\boldsymbol{a}_{n+1} = \frac{1}{\Delta t^2} \left[\frac{12}{11} \boldsymbol{v}_{n+1} \Delta t - \frac{19}{11} \boldsymbol{u}_n + \frac{26}{11} \boldsymbol{u}_{n-1} - \frac{7}{11} \boldsymbol{u}_{n-2}\right], \tag{26}$$

with Δt denoting the time step size and all values subscripted $n + 1$ denoting values of the actual time step. Analogously, the values of the previous time steps are given with n, $n - 1$ and $n - 2$. For the Houbolt time discretization scheme the values of α_1 and α_2 read $\alpha_1 = \dfrac{12}{11 \Delta t}$ and $\alpha_2 = \dfrac{6 \Delta t}{11}$. The proposed choice of the weighting factors for the usage of the Houbolt method is based on a physical weighting in alignment with the contribution in [21] given with

$$\omega_1 = \sqrt{\frac{\Delta t}{\rho}} \quad \text{and} \quad \omega_2 = \sqrt{\frac{\mu}{\Delta t}}. \tag{27}$$

Implementation aspects on the finite element are given in the following Sect. 3.4 and in the Appendix in Table 2 for the solid part.

3.4 Finite Element Discretization in Space

In the following we want to give a description of the discretization of both finite elements for the solid and the fluid part, respectively. Both mixed least-squares finite element formulations presented here are based on stress-velocity functionals, as given in the previous subsections. Thus, the solution variables are the velocities $\boldsymbol{v}$ and stresses $\boldsymbol{\sigma}$. The interpolation of the unknowns are chosen appropriately, such that the mentioned approximation spaces, see (6) and (5), are discretized conformingly. As mentioned in Sect. 2 the discretization in space of the velocity and the stress field are given in terms of Lagrangian interpolation functions denoted with N and Raviart–Thomas shape functions denoted with $\boldsymbol{\psi}$ (see the Appendix), respectively. Furthermore, we introduce the degrees of freedom vector $\boldsymbol{d}^I = [d_1^I, d_2^I]^T$ associated to the velocities in x_1- and x_2-direction of each node I and the vector $\boldsymbol{\beta}^J = [\beta_1^J, \beta_2^J]^T$ denoting the degrees of freedom associated to the stresses at the interpolation sites J. Then we obtain for the discretization of the velocities $\boldsymbol{v} \approx \boldsymbol{v}^h$, the velocity gradient $\nabla \boldsymbol{v} \approx \nabla \boldsymbol{v}^h$ and the divergence of the velocities div $\boldsymbol{v} \approx$ div $\boldsymbol{v}^h$

$$\boldsymbol{v}^h \qquad \text{with the entries} \qquad v_i^h = \sum_I N^I \, d_i^I ,$$

$$\nabla \boldsymbol{v}^h \qquad \text{with the entries} \qquad v_{i,j}^h = \sum_I N_{,j}^I \, v_i^I$$

and

$$\operatorname{div} \boldsymbol{v}^h \qquad \text{with the entries} \qquad v_{i,i}^h = \sum_I N_{,i}^I \, d_i{}^I .$$

Analogously the entries of displacement the field $\boldsymbol{u} \approx \boldsymbol{u}^h$ as well as its gradient $\nabla \boldsymbol{u} \approx \nabla \boldsymbol{u}^h$ and the acceleration field $\boldsymbol{a} \approx \boldsymbol{a}^h$ are calculated from the nodal values $\boldsymbol{u}^I$ and $\boldsymbol{a}^I$ given through the time discretization, see Eqs. (25) and (26). The stress interpolation is given with $\boldsymbol{\sigma} \approx \boldsymbol{\sigma}^h$ and the divergence of the stresses div$\boldsymbol{\sigma} \approx$ div$\boldsymbol{\sigma}^h$, such that

$$\boldsymbol{\sigma}^h \qquad \text{with the entries} \qquad \sigma_{ij}^h = \sum_J \psi_j^J \, \beta_i^J$$

and

$$\operatorname{div} \boldsymbol{\sigma}^h \qquad \text{with the entries} \qquad \sigma_{ij,j}^h = \sum_J \psi_{j,j}^J \, \beta_i^J .$$

The algorithmic treatment based on this discretization is described in the Appendix in Table 1 for the fluid finite element and in Table 2 for the solid finite element, respectively.

4 Numerical Example

In the numerical example we will restrict ourselves to the two-dimensional regime. We consider a channel flow including an elastic wall, which is subjected only to the fluid flow impact of velocities and stresses acting on its boundary. The geometry of this problem is depicted in Fig. 3 with the light gray domain denoting the fluid regime, and the dark gray shading marking the solid domain. All length specifications are given in meter.

On the left edge of the domain an inflow condition is defined for the fluid with $v_{x_1 f}(0, x_2) = \Lambda(t)\, 0.15\, \frac{x_2(5.0-x_2)}{6.25}$ and $v_{x_2 f} = 0$. The upper and lower boundaries of the fluid domain are so-called no slip boundaries, meaning $v_{x_1 f} = v_{x_2 f} = 0$. The lower boundary of the solid domain is fixed, such that $v_{x_1 s} = v_{x_2 s} = 0$, too. Suitable stress boundary conditions are assigned to the right boundary of the domain, which is in the case of a stress-velocity formulation $\beta_1 = \sigma_{11} = 0$. The material parameters are the following for the fluid domain: $\rho_f = 1.0 \frac{\mathrm{kg}}{\mathrm{m}^3}$, $\mu_f = 0.01 \frac{\mathrm{N}s}{\mathrm{m}^2}$, and for the solid

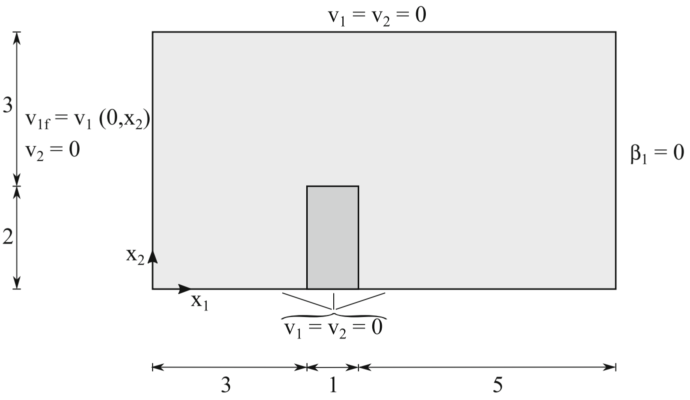

Fig. 3 Channel flow around an elastic wall

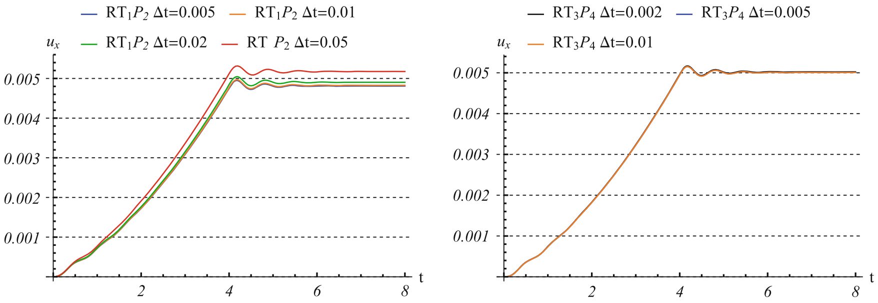

(a) u_{x_1} for RT_1P_2 with Houbolt scheme

(b) u_{x_1} for RT_3P_4 with Houbolt scheme

Fig. 4 Evaluation of the u_{x_1} displacement of node (4, 2) over time at different time step widths for different interpolation orders

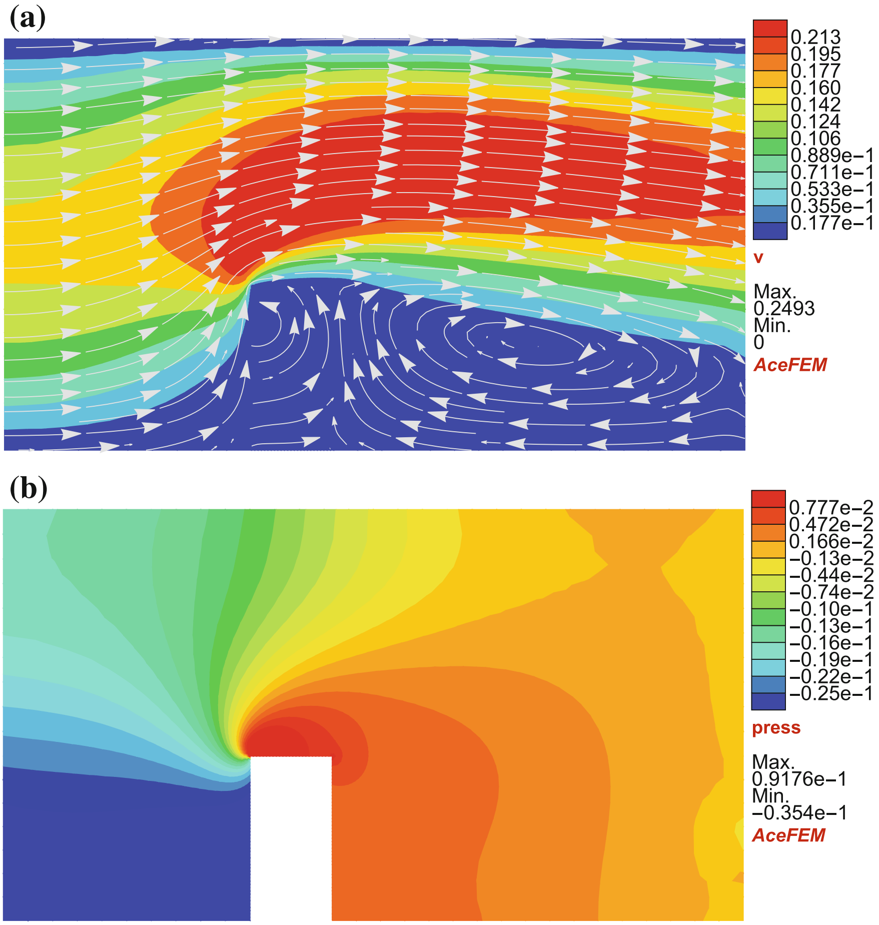

Fig. 5 Plot of **a** the resulting velocity field on the whole domain and **b** pressure distribution in the fluid domain

domain: A density of $\rho_s = 0.12\frac{kg}{\mathrm{m}^3}$ and the Lamé constants $\kappa_s = 33333.3\frac{\mathrm{N}}{\mathrm{m}^2}$ and $\mu_s = 66.71\frac{\mathrm{N}}{\mathrm{m}^2}$. The inflow velocity profile is increased from $\Lambda(t = 0) = 0$ to $\Lambda(t = 4) = 1$ and then hold for $\Lambda(t = t_i) = 1$, for $t_i \in [4, 8]$. In the numerical investigation the horizontal displacement u_{x_1} of node (4, 2) is tracked. Note, this value is computed by default due to the time discretization of the solid domain. The influence of different approximation orders is considered. Additionally, different time increments Δt are considered. Figure 4 shows the results of this investigation.

We find that the Houbolt time integration scheme is stable for the presented investigated time steps. Within the low interpolation formulation larger time steps lead to convergence in the Newton scheme. For the higher interpolation elements a larger time step leads to divergence. Anyways, the low interpolation FEM is not

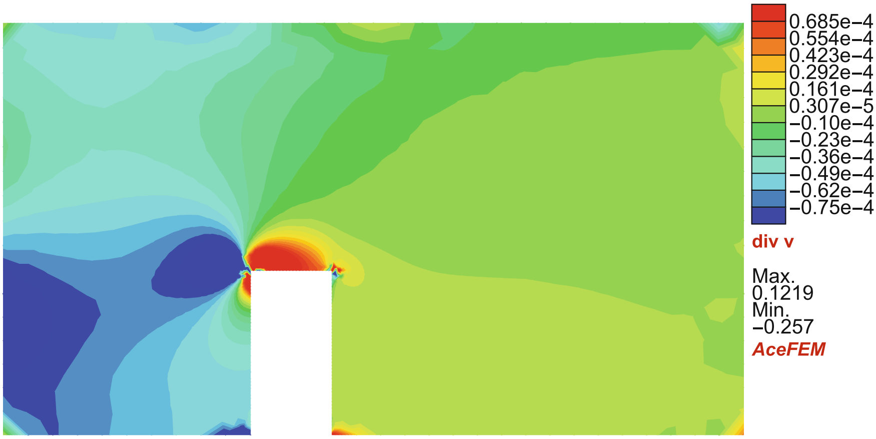

Fig. 6 Plot of the third residual $\mathscr{R}_3^F := \operatorname{div} \boldsymbol{v}$ asking for mass conservation in the fluid domain

approximating a satisfying result. Lower time steps are underestimating the result. Whereas the solutions of the high interpolation elements reach a good result for each of the presented time steps. Considering the solution of the RT_3P_4 simulations, we find that the displacement of node (4, 2) converges after $t \approx 6$ s to $u_{x_1} = 0.0049\,\text{m}$.

Besides, the resulting velocity field including the streamlines on the whole domain is displayed in Fig. 5a. The main stream is clearly visible above the elastic wall, while one large vortex is developed behind the elastic wall. Furthermore, the pressure field of the fluid domain in Fig. 5b shows the gradient of the pressure in the immediate vicinity of the wall. In Fig. 6 the value of the third residual $\mathscr{R}_3^F := \operatorname{div} \boldsymbol{v}$ of the fluid domain is shown. We obtain the highest values at the sharp corners of the flow-around wall, which is in agreement with the pressure distribution in Fig. 5b. This numerical example is carried out using the AceGen and AceFEM packages (version 6.5), see [22, 23], embedded in Mathematica (version 10.1), see [46].

5 Conclusion

The present contribution introduces a least-squares finite element based fluid-structure interaction scheme and provides a numerical example showing the applicability of the method. The Houbolt scheme leads to stable results for the investigated time steps. We find, the higher order interpolation obtains a more accurate result than the lower order approach, which underestimates the result. Within the higher order interpolation scheme the time stepping is more sensitive, such that values larger than $\Delta t = 0.01$ lead to divergence in this example. Investigations on further time integration schemes could be promising for this effect.

Acknowledgements This work was supported by Deutsche Forschungsgemeinschaft (DFG) under grants SCHW 1355/3-1 and SCHR 570/31-1: "Least-Squares Fluid-Struktur-Interaktion für inkompressible Strömungsprozesse". Furthermore, we would like to thank Karl Steeger for fruitful discussions about RT-finite-element spaces.

Appendix

Algorithmic Implementation of Both Finite Element Formulations

Table 1 Algorithm for the SV formulation of the fluid part on element level

- Initialization of basic variables

  $$\boldsymbol{d}^I = \begin{bmatrix} d_1^I \\ d_2^I \end{bmatrix} \quad \boldsymbol{\beta}^J = \begin{bmatrix} \beta_1^J \\ \beta_2^J \end{bmatrix}$$

- Space discretization
  1. Velocities: $v_i^h = \sum_I N^I {d_i}^I, \quad v_{i,j}^h = \sum_I N^I_{,j}\, d_i^I \quad \text{and} \quad v_{i,i}^h = \sum_I N^I_{,i} {d_i}^I$
  2. Stresses $\sigma_{ij}^h = \sum_J \psi_j^J\, \beta_i^J, \quad \sigma_{ij,j}^h = \sum_J \psi_{j,j}^J\, \beta_i^J \quad \text{and} \quad \operatorname{dev} \sigma_{ij}^h = \sigma_{ij}^h - \frac{1}{3}\sigma_{mm}^h \delta_{ij}$

     with the Kronecker delta δ_{ij}

- LS-Functional

  $$\mathscr{F}_{SV\ fluid}(\boldsymbol{\sigma}^h, \boldsymbol{v}^h) = \tfrac{1}{2}\left(||\omega_1 \mathscr{R}_1^F||^2_{L^2(\Omega_e)} + ||\omega_2 \mathscr{R}_2^F||^2_{L^2(\Omega_e)} + ||\omega_3 \mathscr{R}_3^F||^2_{L^2(\Omega_e)} \right),$$

  with $\mathscr{R}_1^F := \operatorname{div} \boldsymbol{\sigma}^h - \rho \nabla \boldsymbol{v}^h \cdot \boldsymbol{v}^h$, $\mathscr{R}_2^F := \operatorname{dev} \boldsymbol{\sigma}^h - 2\mu \nabla^s \boldsymbol{v}^h$, $\mathscr{R}_3^F := \operatorname{div} \boldsymbol{v}^h$,

  $\omega_1 = \frac{1}{\sqrt{\rho}}, \quad \omega_2 = \frac{1}{\sqrt{\mu}} \quad \text{and} \quad \omega_3 = 1$

- Element RHS-Vector $\boldsymbol{P}^e$ and System-Matrix $\boldsymbol{S}^e$

  $\boldsymbol{D}^e = [\boldsymbol{d}^1, ..., \boldsymbol{d}^K, \boldsymbol{\beta}^1, ..., \boldsymbol{\beta}^M]^T$ degree of freedom vector of element e with K and M denoting the number of interpolation sites

```
FOR each element e DO
    $\boldsymbol{P}^e = \frac{\partial \mathscr{F}_{SV\ fluid}}{\partial \boldsymbol{D}^e}$
    $\boldsymbol{S}^e = \frac{\partial \boldsymbol{P}^e}{\partial \boldsymbol{D}^e}$
END DO
```

Table 2 Algorithm for the SV formulation of the solid part on element level

---

- Initialization of basic variables

  $\boldsymbol{d}^I = \begin{bmatrix} d_1^I \\ d_2^I \end{bmatrix} \quad \boldsymbol{\beta}^J = \begin{bmatrix} \beta_1^J \\ \beta_2^J \end{bmatrix}$

- Time discretization - Houbolt scheme
  1. Read from history $(\boldsymbol{u}_n^I, \boldsymbol{u}_{n-1}^I, \boldsymbol{u}_{n-2}^I)$
  2. Calculate at actual time step $n+1$ for each node I

     $\boldsymbol{u}^I{}_{n+1} = \frac{6}{11}\,\boldsymbol{d}^I{}_{n+1}\,\Delta t + \frac{18}{11}\boldsymbol{u}^I{}_n - \frac{9}{11}\boldsymbol{u}^I{}_{n-1} + \frac{2}{11}\boldsymbol{u}^I{}_{n-2}\ ,$

     $\boldsymbol{a}^I{}_{n+1} = \frac{1}{\Delta t^2}\left[\frac{12}{11}\,\boldsymbol{d}^I{}_{n+1}\,\Delta t - \frac{19}{11}\boldsymbol{u}^I{}_n + \frac{26}{11}\boldsymbol{u}^I{}_{n-1} - \frac{7}{11}\boldsymbol{u}^I{}_{n-2}\right]$
  3. Write $\boldsymbol{u}^I{}_{n+1}$ to history

- Space discretization
  1. Displacements and accelerations

     $\nabla^s \boldsymbol{u}^h = \frac{1}{2}(\nabla \boldsymbol{u}^h + (\nabla \boldsymbol{u}^h)^T)$ with the entries of $\nabla \boldsymbol{u}^h$ given with $u_{i,j}^h = \sum\limits_I N_{,j}^I u_i^I$

     and $a_i{}^h = \sum\limits_I N^I a_i^I$ $\;(u_i^I$ and a_i^I from the actual time step $n+1)$
  2. Stresses $\sigma_{ij}^h = \sum\limits_J \psi_j^J\ \beta_i^J$ $\quad$ and $\quad \sigma_{ij,j}^h = \sum\limits_J \psi_{j,j}^J\ \beta_i^J$

- LS-Functional

  $\mathscr{F}_{SV\ solid}(\boldsymbol{\sigma}, \boldsymbol{v}) = \frac{1}{2}\left(\left|\left|\omega_1 \mathscr{R}_1^S\right|\right|_{L^2(\Omega_e)}^2 + \left|\left|\omega_2 \mathscr{R}_2^S\right|\right|_{L^2(\Omega_e)}^2\right),$

  with $\quad \mathscr{R}_1^S := \operatorname{div} \boldsymbol{\sigma}^h + \mathbf{f} - \rho\, \boldsymbol{a}^h\ ,\ \ \mathscr{R}_2^S := \mathbb{C}^{-1} : \boldsymbol{\sigma}^h - \nabla^s \boldsymbol{u}^h\ ,$

  $\omega_1 = \sqrt{\frac{\Delta t}{\rho}}$ and $\omega_2 = \sqrt{\frac{\mu}{\Delta t}}$

- Element RHS-Vector $\boldsymbol{P}^e$ and System-Matrix $\boldsymbol{S}^e$

  $\boldsymbol{D}^e = [\boldsymbol{d}^1, ..., \boldsymbol{d}^K, \boldsymbol{\beta}^1, ..., \boldsymbol{\beta}^M]^T$ degree of freedom vector of element e with K and M denoting the number of interpolation sites

  ```
  FOR each element e DO
      $\boldsymbol{P}^e = \frac{\partial \mathscr{F}_{SV\ solid}}{\partial \boldsymbol{D}^e}$
      $\boldsymbol{S}^e = \frac{\partial \boldsymbol{P}^e}{\partial \boldsymbol{D}^e}$
  END DO
  ```

Raviart–Thomas Vector-Valued Interpolation Functions

Vectorial basis functions $\hat{\boldsymbol{v}}_1^J$ of the reference element for the considered stress interpolation in the RT_1-case are given as

$$\begin{aligned}
\hat{\boldsymbol{v}}_1^1 &= \begin{pmatrix} -8\eta\xi - 8\xi^2 + 6\xi \\ -8\eta^2 - 8\eta\xi + 12\eta + 6\xi - 4 \end{pmatrix} \\
\hat{\boldsymbol{v}}_1^2 &= \begin{pmatrix} 8\xi^2 - 4\xi \\ 8\xi\eta - 2\eta - 6\xi + 2 \end{pmatrix} \\
\hat{\boldsymbol{v}}_1^3 &= \begin{pmatrix} 8\xi^2 - 4\xi \\ 8\xi\eta - 2\eta \end{pmatrix} \\
\hat{\boldsymbol{v}}_1^4 &= \begin{pmatrix} 8\xi\eta - 2\xi \\ 8\eta^2 - 4\eta \end{pmatrix} \\
\hat{\boldsymbol{v}}_1^5 &= \begin{pmatrix} 8\eta\xi - 6\eta - 2\xi + 2 \\ 8\eta^2 - 4\eta \end{pmatrix} \\
\hat{\boldsymbol{v}}_1^6 &= \begin{pmatrix} -8\eta\xi + 6\eta - 8\xi^2 + 12\xi - 4 \\ -8\eta^2 - 8\eta\xi + 6\eta \end{pmatrix} \\
\hat{\boldsymbol{v}}_1^7 &= \begin{pmatrix} -8\eta\xi - 16\xi^2 + 16\xi \\ -8\eta^2 - 16\eta\xi + 8\eta \end{pmatrix} \\
\hat{\boldsymbol{v}}_1^8 &= \begin{pmatrix} -16\eta\xi - 8\xi^2 + 8\xi \\ -16\eta^2 - 8\eta\xi + 16\eta \end{pmatrix} .
\end{aligned}$$

These functions are transformed to the basis functions of the physical space by

$$\bar{\boldsymbol{v}}_1^J = \frac{1}{\det \boldsymbol{T}} \boldsymbol{T} \hat{\boldsymbol{v}}_1^J ,$$

with the transformation matrix $\boldsymbol{T} = \frac{\partial \boldsymbol{x}}{\partial \boldsymbol{\xi}}$, which is constant in here since straight-edged triangle meshes are used. Here $\boldsymbol{x}$ denotes the coordinate vector of the element in the physical space and $\boldsymbol{\xi}$ the coordinate vector of the reference element. Then the vector-valued Raviart–Thomas shape functions for RT_1 in two dimensions are obtained as

$$\psi_1^J = \frac{l}{2} \bar{\boldsymbol{v}}_1^J \qquad \text{and} \qquad \operatorname{div} \psi_1^J = \frac{l}{2} \operatorname{div} \bar{\boldsymbol{v}}_1^J ,$$

with l denoting the associated length of the edge of the interpolation sites $J = 1, \ldots, 6$. The normalization factor $l/2$ is omitted for the interpolation sites inside the element, namely for $J = 7, 8$.

References

1. Ali, A., Reimann, T., Sternel, D.C., Schäfer, M.: Comparison of advanced turbulence modeling approaches for fluid-structure interaction. In: Coupled Problems in Science and Engineering VI, CIMNE (2015)
2. Balzani, D., Deparis, S., Fausten, S., Forti, D., Heinlein, A., Klawonn, A., Quarteroni, A., Rheinbach, Q., Schröder, J.: Numerical modeling of fluid-structure interaction in arteries with anisotropic polyconvex hyperelastic and anisotropic viscoelastic material models at finite strains. Int. J. Numer. Method Biomed. Eng. (2015)
3. Bazilevs, Y., Hsu, M., Kiendl, J., Wüchner, R., Bletzinger, K.: 3D Simulation of wind turbine rotors at full scale. Part II: Fluid - structure interaction modeling with composite blades. Int. J. Numer. Methods Fluids **65**, 236–253 (2011)
4. Bochev, P.B., Gunzburger, M.D.: Least-squares methods for the velocity-pressure-stress formulation of the Stokes equations. Comput. Methods Appl. Mech. Eng. **126**(3–4), 267–287 (1995)
5. Bochev, P.B., Gunzburger, M.D.: Least-Squares Finite Element Methods, 1st edn. Springer, New York (2009)
6. Bodnár, T., Galdi, G., Nečasová, S.: Fluid-Structure Interaction and Biomedical Applications. Springer, Berlin (2014)
7. Boffi, D., Brezzi, F., Fortin, M.: Mixed Finite Element Methods and Applications. Springer, Berlin (2013)
8. Braess, D.: Finite Elemente, 2nd edn. Springer, Berlin (1997)
9. Brooks, A.N., Hughes, T.J.R.: Streamline upwind/Petrov–Galerkin formulations for convection dominated flows with particular emphasis on the incompressible Navier–Stokes equations. Comput. Methods Appl. Mech. Eng. **32**, 199–259 (1982)
10. Bungartz, H.-J., Mehl, M., Schäfer, M.: Fluid Structure Interaction II: Modelling, Simulation, Optimization. Springer, Berlin (2010)
11. Cai, Z., Lee, B., Wang, P.: Least-squares methods for incompressible Newtonian fluid flow: linear stationary problems. SIAM J. Numer. Anal. **42**(2), 843–859 (2004)
12. Cori, J.-F., Etienne, S., Garon, A., Pelletier, D.: High-order implicit Runge–Kutta time integrators for fluid-structure interactions. Int. J. Numer. Methods Fluids **78**, 385–412 (2015)
13. Deang, J.M., Gunzburger, M.D.: Issues related to least-squares finite element methods for the Stokes equations. SIAM J. Sci. Comput. **20**(3), 878–906 (1998)
14. Donea, J., Huerta, A.: Finite Element Methods for Flow Problems. Wiley, New York (2003)
15. Förster, Ch., Wall, W.A., Ramm, E.: Artificial added mass instabilities in sequential staggered coupling of nonlinear structures and incompressible viscous flows. Comput. Methods Appl. Mech. Eng. **196**(7), 1278–1293 (2007)
16. Glück, M., Breuer, M., Durst, F., Halfmann, A., Rank, E.: Computation of fluid-structure interaction on lightweight structures. J. Wind Eng. Ind. Aerodyn. **89**(14), 1351–1368 (2001)
17. Hron, J., Turek, S.: A monolithic FEM solver for an ALE formulation of fluid-structure interaction with configuration for numerical benchmarking. In: European Conference on Computational Fluid Dynamics ECCOMAS CFD (2006)
18. Hughes, T.J.R., Brooks, A.N.: Multi-dimensional upwind scheme with no crosswind diffusion. ASME, Appl. Mech. Div. **34**, 19–35 (1979)
19. Hughes, T.J.R., Franca, L.P., Hulbert, G.M.: A new finite element formulation for computational fluid dynamics: VIII. The Galerkin/Least-squares method for advective-diffusive equations. Comput. Methods Appl. Mech. Eng. **73**, 173–189 (1989)
20. Jiang, B.-N.: The Least-Squares Finite Element Method, Scientific Computation. Springer, Berlin (1998)
21. Kayser-Herold, O., Matthies, H.G.: A unified least-squares formulation for fluid-structure interaction problems. Comput. Struct. **85**, 998–1011 (2007)
22. Korelc, J.: Automatic generation of finite-element code by simultaneous optimization of expressions. Theor. Comput. Sci. **187**(1), 231–248 (1997)

23. Korelc, J.: Multi-language and multi-environment generation of nonlinear finite element codes. Eng. Comput. **18**(4), 312–327 (2002)
24. Küttler, U., Gee, M., Förster, Ch., Comerford, A., Wall, W.A.: Coupling strategies for biomedical fluid - structure interaction problems. Int. J. Numer. Methods Biomed. Eng. **26**, 305–321 (2010)
25. Küttler, U., Wall, W.A.: Fixed-point fluid-structure interaction solvers with dynamic relaxation. Comput. Mech. **43**(1), 61–72 (2008)
26. Münzenmaier, S., Starke, G.: First-order system least squares for coupled Stokes–Darcy flow. SIAM J. Numer. Anal. **49**(1), 387–404 (2011)
27. Nisters, C., Schwarz, A.: Efficient stress-velocity least-squares finite element formulations for the incompressible Navier–Stokes equations. Comput. Methods Appl. Mech. Eng. (2017, in revision)
28. Ozcelikkale, A., Sert, C.: Least-squares spectral element solution of incompressible Navier–Stokes equations with adaptive refinement. J. Comput. Phys. **231**(9), 3755–3769 (2012)
29. Pian, T.H.H., Sumihara, K.: A rational approach for assumed stress finite elements. Int. J. Numer. Methods Eng. **20**, 1685–1695 (1984)
30. Prabhakar, V., Pontaza, J.P., Reddy, J.N.: A collocation penalty least-squares finite element formulation for incompressible flows. Comput. Methods Appl. Mech. Eng. **197**, 449–463 (2008)
31. Raviart, P.-A., Thomas, J.M.: A mixed finite element method for 2-nd order elliptic problems. Mathematical Aspects of Finite Element Methods, pp. 292–315. Springer, Berlin (1977)
32. Reddy, J.N.: Penalty-finite-element analysis of 3-D Navier–Stokes equations. Comput. Methods Appl. Mech. Eng. **35**, 87–97 (1982)
33. Reddy, J.N., Gartling, D.K.: The Finite Element Method in Heat Transfer and Fluid Dynamics, 3rd edn. CRC Press, Boca Raton (2010)
34. Schröder, J., Schwarz, A., Steeger, K.: Least-squares finite element formulations for isotropic and anisotropic elasticity at small and large strains. Advanced Finite Element Technologies. CISM Courses and Lectures, pp. 131–175. Springer, Berlin (2016)
35. Schröder, W.: Summary of Flow Modulation and Fluid-Structure Interaction Findings. Notes on Numerical Fluid Mechanics and Multidisciplinary Design, vol. 109. Springer, Berlin (2010)
36. Schwarz, A., Nickaeen, M., Serdas, S., Nisters, C., Ouazzi, A., Schröder, J., Turek, S.: A comparative study of mixed least-squares FEMs for the incompressible Navier–Stokes equations. Int. J. Comput. Sci. Eng. (2016)
37. Schwarz, A., Schröder, J., Serdas, S., Turek, S., Ouazzi, A., Nickaeen, M.: Performance aspects of a mixed s-v LSFEM for the incompressible Navier–Stokes equations with improved mass conservation. Proc. Appl. Math. Mech. **13**, 97–98 (2013)
38. Schwarz, A., Steeger, K., Schröder, J.: Weighted overconstrained least-squares mixed finite elements for static and dynamic problems in quasi-incompressible elasticity. Comput. Mech. **54**(3), 603–612 (2014)
39. Simo, J.C., Rifai, M.S.: A class of mixed assumed strain methods and the method of incompatible modes. Int. J. Numer. Methods Eng. **29**, 1595–1638 (1990)
40. Starke, G.: An adaptive least-squares mixed finite element method for elasto-plasticity. SIAM J. Numer. Anal. **45**, 371–388 (2007)
41. Tian, F.-B., Dai, H., Luo, H., Doyle, J.F., Rousseau, B.: Fluid-structure interaction involving large deformations: 3D simulations and applications to biological systems. J. Comput. Phys. **258**, 451–469 (2014)
42. Turek, S., Hron, J., Razzaq, M., Wobker, H., Schäfer, M.: Numerical benchmarking of fluid-structure interaction: a comparison of different discretization and solution approaches (2010)
43. van Zuijlen, A.H., Bijl, H.: A higher-order time integration algorithm for the simulation of nonlinear fluid-structure interaction. Nonlinear Anal. Theory Methods Appl. **63**(5–7), e1597–e1605 (2005)
44. Wall, W.A., Genkinger, S., Ramm, E.: A strong coupling partitioned approach for fluid-structure interaction with free surfaces. Comput. Fluids **36**(1), 169–183 (2007)
45. Wilson, E.L., Taylor, R.L., Doherty, W.P., Ghaboussi, J.: Incompatible displacement models. Numer. Comput. Methods Struct. Mech. **43** (1973)

46. Wolfram Research Inc. Mathematica. Campaign: Wolfram Research, Inc. Version 10.1 edition (2015)
47. Zienkiewicz, O.C., Taylor, R.L., Nithiarasu, P.: Fluid-structure interaction. The Finite Element Method for Fluid Dynamics, vol. 3, pp. 423–449 (2014)

Dynamic Analysis of Gradient Poroelastic Solids and Structures

Ioannis P. Pegios, Sofia Papargyri-Beskou and Dimitri E. Beskos

Abstract The present chapter presents a review of previous works of the authors on the subject of the dynamic analysis of gradient poroelastic solids and structures. First, the governing equations of motion of a fluid-saturated poroelastic medium with microstructural (for both the solid and fluid) and microinertia (for the solid) effects are derived. These equations are of an order of two degrees higher than in the classical case and consist of seven equations with seven unknowns in three-dimensions. Second, the propagation of plane harmonic waves in an infinitely extended medium is studied analytically for the low and high frequency range. This is accomplished by separating the equations of motion in their dilatational and rotational parts for which wave dispersion curves can be constructed. Third, a simple one-dimensional boundary value problem, that of the transient behavior of a gradient poroelastic soil column, is solved analytically/ numerically with the aid of numerical Laplace transform. Finally, on the basis of the above, conclusions are drawn and suggestions for future research are made.

1 Introduction

The quasi-static and dynamic theories of linear poroelasticity due to Biot [1, 2] have found many applications in geotechnical engineering, bioengineering and materials science and engineering. A review on the subject of poroelastodynamics up to 2009

I. P. Pegios
School of Sciences and Technology, Hellenic Open University, 26335 Patras, Greece
e-mail: ipegios@gmail.com

S. Papargyri-Beskou (✉)
Department of Civil Engineering, Aristotle University of Thessaloniki,
54124 Thessaloniki, Greece
e-mail: spapargy@civil.auth.gr

D. E. Beskos
Department of Civil Engineering, University of Patras, 26500 Patras, Greece
e-mail: d.e.beskos@upatras.gr

© Springer International Publishing AG 2018

H. Altenbach et al. (eds.), *Advances in Mechanics of Materials and Structural Analysis*, Advanced Structured Materials 80,
https://doi.org/10.1007/978-3-319-70563-7_13

has been reported by Schanz [3], while a very recent book on quasi-static and dynamic poroelasticity has been published by Cheng [4].

For some classes of materials like granular ones, which possess a natural microstructure, classical linear elasticity cannot take into account microstructural effects and resort should be made to higher order theories that do take into account those effects. A general linear theory of elasticity with microstructural effects (both of the micro-stiffness and micro-inertia type) has been developed by Mindlin [5]. The simplest possible version of that theory has two elastic constants (internal length scales) in addition to the two classical elastic moduli, which express the microstructural (micro-stiffness and micro-inertia) effects in a macroscopic manner. Using that simple theory, called gradient elastic theory, various wave propagation problems have been solved (e.g. [6, 7]) and the microstructural effects on dispersion curves have been assessed.

Microstructural effects in fluid-saturated poroelastic media have been studied by Berryman and Thigpen [8] through micro-inertia terms, Aifantis [9] and Vardoulakis and Aifantis [10] through second order gradients for densities and fluid pressure and Ehlers and Volk [11, 12] through micropolar solid rotations. More recently, Sciarra et al. [13] and Madeo et al. [14] developed a poroelastic theory involving gradient effects (micro-stiffness of solid) and studied the one – dimensional consolidation (quasi-static) problem of soil mechanics. Recently, Papargyri-Beskou et al. [15] introduced second order gradient of strain in the stress-strain relation for the solid component of a fluid-saturated poroelastic medium and studied the gradient effect on the dynamic column problem of soil mechanics. Finally, Papargyri-Beskou et al. [16] developed a three-dimensional poroelasticity theory with micro-stiffness effects for both the solid and the fluid and micro-inertia effects for the solid and studied wave dispersion and attenuation in the low frequency range. This work was very recently extended to the high frequency range by Smyrlis et al. [17]. Closing one should also mention the very recent book of Serpieri and Travascio [18] on variational poroelasticity, which also discusses gradient effects as treated in [13, 14].

The present work represents a review of the abovementioned recent works of the authors [15–17] in an effort to provide a unified treatment on the subject of gradient poroelastodynamics.

1.1 Governing Equations of Motion

Consider a fluid saturated poroelastic medium. Following [16] and using indicial notation for vectors and tensors (i, j = 1, 2, 3), one can write down the linearized equations of mass balance and linear momentum balance for the two constituents solid and fluid of a solid-fluid mixture in the form

$$-\dot{n} + \frac{1-n}{\rho_s}\dot{\rho}_s + (1-n)\dot{\varepsilon} = 0 \tag{1}$$

$$-\dot{n}+\frac{n}{\rho_f}\dot{\rho}_f+\bar{Q}^f_{i,i}+n\dot{\varepsilon}=0 \tag{2}$$

$$\sigma^s_{ij,j}=b^s_i+\bar{\rho}_s\ddot{u}_i \tag{3}$$

$$\sigma^f_{ij,j}=b^f_i+\rho_f\dot{\bar{Q}}^f_i+\bar{\rho}_f\ddot{u}_i \tag{4}$$

In the above, indices s and f stand for the solid skeleton and fluid, respectively, n denotes the porosity of the solid, $\bar{\rho}_f=n\rho_f$ and $\bar{\rho}_s=\rho_s(1-n)$ are the relative densities for the fluid and the solid, respectively with ρ_f and ρ_s being the fluid and solid densities, respectively, u_i are the components of the solid displacements, $\varepsilon_{ij}=1/2(u_{i,j}+u_{j,i})$ is the strain tensor of the solid, $\varepsilon=u_{i,i}$ is the dilatation of the solid, $\bar{Q}^f_i=n(\dot{u}^f_i-\dot{u}_i)$ is the relative specific discharge of the fluid with u^f_i being the components of the fluid displacements, σ^s_{ij} and σ^f_{ij} are the partial stress tensors for the solid and fluid, respectively with $\sigma_{ij}=\sigma^s_{ij}+\sigma^f_{ij}$ being the total stress tensor of the composite medium, $b^s_i=-b^f_i$ are the seepage forces and overdots denote time differentiation.

Assuming gradient effects in both the solid and the fluid components one has [16]

$$\sigma^s_{ij}=(1-\mathrm{g}^2\nabla^2)(\lambda\varepsilon\delta_{ij}+2\mu\varepsilon_{ij})+\bar{\rho}_s h^2\ddot{u}_{i,j} \tag{5}$$

$$\sigma^f_{ij}=-\beta\delta_{ij}(1-\theta^2\nabla^2)p \tag{6}$$

In the above, g and h are the length scale parameters (with dimensions of length) of the microstructure and microinertia, respectively, of the solid and θ the length scale parameter (with dimensions of length) of the microstructure of the fluid, p is the fluid pore pressure, λ and μ are the Lamé elastic constants of the solid, β is the coefficient expressing the deformability of the solid as affected by the fluid pressure and $u_{i,j}=\partial u_i/\partial x_j$.

Constitutive equations can also be assumed for n, ρ_f and b^f_i of the form [16]

$$n=\beta\varepsilon+\gamma p \tag{7}$$

$$\dot{\rho}_f=\rho_f\delta(1-\theta^2\nabla^2)p \tag{8}$$

$$b^f_i=\beta\frac{\nu_f}{K}\bar{Q}^f_i \tag{9}$$

In the above, γ is the compressibility of the porous medium, δ is the fluid compressibility, ν_f is the dynamic viscosity of the fluid and K is the permeability in units of length square.

Combining (7) and (1) one obtains

$$\dot{\rho}_s = \frac{\rho_s}{1-n}((\beta + n - 1)\dot{\varepsilon} + \gamma(1 - \theta^2\nabla^2)\dot{p}) \tag{10}$$

and thus, Eq. (1) is replaced by Eq. (10).

The governing equations of motion of the composite medium can now be obtained by substituting the constitutive equations (5)–(9) into the field equations (2)–(4) and express $\bar{Q}_i^f$ in terms of $\dot{u}_i^f$ and $\dot{u}_i$. The result is [16]

$$(1 - \mathrm{g}^2\nabla^2)((\lambda + \mu)u_{k,ki} + \mu\nabla^2 u_i) = -\frac{\beta\nu_f n}{K}(\dot{u}_i^f - \dot{u}_i) + \bar{\rho}_s\ddot{u}_i - \bar{\rho}_s h^2\nabla^2\ddot{u}_i \tag{11}$$

$$-\beta(1 - \theta^2\nabla^2)p_{,i} = n\rho_f\ddot{u}_i^f + \frac{\beta\nu_f n}{K}(\dot{u}_i^f - \dot{u}_i) \tag{12}$$

$$\beta\dot{u}_{i,i} + \mathrm{n}\dot{u}_{i,i}^f + (\gamma + \delta n)(1 - \theta^2\nabla^2)\dot{p} = 0 \tag{13}$$

The above governing equations of motion for a fluid-saturated poroelastic medium with microstructural effects form a system of 7 partial differential equations with 7 unknowns, that is, three solid displacements u_i, three fluid displacements u_i^f and one porewater pressure p. It is observed that for $g = h = \theta = 0$, that is, when there are no microstructural effects, Eqs. (11)–(13) reduce to the classical ones presented as Eqs. (42)–(44) in Beskos [19]. A comparison between these classical equations with the classical ones of Biot [1] done in Beskos [19] reveals that apart from an extra term in Biot's equations, the form of the two sets of classical equations in [1, 19] is the same with some differences in some of the coefficients due to different definitions of partial stresses and seepage forces between the two theories. A comparison between Eqs. (11)–(13) and their corresponding classical ones indicates that inclusion of microstructural parameters raises the spatial order of the differential equations by two as in the case of gradient elasticity [5, 7].

1.2 Wave Propagation Analysis

Application of the divergence and the rot (curl) operators on Eqs. (11) and (12) and employment of Eq. (13) results in the dilatation equations of motion [16]

$$(\lambda + 2\mu)(1 - g^2\nabla^2)\nabla^2\varepsilon = \frac{\beta\nu_f}{K}[(\beta + n)\dot{\varepsilon} + (\gamma + \delta n)(1 - \theta^2\nabla^2)\dot{p}] + \bar{\rho}_s(1 - h^2\nabla^2)\ddot{\varepsilon} \tag{14}$$

$$\begin{aligned} \beta(1 - \theta^2\nabla^2)\nabla^2 p = {} & \rho_f\beta\ddot{\varepsilon} + \rho_f(\gamma + \delta n)(1 - \theta^2\nabla^2)\ddot{p} \\ & + \frac{\beta\nu_f}{K}[(\beta + n)\dot{\varepsilon} + (\gamma + \delta n)(1 - \theta^2\nabla^2)\dot{p}] \end{aligned} \tag{15}$$

and the rotational equations of motion [16]

$$\mu(1-g^2\nabla^2)\nabla^2\boldsymbol{\omega} = n\rho_f\ddot{\boldsymbol{\omega}}^f + \bar{\rho}_s(1-h^2\nabla^2)\ddot{\boldsymbol{\omega}} \tag{16}$$

$$\rho_f\ddot{\boldsymbol{\omega}}^f + \frac{\beta\nu_f}{K}\dot{\boldsymbol{\omega}}^f - \frac{\beta\nu_f}{K}\dot{\boldsymbol{\omega}} = 0 \tag{17}$$

where

$$\varepsilon = u_{i,i} \quad , \quad \boldsymbol{\omega} = \frac{1}{2}\nabla\times\mathbf{u} \quad , \quad \boldsymbol{\omega}^f = \frac{1}{2}\nabla\times\mathbf{u}^f \tag{18}$$

with bold face letters denoting vectors.

Consider first plane harmonic waves in the x-z plane propagating along the z direction in an infinitely extended medium moving according to Eqs. (14) and (15). Thus [16]

$$\boldsymbol{\varepsilon} = A\mathrm{e}^{i(\omega t-\Lambda z)} \quad , \quad p = B\mathrm{e}^{i(\omega t-\Lambda z)} \tag{19}$$

where A and B are amplitudes, $\boldsymbol{\omega}$ the circular frequency, $\boldsymbol{\Lambda}$ the complex wavenumber and $i=\sqrt{-1}$. It can be shown that [16]

$$(\varepsilon, p) = (A, B)\mathrm{e}^{\Delta_p z}\mathrm{e}^{i(\omega t-k_p z)} \tag{20}$$

where k_p and Δ_p are the wavenumber and attenuation coefficient, respectively, for dilatation or P-waves, connected via Λ as $\Lambda = k_p(\omega) + i\Delta_p(\omega)$ with the Λ's obtained as the roots of an algebraic equation of the 8^{th} order [16]. The phase velocity C_p of P-waves is then obtained as $C_p = \omega/k_p(\omega)$.

Consider now plane harmonic waves in the x-z plane propagating along the z direction in an infinitely extended medium moving according to Eqs. (16) and (17). Thus [16]

$$\boldsymbol{\omega} = \mathbf{A}\mathrm{e}^{i(\omega t-\bar{\Lambda} z)} \quad \boldsymbol{\omega}^f = \mathbf{B}\mathrm{e}^{i(\omega t-\bar{\Lambda}_z)} \tag{21}$$

where **A** and **B** are vector amplitudes to be determined and $\bar{\Lambda}$ the complex wavenumber. It can be shown

$$(\boldsymbol{\omega}, \boldsymbol{\omega}^f) = (\mathbf{A}, \mathbf{B})\mathrm{e}^{\Delta_s z}\mathrm{e}^{i(\omega t-k_s z)} \tag{22}$$

where k_s and Δ_s are the wavenumber and attenuation coefficient, respectively, for rotational or S-waves, connected via $\bar{\Lambda}$ as $\bar{\Lambda} = k_s(\omega) + i\Delta_s(\omega)$ with $\bar{\Lambda}$ obtained as the roots of an algebraic equation of the 4^{th} order [16]. The phase velocity C_s of S-waves is then obtained as $C_s = \omega/k_s(\omega)$.

The physical quantities of interest here are the frequency-dependent velocities of propagation $C_{p1,}$ $C_{p2,}$ C_s and the corresponding attenuation coefficients Δ_{p1}, Δ_{p2}, Δ_s. The variation of these quantities with frequency is presented here for various combinations of the microstructural parameters g, h and θ. All quantities are normalized. Thus, C_{p1}, C_{p2} are normalized by $C_{pf} = [(1/\delta)/\rho_f]^{1/2}$, C_s by $C_{rs} = (\mu/\bar{\rho}_s)^{1/2}$,

ω is normalized by $\omega_{rp} = \beta \nu_f / K \bar{\rho}_s$, Δ_{p1} and Δ_{p2} are normalized by ω_{rp}/C_{rp} with $C_{rp} = [(\lambda + 2\mu)/\bar{\rho}_s]^{1/2}$, and Δ_s is normalized by ω_{rs}/C_{rs} with $\omega_{rs} = \beta \nu_f / K \rho_f$.

According to Biot [2], Poiseuille flow in the pores breaks down for frequencies higher than $\omega_t = \pi \nu_f / 4 \rho_f d^2$ where d is the pore diameter. In the low frequency range ($\omega \leq \omega_t$), ν_f is constant, while in the higher frequency range, ν_f is replaced by $\nu_f F(\omega)$, where $F(\omega)$ is a frequency correction factor expressed in terms of Bessel-Kelvin functions. The work in [14] was restricted to the low frequency range. Extension to the high frequency range was done by Smyrlis et al. [17]. For the frequency in the higher range there is an upper bound ω_{u} to ensure that the medium is still a continuum, i.e., the value at which the wavelength becomes of the order of the pore size. Thus $\omega_u = 2\pi C/d$ where C is the phase velocity of the S wave for the soil-fluid mixture computed as $C = (\mu/(\bar{\rho}_s + \bar{\rho}_f))^{1/2}$. Following Beskos et al. [20] and Smyrlis et al. [17], the correction factor F($\boldsymbol{\omega}$) is finally expressed as

$$\omega < \frac{4\nu_f}{d^2 \rho_f}, \qquad F(\omega) = \left(1 + \frac{(d/2)^4 \rho_f^2 \omega^2}{1.152 \nu_f^2}\right) + \mathrm{i} \left(\frac{(d/2)^2 \rho_f \omega}{24 \nu_f} \left(1 - \frac{(d/2)^4 \rho_f^2 \omega^2}{1.440 \nu_f^2}\right)\right) \tag{23}$$

$$\frac{4\nu_f}{d^2 \rho_f} \leq \omega \leq \frac{400 \nu_f}{d^2 \rho_f}, \qquad F(\omega) = \sum_{r=0}^{\infty} \frac{(-\mathrm{r})^r}{(\mathrm{r}!)^2} \left(\frac{i^{3/2} d \rho_f \omega^{1/2}}{4 \nu_f}\right)^{2r} \tag{24}$$

$$\omega > \frac{400\nu_f}{d^2\rho_f}, \quad \begin{array}{l} F(\omega) \approx \left\{ \left(\frac{d}{8\sqrt{2}} \left(\frac{\omega\rho_f}{\nu_f} \right)^{1/2} \right) \left[1 + \left(\frac{3\sqrt{2}}{d} \left(\frac{\nu_f}{\omega\rho_f} \right)^{1/2} \right) + \frac{15\nu_f}{2d^2\rho_f\omega} - \frac{135\nu_f^2}{2d^4\rho_f^2\omega^2} \right] \right\} \\ \mathrm{i} \left\{ \left(\frac{d}{8\sqrt{2}} \left(\frac{\omega\rho_f}{\nu_f} \right)^{1/2} \right) \left[1 - \frac{15\nu_f}{2d^2\rho_f\omega} - \frac{15\sqrt{2}}{d^3} \left(\frac{\nu_f}{\omega\rho_f} \right)^{3/2} - \frac{135\nu_f^2}{8d^4\rho_f^2\omega^2} \right] \right\} \end{array} \tag{25}$$

The numerical results of this section have been obtained on the basis of the values of the coefficients shown in Table 1, which correspond to a fully-saturated poroelastic sandstone. For these values one has $\omega_t = 7.85 \times 10^5 \mathrm{rad/s}$, $\omega_{rp} = 4.352 \times 10^5 \mathrm{rad/s}$ and $\omega_{rs} = 8.838 \times 10^5 \mathrm{rad/s}$. Thus, the low frequency results are valid for $\omega \leq \omega_t$ or for $\widehat{\omega} = \omega/\omega_{rp} \leq \widehat{\omega}_t = 1.804$ and $\widehat{\omega} = \omega/\omega_{rs} \leq \widehat{\omega}_t = 0.888$ for P and S waves, respectively. Finally, $\omega_u = 140 \times 10^5 \mathrm{sec}^{-1}$ and hence $\widehat{\omega}_u = \omega_u/\omega_{rp} = 32.174$ and $\widehat{\omega}_u = \omega_u/\omega_{rs} = 15.840$ for P and S waves, respectively. Using the above numerical data, dispersion and attenuation curves for the two P-waves and the S-wave of the considered gradient poroelastic medium have been obtained for the whole frequency range (low and higher) thereby completing the work in [16], which is restricted only to the low frequency range, i.e., up to $\widehat{\omega}_t$.

Figures 1 and 2 present dispersion curves for the first (fast) P wave for various values of $g = h = \theta$, $g > h$, respectively. One can observe that in all cases with $g = h = \theta = 0$, the present results are identical with the classical results for the special case of the single porosity medium in low and higher frequency range [20],

Table 1 Numerical values of coefficients for water-fully saturated, poroelasic sandstone

Coefficient	Symbol	Numerical value	Units
Lamé constant	λ	2.76×10^9	N/m^2
Lamé constant	μ	2.76×10^9	N/m^2
Porosity	n	0.2364	–
Porosity change due to dilatation	β	0.70	–
Solid density	ρ_s	2.66×10^3	kg/m^3
Water density	ρ_f	1.00×10^3	kg/m^3
Water compressibility	δ	4.67×10^{-10}	1/N m^2
Compressibility of pores	γ	4.24×10^{-9}	1/N m^2
Water dynamic viscosity	ν_f	1.00×10^{-3}	N s/m^2
Muskat permeability	K	7.92×10^{-13}	m^2
Pore diameter	d	1.0×10^{-6}	m

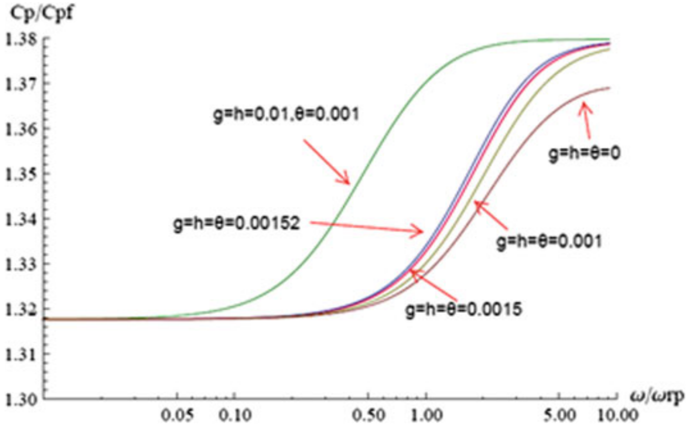

Fig. 1 Dispersion curves for the first (fast) P wave and $g = h = \theta$

as expected. It is also observed in Fig. 1 all dispersion curves start from a value $C_p/C_{pf} = 1.318$ (instead of 1.165 in [16]) at $\omega = 0$ in agreement with [20] and subsequently separate and become horizontal at $\widehat{\omega} = 10$.

Furthermore, one can observe from Fig. 2 that for $g > h = \theta$, and for high frequencies, increasing values of g, h and θ result in higher values of velocity for the same frequency.On the contrary, one can observe from Fig. 3 that for $h > g = \theta$ and for high frequencies, increasing values of h result in lower values of velocity for the same frequencies.

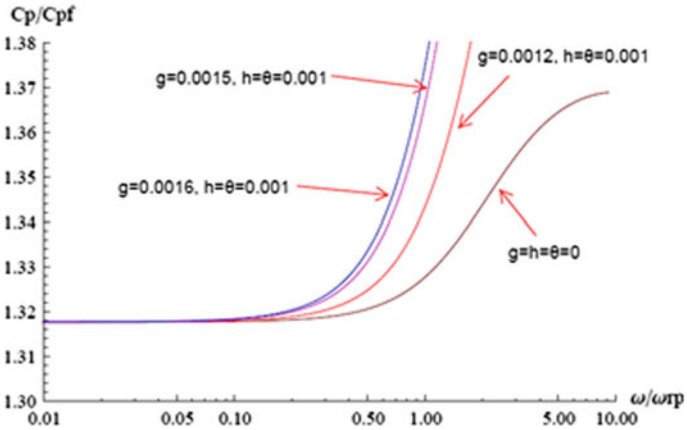

Fig. 2 Dispersion curves for the first (fast) P wave and $g > \theta = h$

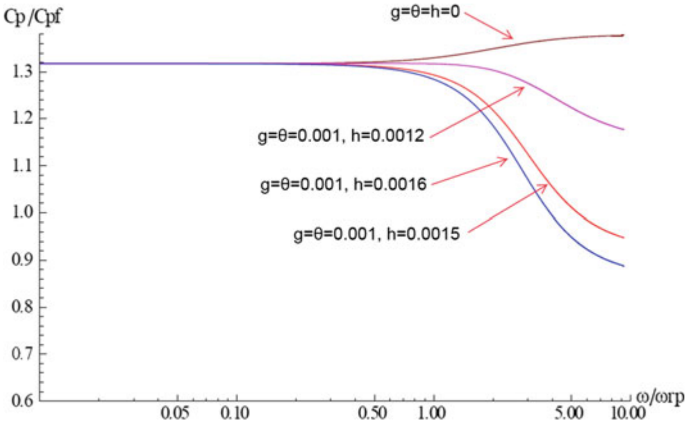

Fig. 3 Dispersion curves for the first (fast) P wave and $h > g = \theta$

Observing now Figs. 4 and 5, dealing with the attenuation curves corresponding to the dispersion ones of Figs. 1 and 2, one can conclude that for $g = h = \theta$ and $g > h$, respectively, increasing values of g, h and θ result in lower values of attenuation with high frequencies. The same also happens for $g < h$ (curves are not shown here due to lack of space).

Dispersion and attenuation curves for the second (slow) P wave are not affected by g, h, θ and hence coincide with the classical ones. Thus, they are identical with those in [16] in the low frequency range and those in [20] for one degree of porosity in both the low and high frequency range, as expected.

Figures 6 and 7 present dispersion curves, for the S wave and $g = h = \theta$ and $g > h = \theta$ respectively. One can observe that for $g = h = \theta = 0$, the present results are identical with the classical results in [20] for the special case of the single porosity

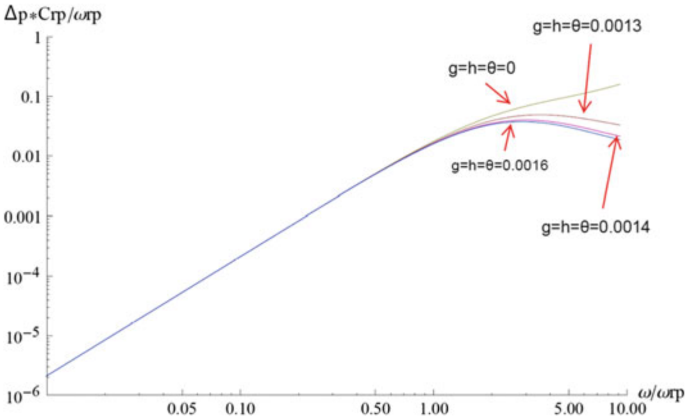

Fig. 4 Attenuation curves for the first (fast) P wave and $g = h = \theta$

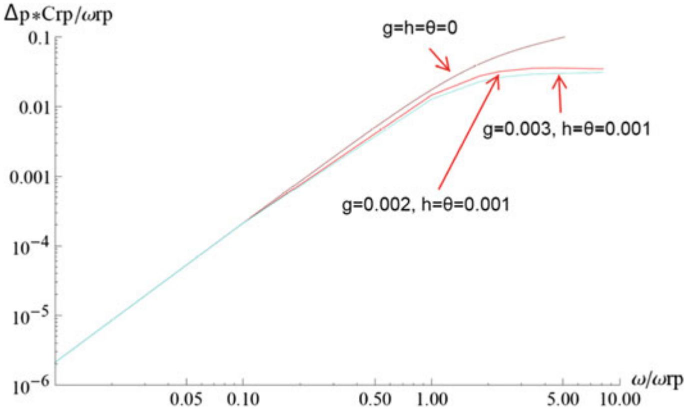

Fig. 5 Attenuation curves for the first (fast) P wave and $g > h = \theta$

medium in the low and high frequency range, as expected. Furthermore, one can observe that for $g > h = \theta$, and $g < h = \theta$, the dispersion curves behave as in the case of fast P-waves.

Figures 8 and 9 present attenuation curves for the S wave and $g = h = \theta$, $g > h = \theta$, respectively. It is observed that while for $\widehat{\omega} \leq 0.01$ there is no any microstructural effect, for $\widehat{\omega} \geq 0.01$ microstructural effects do appear and one has that for increasing values of $g = h = \theta$ or $g > h = \theta$ the attenuation decreases for the same frequency. The same behavior is also observed for the case of $h > g = \theta$ (curves are not shown here due to lack of space).

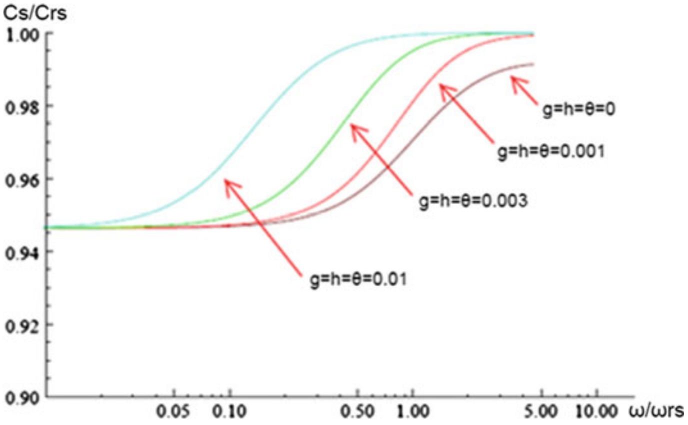

Fig. 6 Dispersion curves for S wave and $g = h = \theta$

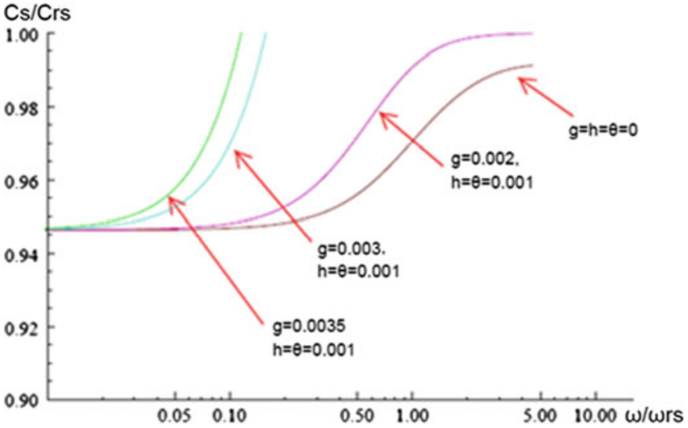

Fig. 7 Dispersion curves for S wave and $g > h = \theta$

1.3 The Dynamic Gradient Poroelastic Column Problem

Consider a fluid-saturated porous gradient elastic layer of height H supported by a rigid and impervious base medium and subjected at its top to a uniformly distributed suddenly applied load, as shown in Fig. 10. This load has a magnitude σ_o and is applied through a rigid porous plate. The problem can be solved by analyzing only a one-dimentional column of the layer under appropriate boundary and initial conditions. For this gradient poroelastic medium it is assumed for simplicity that $h = \theta = 0$ and thus the one-dimensional form of Eqs. (11)–(13) reads as

$$Eu'' - g^2 Eu'''' = \bar{\rho}_s \ddot{u} - \frac{n\beta\nu_f}{K}(\dot{u}^f - \dot{u}) \tag{26}$$

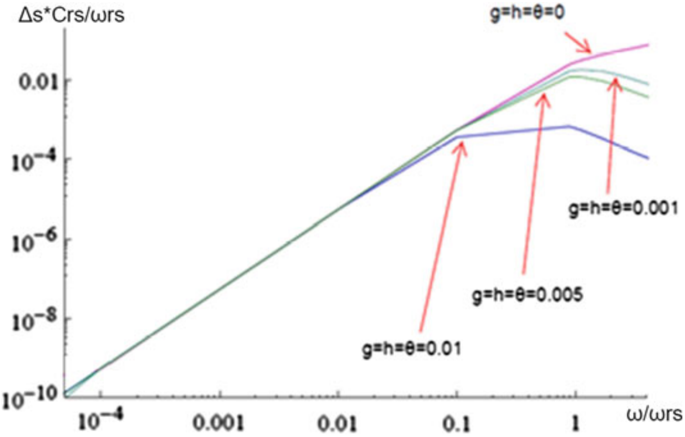

Fig. 8 Attenuation curves for S wave and $g = h = \theta$

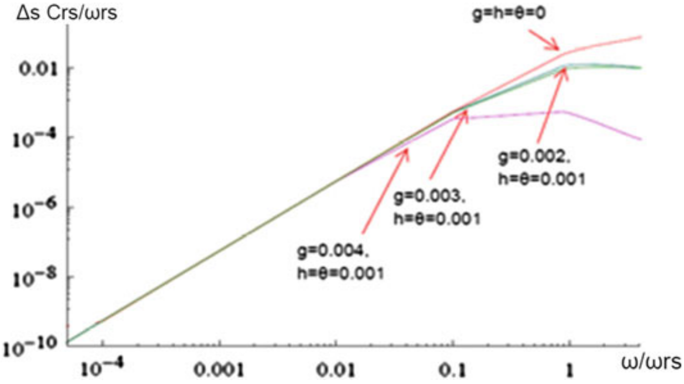

Fig. 9 Attenuation curves for S wave and $g > h = \theta$

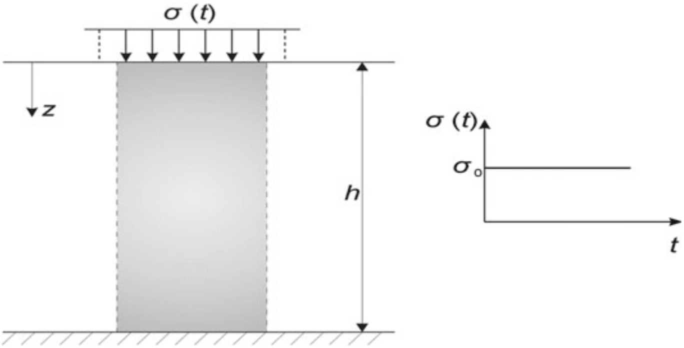

Fig. 10 Geometry and loading of the column problem

$$-np' = n\rho_f \ddot{u}^f + \frac{n^2 \nu_f}{K}(\dot{u}^f - \dot{u}) \tag{27}$$

$$n(\dot{u}^f)' + \beta \dot{u}' + (\gamma + \delta n)\dot{p} = 0 \tag{28}$$

where E is the modulus of elasticity, $u = u\,(\mathrm{z}, t)$ and $u^f = u^f\,(z, t)$ are the displacements of the solid and fluid along the vertical z direction, respectively and primes indicate differentiation along the z direction. The corresponding equations in [15] which are based on Biot's theory extended to the case of gradient elastic skeleton, are of the form

$$Eu'' - g^2 E u'''' = (\tilde{\alpha} - n)p' + \bar{\rho}_s \ddot{u} - \frac{n^2 \nu_f}{K}(\dot{u}^f - \dot{u}) \tag{29}$$

$$-np' = n\rho_f \ddot{u}^f + \frac{n^2 \nu_f}{K}(\dot{u}^f - \dot{u}) \tag{30}$$

$$n(u^f)' + (\tilde{\alpha} - n)u' + \tilde{\beta} p = 0 \tag{31}$$

where the coefficients $\tilde{\alpha}$ and $\tilde{\beta}$ can be found in [15]. One can observe that there are some small differences between Eqs. (29)–(31) and Eqs. (26)–(28) consisting of the extra pressure term in Eq. (29) and some other differences in some of the coefficients, as it has been mentioned in Beskos [19] and at the end of the present Sect. 2. In the following, use will be made of Eqs. (29)–(31) of [15].

The boundary conditions take the form [15]

$$u'(0, t) = -\zeta \sigma_0 / E, \quad u'''(H, t) = 0 \tag{32}$$

$$u(H, t) = u^f(H, t) = 0 \tag{33}$$

$$p(0, t) = p'(H, t) = 0 \tag{34}$$

$$u'''(0, t) = -\sigma_0 (1 - \zeta)/\mathrm{g}^2 E \tag{35}$$

while the initial conditions are given by [15]

$$u(\mathrm{z}, 0) = u^f(\mathrm{z}, 0) = \sigma_0 (H - z)/(E + E^*) \tag{36}$$

$$u'(\mathrm{z}, 0) = (u^f)'(\mathrm{z}, 0) = -\sigma_0/(E + E^*) \tag{37}$$

$$\dot{u}(\mathrm{z}, 0) = \dot{u}^f(\mathrm{z}, 0) = 0 \tag{38}$$

$$p(z, 0) = \sigma_0/(\beta^* + n) \tag{39}$$

where

$$E^* = \tilde{\alpha} n/\tilde{\beta}, \quad \beta^* = E\tilde{\beta}/\tilde{\alpha} \tag{40}$$

Application of Laplace transform with respect to time on Eqs. (29)–(31) under the initial condition (36)–(39) and subsequent elimination of the transformed u^f results in the system of the two ordinary differential equations

$$E\bar{u}'' - g^2 E\bar{u}''\,'' + A_1(\mathrm{s})\bar{u} - A_2(\mathrm{s})\bar{p}' = B(\mathrm{s})(\mathrm{z} - H) \tag{41}$$

$$A_2(\mathrm{s})\bar{u}' - A_3(\mathrm{s})\bar{p}'' + \tilde{\beta}\bar{p} = F(\mathrm{s}) \tag{42}$$

where overbars denote Laplace transformed quantities and $A_1\ (s)$, $A_2\ (s)$, $A_3\ (s)$, $B(s)$ and F(s) are explicitly given in [15]. The solution of the system (41) and (42) is of the form

$$\bar{u} = \bar{u}_h + \bar{u}_p, \quad \bar{p} = \bar{p}_h + \bar{p}_p \tag{43}$$

where

$$\bar{u}_h = \sum_{i=1}^{6} C_{1i} e^{\xi_i z}, \quad \bar{p}_h = \sum_{i=1}^{6} C_{2i} e^{\xi_i z} \tag{44}$$

$$\bar{u}_p = D_1(z - H), \quad \bar{p}_p = D_2 \tag{45}$$

$$C_{2i} = C_{1i} A_2 \xi_i / [A_3 \xi_i^2 - \tilde{\beta})] = C_{1i} f(\xi_i) \tag{46}$$

$$D_1(\mathrm{s}) = B(\mathrm{s})/A_1(\mathrm{s}), \quad D_2(\mathrm{s}) = [F(\mathrm{s})A_1(\mathrm{s}) - B(\mathrm{s})A_2(\mathrm{s})]/A_1(\mathrm{s})\tilde{\beta} \tag{47}$$

with ξ_i being the roots of the sixth order characteristic algebraic equation.

Use of the boundary conditions (32)–(35) in the Laplace transformed domain enables one to determine the 6 unknowns constants C_1i. The time domain response of the system is obtained by a numerical inversion of the transformed solution (43)

Fig. 11 Displacement history at $z = 0$ for soil column with $H = 5\,\mathrm{m}$

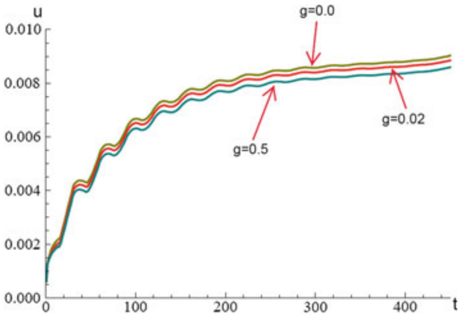

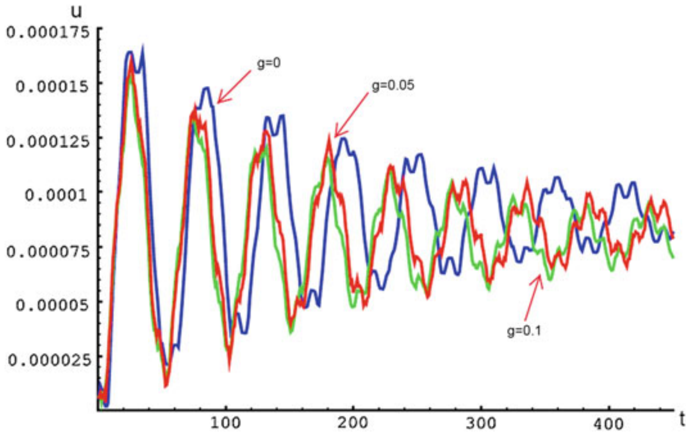

Fig. 12 Displacement history at $z = H/2$ for soil column with $H = 0.1\,\mathrm{m}$

Table 2 Material properties of soil rock types considered

Material	$1/\beta$ [N/m^2]	ν	ρ_s [kg/m^3]	n	K [m^2]	$1/\beta_\mathrm{s}$ [N/m^2]	$1/\beta_\mathrm{f}$ [N/m^2]	ρ_f [kg/m^3]	ν_f [Ns/m^2]
Soil	3.41E+08	0.25	2660	0.45	1.00E-09	2.14E+10	2.14E+09	1000	1.00E-03

with the aid of Durbin's [21] algorithm. Figures 11 and 12 provide the time histories (here the time history is 0.20 sec divided by 500 points in equal intervals) of solid displacement $u(0, t)$ for σ_0 =0.5 MPa, $\zeta = 0.5$.

For Fig. 11 $H = 5\,\mathrm{m}$, the gradient coefficient $g = 0.0, 0.02$ and $0.5\,\mathrm{m}$ although for Fig. 12 $H = 0.1\,\mathrm{m}$ the gradient coefficient $g = 0.0, 0.05$ and $0.1\,\mathrm{m}$ and the values of the remaining constants are those of Table 2. From Figs. 11 and 12 and other figures which can be found in [15] one can observe that the response is oscillatory over time with oscillation amplitudes decreasing with time and that the presence of g results in a small displacement amplitude reduction (stiffening effect).

2 Conclusions and Recommendations for Future Research

On the basis of preceding developments and discussion, the following can be stated:

(1) A general dynamic poroelastic theory including both microstructural and micro-inertia effects has been developed and used to study wave propagation in an infinitely extended medium and to solve the one-dimensional column problem of soil mechanic, under a suddenly applied load.
(2) Concerning the wave propagation analysis presented here for both the low and high frequency ranges

- (i) There are no microstructural effects on either the dispersion or the attenuation curves in the low frequency range.
- (ii) Microstructural effects are significant for higher frequencies and all microstructural parameters (g, h, θ) are important.
- (iii) Dispersion and attenuation curves for the second (slow) P wave exhibit no dependence on the microstructure.
- (iv) Increasing values of g or h result in higher or lower values of dispersive velocities, respectively, and lower values of attenuation for either the fast P or the S wave.

(3) Concerning the dynamic response of the soil column to the suddenly applied load, it was found that the strain gradient effect consists of stiffening the solid skeleton and resulting in lower displacements for those soils for which the column height tends to have comparable dimensions to those of the internal length scale of the material microstructure.

(4) Concerning recommendations for future research on the subject, one can propose the establishment of a variational principle for gradient poroelastodynamics, which will reproduce the governing equations of motion thereby providing a verification of the theory and determine all possible classical and non-classical boundary conditions of the phenomenon. Knowledge of these boundary conditions will enable one to solve correctly more complicated boundary value problems than the simple one-dimentional soil column problem for which non-classical boundary conditions were just the result of an educated guess.

References

1. Biot, M.A.: General theory of three-dimensional consolidation. J. Appl. Phys. **12**, 55–64 (1941)
2. Biot, M.A.: Theory of propagation of elastic waves in a fluid-saturated porous solid: I low frequency range; II higher frequency range. J. Acoust. Soc. Am. **28**, 168–178, 179–191 (1956)
3. Schanz, M.: Poroelastodynamics: linear models, analytical solutions and numerical methods. Appl. Mech. Rev. ASME **62**, 1–15 (2009)
4. Cheng, A.H.D.: Poroelasicity. Springer, Switzerland (2016)
5. Mindlin, R.D.: Micro-structure in linear elasticity. Arch. Ration. Mech. Anal. **16**, 51–78 (1964)
6. Vavva, M.G., Protopappas, V.C., Gergidis, L.N., Charalambopoulos, A., Fotiadis, D.L., Polyzos, D.: Velocity dispersion of guided waves propagating in a free gradient elastic plate: application to cortical bone. J. Acoust. Soc. Am. **125**, 3414–3427 (2009)
7. Papargyri-Beskou, S., Polyzos, D., Beskos, D.E.: Wave dispersion in gradient elastic solids and structures: a unified treatment. Int. J. Solids Stuct. **46**, 3751–3759 (2009)
8. Berryman, J.G., Thigpen, L.: Nonlinear and semi-linear dynamic poroelasticity with microstructure. J. Mech. Phys. Solids **33**, 97–116 (1985)
9. Aifantis, E.C.: Microscopic processes and macroscopic response. In: Desai, C.S., Gallagher, R.H. (eds.) Mechanics of Engineering Materials, pp. 1–22. Wiley, Chichester (1984)
10. Vardoulakis, I., Aifantis, E.C.: On the role of microstructure in the behavior of solids: effects of higher order gradients and internal inertia. Mech. Mater. **18**, 151–158 (1994)
11. Ehlers, W., Volk, W.: On shear band localization phenomena of liquid-saturated granular elastoplastic porous solid materials accounting for fluid viscosity and micropolar solid rotations. Mech. Cohes. Frict. Mater. **2**, 301–320 (1997)

12. Ehlers, W., Volk, W.: On theoretical and numerical methods in the theory of porous media based on polar and non-polar elasto-plastic solid materials. Int. J. Solids Struct. **35**, 4597–4617 (1998)
13. Sciarra, G., Dell'Isola, F., Ianiro, N., Mades, A.: A variational deduction of second gradient poroelasicity, Part I: general theory. J. Mech. Mater. Struct. **3**, 507–526 (2008)
14. Madeo, A., Dell'Isola, F., Ianiro, N., Sciarra, G.: A variational deduction of second gradient poroelasticity II: an application to the consolidation problem. J. Mech. Mater. Stuct. **3**, 607–625 (2008)
15. Papargyri-Beskou, S., Tsinopoulos, S.V., Beskos, D.E.: Transient dynamic analysis of a fluid-saturated porous gradient elastic column. Acta Mech. **222**, 351–362 (2011)
16. Papargyri-Beskou, S., Polyzos, D., Beskos, D.E.: Wave propagation in 3-D poroelastic media including gradient effects. Arch. Appl. Mech. **82**, 1569–1584 (2012)
17. Smyrlis, V.D., Pegios, I.P., Papargyri-Beskou, S.: On wave propagation in gradient poroelasicity. Soil Dyn. Earthq. Eng. **88**, 72–75 (2016)
18. Serpieri, R., Travascio, F.: Variational Continuum Multiphase Poroelasticity. Springer International Publishing AG, Singapore (2017)
19. Beskos, D.E.: Dynamics of saturated rocks. I: equations of motion. J. Eng. Mech. ASCE **115**(5), 982–995 (1989)
20. Beskos, D.E., Vgenopoulou, I., Providakis, C.P.: Dynamics of saturated rocks II: body waves. J. Eng. Mech. ASCE **115**(5), 996–1016 (1989)
21. Durbin, F.: Numerical inversion of Laplace transform: an efficient improvement to Dubner and Abate's method. Comput. J. **17**, 371–376 (1974)

Microstructured Multiferroic Materials: Modelling Approaches Towards Efficiency and Durability

Andreas Ricoeur, Artjom Avakian and Stephan Lange

Abstract Magnetoelectric composites are investigated by numerical simulation. Nonlinear material models describing the magneto-ferroelectric or electro-ferromagnetic behaviors of the two constituents are presented. The ferroelectric model additionally accounts for damage evolution due to micro crack growth. The constitutive equations and weak forms of balance equations have been implemented within a finite element framework. A so-called condensed approach is also elaborated towards multiferroic compounds. Numerical simulations focus on the prediction of local domain orientation, the overall constitutive behaviors, the calculation of magnetoelectric coupling coefficients, and the investigation of damage processes, predominantly during magneto-electric poling, as well as mutual interactions of these aspects. A particle and a laminated composite are compared as examples.

1 Introduction

The coupling of magnetic and electric fields due to the constitutive behavior of a material is commonly denoted as magnetoelectric (ME) effect. The latter is only observed in a few crystal classes exhibiting a very weak coupling, mostly at low temperatures, which can hardly be exploited for technical applications [13, 19, 30]. Much larger coupling coefficients are obtained at room temperature in composite materials with ferroelectric and ferromagnetic constituents. The ME effect is then induced by the strain of matrix and inclusions or of different constituents, respectively, converting electrical and magnetic energies based on the piezoelectric and

---

A. Ricoeur (✉) · A. Avakian · S. Lange
Institute of Mechanics, University of Kassel, Mönchebergstr. 7,
34125 Kassel, Germany
e-mail: ricoeur@uni-kassel.de

A. Avakian
e-mail: artjom.avakian@uni-kassel.de

S. Lange
e-mail: stephan.lange@uni-kassel.de

© Springer International Publishing AG 2018

H. Altenbach et al. (eds.), *Advances in Mechanics of Materials and Structural Analysis*, Advanced Structured Materials 80,
https://doi.org/10.1007/978-3-319-70563-7_14

magnetostrictive effects. From the engineering point of view, this kind of quasistatic conversion of magnetic to electric energy and vice versa is extremely interesting, giving rise to various technical applications. Promising examples are the monitoring of brain activity from weak magnetic fields generated by neuronal activity (magnetoencephalography, MEG) or the storage of digital data based on the principle of electric writing magnetic reading [40].

Some ferromagnetic materials exhibit a pronounced hysteresis behavior, others show an almost reversible nonlinear characteristic. Even two specimens with an identical chemical composition can exhibit qualitatively different features [5–7], depending e.g. on the milling of the powder, the sintering conditions or particle diameters. The reason for the different behaviors is found on the micro scale of domain or BLOCH walls [4, 8]. In this chapter, two approaches are presented for the constitutive modelling of ferromagnetic materials. The one is akin to a model for ferroelectrics and is based on microphysical considerations [1, 26]. It takes advantage of the fact that some aspects of ferromagnetic and ferroelectric behaviors, although originating from completely different processes on the atomic scale, show comparable features on the meso and macro levels. The other approach is purely phenomenological starting from a thermodynamical potential and providing a reversible nonlinear behavior.

The finite element method (FEM) is adopted to solve complex boundary value problems (BVP) based on weak formulations of multiphysical balance laws in connection with the constitutive laws outlined above. User-defined finite elements (FE) have been developed, which are integrated into the commercial FE code ABAQUS providing the solver tool. Additionally, an own pre-and postprocessor has been developed for the sake of conveniently displaying the results of simulations. Due to the brittleness of the investigated materials, large deformations do not appear, thus the FE framework is restricted to linear kinematics. Besides the FEM, a so-called condensed model (CM) is presented here. It does not exhibit a spatial discretization, thus it is not suitable for complex boundary value problems. On the other hand, it is very efficient to investigate multiaxial, multiphysical features of polycrystalline smart materials. The CM approach has been developed for ferroelectric materials [26] including damage evolution in terms of micro crack growth [27].

Among various possible configurations of multiferroic composites, two compositions have been chosen in this chapter, to demonstrate the potential of numerical simulation in the design process. One consists of a ferroelectric matrix with embedded soft ferromagnetic particles, the other is a laminated structure with ferroelectric and hard ferromagnetic layers. The prediction and comparison of ME coupling coefficients is in the focus of the investigations, providing the possibility of functional optimization. These coefficients turn out to be subject to a variety of influencing factors, e.g. the way of magnetoelectric poling, geometrical features or volume fractions of constituents. One important and inevitable aspect is the cracking of the structure in terms of micro crack initiation in the ferroelectric and ferromagnetic materials, as well as delamination of the constituents. The related stress relief reduces the piezoelectric and magnetostrictive coupling, the domain activities and thus the ME coupling efficiency. A second aspect, of course, is the reduction of strength and lifetime of the smart devices. In order to include cracking into the simulations, damage evolution has been incorporated into the ferroelectric constitutive model, accounting for micro crack growth, predominantly driven by residual stresses due to ferroelectric domain switching. Cracking of the ferromagnetic constituent and delamination are not considered so far.

An overview on the state of the art in ferroic constitutive modelling and FE simulation of ME composites is given in [1–3].

2 Constitutive Behaviors: Compilation of Equations

The constitutive frameworks of ferroelectric and reversible and irreversible ferromagnetic behaviors are briefly summarized in this section and compared to each other. The theoretical framework is outlined more detailed in Sect. 3. Ferroelectric materials exposed to electromagnetic fields are described by the following constitutive equations [1]:

$$\begin{aligned} \sigma_{ij} &= C_{ijkl}\left(\varepsilon_{kl} - \varepsilon_{kl}^{\mathrm{irr}}\right) - e_{lij}E_l, \\ D_i &= e_{ikl}\left(\varepsilon_{kl} - \varepsilon_{kl}^{\mathrm{irr}}\right) + \kappa_{il}E_l + P_i^{\mathrm{irr}}, \\ B_i &= \mu_{ij}H_j. \end{aligned} \tag{1}$$

Here, as in the following, the analytical notation is used introducing lower case indices taking values 1, 2, 3 and implying summation over repeated indices. Within a microphysical framework, the irreversible strain $\varepsilon_{kl}^{\mathrm{irr}}$ and polarization P_i^{irr} are due to domain wall motion. Considering plane problems, a grain consists of four domain species separated by 90° - and 180° - domain walls, see Fig. 1. The formulation of a nonlinear constitutive law thus requires four internal variables and associated evolution equations describing the switching of unit cells on the micro level. Due to intended applications within a multiferroic framework, the ferroelectric material is allocated a magnetic permeability expressed by the third equation relating the magnetic field H_j and the induction B_i. The elastic, piezoelectric, dielectric and magnetic permeability tensors C_{ijkl}, e_{ikl}, κ_{il} and μ_{ij} also depend on the internal variables, giving rise to an additional source of nonlinearity, even in the magnetic properties. The other quantities in Eq. (1) are stress σ_{ij}, electric field E_l and electric displacement D_i.

Based on the same ideas as Eq. (1), the ferromagnetic constitutive equations read [2]

$$\begin{aligned} \sigma_{ij} &= C_{ijkl}\left(\varepsilon_{kl} - \varepsilon_{kl}^{\mathrm{irr}}\right), \\ D_i &= \kappa_{il}E_l, \\ B_i &= \mu_{ij}H_j + M_i^{\mathrm{irr}}. \end{aligned} \tag{2}$$

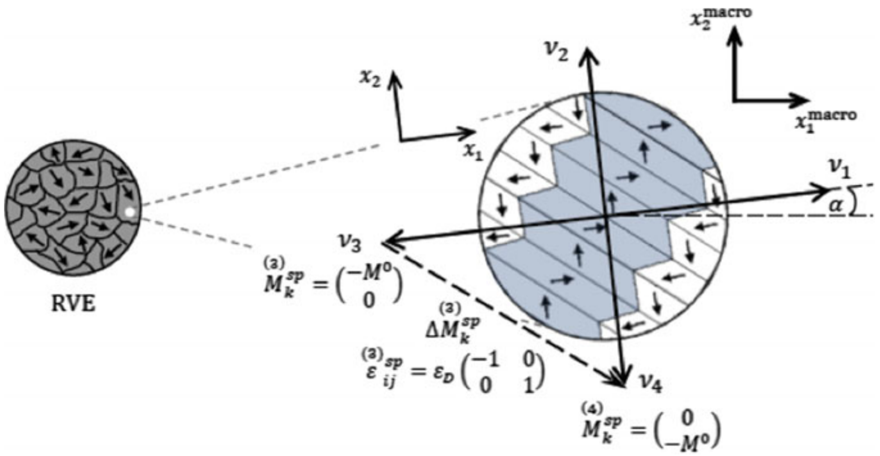
x_2^{macro}
x_1^{macro}
v_2
x_2
x_1
v_1
α
RVE
v_3
$\overset{(3)}{M}{}_k^{sp} = \begin{pmatrix} -M^0 \\ 0 \end{pmatrix}$
$\Delta \overset{(3)}{M}{}_k^{sp}$
$\overset{(3)}{\varepsilon}{}_{ij}^{sp} = \varepsilon_D \begin{pmatrix} -1 & 0 \\ 0 & 1 \end{pmatrix}$
v_4
$\overset{(4)}{M}{}_k^{sp} = \begin{pmatrix} 0 \\ -M^0 \end{pmatrix}$

Fig. 1 Representative volume element (RVE) and global coordinate system $\left(x_1^{\text{macro}}, x_2^{\text{macro}}\right)$, domain pattern and internal variables ν_n representing the magnetic orientations in a grain with local coordinate system (x_1, x_2)

Here, irreversible strain and irreversible magnetization M_i^{irr} or magnetic polarization, respectively, are likewise governed by four internal variables describing BLOCH wall motion due to magnetomechanical driving forces. The affinity to ferroelectricity on the macro- and mesoscales allows for a similar modeling of ferromagnetism covering the essential phenomena. Anyway, in the constitutive framework both physical processes merge into an evolution law for the internal variables, which is based on the magnetoelastic or electroelastic energies, respectively, going along with the changes of the directions of magnetic or electric dipoles.

In contrast to ferroelectricity, piezomagnetic coefficients relating magnetic field and stress or strain and magnetic induction are not involved, accounting for the saturation at larger fields. As a second consequence, the irreversible strain does not directly induce a magnetic induction B_i. Magnetostriction is rather induced by the irreversible part of the strain, which in turn is controlled by the magnetic field but also by mechanical loads. The same way, a strain field has an impact on the magnetic induction via M_i^{irr}. Dielectric properties are allocated by the second equation in Eq. (2) which is linear only at the first glance, since the dielectric constants κ_{il} are controlled by the internal variables in a nonlinear manner. Ferromagnetic materials exhibiting a significant electric conductivity are excluded by the model.

Whereas Eq. (2) generates hysteresis loops, the constitutive equations of nonlinear reversible ferromagnetic behavior are given by

$$\begin{aligned} \dot{\sigma}_{ij}\left(\dot{\varepsilon}_{ij}, \dot{H}_i\right) &= C_{ijkl}\dot{\varepsilon}_{kl} - q_{kij}\left(\varepsilon_{ij}, H_i\right)\dot{H}_k, \\ \dot{D}_i\left(\dot{E}_i\right) &= \kappa_{ij}\dot{E}_j, \\ \dot{B}_i\left(\dot{\varepsilon}_{ij}, \dot{H}_i\right) &= q_{ikl}\left(\varepsilon_{ij}, H_i\right)\dot{\varepsilon}_{kl} + \mu_{ij}\left(\varepsilon_{ij}, H_j\right)\dot{H}_j, \end{aligned} \tag{3}$$

where a rate dependent formulation has been chosen and dots on variables denote time derivatives. The nonlinearity is completely included in the material coefficients depending on the independent variables strain and magnetic field. Due to the reversibility of the constitutive behavior, these functions are unique, not involving any internal variables. The coefficient functions, now including the magnetostrictive tensor $q_{kij}\left(\varepsilon_{ij}, H_i\right)$, have to be chosen in a way to reflect experimental observations. A second requirement is to satisfy thermodynamical consistency by defining a thermodynamical potential yielding all the coefficient functions by differentiation. These purely phenomenological approaches involve several parameters, which are adjusted to specific material behaviors.

3 Constitutive Models for Ferromagnetic Materials

3.1 Physically Motivated Ferromagnetic Model

For the electro- and magnetostatic case ($\dot{B}_i, \dot{D}_i = 0$), the scalar electric and magnetic potentials ϕ^{el} and ϕ^{mag} are motivated from the MAXWELL equations [21]. Their gradients yield electric E_i and magnetic H_i fields [44], just as displacements u_i and strain are related for infinitely small deformations:

$$\varepsilon_{ij} = \frac{1}{2}\left(u_{i,j} + u_{j,i}\right), \quad E_i = -\phi^{\text{el}}_{,i}, \quad H_i = -\phi^{\text{mag}}_{,i}. \tag{4}$$

To define boundary value problems, the balance equation of momentum

$$\sigma_{ij,j} + b_i = \rho \ddot{u}_i \tag{5}$$

has to be considered besides the remaining two MAXWELL equations, not being trivially satisfied within a quasistatic framework. Inertia effects and specific body forces will be neglected in the intended applications, i.e. $b_i = 0$, $\rho\ddot{u}_i = 0$ in Eq. (5). Since free electric volume charges are assumed not to be present in a dielectric material, the mechanical and magneto-/electrostatic balance equations can be specified as

$$\sigma_{ij,j} = 0, \quad D_{i,i} = 0, \quad B_{i,i} = 0\,. \tag{6}$$

For the FE implementation, the weak formulations of these differential equations are required, which are given e.g. in [1] or [2]. CAUCHY's theorem, introducing tractions t_i, is generalized providing the relations

$$t_i = \sigma_{ij} n_j, \quad \omega^{\text{el}}_S = -D_i n_i, \quad \omega^{\text{mag}}_S = -B_i n_i\,, \tag{7}$$

where ω_S^{el} is the surface charge density and ω_S^{mag} is the part of the magnetic flux along the surface normal n_i of the NEUMANN type boundary S_ω. Reversible quantities will now be denoted with a superscript rev. According to a common approach, strain ε_{ij} and magnetic induction B_i are additively decomposed into reversible and irreversible parts:

$$\varepsilon_{ij} = \varepsilon_{ij}^{\mathrm{rev}} + \varepsilon_{ij}^{\mathrm{irr}}, \quad B_i = B_i^{\mathrm{rev}} + M_i^{\mathrm{irr}} \, . \tag{8}$$

The irreversible parts are due to BARKHAUSEN jumps on the microlevel or domain wall motion on the mesoscopic level. It should be noted that a reversibility of $\varepsilon_{ij}^{\mathrm{rev}}$ and B_i^{rev} at this point disregards changes of effective material properties which are, however, incorporated in the implementation. Concerning the electric displacement, just these weak nonlinearities are present due to changes of the dielectric constants κ_{ij} in Eq. (2) as a consequence of BLOCH wall motion, while an explicit nonlinearity due to polarisation rearrangement does not exist, i.e. $P_i^{\mathrm{irr}} = 0$.

The choice of strain, electric and magnetic fields as independent variables is feasible for most engineering applications, thus the constitutive ferromagnetic model is based on the thermodynamical potential $\Psi\left(\varepsilon_{ij}, E_i, H_i\right)$ [2]

$$\begin{aligned} \Psi\left(\varepsilon_{ij}, E_l, H_k\right) = \frac{1}{2} C_{ijkl}\varepsilon_{kl}\varepsilon_{ij} - \frac{1}{2}\kappa_{ij}E_iE_j - \frac{1}{2}\mu_{ij}H_iH_j - \\ - C_{ijkl}\varepsilon_{kl}^{\mathrm{irr}}\varepsilon_{ij} - M_i^{\mathrm{irr}}H_i \, . \end{aligned} \tag{9}$$

The constitutive equations of nonlinear ferromagnetic behavior within a magneto-electric context are then given by

$$\begin{aligned} \sigma_{ij} &= \left.\frac{\partial\Psi\left(\varepsilon_{ij}, E_i, H_i\right)}{\partial\varepsilon_{ij}}\right|_{E_i, H_i} , \\ D_i &= -\left.\frac{\partial\Psi\left(\varepsilon_{ij}, E_i, H_i\right)}{\partial E_i}\right|_{\varepsilon_{ij}, H_i} , \\ B_i &= -\left.\frac{\partial\Psi\left(\varepsilon_{ij}, E_i, H_i\right)}{\partial H_i}\right|_{\varepsilon_{ij}, E_i} , \end{aligned} \tag{10}$$

which coincide with the Eq. (2) from the compilation in Sect. 2. Relating the third constitutive equation to common representations in textbooks, the irreversible magnetization M_i^{irr} is in a more general sense denoted as spontaneous magnetic polarization or magnetization M_i^{sp} according to

$$B_i = \mu_0\left(\delta_{ij} + \chi_{ij}\right)H_j + M_i^{\mathrm{sp}} = \mu_0\mu_{ij}^r H_j + M_i^{\mathrm{sp}} = \mu_{ij}H_j + M_i^{\mathrm{sp}} \, , \tag{11}$$

where δ_{ij} is the KRONECKER identity tensor, χ_{ij} ($\geq$0) the magnetic susceptibility, μ_0 the magnetic permeability of vacuum and μ^r_{ij} are the coefficients of relative permeability of the material ($\geq$1).

On the continuum level, domain wall motion is described by internal variables ν_n, see Fig. 1, for plane problems associated with the four possible orientations of domains in a grain, with the easy axis in the $\langle 100 \rangle$ direction [4, 9, 25, 32]:

$$\dot{\varepsilon}^{\text{irr}}_{ij} = \sum_{n=1}^{4} \overset{(n)}{\varepsilon}{}^{\text{sp}}_{ij} \dot{\nu}_n \ , \quad \dot{M}_i = \sum_{n=1}^{4} \Delta \overset{(n)}{M}{}^{\text{sp}}_i \dot{\nu}_n \ , \tag{12}$$

where $\overset{(n)}{\varepsilon}{}^{\text{sp}}_{ij}$ and $\Delta \overset{(n)}{M}{}^{\text{sp}}_i$ represent the spontaneous strain and change of spontaneous magnetization for the domain n, respectively. The total change of volume fractions of the domain species in a grain resulting from BLOCH wall motion is conserved by the following relations

$$0 \leq \nu_n \leq 1, \quad \sum_{n=1}^{4} \nu_n = 1 \ , \tag{13}$$

where ν_n represents the specific volume of each domain. In all calculations, the generalized state of plane stress will be assumed, i.e. $\sigma_{i3} = 0, \ D_3 = 0, \ B_3 = 0$. The changes of magnetization exhibit three possibilities, ±90° and 180°, for each domain species $n = 1, \ldots, 4$. In Fig. 1, one variant for $n = 3$ is depicted as an example, i.e. $\Delta \overset{(3)}{M}{}^{\text{sp}}_k = \overset{(4)}{M}{}^{\text{sp}}_k - \overset{(3)}{M}{}^{\text{sp}}_k$ for +90°-jumping. Concerning the spontaneous strain, each domain species n is allocated one unique tensor representing ±90° jumping. The rates of volume change of the species $\dot{\nu}_n$, i.e. the time derivatives of the internal variables, play an important role in the thermodynamical formulation of the material law. The evolution of the internal variables ν_n within a domain structure is controlled by an energetic criterion, which has been chosen in the style of ferroelectric switching criteria [2, 20, 24, 26]

$$\Delta w^n = \sigma_{ij} \overset{(n)}{\varepsilon}{}^{\text{sp}}_{ij} + H_i \Delta \overset{(n)}{M}{}^{\text{sp}}_i \geq w^{\text{crit}} \ . \tag{14}$$

The left hand side of the inequality, consisting of mechanical and magnetic contributions, represents the dissipative work Δw^n of BLOCH wall motion due to the jumping of a species n. In-plane, there are three possible jumping variants with the easy axis in the $\langle 100 \rangle$ direction. Based on the idea of ferroelectric switching [20, 23], two different threshold values are introduced:

$$w^{\text{crit}} = \begin{cases} \sqrt{2} M^0 H_{\text{C}}, & \pm 90^\circ \\ 2 M^0 H_{\text{C}}, & 180^\circ \end{cases} \tag{15}$$

where the material parameters H_C and M^0 are coercive field and magnitude of spontaneous magnetization.

On the macroscopic level, an evolution law for the internal variables ν_n controls BLOCH wall motion. Based on Eqs. (14) and (15) the evolution law for a domain species n is

$$\dot{\nu}_n = -\dot{\nu}_n^0 \mathscr{H}\left(\frac{\Delta\tilde{w}^n}{w^{\mathrm{crit}}} - 1\right), \quad \Delta\tilde{w}^n = \max\left(\Delta w^n_{\pm 90^\circ},\ \Delta w^n_{180^\circ}\right), \tag{16}$$

where $\mathscr{H}(\ldots)$ is the HEAVISIDE-function and $\dot{\nu}_n^0$ a model parameter. The latter represents a discrete amount of domain wall motion, which has to be chosen within a numerical context. Equation (16) determines, if the volume of the species n decreases by a magnitude $\mathrm{d}\nu_n^0$ due to local jumping or not. The reduction of ν_n always occurs in favor of another species, satisfying Eq. (13). While the changes of strain and spontaneous magnetization due to BLOCH wall motion are described by Eq. (12), the evolutions of material tangents in a grain are likewise connected to the internal variables, e.g. for the stiffness

$$C_{ijkl} = \sum_{n=1}^{4} \overset{(n)}{C}_{ijkl}\nu_n \quad \rightarrow \quad \dot{C}_{ijkl} = \sum_{n=1}^{4} \overset{(n)}{C}_{ijkl}\dot{\nu}_n = \sum_{n=1}^{4} \frac{\partial C_{ijkl}}{\partial \nu_n}\dot{\nu}_n \tag{17}$$

and similar for all other material tensors.

3.2 Phenomenological Ferromagnetic Model

The constitutive behavior of the ferromagnetic-dielectric material is found to be governed by the thermodynamic potential [3]

$$\begin{aligned}\overline{\Psi}\left(\sigma_p, E_i, H_i\right) = &-\frac{1}{2}S_{11}\sigma_1\sigma_1 - S_{12}\sigma_1\sigma_2 - \frac{1}{2}S_{22}\sigma_2\sigma_2 - S_{66}\sigma_6\sigma_6 - \\ &-\frac{1}{2}\kappa_{11}E_1E_1 - \frac{1}{2}\kappa_{22}E_2E_2 - \frac{1}{2}\mu_{11}^0 H_1H_1 - \frac{\eta_1}{1+\zeta_1 H_1^{-3}}\sigma_1 - \\ &-\frac{\eta_2}{1+\zeta_2 H_1^{-3}}\sigma_2 - \rho\left(H_1 - \xi\ln\left(\xi + H_1\right)\right)\,,\end{aligned} \tag{18}$$

where, in contrast to Eq. (9), stress, electric and magnetic fields are chosen as independent variables. Here, S_{pq}, κ_{ij} and μ_{11}^0 are the coefficients of compliance, dielectric and magnetic permeability tensors, respectively. It is feasible to develop the material model based on stress and magnetic field, since these are the quantities which are commonly controlled in experiments, where e.g. stresses are zero due to free boundaries. In this section the compressed or VOIGT notation is applied, so e.g. σ_6 is the shear stress σ_{12} and S_{12} denotes S_{1122}. Essential features of magnetisation and magnetostriction are appropriately described adapting the constant coefficients η_i, ζ_i, ρ and ξ to experimental curves. Table 4 indicates how to identify the material parameters from experimental data.

Equation (18) has been formulated in a local coordinate system where the x_1-axis is attached to the vector of the H-field. Thus, H_2 does not appear in the potential. The easy axis locally always points in the direction of the magnetic field, since the reversibility, in connection with a vanishing remanence, leads to an immediate magnetisation even at low field intensities. Consequently, the x_1-axes of the local coordinate systems are always attached to the direction of magnetisation and magnetic induction and the material tensors are sparsely populated in these coordinate systems. The potential according to Eq. (18), for curved magnetic flux lines being valid locally and adjusted to the local coordinates, thus contains only these coefficients. In contrast to hard magnetic materials, stresses do not control the direction of magnetisation and the easy axis, respectively, in fact having an impact only on the local magnitudes of the H-field. If boundary conditions are fundamentally changed during the loading process, generally an iteration is required in each load step, adapting the evolving magnetic flux lines and the local coordinate systems to one another. Finally, all fields are transformed into global coordinates, where the material tensors in general are fully populated.

The superscript in the magnetic permeability μ_{11}^0 indicates a constant magnitude in contrast to the function $\overline{\mu}_{11}\left(\sigma_p, H_i\right)$ [3]. The denominators in Eq. (18) cannot be zero since ζ_1 and ζ_2 are always positive, requiring a negative value of H_1 for a division by zero. This is not possible, however, since the local coordinate system is always adapted to the H-field such that $H_1 > 0$. The general constitutive behaviour is obtained by differentiation of Eq. (18) according to

$$\begin{aligned}
\dot{\varepsilon}_p\left(\dot{\sigma}_p, \dot{E}_i, \dot{H}_i\right) &= \frac{-\partial^2\overline{\Psi}}{\partial\sigma_p\partial\sigma_q}\dot{\sigma}_q + \frac{-\partial^2\overline{\Psi}}{\partial\sigma_p\partial E_j}\dot{E}_j + \frac{-\partial^2\overline{\Psi}}{\partial\sigma_p\partial H_j}\dot{H}_j\ , \\
\dot{D}_i\left(\dot{\sigma}_p, \dot{E}_i, \dot{H}_i\right) &= \frac{-\partial^2\overline{\Psi}}{\partial E_i\partial\sigma_q}\dot{\sigma}_q + \frac{-\partial^2\overline{\Psi}}{\partial E_i\partial E_j}\dot{E}_j + \frac{-\partial^2\overline{\Psi}}{\partial E_i\partial H_j}\dot{H}_j\ , \\
\dot{B}_i\left(\dot{\sigma}_p, \dot{E}_i, \dot{H}_i\right) &= \frac{-\partial^2\overline{\Psi}}{\partial H_i\partial\sigma_q}\dot{\sigma}_q + \frac{-\partial^2\overline{\Psi}}{\partial H_i\partial E_j}\dot{E}_j + \frac{-\partial^2\overline{\Psi}}{\partial H_i\partial H_j}\dot{H}_j\ .
\end{aligned} \tag{19}$$

Thus, the rate dependent constitutive framework is given by

$$\begin{aligned}
\dot{\varepsilon}_p\left(\dot{\sigma}_q, \dot{H}_i\right) &= S_{pq}\dot{\sigma}_q + \overline{q}_{jp}\left(H_i\right)\dot{H}_j\ , \\
\dot{D}_i\left(\dot{E}_i\right) &= \kappa_{ij}\dot{E}_j\ , \\
\dot{B}_i\left(\dot{\sigma}_p, \dot{H}_i\right) &= \overline{q}_{iq}\left(H_i\right)\dot{\sigma}_q + \overline{\mu}_{ij}\left(\sigma_p, H_i\right)\dot{H}_j\ .
\end{aligned} \tag{20}$$

Here, $\overline{q}_{jp}$ represents the magnetostrictive tensor. Equation (20) represent nonlinear reversible changes of state since the material tensors are single-valued functions of the independent variables. The electric displacement only depends on the electric field, in a ferromagnetic material not being strongly coupled with mechanical or magnetic fields. Having a closer look, the dielectric properties are controlled by magnetic fields to a certain extent, the latter rotating the axis of transversal isotropy. This effect is intrinsically taken into account by the proposed model due to the local coordinate systems, being attached to the magnetic flux lines, as outlined above. In Eq. (20) bars are added to the magnetic permeability $\overline{\mu}_{ij}\left(\sigma_p, H_i\right)$ and the magnetostrictive coefficients $\overline{q}_{jp}\left(H_i\right)$ to distinguish from quantities based on a different potential. Due to the tensorial representation, Eq. (20) allows for multiaxial loading.

In general, all material coefficients depend on the three independent variables. Experimental observations, however, put this thermodynamical requirement into perspective, showing e.g. a noticeable nonlinearity of the stress–strain curve only for giant magnetostrictive materials. In the potential Eq. (18) and the constitutive relations Eq. (20) the magnetostrictive constants are functions of just the magnetic field and the magnetic permeability is a function of both magnetic field and stress:

$$\overline{q}_{11} = 3\frac{\eta_1\zeta_1 H_1^2}{\left(\zeta_1 + H_1^3\right)^2}, \quad \overline{q}_{12} = 3\frac{\eta_2\zeta_2 H_1^2}{\left(\zeta_2 + H_1^3\right)^2}\,, \tag{21}$$

$$\begin{aligned}\overline{\mu}_{11} = \mu_{11}^0 &+ \frac{6\eta_1\zeta_1 H_1\left(\zeta_1 - 2H_1^3\right)\sigma_1}{\left(\zeta_1 + H_1^3\right)^3} + \frac{6\eta_2\zeta_2 H_1\left(\zeta_2 - 2H_1^3\right)\sigma_2}{\left(\zeta_2 + H_1^3\right)^3} + \\ &+ \frac{\rho\xi}{\left(\xi + H_1\right)^2}\,.\end{aligned} \tag{22}$$

The constant part of the magnetic permeability μ_{11}^0 is intended to represent the linear behaviour of the B-field, once the spontaneous magnetisation is saturated at large magnetic fields [3]. Its magnitude is much smaller than those permeabilities typically found in charts, the latter representing values for much lower magnetic fields. A parameter $\varpi = \mu/\mu^0$ is thus introduced to provide a suitable μ_{11}^0, based on values of relative permeabilities μ_{11}^r available from literature acccording to $\mu_{11}^0 = \mu_{11}/\varpi = \mu_{11}^r\mu_0/\varpi$, where μ_0 is the magnetic permeability of vacuum. The parameter ϖ is calibrated on the basis of experimental plots, typically taking values in the range of a few tens, see appendix.

The constitutive model based on constant coefficients ζ_1, ζ_2 and ξ is suitable for NEUMANN type boundary conditions. The evolution of stress, which is inevitably associated with e.g. a DIRICHLET condition, is however not appropriately taken into account with constant coefficients. A more sophisticated model thus replaces the constant coefficients ζ_1, ζ_2 and ξ by variables depending on stresses and their evolution:

$$\begin{aligned}\zeta_1 = \zeta_1^0 + \zeta_1^\sigma\left(\sigma_1 - \sigma_2\right), \quad \zeta_2 = \zeta_2^0 + \zeta_2^\sigma\left(\sigma_1 - \sigma_2\right), \\ \xi = \xi^0 + \xi^\sigma\left(\sigma_1 - \sigma_2\right) + \hat{\xi}^\sigma\left(\mathrm{d}\sigma_1 - \mathrm{d}\sigma_2\right),\end{aligned} \tag{23}$$

where $\mathrm{d}\sigma_i$ denotes the change of the normal stress σ_i in each load increment and $\zeta_2^\sigma = \zeta_1^\sigma\left(|\sigma_1^s|/|\sigma_2^s|\right)$. Here, $|\sigma_1^s|$ and $|\sigma_2^s|$ represent the absolute values of saturated normal stresses, which can be attained applying realistic magnetic loads.

Unfortunately, their magnitudes are not available from literature. Therefore, both values have been calculated for plane stress conditions, based on the saturation strains $\varepsilon_1^s \approx \eta_1$ and $\varepsilon_2^s \approx \eta_2$ in connection with the stiffness C_{pq}, see appendix Eq. (50). The last term of ξ in Eq. (23) involving the parameter $\hat{\xi}^\sigma$ is crucial, if DIRICHLET boundary conditions or adjacent compliant phases shall be considered. Thus, it is inevitable for the investigation of multiferroic composites, where a ferromagnetic phase may be embedded into a ferroelectric one. For constant mechanical loads σ_1, σ_2 the term vanishes. For displacement boundary conditions both σ_1, σ_2 and $\mathrm{d}\sigma_1$, $\mathrm{d}\sigma_2$ emanate from the solution of the boundary value problem. Introducing the parameters $\zeta_1(\sigma_1, \sigma_2)$, $\zeta_2(\sigma_1, \sigma_2)$ and $\xi(\sigma_1, \sigma_1, \mathrm{d}\sigma_1, \mathrm{d}\sigma_2)$ the MAXWELL relations of thermodynamics are still satisfied [3].

Results of the constitutive model will be investigated in Sect. 6. For the sake of an efficient numerical implementation, the independent mechanical variable is changed from stress to strain, in principle taking another thermodynamical potential $\Psi\left(\varepsilon_p, E_i, H_i\right)$ as a basis. Accordingly, the material tensors are subject to the following transformations:

$$C_{pq} = S_{pq}^{-1}\ , \quad q_{ip} = \overline{q}_{iq} C_{qp}\ , \quad \mu_{ij} = \overline{\mu}_{ij} - \overline{q}_{iq} C_{qp} \overline{q}_{jp}\ . \tag{24}$$

The constitutive equations for the modified set of independent variables are thus given in Eq. (3). Discarding μ_{11}^0 in Eq. (22), Eqs. (24) and (3) yield the magnetic polarization M_i^{sp} according to Eq. (11) instead of B_i. That quantity is equivalent to M_i^{irr} in Eq. (10), however, a different notation is chosen due to the reversible characteristic of the magnetization in the phenomenological model. The specific magnetization m_i, which is commonly depicted in experimental plots, is finally obtained as

$$m_i = \mu_0^{-1} \rho^{-1} M_i^{\mathrm{sp}}\ , \tag{25}$$

where ρ denotes the mass density of the material.

Due to the incremental formulation according to Eq. (3) or (20), the range of the magnetic load $H \in [0, H^{\max}]$ is divided into load increments, controlling the evolution of the magnetomechanical fields in each load step, e.g. the stress evolution $\mathrm{d}\sigma_i$ decreasing or increasing according to the choice of the parameter ΔH, which was chosen $\Delta H = 100\,\mathrm{A/m}$ in the calculations. Accordingly, $\hat{\xi}^\sigma$ in Eq. (23) has to be adapted according to

$$\hat{\xi}^\sigma = \hat{\xi}_0^\sigma \frac{H^{\max}}{\Delta H}\ , \tag{26}$$

where $\hat{\xi}_0^\sigma$ depends on the material and is determined from fitting numerical to experimental magnetization plots under clamped conditions, see Table 4.

4 Condensed Method: Application to Multiferroic Compounds

To investigate the macroscopic behavior of polycristalline ferroic materials based on nonlinear constitutive laws, the FEM is commonly applied, even if structural or geometric issues are irrelevant. The implementation of a discretization scheme is going along with a high computational effort and the solution of the BVP requires high computational costs. Investigating just the material behavior, most predictions, however, are restricted to simple BVP under uni- or biaxial loading and their goal is e.g. the calculation of hysteresis loops. Anyway, the FEM is mostly applied, just to deal with the complex nonlinear material behavior. Interactions of grains are implemented by means of interacting integration points.

In [26, 27, 37] the so-called condensed method (CM) was introduced to investigate the nonlinear polycrystalline material behavior of tetragonal ferroelectrics at a macroscopic material point without any kind of discretization scheme. The CM provides essential issues like various hysteresis loops or residual stresses due to domain wall motion [26]. The latter aspect, in addition, establishes a basis for the modelling of mechanical degradation due to micro crack growth [27, 37]. In this section the CM is extended towards ferromagnetic material behavior and multiferroic bi-material systems. The physically motivated modelling of domain or BLOCH wall motion in ferroelectrics or ferromagnets according to Sect. 3.1 is adopted here. A more detailed representation of the basic idea of the CM can be found in [26, 37].

In Fig. 2 a representative volume element (RVE) of a multiferroic compound under magnetoelectromechanical loading is presented. The ferroelectric (FE) and ferromagnetic (FM) regions might be interpreted as grains, consisting of pure FE or pure FM material, respectively. In the microphysical model, the domain structure of a grain is represented by an arrowed cross, see Fig. 1, where the volume fractions of the four possible orientations of magnetization or polarization are now described

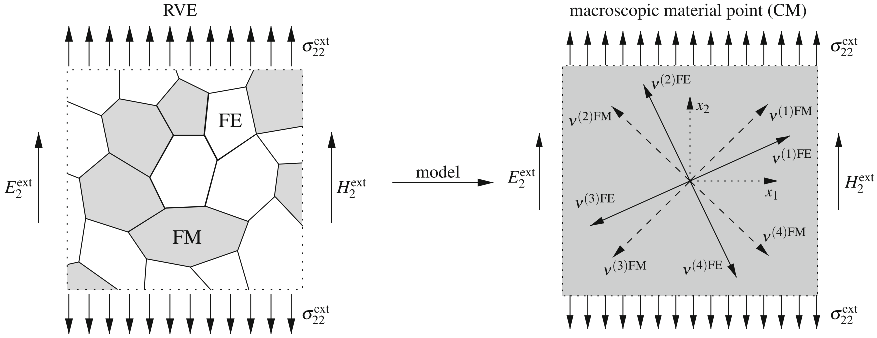

Fig. 2 RVE of a multiferroic compound with distributed ferroelectric (FE) and ferromagnetic (FM) constituents under magnetoelectromechanical loading (left) and illustration of internal variables $\nu^{(i)}$ allocated to single FE and FM domain orientations at a condensed material point (right)

separately by internal variables $\nu^{(i)FM}$ or $\nu^{(i)FE}$ $(i = 1, \ldots, 4)$. Domain switching and rotation of the molecular magnets, respectively, can only occur within the particular arrowed cross, see Fig. 2 (right). In the following a grain will be denoted as a microscopic material point. In the CM, the RVE is condensed to a macroscopic material point where an arbitrary number of grains is collected, whereupon just two of those are depicted in the figure. One major issue which has to be incorporated in the homogenization procedure is the interaction between the microscopic material points.

On the macroscopic scale of an RVE stress σ_{ij}, electric displacement D_i and magnetic induction B_i are microscopic volume averages, specified by angled brackets:

$$\left\langle\sigma_{ij}\right\rangle = \frac{1}{V}\int\limits_V \sigma_{ij}\left(x_l\right)\,\mathrm{d}V\ , \quad \left\langle D_i\right\rangle = \frac{1}{V}\int\limits_V D_i\left(x_l\right)\,\mathrm{d}V\ , \quad \left\langle B_i\right\rangle = \frac{1}{V}\int\limits_V B_i\left(x_l\right)\,\mathrm{d}V\ . \tag{27}$$

Assuming homogeneous fields in a microscopic material point m with the volume $V^{(m)}$, i.e. $\sigma_{ij}^{(m)}$, $D_i^{(m)}$, $B_i^{(m)} = \text{const}$ in $V^{(m)}$, the relations in Eq. (27) turn into

$$\left\langle\sigma_{ij}\right\rangle = \frac{\sum\limits_{m=1}^{M}\sigma_{ij}^{(m)}V^{(m)}}{\sum\limits_{m=1}^{M}V^{(m)}}\ , \quad \left\langle D_i\right\rangle = \frac{\sum\limits_{m=1}^{M}D_i^{(m)}V^{(m)}}{\sum\limits_{m=1}^{M}V^{(m)}}\ , \quad \left\langle B_i\right\rangle = \frac{\sum\limits_{m=1}^{M}B_i^{(m)}V^{(m)}}{\sum\limits_{m=1}^{M}V^{(m)}}\ , \tag{28}$$

where M is the number of microscopic material points per RVE. For the sake of simplicity, it is further assumed that all microscopic materials points have the same size, i.e. $V = MV^{(m)}$. Finally the macroscopic quantities are obtained by the following equations:

$$\left\langle\sigma_{ij}\right\rangle = \frac{1}{M}\sum_{m=1}^{M}\sigma_{ij}^{(m)}\ , \quad \left\langle D_i\right\rangle = \frac{1}{M}\sum_{m=1}^{M}D_i^{(m)}\ , \quad \left\langle B_i\right\rangle = \frac{1}{M}\sum_{m=1}^{M}B_i^{(m)}\ . \tag{29}$$

The average material properties $\left\langle C_{ijkl}\right\rangle$, $\left\langle e_{ikl}\right\rangle$, $\left\langle\kappa_{ij}\right\rangle$ and $\left\langle\mu_{ij}\right\rangle$ are determined likewise [26]. $\sigma_{ij}^{(m)}$, $D_i^{(m)}$ and $B_i^{(m)}$ in Eq. (29) describe the stress, electric displacement and magnetic induction of a microscopic material point m. Depending on the respective material, either ferroelectric or ferromagnetic, the constitutive equations are given by the Eq. (1) or (2). Inserting Eqs. (1) and (2) into Eq. (29), accounting for $M = M_{\mathrm{FE}} + M_{\mathrm{FM}}$, the macroscopic quantities read:

$$\begin{aligned}\langle\sigma_{ij}\rangle = \frac{1}{M}\Bigg(&\sum_{m_{\mathrm{FE}}=1}^{M_{\mathrm{FE}}} C_{ijkl}^{(m_{\mathrm{FE}})}\varepsilon_{kl}^{(m_{\mathrm{FE}})} + \sum_{m_{\mathrm{FM}}=1}^{M_{\mathrm{FM}}} C_{ijkl}^{(m_{\mathrm{FM}})}\varepsilon_{kl}^{(m_{\mathrm{FM}})} - \\ &- \sum_{m_{\mathrm{FE}}=1}^{M_{\mathrm{FE}}} C_{ijkl}^{(m_{\mathrm{FE}})}\varepsilon_{kl}^{\mathrm{irr}(m_{\mathrm{FE}})} - \sum_{m_{\mathrm{FM}}=1}^{M_{\mathrm{FM}}} C_{ijkl}^{(m_{\mathrm{FM}})}\varepsilon_{kl}^{\mathrm{irr}(m_{\mathrm{FM}})} - \\ &- \sum_{m_{\mathrm{FE}}=1}^{M_{\mathrm{FE}}} e_{lij}^{(m_{\mathrm{FE}})} E_l^{(m_{\mathrm{FE}})}\Bigg),\end{aligned} \tag{30}$$

$$\begin{aligned}\langle D_i\rangle = \frac{1}{M}\Bigg(&\sum_{m_{\mathrm{FE}}=1}^{M_{\mathrm{FE}}} e_{ikl}^{(m_{\mathrm{FE}})}\varepsilon_{kl}^{(m_{\mathrm{FE}})} - \sum_{m_{\mathrm{FE}}=1}^{M_{\mathrm{FE}}} e_{ikl}^{(m_{\mathrm{FE}})}\varepsilon_{kl}^{\mathrm{irr}(m_{\mathrm{FE}})} + \\ &+ \sum_{m_{\mathrm{FE}}=1}^{M_{\mathrm{FE}}} \kappa_{il}^{(m_{\mathrm{FE}})} E_l^{(m_{\mathrm{FE}})} + \sum_{m_{\mathrm{FM}}=1}^{M_{\mathrm{FM}}} \kappa_{il}^{(m_{\mathrm{FM}})} E_l^{(m_{\mathrm{FM}})} + \\ &+ \sum_{m_{\mathrm{FE}}=1}^{M_{\mathrm{FE}}} P_i^{\mathrm{irr}(m_{\mathrm{FE}})}\Bigg),\end{aligned} \tag{31}$$

$$\begin{aligned}\langle B_i\rangle = \frac{1}{M}\Bigg(&\sum_{m_{\mathrm{FE}}=1}^{M_{\mathrm{FE}}} \mu_{ij}^{(m_{\mathrm{FE}})} H_j^{(m_{\mathrm{FE}})} + \sum_{m_{\mathrm{FM}}=1}^{M_{\mathrm{FM}}} \mu_{ij}^{(m_{\mathrm{FM}})} H_j^{(m_{\mathrm{FM}})} + \\ &+ \sum_{m_{\mathrm{FM}}=1}^{M_{\mathrm{FM}}} M_i^{\mathrm{irr}(m_{\mathrm{FM}})}\Bigg).\end{aligned} \tag{32}$$

In the following, a generalized VOIGT assumption is taken as a basis. Here, strain, electric and magnetic field are assumed homogeneous in the RVE, thus being identical in all microscopic material points m:

$$\begin{aligned}\langle\varepsilon_{kl}\rangle &= \frac{1}{M}\left(\sum_{m_{\mathrm{FE}}=1}^{M_{\mathrm{FE}}} \varepsilon_{kl}^{(m_{\mathrm{FE}})} + \sum_{m_{\mathrm{FM}}=1}^{M_{\mathrm{FM}}} \varepsilon_{kl}^{(m_{\mathrm{FM}})}\right) = \varepsilon_{kl}^{(m)} = \overline{\varepsilon}_{kl}\ , \\ \langle E_i\rangle &= \frac{1}{M}\left(\sum_{m_{\mathrm{FE}}=1}^{M_{\mathrm{FE}}} E_i^{(m_{\mathrm{FE}})} + \sum_{m_{\mathrm{FM}}=1}^{M_{\mathrm{FM}}} E_i^{(m_{\mathrm{FM}})}\right) = E_i^{(m)} = \overline{E}_i\ , \\ \langle H_i\rangle &= \frac{1}{M}\left(\sum_{m_{\mathrm{FE}}=1}^{M_{\mathrm{FE}}} H_i^{(m_{\mathrm{FE}})} + \sum_{m_{\mathrm{FM}}=1}^{M_{\mathrm{FM}}} H_i^{(m_{\mathrm{FM}})}\right) = H_i^{(m)} = \overline{H}_i\ .\end{aligned} \tag{33}$$

Considering Eq. (33), the macroscopic constitutive equations result from Eqs. (30), (31) and (32):

$$
\begin{aligned}
\langle \sigma_{ij} \rangle &= \langle C_{ijkl} \rangle \overline{\varepsilon}_{kl} - \langle e^{\mathrm{FE}}_{lij} \rangle \overline{E}_l - \langle C^{\mathrm{FE}}_{ijkl} \varepsilon^{\mathrm{irr(FE)}}_{kl} + C^{\mathrm{FM}}_{ijkl} \varepsilon^{\mathrm{irr(FM)}}_{kl} \rangle \,, && (34) \\
\langle D_i \rangle &= \langle e^{\mathrm{FE}}_{ikl} \rangle \overline{\varepsilon}_{kl} + \langle \kappa_{il} \rangle \overline{E}_l - \langle e^{\mathrm{FE}}_{ikl} \varepsilon^{\mathrm{irr(FE)}}_{kl} \rangle + \langle P^{\mathrm{irr(FE)}}_i \rangle \,, && (35) \\
\langle B_i \rangle &= \langle \mu_{ij} \rangle \overline{H}_j + \langle M^{\mathrm{irr(FM)}}_i \rangle \,. && (36)
\end{aligned}
$$

Quantities without the superscript FE or FM have contributions of both constituents. Obviously, the macroscopic fields in Eqs. (34) and (35) do not depend explicitly on the magnetic field, even though e.g. the irreversible strain $\varepsilon^{\mathrm{irr(FM)}}_{kl}$ or the elastic constants $C^{\mathrm{(FM)}}_{ijkl}$ in Eq. (34) are controlled by the magnetic field. On the one hand, this is due to the fact that the ferroelectric material does not exhibit any magnetostriction. On the other hand, the ferromagnetic model neglects piezomagnetic coupling, in order to attain saturation at higher magnetic fields, see Sect. 3.1. Depending on the specific problem the unknowns are chosen among the quantities $\langle \sigma_{ij} \rangle$, $\langle D_i \rangle$, $\langle B_i \rangle$, $\overline{\varepsilon}_{kl}$, $\overline{E}_i$ and $\overline{H}_i$. Assuming stress, electric and magnetic fields as external loads, i.e. $\langle \sigma_{ij} \rangle = \sigma^{\mathrm{ext}}_{ij}$, $\langle E_i \rangle = E^{\mathrm{ext}}_i$ and $\langle H_i \rangle = H^{\mathrm{ext}}_i$, the macroscopic strain $\overline{\varepsilon}_{kl}$ results from Eq. (34):

$$
\overline{\varepsilon}_{kl} = \langle C_{ijkl} \rangle^{-1} \left(\sigma^{\mathrm{ext}}_{ij} + \langle e^{\mathrm{FE}}_{mij} \rangle E^{\mathrm{ext}}_m + \langle C^{\mathrm{FE}}_{ijmn} \varepsilon^{\mathrm{irr(FE)}}_{mn} + C^{\mathrm{FM}}_{ijmn} \varepsilon^{\mathrm{irr(FM)}}_{mn} \rangle \right) = \varepsilon^{(m)}_{kl} \,. \quad (37)
$$

With Eq. (37) the residual stress, e.g. of a microscopic material point m of the ferroelectric phase, is given by:

$$
\begin{aligned}
\sigma^{(m)}_{ij} = {} & C^{(m)}_{ijkl} \Big(\langle C_{mnkl} \rangle^{-1} \big(\sigma^{\mathrm{ext}}_{mn} + \langle C^{\mathrm{(FE)}}_{mnop} \varepsilon^{\mathrm{irr(FE)}}_{op} + C^{\mathrm{(FM)}}_{mnop} \varepsilon^{\mathrm{irr(FM)}}_{op} \rangle + \\
& + \langle e^{\mathrm{(FE)}}_{rmn} \rangle E^{\mathrm{ext}}_r \big) - \varepsilon^{\mathrm{irr}(m)}_{kl} \Big) - e^{(m)}_{lij} E^{\mathrm{ext}}_l \,.
\end{aligned} \quad (38)
$$

From Eq. (38) it is obvious, that in the CM the interaction between the microscopic material points is realized by the strain $\overline{\varepsilon}_{kl}$ in conjunction with the generalized VOIGT assumption.

5 Continuum Damage Model

Two fundamental damage mechanisms are observed in a ME composite: cracking of the two constituents and delamination. The latter will not be considered at this point and cracking will be only allowed in the ferroelectric material. In Fig. 3 the micromechanical motivation of the model is depicted using the example of a particle composite with a ferroelectric matrix. The RVE of the composite shows a few particles and the multiphysical boundary conditions. In the third sketch, the RVE of the ferroelectric matrix with statistically distributed cracks is shown, where the principal stresses σ_I and σ_{II} are the relevant loading quantities, being controlled by magnetic and electric fields as well. Those are part of the driving force being responsible for ferroelectric domain wall motion, giving rise to residual stress. In the model, only cracks being perpendicular to the maximum principal stress are allowed to grow

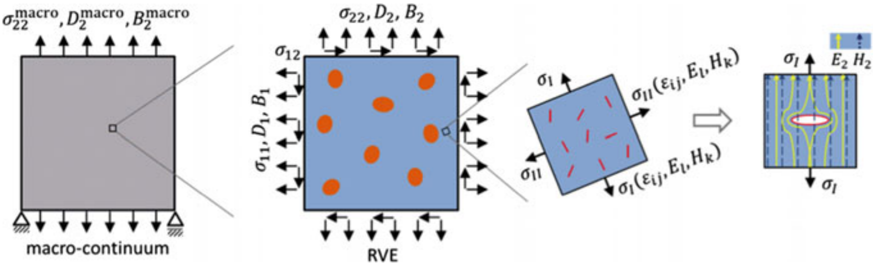
$\sigma_{22}^{\text{macro}}, D_2^{\text{macro}}, B_2^{\text{macro}}$
macro-continuum
σ_{22}, D_2, B_2
σ_{12}
σ_{11}, D_1, B_1
RVE
σ_I
$\sigma_{II}(\varepsilon_{ij}, E_l, H_k)$
σ_{II}
$\sigma_I(\varepsilon_{ij}, E_l, H_k)$
σ_I
E_2 H_2
σ_I

Fig. 3 Damaging of a ME particle composite: micro crack initiation perpendicular to the maximum principal stress σ_I, magnetic field penetrating the crack, electric field circumventing it

following a classical K-factor-based fracture criterion. Assuming a dilute crack distribution, crack interactions can be neglected, thus leaving a single GRIFFITH crack to be considered, as depicted in the last sketch of Fig. 3.

One essential issue in the fracture mechanics of multifunctional materials is the choice of boundary conditions at the crack faces. A comprehensive model is complex, including induced MAXWELL tractions and finite electrical permeabilities [18, 35, 36, 38]. A simple model is implemented here, where the crack is assumed traction-free and electrically impermeable, in Fig. 3 indicated by the solid yellow lines circumventing the crack. Concerning the magnetic field, the crack is assumed to be fully permeable, indicated by the dashed blue lines penetrating the crack. This is justified since, in contrast to the dielectric properties, the magnetic permeabilities of air and of a ferroelectric material are similar by order of magnitude.

In the following, some basic equations of the model are introduced, while the complete theory can be looked up in [17, 27]. Introducing the compressed notations $\Pi_p = \left(\sigma_{ij}, D_i\right)^T$ and $Z_q = \left(\varepsilon_{ij}, -E_i\right)^T$ for generalized stresses and electric displacements, the constitutive equations, linearized with respect to an operating point, are given as

$$\left.\begin{aligned} \langle\sigma_{ij}\rangle &= C^*_{ijkl}\langle\varepsilon_{kl}\rangle - e^*_{lij}\langle E_l\rangle \\ \langle D_i\rangle &= e^*_{ikl}\langle\varepsilon_{kl}\rangle + \kappa^*_{il}\langle E_l\rangle \end{aligned}\right\} \quad \rightarrow \quad \langle\Pi_p\rangle = C^*_{pq}\langle Z_q\rangle \ , \qquad (39)$$
$$\langle B_i\rangle = \mu^*_{ij}\langle H_j\rangle \quad \rightarrow \quad B_i = \mu_{ij}H_j \ ,$$

where angled brackets denote average fields and superscript asterisks represent effective material coefficients. The effective quantities have to be determined from homogenization of the crack RVE, thus the magnetic quantities remain unaffected due to the permeability of the crack. C^*_{pq} is the effective generalized stiffness matrix, comprising homogenized elastic, dielectric and piezoelectric tangent modules. The inverse formulation of the effective constitutive law introduces the generalized stiffness $S^*_{pq} = \left(C^*_{pq}\right)^{-1}$:

$$\langle Z_p \rangle = S^*_{pq} \langle \Pi_q \rangle \,. \tag{40}$$

The generalized strain is decomposed as

$$\langle Z_p \rangle = \langle Z_p \rangle^M + \langle Z_p \rangle^C \tag{41}$$

with $\langle Z_p \rangle^M = S^M_{pq} \Pi^0_q$ for the matrix and $\langle Z_p \rangle^C = S^C_{pq} \Pi^0_q$ for the defect phase. Assuming a generalized REUSS approximation, the average stress is introduced as a constant field, i.e. $\langle \Pi_q \rangle = \Pi^0_q$. Stresses and electric displacements at the boundary of the crack RVE ∂V^C are thus coincident with the average quantities σ^0_{kl} and D^0_n in the domain V^C.

The generalized compliance is likewise decomposed in matrix and defect phase:

$$S^*_{pq} = S^M_{pq} + S^C_{pq} \,. \tag{42}$$

The contribution of micro cracks to the averaged strain and electric field is comprised in $\langle Z_p \rangle^C$ and reads

$$\begin{aligned} \varepsilon^C_{ij} &= \frac{1}{2A} \int_{-a}^{+a} \left(\Delta u_i n_j + \Delta u_j n_i \right) \, dx^c_1 \,, \\ E^C_i &= -\frac{1}{A} \int_{-a}^{+a} \Delta\phi n_i \, dx^c_1 \,, \end{aligned} \tag{43}$$

where Δu_i and $\Delta\phi$ are jumps of displacement and electric potential accross the crack faces and n_j is the unit normal. The area of the plane RVE is denoted as A and a is half the crack length. The GRIFFITH crack RVE and related quantities are depicted in Fig. 4, where x^c_1 is the crack coordinate system.

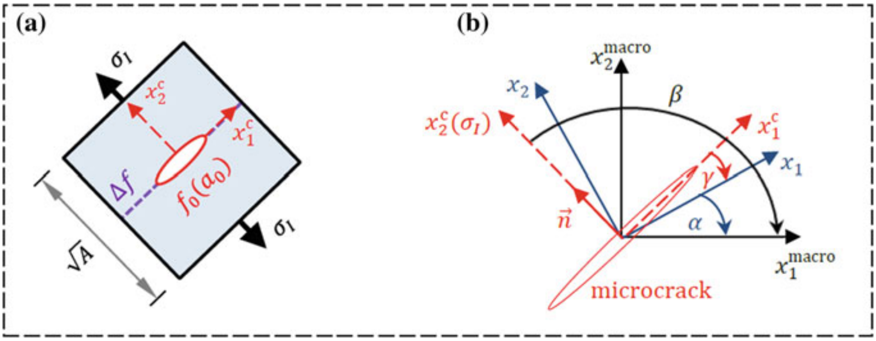

Fig. 4 **a** Dilute crack RVE loaded by principal stress σ_I, initial crack length $2a_0$ and damage parameter f_0; **b** crack with global $\left(x_1^{\text{macro}}, x_2^{\text{macro}}\right)$, local material related (x_1, x_2) and crack $\left(x^c_1, x^c_2\right)$ coordinate systems

The jumps in Eq. (43) are determined from the closed-form solutions of the piezoelectric GRIFFITH crack problem (see e.g. [33, 35, 42], accounting for impermeable electric crack boundary conditions. The generalized effective compliance S^*_{pq} according to Eq. (42) is then obtained as

$$S^M_{pq} = \begin{pmatrix} C_{ijkl} & e_{lij} \\ e_{lij} & -\kappa_{ln} \end{pmatrix}^{-1}, \quad S^C_{pq} = \frac{f\pi}{4} \begin{pmatrix} 0 & 0 & 0 & 0 & 0 & 0 & 0 & 0 & 0 \\ 0 & Y_{22} & 0 & Y_{12} & 0 & Y_{23} & 0 & Y_{24} & 0 \\ 0 & 0 & 0 & 0 & 0 & 0 & 0 & 0 & 0 \\ 0 & Y_{12} & 0 & Y_{11} & 0 & Y_{13} & 0 & Y_{14} & 0 \\ 0 & 0 & 0 & 0 & 0 & 0 & 0 & 0 & 0 \\ 0 & Y_{23} & 0 & Y_{13} & 0 & Y_{33} & 0 & Y_{34} & 0 \\ 0 & 0 & 0 & 0 & 0 & 0 & 0 & 0 & 0 \\ 0 & Y_{24} & 0 & Y_{14} & 0 & Y_{34} & 0 & Y_{44} & 0 \\ 0 & 0 & 0 & 0 & 0 & 0 & 0 & 0 & 0 \end{pmatrix}. \tag{44}$$

The matrix is valid for the crack coordinate system $\left(x_1^c, x_2^c\right)$ defined by the local principal stress axes, see Fig. 4a. The local polarization, being subject to continuous ferroelectric domain evolution, is associated with the local coordinate system (x_1, x_2), see Fig. 4b. The IRWIN matrix Y_{MN} in Eq. (44) is a material property, depending on the direction of polarization.

The local degree of damage is described by the crack density or damage parameter f. Being defined as

$$f = \frac{4a^2}{A} \tag{45}$$

it takes the value $f = 1$ if the crack tips reach the boundary of the RVE, the extension of the latter $\sqrt{A}$ being a model parameter. The mode-I stress intensity factor $K_I^{(n)}$ is applied to quantify the loading, and the related fracture criterion is

$$\sigma_I \sqrt{\pi a_n} = K_I^{(n)} = K_{IC}\ . \tag{46}$$

The fracture toughness K_{IC} can be chosen constant or account for an R-curve behavior, where the crack resistance is controlled by the electric field due to small scale switching at the crack tip [16]. The index n indicates an incremental crack growth in such a way that

$$a_n = a_0 + n \cdot \Delta a, \qquad f_n = f_0 + n \cdot \Delta f\ . \tag{47}$$

Equation (47) is repeated at one external load step as long as the criterion Eq. (46) claims for crack growth, finally initiating the next load step. If $f = 1$ the elastic stiffness is locally reduced to 5% of the undamaged material, the dielectric properties of air are adopted and the piezoelectric coefficients are set to zero.

6 Results

6.1 Ferroelectric, Ferromagnetic and Multiferroic Behavior from FE Simulation

The constitutive models summarized in Sect. 2 have been implemented within the framework of the FE method (for details see [1, 2]). Cobalt ferrite (CF) is employed as an example to demonstrate nonlinear reversible behavior of soft magnetic materials, whereas AlNiCo 35/5 represents a hard magnetic alloy exhibiting pronounced hysteresis behavior. $BaTiO_3$ (BT) is employed as an example to demonstrate nonlinear irreversible behavior of ferroelectric materials. The material data are given in the appendix.

Dielectric and butterfly hysteresis loops for BT are shown in Fig. 5a, b. Both plane stress (esz) and plane strain (evz) are invesigated, depicted by solid blue and dashed black lines, respectively. Qualitatively, there is a good agreement with experimental findings [10, 14, 15]. A quantitative comparison is feasible based on coercive field and remanent strain as well as polarization. From the simulations $E_C = 0.2\,\mathrm{MV/m}$, $\varepsilon_r^{\mathrm{esz}} = 224\,\mathrm{ppm}$, $\varepsilon_r^{\mathrm{evz}} = 208\,\mathrm{ppm}$, $P_r^{\mathrm{esz}} = 73.6\,\mathrm{mC/m^2}$ and $P_r^{\mathrm{evz}} = 72.9\,\mathrm{mC/m^2}$ are the obtained values, being in good agreement with experimental results [39]. Comparing plane strain and plane stress, deviations are predominantly visible in the butterfly loop, where the remanent strain is larger in the plane stress state.

In Fig. 5c, d magnetization M and magnetic induction B as well as strain are plotted versus the magnetic field in x_1–direction, where maximum values of approximately five times the coercive field are applied, i.e. $H_1 = \pm 250\,\mathrm{kA/m}$. The alloy AlNiCo 35/5 has been chosen as an example to demonstrate hard ferromagnetic behavior. Generalized plane stress is assumed in the simulations, i.e. the magnetic induction in perpendicular direction is likewise zero. Equation (2) postulates that the induction B_i and the magnetization M_i^{irr} differ by a term $\mu_{ij} H_j$ which is almost linear in H_j, since nonlinearities in the magnetic permeability, similar as in Eq. (17), play a secondary role. This explains the characteristics of the loops in Fig. 5c, particularly for a saturated magnetization. The dashed red line in the second quadrant is an experimental demagnetization curve, the only part of the loop which is provided by the manufacturer of the material [31]. Anyway, there is a perfect agreement with the numerical prediction. The facts that the coercive magnetization is slightly larger than the coercive induction, while the remanent values are identical are also confirmed experimentally, where $H_C^B = 47\,\mathrm{kA/m}$, $H_C^M = 48\,\mathrm{kA/m}$ and $M_r = B_r = 1.12\,\mathrm{T}$ are given [31]. The butterfly loop in Fig. 5d shows the magnetostrictive properties with a remanent strain $\varepsilon_r = 36\,\mathrm{ppm}$. In contrast to the ferroelectric loop, there is a saturation of the strain at larger loading fields.

Figure 5e, f show the specific magnetization (Eq. (25), $\rho = 5.3\,\mathrm{g/cm^3}$) and strain, respectively, for CF as a soft ferromagnetic alloy, based on the phenomenological constitutive model outlined in Sect. 3.2. Stress-free boundaries are presumed, thus constant values $\zeta_1 = \zeta_1^0$, $\zeta_2 = \zeta_2^0$ and $\xi = \xi^0$ are adopted according to Eq. (23). Furthermore, a generalized state of plane stress is assumed. The curves are nonlinear,

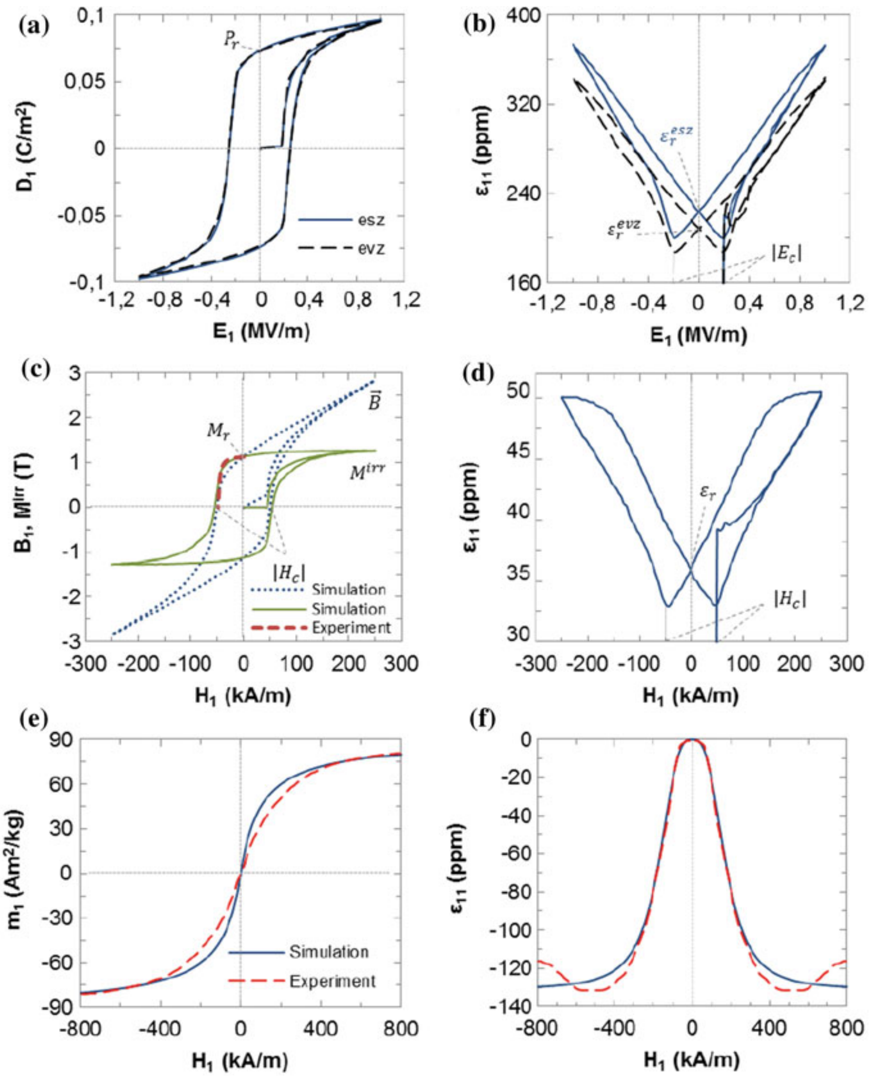

Fig. 5 Constitutive behaviors from FE simulations: **a, b** electric displacement and strain versus electric field for generalized plane stress (esz) and strain (evz) for BT; **c, d** magnetic induction B, magnetization M, (dashed red line: experimental data of demagnetization curve [31]) and strain versus magnetic field for AlNiCo 35/5; **e, f** specific magnetization and strain versus magnetic field for CF (dashed red line: experimental data [5])

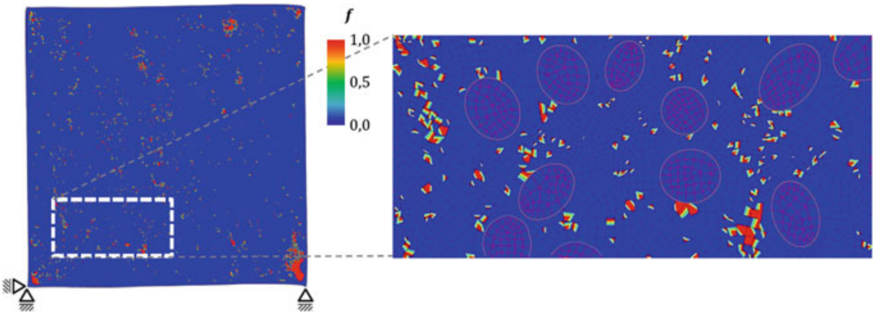

Fig. 6 Damage pattern of a ME particle composite (0,2$CoFe_2O_4$–0,8$BaTiO_3$, matrix: BT) right after electric poling with $E_1 = 5E_C$ and magnetic loading with $H_1 = 1000$ kA/m, see Fig. 8. The local damage parameter $f = 1$ indicates full damage and thus macro crack formation

Table 1 Effective magnetoelectric coupling coefficients of a 0,2$CoFe_2O_4$–0,8$BaTiO_3$ particle composite, where the simulation accounts for linear constitutive relations for both constituents

Coefficients	Linear FEM	Experiment [11, 12]
$g_{11}^{(R)*} = \left.\frac{\Delta\langle D_l\rangle}{\Delta H_k^0}\right\|_{\sigma_{ij},E_n} = \left.\frac{\Delta\langle B_k\rangle}{\Delta E_l^0}\right\|_{\sigma_{ij},H_m}$ [Ns/VC]	$148 \cdot 10^{-12}$	$4.4 \cdot 10^{-12}$

but reversible. Experimental results have been included in the graphs using dashed red lines. The overall coincidence with the simulation is good, without reproducing every detail. Based on the same constitutive model the influence of superimposed bi-axial mechanical stress on the constitutive behavior is investigated in [3].

Based on the material models, in particular nonlinear simulations have been done in order to predict ME coupling coefficients. First of all, however, linear calculations provide upper limiting values to demonstrate the essential role of nonlinear effects stemming from domain switching or damage. Two kinds of composites will be considered: one with a matrix of barium titanate (BT, $BaTiO_3$) with embedded elliptic soft ferromagnetic particles of cobalt ferrite (CF, $CoFe_2O_4$) and a laminated one consisting of three layers of BT and the hard ferromagnetic 0,2AlNiCo 35/5. The particle composite accounts for statistical distributions of particle sizes, shapes and positions. Figure 6 shows an RVE with a magnified excerpt on the right hand side including the FE mesh. Periodic boundary conditions are generally imposed in the FE analyses prior to calculating the coupling coefficients.

For the particle composite experimental values [11, 12] are taken for comparison, where the composition is 80% BT and 20% CF. Table 1 shows a comparison with calculations based on linear piezoelectric and -magnetic constitutive laws. The values differ by two orders of magnitude, the larger coefficient belonging to the calculation.

Several aspects are responsible for this overestimation. First of all, the constitutive laws for both constituents imply perfect poling along the transversal axes,

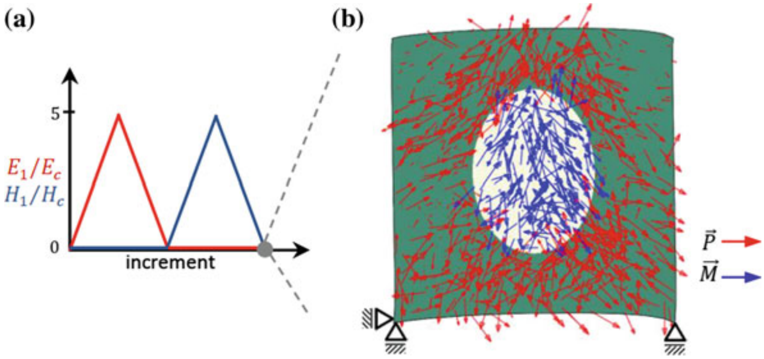

Fig. 7 RVE of an electrically and magnetically poled ME compound with periodically distributed ferromagnetic particles in a ferroelectric matrix ($0.2\text{AlNiCo}\,35/5-0.8\text{BaTiO}_3$): **a** poling load history and **b** vectors of polarization and magnetization

which is far from reality. Figure 7 shows the real states of polarization and magnetization in an example representing the RVE of a periodic particle composite with hard ferromagnetic inclusions. It is obvious that right after the poling, according to the magnetoelectric loading scheme in the left sketch, the vectors of magnetization and polarization are far from being perfectly aligned. Second, the residual stresses induced during the poling process will lead to substantial cracking and delamination between matrix and particles, thus further reducing the ME coupling. A possible crack pattern in the matrix of a non-periodic particle composite after the magnetoelectric poling is indicated in Fig. 6 by the red regions.

Nonlinear simulations are shown next, where the ferroelectric matrix is modelled by the microphysically motivated constitutive law and the particle behavior is described by the phenomenological magnetostrictive law. Calculations are presented, accounting for damage evolution in the matrix on the one hand side and neglecting it on the other. Cracking of the particles and delamination are not considered in any case. The poling process of the initially unpoled materials has to be considered first, in order to induce a piezoelectric effect in the matrix. The magnetostrictive phase, following a nonlinear reversible material law, does not require a magnetic pre-poling. The loading scheme for calculating the ME coupling coefficients is depicted in a small sketch in Fig. 8, whereupon an electric half-cycle with a maximum load of $5E_C$ is followed by a linearly increasing magnetic field up to $H_1 = 1000$ kA/m.

The coupling coefficient $g_{11}^{(R)*}$ in Fig. 8 is determined in the interval of magnetic loading and plotted versus the magnetic field H_1. The right plot is an excerpt of the left one, where the scaling of $g_{11}^{(R)*}$ along the ordinate is different. The red crosses illustrate the scope of experimental results for coupling coefficients. The solid lines represent average electric displacements $\langle D_1\rangle$. Green symbols and lines generally indicate results neglecting damage, blue ones emanate from simulations with damage. The electric displacement is non-zero at $H_1 = 0$ due to the electric poling, in the absence of free charges, leading to a remanent polarization. A depolarization along the x_1-axis

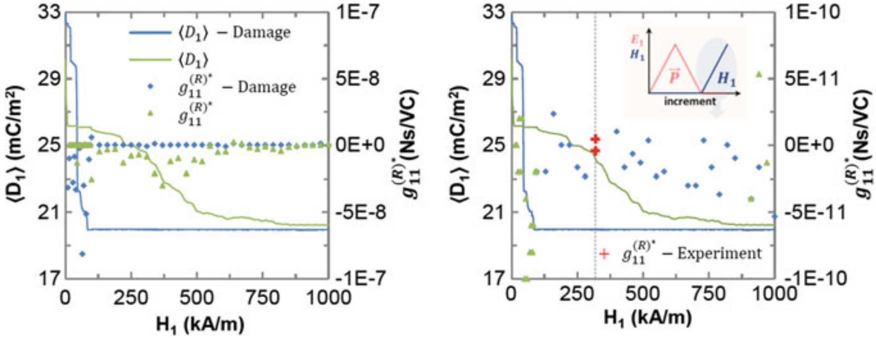

Fig. 8 Average electric displacement $\langle D_1 \rangle$ and ME coupling coefficient $g_{11}^{(R)*}$ for a 0,2$CoFe_2O_4$–0,8$BaTiO_3$ particle composite, see Fig. 6, from numerical simulation; experimental values from [11, 12])

is observed already at low magnetic fields. The reason is the magnetostriction, leading to a compression in the x_1-direction and an extension in x_2. The stress release due to damage on the one hand reduces the slope of reduction in $\langle D_1 \rangle$ for very small magnetic loads, on the other fosters the drop to a stationary value.

The coupling coefficients are calculated from the local derivatives of the $\langle D_1 \rangle (H_1)$-function. Averaging within intervals is necessary to smoothen the results which are depicted by the squared dots. Still there is a considerable scattering, in particular when damage is neglected, whereas the simulation with damage exhibits comparable variance just in the range of small magnetic fields. A general observation is that the ME coupling is obviously reduced by the damage, whose patterns are shown in Fig. 6, where the red regions with $f = 1$ indicate the formation of macro cracks. These are widely dispersed in the ferroelectric matrix, however most of them not being located at the interfaces of matrix and inclusions. Looking at the experimental values of coupling coefficients, they are within the range of those predicted from the model accounting for damage evolution.

Results for the layered composite are considered next. Figure 9c shows the three layers and the mechanical boundary conditions. The middle layer consisting of AlNiCo 35/5 is ferromagnetic, while the outer layers are made of BT. In contrast to the previous simulations of the particle composite, the microphysically motivated constitutive approaches are employed for both ferroelectric and ferromagnetic constituents. In d an excerpt illustrates the damage pattern, the red dots again being interpreted as macroscopic crack formation. In Fig. 9b the ME loading scheme is depicted, starting with an electric poling with a maximum field of strength $5E_C$, followed by a magnetic poling with a maximum of $5H_C$. The ME coupling coefficients are calculated after the poling, increasing an electric field linearly. The reason for imposing the fields along the longer edges is due to the fact that the simulation of the poling process is easier that way than for a perpendicular loading. In reality the middle layer will be poled before assembling the composite. The simulation, however, is based on the whole composite, so the magnetic poling field would have

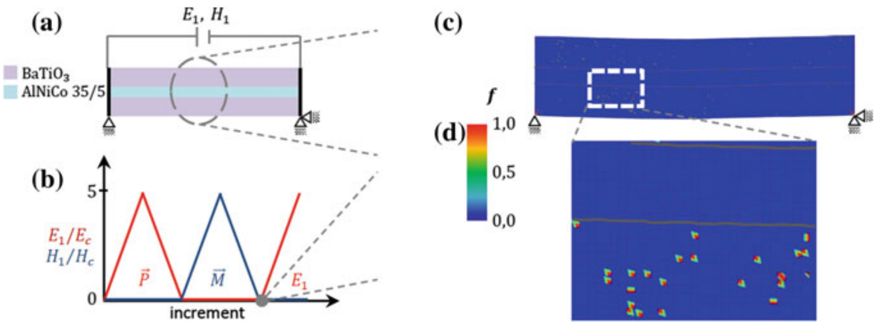

Fig. 9 **a** laminated ME composite (0,2AlNiCo 35/5–0,8BaTiO$_3$) and boundary conditions, **b** load history, **c** FE analysis of displacement ($\times$10) and damage pattern ($f = 1$: macro crack) right after poling

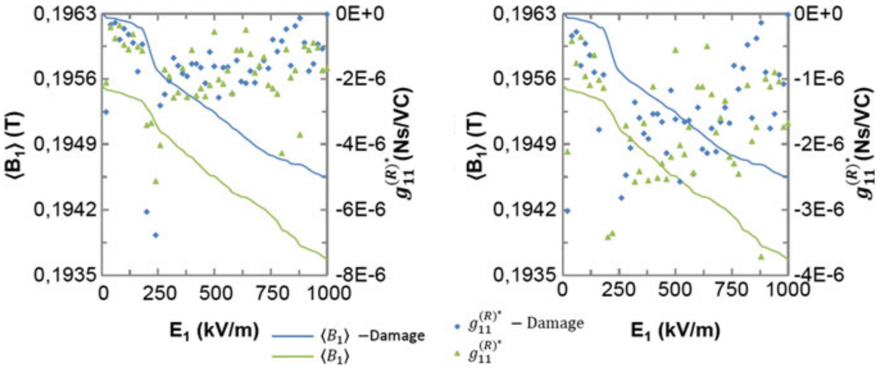

Fig. 10 Laminated composite according to Fig. 9: average magnetic induction $\langle B_1 \rangle$ and effective ME coupling coefficient $g_{11}^{(R)*}$ with different scalings

to penetrate the non-ferromagnetic layers, thus being too weak. The ME coupling coefficients might be even larger for fields along the shorter edges.

In Fig. 10 the average magnetic induction (solid lines) and the ME coupling coefficient (symbols) are plotted versus the electric field. Both magnetic and electric fields are those along the longer edges denoted as x_1-direction. The blue color represents the results including damage, again just in the ferroelectric layers, the green color stands for simulations neglecting damage. The right graph in Fig. 10 magnifies the scaling of the coupling coefficient.

Compared to the particle composite, a first observation is that the range of the induced field, i.e. the magnetic induction, is relatively small, barely exceeding one percent of its total magnitude. The regression caused by electric loading, however, is monotonous, reducing the initial magnetic poling. Comparing the ME coupling efficiency, the coefficients of the laminated composite exceed those of the one with embedded particles by several orders of magnitude, which is the most important outcome at this point. The cracking of the ferroelectric layers, on the other hand, doesn't have a significant impact, neither on the magnetic flux nor on the coupling coefficient. In the plots, the magnetic induction from poling seems to be slightly larger due to damage, the magnitudes, however, indicating a negligible effect.

6.2 Constitutive Behavior and ME Coupling Predicted from the Condensed Method

In this section some results are presented calculated with the condensed method, which is introduced in Sect. 4. First of all, some aspects of pure ferroelectric and ferromagnetic material behavior are considered, finally coupling coefficients of a ME compound are predicted. Figure 11a shows the electromechanical loading scheme for the investigation of a ferroelectric material. Here, N denotes the load increment, $\left|E_2^{\max}\right|$ the amplitude of the applied electric field and $\hat{\sigma}_{11}$ the mechanical load, which is kept constant during a cyclic electric field. According to Fig. 11b the compressive stress $\sigma_{ij}^{\text{ext}} = \left(-\sigma_{11}^{\text{ext}}, 0\right)^T$ is applied perpendicular to the external electric field $E_i^{\text{ext}} = \left(0, E_2^{\text{ext}}\right)^T$.

In Fig. 12a the influence of a perpendicular stress on the electromechanical coupling coefficient k_{22} is investigated, see Fig. 11b. The latter is defined as

$$k_{22} = \sqrt{\frac{\langle e_{22}\rangle^2}{\langle \kappa_{22}\rangle \langle C_{22}\rangle}} \tag{48}$$

and describes the efficiency of conversion of electrical and mechanical energies and vice versa [28]. $\langle C_{22}\rangle$ is the elastic constant in x_2-direction in compressed notation. As shown in [28] by FE simulation, the electromechanical coupling coefficient versus

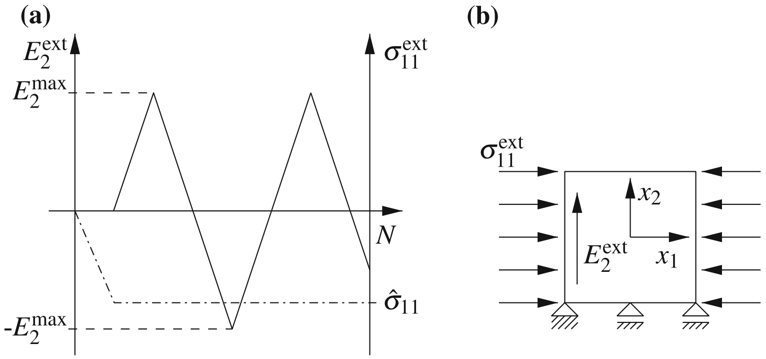

Fig. 11 Electromechanical in-plane loading by stresses σ_{11}^{ext} and perpendicular electric field E_2^{ext}

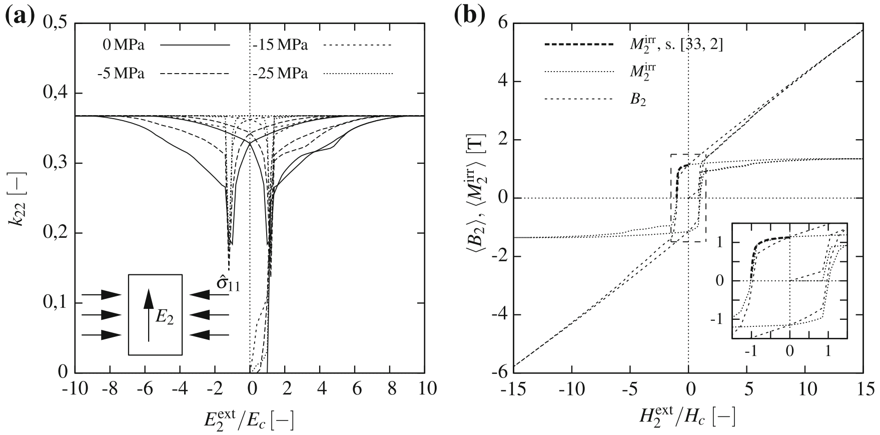

Fig. 12 **a** Electromechanical coupling coefficient k_{22} versus normalized electric field for BT; **b** magnetic induction B_2 and magnetization M_2^{irr} versus normalized magnetic field for AlNiCo 35/5

the normalized electric field exhibits a butterfly-like hysteresis. For a non-polarized polycrystalline material k_{22} vanishes. Increasing the electric field above E_C, k_{22} is augmented due to the domain wall motion. For large fields, a saturation of k_{22} is observed. Concerning the remanent values of the electromechanical coupling coefficient k_{22}^{r} it is obvious, that a compressive perpendicular stress leads to an increasing k_{22}^{r}. The remanent values of Fig. 12a are in a very good agreement with the results in [28], where a micromechanically motivated constitutive model is implemented within a FE framework.

Figure 12b shows the average magnetic induction $\langle B_2 \rangle$ and magnetization $\left\langle M_2^{\mathrm{irr}} \right\rangle$ for a hard ferromagnetic material with pure magnetic loading H_2. The thick dashed line of the second quadrant represents the demagnetization curve taken from [2, 31]. The close-up of Fig. 12b shows a very good agreement between $\left\langle M_2^{\mathrm{irr}} \right\rangle$ of the CM and the experimental data. A comparison of Fig. 5b, where the FEM is used to investigate the nonlinear ferromagnetic material behavior, and Fig. 12b shows a good agreement as well, in particular concerning the demagnetization and remanent magnetization M^{r}. The results of Fig. 12 indicate that the CM is able to predict the macroscopic nonlinear behavior of ferroelectric and ferromagnetic single phase materials.

Figure 13a presents results of a multiferroic compound with 80% barium titanate and 20% cobalt ferrite. The magnetoelectric coupling coefficient $g_{22}^{(\sigma,H)}$ and the average magnetic induction $\langle B_2 \rangle$ are plotted versus the normalized electric field. The nonlinear characteristics of both ferroelectric and ferromagnetic constituents are considered by the microphysical constitutive approach. In that context it should be mentioned that CF is known as hard as well as soft ferromagnet, depending on its processing. In the simulation, the compound is poled applying an unipolar electric field of $E_2^{\max} = 5\,E_C$ and then magnetized with $H_2^{\max} = 15\,H_C$, thus a similar scheme is implemented as depicted in Fig. 9b. Afterwards, an electric field is applied

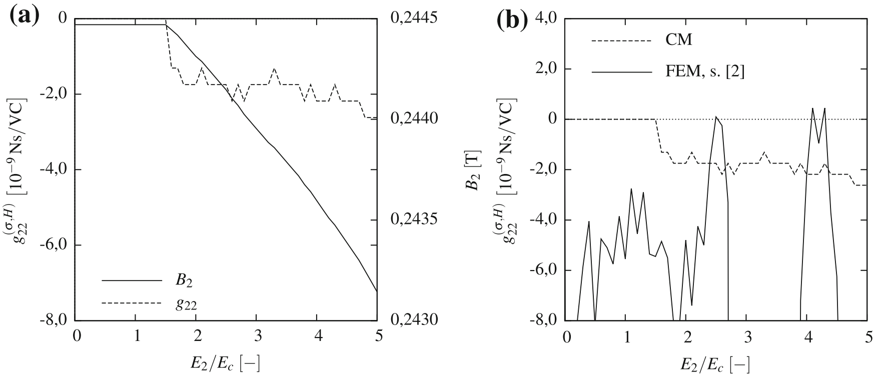

Fig. 13 **a** Magnetoelectric coupling coefficient $g_{22}^{(\sigma,H)}$ and magnetic induction $\langle B_2 \rangle$ versus normalized electric field; **b** comparison of FEM and CM for a 0.2CF–0.8BT multiferroic compound

to calculate the magnetoelectric coupling coefficient according to

$$g_{ij}^{(\sigma,H)} = \left.\frac{\partial \langle B_i \rangle}{\partial E_j^{\text{ext}}}\right|_{\sigma,H} \approx \left.\frac{\Delta \langle B_i \rangle}{\Delta E_j^{\text{ext}}}\right|_{\sigma,H} = \left.\frac{\Delta \langle M_i^{\text{irr}} \rangle}{\Delta E_j^{\text{ext}}}\right|_{\sigma,H}, \tag{49}$$

bearing in mind that σ_{ij}^{ext} and H_i^{ext} are equal to zero, see Fig. 9b. The latter aspect in connection with the generalized VOIGT approximation of the CM, i.e. $\langle H_i \rangle = \bar{H}_i = H_i^{\text{ext}}$, is responsible for the last equality in Eq. (49), leading to a suppression of the linear contribution of H_i to B_i.

Figure 13a reveals that a magnetic field is induced by electric fields above 1.75 E_C, thus the ME coupling is zero for lower fields. The increasing residual stresses in the ferroelectric constituent yield a demagnetization of the ferromagnetic part, leading to a negative ME coupling coefficient. The amount of demagnetization, however, is small and similar to the one in Fig. 10. In Fig. 13b the results of the ME coupling coefficients from the FEM and the CM are compared to each other. The solid line represents the results of the FEM [2] and the dashed line those of the CM. The FEM provides non-zero coupling coefficients already for small electric fields. The main reason therefore are the larger residual stresses in the ferroelectric constituent predicted by the FEM. These are probably caused by geometric features of the composite which cannot be considered in the CM. Nevertheless, the demagnetization of the ferromagnetic constituent is predicted in both cases. The magnitudes of the ME coupling are similar for both simulation approaches.

7 Conclusion

Nonlinear constitutive models for ferroelectric and ferromagnetic materials have been presented within a magneto-electro-mechanical multifield context. The associated finite element implementation enables the simulation of multiferroic composites, in order to determine e.g. the magnetoelectric coupling coefficients or residual stresses due to domain switching. A simple micromechanically motivated damage model has been developed and included, since cracking turns out to have an essential impact, not only on life time but also on the functionality in terms of coupling efficiency. The present damage model thus has to be extended towards cracking in the ferromagnetic phase and delamination of the constituents. The latter aspect will be crucial for laminated composites, where cracking of the material itself turns out to have minor influence on the coupling coefficient. Besides the classical finite element implementation, the constitutive laws have been applied to a so-called condensed method in order to predict nonlinear multiphysical behavior of ferroelecrics, ferromagnetics and multiferroics. The finite element investigations confirm the common experience that the coupling efficiency of laminated composites is much larger compared to embedded particle composites. Nevertheless, more configurations will have to be investigated numerically, including variations of magnetoelectric poling procedures, playing a crucial role. An important aspect, not yet considered in the constitutive and balance equations, is the flux of electric charge. In particular for ferromagnetic materials, the assumption of a dielectric medium often is not quite appropriate.

Appendix

The coefficients of cobalt ferrite (CF) and barium titanate (BT) are listed in Table 2. The coefficient μ_{11} of BT is determined from the magnetic suszeptibility $\chi_v^{\mathrm{CGS}} = -8.47 \cdot 10^{-8}$ at 293.8 K [41] according to $\mu_{11} = \mu_0 \left(\chi_v^{\mathrm{SI}} + 1\right)$ with $\chi_v^{\mathrm{SI}} = 4\pi \chi_v^{\mathrm{CGS}}$. The coefficient μ_{22} was estimated, adapting the transversal isotropy of the dielectric constants κ_{ij} to the magnetic permeability. In the state of maximum magnetostriction the magnetic suszeptibility of CF is $\chi_v^{\mathrm{SI}} = 1.16$, providing a permeability of $\mu_{11} = 2.71 \cdot 10^{-6}\,\mathrm{Ns^2/C^2}$. The coefficient μ_{22} is determined based on the same idea as with BT.

Additionally, the quantities in Table 3 have been identified for the nonlinear reversible constitutive model. Due to the fact, that an appropriate value of μ^r_{11} could not be found in the literature, $\mu^r_{11} = 5$ has been chosen, relying on similar ferromagnetic materials.

Table 4 illustrates the procedure of how to identify the parameters of the constitutive model based on experimental and numerical curves.

Table 2 Material properties of $BaTiO_3$ and $CoFe_2O_4$ [22, 29, 41, 43]

	$BaTiO_3$	$CoFe_2O_4$
C_{11} [GPa]	162	269.5
C_{12} [GPa]	77.5	170
C_{22} [GPa]	166	286
C_{23} [GPa]	76.6	173
C_{44} [GPa]	42.9	45.3
κ_{11} [C/Vm]	$12.57 \cdot 10^{-9}$	$0.093 \cdot 10^{-9}$
κ_{22} [C/Vm]	$11.16 \cdot 10^{-9}$	$0.08 \cdot 10^{-9}$
μ_{11} $[\mathrm{Ns^2/C^2}]$	$1.26 \cdot 10^{-6}$	$2.71 \cdot 10^{-6}$
μ_{22} $[\mathrm{Ns^2/C^2}]$	$1.12 \cdot 10^{-6}$	$2.33 \cdot 10^{-6}$
e_{11} $[\mathrm{C/m^2}]$	18.6	0
e_{12} $[\mathrm{C/m^2}]$	−4.4	0
e_{24} $[\mathrm{C/m^2}]$	11.6	0

Table 3 Parameters of the phenomenological material model adapted to the constitutive behavior of $CoFe_2O_4$

No.	Parameter	Unit	$CoFe_2O_4$
1	η_1	-	$-131 \cdot 10^{-6}$
2	η_2	-	$106 \cdot 10^{-6}$
3	ζ_1^0	$\mathrm{A^3/m^3}$	$5.5 \cdot 10^{15}$
4	ζ_2^0	$\mathrm{A^3/m^3}$	$2.1 \cdot 10^{15}$
5	ζ_1^σ	$\mathrm{A^3/Nm}$	$9 \cdot 10^{10}$
6	ρ	T	0.6
7	ξ^0	N/Vs	$1 \cdot 10^5$
8	ξ^σ	$\mathrm{m^2/Vs}$	0.3
9	ξ_0^σ	$\mathrm{m^2/Vs}$	6
10	ϖ	-	50

Table 4 Identification of the parameters of the phenomenological constitutive model

No.	Parameter	Calibration
1	η_1	Saturation strain ε_{11}^s at $\sigma_{ij} = 0$
2	η_2	Saturation strain ε_{22}^s at $\sigma_{ij} = 0$
3	ζ_1^0	$\varepsilon_{11} - H$ - curve at $\sigma_{ij} = 0$
4	ζ_2^0	$\varepsilon_{22} - H$ - curve at $\sigma_{ij} = 0$
5	ζ_1^σ	$\varepsilon_{11} - H$ - curve at $\sigma_{ij} = \text{const} \neq 0$
6	ρ	Saturation magnetisation (converted in T) at $\sigma_{ij} = 0$
7	ξ^0	$m - H$ - curve at $\sigma_{ij} = 0$
8	ξ^σ	$m - H$ - curve at $\sigma_{ij} = \text{const} \neq 0$
9	ξ_0^σ	$m - H$ - curve (rigidly clamped: $\mathrm{d}\sigma_{ij} \neq 0$)
10	ϖ	Slope of **B** at saturation of magnetisation $(\cdot \mu_0^{-1})$ at $\sigma_{ij} = 0$

Table 5 Parameters of the physically based model adapted to the constitutive behavior of $BaTiO_3$ and AlNiCo 35/5 [10, 22, 34, 39] (in [34] μ^r is denoted as μ_{rec})

Parameter	Unit	$CoFe_2O_4$	AlNiCo 35/5
E_c	MV/m	0.2	-
$H_c = H_{cB}$	kA/m	-	47
P^0	C/m^2	0.26	-
M^0	T	-	1.9
ε_D	–	0.01	0.04
a_0	µm	5	-
f_0	–	0.005	-
K_I^{crit}	$\text{MPa}\sqrt{\text{m}}$	1.4	-

For a plane stress state, the values of σ_{11}^s and σ_{22}^s are calculated as follows:

$$\begin{aligned} \sigma_{11}^s &= C_{11}\eta_1 + C_{12}\eta_2 - \frac{C_{12}}{C_{22}}\left(C_{12}\eta_1 + C_{23}\eta_2\right) \ , \\ \sigma_{22}^s &= C_{12}\eta_1 + C_{22}\eta_2 - \frac{C_{23-}}{C_{22}}\left(C_{12}\eta_1 + C_{23}\eta_2\right) \ . \end{aligned} \tag{50}$$

Moreover, the quantities in Table 5 have been applied for the physically motivated model. Due to the lack of elastic and dielectric constants in literature, the values of Table 2 have been taken for AlNiCo 35/5 as well, assuming the same orders of magnitude.

References

1. Avakian, A., Gellmann, R., Ricoeur, A.: Nonlinear modeling and finite element simulation of magnetoelectric coupling and residual stress in multiferroic composites. Acta Mech. **226**, 2789–2806 (2015)
2. Avakian, A., Ricoeur, A.: Constitutive modeling of nonlinear reversible and irreversible ferromagnetic behaviors and application to multiferroic composites. J. Int. Mater. Sys. Struct. **27**, 2536–2554 (2016)
3. Avakian, A., Ricoeur, A.: An extended constitutive model for nonlinear reversible ferromagnetic behavior under magnetomechanical multiaxial loading conditions. J. Appl. Phys. **121**, 053901 (2017)
4. Bergmann, L., Schaefer, C.: Lehrbuch der Experimentalphysik - 6: Festkörper. de Gruyter, Berlin/New York (2005)
5. Bhame, S.D., Joy, P.A.: Tuning of the magnetostrictive properties of $CoFe_2O_4$ by Mn substitution for Co. J. Appl. Phys. **100**, 113911 (2006)
6. Bhame, S.D., Joy, P.A.: Magnetic and magnetostrictive properties of manganese substituted cobalt ferrite. J. Phys. D Appl. Phys. **40**, 326–3267 (2007)
7. Bhame, S.D., Joy, P.A.: Effect of sintering conditions and microstructure on the magnetostrictive properties of Cobalt Ferrite. J. Am. Ceram. Soc. **91**, 1976–1980 (2008)
8. Bozorth, R.M.: Ferromagnetism. Van Nostrand, New York (1951)

9. Trmolet, Du, de Lacheisserie, E., Gignoux, D., Schlenker, M.: Magnetism - Materials and Applications. Springer, New York (2005)
10. Enderlein, M.: Finite-Elemente-Verfahren zur bruchmechanischen Analyse von RIssen in piezoelektrischen Strukturen bei transienter elektromechanischer Belastung. Dissertation, TU Bergakademie Freiberg, Freiberg (2007)
11. Etier, M.F., Shvartsman, V.V., Salamon, S., Gao, Y., Wende, H., Lupascu, D.C., Raveau, B.: The direct and the converse magnetoelectric effect in multiferroic Cobalt Ferrite-Barium Titanate ceramic composites. J. Am. Ceram. Soc. (2016). https://doi.org/10.1111/jace.14362
12. Etier, M.F., Gao, Y., Shvartsman, V.V., Lupascu, D.C., Landers, J., Wende, H.: Magnetoelectric properties of $0.2CoFe_2O_4$–$0.8BaTiO_3$ composite prepared by organic method. In: Joint 21st IEEE ISAF/11th IEEE ECAPD/IEEE PFM (ISAF/ECAPD/PFM), Aveiro, Portugal, pp. 1–4 (2012)
13. Fiebig, M.: Revival of the magnetoelectric effect. J. Phys. D Appl. Phys. **38**, R123–R152 (2005)
14. Förderreuther, A.: Mechanische Eigenschaften von $BaTiO_3$ - Keramiken unter mechanischer und elektrischer Belastung. Dissertation, Universität Stuttgart, Stuttgart (2003)
15. Förderreuther, A.: Piezoelektrische Eigenschaften. In: Arbeitsbericht im Schwerpunktprogramm "Wechselbeziehung zwischen elektronischen und mechanischen Eigenschaften keramischer Multifunktionswerkstoffe". DFG Geschäftszeichen 322, 734 (1998)
16. Gellmann, R., Ricoeur, A.: Extended semi-analytical investigations of crack growth resistance behavior in ferroelectric materials. Acta Mech. **223**, 2357–2368 (2012)
17. Gellmann, R., Ricoeur, A.: Continuum damage model for ferroelectric materials and its application to multilayer actuators. Smart Mater. Struct. **25**, 055045 (2016)
18. Gellmann, R., Ricoeur, A.: Some new aspects of boundary conditions at crack faces in piezoelectrics. Arch. Appl. Mech. **82**, 841–852 (2012)
19. Hill, N.: Why are there so few magnetic ferroelectrics? J. Phys. Chem. B **104**, 6694–6709 (2000)
20. Hwang, S.C., Lynch, C.S., McMeeking, R.M.: Ferroelectric/ferroelastic interactions and a polarization switching model. Acta Metall Mater. **43**, 2073–2084 (1995)
21. Jackson, J.D.: Classical Electrodynamics. Wiley, New York (1998)
22. Jaffe, B., Cook, W.R., Jaffe, H.: Piezoelectric Ceramics. Academic Press, London (1971)
23. Kamlah, M., Liskowsky, A.C., McMeeking, R.M., Balke, H.: Finite element simulation of a polycristalline ferroelectric based on a multidomain single crystal switching model. Int. J. Solids Struct. **42**, 2949–2964 (2005)
24. Kessler, H., Balke, H.: On the local and average energy release in polarization switching phenomena. J. Mech. Phys. Solids **49**, 953–978 (2001)
25. Kittel, C.: Einführung in die Festkörperphysik. Oldenbourg, München (2006)
26. Lange, S., Ricoeur, A.: A condensed microelectromechanical approach for modeling tetragonal ferroelectrics. Int. J. Solids Struct. **54**, 100–110 (2015)
27. Lange, S., Ricoeur, A.: High cycle fatigue damage and lifetime prediction for tetragonal ferroelectrics under electromechanical loading. Int. J. Solids Struct. **80**, 181–192 (2016)
28. Li, Q., Ricoeur, A., Enderlein, M., Kuna, M.: Evaluation of electromechanical coupling effect by microstructural modeling of domain switching in ferroelectrics. J. Mech. Res. Commun. **37**, 332–336 (2010)
29. Li, J.Y., Dunn, M.L.: Micromechanics of magnetoelectroelastic composite materials: average fields and effective behavior. J. Intell. Mater. Syst. Struct. **9**, 404–416 (1998)
30. Lee, K.Y., Zong, X.C.: Dielectric crack problem for a magnetoelectroelastic strip with functionally graded properties. Arch. Appl. Mech. **82**, 791–807 (2011)
31. Magnetfabrik Bonn GmbH: Alnico 500. DIN-characterization 35-5 (2009)
32. Morrish, A.H.: The Physical Principles of Magnetism. IEEE Press, New York (2001)
33. Park, S.B., Sun, C.T.: Effect of electric field on fracture of piezoelectric ceramics. Int. J. Fract. **70**, 203–216 (1995)
34. Plassmann, W.: Handbuch Elektrotechnik. Grundlagen und Anwendungen für Elektrotechniker. Springer, Wiesbaden (2013)

35. Ricoeur, A., Kuna, M.: Influence of electric field on the fracture of ferroelectric ceramics. J. Eur. Ceram. Soc. **23**, 1313–1328 (2003)
36. Ricoeur, A., Kuna, M.: Electrostatic tractions at crack faces and their influence on the fracture mechanics of piezoelectrics. Int. J. Fract. **157**, 3–12 (2009)
37. Ricoeur, A., Lange, S., Gellmann, R.: Modeling approaches to predict damage evolution and life time of brittle ferroelectrics. In: Hütter, G., Zybell, L. (eds.) Trends, Recent, in Fracture and Damage Mechanics. Springer, Berlin (2015)
38. Ricoeur, A., Gellmann, R., Wang, Z.: Influence of inclined electric fields on the effective fracture toughness of piezoelectric ceramics. Acta Mech. **226**, 491–505 (2015)
39. Rödel, J., Kreher, W.S.: Modeling linear and nonlinear behavior of polycrystalline ferroelectric ceramics. J. Eur. Ceram. Soc. **23**, 2297–2306 (2003)
40. Scott, J.F.: Data storage: multiferroic memories. Nat. Mater. **6**, 256–257 (2007)
41. Stevens, D., Schweinler, H., Sturm, W., Sonder, W.: The magnetic susceptibility of barium titanate. Solid State Div. Semiannu. Prog. Rep. **30**, 13–14 (1956)
42. Sosa, H.: One the fracture mechanics of piezoelectric solids. Int. J. Solids Struct. **29**, 2613–2622 (1992)
43. Tang, T., Yu, W.: Micromechanical modeling of the multiphysical behavior of smart materials using the variational asymptotic method. Smart Mater. Struct. **18**, 125026 (2009)
44. Vanderlinde, J.: Classical Electromagnetic Theory. Springer, Dordrecht (2005)

Biaxial Tensile Tests and Microstructure-Based Inverse Parameter Identification of Inhomogeneous SMC Composites

Malte Schemmann, Sebastian Gajek and Thomas Böhlke

Abstract Discontinuous fiber reinforced composites offer great advantages for high-volume lightweight components. The characterization of their process-dependent, macro-heterogeneous, anisotropic mechanical behavior presents, however, a challenge to composite material science. Biaxial tensile tests allow for the loading of various stress states on the specimen. The inhomogeneous stress and strain fields require an inverse parameter identification. Previous biaxial tensile tests in the elastic range showed fluctuations in the elastic properties within one specimen. Micro CT scans suggested that some of these fluctuations derive from an inhomogeneous fiber orientation distribution. The identification of a generally inhomogeneous stiffness leads, however, to an ill-posed problem which does not allow for a unique solution. We introduce the assumption of linearity between the stiffness tensor and the fiber orientation distribution. This simplification reduces the problem size to five degrees of freedom per specimen which do not depend on fiber orientation distribution. Four of these parameters are identifiable and are determined in a Gauss-Newton type optimization procedure.

1 Introduction

Due to their good formability, economical mass-production and high specific strength and stiffness, discontinuous fiber reinforced polymers are increasingly applied in components in the automotive industry and the mobility sector in general. The appli-

M. Schemmann (✉) · S. Gajek · T. Böhlke
Institute of Engineering Mechanics, Chair for Continuum Mechanics, Karlsruhe Institute of Technology (KIT), Kaiserstraße 10, 76131 Karlsruhe, Germany
e-mail: malte.schemmann@kit.edu

S. Gajek
e-mail: sebastian.gajek@student.kit.edu

T. Böhlke
e-mail: thomas.boehlke@kit.edu

© Springer International Publishing AG 2018

H. Altenbach et al. (eds.), *Advances in Mechanics of Materials and Structural Analysis*, Advanced Structured Materials 80,
https://doi.org/10.1007/978-3-319-70563-7_15

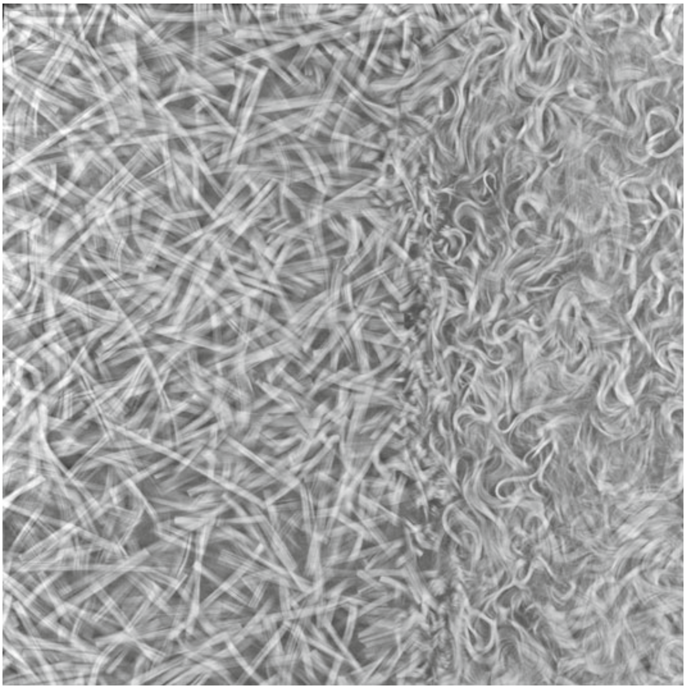

Fig. 1 CT scan of a macro-heterogeneous SMC microstructure that shows to different flow regions: almost straight fibers on the left side and curly fibers on the right third of the image, specimen dimensions: 73 mm × 73 mm × 3 mm

cation of this class of materials is, however, hindered by a lack of a detailed understanding of its mechanical behavior.

The material class under consideration is the discontinuous fiber reinforced thermoset, Sheet Molding Compound (SMC). Specifically, glass fiber reinforced Unsaturated Polyester Polyurethane Hybrid (UPPH) resin is under consideration. The fibers have a length of 25 mm. Typically, parts of SMC such as structural automotive components are manufactured by compression molding of prepregs. This forming process leads to a heterogeneous fiber orientation distribution. An example for such a heterogeneous microstructure is shown in a slice of a Computed tomography (CT) scan in Fig. 1. Here, characteristic flow regions developed during moldfilling. As a result, the material behavior is spatially heterogeneous and anisotropic in a process sensitive way [10].

Within the virtual process chain, this heterogeneity has been taken into account in moldfilling analysis [1, 17] and homogenization approaches [3, 16] for discontinuous fiber reinforced polymers. The mechanical characterization of heterogeneous composites has been considered in great detail in the literature by the assumption of homogeneously distributed material properties within the specimen. However, the consideration of heterogeneous specimens is in an early stage of research.

For the heterogeneous stress and strain state and multiaxial loading even in cruciform specimen with homogeneous properties, it is, in general, not possible to analytically identify the material parameters of a constitutive equation. Therefore, an inverse parameter identification method is needed. Schnur and Zabras [23] introduce a coupled procedure that links finite element simulations to an optimization method for inverse parameter identification. Through the minimization of a goal function that describes the deviation of a simulation and the experiment, the unknown material parameters are identified.

In the past, many approaches were suggested for the optimization of the goal function. A key benefit of gradient free procedures such as neural network computation [4] and evolutionary algorithms [18] is that no additional model information is needed. These procedures, however, usually result in comparably high computational cost. An overview of different gradient methods for inverse parameter identification is given by Ponthot and Kleinermann [19]. The required gradient can either be estimated by a finite difference scheme [5, 23] or calculated analytically [12, 13]. The latter one requires modifications in the finite element code. The development of full field measurement techniques allows for a parameter identification with inhomogeneous displacement and strain fields. Lecompte et al. [11] identified the anisotropic elastic behavior of glass fiber reinforced epoxy. Through using a goal function that compares strain fields, the needed gradient for the optimization method can be obtained analytically using the constitutive equations without making adjustments to the finite element code.

A direct tensor notation is preferred throughout the text. Tensor components are expressed by latin indices, and Einstein's summation convention is applied. components of vectors and tensors refer to the orthonormal basis $\{\mathbf{e}_1, \mathbf{e}_2, \mathbf{e}_3\}$. Vectors and second-order tensors are denoted by lowercase and uppercase bold letters, e.g., $\mathbf{a}$ and $\mathbf{A}$, respectively. Fourth-order tensors are denoted by, e.g., $\mathbb{A}$, $\mathbb{B}$, …. Additionally, second and higher-order tensors can be written as $\mathbb{A}_{\langle\alpha\rangle}$, where α indicates the tensor rank. The composition of two second-order or two fourth-order tensors is formulated by $\mathbf{AB}$ and $\mathbb{AB}$. A linear mapping of second-order tensors by a fourth-order tensor is written as $\mathbf{A} = \mathbb{C}[\mathbf{B}]$. The scalar product is denoted by $\mathbf{A} \cdot \mathbf{B}$. The dyadic product operator $\otimes$ is defined as $(\mathbf{A} \otimes \mathbf{B})\,[\mathbf{C}] = (\mathbf{B} \cdot \mathbf{C})\,\mathbf{A}$, higher-order dyadic products of the same tensor are indicated by $\mathbf{n}^{\otimes\alpha} = \mathbf{n} \otimes \cdots \otimes \mathbf{n}$, where $\mathbf{n}^{\otimes\alpha}$ is a tensor with the rank α times the rank of $\mathbf{n}$. The identity on symmetric second-order tensors is denoted by $\mathbb{I}^{\mathrm{S}}$. Completely symmetric and traceless, i.e. irreducible tensors are denoted with a prime, e.g., $\mathbf{A}'$. Column vectors and matrices are noted with underscores, e.g., $\underline{p}$, $\underline{\underline{A}}$.

2 Experimental Procedure

The specimens are tested in an electro-mechanical biaxial tensile testing machine from Zwick. Four independent axes allow for a maximum load of 150 kN. Figure 2 (left) shows the setup of the machine. Five markers for integrated strain measurements are located on the lower side of the specimen. These markers are traced by the

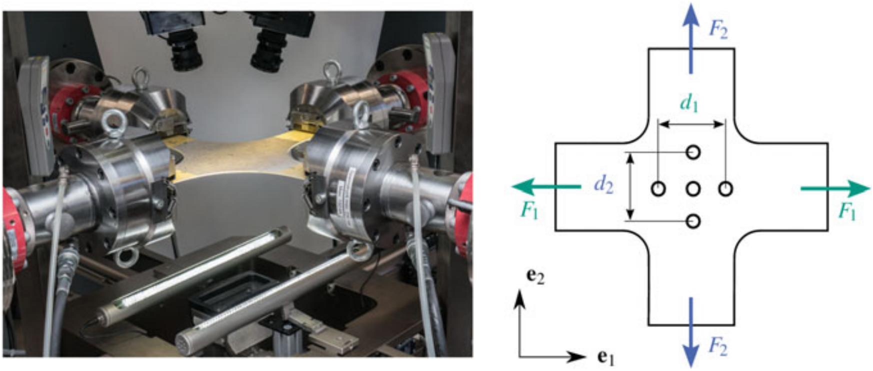

Fig. 2 Biaxial tensile testing machine (left) and cruciform specimen with markers for displacement measurement (right)

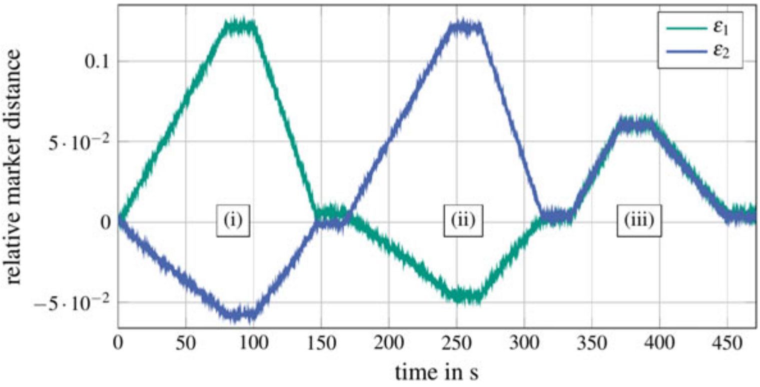

Fig. 3 Experimental procedure: strain path

integrated strain measurement system Video XTens. The distances between opposing points d_1 and d_2 (see Fig. 2 (right)) are used for the load control. Additionally, the marker positions are used for the active midpoint control of the system which allows for load application without bending in specimen's arms, even for highly heterogeneous specimen. On the upper side of the specimen, a speckle pattern is applied which is used for full-field strain measurements with the GOM ARAMIS 4M grayscale image correlation system.

Figure 3 shows the prescribed strain path, and Fig. 4 the force path over the three loading steps of the experiments. Firstly (i), the specimen is loaded with a relative marker distance or average technical strain ε_1. The perpendicular axes are in the $\mathbf{e}_2$-direction and controlled in such a way that the force remains at a low contact force. This strain is maintained whereas the viscosity of the material leads to a decrease of the tension forces. Secondly (ii), after a relaxation time, the $\mathbf{e}_2$-direction is tested equivalently. Thirdly (iii), an equibiaxial load is applied to the specimen.

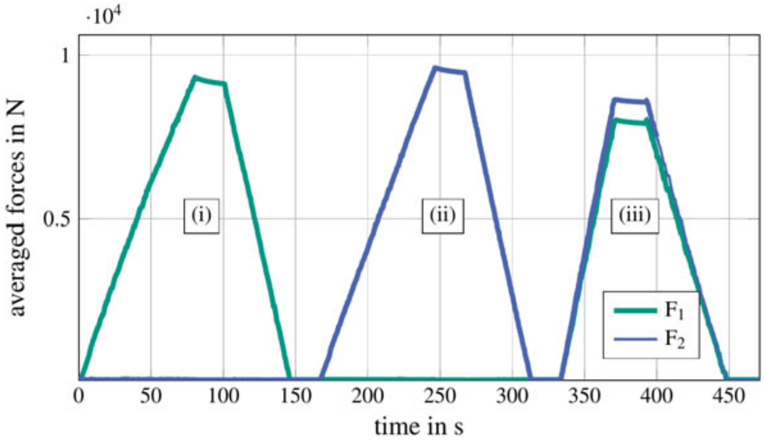

Fig. 4 Experimental procedure: force path

3 Inverse Parameter Identification

In biaxial tensile experiments, the stress and strain fields in the specimen are heterogeneous. Due to this heterogeneity, the material parameters cannot be identified directly, but may be obtained by the solution of an inverse problem. The direct problem is defined by the strain displacement relation, the balance of linear momentum, the boundary conditions and Hooke's law for the constitutive relation between the stress tensor $\boldsymbol{\sigma}$ (with $\boldsymbol{\sigma} = \boldsymbol{\sigma}^{\mathsf{T}}$) and strain tensor $\boldsymbol{\varepsilon}$ with a position-dependent stiffness $\mathbb{C}(\mathbf{x})$

$$\boldsymbol{\sigma} = \mathbb{C}\,(\mathbf{x})\,[\boldsymbol{\varepsilon}]\,. \tag{1}$$

The quasi-static boundary value problem - using these relations - is solved with the FE software ABAQUS.

Furthermore, if the numerically calculated strain field is $\boldsymbol{\varepsilon}^{\text{sim}} \in \mathscr{U}^{\text{sim}}$, whereas $\mathscr{C}$ is the space of stiffness tensors and $\mathscr{U}^{\text{sim}}$ the solution space of the FEM for strains, the inverse problem can be defined by:

$$\text{find}\ \ \mathbb{C}(\mathbf{x}) \in \mathscr{C},\ \ \text{that resolves}\ \ \boldsymbol{\varepsilon}^{\text{sim}}\,(\mathbb{C}(\mathbf{x})) = \boldsymbol{\varepsilon}^{\text{exp}}. \tag{2}$$

In general, the equality of the strain fields $\boldsymbol{\varepsilon}^{\text{exp}}$ and $\boldsymbol{\varepsilon}^{\text{sim}}(\mathbb{C}(\mathbf{x}))$ cannot be assured. This discrepancy derives from measurement uncertainties or modeling errors [13]. A solution of the inverse problem is, however, obtained by minimizing the correlation function $f(\mathbb{C}(\mathbf{x}))$ that describes the error of the experimental and simulated strains. The vector $\underline{r}(\mathbb{C}(\mathbf{x}))$ quantifies the deviation of the strain fields. In $f(\mathbb{C}(\mathbf{x}))$ and $\underline{r}(\mathbb{C}(\mathbf{x}))$, only the measurable in-plane strains are considered

$$\underline{r}(\mathbb{C}(\mathbf{x})) = \begin{pmatrix} \varepsilon^{\text{sim}}_{11,i,j}(\mathbb{C}(\mathbf{x})) - \varepsilon^{\text{exp}}_{11,i,j} \\ \varepsilon^{\text{sim}}_{22,i,j}(\mathbb{C}(\mathbf{x})) - \varepsilon^{\text{exp}}_{22,i,j} \\ \gamma^{\text{sim}}_{12,i,j}(\mathbb{C}(\mathbf{x})) - \gamma^{\text{exp}}_{12,i,j} \\ \vdots \end{pmatrix}_{i=1\ldots K, j=1\ldots N} . \tag{3}$$

Since the meshes of the experimentally measured strain field is discretized much finer than the FEM simulation solution, both strain fields are compared in a comparison mesh. A mapping algorithm interpolates the strain fields on a comparison mesh with the spatial coordinates $\mathbf{x}_i \in \Omega,\ i = 1\ldots K$ and discrete times $t_j \in \mathscr{T},\ j = 1\ldots N$.

Using the strain vector $\underline{\varepsilon} = (\varepsilon_{11}, \varepsilon_{22}, \gamma_{12})^T$, the error function $\underline{f}(\mathbb{C}(\mathbf{x}))$ and the strain deviation $\underline{r}(\mathbb{C}(\mathbf{x}))$, the inverse problem can be rewritten as

$$f(\mathbb{C}(\mathbf{x})) = ||\underline{r}(\mathbb{C}(\mathbf{x}))||_2^2 = \underline{r}(\mathbb{C}(\mathbf{x}))^{\mathsf{T}}\underline{r}(\mathbb{C}(\mathbf{x})) \rightarrow \min_{\mathbb{C}(\mathbf{x}) \in \mathscr{C}} . \tag{4}$$

The results of experiments with the identification of a homogeneous anisotropic stiffness and consideration of viscous effects in SMC and long fiber reinforced thermoplastics can be found in [21]. These results are compared with homogenized material over the whole specimen with the interaction direct derivative (IDD) estimate [22].

3.1 Note on Fiber Orientation Tensors

Despite the fact that the material microstructure and part dimensions do not show scale separation (see Fig. 1), mean field modeling is widely used in literature and within this paper. Here, SMC is considered as a two-phase microstructure that consists of the UPPH matrix phase Ω_{M} and glass fibers Ω_{F}. The matrix is characterized by the isotropic matrix stiffness $\mathbb{C}_{\text{M}}$ and the corresponding volume fraction c_{M}. The fibers are modeled as straight fibers, therefore, fiber curvature is neglected. Additionally, it is assumed that all fibers have the same isotropic stiffness $\mathbb{C}_{\text{F}}$ and aspect ratio a_{v}. The orientation of each fiber is characterized by the unit vector $\mathbf{n}$, as shown in Fig. 5. The total fiber volume fraction is $c_{\text{F}} = 1 - c_{\text{M}}$. The fiber orientation distribution function

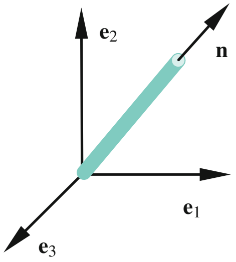

Fig. 5 A single fiber with the orientation **n**

(FODF) specifies the volume fraction $\mathrm{d}v/v$ of fibers with the orientation $\mathbf{n}$ with respect to all fibers (see, i.e. [15, 25]):

$$\frac{\mathrm{d}v}{v}(\mathbf{n}) = f\,(\mathbf{n})\;\mathrm{d}S. \tag{5}$$

Here, $\mathrm{d}S$ is the surface element on the unit sphere $S := \{\mathbf{n} \in \mathbb{R}^3 : \|\mathbf{n}\| = 1\}$. The FODF is symmetric, normalized and non-negative:

$$f(\mathbf{n}) = f(-\mathbf{n}), \quad \int_S f(\mathbf{n})\,\mathrm{d}S = 1, \quad f(\mathbf{n}) \geq 0\ \forall \mathbf{n} \in S. \tag{6}$$

Tucker [1] introduced the fiber orientation tensors (FOT) of second $\mathbf{N}$, fourth $\mathbb{N}_{\langle 4\rangle}$ and n^{th}-order $\mathbb{N}_{\langle n\rangle}$ as follows:

$$\mathbf{N} = \int_S f(\mathbf{n})\mathbf{n}\otimes\mathbf{n}\,\mathrm{d}S, \quad \mathbb{N} = \int_S f(\mathbf{n})\mathbf{n}\otimes\mathbf{n}\otimes\mathbf{n}\otimes\mathbf{n}\,\mathrm{d}S, \quad \mathbb{N}_{\langle n\rangle} \overset{n\geq 4}{=} \int_S f(\mathbf{n})\mathbf{n}^{\otimes n}\,\mathrm{d}S. \tag{7}$$

Kanatani [9] calls these tensors orientation tensors of first kind. Equation (6) implicates that $\mathbf{A}$ is completely symmetric and normalized. Higher order tensors of the same kind provide complete information about lower orders,

$$N_{ij} = N_{ji}, \quad N_{ijkl} = N_{jikl} = N_{klij} = N_{ikjl}, \quad N_{ii} = 1, \quad N_{ijkk} = N_{ij}. \tag{8}$$

Kanatani [9] introduced fabric tensors of the third kind $\mathbb{D}_{\langle n\rangle}$ as follows. Orientation tensors of third kind are deviatoric and fully symmetric [6]. Therefore, the n^{th}-order orientation tensor of third kind has $2n+1$ independent components. These irreducible orientation tensors are traceless and fully symmetric:

$$D_{ii} = 0, \quad D_{ijkl} = D_{jikl} = D_{klij} = D_{ikjl}, \quad D_{iikl} = 0_{kl}. \tag{9}$$

By using the orientation tensors of first kind $\mathbb{N}_{\langle n\rangle}$, the orientation tensor of the third kind can be obtained by

$$\mathbb{D}'_{\langle n\rangle} = \frac{2n+1}{2^n}\binom{2n}{n}\mathbb{N}'_{\langle n\rangle}, \tag{10}$$

where $\binom{n}{k}$ are the binomial coefficient. The index notation for the deviatoric part of a n^{th}-order symmetric tensors can be found in [9]. An approximation of the FODF by orientation tensors of the third kind is given by

$$f(\mathbf{n}) = \frac{1}{4\pi}\left(D_{\langle 0\rangle} + \mathbf{D}'_{\langle 2\rangle}\cdot\mathbf{n}\otimes\mathbf{n} + \mathbb{D}'_{\langle 4\rangle}\cdot\mathbf{n}\otimes\mathbf{n}\otimes\mathbf{n}\otimes\mathbf{n} + \cdots\right). \tag{11}$$

3.2 Implications by the Assumption of the Linearity Between the Stiffness Tensor and the Fiber Orientation Tensor

The harmonic decomposition of the fully anisotropic stiffness tensor [2, 7, 20, 24] yields

$$\underbrace{\mathbb{C}}_{21} = \underbrace{\underbrace{\overbrace{k_1\mathbb{P}_1 + k_2\mathbb{P}_2}^{\mathbb{C}_{\text{iso}}}}_{2} + \underbrace{\overbrace{\mathbf{I}\otimes\mathbf{H}_1^{'} + \mathbf{H}_1^{'}\otimes\mathbf{I}}^{\mathbb{C}_{\text{H21}}}}_{5} + \underbrace{\overbrace{4\mathbb{J}(\mathbf{H}_2^{'})}^{\mathbb{C}_{\text{H22}}}}_{5} + \underbrace{\overbrace{\mathbb{H}^{'}}^{\mathbb{C}_{\text{H4}}}}_{9}}_{21}, \tag{12}$$

where the operator $\mathbb{J}$ is defined as

$$4\mathbb{J}[\mathbf{A}] = \left(A_{im}\delta_{jn} + A_{in}\delta_{jm} + A_{jn}\delta_{im} + A_{jm}\delta_{in}\right)\mathbf{e}_i\otimes\mathbf{e}_j\otimes\mathbf{e}_m\otimes\mathbf{e}_n. \tag{13}$$

The two isotropic projectors are $\mathbb{P}_1 = (\mathbf{I}\otimes\mathbf{I})/3$ and $\mathbb{P}_2 = \mathbb{I}^S - \mathbb{P}_1$, $\mathbb{I}^S$ denotes the fourth-order identity on symmetric second-order tensors. The tensors $\mathbf{H}_1'$, $\mathbf{H}_2'$ and $\mathbb{H}'$ are completely symmetric and traceless. The coefficients h_1 and h_2 assemble the isotropic part $\mathbb{C}_{\text{iso}}$, $\mathbb{C}_{\text{H21}}$ and $\mathbb{C}_{\text{H22}}$ are first and second deviatoric parts, $\mathbb{C}_{\text{CH4}}$ is the harmonic part. The numbers below the quantities, i.e. in Eq. (12), indicate the number of independent components of each tensor. The assumption of linearity between $\mathbb{C}$ and the fiber orientation tensors $\mathbf{D}_{\langle 2\rangle}^{'}$, $\mathbb{D}_{\langle 4\rangle}^{'}$ lead to the following relationship:

$$\mathbb{C} = \underbrace{k_1\mathbb{P}_1 + k_2\mathbb{P}_2}_{2} \quad + \underbrace{\alpha(\mathbf{I}\otimes\mathbf{D}_{\langle 2\rangle}^{'} + \mathbf{D}_{\langle 2\rangle}^{'}\otimes\mathbf{I})}_{1} \quad + \underbrace{\beta\mathbb{J}(\mathbf{D}_{\langle 2\rangle}^{'})}_{1} \quad + \underbrace{\gamma\mathbb{D}_{\langle 4\rangle}^{'}}_{1}. \tag{14}$$

If $\mathbb{D}_{\langle 4\rangle}$ and $\mathbf{D}_{\langle 2\rangle}$ are known, this assumption reduces the number of unknown parameters from 21 (anisotropic elasticity) to five, namely k_1, k_2, α, β and γ. These parameters depend on the matrix and the fiber properties, the volume fraction, the fiber geometry, but not the fiber orientation distribution. Therefore, we assume these parameters as constant within the specimen. The material inhomogeneity derives only from an inhomogeneous fiber orientation distribution which can be obtained, i.e. by micro CT analysis or moldfilling simulations.

3.3 Numerical Treatment of the Optimization

Since k_1 only describes the relation between the stress and the volume change or trace of the strain $\text{tr}(\boldsymbol{\varepsilon}) = \varepsilon_{11} + \varepsilon_{22} + \varepsilon_{33}$ and ε_{33}, and the out of plane strain is not measurable (Eq. (3)), the parameter k_1 is indifferent with the goal function. If all the other parameters are combined into the parameter vector $\underline{p} = (k_2, \alpha, \beta, \gamma)$ the stiffness can be written as

$$\mathbb{C}(\mathbf{x}) = \mathbb{C}(\underline{p}, k_1, \mathbf{D}_{\langle 2\rangle}^{'}(\mathbf{x}), \mathbb{D}_{\langle 4\rangle}^{'}(\mathbf{x})) = \mathbb{C}(\underline{p}). \tag{15}$$

A reformulation of the optimization problem leads to

$$f(\underline{p}) = \underline{r}(\underline{p})^{\mathsf{T}}\underline{r}(\underline{p}) \rightarrow \min_{\underline{p}\in\mathscr{P}} . \tag{16}$$

The given problem is nonlinear and solved numerically. To identify the unknown parameters $\underline{p}$, a Gauss-Newton optimization procedure is used [11]. This procedure is based on the classical Newton's optimization method

$$\underline{p}^{k+1} = \underline{p}^{k} - \left[\underline{\underline{H}}(\underline{p}^{k})\right]^{-1} \nabla f(\underline{p}^{k}). \tag{17}$$

The gradient of Eq. 16 can be written as

$$\nabla f(\underline{p}) = 2\underline{\underline{J}}(\underline{p})^{\mathsf{T}}\underline{r}(\underline{p}), \text{ with the Jacobian} \qquad J_{ij}(\underline{p}) = \frac{\partial r_i(\underline{p})}{\partial p_j}. \tag{18}$$

The Gauss-Newton-Approximation of the Hessian can than be expressed as

$$H\,\underline{\underline{H}}(\underline{p}) = 2\underline{\underline{J}}(\underline{p})^{\mathsf{T}}\underline{\underline{J}}(\underline{p}) + 2\underline{\underline{G}}(\underline{p}), \text{ with} \qquad G_{ij}(\underline{p}) = \sum_{k=1}^{N\cdot K} \frac{\partial^2 r_k(\underline{p})}{\partial p_i \partial p_j} r_k(\underline{p}). \tag{19}$$

Negligence of $\underline{\underline{G}}(\underline{p})$ yields the Gauss-Newton optimization method

$$\underline{p}^{k+1} = \underline{p}^{k} - \left[\underline{\underline{J}}(\underline{p}^{k})^{\mathsf{T}}\underline{\underline{J}}(\underline{p}^{k})\right]^{-1} \underline{\underline{J}}(\underline{p}^{k})^{\mathsf{T}}\underline{r}(\underline{p}^{k}). \tag{20}$$

The Jacobian required for the Gauss-Newton optimization method is assembled by partial derivatives of the strain field with respect to the parameter vector $\underline{p}$. These entries are estimated by the constitutive equation $\boldsymbol{\sigma} = \mathbb{C}(\mathbf{x})[\boldsymbol{\varepsilon}]$ while assuming the stress field is independent of $\underline{p}$

$$\frac{\partial \boldsymbol{\varepsilon}}{\partial p_i} = -\mathbb{C}^{-1}\frac{\partial \mathbb{C}}{\partial p_i}[\boldsymbol{\varepsilon}]. \tag{21}$$

This assumption was successfully used in the identifications of homogeneous parameters and showed significant increase performance [11]. In the context of this work, the comparison to a finite difference scheme of $\partial\boldsymbol{\varepsilon}/\partial p_i$ showed a difference in the converged material properties of up to 10%. Therefore, the solution with the analytic derivative (Eq. 21) was used as a starting value for the optimization with the finite difference scheme, which had a significant higher computational cost because in each iteration, solutions for small fluctuations of p_i had to be calculated. As mentioned in above, due to the lack of reliable measurement techniques to measure the out of plane strain of the specimen, the parameter k_1 is not identifiable. Its value is obtained through a Mori–Tanaka [14] homogenization in the following way $k_1 = \frac{1}{3}\mathbb{P}_1 \cdot \mathbb{C}_{\mathrm{MT}}$.

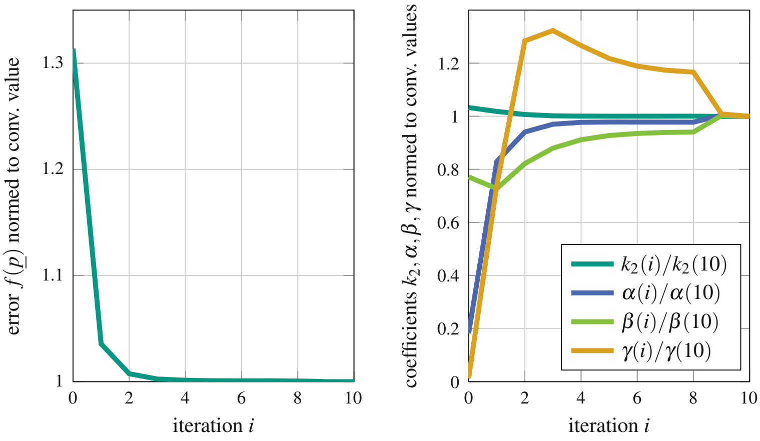

Fig. 6 Reduction of error in the optimization process (left) and evolution of coefficients (right), iterations 1–8 obtained by Gauss-Newton procedure with analytic Jacobian (Eq. 21), iterations 9–10 obtained by finite difference scheme

Gradient based optimization algorithms are, generally, highly sensitive to a deviation of start values. Hartmann and Gilbert [8] showed that for the case of homogeneous isotropic elasticity (surface strain and force measurement including some measuring uncertainties), the material parameters can be identified at sufficient precision. However, to minimize the risk of convergence problems, the start values to the Gauss-Newton method are obtained in the following way.

An inverse parameter identification is used to identify the homogeneous stiffness of the specimen. In the following step, the heterogeneous stiffness tensor (Sect. 3.2) is fitted to the homogeneous stiffness tensor using a least-square approach and a genetic optimization algorithm. The obtained values for k_2, α, β, γ are now used as starting values.

Figure 6 (left) shows the convergence behavior of the described optimization procedure. In average, the Gauss-Newton algorithm converges in less than 10 iterations, whereas convergence is achieved when the relative change of every parameter is below 1%. The plot in Fig. 6 left shows the reduction of the error function $f(\underline{p})$ over the Gauss-Newton iterations i. An error reduction of about 25% was obtained. Figure 6 (right) shows the evolution of the four parameters k_2, α, β and γ normed to its converged values.

4 Results and Discussion

Figures 7 and 8 depict a comparison between measured and simulated strain fields for two different biaxial tensile specimens for the load case of equibiaxial tension. For Fig. 7, the fiber volume fraction of the specimen is 22%, and for Fig. 8 it is

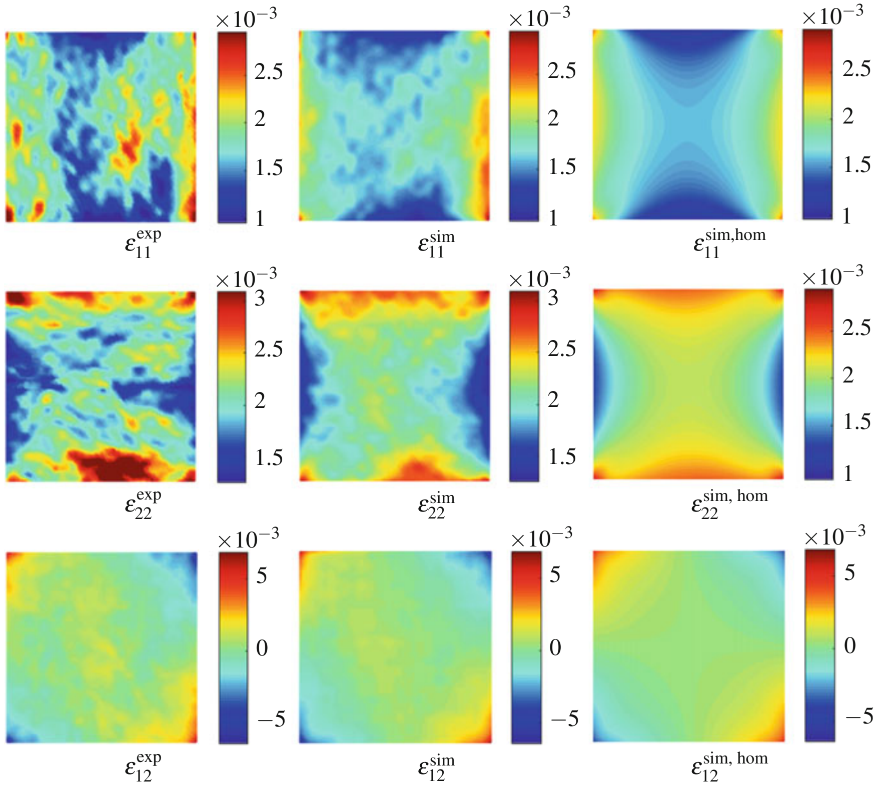

Fig. 7 Comparisons of the strain fields for the load case of equibiaxial tension. The fiber volume fraction of the specimen is 22%. Left column: measured strain field by digital image correlation. Middle column: fitted under the assumption of linearity between the fiber orientation tensor and stiffness tensor. Right: fitted with a homogeneous stiffness over the specimen

29%. The left columns of both figures show the measured strain field by digital image correlation. The middle column shows the strain fields obtained by finite element simulations with the consideration of a heterogeneous material behavior, see Sects. 3.2 and 3.3. The right column shows finite element results for a homogeneous stiffness. This stiffness was identified in a state-of-the-art standard procedure [22], that is similar to the heterogeneous one mentioned above.

Measurement errors at low strains such as 0.2–0.5%, and the evaluation of only five specimens (two are only shown within this paper) requires to exercise caution to avoid over-interpretation of the results. Some to the authors reliable findings are, however, collected in the following.

First, the measured and homogeneously simulated strain fields show significant fluctuations which additionally motivates an identification of inhomogeneous material properties.

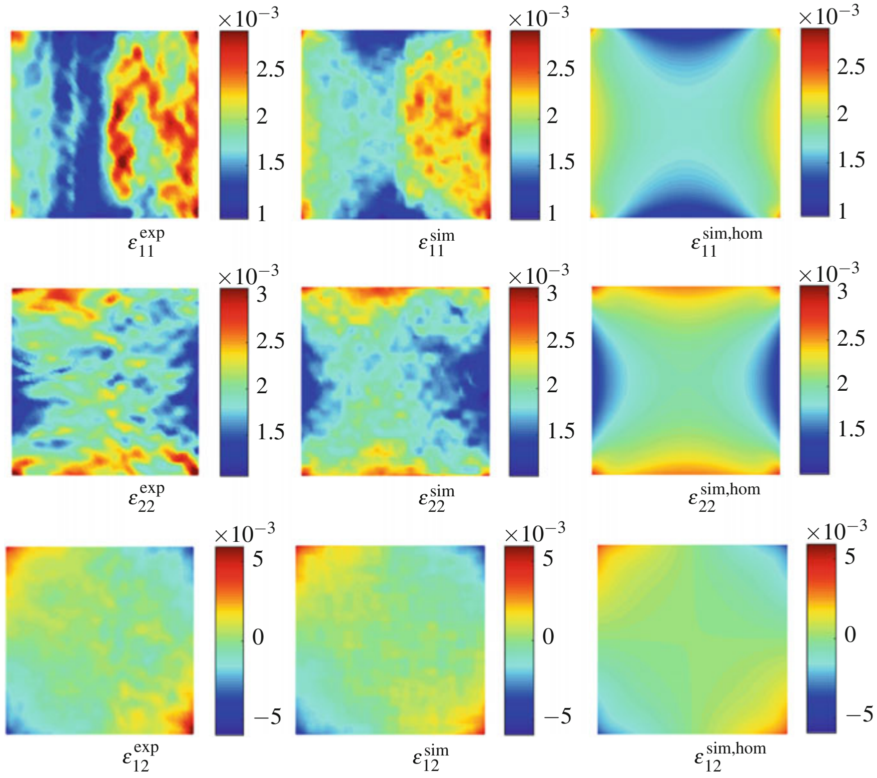

Fig. 8 Comparisons of the strain fields for the load case of equibiaxial tension. The fiber volume fraction of the specimen is 29%. Left column: measured strain field by digital image correlation. Middle column: fitted under the assumption of linearity between the fiber orientation tensor and stiffness tensor. Right: fitted with a homogeneous stiffness over the specimen

The new approach (middle column) covers tendencies of these fluctuations. The normal strains in Figs. 7 and 8 seem to reproduce the measured strain field not only qualitatively but also quantitatively. A slice of the CT scan of the specimen in Fig. 8 is depicted in Fig. 1. The CT scan shows a typical SMC fiber orientation on the left two third of the specimen, whereas on the right side of the specimen, the moldflow induced an increased amount of fiber bending. The consideration of the measured strains in the $\mathbf{e}_1$-direction shows an increase on the right side. This suggests a lower stiffness in this area which may derive from the microstructure described above. Similarly, on the lower left side of the image, the fibers seem to be orientated dominantly horizontal, therefore reduction of the stiffness in the vertical direction could explain the higher strains.

5 Conclusions

In contrast to common testing procedures, we introduced a method to characterize the microstructure based heterogeneity of SMC in biaxial tensile tests. The micromechanically-motivated assumption of linearity between stiffness and fiber orientation distribution reduced the problem dimension to four identifiable parameters, even for a highly heterogeneous fiber orientation distribution. Volumetric compression is not measurable. However, all other components of the stiffness tensor were obtained in a single biaxial tensile specimen (plane stress) in one experiment.

Compared to traditional homogenization schemes, the introduced approach requires one measurement per fiber volume fraction and aspect ratio to predict the stiffness for any fiber orientation distribution. New measurements are required for a different fiber volume fraction or fiber aspect ratio. Homogenization approaches on the other hand do not require tests of the composite, however the elastic properties of the phases are needed as an input.

Acknowledgements The micro CT scans of the SMC material were performed by Pascal Pinter from the Institute of Applied Materials (KIT). The plates were manufactured by David Bücheler and Martin Hohberg at the Fraunhofer Institute of Chemical Technology in Pfinztal Germany. We would like to thank these partners for the great cooperation.

The research documented in this manuscript has been funded by the German Research Foundation (DFG) within the International Research Training Group Integrated engineering of continuous-discontinuous long fiber reinforced polymer structures (GRK 2078). The support by the German Research Foundation (DFG) is gratefully acknowledged.

References

1. Advani, S.G., Tucker III, C.L.: The use of tensors to describe and predict fiber orientation in short fiber composites. J. Rheol. **31**(8), 751–784 (1987). https://doi.org/10.1122/1.549945
2. Böhlke, T., Jöchen, K., Piat, R., Langhoff, T.A., Tsukrov, I.: Elastic properties of pyrolytic carbon with axisymmetric textures. Tech. Mech. **30**(4), 343–353 (2010)
3. Buck, F., Brylka, B., Müller, V., Müller, T., Weidenmann, K.A., Hrymak, A.N., Henning, F., Böhlke, T.: Two-scale structural mechanical modeling of long fiber reinforced thermoplastics. Compos. Sci. Technol. **117**, 159–167 (2015). https://doi.org/10.1016/j.compscitech.2015.05.020
4. Chamekh, A., Bel Hadj Salah, H., Hambli, R.: Inverse technique identification of material parameters using finite element and neural network computation. Int. J. Adv. Manuf. Technol. **44**(1–2), 173–179 (2009). https://doi.org/10.1007/s00170-008-1809-6
5. Cooreman, S., Lecompte, D., Sol, H., Vantomme, J., Debruyne, D.: Identification of mechanical material behavior through inverse modeling and DIC. Exp. Mech. **48**(4), 421–433 (2007). https://doi.org/10.1007/s11340-007-9094-0
6. Ehrentraut, H., Muschik, W.: On symmetric irreducible tensors in d dimensions introduction and motivation. Int. J. Phys. Eng. Sci. 149–159 (1998). https://doi.org/10.1007/s007770050048
7. Forte, S., Vianello, M.: Symmetry classes for elasticity tensors. J. Elast. **43**(2), 81–108 (1996). https://doi.org/10.1007/BF00042505
8. Hartmann, S., Gilbert, R.R.: Identifiability of material parameters in solid mechanics. Arch. Appl. Mech. 1–24 (2017). https://doi.org/10.1007/s00419-017-1259-4

9. Kanatani, K.I.: Distribution of directional data and fabric tensors. Int. J. Eng. Sci. **22**(2), 149–164 (1984). https://doi.org/10.1016/0020-7225(84)90090-9
10. Katayama, T., Shinohara, M., Hakotani, M., Kitade, A., Kono, D.: Development of CAE for predicting stiffness of SMC structure estimation of young's modulus in rib part. J. Mater. Process. Technol. **119**(13), 237–243 (2001). https://doi.org/10.1016/S0924-0136(01)00958-X
11. Lecompte, D., Smits, A., Sol, H., Vantomme, J., Van Hemelrijck, D.: Mixed numerical-experimental technique for orthotropic parameter identification using biaxial tensile tests on cruciform specimens. Int. J. Solids Struct. **44**(5), 1643–1656 (2007). https://doi.org/10.1016/j.ijsolstr.2006.06.050
12. Mahnken, R., Stein, E.: A unified approach for parameter identification of inelastic material models in the frame of the finite element method. Comput. Methods Appl. Mech. Eng. **136**(3–4), 225–258 (1996a). https://doi.org/10.1016/0045-7825(96)00991-7
13. Mahnken, R., Stein, E.: Parameter identification for viscoplastic models based on analytical derivatives of a least-squares functional and stability investigations. Int. J. Plast. **12**(4), 451–479 (1996b)
14. Mori, T., Tanaka, K.: Averate stress in matrix and average elastic energy of materials with misfitting inclusions. Acta Metall. **21**, 571–574 (1973)
15. Müller, V., Böhlke, T.: Prediction of effective elastic properties of fiber reinforced composites using fiber orientation tensors. Compos. Sci. Technol. **130**, 36–45 (2016). https://doi.org/10.1016/j.compscitech.2016.04.009
16. Müller, V., Kabel, M., Andrä, H., Böhlke, T.: Homogenization of linear elastic properties of short-fiber reinforced composites a comparison of mean field and voxel-based methods. Int. J. Solids Struct. **67**, 56–70 (2015). https://doi.org/10.1016/j.ijsolstr.2015.02.030
17. Osswald, T.A., Tucker, C.L.: Compression mold filling simulation of non-planar parts. Int. Polym. Process. **5**(2), 79–87 (1989). https://doi.org/10.3139/217.900079
18. Pan, W., Boyle J., Ramlan, M., Dun, C., Ismail, M., Hakoda, K.: Material plastic properties characterization using a generic algorithm and finite element method modelling of the plane-strain small punch test. STP Conference, Ostrava, Czech Republic (2010)
19. Ponthot, J.P., Kleinermann, J.P.: A cascade optimization methodology for automatic parameter identification and shape/process optimization in metal forming simulation. Comput. Methods Appl. Mech. Eng. **195**(41–43), 5472–5508 (2006). https://doi.org/10.1016/j.cma.2005.11.012
20. Rychlewski, J.: A qualitative approach to Hooke's tensors. Part I. Arch. Mech. **52**(4–5), 737–759 (2000)
21. Schemmann, M., Brylka, B., Gajek, S., Böhlke, T.: Parameter identification by inverse modelling of biaxial tensile tests for discontinous fiber reinforced polymers. Proc. Appl. Math. Mech. **15**(1), 355–356 (2015a). https://doi.org/10.1002/pamm.201510168
22. Schemmann, M., Brylka, B., Müller, V., Kehrer, M.L., Böhlke, T.: Mean field homogenization of discontinous fiber reinforced polymers and parameter identification of biaxial tensile tests through inverse modeling. In: Proceedings of 20th International Conference on Composite Materials, vol. 20 (2015b)
23. Schnur, D., Zabaras, N.: An inverse method for determining elastic material properties and a material interface. **33**, 2039–2057 (1992)
24. Schouten, J.A.: Der Ricci-Kalkül, Grundlehren der mathematischen Wissenschaften, vol. 10. Springer, Berlin, Heidelberg (1924). https://doi.org/10.1007/978-3-662-06545-7
25. Zheng, Q.S., Du, D.X.: An explicit and universally applicable estimate for the effective properties of multiphase composites which accounts for inclusion distribution. J. Mech. Phys. Solids **49**(11), 2765–2788 (2001). https://doi.org/10.1016/S0022-5096(01)00078-3

Configurational Forces in a Phase Field Model for Dynamic Brittle Fracture

Alexander Schlüter, Charlotte Kuhn and Ralf Müller

Abstract In this work, the concept of configurational forces is proposed to enhance the post-processing of phase field simulations for dynamic brittle fracture. A local configurational force balance is derived by taking the gradient of the Lagrangian density of the phase field fracture problem. It is shown that the total configurational forces computed for a crack tip control volume are closely related to the Griffith criterion of classical fracture mechanics. Finally, the evaluation of the configurational within the finite element framework is demonstrated by two examples.

1 Introduction

The numerical analysis of dynamic brittle fracture by so-called phase field models has gained attention in recent years, see e.g. Hofacker and Miehe [12], Borden et. al. [3], Steinke et al. [30], Li et al. [17] and Schlüter et al. [28, 29]. In phase field models for fracture, a scalar order parameter, the phase field, represents cracks in a continuous manner, i.e. there is a smooth transition zone in which the phase field varies from a value indicating undamaged material to another value that indicates completely broken material. Hence, the distribution of the phase field variable can be seen as a regularized approximation of the crack. Crack growth is governed by two coupled partial differential equations: the equation of motion and the phase field evolution equation. These are the Euler–Lagrange equations of Hamilton's principle

---

A. Schlüter (✉)
Computational Mechanics and Institute of Applied Mechanics,
University of Kaiserslautern, P.O.Box 3049, 67653 Kaiserslautern, Germany
e-mail: aschluet@rhrk.uni-kl.de

C. Kuhn
Computational Mechanics, University of Kaiserslautern, Kaiserslautern, Germany
e-mail: chakuhn@rhrk.uni-kl.de

R. Müller
Institute of Applied Mechanics, University of Kaiserslautern, Kaiserslautern, Germany
e-mail: ram@rhrk.uni-kl.de

© Springer International Publishing AG 2018
H. Altenbach et al. (eds.), *Advances in Mechanics of Materials and Structural Analysis*, Advanced Structured Materials 80,
https://doi.org/10.1007/978-3-319-70563-7_16

if, following Griffith's [9] idea, the fracture energy is interpreted as a part of the potential energy. Phase field models for dynamic brittle fracture have been able to predict fracture phenomena like crack branching and intersonic fracture in good agreement with experiments and theoretical predictions, e.g. in Schlüter et al. [28], Borden et al. [3] and Li et al. [17]. However, often it is difficult to gain deeper insight into the computational results and some features of the computational results remain obscure.

The development of the concept of configurational forces on the other hand started with Eshelby's pioneering work [7] and has since been extended and applied to various fields, see e.g. the textbooks of Gurtin [10], Kienzler and Herrmann [13] and Maugin [18, 19]. Configurational forces represent the change of potential energy of a body with respect to certain quantities that characterize the material configuration, i.e. the size and shape of cracks or the position of an inclusion. This energetic point of view of material changes links the concept of configurational forces to phase field models for fracture. Indeed, configurational forces in a phase field model for fracture have been studied in Kuhn and Müller [15], Kuhn [14] and Hakim and Karma [11] for the quasi-static case where inertia terms are neglected. In this case, the configurational force components acting on a crack tip are related to well-known quantities of fracture mechanics such as the path-independent $\mathscr{J}$-integral, see Rice [27], and the fracture resistance. In contrast to numerical strategies that rely on the configurational forces in order to model crack propagation such as in Miehe and Gürses [21] and Özenç et al. [25], the evaluation of the configurational forces is not a necessity in phase field fracture models. In the context of phase field fracture models, configurational forces should rather be understood as a post-processing tool that enhances the understanding of the simulations.

In this work, the idea to consider configurational forces for a phase field fracture model from Kuhn and Müller [15] is extended to the dynamic case. After a brief introduction of the employed phase field model for dynamic fracture, a configurational force balance is derived by considering the gradient of the Lagrangian of the fracture problem. This balance describes the energetic changes associated with a translation of a crack tip, i.e. crack growth, and is used to highlight the relation of the phase field model to the Griffith criterion of classical fracture mechanics. Lastly, two dynamic fracture problems are solved numerically. The analysis of the results relies on the computed configurational forces and reveals interesting features of the simulations.

2 A Phase Field Model for Dynamic Brittle Fracture

We consider a homogeneous body $\Omega \subset \mathbb{R}^2$ with external boundary $\partial\Omega$ that consists of linear elastic material with Lamé parameters λ and μ as well as mass density ρ. The speed of surface waves in this elastic medium, the Rayleigh wave speed, can be approximated by

$$c_r \approx \frac{0.87 + 1.12\nu}{1+\nu}\sqrt{\frac{\mu}{\rho}}, \tag{1}$$

see Rahman and Michelitsch [26], where

$$\nu = 2\frac{\lambda}{\lambda+\mu} \tag{2}$$

is the Poisson's ratio. The motion of the body is described in terms of the displacement field $\mathbf{u}(\mathbf{x}, t) = u_1\mathbf{e}_1 + u_2\mathbf{e}_1$, where $\mathbf{e}_1$ and $\mathbf{e}_2$ are the unit vectors in x_1- and x_2-direction of a cartesian coordinate system. Physical internal forces are represented by the Cauchy stress tensor $\sigma(\mathbf{x}, t)$. The fields have to satisfy Dirichlet boundary conditions

$$\mathbf{u}(\mathbf{x}, t) \;=\; \mathbf{u}^*(t) \tag{3}$$

on $\partial\Omega_{\mathbf{u}}$ and traction boundary conditions

$$\sigma\mathbf{n} \;=\; \mathbf{t}^*(t) \tag{4}$$

on $\partial\Omega_{\mathbf{t}}$, where $\mathbf{n}$ is the outward normal vector on the boundary $\partial\Omega = \partial\Omega_{\mathbf{u}} \cup \partial\Omega_{\mathbf{t}}$. In addition, initial conditions

$$\mathbf{u}(\mathbf{x}, t_0) = \mathbf{u}_0(\mathbf{x}) \tag{5}$$

and

$$\dot{\mathbf{u}}(\mathbf{x}, t_0) = \mathbf{v}_0(\mathbf{x}), \tag{6}$$

where $\dot{(*)} = \frac{\partial(*)}{\partial t}$ indicates the material time derivative, have to be provided. The linearized strain tensor

$$\varepsilon = \frac{1}{2}\left(\mathrm{grad}\mathbf{u} + (\mathrm{grad}\mathbf{u})^T\right) \tag{7}$$

serves as a strain measure. Cracks are denoted as Γ, see Fig. 1a, and are approximated by an order parameter $s(\mathbf{x}, t) \in [0, 1]$ which varies continuously from $s = 1$ in undamaged material to $s = 0$ in fully broken material, as displayed in Fig. 1b. To be precise, the cracks Γ are replaced by the zero set of s and the surface measure of Γ is approximated by the crack surface density per unit volume which is formulated in terms of the order parameter

$$\gamma = \frac{(1-s)^2}{4l} + l|\nabla s|^2 \tag{8}$$

as proposed in Bourdin [4]. The integral

$$\int_{\Omega} \gamma \,\mathrm{d}V \tag{9}$$

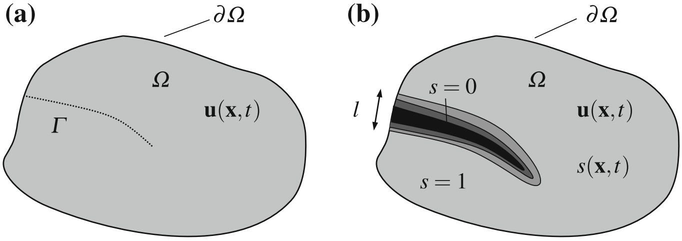

Fig. 1 **a** Fractured body with internal discontinuity (sharp crack) Γ **b** and smooth representation of the crack by means of a phase field $s(\mathbf{x}, t)$

yields the surface measure of the crack set Γ. Initial cracks in the material are modelled by specifying initial conditions

$$s(\mathbf{x}, t_0) = 0 \tag{10}$$

for the order parameter. Following Griffith's idea, the crack Γ is associated with a fracture energy that is required to create the crack surface. The phase field is used to approximate this fracture energy in a regularized manner, i.e.

$$\int_{\Gamma} \mathscr{G}_c \, \mathrm{d}A \approx \int_{\Omega} \psi^s \mathrm{d}V = E^s, \tag{11}$$

where

$$\psi^s = \mathscr{G}_c \gamma \tag{12}$$

is the fracture energy density per unit volume. The parameter $\mathscr{G}_c$ denotes the fracture resistance which is assumed to be a constant material parameter. The length-scale parameter l controls the width of the phase field approximated crack, i.e. an increase of l causes the width of the transition zone between broken and unbroken material to increase as well. It can be shown that the volume integral on the right-hand side of approximation (11) converges to the surface integral on the left-hand side if $l \to 0$, as illustrated in Miehe et al. [23]. In order to model the degradation of stiffness in broken material, the phase field s is linked to the elastic energy of the body, i.e.

$$E^e = \int_{\Omega} \psi^e(\varepsilon, s) \; \mathrm{d}\Omega. \tag{13}$$

where the strain energy density is given by

$$\psi^e(\varepsilon, s) = \psi^e_-(\varepsilon) + g(s)\psi^e_+(\varepsilon)\,. \tag{14}$$

The strain energy density is decomposed in a crack driving part ψ_+^e that is affected by a degradation function $g(s)$ and a part that is associated with compressive strain states ψ_-^e. In the literature, there are several propositions to implement this decomposition, which all aim to prevent unphysical fracture behaviour in compressive load states. The model of Miehe et al. [22] proposes a split based on a spectral decomposition of ε whereas Strobl and Seelig [31] actually take the orientation of the phase field crack into account. The approach used in this work follows the publication of Amor et al. [1] and is based on a volumetric-deviatoric decomposition of the strain tensor ε. The degradation function $g(s)$ models the loss of stiffness in broken material by reducing the strain energy accordingly, i.e. it has to satisfy $g(1) = 1$ and $g(0) = 0$. The compressive strain energy is not affected by $g(s)$ which models the impenetrability of cracks during crack closure, i.e. no degradation of the compressive stress, see (16). In this work, the degradation function is chosen to be

$$g(s) = a(s^3 - s^2) + 3s^2 - 2s^3, \quad \text{where} \quad a = 0.1 \tag{15}$$

as proposed in Borden [2]. An additional consequence of leaving ψ_-^e unaffected by s is that crack growth is not driven by compressive load states, which becomes apparent in (23). The stress is

$$\sigma = \frac{\partial \psi^e}{\partial \varepsilon} = \frac{\partial \psi_-^e}{\partial \varepsilon} + g(s)\frac{\partial \psi_+^e}{\partial \varepsilon}. \tag{16}$$

The kinetic energy of the body is assumed not to be affected by the phase field, i.e.

$$K(\dot{\mathbf{u}}) = \int_\Omega k \,\mathrm{d}V, \quad \text{where} \quad k = \frac{1}{2}\rho\dot{\mathbf{u}} \cdot \dot{\mathbf{u}}. \tag{17}$$

Eventually, the dynamic fracture problem can be stated using Hamilton's principle

$$\delta \int_{t_1}^{t_2} L \,\mathrm{d}t = 0, \tag{18}$$

for arbitrary times $t_1 < t_2$. The Lagrangian is given by

$$L = \int_\Omega \mathscr{L} \,\mathrm{d}V + P, \tag{19}$$

where

$$P = \int_{\partial\Omega_\mathbf{t}} \mathbf{t}^* \cdot \mathbf{u} \,\mathrm{d}A \tag{20}$$

is the work of external forces - neglecting volume forces - acting on the boundary $\partial\Omega_\mathbf{t}$ and

$$\mathscr{L}\left(\dot{\mathbf{u}}, \varepsilon, s, \nabla s\right) = k(\dot{\mathbf{u}}) - \psi^e\left(\varepsilon, s\right) - \psi^s\left(s, \nabla s\right) \tag{21}$$

is the Lagrangian density per unit volume. The Euler–Lagrange equations following from (18) are the equation of motion

$$\rho \ddot{\mathbf{u}} - \operatorname{div} \sigma = \mathbf{0}, \tag{22}$$

and the phase field equation

$$\frac{\partial \psi}{\partial s} - \operatorname{div}\left(\frac{\partial \psi}{\partial \nabla s}\right) = 0 \quad \Leftrightarrow \quad g'(s)\psi^e_+ - \mathscr{G}_c\left[2l\Delta s + \frac{1-s}{2l}\right] = 0, \tag{23}$$

with

$$\psi = \psi^e + \psi^s, \tag{24}$$

as well as the traction boundary conditions

$$\sigma \mathbf{n} = \mathbf{t}^* \quad \text{on } \partial\Omega_t \tag{25}$$

and the Neumann boundary conditions for the phase field

$$\nabla s \cdot \mathbf{n} = 0 \quad \text{on } \partial\Omega. \tag{26}$$

The Dirichlet boundary conditions for the displacement field have to be specified as shown in (3) but do not follow directly from Hamilton's principle. An additional constraint on the phase field s is necessary to impose the irreversibility of fracture. This is achieved by defining homogeneous Dirichlet boundary conditions

$$s(\mathbf{x}, t > t^*_{\mathbf{x}}) = 0 \quad \text{if} \quad s(\mathbf{x}, t^*_{\mathbf{x}}) = 0 \tag{27}$$

on the crack field. Herein, $t^*_{\mathbf{x}}$ is the time when the crack field becomes zero at the location $\mathbf{x}$ for the first time. The extension (27) allows for partial reversibility of the phase field because s is interpreted as an indicator field for cracks rather than a damage variable. Since only the zero set of s is interpreted as the crack, the extension (27) prevents unphysical crack healing. Details on the implementation in a finite element scheme can be found in Kuhn [14] whereas details on the interpretation of the phase field as a damage-like variable and the corresponding irreversibility constraint can be found in Miehe et al. [23].

3 Configurational Force Balance for a Phase Field Model for Dynamic Brittle Fracture

Crack growth corresponds to a translation of the crack tip with respect to its coordinates $\mathbf{z}$ in the reference configuration. As explained in Kienzler and Herrmann [13], a configurational force balance law that captures the energy change due to a translation of the considered defect, in our case the crack tip, can be found by taking the gradient of the Lagrangian density. In the phase field model, the evolution of the phase field is governed by the Lagrangian (19) but also by the irreversibility constraint (27). Thus, a configurational force balance law derived by taking the gradient of the Lagrangian density without incorporating the irreversibility constraint does only describe the fracture process as long as the load is high enough to sustain the cracks and the irreversibility constraint does not play a role. We still follow the gradient of the Lagrangian approach to derive the configurational force balance but discuss the neglected irreversibility condition as part of the interpretation of the computational results in Sect. 5. In order to determine the energetic driving force on a particular crack tip, the Lagrangian density $\mathscr{L}$ is considered to additionally be a function of the position of that crack tip $\mathbf{z}$ and the gradient

$$-\nabla\mathscr{L}\left(\dot{\mathbf{u}}, \varepsilon, s, \nabla s, \mathbf{z}\right) = \left(\frac{\partial\psi}{\partial s}s_{,k} + \frac{\partial\psi}{\partial s_{,i}}s_{,ik} + \frac{\partial\psi}{\partial\varepsilon_{ij}}\varepsilon_{ij,k} - \frac{\partial k}{\partial\dot{u}_i}\dot{u}_{i,k} - \frac{\partial\mathscr{L}}{\partial z_i}z_{i,k}\right)\mathbf{e}_k \tag{28}$$

is computed. Employing Einstein's summation convention and making use of the identities

$$\frac{\partial\psi}{\partial s_{,i}}s_{,ik} = \left(s_{,k}\frac{\partial\psi}{\partial s_{,i}}\right)_{,i} - \left(\frac{\partial\psi}{\partial s_{,i}}\right)_{,i}s_{,k} \tag{29}$$

and

$$\frac{\partial\psi}{\partial\varepsilon_{ij}}\varepsilon_{ij,k} = \left(u_{j,k}\sigma_{ji}\right)_{,i} - u_{i,k}\sigma_{ij,j} \tag{30}$$

the components of Eq. (28) can be rewritten as

$$\begin{aligned} -\mathscr{L}_{,k} = & \frac{\partial\psi}{\partial s}s_{,k} + \left(s_{,k}\frac{\partial\psi}{\partial s_{,i}}\right)_{,i} - \left(\frac{\partial\psi}{\partial s_{,i}}\right)_{,i}s_{,k} \\ & + \left(u_{j,k}\sigma_{ji}\right)_{,i} - u_{i,k}\sigma_{ij,j} - \frac{\partial k}{\partial\dot{u}_i}\dot{u}_{i,k} - \frac{\partial\mathscr{L}}{\partial z_i}z_{i,k} \end{aligned} \tag{31}$$

By means of the equation of motion (22), the evolution Eq. (23) and the definition of the linear momentum

$$\mathbf{p} = \frac{\partial k}{\partial\dot{u}_k}\mathbf{e}_k = \rho\dot{\mathbf{u}} \tag{32}$$

we obtain

$$-\nabla\mathscr{L} = \left(\left(s_{,k}\frac{\partial\psi}{\partial s_{,i}} + u_{j,k}\sigma_{ji}\right)_{,i} - u_{i,k}\dot{p}_i - p_i\dot{u}_{i,k} - \frac{\partial\mathscr{L}}{\partial z_i}z_{i,k}\right)\mathbf{e}_k \tag{33}$$

which with

$$-\nabla\mathscr{L} = -(\mathscr{L}\delta_{ki})_{,i}\,\mathbf{e}_k, \qquad \delta_{ij} = \begin{cases} 1 \text{ if } i = j \\ 0 \text{ else} \end{cases} \tag{34}$$

can be recast in the form

$$\mathbf{g} = \mathrm{div}\Sigma - \dot{\mathfrak{p}}. \tag{35}$$

Here, the configurational stress tensor

$$\Sigma = \Sigma^e + \Sigma^s \tag{36}$$

consisting of the dynamic Eshelby stress tensor or elastic part of the configurational stress tensor

$$\Sigma^e = \big(\big(\psi^e - k\big)\delta_{ij} - u_{k,i}\sigma_{kj}\big)\,\mathbf{e}_i \otimes \mathbf{e}_j, \tag{37}$$

and the cohesive configurational stress tensor

$$\Sigma^s = \left(\psi^s\delta_{ij} - s_{,i}\frac{\partial\psi}{\partial s_{,j}}\right)\mathbf{e}_i \otimes \mathbf{e}_j \tag{38}$$

has been introduced. The symbol "⊗" denotes the dyadic product. The expression

$$\mathfrak{p} = -u_{i,k}p_i\,\mathbf{e}_k = -\,(\mathrm{grad}\mathbf{u})^T\,\mathbf{p} \tag{39}$$

denotes the so-called pseudo-momentum, see e.g. Maugin and Trimarco [20], whereas the quantity

$$\mathbf{g} = -z_{i,k}\frac{\partial\mathscr{L}}{\partial z_i}\mathbf{e}_k \tag{40}$$

is the local contribution of the state $[\dot{\mathbf{u}}(\mathbf{x},t), \varepsilon(\mathbf{x},t), s(\mathbf{x},t), \nabla s(\mathbf{x},t)]$ at $\mathbf{x}$ to the energetic driving force that acts on the crack tip $\mathbf{z}$. Alternatively, $\mathbf{g}$ might be interpreted as a measure of the change of $\mathscr{L}$ at $\mathbf{x}$ due to an infinitesimally small translation of the crack tip $\mathbf{z}$. By integration over a subdomain R of Ω, a global form of the configurational force balance

$$\begin{gathered} \underbrace{\int_R \mathbf{g}\,\mathrm{d}V}_{\mathbf{G}_R} = \underbrace{\int_R \mathrm{div}\Sigma^e\,\mathrm{d}V}_{\mathbf{G}^e_R} + \underbrace{\int_R \mathrm{div}\Sigma^s\,\mathrm{d}V}_{\mathbf{G}^s_R} - \underbrace{\int_R \dot{\mathfrak{p}}\,\mathrm{d}V}_{-\mathfrak{P}_R}, \\ \mathbf{G}_R = \mathbf{G}^e_R + \mathbf{G}^s_R + \mathfrak{P}_R \end{gathered} \tag{41}$$

is obtained. In contrast to $\mathbf{g}$, the quantity $\mathbf{G}_R$ represents the resulting configurational force on $\mathbf{z}$ of the states $[\dot{\mathbf{u}}(\mathbf{x},t), \varepsilon(\mathbf{x},t), s(\mathbf{x},t), \nabla s(\mathbf{x},t)]$ of all $\mathbf{x}$ inside R.

4 Discussion of the Configurational Force Balance

In this section, the configurational force balances that were established in the previous section are discussed. In particular, their role as a means to highlight the connection between phase models for dynamic brittle fracture and Griffith's description of brittle fracture in the framework of dynamic linear elastic fracture mechanics (LEFM) is explained.

To this end, we consider a LEFM model of the crack tip and the region surrounding it, see Fig. 2a as well as the corresponding phase field representation, see Fig. 2b. In order to evaluate the relevant energetic driving forces on a particular crack tip, suitable control volumes should at least contain all particles that constitute the near tip region and no other crack tip. Hence, a disc with radius δ that is centered around the crack tip $\mathbf{z}$

$$D_\delta(t) = \{\mathbf{x}(t) \in \Omega : \|\mathbf{x}(t) - \mathbf{z}(t)\| \leq \delta\} \tag{42}$$

is chosen as a control volume for the phase field problem and a ξ-η-coordinate system is introduced where $\mathbf{e}_\xi$ is tangential to the crack path at $\mathbf{z}$. The control volume for the respective LEFM problem, is bounded by the contour $\partial D'_\delta$ and the crack faces as displayed in Fig. 2a. Presume that

A: *the boundary conditions at the crack faces are adequately modeled by* (14).

In that case,

B: *the displacements* $\mathbf{u}$ *in* D_δ *but outside the subset* $R_s \subset D_\delta$ *where the phase field is significantly different from* $s = 1$ *are assumed to be a good approximation of the displacements* $\mathbf{u}'$ *that are obtained for the otherwise identical problem formulated in the framework of dynamic linear elastic fracture mechanics, see Fig. 1a. The size of* R_s *depends on the length-scale parameter* l *which is assumed to be small compared to* δ*. Consequently, it is also* $\partial D_{\delta,A\to B} \approx \partial D_\delta$.

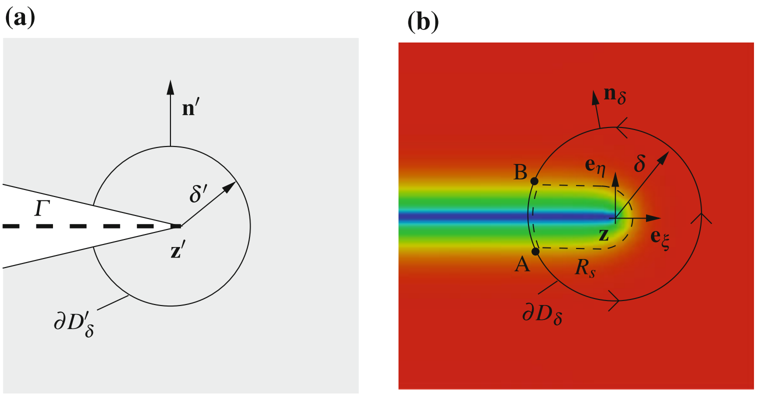

Fig. 2 **a** Crack tip region of a problem formulated in the framework of linear elastic fracture mechanics (LEFM) and **b** the associated phase field representation of the crack tip region

Assumption B is motivated by the proofs of Γ-convergence for the quasi-static phase field model, e.g. in Chambolle [5] which establish a link between the global energies and their minimizers obtained in a free-discontinuity model on the one hand and a phase field model on the other hand. Furthermore, we choose

C: D_δ to be small enough compared to a typical length-scale L of the problem to ensure that the fields on $\partial D_\delta \setminus \partial D_{\delta,B\rightarrow A}$ and $\partial D'_\delta$ are the universal crack tip fields known from linear elastic fracture mechanics.

Addtionally,

D: *it is assumed that the fields in D_δ are smooth enough to allow the gradient and divergence operations.*

Assumption C justifies that for any fields $\phi\,(\mathbf{x}, t)$ that show high gradients in the near-tip region the "transport condition of the singularity" assumption

E:

$$\frac{\partial \phi}{\partial t} \approx -\nabla \phi \cdot \mathbf{v}, \tag{43}$$

with the crack tip velocity

$$\mathbf{v} = \frac{\mathrm{d}}{\mathbf{z}} \mathrm{d}t \tag{44}$$

is made, see Ehrlacher [6]. In particular,

$$-\,\dot{\mathbf{u}} \approx (\mathrm{grad}\mathbf{u})\,\mathbf{v} \quad \text{and} \quad -\,\ddot{\mathbf{u}} \approx (\mathrm{grad}\dot{\mathbf{u}})\,\mathbf{v} \tag{45}$$

is used which also implies

$$\dot{k} = \rho \ddot{\mathbf{u}} \cdot \dot{\mathbf{u}} \approx -\nabla k \cdot \mathbf{v}. \tag{46}$$

In order to find out how the configurational force balances relate to the energy release rate known from dynamic linear elastic fracture mechanics, the working of the dynamic Eshelby stress tensor and the pseudo-momentum on D_δ are considered. With the definition of the dynamic Eshelby stress tensor (37), of the pseudo-momentum (39), the divergence theorem, the symmetry of the stress tensor, the fact that $\mathbf{v}$ is constant in D_δ, (45) and $(46)_1$ we obtain

$$\begin{aligned} &\left[\int_{\partial D_\delta} \boldsymbol{\Sigma}^e \mathbf{n}_\delta \,\mathrm{d}A\right] \cdot \mathbf{v} - \left[\int_{D_\delta} \dot{\mathbf{p}} \;\mathrm{d}V\right] \cdot \mathbf{v} \\ =&\left[\int_{\partial D_\delta} \left(\psi^e - k\right) \mathbf{n}_\delta \,\mathrm{d}A\right] \cdot \mathbf{v} - \left[\int_{\partial D_\delta} \left((\mathrm{grad}\mathbf{u})^T \sigma\right) \mathbf{n}_\delta \,\mathrm{d}A\right] \cdot \mathbf{v} \\ &+ \left[\int_{D_\delta} \left((\mathrm{grad}\mathbf{u})^T \dot{\mathbf{p}} + (\mathrm{grad}\dot{\mathbf{u}})^T \mathbf{p}\right) \mathrm{d}V\right] \cdot \mathbf{v} \\ =&\int_{\partial D_\delta} \left(\left(\psi^e - k\right) \mathbf{v} \cdot \mathbf{n}_\delta \; - \sigma \dot{\mathbf{u}} \cdot \mathbf{n}_\delta\right) \,\mathrm{d}A - 2\int_{D_\delta} \dot{k} \,\mathrm{d}V. \end{aligned} \tag{47}$$

Application of the gradient theorem to the kinetic energy density

$$\int_{D_\delta} \nabla k \, \mathrm{d}V = \int_{\partial D_\delta} k \mathbf{n}_\delta \, \mathrm{d}A, \tag{48}$$

taking the dot product with $\mathbf{v}$ on both sides and using (46) results in

$$\int_{D_\delta} \dot{k} \, \mathrm{d}V \approx - \int_{\partial D_\delta} k \mathbf{n}_\delta \, \mathrm{d}A \cdot \mathbf{v}. \tag{49}$$

Thus, we obtain from (47) and (49)

$$\left[\int_{\partial D_\delta} \boldsymbol{\Sigma}^e \mathbf{n}_\delta \, \mathrm{d}A \right] \cdot \mathbf{v} - \left[\int_{D_\delta} \dot{\mathfrak{p}} \, \mathrm{d}V \right] \cdot \mathbf{v} \approx \int_{\partial D_\delta} \left(\left(\psi^e + k \right) \mathbf{n}_\delta \cdot \mathbf{v} + \sigma \dot{\mathbf{u}} \cdot \mathbf{n}_\delta \right) \, \mathrm{d}A. \tag{50}$$

Division by the absolute value of the crack tip velocity v and making use of $\mathbf{v} \approx v \mathbf{e}_\xi$ yields

$$\left(\mathbf{G}^e_{D_\delta} + \mathfrak{P}_{D_\delta} \right) \cdot \mathbf{e}_\xi \approx \frac{1}{v} \int_{\partial D_\delta} \left(\left(\psi^e + k \right) \mathbf{n}_\delta \cdot \mathbf{v} + \sigma \dot{\mathbf{u}} \cdot \mathbf{n}_\delta \right) \, \mathrm{d}A. \tag{51}$$

From assumptions B it follows that

$$\begin{aligned} &\frac{1}{v} \int_{\partial D_{\delta, A \to B}} \left(\left(\psi^e + k \right) \mathbf{n}_\delta \cdot \mathbf{v} + \sigma \dot{\mathbf{u}} \cdot \mathbf{n}_\delta \right) \mathrm{d}A \\ \approx &\frac{1}{v'} \int_{\partial D'_\delta} \left(\left(\psi^{e\prime} + k' \right) \mathbf{n}' \cdot \mathbf{v}' + \sigma' \dot{\mathbf{u}}' \cdot \mathbf{n}' \right) \, \mathrm{d}A \end{aligned} \tag{52}$$

where the boundary is split into two segments $\partial D_{\delta, A \to B}$ and $\partial D_{\delta, B \to A}$, see Fig. 2b. Herein, $(\cdot)'$ marks the respective quantities obtained in the otherwise identical problem formulated in the framework of linear elastic fracture mechanics. Presuming that the tip domain is indeed small, see assumption C, the integrals in (52) are path-independent and the dynamic energy release rate is

$$\mathscr{G} = \frac{1}{v'} \int_{\partial D'_\delta} \left(\left(\psi^{e\prime} + k' \right) \mathbf{n}' \cdot \mathbf{v}' + \left(\sigma' \dot{\mathbf{u}}' \right) \cdot \mathbf{n}' \right) \, \mathrm{d}A, \tag{53}$$

e.g. see Freund [8]. By means of (53) and the relations (51) and (52) we eventually obtain a link between the configurational forces in the phase field model and quantities from classical fracture mechanics as

$$\mathscr{G} \approx \left(\mathbf{G}^e_{D_\delta} + \mathfrak{P}_{D_\delta} \right) \cdot \mathbf{e}_\xi. \tag{54}$$

In order to obtain an interpretation of the cohesive configurational stress the procedure described in Kuhn [14] is followed. Firstly, the divergence theorem is applied to the second term on the right-hand side of (41), i.e.

$$\mathbf{G}^s_{D_\delta} = \int_{D_\delta} \operatorname{div}\Sigma^s \,\mathrm{d}V = \int_{\partial D_\delta} \Sigma^s \mathbf{n}_\delta \,\mathrm{d}A = \int_{\partial D_{\delta,A\to B}} \Sigma^s \mathbf{n}_\delta \,\mathrm{d}A + \int_{\partial D_{\delta,B\to A}} \Sigma^s \mathbf{n}_\delta \,\mathrm{d}A. \tag{55}$$

On the first segment $\Sigma^s|_{\partial D_{\delta,A\to B}} = \mathbf{0}$ since $s \equiv 1$. If the second segment is sufficiently far away from the crack tip, i.e. assumption B is fulfilled and the crack is straight inside D_δ, it is reasonable to assume that the phase field has the same shape in η-direction as the 1D solution derived in Kuhn [14],

$$s(x_1, x_2)|_{\partial D_{\delta,B\to A}} = 1 - \exp\left(-\frac{|\eta|}{2l}\right). \tag{56}$$

Thus, it is

$$\Sigma^s\big|_{\partial D_{\delta,B\to A}} = \begin{pmatrix} \psi^s & 0 \\ 0 & 0 \end{pmatrix} \tag{57}$$

with

$$\psi^s = \frac{\mathscr{G}_c}{2l} \exp\left(-\frac{|\eta|}{l}\right). \tag{58}$$

Eventually these considerations yield

$$\mathbf{G}^s_{D_\delta} = \int_{\partial D_{\delta,B\to A}} \Sigma^s \mathbf{n} \,\mathrm{d}A = \int_{\partial D_{\delta,B\to A}} \begin{pmatrix} -\psi^s \\ 0 \end{pmatrix} \mathrm{d}\eta = \begin{pmatrix} -\mathscr{G}_c \\ 0 \end{pmatrix} = -\mathscr{G}_c \mathbf{e}_\xi. \tag{59}$$

Hence, with (54), (59) and (41) we find that the configurational force balance applied to an appropriately small crack tip disc D_δ in the form

$$\mathbf{G}_{D_\delta} \cdot \mathbf{e}_\xi = \left(\mathbf{G}^e_{D_\delta} + \boldsymbol{\mathfrak{P}}_{D_\delta} + \mathbf{G}^s_{D_\delta}\right) \cdot \mathbf{e}_\xi = 0 \tag{60}$$

is closely related to the Griffith condition for stable crack growth

$$\mathscr{G} = \mathscr{G}_c. \tag{61}$$

The Griffith condition is fulfilled if $\mathbf{G}_{D_\delta} = \mathbf{0}$, i.e. the crack driving forces $\mathbf{G}^e_{D_\delta} + \boldsymbol{\mathfrak{P}}_{D_\delta}$ balance the cohesive configurational force $\mathbf{G}^s_{D_\delta}$.

In order to judge whether the size of the control volume D_δ is chosen large enough in order to comply with assumption B, we consider a second tip disc control volume R with radius $\delta_R > \delta$ and a third control volume $R_\delta = R \setminus D_\delta$ that does not include the crack tip, any other crack tip nor the regions dominated by the stress concentrations surrounding them. It is

$$\int_R \left(\operatorname{div}\boldsymbol{\Sigma}^e - \dot{\mathfrak{p}}\right) \,\mathrm{d}V = \int_{R_\delta} \left(\operatorname{div}\boldsymbol{\Sigma}^e - \dot{\mathfrak{p}}\right) \,\mathrm{d}V + \int_{D_\delta} \left(\operatorname{div}\boldsymbol{\Sigma}^e - \dot{\mathfrak{p}}\right) \,\mathrm{d}V. \tag{62}$$

The integral $\int_{R_\delta} \left(\operatorname{div}\boldsymbol{\Sigma}^e - \dot{\mathfrak{p}}\right)\, \mathrm{d}V$ represents the crack-extending energetic driving force on $\mathbf{z}$ that results from the states $[\dot{\mathbf{u}}(\mathbf{x}, t), \varepsilon(\mathbf{x}, t), s(\mathbf{x}, t),]$ of all $\mathbf{x}$ inside R_δ, see (41). Since no stress concentration is located in R_δ, it is

$$\left|\int_{R_\delta} \left(\operatorname{div}\Sigma^e - \dot{\mathfrak{p}}\right)\, \mathrm{d}V\right| \ll \left|\int_{D_\delta} \left(\operatorname{div}\Sigma^e - \dot{\mathfrak{p}}\right)\, \mathrm{d}V\right|. \tag{63}$$

From (62) it follows

$$\int_{R} \left(\operatorname{div}\Sigma^e - \dot{\mathfrak{p}}\right)\, \mathrm{d}V \approx \int_{D_\delta} \left(\operatorname{div}\Sigma^e - \dot{\mathfrak{p}}\right)\, \mathrm{d}V. \tag{64}$$

Equation (64) implies that the value of the above integral is insensitive to a further increase of the size of the control volume if the crack tip field is sufficiently contained in D_δ. Hence, δ is chosen large enough, if (64) is fulfilled for $\delta_R > \delta$.

By taking the dot product with $\mathbf{e}_\xi$ on both sides of (64), we obtain by means of (54)

$$\mathscr{G} \approx \int_{R} \left(\operatorname{div}\Sigma^e - \dot{\mathfrak{p}}\right)\, \mathrm{d}V \cdot \mathbf{e}_\xi \tag{65}$$

Relation (59) holds for larger control volumes as well as long as the crack is straight and aligned with $\mathbf{e}_\xi$. Hence, under these conditions, the configurational force balance in the form (60) can be applied to a large control volume and still be related to the Griffith condition (61).

5 Numerical Examples

In order to demonstrate the significance of the derived configurational force balances for the analysis of phase field simulations of fracture, two numerical experiments are performed. The set of coupled Eqs. (22) and (23) is solved by a finite element scheme with bilinear shape functions, implicit time integration and automatic step size control, see Schlüter et al. [29] for details. The degradation function used in Schlüter et al. [29] differs from the general cubic formulation used in this work, which may raise the question whether this variation has any consequences for the numerical solution strategy. Indeed, in Kuhn et al. [16] a monolithic finite element scheme with bilinear shape functions proved to have difficulties predicting crack nucleation in previously undamaged material if a degradation function of the type (15) with $a = 0$ was used. However, these difficulties are removed for $a > 0$. Furthermore, crack nucleation in pristine material is not considered in this work. Consequently, the chosen numerical solution strategy is assumed to be suitable for the presented problems. The computation of the configurational forces within the finite element framework is explained in Müller et al. [24], Kuhn and Müller [15] and Kuhn [14].

5.1 Crack Arrest

To begin with, a tension-loaded specimen with an initial crack as depicted in Fig. 3a is considered. The length-scale parameter is set to $l = 0.02L$ and the element size h of the regular mesh is small enough to resolve the phase field crack properly, i.e. $h = 2l$. The Lamé parameters of the material are $\lambda = \mu$, i.e. the Poisson's ratio is $\nu = \frac{1}{4}$. The applied displacement, $\mathbf{u}^*(t) = \pm\, u^*(t)\, \mathbf{e}_2$, is controlled such that after initial crack growth in x_1-direction - with crack speeds of around half the Rayleigh wave speed c_r- the crack arrests and the velocity drops to zero, see the magenta line in Fig. 3b. The maximum applied displacement is $u_{max} = 0.8\sqrt{\mathscr{G}_c L/2\mu}$ which causes the crack to extend from its initial size of $0.5L$ to its final length of $1.53L$. The crack speed is calculated from a post-processing regression analysis of a series of subsequent crack tip positions. Herein, the current crack tip position $\mathbf{z}(t)$ is identified with the position of the node I that is the most advanced on the crack path and fullfills $s_I = 0$. Subsequently, a polynomial is fitted to this discrete representation of the crack tip location in order to get a smoothed representation of the crack tip position as a function of t

$$\tilde{\mathbf{z}}(t) \approx \mathbf{z}(t), \tag{66}$$

which allows to compute the crack speed as

$$\mathbf{v} = \dot{\tilde{\mathbf{z}}} \tag{67}$$

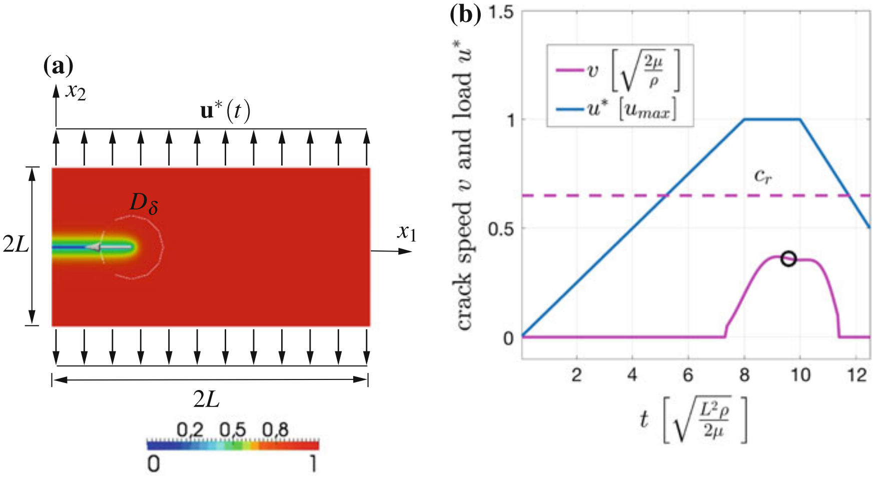

Fig. 3 **a** Phase field s (contour), domain D_δ (circle), total configurational force $\underline{\mathbf{G}}_{D_\delta}$ in the unloaded state (arrow). **b** Applied load u^* and crack speed v (solid lines), Rayleigh wave speed (dashed line) and the point in time (black circle) at which the convergence study displayed in Fig. 4a is performed

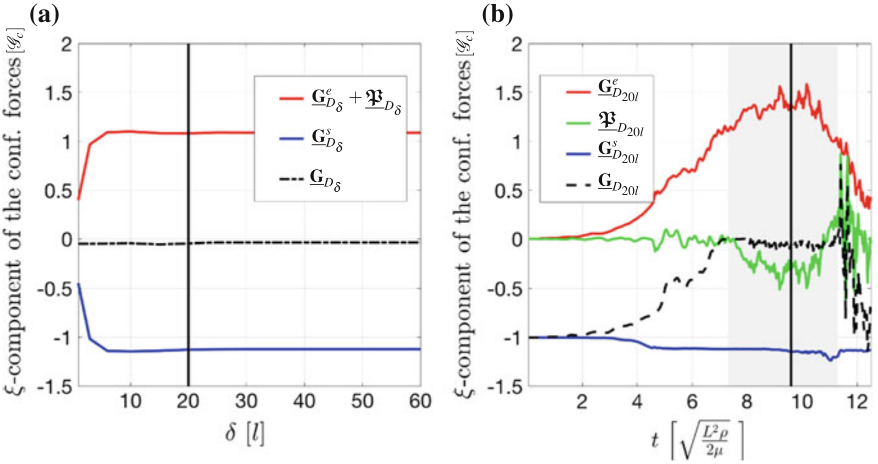

Fig. 4 **a** configurational force components evaluated at time $t = 9.6\sqrt{L^2\rho/2\mu}$ for different radii of the control volume. **b** ξ-components of the configurational forces for a tip disc control volume with a radius of $\delta = 20l$, see also the vertical black line in Fig. 4a, period of crack growth (grey area) and point in time at which Fig. 4a is recorded (vertical black line)

and the tangential vector as

$$\mathbf{e}_\xi = \frac{\mathbf{v}}{|\mathbf{v}|}, \tag{68}$$

see also Fig. 6a.

Figure 4a shows the ξ-component of the configurational forces $\underline{G}^e_\xi + \underline{\mathfrak{P}}_\xi$, $\underline{G}^s_\xi$ and $\underline{G}_\xi$ evaluated at time $t = 9.6\sqrt{L^2\rho/2\mu}$ for different sizes of the tip control volume. The index $(*)_{D_\delta}$ is skipped for clarity from this point on, whereas the underbar notation $\underline{*}$ indicates that the respective quantities are evaluated numerically. It can be observed that control volumes with a radius smaller than $\delta = 10l$ do not yield converged values of the configurational force components $\underline{G}^e_\xi + \underline{\mathfrak{P}}_\xi$ and $\underline{G}^s_\xi$. In this case, the tip disc is too small compared to l to include the near tip stress field or to evaluate the cohesive fracture resistance force correctly. Thus, assumption B, see the previous chapter, is violated and the computed configurational forces cannot be related in any way to the energy release rate $\mathscr{G}$ or the fracture resistance $\mathscr{G}_c$. Larger control volumes however approve that - apart from a slight overestimation of the cohesive configurational force which is typical for finite element discretizations of phase field models for fracture, see e.g. Kuhn [14] and Borden [2] - the cohesive force is $\underline{G}^s_\xi \approx -\mathscr{G}_c$. Thus, the cohesive configurational force $\underline{G}^s_\xi$ represents the materials resistance to crack propagation in accordance with (59). The part $\underline{G}^e_\xi + \underline{\mathfrak{P}}_\xi$ on the other hand is the crack driving component which counteracts the cohesive force $\underline{G}^s_\xi$. For all control volumes, the total tip configurational force is $\underline{G}_\xi \approx 0$, which underlines the phase field model's connection to the Griffith condition (61). The crack tip control volume needs to be chosen large enough such that $\underline{\mathbf{G}}^e + \underline{\mathfrak{P}}$ is insensitive to a further increase of the radius δ, see (63). As can be observed in Fig. 4**a** this is fulfilled for a size of at least $\delta = 10l$. For further analysis, we choose $\delta = 20l$ in this example, see also the vertical black line in Fig. 4a.

Figure 4b shows records of the configurational forces with respect to time for a control volume of size $\delta = 20\,l$. Initially, only the cohesive configurational force is non-zero and its ξ-component agrees well with $\mathscr{G}_c$ as mentioned above. Over the course of the simulation this does not change significantly, except for a slight increase of $|\underline{G}_\xi^s|$ well before crack initiation. The elastic component of the configurational force $\underline{G}_\xi^e$ is the crack driving force. It is controlled by the applied displacement load, see also Fig. 3b, and decreases as soon as the displacement load is reduced. Inertial effects are present even before crack initiation at time $t \approx 7.3\sqrt{L^2\rho/2\mu}$ which becomes apparent in the nonzero pseudo-momentum $\underline{\mathfrak{P}}_\xi$. However, up to crack initiation $\underline{\mathfrak{P}}_\xi$ oscillates around zero and only shows a clear trend to negative values during the period of crack propagation $7.3\sqrt{L^2\rho/2\mu} < t < 11.3\sqrt{L^2\rho/2\mu}$ where it reaches peak values of around $-0.5\mathscr{G}_c$. Thus, in this stage of the simulation $\underline{\mathfrak{P}}_\xi$ represents a resistance to crack propagation which is in contrast to $\underline{G}_\xi^s$ due to inertial effects and not due to the cohesion of material particles. Note that the Griffith condition $\underline{G}_\xi \approx 0$ is fulfilled during crack growth. In the last stages of crack growth, i.e. for $t > 10.9\sqrt{L^2\rho/2\mu}$, positive values of $\underline{\mathfrak{P}}_\xi$ can be observed which imply a crack driving inertial force. It can be concluded that there is an inertial resistance to crack deceleration that keeps the crack growing although $\underline{G}_\xi^e$ does not provide a sufficiently large crack driving force anymore to overcome the material resistance $\underline{G}_\xi^s$. Eventually, $\underline{G}_\xi^e$ drops to the point that the Griffith condition is no longer satisfied and the crack stops. Initially, the total configurational force is $\underline{G}_\xi \approx -\mathscr{G}_c$, since the crack tip is unloaded and thus $\underline{G}_\xi^e = 0$ and $\underline{\mathfrak{P}}_\xi = 0$ but the material's resistance $\underline{G}_\xi^s = -\mathscr{G}_c$ is non-zero. A negative ξ-component of the total configurational force implies that the resulting energetic driving force on the crack tip favors a recession of the crack, i.e. crack healing. Hence, an according evolution of the order parameter should take place in this subcritical load state. However, such an evolution of s is prevented by the irreversibility constraint (27). The irreversibility constraint counteracts the crack closing energetic driving force $\underline{G}_\xi^s$ in subcritical load states but - since the antagonistic irreversibility force is not accounted for in the configurational force balances (35) and (41) - $\underline{G}_\xi \approx -\mathscr{G}_c$ follows.

This example demonstrates the main character of the different components of the crack tip configurational force. The elastic part $\underline{G}_\xi^e$ is the crack driving energetic force, whereas $\underline{G}_\xi^s$ and $\underline{\mathfrak{P}}_\xi$ represent the material's and the inertial resistance to crack propagation. During crack deceleration the inertial forces may also play a crack driving role, i.e. $\underline{\mathfrak{P}}_\xi > 0$. The fact that $\underline{G}_\xi \approx 0$ during crack propagation highlights the connection of the phase field model to Griffith's description of crack growth. Furthermore, it is found that states at which $\underline{G}_\xi < 0$ have to be interpreted as subcritical load states where the irreversibility constraint (27) comes into effect. Additionally, it is observed that the size of the control volume needs to be large enough compared to the length-scale parameter l in order to yield useful results, e.g. $\delta > 20l$. Above this critical size, the configurational force components $\underline{G}_\xi^e + \underline{\mathfrak{P}}_\xi$, $\underline{G}_\xi^s$ and $\underline{G}_\xi$ are insensitive to a further increase of the size of the control volume.

5.2 *Branching*

In this section, the concept of configurational forces is employed to study dynamic crack branching in the phase field model. A body with an initial crack as displayed in Fig. 5a is considered. The Lamé parameters of the material are $\lambda = \mu$, i.e. $\nu = 1/4$. Again, a regular mesh with an element size of $h = 2\,l$ is used where the length-scale parameter is set to $l = 0.005\,L$. The traction load $\mathbf{t}^* = \pm t^*\mathbf{e}_2$ is increased linearly to its maximum value of $t_{max} = 1.0\sqrt{2\mu\mathscr{G}_c/L}$ and afterwards held constant, see Fig. 5b. The crack originally propagates in x_1-direction and eventually branches, see the crack pattern displayed in Fig. 6a. It is not possible to unambiguously identify the moment of branching since the diffuse phase field representation of the crack surface does not allow to identify distinct crack tips in the very early stages of the branching process. Instead, branching is announced by a period A of crack widening and the formation of bulges indicating the directional instability of the crack, see Fig. 6b. Subsequently, pronounced bulging of the crack tip initiates crack branching and eventually two distinct crack tips can be identified. This branching period is denoted as B and lasts from $t = 1.63\sqrt{L^2\rho/2\mu}$ to $t = 1.76\sqrt{L^2\rho/2\mu}$, see also Figs. 5b and 6b.

The crack speed - recorded for the lower branch - reaches its maximum value of $v \approx 0.56c_r$ right after branching occurs, see the magenta line in Fig. 5b. The configurational force components acting on a control volume of size $\delta = 15l$ are displayed in Fig. 6b. In addition to the computed data (thin lines) the corresponding moving average filtered data sets (thick lines) are plotted. The filtered data corresponds to the unweighted mean of the data of the last 30 time steps and the resulting lag is corrected. This post-processing step is necessary to make the strongly oscillating configurational forces more accessible to interpretation. After this smoothing step it becomes obvious that the main characteristics of the configurational force components from the previous numerical example remain the same. Again, $\underline{G^e_\xi} > 0$ is

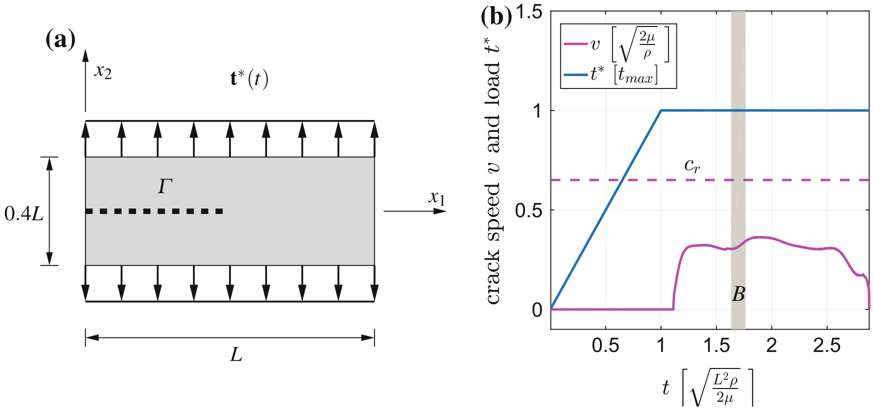

Fig. 5 **a** Setup for the branching problem and **b** crack speed v and applied traction load t^*. The period of crack branching B is indicated by the grey region

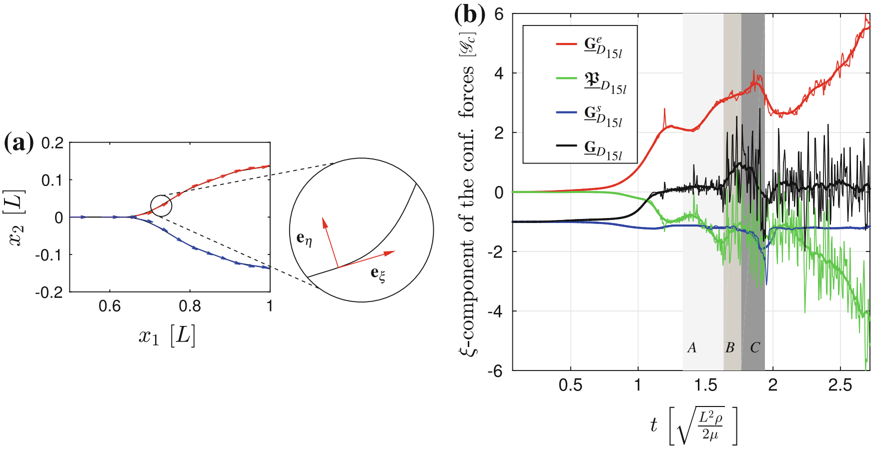

Fig. 6 **a** representation of the crack pattern by successive crack tip positions $\tilde{\mathbf{z}}$ (black lines), tangential vectors $\mathbf{e}_\xi$ for the lower (blue arrows) and upper (red arrows) branch, illustration of the ξ-η-coordinate system. **b** ξ-components of the configurational forces for a tip disc control volume with a radius of $\delta = 15l$ (thin lines) and corresponding moving average filtered data (thick lines). The stages of branching A, B, C are indicated by regions of different shades of grey

the crack driving force whereas $\underline{G}^s_\xi < 0$ and $\underline{\mathfrak{P}}_\xi < 0$ represent the material and inertial resistance to crack propagation. In contrast to the previous example however, the total configurational force acting on the crack tip is slightly larger than zero in the phase of notable crack widening A, and shows peak averaged values of around $\underline{G}_\xi \approx 1.0\,\mathscr{G}_c$ during crack branching, i.e. phase B. This suggests that the crack driving force exceeds the inertial and material resistance and thus, an additional crack tip is formed to transform sufficient amounts of energy. Period C that lasts from $t = 1.76\sqrt{L^2\rho/2\mu}$ to $t = 1.94\sqrt{L^2\rho/2\mu}$ denotes the period where branching already took place but the two crack tips are still located in D_{15l}. In this phase, domain independence of $\underline{G}^e_\xi + \underline{\mathfrak{P}}_\xi$, i.e. (63), is not valid since more than one stress concentration is contained in D_{15l}. Note that the cohesive configurational force $\underline{G}^s_\xi$ peaks significantly later than $\underline{G}_\xi$, i.e. at the end of C, driving the total configurational force $\underline{G}_\xi$ back to zero. The absolute values of the inertial configurational force before branching of $|\underline{\mathfrak{P}}_\xi| > 1.0\mathscr{G}_c$ exceed the maximum values of the previous, non-branching example.

The various components of the tip configurational force are displayed in Fig. 7 for different sizes of the crack tip control volume ranging from $\delta = 10l$ to $\delta = 20l$. As expected, the elastic configurational force $\underline{G}^e_\xi$ and the pseudo-momentum $\underline{\mathfrak{P}}_\xi$ for themselves are clearly dependent on the size of the control volume, since their graphs (quantitatively) vary significantly for different δ, see Fig. 7a. The sum $\underline{G}^e_\xi + \underline{\mathfrak{P}}_\xi$, plotted in Fig. 7b, on the other hand is less sensitive to the size of the control volume, which is in good agreement with the considerations that led to (63), see Fig. 7b. A significant difference in the graphs of $\underline{G}^e_\xi + \underline{\mathfrak{P}}_\xi$ can however be noted directly after

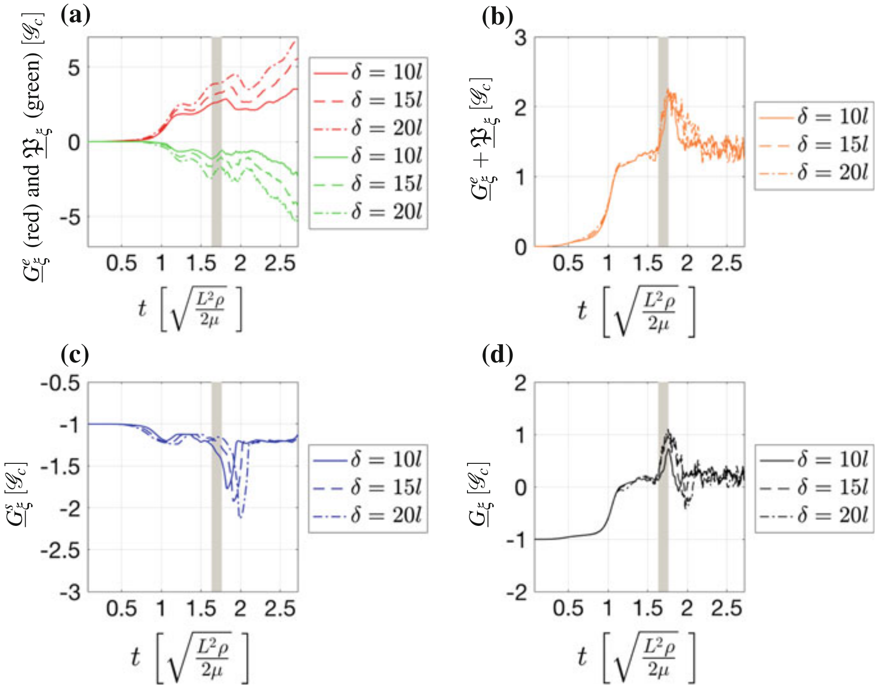

Fig. 7 Configurational force components for different radii of the tip disc: **a** the elastic part $\underline{G}^e_\xi$ (red) and the pseudo-momentum $\underline{\mathfrak{P}}_\xi$ (green), **b** the sum of the elastic part and the pseudo-momentum $\underline{G}^e_\xi + \underline{\mathfrak{P}}_\xi$, **c** the cohesive configurational force $\underline{G}^s_\xi$ and **d** the total configurational force $\underline{G}_\xi$. The branching period B is indicated by the grey region

crack branching. This is due to the fact that the second crack tip may still be contained in a larger control volume while it is not located in a smaller control volume anymore. The quantity $\underline{G}^e_\xi + \underline{\mathfrak{P}}_\xi$ corresponds to the dynamic energy release rate, see (65), and reaches values larger than $1.3\,\mathscr{G}_c$ with an increasing tendency prior to branching and $\sim 2.0\,\mathscr{G}_c$ during the period of crack branching B.

The cohesive configurational forces show pronounced peak values. Their magnitude as well as the time of their occurrence is clearly dependent on δ, see Fig. 7c. The peak occurs right before the second crack tip exits the respective control volume, i.e. at the end of period C, and is thus delayed for larger control volumes. Larger control volumes also contain a larger part of the second crack (tip) and hence the absolute value of $\underline{G}^s_\xi$ is larger as well. Apart from these features, the cohesive configurational force provides a resistance to crack propagation slightly larger than $\mathscr{G}_c$ as explained in the previous example.

The total configurational force $\underline{G}_\xi$ also shows a low sensitivity on δ. All graphs in Fig. 7d have a significant peak during crack branching in common. Its magnitude ranges from $\underline{G}_\xi \approx 0.7\mathscr{G}_c$ for $\delta = 10\,l$ to $\underline{G}_\xi \approx 1.0\mathscr{G}_c$ for $\delta = 20\,l$. In contrast to the crack arrest simulation however, $\underline{G}_\xi$ is slightly larger than zero before and after crack branching. Consequently, the Griffith condition (61) is not perfectly fulfilled but the crack driving force exceeds the cohesive material resistance.

The evaluation of the configurational forces in this numerical example suggest that a critical energy release rate $\mathscr{G} \approx \underline{G}^e_\xi + \underline{\mathfrak{P}}_\xi$ and total configurational force $\underline{G}_\xi$ go along with dynamic crack branching. Furthermore, it shows that the energy release rate $\mathscr{G} \approx \underline{G}^e_\xi + \underline{\mathfrak{P}}_\xi$, the cohesive configurational force $\underline{G}^s_\xi$ and the total configurational force $\underline{G}_\xi$ are less sensitive to the size of the crack tip control volume than $\underline{G}^e_\xi$ and $\underline{\mathfrak{P}}_\xi$, which is in good agreement with the considerations made in Sect. 4.

6 Conclusions

In this work, the concept of configurational forces is proposed to enhance the post-processing and the interpretation of the results of phase field simulations for dynamic brittle fracture. A local configurational force balance is derived by taking the gradient of the Lagrangian density of the phase field fracture problem. It is shown that the total configurational forces computed for a crack tip control volume are closely related to the Griffith criterion of classical fracture mechanics.

The relevance of the configurational forces as a post-processing tool for dynamic phase field simulations is illustrated by means of two examples. The first example deals with a crack arrest scenario, where an initially fast growing crack stops again. Here, the inertial resistance to crack propagation at high crack speeds can be visualized by considering the pseudo-momentum of the crack tip. Furthermore, the connection to the Griffith criterion is established by noting that the total configurational force tangential to the direction of crack growth is approximately zero during crack propagation. The second numerical example deals with the phenomenon of dynamic crack branching. In this case, configurational forces yield interesting insights in the simulations. Right before branching, the absolute value of the crack driving configurational force exceeds the resistant cohesive configurational force by a factor of around two. This indicates that an additional crack tip needs to be nucleated in order to match the energy flux to the crack tip with the energy that can be dissipated during the creation of the new fracture surface. Furthermore, the observation of these critical values of the crack driving force enable the identification of crack branching even before two distinct crack tips can be observed in contour plots of the phase field variable.

It is concluded that the concept of configurational forces is indeed helpful to reveal features of phase field simulations for dynamic brittle fracture. Furthermore, the decomposition of the configurational force acting on a phase field crack tip and the interpretation of its components highlight the relation of the model to Griffith's energetic description of brittle fracture.

Acknowledgements The financial support within the International Research Training Group 2057 is gratefully acknowledged.

References

1. Amor, H., Marigo, J.J., Maurini, C.: Regularized formulation of the variational brittle fracture with unilateral contact: numerical experiments. J. Mech. Phys. Solid **57**(8), 1209–1229 (2009)
2. Borden, M.J.: Isogeometric analysis of phase-field models for dynamic brittle and ductile fracture. Ph.D. thesis, The university of Texas at Austin (2012)
3. Borden, M.J., Verhoosel, C.V., Scott, M.A., Hughes, T.J.R., Landis, C.M.: A phase-field description of dynamic brittle fracture. Comput. Methods Appl. Mech. Eng. **217–220**, 77–95 (2012)
4. Bourdin, B.: Numerical implementation of the variational formulation of quasi-static brittle fracture. Interfaces Free Bound **9**, 411–430 (2007)
5. Chambolle, A.: An approximation result for special functions with bounded deformation. J. Math. Pure Appl. **83**(7), 929–954 (2004)
6. Ehrlacher, A.: Path independent integral for the calculation of the energy release rate in elastodynamics. Adv. Fract. Res. **5**, 2187–2195 (1981)
7. Eshelby, J.D.: The force on an elastic singularity. Philosoph. Trans. R. Soc. Lond. A **244**(877), 87–112 (1951)
8. Freund, L.B.: Dynamic Fracture Mechanics. Cambridge University Press, Cambridge (1990)
9. Griffith, A.A.: The phenomena of rupture and flow in solids. Philosoph. Trans. R. Soc. Lond. A **221**, 163–198 (1921)
10. Gurtin, M.E.: Configurational Forces as Basic Concepts of Continuum Physics. Applied Mathematical Sciences. Springer, New York (2000)
11. Hakim, V., Karma, A.: Laws of crack motion and phase-field models of fracture. J. Mech. Phys. Solid **57**(2), 342–368 (2009)
12. Hofacker, M., Miehe, C.: A phase field model of dynamic fracture: robust field updates for the analysis of complex crack patterns. Int. J. Numer. Methods Eng. **93**(3), 276–301 (2013)
13. Kienzler, R., Herrmann, G.: Mechanics in Material Space: With Applications to Defect and Fracture Mechanics. Engineering Online Library. Springer, Berlin (2000)
14. Kuhn, C.: Numerical and analytical investigation of a phase field model for fracture. Ph.D. thesis, Technische Universität Kaiserslautern (2013)
15. Kuhn, C., Müller, R.: Configurational forces in a phase field model for fracture. In: 18th European Conference on Fracture. DVM (2010)
16. Kuhn, C., Schlüter, A., Müller, R.: On degradation functions in phase field fracture models. Appl. Mech. Rev. **57**(2), (2015)
17. Li, T., Marigo, J.J., Guilbaud, D.: Numerical investigation of dynamic brittle fracture via gradient damage models. Adv. Model. Simul. Eng. Sci. **3**(1), 26 (2016). https://doi.org/10.1186/s40323-016-0080-x
18. Maugin, G.A.: Material Inhomogeneities in Elasticity. Applied Mathematics and Mathematical Computation. Taylor and Francis, London (1993)
19. Maugin, G.A.: Configurational Forces: Thermomechanics, Physics, Mathematics, and Numerics. CRC Series-Modern Mechanics and Mathematics. Taylor and Francis, London (2010)
20. Maugin, G.A., Trimarco, C.: Pseudomomentum and material forces in nonlinear elasticity: variational formulations and application to brittle fracture. Acta Mech. **94**(1), 1–28 (1992). https://doi.org/10.1007/BF01177002
21. Miehe, C., Grses, E.: A robust algorithm for configurational-force-driven brittle crack propagation with r-adaptive mesh alignment. Int. J. Numer. Methods Eng. **72**(2), 127–155 (2007). https://doi.org/10.1002/nme.1999
22. Miehe, C., Hofacker, M., Welschinger, F.: A phase field model for rate-independent crack propagation: robust algorithmic implementation based on operator splits. Comput. Methods Appl. Mech. Eng. **199**(45–48), 2765–2778 (2010)
23. Miehe, C., Welschinger, F., Hofacker, M.: Thermodynamically consistent phase-field models for fracture: variational principles and multi-field FE implementations. Int. J. Numer. Methods Eng. **83**(10), 1273–1311 (2010)

24. Mueller, R., Kolling, S., Gross, D.: On configurational forces in the context of the finite element method. Int. J. Numer. Methods Eng. **53**(7), 1557–1574 (2002)
25. Özenç, K., Chinaryan, G., Kaliske, M.: A configurational force approach to model the branching phenomenon in dynamic brittle fracture. Eng. Fract. Mech. **157**(Complete), 26–42 (2016). https://doi.org/10.1016/j.engfracmech.2016.02.017
26. Rahman, M., Michelitsch, T.: A note on the formula for the rayleigh wave speed. Wave Motion **43**(3), 272–276 (2006)
27. Rice, J.R.: A path independent integral and the approximate analysis of strain concentration by notches and cracks. J. Appl. Mech. **35**, 379–386 (1968)
28. Schlüter, A., Kuhn, C., Müller, R., Gross, D.: An investigation of intersonic fracture using a phase field model (2016). https://doi.org/10.1007/s00419-015-1114-4
29. Schlüter, A., Willenbücher, A., Kuhn, C., Müller, R.: Phase field approximation of dynamic brittle fracture. Comput. Mech. 1–21 (2014)
30. Steinke, C., Özenç, K., Chinaryan, G., Kaliske, M.: A comparative study of the r-adaptive material force approach and the phase-field method in dynamic fracture
31. Strobl, M., Seelig, T.: On constitutive assumptions in phase field approaches to brittle fracture. Procedia Struct. Integr. **2**, 3705–3712 (2016). https://doi.org/10.1016/j.prostr.2016.06.460, http://www.sciencedirect.com/science/article/pii/S2452321616304796

A Multi-layer Piezocomposite Model and Application on Controlled Smart Structures

Georgios Tairidis, Georgia Foutsitzi and Georgios E. Stavroulakis

Abstract In smart structural applications, multi-layered piezocomposite plates are very common for the study of active control applications. In this paper a finite element formulation is presented to model the static and dynamic response of laminated composite plates containing integrated piezoelectric sensors and actuators subjected to electrical and mechanical loadings. The formulation is based on a third order shear deformation theory and Hamilton's principle. A nine-noded C^0 plate element is implemented for the analysis. The element was developed to include stiffness and the electromechanical coupling of the piezoelectric sensor/actuator layers. The electric potential is assumed to vary linearly through the thickness for each piezoelectric sublayer. The model is validated by comparing with existing results documented in the literature. A displacement and optimal LQR control algorithm is used for the active control of the static deflection and of the dynamic response of the plates with surface bonded piezoelectric sensors and actuators layers or patches. The main aspects of the application of the present model are discussed through a set of numerical examples.

G. Tairidis · G. E. Stavroulakis (✉)
School of Production Engineering and Management, Institute of Computational Mechanics and Optimization, Technical University of Crete, University Campus, 73100 Chania, Greece
e-mail: gestavr@dpem.tuc.gr

G. Tairidis
e-mail: tairidis@gmail.com

G. Foutsitzi
Department of Accounting and Finance, Technological Educational Institution of Epirus, Preveza 48100, Greece
e-mail: gfoutsi@teiep.gr

© Springer International Publishing AG 2018

H. Altenbach et al. (eds.), *Advances in Mechanics of Materials and Structural Analysis*, Advanced Structured Materials 80,
https://doi.org/10.1007/978-3-319-70563-7_17

1 Introduction

Smart composite structures have attracted a great deal of attention in the last few decades due to their significant potential applicability in various industrial and research areas. Piezocomposites constitute a significant class of smart structures and have been studied extensively. Dealing with smart composite structures requires the possibility of modelling and simulation of their behavior. Stress and strain distribution within a multilayer composite may require careful approximation that deviates from classical thin plate theories. This is mainly due to the higher contribution of shear and the effect of weak points like glue layers and interfaces. It is widely accepted that higher-order shear deformation theory (HSDT) is essentially required for the accurate modelling of thick plates. If one uses the classical plate theory for modelling of thick laminated structures made of advanced composites (e.g. graphite/epoxy, boron/epoxy) whose elastic to shear modulus ratios are very large, the errors in deflections, stresses, natural frequencies and buckling loads become higher. Reddy [1] also showed that HSDT improves the in-plane response even in the case of thin laminated composite structure. Thus, if the substrate of a smart structure is a multilayered laminated composite structure, one should consider the effect of transverse shear deformation to obtain an accurate response. A variety of higher order lamination theories has been proposed in order to improve the transverse shear stress calculation. Kant and Manjunatha [2] developed a nine-node finite element (FE) having seven degrees of freedom per node to perform free vibration analysis of unsymmetrically laminated multilayered plates. Goswami [3] presented a simple C^0 FE formulation for nine-node FE with six degrees of freedom based on HSDT. Lee and Kim [4] developed a four-node laminated plate element by using a higher order shear deformation theory and assumed strains to perform the FE analysis of laminated composite plate structures.

The recent advances in smart structures have prompted interest in more accurate modelling and simulation of their coupled electro-mechanical behavior for active control applications. FE models for piezoelectric composite beams and plates have been reported in Refs. [5]–[12]. Ray et al. [13] developed a two-dimensional eight-noded isoparametric finite element for modelling the distributed coupled electromechanical behavior of smart structures using higher-order displacement theory. In Ref. [14] a higher-order, shear-flexible piezolaminated C^1 QUAD 8 multi-layer composite plate finite element with 48 elastic degrees of freedom per element and 9 electric degrees of freedom per element per piezoelectric layer has been presented for the analysis of multi-layer smart composite structures. The electric potential is assumed to vary quadratically over the thickness, following [15], representing the potential induced due to bending deformation more accurately, by interpolating using nodal mid-plane electric potentials and one electric degree of freedom representing the potential difference between the top and bottom surfaces of the piezoelectric layer. Phung–Van et al. [16] presented a simple and effective formulation to investigate static, free vibration and dynamic control of piezoelectric composite plates integrated with sensors and actuators, based on isogeometric analysis and higher order shear deformation theory. Recently, the static behavior of a laminated composite flat panel, surface bonded with and without piezoelectric and/or magnetostrictive layers, have been analyzed in [17]. The plate has been modeled in the framework of the HSDT mid-plane kinematics discretised using suitable FEM with sixteen degrees of freedom.

Additionally, several other analytical and numerical methods [18–20] are promising to solve various piezoelectric structures.

The objective of this work is to develop a finite element model for active control of multilayer piezocomposite plates using higher order shear deformation displacement theory. The core elastic part of the smart plate is a laminate made of several plies with different material orientations. The plate is integrated with piezoelectric layers or patches polarized in the thickness direction. The overall structure is considered as a laminated plate with the integrated piezoelectric and sensor layers as the bounding plies of the laminated plate. In order to create a flexible model, suitable for both classical (statics, dynamics, control) as well as advanced applications (delamination, damage, consideration of glue material), a nine-node quadrilateral finite element is developed. The formulation is based on the third order shear deformation theory that accounts for parabolic distribution of the transverse shear strains through the thickness of the plate and rotary inertial effects [2] and has been extended to incorporate the piezoelectric sensors and actuators layers. To illustrate the accuracy of the present finite element model, a comparison of results with published ones is presented. Moreover, the shape control and active vibration suppression of a cantilever composite plate are studied, in order to demonstrate some of the capabilities of the model.

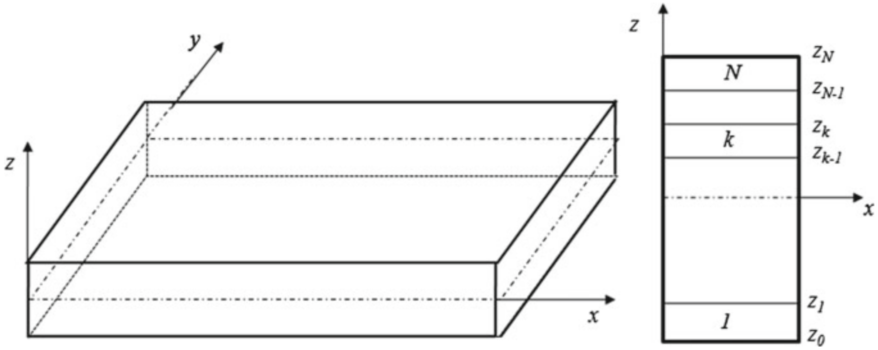

Fig. 1 Geometry of the smart piezocomposite plate

2 Governing Equations

Consider a piezocomposite plate structure consisting of several layers, including piezoelectric layers, as shown in Fig. 1. All layers are perfectly bonded. The plate has length a, width b, total thickness h and consists of N layers with the principal material coordinates of the k -th lamina oriented at an angle θ_k to the laminate coordinate x. The xy plane coincide with the midplane of the plate, with the z-axis being normal to the midplane. The piezoelectric layers are much thinner than the host structure and they have poling direction along z-axis. For simplicity of the notation, all the layers of the laminate will be considered as piezoelectric. Elastic layers are then obtained by making their piezoelectric constants vanish.

2.1 Mechanical Displacement and Strains

The mechanical behaviour of the structure is modelled by the 3rd order displacement theory developed by Kant et al. [2] as follows

$$\begin{aligned} u_1(x, y, z, t) &= u(x, y, t) + z\theta_x(x, y, t) + z^3\theta_x^*(x, y, t) \\ u_2(x, y, z, t) &= v(x, y, t) + z\theta_y(x, y, t) + z^3\theta_y^*(x, y, t) \\ u_3(x, y, z, t) &= w(x, y, t) \end{aligned} \tag{1}$$

where, u_1, u_2, u_3 are the displacements at any point of the plate along the (x, y, z) coordinates, u, v, w are the displacements associated with a point on the mid-plane of the plate and θ_x, θ_y are the normal rotations about the y and x -axes, respectively. The functions θ_x^*, θ_y^* are the higher order terms of Taylor series expansion defined at the mid-surface.

The in-plane strains are thus expressed by the following equation

$$\{\varepsilon_b\} = \{\varepsilon_{xx}, \varepsilon_{yy}, \gamma_{xy}\}^T = \{\varepsilon_{b0}\} + z\{k\} + z^3\{k^*\} \tag{2}$$

where

$$\{\varepsilon_{0b}\} = \left\{\frac{\partial u}{\partial x}, \frac{\partial v}{\partial y}, \left(\frac{\partial u}{\partial y} + \frac{\partial v}{\partial x}\right)\right\}^T, \{k\} = \left\{\frac{\partial \theta_x}{\partial x}, \frac{\partial \theta_y}{\partial y}, \left(\frac{\partial \theta_x}{\partial y} + \frac{\partial \theta_y}{\partial x}\right)\right\}^T,$$

$$\{k^*\} = \left\{\frac{\partial \theta_x^*}{\partial x}, \frac{\partial \theta_y^*}{\partial y}, \left(\frac{\partial \theta_x^*}{\partial y} + \frac{\partial \theta_y^*}{\partial x}\right)\right\}^T,$$

The transverse shear strains are given by

$$\{\varepsilon_s\} = \{\gamma_{yz}, \gamma_{xy}\}^T = \{\varepsilon_{0s}\} + z^2\{k_s\} \tag{3}$$

where

$$\{\varepsilon_{0s}\} = \left\{\psi_x, \psi_y\right\}^T = \left\{\theta_y + \frac{\partial w}{\partial y}, \theta_x + \frac{\partial w}{\partial x}\right\}^T, \{k_s\} = \left\{\psi_x^*, \psi_y^*\right\}^T = \left\{3\theta_y^*, 3\theta_x^*\right\}^T.$$

2.2 Constitutive Equations of Piezoelectric Lamina

The linear constitutive equations for the k -th piezoelectric lamina with reference to its principal axes are given by:

$$\begin{aligned} \{\hat{\sigma}\}_k &= [\bar{Q}]_k\{\hat{\varepsilon}\} - [\bar{e}]_k^T\{E\}_k \\ \{\hat{D}\}_k &= [\bar{e}]_k\{\hat{\varepsilon}\} + [\bar{\xi}]_k\{E\}_k \end{aligned} \tag{4}$$

where $\{\hat{\sigma}\}$,$\{\hat{\varepsilon}\}$, $\{\hat{D}\}$ and $\{E\}$ are stress, strain, electric displacement and electric field vector, respectively. $[\bar{Q}]$, $[\bar{e}]$ and $[\bar{\xi}]$ are plane-stress reduced stiffness coefficients, the piezoelectric coefficients and the permittivity constant matrices, respectively. In the above equations, a superscript T denotes the transpose of a matrix. Equation (4a) describes the inverse piezoelectric effect and Eq. (4b) describes the direct piezoelectric effect. Next, we assume that the piezoelectric material exhibits orthorhombic 2 mm symmetry. After transforming Eq. (4) to the global coordinate system (x, y, z) and separating the bending and shear related variables, the constitutive Eq. (4) becomes

$$\begin{aligned} \{\sigma_b\} &= [Q_b]\{\varepsilon_b\} - [e_b]^T\{E\} \\ \{\sigma_s\} &= [Q_s]\{\varepsilon_s\} - [e_s]^T\{E\} \\ \{D\} &= [e_b]\{\varepsilon_b\} + [e_s]\{\varepsilon_s\} + [\xi]\{E\} \end{aligned} \tag{5}$$

where $\{\sigma_b\} = \{\sigma_{xx}, \sigma_{yy}, \tau_{xy}\}^T$, $\{\sigma_s\} = \{\tau_{yz}, \tau_{xz}\}^T$ and

$$[Q_b]_k = \begin{bmatrix} Q_{11} & Q_{12} & Q_{16} \\ Q_{21} & Q_{22} & Q_{26} \\ Q_{16} & Q_{26} & Q_{66} \end{bmatrix}, \quad [Q_s] = \begin{bmatrix} Q_{44} & Q_{45} \\ Q_{45} & Q_{55} \end{bmatrix}$$

$$[e_b] = \begin{bmatrix} 0 & 0 & 0 \\ 0 & 0 & 0 \\ e_{31} & e_{32} & e_{36} \end{bmatrix}, [e_s] = \begin{bmatrix} e_{14} & e_{15} \\ e_{25} & e_{25} \\ 0 & 0 \end{bmatrix}, [\xi] = \begin{bmatrix} \xi_{11} & \xi_{12} & 0 \\ \xi_{21} & \xi_{22} & 0 \\ 0 & 0 & \xi_{33} \end{bmatrix} \tag{6}$$

In Eq. (6), Q_{kl}, e_{kl} and ξ_{kl} are the transformed reduced elastic, piezoelectric and permittivity constants of the kth lamina, respectively. The detailed expressions for transformed material constants can be obtained from [21]. For non-piezoelectric layer the material constants e_{kl} and ξ_{kl} should be zero.

2.3 Electric Field

It is assumed that the electric field acts in the thickness direction. Also, this paper considers piezoelectric elements with electrodes on the top and bottom surfaces and poled in the thickness direction. Thus, for most of the typical piezoelectric laminate structures with relatively small thickness of the piezolayers in comparison to the overall laminate thickness, the electric field inside the k-th piezoelectric layer can be expressed as

$$\{E\}_k = [B_\phi]_{p_k} \phi^{p_k} \tag{7}$$

where

$$[B_\phi]_{p_k} = \begin{bmatrix} 0 & 0 & -\frac{1}{h^{p_k}} \end{bmatrix}$$

and h^{p_k}, ϕ^{p_k} are the thickness and the difference of electric potential between the electrodes covering the surface on each side of the piezoelectric layer p_k. It should be noted that such formulation gives one electric degree of freedom per layer per element of the electric field.

2.4 Finite Element Formulation

It is well known that the analytical solutions of laminated composite structure bonded with and without functional materials are very tough due to their material and geometrical complexities. However, FEM has been proved to be a robust numerical tool for such kind of complex analysis. In this present study, the smart plate model has been discretized using a nine nodded isoparametric quadrilateral Lagrangian element with seven degrees of freedom (DOF) per node. The element is developed to include the stiffness and the electromechanical coupling of the piezoelectric sensor/actuator layers. The generalized displacement vector for any point within a typical element e may be expressed as:

$$\{\bar{u}(x, y, t)\} \equiv \{u, v, w, \theta_x, \theta_y, \theta_x^*, \theta_y^*\}^T = [N_u]\{d\}_e = \sum_{i=1}^{9} (N_i [I]_{7\times 7} \{d_i\}_e) \tag{8}$$

where $\{d_i\}_e = \{u_i, v_i, w_i, \theta_{xi}, \theta_{yi}, \theta_{xi}^*, \theta_{yi}^*\}^T$ corresponding to the i-th node of the element and N_i are the shape functions.

Substituting (8) into Eqs. (2) and (3) gives:

$$\{\varepsilon(x, y, t)\} = [B]\{d\}_e = \sum_{i=1}^{9} ([B_i]\{d_i\}_e) \tag{9}$$

or equivalent:

$$\{\bar{\varepsilon}\} = \begin{Bmatrix} \{\varepsilon_{b0}\} \\ \{k\} \\ \{k^*\} \\ \{\varepsilon_{s0}\} \\ \{k_s\} \end{Bmatrix} = \begin{bmatrix} [B_b] \\ [B_k] \\ [B_{k^*}] \\ [B_s] \\ [B_{ks}] \end{bmatrix} \{d\}_e = \sum_{i=1}^{9} \left(\begin{bmatrix} [B_b]_i \\ [B_k]_i \\ [B_{k^*}]_i \\ [B_s]_i \\ [B_{ks}]_i \end{bmatrix} \{d_i\}_e \right)$$

where

$$[B_b]_i = \begin{bmatrix} \partial_x & 0 & 0 & 0 & 0 & 0 & 0 \\ 0 & \partial_y & 0 & 0 & 0 & 0 & 0 \\ \partial_y & \partial_x & 0 & 0 & 0 & 0 & 0 \end{bmatrix} N_i, \quad [B_k]_i = \begin{bmatrix} 0 & 0 & 0 & \partial_x & 0 & 0 & 0 \\ 0 & 0 & 0 & 0 & \partial_y & 0 & 0 \\ 0 & 0 & 0 & \partial_y & \partial_x & 0 & 0 \end{bmatrix} N_i$$

$$[B_{k^*}]_i = \begin{bmatrix} 0 & 0 & 0 & 0 & 0 & \partial_x & 0 \\ 0 & 0 & 0 & 0 & 0 & 0 & \partial_y \\ 0 & 0 & 0 & 0 & 0 & \partial_y & \partial_x \end{bmatrix} N_i, \quad [B_s]_i = \begin{bmatrix} 0 & 0 & \partial_x & 1 & 0 & 0 & 0 \\ 0 & 0 & \partial_y & 0 & 1 & 0 & 0 \end{bmatrix} N_i$$

$$[B_{k_s}]_i = \begin{bmatrix} 0 & 0 & 0 & 0 & 0 & 3 & 0 \\ 0 & 0 & 0 & 0 & 0 & 0 & 3 \end{bmatrix} N_i$$

and $\partial_x = \frac{\partial}{\partial x}$, $\partial_y = \frac{\partial}{\partial y}$.

In general, piezocomposite structures may comprise more than one piezoelectric layer, e.g. a number of N_{pe} piezoelectric layers. Therefore, electrical quantities are observed layerwise, and in the finite element model they are given in the condensed form of vectors $\{E\}_e$ and $\{\phi\}_e$ defined on the element level.

Thus after the discretization of the structure, the differences of electric potentials of all piezoelectric layers across the thickness of the element can be expressed as:

$$\{\phi\}_e = \{\phi^1, \phi^2, \ldots, \phi^{N_{pe}}\}^T \tag{10}$$

where N_{pe} is the number of the piezoelectric layers of the e^{th} element. The electric field distribution can be written as:

$$\{E\}_e = [B_\phi]\{\phi\}_e$$

where $[B_\phi] = diag([B_\phi]_1, [B_\phi]_2, \ldots, [B_\phi]_{Npe})$ is the electric field-electric potential matrix, which has a diagonal form since the difference of electric potentials of a piezo-layer affects the electric field only of the very same layer.

2.5 Variational Principle

This formulation will be based on the Hamilton variational principle in which the strain potential energy, kinetic energy and work are considered for the entire structure. Since we are dealing with the piezoelectric continuum, the Lagrangian will be properly adapted in order to include the contribution from the electrical field besides the contribution from the mechanical field. The most general form of this variational principle is stated as:

$$\int_0^T (\delta T - \delta U + \delta W)\,\mathrm{d}t \tag{11}$$

where T is the total kinetic energy, U is the total strain energy and W is the work done by the loads.
The strain energy of a piezocomposite element is given by:

$$\begin{aligned}
U &= \frac{1}{2}\int_{V_e} (\{\varepsilon_b\}^T\{\sigma_b\} + \{\varepsilon_s\}^T\{\sigma_s\})\,\mathrm{d}V \\
&= \frac{1}{2}\int_{V_e} (\{\varepsilon_{b0}\}^T[Q_b]\{\varepsilon_{b0}\} + \{\varepsilon_{b0}\}^T z[Q_b]\{k\} + \{\varepsilon_{b0}\}^T z^3[Q_b]\{k^*\} \\
&\quad +\{k\}^T z[Q_b]\{\varepsilon_{b0}\} + \{k\}^T z^2[Q_b]\{k\} + \{k\}^T z^4[Q_b]\{k^*\} \\
&\quad +\{k^*\}^T z^3[Q_b]\{\varepsilon_{b0}\} + \{k^*\}^T z^4[Q_b]\{k\} + \{k^*\}^T z^6[Q_b]\{k^*\} \\
&\quad +\{\varepsilon_{s0}\}^T[Q_s]\{\varepsilon_{s0}\} + \{\varepsilon_{s0}\}^T z^2[Q_s]\{k_s\} \\
&\quad +\{k_s\}^T z^2[Q_s]\{\varepsilon_{s0}\} + \{k_s\}^T z^4[Q_s]\{k_s\} \\
&\quad -\{\varepsilon_{b0}\}^T[e_b]^T\{E\} - \{k\}^T z[e_b]^T\{E\} - \{k^*\}^T z^3[e_b]^T\{E\} \\
&\quad -\{\varepsilon_{s0}\}^T[e_s]^T\{E\} - \{k_s\}^T z[e_s]^T\{E\})\,\mathrm{d}V \\
&= \frac{1}{2}\int_{V_e} \begin{bmatrix} \{\varepsilon_{b0}\} \\ \{k\} \\ \{k^*\} \\ \{\varepsilon_{s0}\} \\ \{k_s\} \end{bmatrix}^T \begin{bmatrix} [Q_b] & z[Q_b] & z^3[Q_b] & 0 & 0 \\ z[Q_b] & z^2[Q_b] & z^4[Q_b] & 0 & 0 \\ z^3[Q_b] & z^4[Q_b] & z^6[Q_b] & 0 & 0 \\ 0 & 0 & 0 & [Q_s] & z^2[Q_s] \\ 0 & 0 & 0 & z^2[Q_s] & z^4[Q_s] \end{bmatrix} \begin{bmatrix} \{\varepsilon_{b0}\} \\ \{k\} \\ \{k^*\} \\ \{\varepsilon_{s0}\} \\ \{k_s\} \end{bmatrix} \mathrm{d}V
\end{aligned}$$

$$-\frac{1}{2}\int\limits_{V_e}\begin{bmatrix}\{\varepsilon_{b0}\}\\ \{k\}\\ \{k^*\}\\ \{\varepsilon_{s0}\}\\ \{k_s\}\end{bmatrix}^T \begin{bmatrix}[\varepsilon_b]^T\\ z[\varepsilon_b]^T\\ z^3[\varepsilon_b]^T\\ [\varepsilon_s]^T\\ z^2[\varepsilon_s]^T\end{bmatrix}\{E\}\mathrm{d}V$$

$$=\frac{1}{2}\int\limits_{V_e}(\{\bar{\varepsilon}\}^T[\mathscr{D}(z)]\{\bar{\varepsilon}\}-\{\bar{\varepsilon}\}^T[\mathscr{E}(z)]\{E\})\mathrm{d}V \tag{12}$$

where V_e is the volume of an element. Substituting for $\{\varepsilon_{b0}\}$, $\{k\}$, $\{k^*\}$, $\{\varepsilon_{s0}\}$, $\{k_s\}$ and $\{E\}$ in Eq. (12), U can be written as:

$$U=\frac{1}{2}\{d\}_e^T[K_{uu}]_e\{d\}_e-\frac{1}{2}\{d\}_e^T[K_{u\phi}]_e\{\phi\}_e \tag{13}$$

where

$$[K_{uu}]_e=\sum_{k=1}^{N}\left[\int\limits_{V_k}([B]^T[\mathscr{D}(z)]_k[B]\mathrm{d}V_k\right]$$

$$[K_{u\phi}]_e=\left[\int\limits_{V_{p_1}}[B]^T[\mathscr{E}(z)]_{p_1}[B_\phi]_{p_1}\mathrm{d}V_{p_1}\int\limits_{V_{p_2}}[B]^T[\mathscr{E}(z)]_{p_2}[B_\phi]_{p_2}\mathrm{d}V_{p_2}\dots\right.$$
$$\left.\dots\int\limits_{V_{p_{N_e}}}[B]^T[\mathscr{E}(z)]_{p_{N_e}}[B_\phi]_{p_{N_e}}\mathrm{d}V_{p_{N_e}}\right]$$

and V_k is the volume of the k-th layer, V_{p_k} is the volume of the p_k-th piezoelectric layer inside an element and N is the number of lamina.

The element kinetic energy is given by:

$$T=\frac{1}{2}\sum_{i=1}^{N}\int\limits_{V_k}\rho_k\left[\{\dot{u_1}\}^2+\{\dot{u_1}\}^2+\{\dot{u_1}\}^2\right]\mathrm{d}V_k \tag{14}$$

where ρ_k is the density of the k-th layer. Substituting the displacements relations (1), Eq. (14) becomes:

$$T=\frac{1}{2}\sum_{i=1}^{N}\int\limits_{V_k}\rho_k[\dot{u}^2+2z\dot{u}\dot{\theta}_x+2z^3\dot{u}\dot{\theta}_x^*+\dot{v}^2+2z\dot{v}\dot{\theta}_y+2z^3\dot{v}\dot{\theta}_y^*+\dot{w}^2$$
$$+z^2\dot{\theta}_x^2+2z^4\dot{\theta}_x\dot{\theta}_x^*+z^6(\dot{\theta}_x^*)^2+z^2\dot{\theta}_y^2+2z^4\dot{\theta}_y\dot{\theta}_y^*+z^6(\dot{\theta}_y^*)^2]\mathrm{d}V_k$$

$$= \frac{1}{2}\sum_{k=1}^{N}\int_{V_k}\rho_k \begin{Bmatrix} u \\ v \\ w \\ \theta_x \\ \theta_x^* \\ \theta_y \\ \theta_y^* \end{Bmatrix}^T \begin{bmatrix} 1 & 0 & 0 & z & 0 & z^3 & 0 \\ 0 & 1 & 0 & 0 & z & 0 & z^3 \\ 0 & 0 & 1 & 0 & 0 & 0 & 0 \\ z & 0 & 0 & z^2 & 0 & z^4 & 0 \\ 0 & z & 0 & 0 & z^2 & 0 & z^4 \\ z^3 & 0 & 0 & z^4 & 0 & z^6 & 0 \\ 0 & z^3 & 0 & 0 & z^4 & 0 & z^6 \end{bmatrix} \begin{Bmatrix} u \\ v \\ w \\ \theta_x \\ \theta_x^* \\ \theta_y \\ \theta_y^* \end{Bmatrix} \mathrm{d}V$$

$$= \frac{1}{2}\sum_{k=1}^{N}\int_{V_k}\{\dot{\bar{u}}\}^T[I(z)]_k\{\dot{\bar{u}}\}\mathrm{d}V \tag{15}$$

Substituting Eq. (8) in the relation (15), one obtains:

$$T = \frac{1}{2}\{\dot{d}\}_e^T[M]_e\{\dot{d}\}_e \tag{16}$$

where

$$[M]_e = \int_{A_e}\sum_{k=1}^{N}\int_{z_{k-1}}^{z_k}[N]^T[I(z)]_k[N]\mathrm{d}z\mathrm{d}A$$

where A_e is the area of the element and z_{k-1}, z_k are the z coordinates of laminates corresponding to the top and bottom surface of the k-th layer.

The total work W is the sum of the work done by the electrical forces W_E and the work done by the mechanical forces W_m. Using constitutive relations, strain displacement and electric field-electric potential relations, the element electrical energy can be written as:

$$\begin{aligned} W_E &= \frac{1}{2}\sum_{k=1}^{N_{pe}}\int_{V_{pk}}\{E\}_k^T\{D\}_k\mathrm{d}V = \frac{1}{2}\sum_{k=1}^{N_{pe}}\int_{V_{pk}}\{E\}_k^T([e_b]_k\{\varepsilon_b\} + [e_s]_k\{\varepsilon_s\} + [\xi]_k\{E\}_k)\mathrm{d}V \\ &= \frac{1}{2}\{\phi\}_e^T\int_{V_p}[B_\phi]^T[\xi][B]\mathrm{d}V\{d\}_e + \frac{1}{2}\{\phi\}_e^T\int_{V_p}[B_\phi]^T[\xi][B_\phi]\mathrm{d}V\{\phi\}_e \\ &= \frac{1}{2}\{\phi\}_e^T[K_{\phi u}]_e\{d\}_e + \frac{1}{2}\{\phi\}_e^T[K_{\phi\phi}]_e\{\phi\}_e \end{aligned} \tag{17}$$

where

$$[K_{\phi\phi}]_e = diag\left(\int\limits_{V_{p1}} [B_\phi]^T_{p_1}[\xi]_{p_1}[B_\phi]_{p_1}\mathrm{d}V_{p_1}, \int\limits_{V_{p2}} [B_\phi]^T_{p_2}[\xi]_{p_2}[B_\phi]_{p_2}\mathrm{d}V_{p_2}, \ldots, \right.$$
$$\left. \ldots, \int\limits_{V_{p_{N_e}}} [B_\phi]^T_{p_{N_e}}[\xi]_{p_{N_e}}[B_\phi]_{p_{N_e}}\mathrm{d}V_{p_{N_e}}\right)$$

$[K_{\phi u}]_e = [K_{\phi\phi}]_e^T$ and V_p is the volume of the piezoelectric layer.

The work done by the mechanical forces is given by:

$$\begin{aligned}
W_m &= \{\bar{u}\}^T\{f_c\} + \int\limits_{S_1}\{\bar{u}\}^T\{f_s\}\mathrm{d}S + \int\limits_{V}\{\bar{u}\}^T\{f_v\}\mathrm{d}V - \int\limits_{S_2}\{E\}^T\{f_\phi\}\mathrm{d}S \\
&= \{d\}_e^T[N]^T\{f_c\} + \{d\}_e^T\int\limits_{S_1}[N]^T\{f_s\}\mathrm{d}S + \{d\}_e^T\int\limits_{V}[N]^T\{f_v\}\mathrm{d}V - \\
&- \{\phi\}_e^T\int\limits_{S_2}[B_\phi]^T\{f_\phi\}\mathrm{d}S \\
&= \{d\}_e^T\{F_m\}_e + \{\phi\}_e^T\{F_\phi\}_e
\end{aligned} \tag{18}$$

In Eq. (18), $\{f_c\}$ denotes the concentrated forces intensity, $\{f_s\}$ and $\{f_v\}$ denote the surface and volume force intensity, respectively and $\{f_\phi\}$ denotes the surface charge density. S_1 and S_2 are the surface areas where the mechanical forces and electrical charge are applied, respectively. $\{F_m\}_e$ are the applied mechanical forces at each element and $\{F_\phi\}_e$ are the applied electrical charges at each element.

2.6 Equations of Motion

Using Hamilton s principle (11) the resultant global FE spatial model, governing the motion and electric charge equilibrium, is given by:

$$\begin{aligned}
[M]\left\{\ddot{d}\right\} + [K_{uu}]\{d\} + \left[K_{u\phi}\right]\{\phi\} &= \{F_m\} \\
\left[K_{\phi u}\right]\{d\} + \left[K_{\phi\phi}\right]\{\phi\} &= \left\{F_\phi\right\}
\end{aligned} \tag{19}$$

where $\{d\}$ and $\{\phi\}$ are the global mechanical and electrical DoFs vectors, $[M]$ is the global mass matrix, $[K_{uu}]$, $\left[K_{u\phi}\right] = \left[K_{u\phi}\right]^T$ and $\left[K_{\phi\phi}\right]$ are the global mechanical stiffness, mechanical-electrical coupling stiffness and dielectric stiffness matrices respectively. $\{F_m\}$ and $\left\{F_\phi\right\}$ are the respective global mechanical and electrical loading vectors.

Next we assume that the electrical DoFs vector in Eq. (19) can be divided into the actuating and sensing DoFs, $\{\phi\}_e = \{\phi_a, \phi_s\}^T$, where the subscripts a and s denote the actuating and sensing capabilities. Hence, considering open-circuit electrodes, and in that case $\left\{F_\phi\right\} = 0$, the non-specified potential differences in (19) can be statically condensed and the equations of motion and charge equilibrium become:

$$\begin{aligned}[M]\left\{\ddot{d}\right\} + \left[K_{uu}^*\right]\{d\} &= \{F_m\} - \left[K_{u\phi}\right]_a \{\phi\}_a \\ \{\phi\}_s &= -\left[K_{\phi\phi}\right]_s^{-1}\left[K_{\phi u}\right]_s \{d\}\end{aligned} \tag{20}$$

where $\left[K_{uu}^*\right] = [K_{uu}] - \left[K_{u\phi}\right]_s \left[K_{\phi\phi}\right]_s^{-1} \left[K_{\phi u}\right]_s$.

Equation (20) can be used in smart structures applications such as vibration control, static or dynamic shape control, etc. In shape control applications, the piezoelectric layers are used as actuators. In addition the time-dependent momentum forces become zero. Thus, all the electrical degrees are considered as known quantities and the coupled equations (20) reduce to pure mechanical ones:

$$[K_{uu}]\{d\} = \{F_m\} - \{F_{el}\} \tag{21}$$

where $\{F_{el}\} = \left[K_{u\phi}\right]\{\phi\}$ is the electrical force vector due to the actuation.

2.7 Modal Model in Terms of State Space

The application of the active control methods in dynamic structural problem requires the use of a state space model. Before we obtain this kind of equations, a mode superposition method is adopted to obtain an approximate reduced-order dynamic model of the system with uncoupled equations of motion in the modal coordinates. Hence $\{d(t)\}$ can be approximated by:

$$\{d\} \approx \sum_{i=1}^{r} \Phi_j \eta_j = [\Phi]\{\eta\} \tag{22}$$

where $[\Phi] = [\Phi_1, \Phi_2, \cdots, \Phi_r]$ is the truncated modal matrix and $\{\eta\} = \{\eta_1, \eta_2, \cdots, \eta_r\}$ is the modal coordinate vector. Substituting Eq. (22) into Eq. (20) leads to:

$$\{\ddot{\eta}\} + \left[\Omega^2\right]\{\eta\} = [\Phi]^T\{F_m\} - [\Phi]^T\left[K_{u\phi}\right]_\alpha \{\phi\}_\alpha \tag{23}$$

$$\{\phi\}_s = -\left[K_{\phi\phi}\right\}_s^{-1}\left[K_{u\phi}\right]_s [\Phi]^T\{\eta\} \tag{24}$$

Also, using the modal approach, structural damping can be easily introduced as:

$$\{\ddot{\eta}\} + [\Lambda]\{\dot{\eta}\} + [\Omega]\{\eta\} = [\Phi]^T\{F_m\} - [\Phi]^T\left[K_{u\phi}\right]_\alpha \{\phi\}_\alpha \tag{25}$$

where $[\Lambda]$ is a diagonal modal damping matrix with the generic term $2\xi_i\omega_i$, where ξ_i is the modal damping ratio and ω_i the undamped natural frequency of the i-th mode.

For control design, the Eqs. (25) and (24) are transformed into state-space form as follows:

$$\{\dot{x}\} = [A]\{x\} + [B]\left\{u_\phi\right\} + \{f\} \tag{26}$$

$$\{\phi\}_s = \{y\} = \{C\}\{x\} \tag{27}$$

where $\{x\} = \{\eta, \dot{\eta}\}^T$ is the state vector, $[A]$ is the system matrix, $[B]$ is the control matrix, $\{f\}$ is the disturbance input vector and $\left\{u_\phi\right\} = \{\phi\}_\alpha$ is the control input to the actuator.

These matrices are given by

$$[A] = \begin{bmatrix} [0] & [I] \\ \left[-\Omega^2\right] & [\Lambda] \end{bmatrix} \qquad [B] = \begin{bmatrix} [0] \\ -[\Phi]^T\left[K_{u\phi}\right]_a \end{bmatrix}$$

$$\{f\} = \begin{bmatrix} [0] \\ [\Phi]^T\{F_m\} \end{bmatrix} \qquad [C] = \left[-\left[K_{\phi\phi}\right]_s^{-1}\left[K_{\phi u}\right]_s[\Phi]\,[0]\right] \tag{28}$$

2.8 Control Law

The state-space system Eq. (26) is now applied to the design of an optimal controller. The control algorithm considered here is the linear quadratic regulator (LQR) controller. The control voltage in this case is given by:

$$\{u_\phi\} = [G]\{x\} \tag{29}$$

in which the feedback control gain $[G]$ is obtained so as to minimize the quadratic cost function of the form:

$$J = \frac{1}{2}\int_0^\infty \left(\{x\}^T[Q]\{x\} + \{u\}^T[R]\{u\}\right)\mathrm{d}t \tag{30}$$

subjected to system equation (26). $[Q]$ and $[R]$ are the semi-positive-definite and positive-definite weighting matrices on the outputs and control inputs, respectively. In our case higher values in $[Q]$ mean that we demand more vibration suppression ability from the controller, while larger values in $[R]$ put more interest in limiting the control effort. Assuming infinite optimization horizon and full state feedback, the control gain $[G]$ in (29) is given by:

$$[G] = -[R]^{-1}[B]^T[P] \tag{31}$$

where $[P]$ is a solution of the Riccati equation.

$$[A]^T[P] + [P][A] - [P][B][R]^{-1}[B]^T[P] + [Q] = 0 \tag{32}$$

An advantage of the linear quadratic formulation of the problem is the linearity of the control law, which leads to easy analysis and practical implementation. Another advantage is that the values of the gain and phase margins imply stability, good disturbance rejection and good tracking.

A computer program has been developed in MATLAB to perform all the necessary computations. Reduced integration technique is adopted to avoid shear and membrane locking during computation.

3 Numerical Applications

In this section, the formulation and finite element code developed in the present work is validated with existing results documented in the literature. For static deflection, a piezoelectric bimorph cantilever beam is considered and for dynamic analysis a cantilever piezocomposite plate is considered. After the validation work, shape control and vibration suppression of piezocomposite multilayer plate is investigated.

3.1 Validation Example 1

To validate the static analysis, a piezoelectric bimorph cantilever beam (100 × 5 × 1 mm) constructed of two layers of PVDF bonded together and polarized in opposite directions is considered. The total height or thickness is 0.001 m, the length is 0.1 m and the width is 0.005 m. The cantilever is fixed on the left end and electric potential is applied such that the top layer is $0.5V$ and the bottom layer is $0.5\ V$. The material properties of the PVDF material are given as: $E_1 = E_2 = 2.0\ E^9 \mathrm{N/m}^2$, $G_{12} = G_{13} = G_{23} = 7.75\ E^9 \mathrm{N/m}^2$ and $e_{31} = 0.046$ N/Vm. The bimorph beam is modelled using five beam elements of equal length. This particular example has been considered by several researchers (see e.g. [5–7]). The numerical results for the present method are compared with results from other methods in Table 1. Veley and Rao [6] used a 2D plane stress element modified with pseudo-nodes to include the electric potential DOF. Tzou and Ye [7], using triangular shell elements which have both mechanical (using FOSDT) and electrical DOFs, showed that they produced better results than the thin solid linear elements used by Tzou [7]. Chee et al. [10] used a mixed finite element model, which uses Hermitian beam elements with electric potential incorporated via the layerwise formulation. The present results fit exactly with those of Chee et al. and has a high correlation with Tzou 's theoretical shell solutions and the results of Veley and Rao. This comparison suggests that

Table 1 Transverse Displacement w (m) of the bimorph beam

Nodes	x (m)	Present	FE-Chee et al. [10]	Theory-Tzou et al. [7]	FEM Veley et al. [6]
1	0.00	0.00	0.00	0.00	0.00
2	0.02	1.380×10^{-8}	1.380×10^{-8}	1.380×10^{-8}	1.380×10^{-8}
3	0.04	5.520×10^{-8}	5.520×10^{-8}	5.520×10^{-8}	5.520×10^{-8}
4	0.06	1.242×10^{-7}	1.242×10^{-7}	1.240×10^{-7}	1.240×10^{-7}
5	0.08	2.208×10^{-7}	2.208×10^{-7}	2.210×10^{-7}	2.210×10^{-7}
6	0.10	3.450×10^{-7}	3.450×10^{-7}	3.450×10^{-7}	3.450×10^{-7}

the developed finite element code is capable of analyzing cases where piezoelectric material in the structures is used for actuation.

3.2 *Validation Example 2*

To validate the dynamic analysis, a cantilever composite plate (20×20 cm) with continuous piezoceramic layers bonded to the surface (top and bottom) is considered (Fig. 2). The stacking sequence the composite is antisymmetric angle-ply ($[-45^o/45^o/-45^o/45^o]$). The plate is made of T300/976 graphite-epoxy composite and the piezoceramic is PZT G1195N. The material properties are given in Table 2. The total thickness of the composite is 1 mm and each layer has the same thickness (0.25 mm); the thickness of each PZT is 0.1 mm. The plate is modelled using the present nine-node elements with a mesh size of 6×6. The first ten circular frequencies based on the present element are compared with those obtained by Lam et al., [8] in Table 3. Lam et al. [8] used a rectangular nonconforming plate bending element

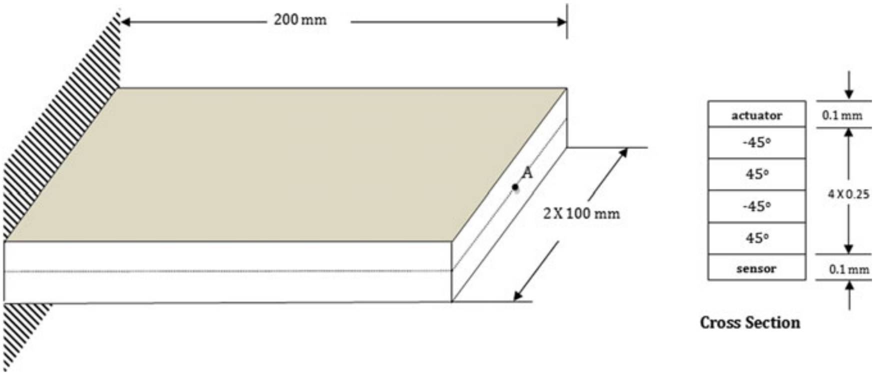

Fig. 2 The cantilever piezocomposite plate

Table 2 Material properties of T300/976 graphiteepoxy composites and PZT G1195N piezoceramics

	T300/976	PZT
Young's moduli (GPa):		
E_1	150.0	63.0
E_2	9.0	63.0
Poisson ratio:	0.3	0.3
Shear moduli (GPa):		
G_{12}	7.1	24.2
$G_{23} = G_{13}$	2.5	24.2
Density $\rho (kgm^{-3})$	1600	7600
Piezoelectric constants (mV^{-1}):		
$d_{31} = d_{32}$	–	254×10^{-12}
Electrical permittivity (Fm^{-1}):		
$\xi_{11} = \xi_{22}$	–	15.3×10^{-9}
ξ_{33}	–	15.0×10^{-9}

Table 3 Natural frequencies (in Hz) for the piezocomposite plate

Mode	Results of Lam et al. [8]	Present
1	21.7558	21.4655
2	64.6483	63.3468
3	130.8456	130.8108
4	185.9157	182.4012
5	221.4875	218.2537
6	382.2130	381.9080
7	407.1130	395.6595
8	415.6272	410.8062
9	482.9578	476.3271
10	669.5056	642.7275

based on classical plate theory. It can be easily observed that the present values are showing good agreement with the results of Lam et al. and the difference between the results are within the expected line. The minor difference was expected because the model of Ref. [8] used low order classical displacement field.

3.3 Shape Control Applications

Having validated the model and finite element method code, we present a numerical example to demonstrate the use of this code for the simulation of the response of laminated composite plates with integrated piezoelectric sensor and actuator in active

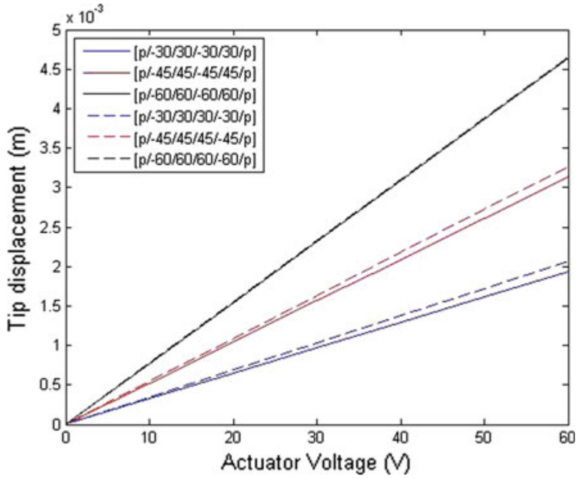

Fig. 3 Effect of symmetric and asymmetric ply orientation on the deflection of point A for different applied voltage

deformations and vibration control. The physical model is the same as in the previous dynamic study.

First, the static analysis and deformation control of the composite plate are presented. In the static analysis, all the piezoceramics on the upper and lower surfaces of the plate are used as actuators. Equal voltages with opposite signs are applied across the thickness of the upper and lower piezoelectric layer, respectively. Figure 3 shows the corresponding displacements at the tip point A for different applied actuator voltages under different symmetric angle-ply lay up $[p/\theta/\theta/\theta/\theta/p]$ and antisymmetric angle-ply layup $[p/\theta/\theta/\theta/\theta/p]$. It can be concluded from Fig. 3 that there is a linear relationship between the plate s centerline deflection and the actuator 's input voltage. Also, it is observed that with an increase in the angle θ, an increase of tip deflection is obtained under same applied actuator voltage in both type of layup. However, deflection is more in case of the symmetric angle-ply lay up than the antisymmetric angle-ply lay up.

For practical applications one would like to know the optimal actuation value with respect to a given shape control task. A first attempt has been done here by classical trial and error techniques. After some numerical experiments the more satisfactory results are shown in Fig. 4.

The centerline deflection under the action of a uniform distributed load of $100\,\mathrm{N\,m^{-2}}$ for different values of the actuation is shown in Fig. 3. The task has been the reduction of plate's deflections due to loading. The results are directly comparable with that published in paper [8].

Fig. 4 The centerline deflection under uniform load and different actuator input voltages

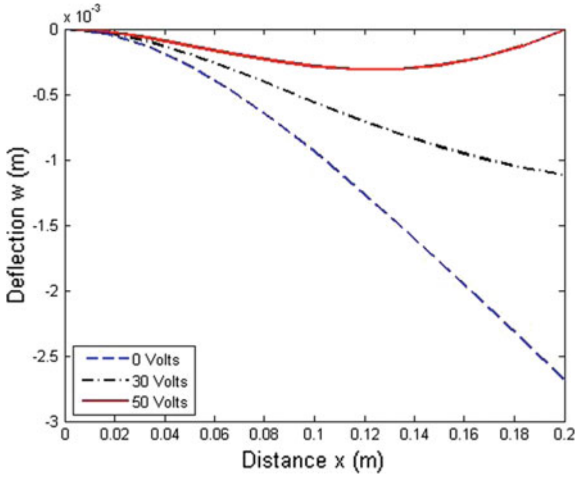

3.4 Vibration Control Applications

In order to investigate the active vibration control of the composite plate, the same structure as in validation example 2 is considered again except that the piezoelectric layers are not located on the entire top and bottom faces of the plate. In the present case, only the first six elements near the clamped edge are covered (on the top and bottom) by piezoelectric patches. In vibration control, the upper piezoceramics serve as sensors and the lower ones as actuators. The first six modes are used in the modal space analysis and an initial modal damping ratio for each of the modes is assumed to be 0.4%. The plate is subjected to a vertical impulse at its tip and the disturbance in a structure is suppressed by using the linear quadratic regulator (LQR) as a control measure.

To design the feedback control using LQR, the appropriate selection of the weighting matrices $[Q]$ and $[R]$ plays a vital role. To estimate the weighting matrices and provide an insight into weighting matrices on structural response and actuator voltage, the effect of $[Q]$ and $[R]$ on vibration response and control voltage is investigated in the following.

The value of the $[Q]$ matrix is changed as $(10^5, 10^6, 10^7)$ $I_{12\times12}$ in the LQR procedure given by Eqs. (29) and (31), while the value of $[R]$ is kept constant as $[R] = \gamma\ I_{36\times36}$ with $\gamma = 1$. One should note that the order of matrix $[Q]$ is determined according to the number of state variables, $\{x\}$, which is defined by the number of vibration modes considered in the control system. Here, the first six modes the vibration control is considered. Similarly, the order of matrix $[R]$ is determined according to the number of actuators of the system. In the present example, each finite element is assumed to covered by an actuator requiring a dimension of 36×36 for matrix $[R]$. The LQR function in MATLAB is used to find the optimal gain, which decides the gain based on the system matrix, disturbance matrix and control matrix

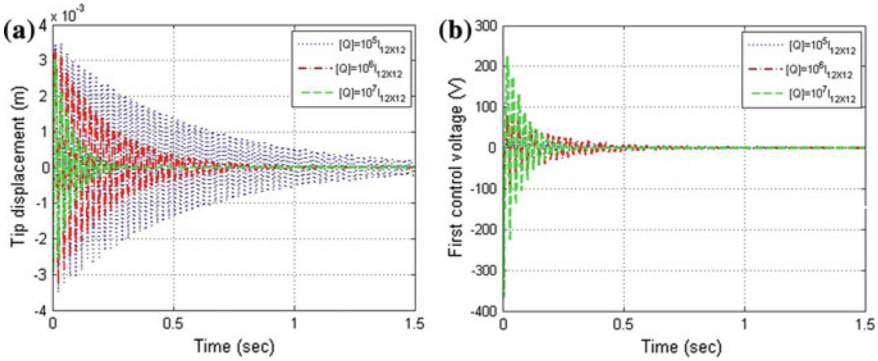

Fig. 5 Effect of the [Q] matrix coefficient on **a** tip displacement and **b** applied voltage

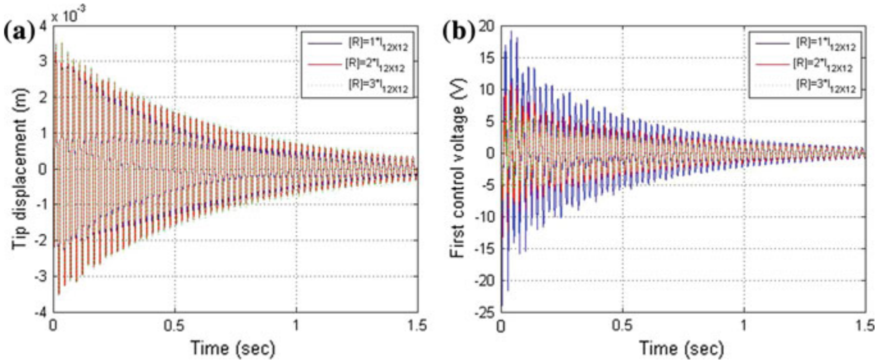

Fig. 6 Effect of the [R] matrix coefficient on **a** tip displacement and **b** applied voltage

as explained in Eq. (29). Using the determined feedback control, the tip displacement and the control voltage for the first mode of the smart laminated plate are obtained as shown in Fig. 5. It is observed that the higher value of $[Q]$ results in lower settling time but higher applied voltage (Fig. 5).

In another investigation, the coefficient γ of the $[R]$ matrix is changed from 1 to 3 in the LQR procedure, while the value of $[Q]$ is kept constant as $[Q] = 10^5\ I_{12\times 12}$. Next, the feedback gain is determined according to each $[R]$ value. Using the determined feedback control, the tip displacement and control voltage of the first actuator are obtained as shown in Fig. 6. It is observed that increasing the value of the $[R]$ matrix decreases the required electric voltage but, on the other hand, it increases the settling time.

4 Conclusion

In this work, a theoretical and FE formulation for the analysis of anisotropic piezocomposite laminated plates was presented. The formulation was based on the third order shear deformation theory that accounts for parabolic distribution of the transverse shear strains through the thickness of the plate and rotary inertial effects and has been extended to incorporate the piezoelectric sensors and actuators layers. To implement the model, a nine-noded isoparametric element with seven degree of freedom per node and one electric degree of freedom per element per piezoelectric layer has been proposed. The element was developed to include stiffness and the electromechanical coupling of the piezoelectric sensor/actuator layers. Numerical experiments using a computer code, whose algorithm is based on the present finite element model, produced results that correlated well with other published results. After the validation work, numerical illustrations have been presented to study shape and vibration control of a cantilever piezocomposite plate. The effects of laminate configuration and applied voltage on shape control of the smart system have been investigated in this simulation study. Finally, the active vibration control performance of the piezocomposite plate was studied by applying LQR optimal control based on full state feedback assumption. The effects of weighting matrices on controlled response of the smart system have also been investigated.

More complicated adaptive fuzzy and neurofuzzy controllers have been recently studied by the authors [22]–[25] and can be used for control applications of the created model. Furthermore, extension to geometric or material nonlinearity is possible, within classical Newton–Raphson approaches.

References

1. Reddy, J.N.: A simple higher-order theory for laminated composite plate. J. Appl. Mech. **51**, 745–752 (1984)
2. Kant, T., Mallikarjuna, : A higher-order theory for free vibration of unsymmetrically laminated compositeand sandwich plates- Finite element evaluations. Comp. Struct. **32**(2a5), 1125–1132 (1989)
3. Goswami, S.: A C^0 plate bending element with refined shear deformation theory for composite structures. Compos. Struct. **72**, 375–382 (2006)
4. Lee, S.J., Kim, H.R.: FE analysis of laminated composite plates using a higher order shear deformation theory with assumed strains. Lat. Am. J. Solids Struct. **10**, 523–547 (2013)
5. Hwang, W.S., Park, H.C.: Finite element modelling of piezoelectric sensors and actuators. AIAA J. **31**, 930–937 (1993)
6. Veley D., Rao S.S.: Two-dimensional finite element modeling of composites with embedded piezoelectrics Collection Technical Papers Proceedings of the AIAA/ASME/ASCE/AHS/ASC Structures, Structural Dynamics and Materials Conference, vol. 5, pp 2629–2633 (1994)
7. Tzou, H.S., Ye, R.: Analysis of piezoelastic structures with laminated piezoelectric triangle shell elements. AIAA J. **34**, 110–115 (1996)
8. Lam, K.Y., Peng, X.Q., Liu, G.R., Reddy, J.N.: A finite-element model for piezoelectric composite laminates. Smart Mater. Struct. **6**, 583–591 (1997)

9. Peng, X.Q., Lam, K.Y., Liu, G.R.: Active vibration control of composite beams with piezoelectric: a finite element model with third order theory. J. Sound Vib. **209**, 635–650 (1998)
10. Chee, C.Y.K., Tong, L., Steven, G.P.: A mixed model for composite beams with piezoelectric actuators and sensors. Smart Mater. Struct. **8**, 417–432 (1999)
11. Wang, S.Y., Quek, S.T., Ang, K.K.: Vibration control of smart piezoelectric composite plates Smart Mater. Struct. **10**, 637–644 (2001)
12. Marinković, D., Köppe, H., Gabbert, U.: Numerically efficient finite element formulation for modeling active composite laminates. Mech. Adv. Mater. Struct. **13**(5), 379–379 (2006)
13. Ray, M.C., Bhattacharyya, R., Samanta, B.: Static analysis of an intelligent structure by the finite element method. Comp. Struc. **52**(4), 617–631 (1994)
14. Balamurugan, V., Narayanan, S.: A piezoelectric higher-order plate element for the analysis of multi-layer smart composite laminates. Smart Mater. Struct. **16**, 2026–2039 (2007)
15. Kogl, M., Bucalem, M.L.: A family of piezoelectric MITC plate elements. Comput. Struct. **83**, 1277–1297 (2005)
16. Phung-Van, P., De Lorenzis, L., Thai, C.H., Abdel-Wahab, M., Nguyen-Xuan, H.: Analysis of laminated composite plates integrated with piezoelectric sensors and actuators using higher-order shear deformation theory and isogeometric finite elements. Comput. Mater. Sci. **96**(Part B), 495–495 (2015)
17. Dutta, G., Panda, S.K., Mahapatra, T.R., Singh, V.K.: Electro-magneto-elastic response of laminated composite plate: A finite element approach. Intern. J. Appl. Comput. Math. **3**(3), 2573–2592 (2017). https://doi.org/10.1007/s40819-016-0256-6
18. Kienzler, R.: On Consistent Second-Order Plate Theories. In: Kienzler, R., Ott, I., Altenbach, H. (eds.) Theories of Plates and Shells: Critical Review and New Applications, pp. 85-96, Springer, Berlin (2004). https://doi.org/10.1007/978-3-540-39905-6_11
19. Schneider, P., Kienzler, R., Böhm, M.: Modeling of consistent second-order plate theories for anisotropic materials. Z. angew. Math. Mech. **94**, 21–42 (2014). https://doi.org/10.1002/zamm.201100033
20. Bousahla, A.A., Houari, M.S.A., Tounsi, A., Bedia, E.A.A.: A novel higher order shear and normal deformation theory based on neutral surface position for bending analysis of advanced composite plates. Int. J. Comput. Methods **11**(6), 1350082 (2014). https://doi.org/10.1142/S0219876213500825
21. Reddy, N.J.: Mechanics of Laminated Composite Plates: Theory and Analysis, CRC: New York, NY, USA (1997)
22. Marinaki, M., Marinakis, Y., Stavroulakis, G.E.: Fuzzy control optimized by a multi-objective particle swarm optimization algorithm for vibration suppression of smart structures. Struct. Multidiscip. Optim. **43**, 29–42 (2011). https://doi.org/10.1007/s00158-010-0552-4
23. Tairidis, G., Foutsitzi, G., Koutsianitis, P., Stavroulakis, G.E.: Fine tunning of a fuzzy controller for vibration suppression of smart plates using genetic algorithms. Adv. Eng. Softw. **101**, 123–135 (2016)
24. Tairidis, G.,: Optimal design of smart structures with intelligent control. PhD. Thesis, Technical University of Crete, Greece. http://hdl.handle.net/10442/hedi/38484Cited17April2017
25. Koutsianitis, P., Tairidis, G.K., Drosopoulos, G.A., Foutsitzi, G.A., Stavroulakis, G.E.: Effectiveness of optimized fuzzy controllers on partially delaminated piezocomposites. Acta Mech. **228**, 1373–1392 (2017). https://doi.org/10.1007/s00707-016-1771-6

Optimal Design of Disks Under Large Creep Deformation

Aneta Ustrzycka, Krzysztof Szuwalski and Zbigniew L. Kowalewski

Abstract Optimal distribution of thickness in the class of polynomial functions for rotating axisymmetric disks with respect to the mixed creep rupture time are found. Two effects lead to damage: reduction of transversal dimensions and growth of microcracks are simultaneously taken into account. The former requires the finite strain analysis, the latter is described by the Kachanov's evolution equation. Behaviour of the material is described by nonlinear Norton's law, generalized for Cauchy true stress and logarithmic strain, and the shape change law in the form of similarity of Cauchy true stress and logarithmic strain deviators. For optimal shapes, changes of geometry of the disk and continuity function are presented. The theoretical considerations based on the perception of the structural components as some highlighted objects with defined properties are presented.

Keywords Optimal disk · Mixed creep rupture · Optimal design

1 Introduction

For over 300 years, the optimal design problems of structural elements have been an object of interest for scientist from all over the world. It is an interdisciplinary domain combining not only mechanics and physics, but also theory of optimal design and IT. Each science domain mentioned earlier has a direct influence on the results of optimal design. Technical progress achieved in advanced technology increases growth of demands for effective tools in the range of strength of materials. Scientific research

---

A. Ustrzycka · Z. L. Kowalewski (✉)
Institute of Fundamental Technological Research, Polish Academy
of Sciences, Pawińskiego 5B, 02-106 Warsaw, Poland
e-mail: zkowalew@ippt.pan.pl

A. Ustrzycka
e-mail: austrzyc@ippt.pan.pl

K. Szuwalski
Cracow University of Technology, Warszawska 24, 31-155 Kraków, Poland
e-mail: krzysztof.szuwalski@pk.edu.pl

© Springer International Publishing AG 2018

H. Altenbach et al. (eds.), *Advances in Mechanics of Materials and Structural Analysis*, Advanced Structured Materials 80,
https://doi.org/10.1007/978-3-319-70563-7_18

stimulates a development in this domain offering new technological opportunities making their application beneficial for industry.

The problem of structural optimization under creep conditions is a relatively young subject and offers a wide scope of investigations. Operational loadings of structural elements are usually long-lasting, quite often acting at elevated temperatures promoting large permanent deformation. Creep deformation is defined as a process carried out at long-lasting loadings at elevated temperature, during which the values of stress and strain caused by structural loadings undergo change in time. This problem is of special significance in many branches of industry, beginning from energetics (steam boilers, turbine blades), thermal power plants (pipelines) in chemical industry, defense industry (military equipment) to space research. A general approach to the creep problem, especially in multi-axial stress state was presented by Martin and Leckie [29], Hayhurst [19] and Betten [1]. Contemporary creep research is carried out for already used materials as well as for new ones such as: composites [15, 22], graded materials [25, 26, 44], intermetallic [2, 24] and many others. Among many new possible criteria of optimization, such as stiffness after given time, stress relaxation, one of the most important seems to be time to creep rupture. A broad presentation of various objective functions with division on time-dependent and time-independent was given by Życzkowski [45, 46]. Most papers on optimal structural design are based on the brittle creep rupture theory proposed by Kachanov (small deformation theory). It was due to its relative simplicity - theory based on principle rigidification. Optimal solutions with respect to brittle creep rupture often coincide with uniform strength structures. In such a way the optimal solutions have been found by: Rysz [34] for cylinders; by Ganczarski and Skrzypek [11] for prestressed disks; Gunneskov [17] for rotating disks. In the work published by Hoff [20], the moment of failure of a bar under tension is defined as the one at which the cross-sectional area becomes zero as a result of quasiviscous flow. It was shown that the calculated results are in a good agreement with the experimental data [5, 13, 14, 27, 28, 30]. Applications of the ductile rupture theory, proposed by Hoff in optimization problems are rather scarce, because they require the finite deformation theory. First time it was used by Szuwalski [36] for optimization of bars under nonuniform tension. Some problems of prismatic tension rods were discussed by Pedersen [32, 33] and Shimanovskii and Shalinskii [35]. Their approach introduces not only physical nonlinearities, connected with creep law, but also geometrical ones, resulting from the finite deformation theory. Additional time factor and presence of body forces depending on the spatial coordinate complicate analysis of the problem. The optimal full disks with respect to ductile creep rupture time were found by Szuwalski [36, 37]. The first attempts to find a solution for annular disks were made by Szuwalski and Ustrzycka [39–41]. Earlier, some problems of optimal design for annular rotating disks were discussed by Farshi and Bidabadi [9]. Analytical solutions for the elastic-plastic stress distribution in rotating annular disks were obtained by Çğallioğlu et al. [3], Gun [16] and Golub [12]. The ductile creep rupture analysis for the elastoplastic disks was carried by Dems and Mróz [4], Ahmet and Erslan [6], Jahed et al. [21] and Golub et al. [14]. Modifications of the Hoff's model was proposed by Golub and Teteruk [13]. The influence of boundary conditions on optimal shape was investigated by Pedersen [33] and later by Szuwalski and Ustrzycka [38]. The elastic–plastic analysis of rotating disks was presented by Vivio and Vullo [42, 43], Eraslan [6–8], Gamer [10], Guven [18] and Orcan and Eraslan [31]. Hoff's definition of rupture - reduction of transversal dimensions of structures to zero (infinite large strains) has certain limitations. It predicts, contrary to observations, that creep does not result in damage of structure. Also, his scheme does not explain fractures at small strains (brittle rupture) and the change of character of rupture (from ductile to brittle). Application of mixed rupture theory proposed by Kachanov [23] takes into account both: geometrical changes - diminishing of transversal dimensions resulting from large deformation and growth of microcracks. Theory of shape optimization was proposed currently by Szuwalski and Ustrzycka for bars under nonuniform tension (2012) and rotating full disk (2013). Problems of structural optimization under creep conditions show specific features. The constitutive equations are often strongly nonlinear. Additional time factor causes that all differential equations describing process are the partial ones. Such problems require the finite strain approach, i.e. resignation of the rigidification theorem and analysis of already deformed body using Cauchy true stress and logarithmic strain. The analytical equations describing the shapes of axisymmetric rotating discs, optimal with respect to mixed time rupture, are derived. The numerical procedure for solving these equations is proposed and same final results are presented in the form of diagrams. The problems of optimal shape are difficult, but important in view of metal structures working at elevated temperatures.

2 Optimal Design of Full Disks with Respect to Mixed Creep Rupture Time

2.1 Mathematical Model of Disk with Respect to the Mixed Creep Rupture Time

The problem of optimal shape of rotating full disk is investigated with respect to mixed creep rupture time under complex stress state. Microcracking and diminishing of transversal dimensions from the beginning of creep process is assumed. Such an approach introduces not only physical nonlinearities, connected with creep law (usually Norton's law), but also geometrical ones, resulting from the finite deformation theory. Additional time factor leads to an increase of model complexity. The whole creep process must be analyzed from its beginning up to rupture. The concept of the mathematical description of mixed creep rupture requires examination of the entire process, taking into account geometrical changes. The problem is solved in material coordinates (Lagrangian description) and all parameters in the initial state, for time equal to zero, are denoted by capital letters, while current values of these parameters by the same small letters. Due to axial symmetry, all quantities will be functions of two independent variables: radius R and time t. The disk rotates with

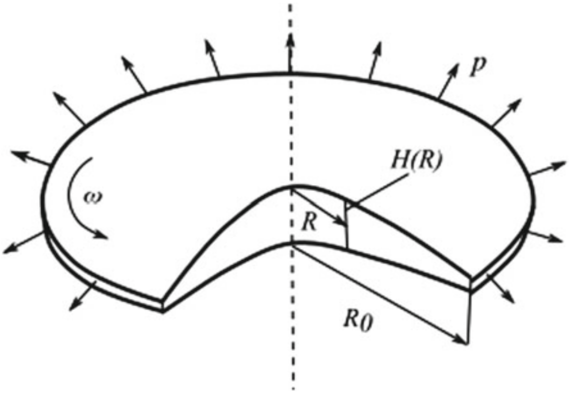

Fig. 1 Element of the deformed disk

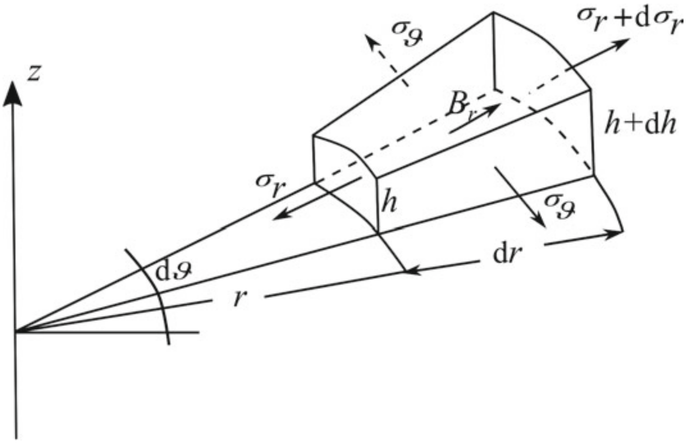

Fig. 2 Deformed element of the disk

constant angular velocity ω and the body forces connected with own mass of the disk are taken into account, Fig. 1.

Arbitrarily chosen small element of the disk, limited previously by two cylindrical surfaces of radii R and $R + \mathrm{d}R$, and two planes forming the angle after deformation are shown in Fig. 2. The internal equilibrium condition for plane stress state takes the form

$$\frac{1}{hr'}\frac{\partial}{\partial R}(h\sigma_r) + \frac{\sigma_r - \sigma_\vartheta}{r} + \frac{\gamma}{g}\omega^2 r = 0 \tag{1}$$

where: σ_r - current value of radial stress and σ_ϑ current value of circumferential stress, h - current thickness, γ - specific weight of material and g - acceleration of gravity, $r^{'}$ - derivative of spatial coordinate r with respect to material one R. Assumption of incompressibility leads to

$$HRdR = hrdr \tag{2}$$

where R stands for the material coordinate of the discussed point, while r for the spatial one, H for initial, and h for current thickness of the disk. Finite strain components require logarithmic measure of deformation

$$\epsilon_r = \ln\frac{\partial r}{\partial R} = \ln r', \quad \epsilon_\vartheta = \ln\frac{r}{R}, \quad \epsilon_z = \ln\frac{h}{H} \tag{3}$$

where a prime denotes the derivative with respect to the material coordinate, and their rates denoted by overdots

$$\dot{\epsilon}_r = \frac{\dot{r}'}{r'}, \quad \dot{\epsilon}_\vartheta = \frac{\dot{r}}{r}, \quad \dot{\epsilon}_z = \frac{\dot{h}}{h} \tag{4}$$

Here, physical relation in the form of deviators similarity of true Cauchy stress D_σ and logarithmic strain rate $D_{\dot{\epsilon}}$ is adopted

$$D_{\dot{\epsilon}} = \frac{3}{2}\frac{\dot{\epsilon}_\mathrm{e}}{\sigma_\mathrm{e}} D_\sigma \tag{5}$$

where σ_e denotes the effective stress, according to the Huber–Mises–Hencky hypothesis generalized to the true Cauchy stress

$$\sigma_\mathrm{e} = \left\{\frac{1}{2}\left[(\sigma_1 - \sigma_2)^2 + (\sigma_2 - \sigma_3)^2 + (\sigma_3 - \sigma_1)^2\right]\right\}^{\frac{1}{2}} \tag{6}$$

and, respectively, $\dot{\epsilon_e}$ is the effective strain rate

$$\dot{\epsilon}_\mathrm{e} = \frac{\sqrt{2}}{3}\left\{\left[(\dot{\epsilon}_1 - \dot{\epsilon}_2)^2 + (\dot{\epsilon}_2 - \dot{\epsilon}_3)^2 + (\dot{\epsilon}_3 - \dot{\epsilon}_1)^2\right]\right\}^{\frac{1}{2}} \tag{7}$$

The material of the disk fulfills Norton's creep law:

$$\dot{\epsilon}_\mathrm{e} = k\sigma_\mathrm{e}^n \tag{8}$$

Finally, taking Eq. (8) leads to the following expressions

$$\begin{aligned}
\dot{\epsilon}_1 &= \frac{3}{2}k\sigma_\mathrm{e}^{n-1}(\sigma_1 - \sigma_\mathrm{m}) \\
\dot{\epsilon}_2 &= \frac{3}{2}k\sigma_\mathrm{e}^{n-1}(\sigma_2 - \sigma_\mathrm{m}) \\
\dot{\epsilon}_3 &= \frac{3}{2}k\sigma_\mathrm{e}^{n-1}(\sigma_3 - \sigma_\mathrm{m})
\end{aligned} \tag{9}$$

where

$$\sigma_{\mathrm{m}} = \frac{1}{3}(\sigma_1 + \sigma_2 + \sigma_3) \tag{10}$$

stands for the mean true Cauchy stress. The following compatibility equation results from definitions of logarithmic strain, cf. Eq. (3)

$$\epsilon_r = \epsilon_\vartheta + \ln\left(1 + R\frac{\partial \epsilon_\vartheta}{\partial R}\right) \tag{11}$$

which, after derivation with respect to time, takes the form

$$\dot{\epsilon_r} - \dot{\epsilon_\vartheta} = \frac{R\frac{\partial \dot{\epsilon_\vartheta}}{\partial R}}{1 + R\frac{\partial \epsilon_\vartheta}{\partial R}} \tag{12}$$

Substitution of the first two Eqs. (9) and (3) makes it possible to rewrite this equation in the form of the relation between stress components. Compatibility condition after some rearrangements takes the form

$$\begin{aligned} &\sigma_r^{'}\left[(n-1)\left(2\sigma_r - \sigma_\vartheta\right)\left(2\sigma_\vartheta - \sigma_r\right) - 2\sigma_{\mathrm{e}}^2\right] + \\ &+ \sigma_\vartheta^{'}\left[(n-1)\left(2\sigma_\vartheta - \sigma_r\right)^2 + 4\sigma_{\mathrm{e}}^4\right] = 6\sigma_{\mathrm{e}}^2\frac{r^{'}}{r}\left(\sigma_r - \sigma_\vartheta\right) \end{aligned} \tag{13}$$

The shape change law assumed in the form of similarity of the true Cauchy stress and logarithmic strain velocity deviators leads to

$$\frac{\dot{r}}{r} = \frac{1}{2}k\sigma_{\mathrm{e}}^{n-1}\left(2\sigma_\vartheta - \sigma_r\right) \tag{14}$$

To find the mixed rupture time, the evolution equation proposed by Kachanov will be applied

$$\frac{\partial \Psi}{\partial t} = -D\left[\frac{\sigma_{\mathrm{e}}}{\Psi}\right]^m \tag{15}$$

in which D and m are material constants. Continuity function Ψ is defined by the ratio of effective cross-sectional area a_{e} to the total area a

$$\Psi = \frac{a_{\mathrm{e}}}{a} \tag{16}$$

Contrary to the brittle rupture theory, σ_{e} denotes here the effective true Cauchy stress - related to the current cross-section a (geometrical changes are taken into account). Damage is characterized by the continuity function $0 \leqslant \Psi \leqslant 1$. At the initial state (no damage): $\Psi = 1$, as time goes on, it decreases. Rupture occurs when the continuity function reaches a critical value $\Psi = 0$. The internal equilibrium condition Eq. (1) incompressibility condition Eq. (2), compatibility condition, in the form of the relation between stresses Eq. (13), the shape change law Eq. (14) and evolution equation Eq. (15) form the set of five equations with five unknowns: true Cauchy stress σ_r and σ_ϑ, spatial coordinate r, current thickness of the disk h, and continuity function Ψ.

$$\frac{1}{hr'}\frac{\partial}{\partial R}\left(h\sigma_r\right)+\frac{\sigma_r-\sigma_\vartheta}{r}+\frac{\gamma}{g}\omega^2 r=0$$

$$\sigma_\vartheta' = \frac{6\sigma_{\mathrm{e}}^2\left(\sigma_r-\sigma_\vartheta\right)\dfrac{r'}{r}-\sigma_r'\left[(n-1)\left(2\sigma_r+\sigma_\vartheta\right)\left(2\sigma_\vartheta+\sigma_r\right)-2\sigma_{\mathrm{e}}^2\right]}{\left[(n-1)\left(2\sigma_r+\sigma_\vartheta\right)^2+4\sigma_{\mathrm{e}}^2\right]} \tag{17}$$

$$\frac{\dot r}{r}=\frac{1}{2}k\sigma_{\mathrm{e}}^{n-1}\left(2\sigma_\vartheta-\sigma_r\right)$$

$$HR\mathrm{d}R=hrdr$$

$$\frac{\partial\Psi}{\partial t}=-D\left[\frac{\sigma_{\mathrm{e}}}{\Psi}\right]^m$$

Initially, the disk remains undeformed, therefore, the initial conditions take the form

$$r\left(R,0\right)=R,\ h\left(R,0\right)=H\left(R\right) \tag{18}$$

The boundary conditions on the disk axis are as follows

$$r\left(0,t\right)=0,\ \dot r\left(0,t\right)=0 \tag{19}$$

$$\sigma_r\left(0,t\right)=\sigma_\vartheta\left(0,t\right) \tag{20}$$

Further, it is assumed that the traction at the external edge of the disk results from the constant mass $M=$ const. uniformly distributed throughout the whole creep process. The total radial force at the external radius is equal to

$$N_r\left(R_0\right)=M\omega^2 r\left(R_0,t\right) \tag{21}$$

and the radial stress is equal to the tensile pressure

$$\sigma_r\left(R_0\right)=p=\frac{N_r\left(R_0\right)}{2\pi r\left(R_0\right)h\left(R_0\right)}=\frac{M\omega^2}{2\pi h\left(R_0\right)} \tag{22}$$

The set of five equations Eq. (17) allows to specify the mixed creep rupture time. It is the time after which the rupture criterion adopted in the following form is fulfilled at least in one place

$$\exists R:\left(R\in\langle 0,R_0\rangle\wedge\Psi\in\langle 1,0\rangle\wedge\Psi|_{t_*^m}\to 0\right) \tag{23}$$

Theoretically, according to the Kachanov's proposal, time after which the continuity function diminishes to zero is the time of mixed rupture $t_*^{(m)}$.

A parametric optimization, where the initial shape is defined by polynomial function, was applied. Let us consider an optimality criterion in the form

$$(\exists! H\left(R\right) \in f)\, t_*|_{V=const.} \longrightarrow max \tag{24}$$

where functions $f : \mathbf{R} \longrightarrow \mathbf{R}$, $R \longrightarrow b_0 + b_1 R + b_2 R^2 + \cdots + b_i R^i$, for all arguments $R \in \langle A, B\rangle$, $i \in \mathbf{N} \setminus \{0\}$ (i is a non-negative integer) and $b_i \in \mathbf{R}$ are constant for a given and fixed volume of the structure. The latter can be treated as a limitation. The initial profile of a full disk is sought in the class of polynomial functions.

2.2 Numerical Solutions

For the sake of numerical calculations, dimensionless quantities are introduced. Both material and spatial coordinates are related to the initial external radius R_0

$$\hat{R} = \frac{R}{R_0}, \quad \hat{r} = \frac{r}{R_0} \tag{25}$$

The thickness of the disk is related to the mean thickness h_m of the full disk of volume V and radius R_0

$$h_m = \frac{V}{\pi R_0^2} \tag{26}$$

Dimensionless thicknesses of the initial and current disk related to the mean thickness Eq. (26), are respectively

$$\hat{H} = \frac{\pi R_0^2}{V} H, \quad \hat{h} = \frac{\pi R_0^2}{V} h \tag{27}$$

Dimensionless stress is referred to stress calculated using a rigidification theorem in the motionless full plane disk subject to tension with uniform pressure p Eq. (22)

$$s = \frac{M\omega^2}{2\pi h_m} = \frac{M\omega^2 R_0^2}{2V} \tag{28}$$

Radial loading at radius R_0 of the rotating disk results from mass M uniformly distributed on the external edge

$$\sigma_r\left(r\right) = p = \frac{M\omega^2}{2\pi h\left(R_0\right)} \tag{29}$$

Finally, the dimensionless stress is equal to

$$\hat{\sigma}_i = \frac{2V}{M\omega^2 R_0^2}, \forall i = \{r, \vartheta\}. \tag{30}$$

Consequently, the dimensionless time is defined

$$\hat{t} = \frac{t}{t_0^{(d)}} \tag{31}$$

where: $t_0^{(d)}$ stands for the time of ductile rupture for full plane disk. To evaluate the time of ductile rupture for full plane disk, the equation resulting from Eq. (9) may be used

$$\dot{\epsilon}_z = \frac{\dot{h}}{h} = \frac{3}{2} k \sigma_{\mathrm{e}}^{n-1} (\sigma_z - \sigma_m) \tag{32}$$

where the effective stress reads

$$\sigma_{\mathrm{e}} = \sigma_r = \sigma_\vartheta = p \tag{33}$$

and the mean stress can be written as

$$\sigma_m = \frac{2}{3} p \tag{34}$$

Applying the above equations to Eq. (22) leads to the relationship

$$\frac{1}{h}\frac{dh}{dt} = -k \left(\frac{M\omega^2}{2\pi h}\right)^n \tag{35}$$

which describes a change of thickness in time. The initial condition takes form

$$h\,(t = 0) = h_{\mathrm{m}} \tag{36}$$

The condition of ductile rupture $h \rightarrow 0$ enables calculation of the time of ductile rupture $t_0^{(d)}$

$$t_0^{(d)} = \frac{1}{nk \left(\dfrac{M\omega^2}{2\pi h_m}\right)^n} = \frac{1}{nks^n} \tag{37}$$

Finally, the dimensionless time Eq. (31) is defined

$$\hat{t} = nks^n t \tag{38}$$

To avoid a large number of material constants in numerical calculations, the new parameter Θ is introduced. This parameter is equal to the ratio of the brittle rupture time to the ductile rupture time for the prismatic bar subject to uniform tension under the initial stress s Eq. (28)

$$\Theta = \frac{t_{\mathrm{pr}}^{(K)}}{t_{\mathrm{pr}}^{(H)}} = \frac{nks^{n}}{(m+1)Ds^{m}} \tag{39}$$

The parameter Θ contains four material constants: n and k in Norton's law Eq. (8), m and D in evolution equation Eq. (15). In some way, it describes sensitivity of material to the damage type: brittle or ductile. The mathematical model of mixed creep rupture is finally described by the system of five partial differential equations in the dimensionless form

$$\begin{gathered}
\hat{\sigma}_r^{'} = \frac{\hat{r}^{'}}{\hat{r}} \left(\hat{\sigma}_r - \hat{\sigma}_\vartheta\right) - 2\hat{r}\hat{r}^{'} \mu - \frac{\hat{h}^{'}}{\hat{h}} \hat{\sigma}_r \\
\hat{\sigma}_\vartheta^{'} = \frac{6\hat{\sigma}_e^2 \left(\hat{\sigma}_r - \hat{\sigma}_\vartheta\right) \frac{\hat{r}^{'}}{\hat{r}} - \hat{\sigma}_r^{'} \left[(n-1)\left(5\hat{\sigma}_r\hat{\sigma}_\vartheta - 2\hat{\sigma}_r^2 - 2\hat{\sigma}_\vartheta^2\right) - 2\hat{\sigma}_e^2\right]}{(n-1)\left(2\hat{\sigma}_\vartheta - \hat{\sigma}_r\right)^2 + 4\hat{\sigma}_e^{'}} \\
\frac{d\hat{r}}{d\hat{t}} = \frac{\hat{r}}{2n} \left(\hat{\sigma}_r^2 + \hat{\sigma}_\vartheta^2 - \hat{\sigma}_r\hat{\sigma}_\vartheta\right)^{\frac{n-1}{2}} \left(2\hat{\sigma}_\vartheta - \hat{\sigma}_r\right) \\
\hat{h} = \frac{\hat{H}\hat{R}}{\hat{r}^{'}\hat{r}} \\
\frac{\partial \Psi}{\partial \hat{t}} = \frac{-1}{(m+1)\,\Theta} \left[\frac{\hat{\sigma}_{\mathrm{e}}}{\Psi}\right]^{m}
\end{gathered} \tag{40}$$

where μ is the ratio of disk's own mass to the mass distributed at the external radius

$$\mu = \frac{\gamma V}{gM} \tag{41}$$

The above equations set Eq. (40) contains five unknowns: true Cauchy stress components σ_r and σ_ϑ, current thickness h, spatial radial coordinate r and continuity function Ψ. The initial conditions Eq. (18) can be expressed in the following dimensionless form

$$\hat{r}\left(\hat{R}, 0\right) = \hat{R},\ \hat{h}\left(\hat{R}, 0\right) = \hat{H}\left(\hat{R}\right) \tag{42}$$

while the boundary conditions Eqs. (19) and (20) can be described by

$$\hat{r}\left(0, \hat{t}\right) = 0,\ \hat{\dot{r}}\left(0, \hat{t}\right) = 0,\ \hat{\sigma_r}\left(0, \hat{t}\right) = \hat{\sigma_\vartheta}\left(0, \hat{t}\right) \tag{43}$$

The condition at external radius Eq. (22), where the mass M is distributed, may be written in the dimensionless form

$$\hat{\sigma_r}\left(1, \hat{t}\right) = \frac{1}{\hat{h}}\left(1, \hat{t}\right) \tag{44}$$

The function $\hat{H}(\hat{R})$ describing the initial profile of the disk is expressed by the fourth equation in set Eq. (40) and by the initial conditions Eq. (42). It is necessary to know this function in order to solve the set Eq. (40). Since this function is being sought in the optimisation process, a parametric optimisation is applied. We are looking for the best possible function $\hat{H}(\hat{R})$, leading to the longest lifetime under the mixed rupture in the class of polynomial functions assumed. In order to perform an optimisation procedure, the rupture and optimality criteria are introduced. We must follow the whole creep process step by step for each new initial geometry of the disk up to the moment of fulfilling of rupture criterion in order to establish the mixed creep rupture time. The numerical algorithm consists of two blocks, which are sequentially activated (Fig. 3).

In the first block, the stress distribution is found for a given geometry of disk. It requires integration of two first equations of set Eq. (54) and initial conditions Eq. (56). A width of the disk was divided initially into fifty parts of equal length. The program assigns a procedure using the fourth order Runge–Kutta method. The values of stresses in the middle of disk must be assumed in such a way that the result of integration satisfies the boundary condition Eq. (58) for a given accuracy. To this aim, the recurrential procedure must be applied, because initial values of stress at the external edge of the disk are unknown. In this way, the distribution of true Cauchy stress components with help of the evolution equation may be found (the last one in the set Eq. (54). This makes it possible to establish the distribution of continuity function Ψ. Subsequently, the rupture criterion is checked, and a new geometry of the disk is calculated.

In the second block, for already known distribution of stress the integration with respect to time is made, and the new geometry of the disk is calculated. The third equation in set Eq. (54) is integrated with respect to time using Euler's method. The time step varies, at the beginning of the creep process it may be larger (slow geometry changes), it must be small for time close to the rupture time, since process accelerates significantly. The new spatial coordinates of the knot points are found (third equation in set Eq. (54), after that the current thickness h is calculated from the incompressibility condition (fourth equation in set Eq. (54). In this way, the new geometry of deformed disk is found, stress distribution may be calculated repeating the procedure of part I. All time steps are summarized giving the total time of the work for a given disk. The calculations are carried out until the mixed rupture condition is satisfied, i.e. the continuity function reaches the critical value 0.001. As a consequence, the creep process can be treated as finished and the time to mixed rupture determined.

Among the results obtained for many initial shapes of the disk described by the assumed polynomial function one can indicate the best solution leading to the longest time to mixed creep rupture. This is the optimal disk.

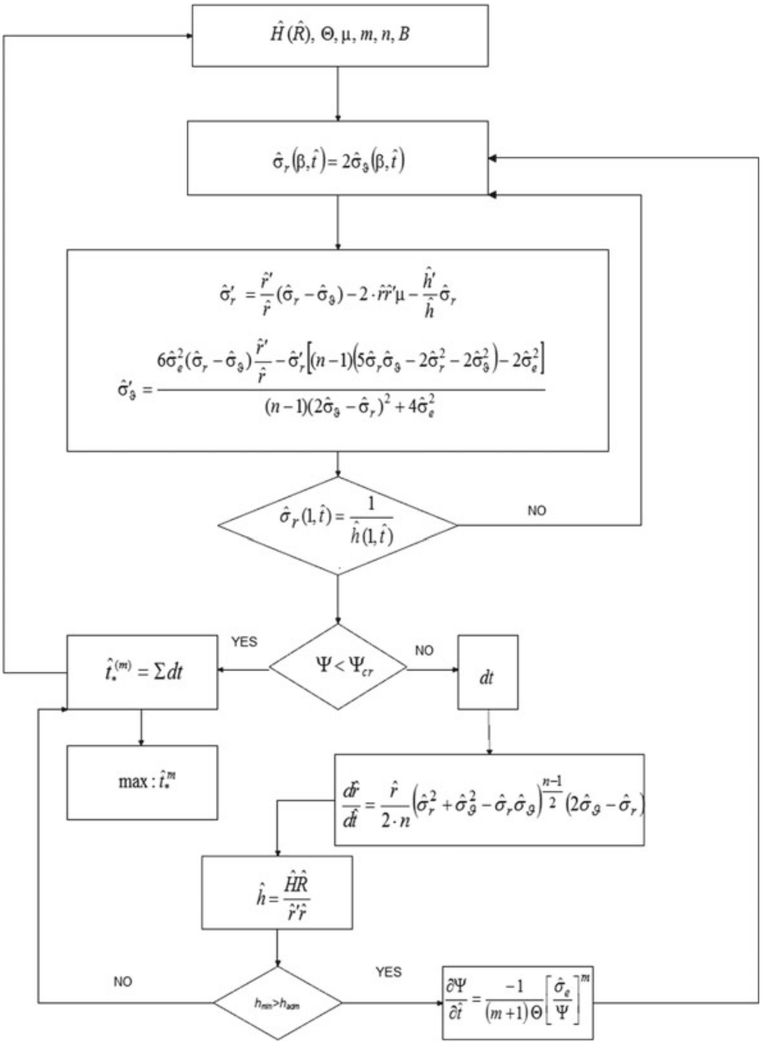
$\hat{H}(\hat{R})$, Θ, μ, m, n, B
$\hat{\sigma}_r(\beta,\hat{t}) = 2\hat{\sigma}_\vartheta(\beta,\hat{t})$
$\hat{\sigma}'_r = \frac{\hat{r}'}{\hat{r}}(\hat{\sigma}_r - \hat{\sigma}_\vartheta) - 2\cdot\hat{r}\hat{r}'\mu - \frac{\hat{h}'}{\hat{h}}\hat{\sigma}_r$
$\hat{\sigma}'_\vartheta = \frac{6\hat{\sigma}_e^2(\hat{\sigma}_r - \hat{\sigma}_\vartheta)\frac{\hat{r}'}{\hat{r}} - \hat{\sigma}'_r\left[(n-1)(5\hat{\sigma}_r\hat{\sigma}_\vartheta - 2\hat{\sigma}_r^2 - 2\hat{\sigma}_\vartheta^2) - 2\hat{\sigma}_e^2\right]}{(n-1)(2\hat{\sigma}_\vartheta - \hat{\sigma}_r)^2 + 4\hat{\sigma}_e^2}$
$\hat{\sigma}_r(1,\hat{t}) = \frac{1}{\hat{h}(1,\hat{t})}$
NO
YES
$\Psi < \Psi_{cr}$
NO
$\hat{t}_*^{(m)} = \Sigma dt$
dt
max : $\hat{t}_*^m$
$\frac{d\hat{r}}{d\hat{t}} = \frac{\hat{r}}{2\cdot n}\left(\hat{\sigma}_r^2 + \hat{\sigma}_\vartheta^2 - \hat{\sigma}_r\hat{\sigma}_\vartheta\right)^{\frac{n-1}{2}}(2\hat{\sigma}_\vartheta - \hat{\sigma}_r)$
$\hat{h} = \frac{\hat{H}\hat{R}}{\hat{r}'\hat{r}}$
NO
$h_{min} > h_{adm}$
YES
$\frac{\partial\Psi}{\partial\hat{t}} = \frac{-1}{(m+1)\Theta}\left[\frac{\hat{\sigma}_e}{\Psi}\right]^m$

Fig. 3 Numerical algorithm for the finite creep deformation analysis and optimization procedure

For the arbitrary chosen initial geometry: $\hat{H}(\hat{R}) = 0.8 - \hat{R} + 2.1\hat{R}^2$, an influence of parameters m and Θ on time to the mixed rupture $t^{(m)}$ can be investigated (see Fig. 4).

The Θ parameter Eq. (53) characterizes sensitivity of a material to a type of rupture Fig. 4. As the Θ parameter increases, the material sensitivity to cracking decreases and geometrical variation decides when time to rupture is achieved. Above the critical value of Θ parameter, the material can be treated as destroyed due to diminishing

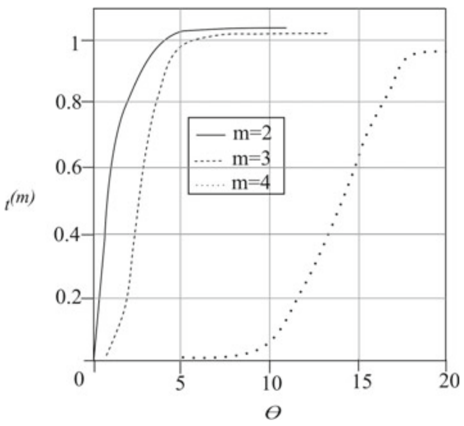

Fig. 4 Influence of parameters m and Θ on time to mixed rupture $t^{(m)}$

of transversal dimensions, and as a consequence, time to rupture is equal to that for ductile rupture obtained.

2.3 Optimal Solutions

2.3.1 Uniparametric Optimization

Firstly, the optimal solutions for the problem of rotating full disk with respect to mixed creep rupture time are sought in the class of linear functions:

$$\hat{H}\left(\hat{R}, u_0, u_1\right) = u_0 + u_1 \hat{R} \tag{45}$$

Parameters u_0 and u_1 (uniparametric optimisation), which optimal values are sought, are linked together by the condition of given volume V:

$$u_1 = \frac{3}{2}(1 - u_0) \tag{46}$$

Parameter u_0 is treated as a free steering one (uniparametric optimisation). Values of it are limited by the condition of nonnegative thickness at the external edge:

$$\hat{H}(1) > 1 \rightarrow 1 \leq u_0 \leq 3 \tag{47}$$

An influence of two important parameters is investigated: μ as the ratio of own mass of the disk to mass uniformly distributed at the external edge, and Θ ratio of the brittle rupture time and ductile rupture time of the prismatic bar subject to uniform tension under the stress expressed by Eq. (28).

Table 1 Profiles of optimal disks for $n = 3$ and $m = 2$ and for three different values of parameter Θ and μ

	$\Theta = 0.3$	$\Theta = 0.8$	$\Theta = 3$
$\mu = 0.1$	$\hat{H}(\hat{R}) = 1.12–0.15\hat{R}$	$\hat{H}(\hat{R}) = 0.69–0.45\hat{R}$	$\hat{H}(\hat{R}) = 1.09–0.15\hat{R}$
$\mu = 1$	$\hat{H}(\hat{R}) = 1.21–0.33\hat{R}$	$\hat{H}(\hat{R}) = 1.42–0.61\hat{R}$	$\hat{H}(\hat{R}) = 1.91–1.35\hat{R}$
$\mu = 10$	$\hat{H}(\hat{R}) = 2.01–1.52\hat{R}$	$\hat{H}(\hat{R}) = 2.09–1.65\hat{R}$	$\hat{H}(\hat{R}) = 2.1–1.65\hat{R}$

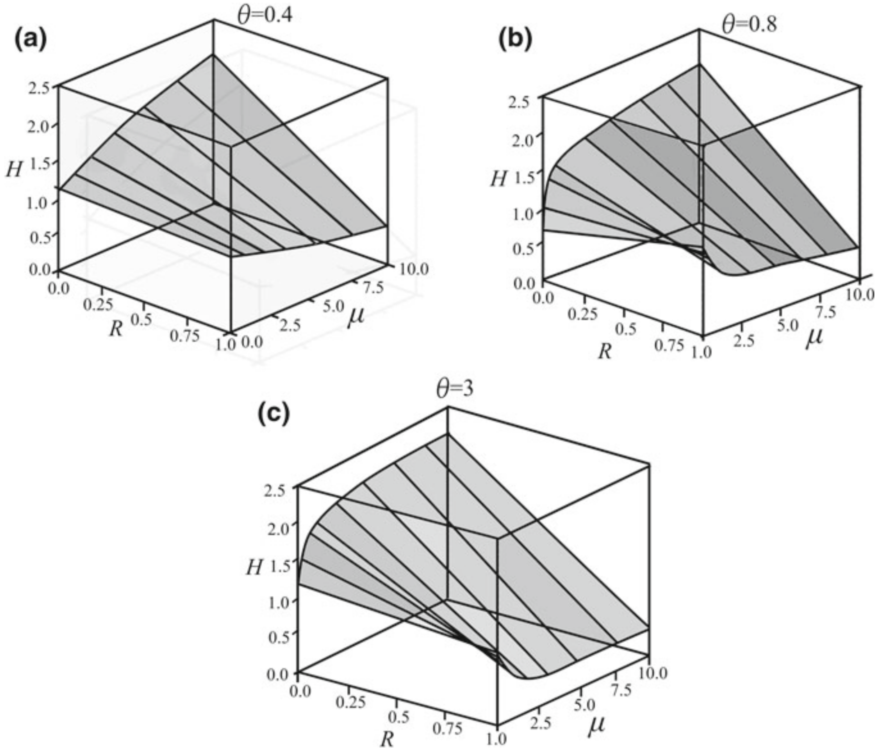

Fig. 5 Profiles of the optimal disks for $n = 3$ and $m = 2$ and for three different values of parameter Θ

Profiles of optimal disks for uniparametric optimization are shown in Table 1 as a function of the parameter μ for three different values of parameter Θ.

The solutions strongly depend on the ratio Θ and μ (Fig. 5). When the mass M is very large in comparison to the disk's own mass (small values of μ), optimal disks are close to flat ones. For larger values of parameter Θ (ductile materials), the thickness of optimal disks in the vicinity of external edge grows. For larger values of parameters μ (small mass M at the external radius), the mass of the disk is distributed as close to the rotation axis as possible.

2.3.2 Biparametric Optimization

Better results may be obtained for disks, that initial shape is defined by quadratic function:

$$\hat{H}\left(\hat{R}, b_0, b_1, b_2\right) = b_0 + b_1\hat{R} + b_2\hat{R}^2, \quad b_2 \neq 0 \tag{48}$$

In the case of quadratic functions, three parameters are considered. Finding the optimal values for these parameters takes much more time than for the uniparametric optimization. From three parameters in this function, only two of them may be treated as free ones, the third one results from the given volume of disk:

$$\hat{V} = \int_0^1 2\pi \left(b_0 + b_1\hat{R} + b_2\hat{R}^2\right) \hat{R} d\hat{R} = \pi \tag{49}$$

Including Eq. (49), one can obtain the following formula:

$$b_2 = 2 - 2b_0 - \frac{4}{3}b_1 \tag{50}$$

In the process of biparametric optimization, we look for such parameters b_0 and b_1, that give the longest values of the time to ductile creep rupture. Some limitations may be imposed on these parameters. One may expect that for the rotating disk with centrifugal forces, its thickness should diminish with an increase of radius (although sometimes this limitation may be violated). It leads to:

$$\frac{d\hat{H}(\hat{R})}{d\hat{R}} \leq 0 \longrightarrow b_0 < 2 - \frac{1}{3}b_1 \tag{51}$$

Obviously, the thickness at the external radius (and on the whole width of the disk) must be positive, that means:

$$\hat{H}(1) > 0 \longrightarrow b_0 < 1 - \frac{5}{12}b_1 \tag{52}$$

Finally, in the plane of free parameters b_0 and b_1, the search range at the beginning of numerical calculation will be restricted to the triangle area designated by continuous lines shown in Fig. 6.

Profiles of optimal disks for the biparametric optimization are shown in Fig. 7. For smaller parameter μ (the own mass almost neglected), the growth of thickness at the external edge was observed. The optimal solutions have minimum inside the disk width.

The larger thickness at the external edge works as some kind of reinforcement, which slows down the creep process, and thanks to it, the time to mixed rupture may be longer. For larger parameter Θ (brittle materials), this effect is weaker.

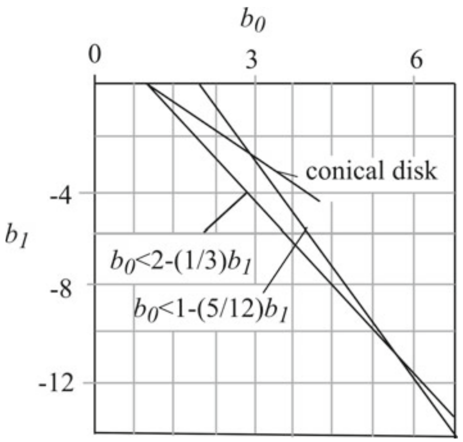

Fig. 6 Range of the expected b_0 and b_1 optimal parameters for $n = 6$, $\beta = 0.5$, $\mu = 1$

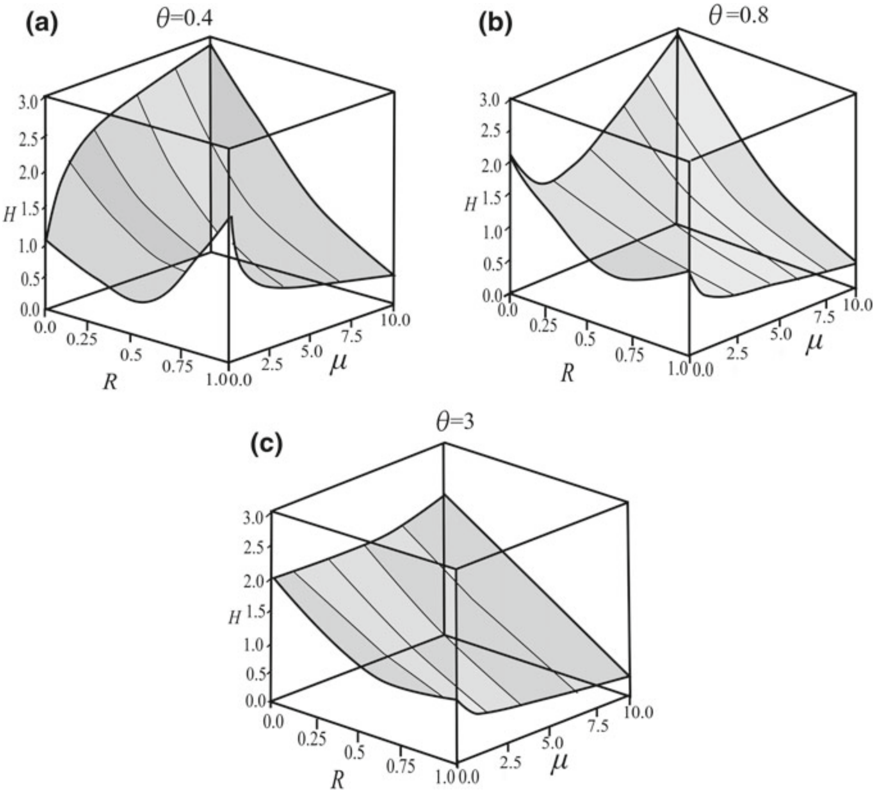

Fig. 7 Optimal shapes of the disks for biparametric optimisation

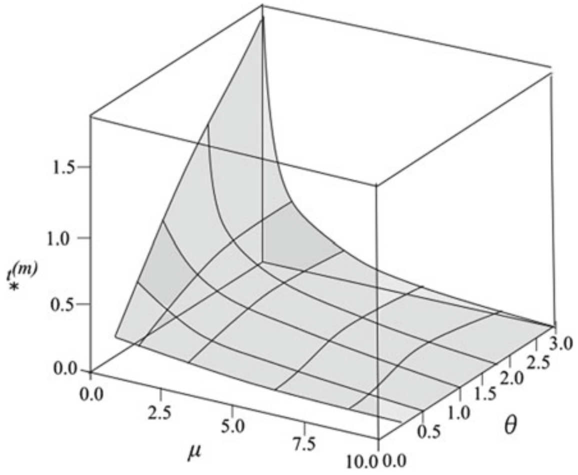

Fig. 8 Time to mixed rupture for the disks with optimal biparametric shapes in terms of μ and Θ

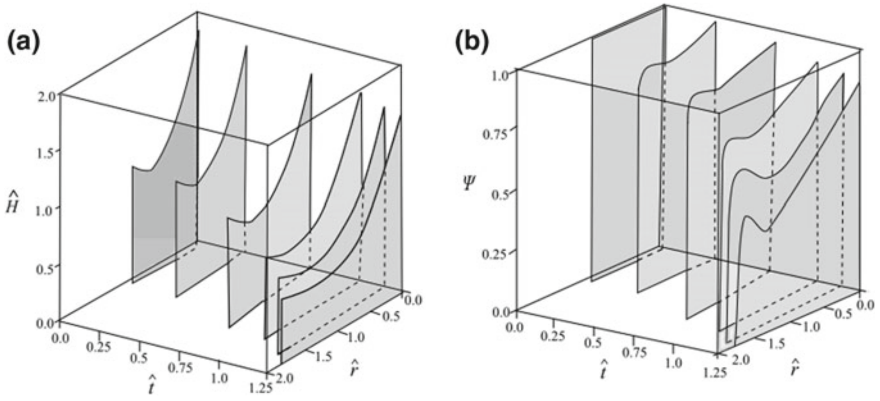

Fig. 9 Creep process for selected time intervals

The time to mixed rupture for optimal shapes of the disks with the same volume, as a function of the parameters μ and Θ for biparametric optimisation is shown in Fig. 8. The longest time to mixed creep rupture for optimal disks is observed for larger parameter Θ (brittle materials) and smaller μ (the own mass almost neglected). Increase of μ, for all kind of materials (brittle and ductile) leads to decrease of the lifetime of the full disks. Changes of a profile for the optimal disk are shown in Fig. 9a, while in Fig. 9b the corresponding distribution of the continuity function is illustrated for the same time intervals. The results are presented for optimal disks using the following parameters: $\mu = 0.1, n = 3, \Theta = 3$, where an initial shape is described by function $\hat{H}(\hat{R}) = 2 - 3\hat{R} + 2\hat{R}^2$. It was observed, that despite the strengthening of the external edge of the disk, the rupture criterion for the continuity function is fulfilled. Inside the disk the values of function are quite large. This effect is only achieved for the disks of initial profile described by the quadratic function Eq. (48).

2.3.3 Modified Disk of Uniform Strength

One may expect that disks of uniform initial strength, in which both radial and circumferential stresses are the same for $0 \leq R \leq B$ and close to optimum with respect to mixed rupture time. Such disks are described by formula:

$$\hat{H}_{\mathrm{us}}(\hat{R}) = \frac{1}{\hat{\Sigma}} \exp\left[\frac{\mu}{\hat{\Sigma}}\left(1 - \hat{R}^2\right)\right] \tag{53}$$

where: $\hat{\Sigma}$ - dimensionless equalized initial stress, calculated under assumption of the constant volume:

$$\hat{\Sigma} = \frac{\mu}{\ln(1+\mu)} \tag{54}$$

It may be slightly corrected in order to obtain the longest creep lifetime. Correction may be adopted in the form of the third degree polynomial function:

$$\hat{H}_{\mathrm{cor}} = p_0 + p_2\hat{R}^2 + p_3\hat{R}^3 \tag{55}$$

without the linear element. As a consequence, the thickness derivative in the middle of the disk is equal to zero.

As the correction cannot change the total volume of the bar, only two coefficients in Eq. (55) may be treated as free, while the third one can be determined from the constant volume condition:

$$p_3 = -\frac{5}{2}p_0 - \frac{5}{4}p_2 \tag{56}$$

An initial shape of the disk was proposed for different values of these parameters using expression

$$\hat{H}(\hat{R}) = \hat{H}_{us}(\hat{R}) + \hat{H}_{cor}(\hat{R}) \tag{57}$$

and then carrying out integration of the set of equations Eq. (40). Calculations were carried for $\mu = 0.1$, $\Theta = 3$, exponent in Norton's law $n = 3$ and exponent in Kachanov's law $m = 2$. The comparison between the optimal shapes of the uniform strength disk and uni- and biparametric optimisation is presented in Fig. 10.

The optimal solution of the disks are presented on the time axis. As expected, the corrected shape of uniform initial strength disk provides the longest time of mixed creep rupture. The parabolic disk enlarges this time around 14%. The lifetime of corrected disk of uniform strength is 70% longer than that of conical disk.

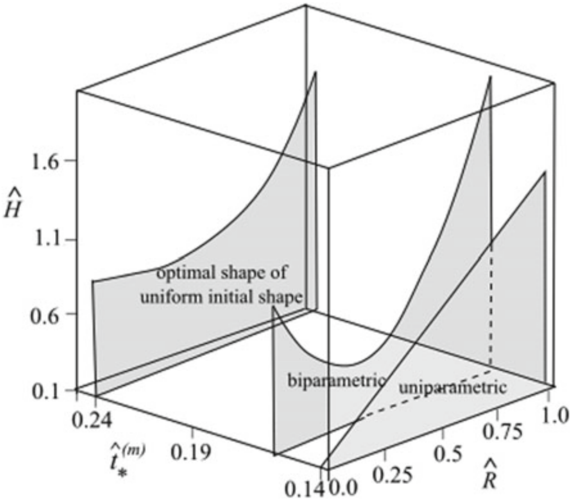

Fig. 10 Optimal shape of the corrected uniform initial strength disks compared to the uni- and biparametric optimisation

3 Optimal Design of Annular Disks with Respect to Mixed Creep Rupture Time

3.1 *Mathematical Model of Annular Disk with Respect the Mixed Creep Rupture Time*

The initial shape of rotating annular disk is sought for the given internal and external radii A and B and given volume V (Fig. 11), ensuring the longest time to mixed creep rupture. In the case of the annular disk (volume V and initial radii A and B are given)

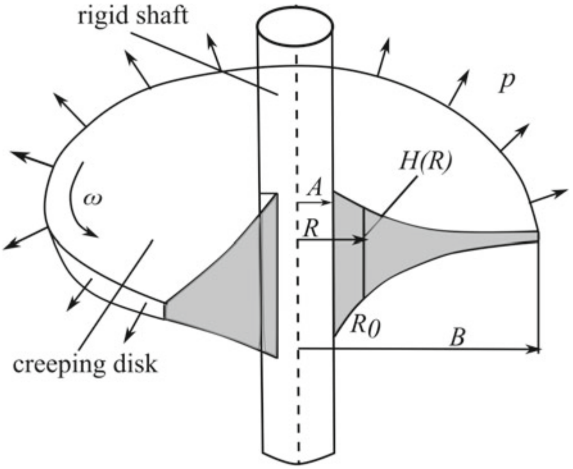

Fig. 11 Model of the annular rotating disk

rotating with constant angular velocity ω, (the properties of material are known, mass M is uniformly distributed at the external edge), the optimization problem can be formulated in the following way:

- for given $V, A, B, \omega, \gamma, M$
- we look for such $H(R, b_0, b_1, b_2) = b_0 + b_1 R + b_2 R^2$
- that $t_*^{(m)} \longrightarrow \max$

The problem seems to be of great importance for rotors of jet engines and power plant turbines working at high temperatures. In such cases the creep effects must be taken into account. Also, the body forces are of great importance. The axially symmetric problem (all variables depend on the single material coordinate only, a radius) is described using material Lagrangean coordinate denoted by capital R. Corresponding spatial coordinate r may be treated as a measure of deformation. The external loading of the disk results from centrifugal force acting on the blades of total mass M put at the external edge of the disk, under assumption that they are uniformly distributed. Moreover, the body forces connected with the own mass of the disk are taken into consideration. Both types of loading depend on the spatial coordinate, and change according to the disk deformation within the creep process. The mathematical model of mixed creep rupture is finally described by the system of five partial differential equations in the dimensionless form:

$$\hat{\sigma}_r^{'} = \frac{\hat{r}^{'}}{\hat{r}}\left(\hat{\sigma}_r - \hat{\sigma}_\vartheta\right) - 2\hat{r}\hat{r}^{'}\mu - \frac{\hat{h}^{'}}{\hat{h}}\hat{\sigma}_r \tag{58}$$

$$\sigma_\vartheta^{'} = \frac{6\sigma_e^2\left(\sigma_r - \sigma_\vartheta\right)\dfrac{r^{'}}{r} - \sigma_r^{'}\left[(n-1)\left(2\sigma_r + \sigma_\vartheta\right)\left(2\sigma_\vartheta + \sigma_r\right) - 2\sigma_e^2\right]}{\left[(n-1)\left(2\sigma_r + \sigma_\vartheta\right)^2 + 4\sigma_e^2\right]} \tag{59}$$

$$\frac{d\hat{r}}{d\hat{t}} = \frac{\hat{r}}{2n}\left(\hat{\sigma}_r^2 + \hat{\sigma}_\vartheta^2 - \hat{\sigma}_r\hat{\sigma}_\vartheta\right)^{\frac{n-1}{2}}\left(2\hat{\sigma}_\vartheta - \hat{\sigma}_r\right) \tag{60}$$

$$\hat{h} = \frac{\hat{H}\hat{R}}{\hat{r}^{\prime}\hat{r}} \tag{61}$$

$$\frac{\partial\Psi}{\partial\hat{t}} = \frac{-1}{(m+1)\,\Theta}\left[\frac{\hat{\sigma}_e}{\Psi}\right]^m \tag{62}$$

In the case of annular disk an additional parameter is used:

$$\beta = \frac{A}{B} \tag{63}$$

where: β is the ratio of internal and external radii. A set of equations Eqs. (58)–(62) written in the above form is convenient for numerical calculations.

3.2 Influence of Boundary Conditions

3.2.1 Disk Clamped on a Rigid Shaft

At the beginning of creep process (for $t = 0$), the disk remains undeformed, therefore, the initial conditions take the form:

$$\hat{r}\left(\hat{R},0\right) = \hat{R},\quad \hat{h}\left(\hat{R},0\right) = \hat{H}\left(\hat{R}\right) \tag{64}$$

Boundary conditions at internal radius may be written:

$$\hat{h}\left(\beta,\hat{t}\right) = \hat{H}(\beta,0),\quad \hat{r}\left(\beta,\hat{t}\right) = \beta \tag{65}$$

Since we are looking for the stress distribution, this boundary condition should be rewritten in terms of stress. Taking advantage of shape change law Eq. (60), the condition at the internal edge can be written as follows:

$$\dot{\hat{r}}(\beta,\hat{t}) = 0 \tag{66}$$

It leads to relation of stress at the internal edge

$$\hat{\sigma}_r(\beta,\hat{t}) = 2\hat{\sigma}_\vartheta(\beta,\hat{t}) \tag{67}$$

By introduction of dimensionless parameters into the condition at external radius Eq. (65), where the mass M is distributed:

$$\frac{\hat{\sigma}_r(b)M\omega^2b^2}{2V} = \frac{M\omega^2b^2}{2V\hat{h}(b)} \tag{68}$$

one can get a condition at the external radius B in the following form:

$$\hat{\sigma}_r(1,t) = \frac{1}{\hat{h}(1,t)} \tag{69}$$

The numerical algorithm consists of three steps:

The first step – for given geometry of the disk, the true Cauchy stress distribution is established from Eqs. (58) and (59). We don't know values of stress at the internal edge of the disk, so it is necessary to assume them arbitrarily, remmembering that the boundary condition at the external edge of the disk must be fulfilled.

The second step – distribution of the Cauchy stress found in the first step, makes it possible to establish a new geometry of the disk from Eqs. (60) and (61).

The third step – from Eq. (62) a distribution of continuity function Ψ is calculated. If its minimum value satisfies the rupture criterion, the creep process is finished –

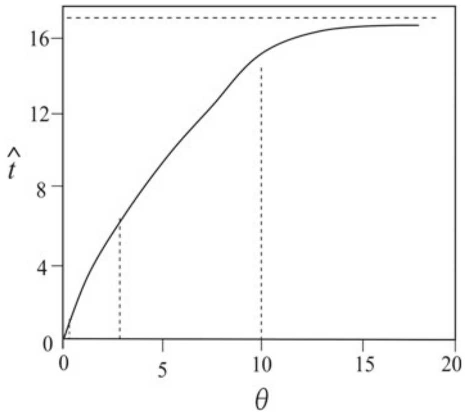

Fig. 12 Influence of parameter Θ on the time to rupture for the disk clamped on the shaft

the time to mixed rupture is found. Due to the inability in order to write the objective function (mixed rupture time) as an explicit function of the optimization parameters (initial profile of the disk) the parametric optimization is applied (search method). To establish the range of parameter Θ arbitrary taken the disk described by the equation $\hat{H}(\hat{R}) = 0.8 - \hat{R} + 2.1\hat{R}^2$, was investigated. The parameter Θ is defined here identically as for full disks, Eq. (39), where it has significant influence on the time to rupture. The results are presented in Fig. 12.

By increasing of Θ, the time to rupture becomes longer for the disk clamped on the rigid shaft. This is observed up to the values of Θ equal to 11 approximately. For higher values of Θ, the influence of brittle rupture becomes so small in comparison to ductile effect, that rupture effects result almost from geometrical variations only. Time to rupture for $\Theta \geq 11$ coincides with that for ductile rupture obtained. For numerical calculations three values $\Theta = 0.4$, $\Theta = 3$ and $\Theta = 10$ were taken into account. Initially, the optimal solution was sought among the conical disks which initial shape is described by the formula:

$$\hat{H}\left(\hat{R}; u_0, u_1\right) = u_0 + u_1\hat{R} \tag{70}$$

Using condition of constant volume leads to:

$$u_1 = \frac{3}{2}(1 - u_0) \tag{71}$$

and as a consequence, only one free parameter u_0 remains. Optimal solutions for the disks clamped on the rigid shaft for various Θ are presented in Fig. 13 for $\beta = 0.1$ and $\mu = 0.1$.

For $\Theta = 0.4$, the optimal profile of the conical disk becomes almost flat. For higher Θ, the mass moves toward the internal edge. It was expected that the results

Fig. 13 Optimal profiles of conical disk clamped on the rigid shaft, $\beta = 0.1$, $\mu = 0.1$

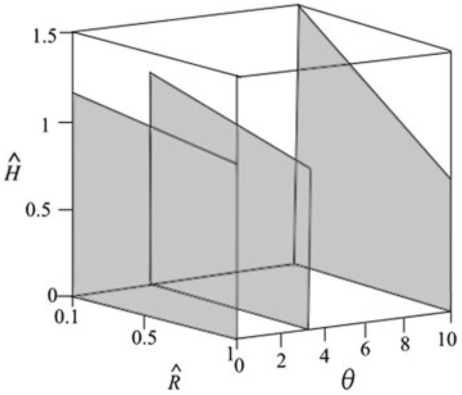

presented earlier can be improved by expanding the class of functions, in which the optimal solution is sought. In the next step the biparametric optimization was used.

An initial shape is defined by quadratic function:

$$\hat{H}\left(\hat{R}, b_0, b_1, b_2\right) = b_0 + b_1\hat{R} + b_2\hat{R}^2, \quad b_2 \neq 0 \tag{72}$$

From three parameters in this function, only two of them may be treated as free ones, the third results from the given volume of disk:

$$\hat{V} = \int_0^1 2\pi\left(b_0 + b_1\hat{R} + b_2\hat{R}^2\right)\hat{R}d\hat{R} = \pi \tag{73}$$

in which:

$$b_2 = \frac{2 - \frac{4}{3}b_1(1-\beta^3) - 2b_0(1-\beta^2)}{1-\beta^4} \tag{74}$$

The search process for biparametric optimisation is much more time consumable. For determined values of b_0, the time to mixed rupture is calculated for various b_1. In such a way, parameter b_1 leading to the longest lifetime may be found. This procedure is repeated for subsequent values of b_0. Finally, the optimal solution is established as "maximum maximorum" of all disks investigated (sometimes almost hundred). Optimal shapes of the disks for biparametric optimisation are shown in Fig. 14.

The optimal shape of disk for $\Theta = 0.4$ is characterized by the large increase of thickness at the external edge. In spite of larger centrifugal forces, the external edge works as a kind of reinforcement slowing down the creep process. For larger Θ such effect does not occur.

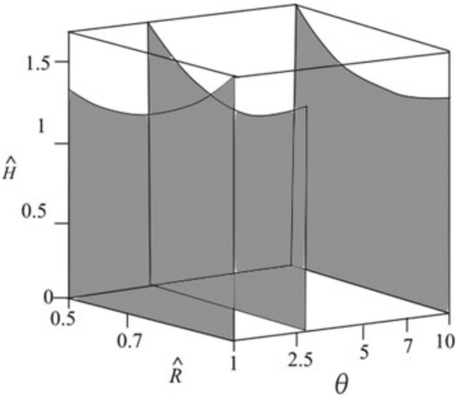

Fig. 14 Optimal shapes of the disks clamped on the rigid shaft, $\beta = 0.5$, $\mu = 0.1$

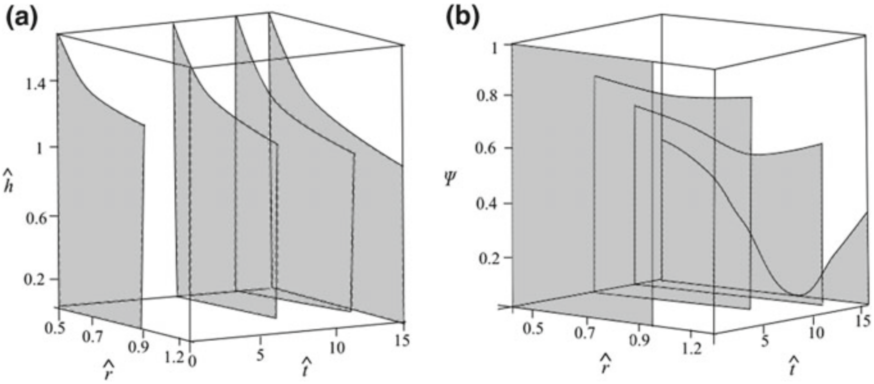

Fig. 15 Time intervals of creep process for $\beta = 0.5$, $\mu = 0.1$ and $\Theta = 3$

The creep process of the optimal disk with initial profile described by the function:

$$\hat{H}\left(\hat{R}\right) = 3.51 - 5\hat{R} + 2.76\hat{R}^2 \tag{75}$$

is presented in Fig. 15, showing changes of shape (A) and continuity function distribution (B) in terms of time. A distribution of the continuity function at rupture is not uniform, criterion of rupture is fulfilled inside the disk at single point. For other radii the values of function are non-zero and at the internal and external edges they are quite large. This effect is attributed only to the disks of initial profile described by the quadratic function, Eq. (72).

One may expect that disks of uniform initial strength, in which the radial and circumferential stress components are equal and independent of the radius, will be close to the optimal profiles with respect to the mixed rupture time.

3.2.2 Disk Fastened on the Rigid Shaft, with Changing Thickness in the Place of Joint

Analysis of the disk fastened to the rigid shaft is carried out in such a way that enables displacement on the one hand and variation of thickness in this place (e.g. spline joint) on the other. The boundary and initial conditions are the same as in Sect. 4.2.1, Eqs. (65), (67) and (69). Only the condition represented by Eq. (66) is eliminated, what means that thickness of the disk at the joint with the shaft will diminish throughout the creep process. An influence of the parameter Θ on the time to rupture of disk fastened to the rigid shaft, with possible change of thickness was investigated for the annular disk described by the equation $\hat{H}(\hat{R}) = 0.8 - \hat{R} + 2.1\hat{R}^2$. The results are presented in Fig. 16.

Taking advantage of these results the following values of Θ were chosen for numerical calculations: $\Theta = 0.4$, $\Theta = 3$ and $\Theta = 10$. It turned out, that parameter Θ has no influence on the optimal shape of conical disk (due to small width of the disk, Fig. 17), which is described by the equation:

$$\hat{H}\left(\hat{R}\right) = 1.87 - 0.74\hat{R} \tag{76}$$

The optimal shapes of disks fastened to the rigid shaft with possible thickness variation are shown in Fig. 18 for the biparametric optimisation. For $\Theta = 0.4$ and $\Theta = 3$ the optimal shapes of disk have a reinforcement of the external edge (an increase of the thickness). For larger Θ, the effect vanishes.

Figure 19 elaborated for the optimal disk:

$$\hat{H}(\hat{R}) = 4.39 - 8\hat{R} + 5.05\hat{R}^2 \tag{77}$$

shows the time intervals of the optimal profile for the annular disk fastened to the rigid shaft (Fig. 19a) and the continuity function (Fig. 19b).

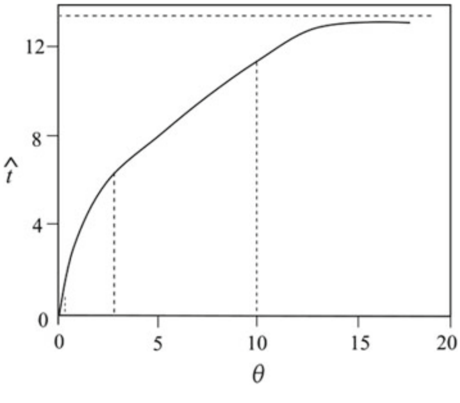

Fig. 16 Influence of parameter Θ on the time to rupture of disk fastened to the rigid shaft, with possible thickness variation in the place of joint

Fig. 17 The optimal shapes of disks fastened to the rigid shaft - uniparametric optimisation, $\beta = 0.5$, $\mu = 0.1$

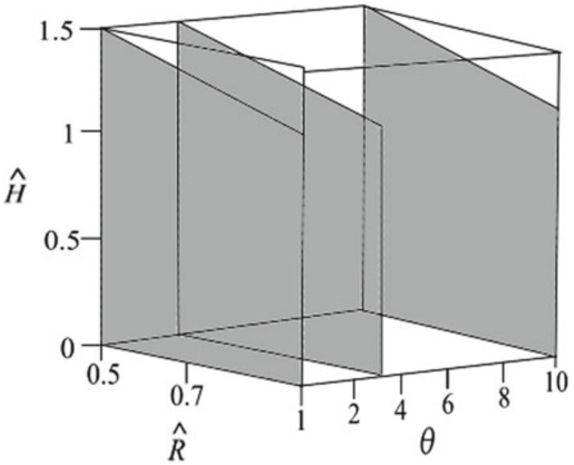

Fig. 18 The optimal shapes of disks fastened to the rigid shaft - biparametric optimisation, $\beta = 0.5$, $\mu = 0.1$

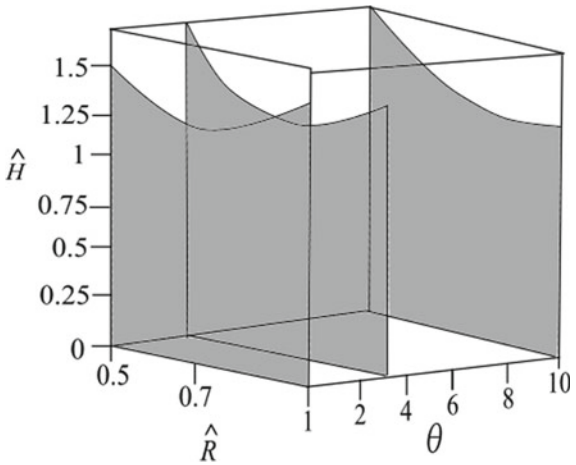

The geometrical variations of a disk profile are not significant in the creep process. Due to small width of the disk, the thickness variation at the internal edge is not too large, although possible.

3.2.3 Disk with Free Inner Edge

Boundary condition at the internal radius is described by the following expression:

$$\hat{\sigma}_r\left(\beta,\hat{t}\right) = 0 \tag{78}$$

and at the external radius by the following equations:

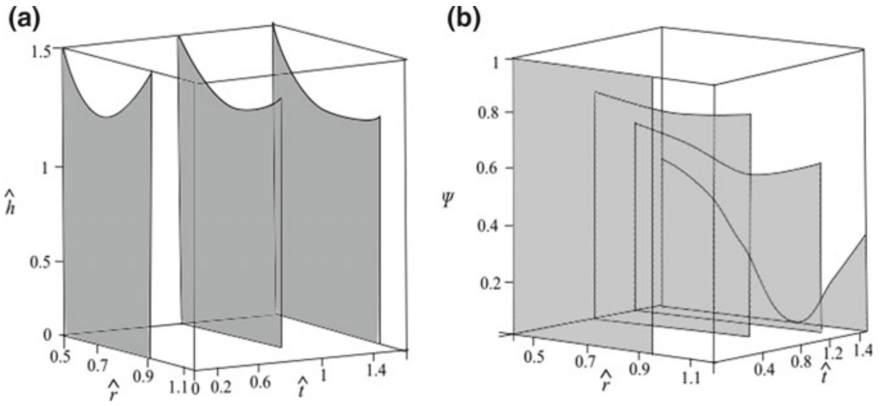

Fig. 19 Time intervals of the optimal profile and the continuity function for $\beta = 0.5$, $\mu = 0.1$, $\Theta = 3$

Fig. 20 The optimal profiles of the conical disk with free internal edge, $\beta = 0.1$, $\mu = 0.1$

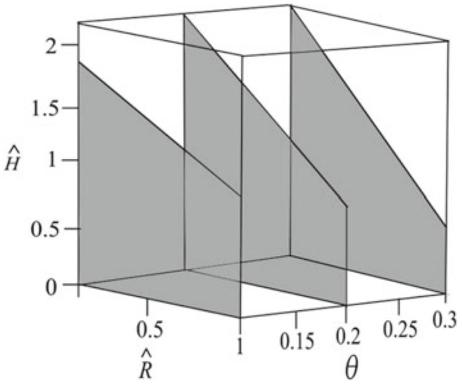

$$\hat{\sigma}_r(1, t) = \frac{1}{\hat{h}(1, t)} \tag{79}$$

The optimal profiles for the conical disk are plotted in Fig. 20 as a function of parameter Θ for the boundary conditions defined.

The optimal profiles for the conical disks with free internal edge are characterized by significant reduction of thickness at the external radius, even larger than for the disk clamped to the rigid shaft. The optimal shapes of the free disks are shown in Fig. 21 for the biparametric optimization.

The reinforcement of the disk external edge is observed for $\Theta = 0.1$. In the case of $\Theta = 0.2$ and $\Theta = 0.3$ the optimal shapes are characterized by reduction of the disk thickness toward the external edge. An example of the optimal profiles can be expressed as follows:

$$\hat{H}\left(\hat{R}\right) = 4.09 - 5.01\hat{R} + 1.79\hat{R} \tag{80}$$

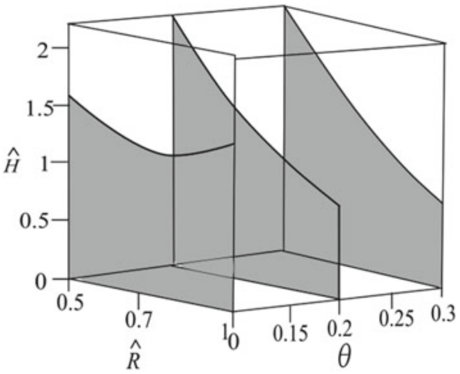

Fig. 21 The optimal shape for the disk with free internal edge, $\beta = 0.5$, $\mu = 0.1$

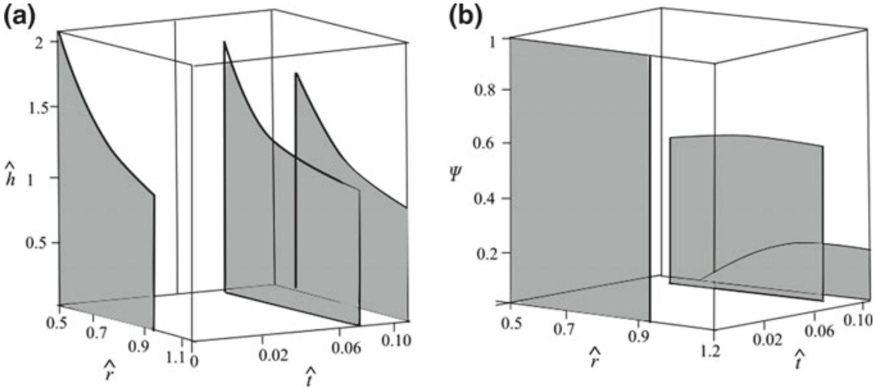

Fig. 22 Time intervals of the optimal profile for free edge and the continuity function, $\beta = 0.5$, $\mu = 0.1$, $\Theta = 0.2$

The time intervals of the disk profile and continuity function are shown in Fig. 22a, b, respectively.

Time intervals of the optimal profile and the continuity function indicate, that the rupture criterion of the disk is fulfilled at the internal edge, despite of the significant reinforcement of the thickness at this point.

4 Conclusions

Time-dependent properties of materials make it possible to formulate various problems of structure optimization under creep conditions. The problem of optimal design with respect to ductile and mixed creep rupture time turns out to be a very complicated one. In spite of physical nonlinearites (Norton's creep law), also geometrical nonlinearities are introduced, due to necessity of finite deformation theory application. Moreover, additional time factor causes that all differential equations describing process are the partial ones.

All these complications caused, that the parametric optimization was applied – the initial shape of the disk was described by polynomial function. The best solution was sought among disks with initial shape described by linear (one free parameter), or quadratic (two free parameters) functions. Better result, longer times to mixed creep rupture were obtained for biparametric optimization.

Significant influence on optimal solution of parameter Θ describing sensitivity of material on brittle, or ductile rupture was observed. Also ratio of own mass of the disk and mass placed at the external edge μ is of great importance.

References

1. Betten, J.: Mathematical modelling of materials behaviour under creep conditions. Appl. Mech. Rev. **54**(2), 107–132 (2001)
2. Castillo-Rodríguez, M., Nó, M.L., Jiménez, J.A., Ruano, O.A., San, Juan J.: High temperature internal friction in a Ti-46Al-1Mo-0.2Si intermetallic, comparison to creep behaviour. Acta Mater. **103**, 46–56 (2016)
3. Çğallioğlu, H., Topcu, M., Tarakcilar, A.R.: Elastic-plastic stress analysis on orthotropic rotating disc. Int. J. Mech. Sci. **48**, 985–990 (2006)
4. Dems, K., Mróz, Z.: Shape sensitivity analysis and optimal design of disks and plates with strong discontinuities of kinematic fields. Int. J. Solids Struct. **29**(4), 437–463 (1992)
5. Dorn, J.E.: Some fundamental experiments on high temperature creep. J. Mech. Phys. Solids **3**(2), 85 (1955)
6. Eraslan, A.N.: Elastic-plastic deformations of rotating variable thickness annular disks with free, pressurized and radially constrained boundary conditions. Int. J. Mech. Sci. **45**(4), 643–667 (2003)
7. Eraslan, A.N., Orcan, Y.: Elastic-plastic deformation of a rotating solid disk of exponentially varying thickness. Mech. Mater. **34**, 423–432 (2002)
8. Eraslan, A.N., Orcan, Y.: On the rotating elastic-plastic solid disks of variable thickness having concave profiles. Int. J. Mech. Sci. **44**, 1445–1466 (2002)
9. Farshi, B., Bidabadi, J.: Optimum design of inhomogeneous rotating discs under secondary creep. Int. J. Press. Vessels Pip. **85**, 507–515 (2008)
10. Gamer, U.: Elastic-plastic deformation of the rotating solid disk. Ingenieur-Arch. **54**, 345–354 (1984)
11. Ganczarski, A., Skrzypek, J.: Optimal shape of prestressed disks in creep. J. Struct. Mech. **2**, 141–160 (1976)
12. Golub, V.P.: Derivation of creep long-term fracture criteria under plane state of stress. Int. J. Mech. Sci. **47**(12), 1807–1826 (2005)
13. Golub, V.P., Teteruk, R.G.: Evaluating the time to ductile fracture under creep conditions. Int. Appl. Mech. **30**(11), 898–905 (1994)
14. Golub, V.P., Romanov, A.V., Romanova, N.V.: Nonlinear creep and ductile creep rupture of perfectly elastoplastic rods under tension. Int. Appl. Mech. **44**(4), 459–470 (2008)
15. Grabovsky, Y.: Optimal design problems for two-phase conducting composites with weakly discontinuous objective functionals. Adv. Appl. Math. **27**, 683–704 (2001)
16. Gun, H.: Two-dimensional boundary element analysis of creep continuum damage problems with plastic effects. Comput. Mater. Sci. **41**(3), 322–329 (2008)
17. Gunneskov, O.: Optimal design of rotating disks in creep. J. Struct. Mech. **4**(2), 141–160 (1976)

18. Guven, U.: Elastic-plastic stresses in a rotating annular disk of variable thickness and variable density. Int. J. Mech. Sci. **34**, 133–8 (1992)
19. Hayhurst, D.R.: Creep rupture under multi-axial states of stress. J. Mech. Phys. Solids **20**, 381–390 (1972)
20. Hoff, N.J.: The necking and rupture of rods subjected to constant tensile loads. J. Appl. Mech. Trans. ASME **20**, 105–112 (1953)
21. Jahed, H., Farshi, B., Bidabadi, J.: Minimum weight design of inhomogeneous rotating discs. Int. J. Press. Vessels Pip. **82**, 35–41 (2005)
22. Jiang, L.: Optimal design of equipment for al in-situ composites fabricated by reaction synthesis. In: International Conference on Measuring Technology and Mechatronics Automation, vol. 2, pp. 832–836 (2010)
23. Kachanov, L.M.: Creep Theory. Fizmatgiz, Moskwa (1960)
24. Kastenhuber, M., Rashkova, B., Clemens, H., Mayer, S.: Effect of microstructural instability on the creep resistance of an advanced intermetallic g-TiAl based alloy. Intermetallics **80**, 1–9 (2017)
25. Kordkheili, S.A.H., Naghdabadi, R.: Thermoelastic analysis of a functionally graded rotating disk. Compos. Struct. **79**(4), 508–516 (2007)
26. Kou, X.Y., Parks, G.T., Tan, S.T.: Optimal design of functionally graded materials using a procedural model and particle swarm optimisation. Comput. Aided Design **44**(4), 300–310 (2012)
27. Kowalewski, Z.L., Mackiewicz, S., Szelżek, J., Pietrzak, K., Augustyniak, B.: Evaluation of damage in steels subjected to prior deformation - destructive and nondestructive techniques. J. Multiscale Model. 479–499 (2009)
28. Lin, J., Kowalewski, Z.L., Cao, J.: Creep rupture of copper and aluminum alloy under combined loadings - experiments and their various descriptions. Int. J. Mech. Sci. **47**, 1038–1058 (2005)
29. Martin, J.B., Leckie, F.A.: On the creep rupture of structures. J. Mech. Phys. Solids **20**, 223–238 (1972)
30. Mentl, V.: An application of a phenomenological theory of creep damage. Mater. High Temp. **23**, 195–200 (2006)
31. Orcan, Y., Eraslan, A.N.: Elastic-plastic stresses in linearly hardening rotating solid disks of variable thickness. Mech. Res. Commun. **29**, 269–281 (2002)
32. Pedersen, P.: On optimal shapes in materials and structures. Struct. Multidisc. Optim. **19**, 169–182 (2000)
33. Pedersen, P.: On the influence of boundary conditions, Poisson's ratio and material non-linearity on the optimal shape. Int. J. Solids Struct. **38**(3), 465–477 (2001)
34. Rysz, M.: Optimal design of a thick-walled pipeline cross-section against creep rupture. Acta Mech. **1**(4), 83–102 (1987)
35. Shimanovskii, A.V., Shalinskii, V.V.: Physically and geometrically nonlinear deformation of bars: numerical analytic problem-solving. Int. Appl. Mech. **45**(5), 572–577 (2009)
36. Szuwalski, K.: Optimal design of bars under nonuniform tension with respect to ductile creep rupture. Mech. Struct. Mach. **3**, 303–319 (1989)
37. Szuwalski, K.: Nohomogeneous bars optimal with respect to ductile creep rupture. Eng. Opt. **25**, 54–60 (1995)
38. Szuwalski, K., Ustrzycka, A.: Optimal design of bars under nonuniform tension with respect to mixed creep rupture time. Int. J. Non-Linear Mech. **47**, 55–60 (2012)
39. Szuwalski, K., Ustrzycka, A.: The influence of boundary conditions on optimal shape of annular disk with respect to ductile creep rupture time. Eur. J. Mech. A-Solids **37**, 79–85 (2013)
40. Szuwalski, K., Ustrzycka, A.: Optimal design of full disks with respect to mixed creep rupture time. Eng. Struct. **20**, 1728–1734 (2013)
41. Szuwalski, K., Ustrzycka, A.: Mathematical and numerical modelling of large creep deformations for annular rotating disks. Appl. Math. Mech. Engl. Ed. **36**, 1441–1448 (2015)
42. Vivio, F., Vullo, V.: Elastic stress analysis of rotating converging conical disks subjected to thermal load and having variable density along the radius. Int. J. Solids Struct. **44**(24), 7767–7784 (2007)

43. Vivio, F., Vullo, L.: Elastic-plastic analysis of rotating disks having non-linearly variable thickness: residual stresses by overspeeding and service stress state reduction. Ann. Solid Struct. Mech. **1**(2), 87–102 (2010)
44. Zenkour, A.M.: Elastic deformation of the rotating functionally graded annular disk with rigid casing. J. Mater. Sci. **43**(23), 9717–9724 (2007)
45. Życzkowski, M.: Optimal structural design in rheology. J. Appl. Mech. **38**(1), 39–46 (1971)
46. Życzkowski, M.: Optimal structural design under creep conditions. Appl. Mech. Rev. **12**, 453–461 (1988)

A J-Interaction Integral to Compute Force Stress and Couple Stress Intensity Factors for Cracks in Functionally Graded Micropolar Materials

Hongjun Yu and Meinhard Kuna

Abstract In contrast to classical elasticity, the micropolar continuum theory allows to describe materials with significant microstructural effects, such as particulate, granular and porous composites. Such materials show a size effect and have often a spatially varying distribution of mechanical properties. This contribution focuses on the establishment of the interaction integral (I-integral) for decoupling the force stress intensity factors (FSIFs) and couple stress intensity factors (CSIFs) of a crack in functionally graded micropolar material (FGMM). The I-integral is derived from the J-integral by superimposing an auxiliary field on the actual field. The auxiliary field is examined using three different definitions including the constant-constitutive-tensor (CCT) formulation, the non-equilibrium (NE) formulation and the incompatibility (IC) formulation. The NE and IC formulations are more appropriate than the CCT formulation because the I-integral using the CCT formulation involves strain gradients and curvature gradients, which may cause loss of accuracy in numerical calculations. Furthermore, we introduce the patched extended finite element method (patched-XFEM), which replaces crack-tip enrichment functions from the XFEM by a local refined mesh to improve the numerical precision. The I-integral in combination with the patched-XFEM is employed to examine numerically the influence of material parameters on the FSIFs and CSIFs.

H. Yu
Department of Astronautic Science and Mechanics, Harbin Institute
of Technology, Harbin 150001, China
e-mail: yuhongjun@hit.edu.cn

M. Kuna (✉)
Technische Universität Bergakademie Freiberg, Institute of Mechanics
and Fluid Dynamics, 09596 Freiberg, Germany
e-mail: meinhard.kuna@imfd.tu-freiberg.de

© Springer International Publishing AG 2018

H. Altenbach et al. (eds.), *Advances in Mechanics of Materials and Structural Analysis*, Advanced Structured Materials 80,
https://doi.org/10.1007/978-3-319-70563-7_19

1 Introduction

The micropolar continuum theory is preferable to describe materials where microstructural effects are significant, such as particulate, granular and porous composites, whereas the classical continuum theory does not enable it. A current overview about micropolar continuum theory can be found in [1–3]. The micropolar continuum concept was first proposed by Cosserat and Cosserat [4], who introduced three rotational degrees of freedom, in addition to translational degrees of freedom. The micropolar continuum did not receive much attention until the elaborate studies of Eringen [5, 6], who introduced a general theory of a microelastic continuum. Cowin [7] used an internal length to describe the size effect and the coupling number N to characterize a continuous transition from classical elasticity to micropolar elasticity. The size effect was first observed by researchers [8–12] in foam and porous materials. The experiments [11, 12] showed that the porous specimens behaved much stiffer than expected from classical elasticity under torsion of slender cylinders and under bending of plates and beams, but size effects were not observed in tension. In particular, the micropolar elastic theory accurately fits the experimental data for the effective stiffness of bone samples from the osteon to the whole bone [12, 13]. Moreover, many natural porous materials show a spatially gradation of the mechanical properties to match an optimal design. Nevertheless, issues of fracture and fatigue have to be considered to maintain high strength and durability.

Through analyzing a crack in an infinite two-dimensional (2D) micropolar medium, researchers [14, 15] found that both force stresses and couple stresses near a crack tip have an $r^{-1/2}$ singularity. They proposed to use the force stress intensity factors (FSIFs) and couple stress intensity factors (CSIFs) to characterize the crack-tip fields. Paul and Sridharan [16, 17] analyzed the influence of the micropolar constitutive material parameters on the FSIFs and CSIFs for penny-shaped and Griffith cracks in a micropolar medium. They found that both the mode-I FSIF and the CSIF depend on the internal length parameter as well as the coupling number N. Sridharan [18] analyzed an insulated penny-shaped crack in micropolar media under uniform heat-flow loading. He found that the mode-II FSIF depends on the intrinsic length parameter and the coupling number N, and that its value remains higher than those obtained from the classical continuum theory. Diegele et al. [19] provided the near-tip asymptotic field solutions for a mixed-mode crack in a 2D isotropic micropolar solid. They showed that aside from two FSIFs and one CSIF characterizing the singular terms, two constant force stresses and one constant couple stress are involved in the expressions of force stresses and couple stresses, respectively. Recently, a number of research works on fracture of micropolar materials have been carried out in theoretical [20–25] and numerical approaches including the finite element method (FEM) [26, 27] the boundary element method (BEM) [28, 29] and the extended finite element method (XFEM) [30, 31].

In practical numerical calculations, only few methods are effective to extract the crack-tip fracture parameters for micropolar elasticity. Jaric [32] proposed a path-independent J-integral that equals the crack-tip energy release rate. However, the mixed-mode FSIFs and CSIFs cannot be decoupled from the J-integral. An effective approach to decouple the mode-I FSIF, the mode-II FSIF and the in-plane CSIF is the I-integral [33], which is derived from the J-integral based on the superposition of the actual field and an auxiliary field. The I-integral was first proposed by Stern et al. [34] for classical elastic media. As the auxiliary field can be designed freely, the I-integral allows not only to decouple the mixed-mode SIFs, but also to extract the crack-tip T-stress [35]. The I-integral was developed for functionally graded materials (FGMs) [36, 37] which is a category of nonhomogeneous materials with properties varying continuously with location. Compared to the analytical models for FGMs [38, 39], the I-integral is easily implemented in practical fracture analyses. The merit of the I-integral is demonstrated in crack analyses of FGMs, bi-materials, and fiber-reinforced composites [40–45]. Recently, Yu et al. [33] developed the I-integral for extracting the FSIFs and CSIFs of micropolar materials and proved that the I-integral is domain-independent for interfaces.

The present contribution aims to discuss the validity of the I-integral for functionally graded micropolar materials (FGMMs) through the selection of different applicable auxiliary fields. The outline is as follows. Section 2 briefly introduces the micropolar elastic theory and the linear elastic fracture theory for FGMMs. Section 3 discusses three applicable auxiliary fields and derives the domain forms of the I-integral. Section 4 introduces briefly the patched XFEM. Several examples are provided in Sect. 5 to verify the validity of the auxiliary fields. Finally, a summary is given in Sect. 6.

2 Fracture Mechanics of FGMMs

2.1 Governing Equations for Micropolar Elasticity

In the micropolar continuum theory, each material point has six degrees of freedom, including three displacement components and three micro-rotation components. For a centrosymmetric isotropic micropolar solid without body forces and body couples, the governing equations are as follows [46]:

- Kinematic equations:

$$\begin{aligned} \varepsilon_{ij} &= u_{j,i} - e_{ijk}\phi_k \\ \chi_{ij} &= \phi_{j,i} \end{aligned} \tag{1}$$

  where u_j and ϕ_k are the components of displacement and micro-rotation vectors, respectively, ε_{ij} and χ_{ij} are the components of microstrain and curvature tensors, respectively, and e_{ijk} is the permutation tensor. The subscripts $i,\ j,\ k$ and l range from (1) to (3), and the repetition of a subscript in a term denotes a summation with respect to that index over its range. A comma denotes a partial derivative.

- Equilibrium equations (without body forces and body couples):

$$\begin{aligned} &\sigma_{ji,j} = 0 \\ &m_{ji,j} + e_{ijk}\sigma_{jk} = 0 \end{aligned} \tag{2}$$

- Constitutive equations:

$$\begin{aligned} \sigma_{ij} &= A_{ijkl}\varepsilon_{kl} = \lambda\varepsilon_{kk}\delta_{ij} + (\mu+\kappa)\varepsilon_{ij} + \mu\varepsilon_{ji} \\ m_{ij} &= B_{ijkl}\chi_{kl} = \alpha\chi_{kk}\delta_{ij} + \gamma\chi_{ij} + \beta\chi_{ji} \end{aligned} \tag{3}$$

where σ_{ij} and m_{ij} are the force stress and couple stress tensors, respectively, λ and μ are Lamé's constants, and κ, α, β and γ are the micropolar material parameters. The stress is also expressed by the macrostrain tensor $e_{ij} = (u_{i,j} + u_{j,i})/2$ and the macrorotation vector $r_k = e_{klm}u_{m,l}/2$ as $\sigma_{ij} = \lambda e_{kk}\delta_{ij} + (2\mu+\kappa)e_{ij} + \kappa e_{ijk}(r_k - \phi_k)$. For micropolar elasticity, the shear modulus G, Young's modulus E and Poisson's ratio ν are given by [20]:

$$G = \mu + \frac{\kappa}{2}, \quad \nu = \frac{\lambda}{2\lambda + 2G}, \quad E = 2G(1+\nu) \tag{4}$$

In addition, the characteristic length in torsion l_t, and the characteristic length in bending, l_b and the coupling number N given by [20]

$$l_t = \sqrt{\frac{\beta+\gamma}{2G}}, \quad l_b = \sqrt{\frac{\gamma}{4G}}, \quad N = \sqrt{\frac{\kappa}{2G+\kappa}} \tag{5}$$

are used to describe the micropolar materials. Due to the existence of two internal characteristic lengths, the micropolar theory is capable to predict size effects. The coupling number N satisfies the relation $0 \le N \le 1$, where $N = 0$ corresponds to the classical elastic theory and $N = 1$ the couple stress theory. The micropolar constants satisfy the following inequalities [1, 46–48]:

$$\begin{aligned} &3\lambda + 2G \ge 0, \qquad && G \ge 0, \quad \kappa \ge 0 \\ &3\alpha + \beta + \gamma \ge 0, && -\gamma \le \beta \le \gamma \end{aligned} \tag{6}$$

2.2 *Crack-Tip Asymptotic Fields in FGMMs*

Let's consider a 2D functionally graded micropolar body occupying the space R with a crack as shown in Fig. 1. Only in-plane displacement components u_1, u_2 and micro-rotation component ϕ_3 are non-zero, and thus the governing equations are simplified to:

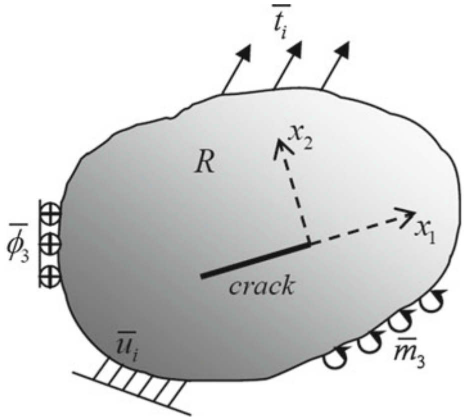

Fig. 1 A two-dimensional functionally graded micropolar solid with an inclined crack

$$\varepsilon_{ij} = u_{j,i} - e_{ij3}\phi_3, \qquad \chi_{i3} = \phi_{3,i} \tag{7}$$

$$\sigma_{ji,j} = 0, \qquad m_{i3,i} + e_{ij3}\sigma_{ij} = 0 \tag{8}$$

$$\sigma_{ij} = A_{ijkl}(\mathbf{x})\varepsilon_{kl}, \qquad m_{i3} = \gamma(\mathbf{x})\chi_{i3} \tag{9}$$

The material parameters $A_{ijkl}(\mathbf{x})$ $(i, j, k, l = 1, 2)$ and $\gamma(\mathbf{x})$ are spatially continuous and piecewise differentiable in domain R. The boundary conditions are given by

$$\begin{aligned} u_i &= \bar{u}_i \text{ on } \partial R^u, & \sigma_{ij}n_i &= \bar{t}_j \text{ on } \partial R^\sigma \\ \phi_3 &= \bar{\phi}_3 \text{ on } \partial R^\phi, & m_{i3}n_i &= \bar{m}_3 \text{ on } \partial R^m \end{aligned} \tag{10}$$

where $\partial R = \partial R^u + \partial R^\sigma = \partial R^\phi + \partial R^m$ is the boundary of R, $\bar{t}_i$ and $\bar{m}_3$ are the force traction and the couple traction, respectively, on the boundary, $\bar{u}_i$ and $\bar{\phi}_3$ are the displacement and the micro-rotation, respectively, prescribed on the boundary, and n_i is the unit outward normal vector to the boundary.

In a small circular region R_ε around the crack tip, the dependence of material parameters on coordinates $\mathbf{x} = x_i\,\mathbf{e}_i$ in FGMMs $A_{ijkl}(\mathbf{x})$ and $\gamma(\mathbf{x})$ can be expressed in a Taylor series expansion as

$$\begin{aligned} A_{ijkl}(r,\theta) &= A^0_{ijkl} + rA^{(1)}_{ijkl}(\theta) + \frac{r^2}{2}A^{(2)}_{ijkl}(\theta) + \ldots \equiv A^0_{ijkl} + \tilde{A}_{ijkl} \\ \gamma(r,\theta) &= \gamma_0 + r\gamma^{(1)}(\theta) + \frac{r^2}{2}\gamma^{(2)}(\theta) + \ldots \equiv \gamma_0 + \tilde{\gamma} \end{aligned} \tag{11}$$

where A^0_{ijkl} and γ_0 are the local material constants evaluated at the crack tip, $A^{(n)}_{ijkl}(\theta)$ and $\gamma^{(n)}(\theta)$ are angular functions with $n = 1, 2, \ldots$. $\tilde{A}_{ijkl} \sim O(r)$ and $\tilde{\gamma} \sim O(r)$ are higher order terms of material parameters. Substituting Eq. (11) into Eqs. (7)–(9) yields

$$\begin{aligned}&(A^0_{ijkl} + \tilde{A}_{ijkl})(u_{l,kj} - e_{kl3}\phi_{3,j}) + \tilde{A}_{ijkl,j}(u_{l,k} - e_{kl3}\phi_3) = 0,\\ &(\gamma_0 + \tilde{\gamma})\phi_{3,ii} + \tilde{\gamma}_{,i}\phi_{3,i} + e_{ij3}(A^0_{ijkl} + \tilde{A}_{ijkl})(u_{l,k} - e_{kl3}\phi_3) = 0\end{aligned} \tag{12}$$

Following Ref. [19], we assume that

$$\begin{aligned}u_i(r,\theta) &= u_i^{(0)}(\theta)r^s + u_i^{(1)}(\theta)r^{s+1/2} + u_i^{(2)}(\theta)r^{s+1} + \ldots,\\ \phi_3(r,\theta) &= \phi_3^{(0)}(\theta)r^s + \phi_3^{(1)}(\theta)r^{s+1/2} + \phi_3^{(2)}(\theta)r^{s+1} + \ldots\end{aligned} \tag{13}$$

where the superscript s is an unspecified positive number. If the region R_ε is sufficiently small, the influence of higher-order terms of material constants can be ignored. Keeping the singular terms of $O(r^{s-2})$ and $O(r^{s-3/2})$ and ignoring higher-order terms, one can simplify (12) as

$$A^0_{ijkl}u_{l,kj} = 0, \qquad \gamma_0\phi_{3,ii} = 0 \tag{14}$$

The expressions in Eq. (14) are identical to those for a homogeneous micropolar solid with material constants evaluated at the crack tip in FGMMs. Adopting the solution process given in Ref. [19], one obtains the result that in the vicinity of the crack tip, both the displacement and micro-rotation have a $r^{1/2}$-singularity. The terms $u_i^{(0)}$, $u_i^{(1)}$, $\phi_3^{(0)}$ and $\phi_3^{(1)}$ are identical to those given by Diegele et al. [19] for homogeneous micropolar materials, while the terms $u_i^{(n)}$ and $\phi_3^{(n)}$ ($n \geq 2$) for FGMMs are different from those in [19] due to the nonhomogeneity of material property. Therefore, for the generalized plane strain condition, the expressions of u_i and ϕ_3 are given by

$$\begin{aligned}u_1 &= \left[K_I f_1^I(\theta) + K_{II} f_1^{II}(\theta)\right]\sqrt{\frac{r}{2\pi}}\\ &\quad + \left(k_I\frac{1-\nu_0}{2G_0}\cos\theta + k_{II}\frac{2G_0+\kappa_0}{4G_0\kappa_0}\sin\theta\right)r + O(r^{3/2}) + \ldots\\ u_2 &= \left[K_I f_2^I(\theta) + K_{II} f_2^{II}(\theta)\right]\sqrt{\frac{r}{2\pi}}\\ &\quad - \left(k_I\frac{\nu_0}{2G_0}\sin\theta + k_{II}\frac{2G_0-\kappa_0}{4G_0\kappa_0}\cos\theta\right)r + O(r^{3/2}) + \ldots\end{aligned} \tag{15}$$

$$\phi_3 = \frac{L_3}{\gamma_0}\sqrt{\frac{2r}{\pi}}\sin\frac{\theta}{2} + \frac{l_3}{\gamma_0}r\cos\theta + O(r^{3/2}) + \ldots \tag{16}$$

The crack-tip force stresses and couple stresses are expressed as

$$\sigma_{ij} = \frac{1}{\sqrt{2\pi r}}\left[K_I g_{ij}^I(\theta) + K_{II} g_{ij}^{II}(\theta)\right] + \left(k_I\delta_{i1}\delta_{j1} + k_{II}\delta_{i1}\delta_{j2}\right) + O(r^{1/2}) + \ldots \tag{17}$$

$$m_{i3} = \frac{L_3}{\sqrt{2\pi r}}\left(-\delta_{i1}\sin\frac{\theta}{2} + \delta_{i2}\cos\frac{\theta}{2}\right) + l_3\delta_{i1} + O(r^{1/2}) + \ldots \tag{18}$$

where $K_I = \lim_{r\to 0}\{\sqrt{2\pi r}\,\sigma_{22}|_{\theta=0}\}$, $K_{II} = \lim_{r\to 0}\{\sqrt{2\pi r}\,\sigma_{21}|_{\theta=0}\}$ and $L_3 = \lim_{r\to 0}\{\sqrt{2\pi r}\, m_{23}|_{\theta=0}\}$ are the mode-I FSIF, mode-II FSIF and in-plane CSIF, respectively. The coefficients k_I, k_{II}, and l_3 represent constant stress terms due to crack opening, crack sliding and in-plane micro-rotation, respectively. It can be observed that both the normal stress σ_{11} and the shear stress σ_{12} have a constant term. This is different from the classical fracture mechanics, where only the normal stress $\sigma_{11} = T$ has a constant term. The angular functions f_i^I, f_i^{II}, g_i^I, and g_i^{II} for the generalized plane strain condition are given by [33]:

$$\begin{aligned} f_1^I &= \frac{S_0}{4G_0}\left[(5-4\nu_0)\cos\frac{\theta}{2} - \cos\frac{3\theta}{2}\right] - \frac{\nu_0}{G_0}\cos\frac{\theta}{2} \\ f_2^I &= \frac{S_0}{4G_0}\left[(3-4\nu_0)\sin\frac{\theta}{2} - \sin\frac{3\theta}{2}\right] + \frac{1-\nu_0}{G_0}\sin\frac{\theta}{2} \end{aligned} \tag{19}$$

$$\begin{aligned} f_1^{II} &= \frac{S_0}{4G_0}\left[(5-4\nu_0)\sin\frac{\theta}{2} + \sin\frac{3\theta}{2}\right] + \frac{1-\nu_0}{G_0}\sin\frac{\theta}{2} \\ f_2^{II} &= \frac{S_0}{4G_0}\left[(4\nu_0-3)\cos\frac{\theta}{2} - \cos\frac{3\theta}{2}\right] + \frac{\nu_0}{G_0}\cos\frac{\theta}{2} \end{aligned} \tag{20}$$

$$\begin{aligned} g_{11}^I &= \frac{S_0}{4}\left(3\cos\frac{\theta}{2} + \cos\frac{5\theta}{2}\right), \quad & g_{12}^I &= \frac{S_0}{4}\left(3\sin\frac{\theta}{2} + \sin\frac{5\theta}{2}\right) - \sin\frac{\theta}{2} \\ g_{21}^I &= \frac{S_0}{4}\left(-\sin\frac{\theta}{2} + \sin\frac{5\theta}{2}\right), \quad & g_{22}^I &= \frac{S_0}{4}\left(\cos\frac{\theta}{2} - \cos\frac{5\theta}{2}\right) + \cos\frac{\theta}{2} \end{aligned} \tag{21}$$

$$\begin{aligned} g_{11}^{II} &= \frac{S_0}{4}\left(-3\sin\frac{\theta}{2} - \sin\frac{5\theta}{2}\right) - \sin\frac{\theta}{2}, \quad & g_{12}^{II} &= \frac{S_0}{4}\left(3\cos\frac{\theta}{2} + \cos\frac{5\theta}{2}\right) \\ g_{21}^{II} &= \frac{S_0}{4}\left(-\cos\frac{\theta}{2} + \cos\frac{5\theta}{2}\right) + \cos\frac{\theta}{2}, \quad & g_{22}^{II} &= \frac{S_0}{4}\left(-\sin\frac{\theta}{2} + \sin\frac{5\theta}{2}\right) \end{aligned} \tag{22}$$

The micropolar constant S_0 is defined by

$$S_0 = \frac{1 - 2(1 - \nu_0)N_0^2}{1 + 2(1 - \nu_0)N_0^2} \tag{23}$$

where $N_0 = \sqrt{\kappa_0/(2G_0 + \kappa_0)}$ is the coupling number evaluated at the crack tip. The constant S_0 satisfies the relation $\frac{1}{1.5-\nu_0} - 1 \leq S_0 \leq 1$ due to $0 \leq N_0 \leq 1$. It can be observed that the above angular functions f_i^I, f_i^{II}, g_i^I, and g_i^{II} degenerate to the corresponding functions of classical elastic theory for $N_0 = 0$ and to the couple stress theory for $N_0 = 1$ [20]. For the generalized plane stress condition, Poisson's ratio in the above expressions must be replaced with $\nu_0/(1 + \nu_0)$. Researchers [49, 50] found that the nature of the near tip displacement for FGMs is precisely the same as for homogeneous materials (the form of the terms proportional to $r^{1/2}$ and r in the displacement expression for FGMs is identical to that for homogeneous materials). It is also the case for the near tip displacement and micro-rotation of FGMMs.

3 Interaction Integral (I-integral)

The J-integral for a micropolar material is given by [51]

$$J = \lim_{\Gamma_\varepsilon \to 0} \int_{\Gamma_\varepsilon} \left[\frac{1}{2}(\sigma_{jk}\varepsilon_{jk} + m_{j3}\chi_{j3})\delta_{i1} - \sigma_{ij}u_{j,1} - m_{i3}\phi_{3,1} \right] n_i d\Gamma \, , \tag{24}$$

where Γ_ε is an integral contour around the crack tip, as shown in Fig. 2. Superimposing an auxiliary field $(u_i^{aux}, \phi_3^{aux})$ on the actual field (u_i, ϕ_3) of the considered crack problem leads to a new state for which the J-integral is given by

$$J^{(S)} = \lim_{\Gamma_\varepsilon \to 0} \int_{\Gamma_\varepsilon} \left\{ \begin{array}{c} \frac{1}{2}[(\sigma_{jk} + \sigma_{jk}^{aux})(\varepsilon_{jk} + \varepsilon_{jk}^{aux}) + (m_{j3} + m_{j3}^{aux})(\chi_{j3} + \chi_{j3}^{aux})]\delta_{i1} \\ -(\sigma_{ij} + \sigma_{ij}^{aux})(u_{j,1} + u_{j,1}^{aux}) - (m_{i3} + m_{i3}^{aux})(\phi_{3,1} + \phi_{3,1}^{aux}) \end{array} \right\} n_i d\Gamma \tag{25}$$

Fig. 2 Integral paths around the crack tip

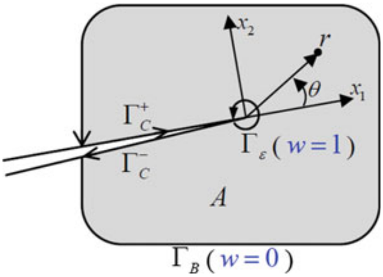

Expanding the J-integral and extracting the cross terms, one obtains the I-integral [33]

$$I = \lim_{\Gamma_\varepsilon \to 0} \int_{\Gamma_\varepsilon} \begin{bmatrix} \frac{1}{2}(\sigma_{jk}^{aux}\varepsilon_{jk} + \sigma_{jk}\varepsilon_{jk}^{aux} + m_{j3}^{aux}\chi_{j3} + m_{j3}\chi_{j3}^{aux})\delta_{i1} \\ -\sigma_{ij}^{aux}u_{j,1} - \sigma_{ij}u_{j,1}^{aux} - m_{i3}^{aux}\phi_{3,1} - m_{i3}\phi_{3,1}^{aux} \end{bmatrix} n_i d\Gamma \qquad (26)$$

The auxiliary field must be defined prior to the computation of the I-integral.

3.1 Three Formulations of the Auxiliary Field

Kim and Paulino [37] proposed three formulations of the auxiliary field for functionally graded materials, i.e. a constant-constitutive-tensor (CCT) formulation, a nonequilibrium (NE) formulation and an incompatibility (IC) formulation. Rao and Kuna [52, 53] showed the validity of these three definitions for functionally graded piezoelectric and magnetoelectroelastic materials. Similarly, three formulations are defined for FGMMs here. All of these three formulations adopt the same definitions for the auxiliary displacement and micro-rotation, i.e.

$$\begin{aligned} u_i^{aux} &= \left[K_I^{aux} f_i^I(\theta) + K_{II}^{aux} f_i^{II}(\theta)\right]\sqrt{\frac{r}{2\pi}} \\ \phi_3^{aux} &= \frac{L_3^{aux}}{\gamma_0}\sqrt{\frac{2r}{\pi}}\sin\frac{\theta}{2}, \end{aligned} \qquad (27)$$

where K_I^{aux}, K_{II}^{aux} and L_3^{aux} are the auxiliary mode-I FSIF, mode-II FSIF and in-plane CSIF, respectively. The angular functions f_i^I and f_i^{II} are identical to those in Eqs. (19) and (20). However, different formulations are used to define the auxiliary force stress, couple stress, microstrain and curvature, i.e.

- CCT formulation

$$\varepsilon_{ij}^{aux} = u_{j,i}^{aux}, \qquad \chi_{i3}^{aux} = \phi_{3,i}^{aux} \qquad (28)$$

$$\sigma_{ij}^{aux} = A_{ijkl}^{0}\varepsilon_{kl}^{aux}, \qquad m_{i3}^{aux} = \gamma_0\chi_{i3}^{aux} \qquad (29)$$

In the CCT formulation, all auxiliary variables are the asymptotic analytical solutions of a crack in an infinite homogeneous micropolar plate. Here, the material constants in the auxiliary constitutive Eq. (29) are different from those in the actual constitutive Eq. (3). As a result, the auxiliary field satisfies the equilibrium equations $\sigma_{ij,i}^{aux} = 0$ and $m_{i3,i}^{aux} = 0$, but violates the relations $\sigma_{ij}^{aux} \neq A_{ijkl}(\mathbf{x})\varepsilon_{kl}^{aux}$ and $m_{i3}^{aux} \neq \gamma(\mathbf{x})\chi_{i3}^{aux}$ for any coordinate apart from the crack tip.

- NE formulation

$$\varepsilon_{ij}^{aux} = u_{j,i}^{aux}, \qquad \chi_{i3}^{aux} = \phi_{3,i}^{aux} \tag{30}$$

$$\sigma_{ij}^{aux} = A_{ijkl}\varepsilon_{kl}^{aux}, \qquad m_{i3}^{aux} = \gamma\chi_{i3}^{aux} \tag{31}$$

In the NE formulation, the auxiliary force stress and couple stress are not the asymptotic analytical solutions of a crack in a homogeneous micropolar plate, but defined using the actual material properties of FGMMs. As a result, the auxiliary field does not satisfy the equilibrium equations, i.e. $\sigma_{ij,i}^{aux} \neq 0$ and $m_{i3,i}^{aux} \neq 0$.

- IC formulation

$$\sigma_{ij}^{aux} = A_{ijkl}^{0}u_{l,k}^{aux}, \qquad m_{i3}^{aux} = \gamma_0\phi_{3,i}^{aux} \tag{32}$$

$$\varepsilon_{ij}^{aux} = A_{ijkl}^{-1}\sigma_{kl}^{aux}, \qquad \chi_{i3}^{aux} = \gamma^{-1}m_{i3}^{aux} \tag{33}$$

In the IC formulation, the auxiliary force stress and couple stress are the asymptotic analytical solutions of a crack in a homogeneous micropolar plate so that $\sigma_{ij,i}^{aux} = 0$ and $m_{i3,i}^{aux} = 0$, whereas the auxiliary strain and curvature are defined using the actual material properties which results in $\varepsilon_{ij}^{aux} \neq u_{j,i}^{aux}$ and $\chi_{i3}^{aux} \neq \phi_{3,i}^{aux}$.

For homogeneous materials, all of the above three formulations coincide with each other, whereas none of the above three formulations satisfies all three governing relations for FGMMs, i.e. the constitutive, equilibrium and compatibility equations.

3.2 Numerical Calculation of the I-Integral

For practical calculations, the infinitesimal contour integral Eq. (26) must be converted into an equivalent domain integral. A traction-free crack is considered for which the crack-face boundary conditions are

$$n_i\sigma_{ij} = 0, \quad n_i m_{ij} = 0, \quad \text{on } \Gamma_C^+ \text{ and } \Gamma_C^- \tag{34}$$

where Γ_C^+ and Γ_C^- represent the top and bottom faces of a crack, respectively. As shown in Fig. 2, we convert the I-integral into an equivalent domain integral by Gauss' theorem as

$$I = \int_A \frac{\partial}{\partial x_i}\left\{\left[\begin{array}{c} \sigma_{ij}^{aux}u_{j,1} + \sigma_{ij}u_{j,1}^{aux} + m_{i3}^{aux}\phi_{3,1} + m_{i3}\phi_{3,1}^{aux} \\ -\frac{1}{2}(\sigma_{jk}^{aux}\varepsilon_{jk} + \sigma_{jk}\varepsilon_{jk}^{aux} + m_{j3}^{aux}\chi_{j3} + m_{j3}\chi_{j3}^{aux})\delta_{i1} \end{array}\right] w\right\} dA \tag{35}$$

where a smooth weighting function w is introduced with values varying from 1 on Γ_ε to 0 on Γ_B. Applying the auxiliary fields defined above, one can simplify the I-integral as follows:

- I-integral using the CCT formulation

$$
\begin{aligned}
I = {} & \int_A \left[\begin{array}{c} \sigma_{ij}^{aux} u_{j,1} + \sigma_{ij} u_{j,1}^{aux} - \frac{1}{2}(\sigma_{jk}^{aux} \varepsilon_{jk} + \sigma_{jk} \varepsilon_{jk}^{aux}) \delta_{i1} \\ + m_{i3}^{aux} \phi_{3,1} + m_{i3} \phi_{3,1}^{aux} - \frac{1}{2}(m_{j3}^{aux} \chi_{j3} + m_{j3} \chi_{j3}^{aux}) \delta_{i1} \end{array} \right] w_{,i} \, dA \\
& + \int_A \left[(\sigma_{12}^{aux} - \sigma_{21}^{aux}) \phi_{3,1} - (\sigma_{12} - \sigma_{21}) \phi_{3,1}^{aux} \right] w dA \\
& + \frac{1}{2} \int_A \left[\begin{array}{c} (A_{ijkl} - A_{ijkl}^0)(\varepsilon_{ij} \varepsilon_{kl,1}^{aux} - \varepsilon_{ij}^{aux} \varepsilon_{kl,1}) - A_{ijkl,1} \varepsilon_{ij} \varepsilon_{kl}^{aux} \\ + (\gamma - \gamma_0)(\chi_{i3} \chi_{i3,1}^{aux} - \chi_{i3}^{aux} \chi_{i3,1}) - \gamma_{,1} \chi_{i3} \chi_{i3}^{aux} \end{array} \right] w \, dA
\end{aligned} \tag{36}
$$

- I-integral using the NE formulation

$$
\begin{aligned}
I = {} & \int_A \left(\begin{array}{c} \sigma_{ij}^{aux} u_{j,1} + \sigma_{ij} u_{j,1}^{aux} - \sigma_{jk} \varepsilon_{jk}^{aux} \delta_{i1} \\ + m_{i3}^{aux} \phi_{3,1} + m_{i3} \phi_{3,1}^{aux} - m_{j3} \chi_{j3}^{aux} \delta_{i1} \end{array} \right) w_{,i} \, dA \\
& + \int_A \left[(\sigma_{12}^{aux} - \sigma_{21}^{aux}) \phi_{3,1} - (\sigma_{12} - \sigma_{21}) \phi_{3,1}^{aux} \right] w dA \\
& + \int_A \left(\sigma_{ij,i}^{aux} u_{j,1} - A_{ijkl,1} \varepsilon_{ij} \varepsilon_{kl}^{aux} + m_{i3,i}^{aux} \phi_{3,1} - \gamma_{,1} \chi_{i3} \chi_{i3}^{aux} \right) w \, dA
\end{aligned} \tag{37}
$$

- I-integral using the IC formulation

$$
\begin{aligned}
I = {} & \int_A \left(\begin{array}{c} \sigma_{ij}^{aux} u_{j,1} + \sigma_{ij} u_{j,1}^{aux} - \sigma_{jk}^{aux} \varepsilon_{jk} \delta_{i1} \\ + m_{i3}^{aux} \phi_{3,1} + m_{i3} \phi_{3,1}^{aux} - m_{j3}^{aux} \chi_{j3} \delta_{i1} \end{array} \right) w_{,i} \, dA \\
& + \int_A \left[(\sigma_{12}^{aux} - \sigma_{21}^{aux}) \phi_{3,1} - (\sigma_{12} - \sigma_{21}) \phi_{3,1}^{aux} \right] w dA \\
& + \int_A \left\{ [(A_{ijkl}^0)^{-1} - A_{ijkl}^{-1}] \sigma_{ij} \sigma_{kl,1}^{aux} + (\gamma_0^{-1} - \gamma^{-1}) m_{i3} m_{i3,1}^{aux} \right\} w \, dA
\end{aligned} \tag{38}
$$

It can be observed that each of the above three domain forms of the I-integral contains three parts, whereby the third integral caused by material nonhomogeneity vanishes for homogeneous micropolar materials. The I-integral using the CCT formulation Eq. (36) contains strain gradient ($\varepsilon_{kl,1}$), curvature gradient ($\chi_{i3,1}$) and material property gradient ($A_{ijkl,1}$ and $\gamma_{,1}$). The I-integral using the NE formulation Eq. (37) contains neither strain gradient nor curvature gradient, but contains material property gradient. The I-integral using the IC formulation Eq. (38) contains none of them.

Since the I-integral using the CCT formulation contains strain and curvature gradients, its numerical computation will lose accuracy. Therefore, the NE and IC formulations are more appropriate than the CCT formulations for FGMMs. In addition, the I-integral using the IC formulation is effective for micropolar composites due to its domain-independence for interfaces [19].

3.3 Extraction of the FSIFs and CSIFs

In order to derive the relations between the I-integral and the intensity factors, we take the integral path Γ_ε along a circle of radius r. Substituting $d\Gamma = rd\theta$ into Eq. (26) yields

$$I = \lim_{r\to 0}\int_{-\pi}^{\pi}\begin{bmatrix} \frac{1}{2}(\sigma_{jk}^{aux}\varepsilon_{jk} + \sigma_{jk}\varepsilon_{jk}^{aux} + m_{j3}^{aux}\chi_{j3} + m_{j3}\chi_{j3}^{aux})\delta_{i1} \\ \\ -\sigma_{ij}^{aux}u_{j,1} - \sigma_{ij}u_{j,1}^{aux} - m_{i3}^{aux}\phi_{3,1} - m_{i3}\phi_{3,1}^{aux} \end{bmatrix} n_i r d\theta\,. \tag{39}$$

In a small region R_ε around the crack tip, the material constants A_{ijkl}^{-1} and γ^{-1} can be expressed using a Taylor series expansion as

$$\begin{aligned} A_{ijkl}^{-1}(r,\theta) &= (A_{ijkl}^{0})^{-1} + r\frac{\partial A_{ijkl}^{-1}}{\partial r}(\theta) + \frac{r^2}{2}\frac{\partial^2 A_{ijkl}^{-1}}{\partial r^2}(\theta) + \ldots. \\ \gamma^{-1}(r,\theta) &= \gamma_0^{-1} + r\frac{\partial \gamma^{-1}}{\partial r}(\theta) + \frac{r^2}{2}\frac{\partial^2 \gamma^{-1}}{\partial r^2}(\theta) + \ldots. \end{aligned} \tag{40}$$

As $r \to 0$, only the singular terms in the expansions of σ_{ij}, m_{i3}, $u_{j,i}$, $\phi_{3,i}$, ε_{ij}^{aux} and χ_{i3}^{aux} contribute to the I-integral. Substituting Eq. (40), the actual and auxiliary fields into Eq. (39) yields

$$I = \frac{1+S_0}{E'_0}(K_I K_I^{aux} + K_{II}K_{II}^{aux}) + \frac{L_3 L_3^{aux}}{\gamma_0} \tag{41}$$

where

$$E'_0 = \begin{cases} E_0 & \text{(plane stress)} \\ \frac{E_0}{1-\nu_0^2} & \text{(plane strain)} \end{cases} \tag{42}$$

Taking the vector $[K_I^{aux},\ K_{II}^{aux},\ L_3^{aux}]$ sequentially to be $[1,\ 0,\ 0]$, $[0,\ 1,\ 0]$ and $[0,\ 0,\ 1]$, one can compute the corresponding I-integrals $I^{(K_I)}$, $I^{(K_{II})}$ and $I^{(L_3)}$, so that the FSIFs and CSIFs can be solved according to the relations

$$K_I = \frac{E'_0}{1+S_0}I^{(K_I)}, \quad K_{II} = \frac{E'_0}{1+S_0}I^{(K_{II})}, \quad L_I = \gamma_0 I^{(L_3)}. \tag{43}$$

4 Patched XFEM for Micropolar Materials

Through embedding local solutions of boundary-value problems into the finite element approximation, the extended finite element method (XFEM) [54] allows cracks and material interfaces to be tackled independently of the mesh. The XFEM can greatly facilitate the modeling process, especially for crack propagation problems. Recently, the XFEM has been developed for micropolar elasticity [30, 31], too. The displacement approximation in the XFEM usually contains the standard finite element shape functions, the enrichment for crack faces and the enrichment for crack tips. The enrichment for crack faces is only a function of position, whereas the enrichment for crack tips is dependent on material constitutive equation. The use of the crack-tip enrichment is mainly used to improve the numerical accuracy. If the finite element mesh is sufficiently fine and the I-integrals are applied, it is not necessary to use the crack-tip enrichment functions. For FGMMs, we herein adopt the displacement and micro-rotation approximations as

$$\begin{Bmatrix} u_1^h(\mathbf{x}) \\ u_2^h(\mathbf{x}) \\ \phi_3^h(\mathbf{x}) \end{Bmatrix} = \sum_{p\in S_N} N_p(\mathbf{x}) \begin{Bmatrix} u_1^p \\ u_2^p \\ \phi_3^p \end{Bmatrix} + \sum_{p\in S_H} N_p(\mathbf{x})\bar{H}_p(\mathbf{x}) \begin{Bmatrix} b_1^p \\ b_2^p \\ b_3^p \end{Bmatrix} \tag{44}$$

Here, u_i^p, ϕ_3^p and b_i^p are the nodal displacements, nodal micro-rotation, and the additional degrees of freedom, respectively. $N_p(\mathbf{x})$ is the standard finite element shape function, $\bar{H}_p(\mathbf{x}) = H(\mathbf{x} - \bar{\mathbf{x}}) - H(\mathbf{x}_p - \bar{\mathbf{x}})$ is the shifted enrichment function for a crack face, where $\mathbf{x}$, $\mathbf{x}_p$ and $\bar{\mathbf{x}}$ denote an arbitrary point, the nodal point and the point on a crack face, respectively. S_N and S_H are the set of standard nodes and the set of enriched nodes, respectively. For a n-node element cut by a crack, the nodal degrees-of-freedom are expressed as

$$\begin{aligned} \{\mathbf{a}\} &= \begin{bmatrix} u_1^{(1)} \; u_2^{(1)} \; \phi_3^{(1)} \; ... \; u_1^{(n)} \; u_2^{(n)} \; \phi_3^{(n)} \end{bmatrix}^{\mathrm{T}} \\ \{\mathbf{b}\} &= \begin{bmatrix} b_1^{(1)} \; b_2^{(1)} \; b_3^{(1)} \; ... \; b_1^{(n)} \; b_2^{(n)} \; b_3^{(n)} \end{bmatrix}^{\mathrm{T}} \end{aligned} \tag{45}$$

The displacement and micro-rotation are expressed in matrix form as

$$\begin{Bmatrix} \mathbf{u}^h \\ \phi_3^h \end{Bmatrix} = \begin{bmatrix} \mathbf{N}^a \; \mathbf{N}^b \end{bmatrix} \begin{Bmatrix} \mathbf{a} \\ \mathbf{b} \end{Bmatrix} \tag{46}$$

Here, $[\mathbf{N}^a] = \begin{bmatrix} N_{(1)}\mathbf{I} \; N_{(2)}\mathbf{I} \; ... \; N_{(n)}\mathbf{I} \end{bmatrix}$, $[\mathbf{N}^b] = \begin{bmatrix} \bar{H}_{(1)}N_{(1)}\mathbf{I} \; \bar{H}_{(2)}N_{(2)}\mathbf{I} \; ... \; \bar{H}_{(n)}N_{(n)}\mathbf{I} \end{bmatrix}$, and $\mathbf{u} = \begin{bmatrix} u_1 \; u_2 \end{bmatrix}^{\mathrm{T}}$, where $\mathbf{I}$ is an identity matrix of order 3. The strain and curvature are expressed in matrix form as

$$\begin{Bmatrix} \varepsilon \\ \chi \end{Bmatrix} = \begin{bmatrix} \mathbf{B}^a \; \mathbf{B}^b \end{bmatrix} \begin{Bmatrix} \mathbf{a} \\ \mathbf{b} \end{Bmatrix} \tag{47}$$

Here, $\{\varepsilon\} = [\varepsilon_{11}\ \varepsilon_{12}\ \varepsilon_{21}\ \varepsilon_{22}]^{\mathrm{T}}$, $\{\chi\} = [\chi_{13}\ \chi_{23}]^{\mathrm{T}}$, $[\mathbf{B}^a] = \left[\mathbf{B}_{(1)}\ \mathbf{B}_{(2)}\ \ldots\ \mathbf{B}_{(n)}\right]$ and $[\mathbf{B}^b] = \left[\bar{H}_{(1)}\mathbf{B}_{(1)}\ \bar{H}_{(2)}\mathbf{B}_{(2)}\ \ldots\ \bar{H}_{(n)}\mathbf{B}_{(n)}\right]$, where

$$[\mathbf{B}_p] = \begin{bmatrix} N_{p,1} & 0 & 0 \\ 0 & N_{p,1} & -N_p \\ N_{p,2} & 0 & N_p \\ 0 & N_{p,2} & 0 \\ 0 & 0 & N_{p,1} \\ 0 & 0 & N_{p,2} \end{bmatrix},\ p = (1),\ \ldots\ (n)$$

Substituting Eq. (47) into the weak forms of the governing equations

$$\int_R \left\{\delta\varepsilon^{\mathrm{T}}\ \delta\chi^{\mathrm{T}}\right\}[\mathbf{C}(\mathbf{x})]\begin{Bmatrix}\varepsilon \\ \chi\end{Bmatrix} dV = \int_{\partial R^{\sigma}} \left\{\delta\mathbf{u}^{\mathrm{T}}\ \delta\phi_3\right\}\begin{Bmatrix}\mathbf{t} \\ m_3\end{Bmatrix} dS\,, \tag{48}$$

one obtains the linear equations

$$\begin{bmatrix}\mathbf{K}^e_{aa} & \mathbf{K}^e_{ab} \\ \mathbf{K}^e_{ba} & \mathbf{K}^e_{bb}\end{bmatrix}\begin{Bmatrix}\mathbf{a} \\ \mathbf{b}\end{Bmatrix} = \begin{Bmatrix}\mathbf{F}^e \\ \mathbf{0}\end{Bmatrix}. \tag{49}$$

Here, $\mathbf{C}(\mathbf{x})$ is material matrix of FGMMs, $\mathbf{t} = \left[t_1\ t_2\right]^{\mathrm{T}}$ is the traction vector. The element stiffness matrices and the nodal force vector for one element e are

$$\begin{aligned}
[\mathbf{K}^e_{aa}] &= \int_{V^e} [\mathbf{B}^a]^{\mathrm{T}}[\mathbf{C}(\mathbf{x})][\mathbf{B}^a]dV \\
[\mathbf{K}^e_{bb}] &= \int_{V^e} [\mathbf{B}^b]^{\mathrm{T}}[\mathbf{C}(\mathbf{x})][\mathbf{B}^b]dV \\
[\mathbf{K}^e_{ab}] &= \int_{V^e} [\mathbf{B}^a]^{\mathrm{T}}[\mathbf{C}(\mathbf{x})][\mathbf{B}^b]dV = [\mathbf{K}^e_{ba}]^{\mathrm{T}}
\end{aligned} \tag{50}$$

.

$$\{\mathbf{F}^e\} = \int_S [\mathbf{N}^a]^{\mathrm{T}}\begin{Bmatrix}\mathbf{t} \\ m_3\end{Bmatrix} dS \tag{51}$$

For plane strain condition, the material matrix $\mathbf{C}$ is expressed as

$$[\mathbf{C}] = \begin{bmatrix} \lambda + 2G & 0 & 0 & \lambda & & \\ 0 & G + \kappa/2 & G - \kappa/2 & 0 & \multicolumn{2}{c}{\mathbf{0}} \\ 0 & G - \kappa/2 & G + \kappa/2 & 0 & & \\ \lambda & 0 & 0 & \lambda + 2G & & \\ & & \mathbf{0} & & \gamma & 0 \\ & & & & 0 & \gamma \end{bmatrix}$$

while for plane stress condition, the parameter λ in the material matrix $\mathbf{C}$ should be replaced with $2G\lambda/(2G + \lambda)$.

In order to achieve satisfactory precision in the region around the crack tip, Yu et al. [45] proposed to patch a refined mesh on the main mesh. The technique was referred to as the patched XFEM. When the crack propagates, the patched mesh goes together with the crack tip. For FGMMs, the nonhomogeneous >>graded<< element technique [40] is adopted, namely, the material properties at each integration point are used in the calculation of the above element stiffness matrices.

5 Numerical Examples

In this section, internal and edge cracks are studied sequentially to verify the validity of different auxiliary fields and to examine the influence of material parameters on the FSIFs and CSIFs.

5.1 *Internal Cracks*

Figure 3(a) shows an inclined crack of length $2a$ and angle ω located in a square plate of length $2W$ subjected to tensile load $\sigma_{app} = \sigma_o e^{\eta x_1}$. Young's modulus varies with x_1 according to $E = E_o e^{\eta x_1}$, whereas Poisson's ratio ν, the coupling number N, and the characteristic length l_b remain constant in the entire plate. The data used in numerical analysis are as follows: $\sigma_o = 1\,\text{MPa}$, $E_o = 1\,\text{GPa}$, $\nu = 0.3$ and $l_b = 0.01\,\text{mm}$.

Example 1: An Infinite Square Plate with an Inclined Crack
First, the geometric parameters $a = 1\,\text{mm}$ and $W = 20\,\text{mm}$, the material gradient parameter $\eta = 0$ and the coupling number $N = 0.01$ are used to model an infinite homogeneous classical elastic plate, for which the analytical solution of the FSIFs is given by

$$\begin{aligned} K_I &= \sigma_o \sqrt{\pi a} \cos^2\omega \\ K_{II} &= \sigma_o \sqrt{\pi a}\ \sin\omega \cos\omega \end{aligned} \tag{52}$$

Then, the geometric and material parameters are set to $a = 1\,\text{mm}$, $W = 10\,\text{mm}$, $\beta = 0.5$ and $N = 0.01$ to model a functionally graded classical elastic plate. The classical elastic plate with such a configuration was investigated by Dolbow and Gosz [36]. As shown in Fig. 3b, the finite element mesh consists of 1945 eight-node quadrilateral (Q8) and 24 six-node quarter-point (T6qp) singular elements around the crack tips, with a total of 1969 elements and 6026 nodes.

As shown in Fig. 3c, the region being comprised of elements totally and partially enclosed by a circle C_I of radius R_I is selected to be the integration domain. In this example, $R_I = 6h_e$, where $h_e = 0.012$ is the radial edge length of an element at the crack tip. A right-hand Cartesian coordinate frame (x_1, x_2, x_3) is used, which

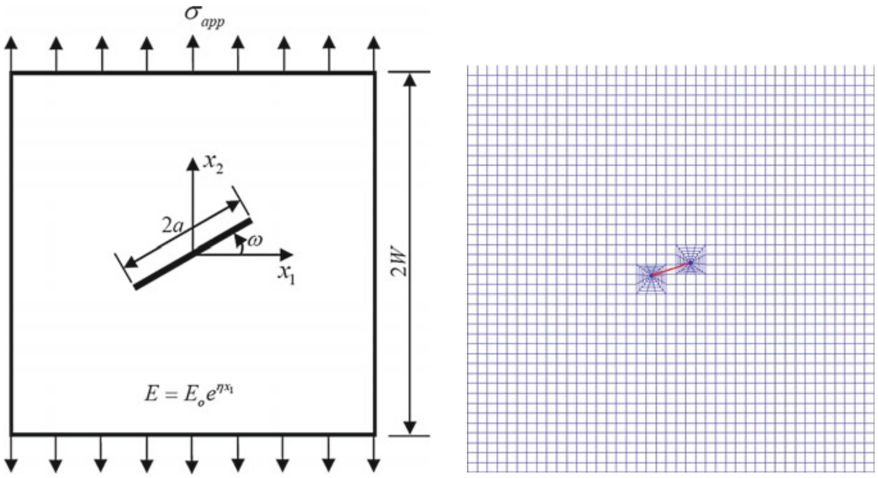

(a) Geometry and boundary conditions (b) Finite element mesh

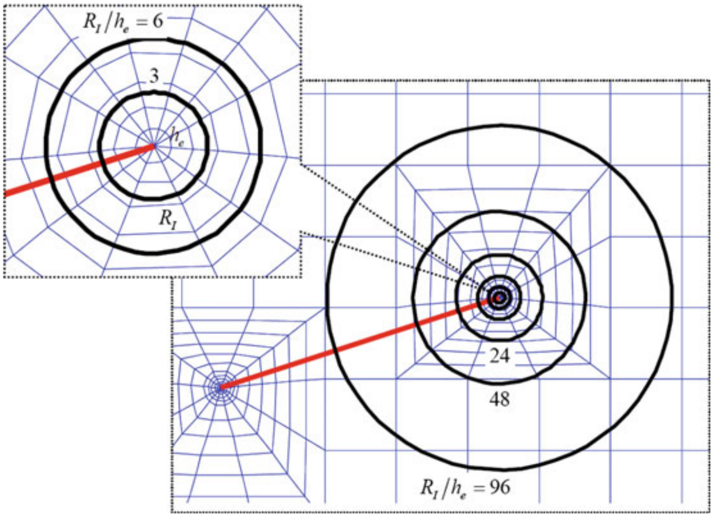

(c) Integral domains determined by a circle C_I of radius R_I

Fig. 3 A cracked micropolar plate under tension

leads to negative CSIF values for this example. The negative sign in the CSIFs just denotes the direction and thus, the normalized CSIFs $-L_3/L_0$ are given in the tables. Tables 1 and 2 list the normalized intensity factors K_I/K_0 , K_{II}/K_0 and $-L_3/L_0$ for a homogeneous plate $(\eta = 0)$ and for a functionally graded plate $(\eta = 0.5)$, respectively, where the reference factors $K_0 = \sigma_o\sqrt{\pi a}$ and $L_0 = l_b K_0$ are used for the internal crack. The results show that all three formulations of I-integral generate the same results for the homogeneous plate. For the functionally graded plate, the IC

Table 1 Normalized FSIFs and CSIFs at the right tip of a crack in an infinite homogeneous plate (Example 1: $a/W = 0.05,\ \eta = 0,\ N = 0.01,\ R_I/h_e = 6$)

	CCT formulation			NE formulation			IC formulation			Analytical	
ω (°)	$\frac{K_I}{K_0}$	$\frac{K_{II}}{K_0}$	$-\frac{L_3}{L_0}$	$\frac{K_I}{K_0}$	$\frac{K_{II}}{K_0}$	$-\frac{L_3}{L_0}$	$\frac{K_I}{K_0}$	$\frac{K_{II}}{K_0}$	$-\frac{L_3}{L_0}$	$\frac{K_I}{K_0}$	$\frac{K_{II}}{K_0}$
0	1.002	0.000	0.006	1.002	0.000	0.006	1.002	0.000	0.006	1.000	0.000
18	0.908	0.293	0.005	0.908	0.293	0.005	0.908	0.293	0.005	0.905	0.294
36	0.656	0.478	0.004	0.656	0.478	0.004	0.656	0.478	0.004	0.655	0.476
54	0.348	0.477	0.002	0.348	0.477	0.002	0.348	0.477	0.002	0.346	0.476
72	0.095	0.295	0.001	0.095	0.295	0.001	0.095	0.295	0.001	0.096	0.294

Table 2 Normalized FSIFs and CSIFs of a crack in a functionally graded plate (Example 1: $a/W = 0.1,\ \eta = 0.5,\ N = 0.01,\ R_I/h_e = 6$)

	CCT formulation			NE formulation			IC formulation			Ref. [36]	
ω (°)	$\frac{K_I}{K_0}$	$\frac{K_{II}}{K_0}$	$-\frac{L_3}{L_0}$	$\frac{K_I}{K_0}$	$\frac{K_{II}}{K_0}$	$-\frac{L_3}{L_0}$	$\frac{K_I}{K_0}$	$\frac{K_{II}}{K_0}$	$-\frac{L_3}{L_0}$	$\frac{K_I}{K_0}$	$\frac{K_{II}}{K_0}$
Right tip											
0	1.450	–0.001	0.010	1.451	–0.001	0.010	1.451	–0.001	0.010	1.445	0.000
18	1.308	0.348	0.009	1.310	0.348	0.009	1.310	0.348	0.009	1.303	0.353
36	0.936	0.558	0.006	0.937	0.558	0.006	0.937	0.558	0.006	0.930	0.560
54	0.495	0.538	0.003	0.496	0.538	0.003	0.496	0.538	0.003	0.488	0.540
72	0.146	0.316	0.001	0.146	0.316	0.001	0.146	0.316	0.001	0.142	0.316
Left tip											
0	0.683	–0.001	0.003	0.682	–0.001	0.003	0.682	–0.001	0.003	0.681	0.000
18	0.627	0.213	0.003	0.626	0.213	0.003	0.626	0.213	0.003	0.623	0.213
36	0.466	0.368	0.002	0.466	0.367	0.002	0.466	0.367	0.002	0.467	0.364
54	0.252	0.398	0.002	0.251	0.398	0.002	0.251	0.398	0.002	0.251	0.396
72	0.060	0.269	0.001	0.060	0.269	0.001	0.060	0.269	0.001	0.062	0.268

formulation and the NE formulation deliver the same results, which have a difference of less than 1.0% with the results computed using the CCT formulation. All CSIF values approach zero, which indicates that it is reasonable to use the coupling number $N = 0.01$ to simulate a classical elastic plate. The present FSIFs are compared with the analytical results of Eq. (52) (see Table 1) and those published in Ref. [36] (see Table 2). An agreement within 1.0% is shown for all three formulations.

Example 2: A Functionally Graded Plate with an Inclined Crack

The geometric and material parameters are set to $a = 1\,\text{mm}$, $W = 10\,\text{mm}$, $\eta = 0.5$ and $N = 0.01$ and $N = 0.5$ to model a functionally graded micropolar plate. As shown in Fig. 3c, six integration domains of $R_I/h_e = 3$, 6, 12, 24, 48 and 96 are used to compute the FSIFs and CSIFs in order to verify the domain-independence of the

Table 3 Normalized FSIFs and CSIFs of a crack in a functionally graded plate (Example 2: $a/W = 0.1,\ \eta = 0.5,\ N = 0.01,\ \omega = 18°$)

	CCT formulation			NE formulation			IC formulation		
$\frac{R_I}{h_e}$	$\frac{K_I}{K_0}$	$\frac{K_{II}}{K_0}$	$-\frac{L_3}{L_0}$	$\frac{K_I}{K_0}$	$\frac{K_{II}}{K_0}$	$-\frac{L_3}{L_0}$	$\frac{K_I}{K_0}$	$\frac{K_{II}}{K_0}$	$-\frac{L_3}{L_0}$
Right tip									
3	1.309	0.347	0.009	1.310	0.347	0.009	1.310	0.347	0.009
6	1.308	0.348	0.009	1.310	0.348	0.009	1.310	0.348	0.009
12	1.306	0.348	0.009	1.309	0.348	0.009	1.309	0.348	0.009
24	1.304	0.348	0.009	1.309	0.349	0.009	1.309	0.349	0.009
48	1.297	0.348	0.009	1.309	0.349	0.009	1.309	0.349	0.009
96	1.283	0.344	0.009	1.308	0.349	0.009	1.308	0.349	0.009
$D_r(\%)$	2.0	1.1	0.0	0.2	0.6	0.0	0.2	0.6	0.0
Left tip									
3	0.627	0.213	0.003	0.626	0.212	0.003	0.626	0.212	0.003
6	0.627	0.213	0.003	0.626	0.213	0.003	0.626	0.213	0.003
12	0.627	0.213	0.003	0.626	0.213	0.003	0.626	0.213	0.003
24	0.630	0.214	0.003	0.626	0.213	0.003	0.626	0.213	0.003
48	0.630	0.215	0.003	0.626	0.213	0.003	0.626	0.213	0.003
96	0.634	0.219	0.003	0.626	0.213	0.003	0.626	0.213	0.003
$D_r(\%)$	1.1	2.8	0.0	0.0	0.5	0.0	0.0	0.5	0.0

I-integrals. The relative deviation $D_r = |(K_{\max} - K_{\min})/K_{\text{mean}}| \times 100\%$ is used to estimate the difference of the intensity factors computed using different integration domains, where $K_{\max}$, $K_{\min}$ and K_{mean} denote the maximum, minimum and average values of the intensity factors, respectively.

Tables 3 and 4 list the normalized intensity factors for $N = 0.01$ and $N = 0.5$, respectively. The relative deviation D_r for both the NE formulation and the IC formulation does not exceed 1.0%, whereas D_r for the CCT formulation is about 3.0%. It indicates that the computation of the strain gradient probably causes numerical inaccuracy in finite element analysis. In addition, a relatively weaker convergence is observed for the CCT formulation when the size of integration domain increases, which is in accordance with the discussion for classical FGMs, see [37]. Therefore, the NE and IC formulations are more appropriate than the CCT formulation for FGMMs.

Example 3: Influence of Coupling and Gradation

First, the geometric parameters are set fixed to $a = 1$ mm, $W = 10$ mm and $\omega = 18°$. We take the coupling number $N = 0.01 \sim 0.99$ and gradation factor $\eta = 0 \sim 0.5$ in order to study their influence on the FSIFs and CSIFs. The IC formulation is used to compute the FSIFs and CSIFs, which are shown in Fig. 4a, b. Irrespective of whether the material is homogenous ($\eta = 0$) or nonhomogeneous ($\eta = 0.5$), all FSIFs and

Table 4 Normalized FSIFs and CSIFs of a crack in a functionally graded micropolar plate (Example 2: $a/W = 0.1,\ \eta = 0.5,\ N = 0.5,\ \omega = 18°$)

	CCT formulation			NE formulation			IC formulation		
$\frac{R_I}{h_e}$	$\frac{K_I}{K_0}$	$\frac{K_{II}}{K_0}$	$-\frac{L_3}{L_0}$	$\frac{K_I}{K_0}$	$\frac{K_{II}}{K_0}$	$-\frac{L_3}{L_0}$	$\frac{K_I}{K_0}$	$\frac{K_{II}}{K_0}$	$-\frac{L_3}{L_0}$
Right tip									
3	1.406	0.404	0.805	1.407	0.405	0.806	1.407	0.405	0.806
6	1.405	0.404	0.805	1.407	0.405	0.806	1.407	0.405	0.806
12	1.402	0.404	0.805	1.407	0.405	0.807	1.407	0.405	0.807
24	1.397	0.404	0.805	1.407	0.405	0.807	1.407	0.405	0.807
48	1.386	0.402	0.804	1.406	0.405	0.807	1.406	0.405	0.807
96	1.366	0.397	0.804	1.406	0.406	0.807	1.406	0.406	0.807
$D_r(\%)$	2.9	1.8	0.1	0.1	0.2	0.1	0.1	0.2	0.1
Left tip									
3	0.675	0.246	0.385	0.675	0.246	0.385	0.675	0.246	0.385
6	0.676	0.247	0.386	0.675	0.246	0.385	0.675	0.246	0.385
12	0.677	0.247	0.386	0.674	0.246	0.386	0.674	0.246	0.386
24	0.679	0.248	0.386	0.674	0.246	0.386	0.674	0.246	0.386
48	0.682	0.249	0.387	0.674	0.246	0.386	0.674	0.246	0.386
96	0.688	0.253	0.387	0.674	0.246	0.386	0.674	0.246	0.386
$D_r(\%)$	1.9	2.8	0.5	0.1	0.0	0.3	0.1	0.0	0.3

CSIFs at both crack tips increase monotonically as the coupling number N increases. As shown in Fig. 5a, b, for both $N = 0.01$ and $N = 0.5$, all FSIFs and CSIFs at the right (left) crack tip increase (decrease) monotonically as the gradient parameter η increases.

Next, the geometric and material parameters are set fixed to $W = 10\,\text{mm}, \omega = 18°$, $N = 0.5$, and $\eta = 0$ and 0.5, and the crack length is taken to be $a = 1 \sim 6\,\text{mm}$ in order to verify its influence on the normalized intensity factors. For a homogeneous micropolar plate, as shown in Fig. 6a, all FSIFs and CSIFs at both crack tips increase as the crack length a increases. Contrary, for a functionally graded micropolar plate ($\eta = 0.5$), as shown in Fig. 6b, all FSIFs and CSIFs at the right (left) crack tip increase (decrease) monotonically with growing crack length a. This example indicates that the material property gradient substantially affects the varying trend of the FSIFs and CSIFs.

5.2 *Edge Cracks*

As shown in Fig. 7, the second model is a rectangular plate of length $2H = 20\,\text{mm}$ and width $W = 11\,\text{mm}$ subjected to tension loading $\sigma_{app} = 100\,\text{MPa}$, which contains an

Fig. 4 Normalized FSIFs and CSIFs versus the coupling number N in **a** a homogeneous plate of $\eta = 0$ and **b** a functionally graded plate of $\eta = 0.5$ (Example 3)

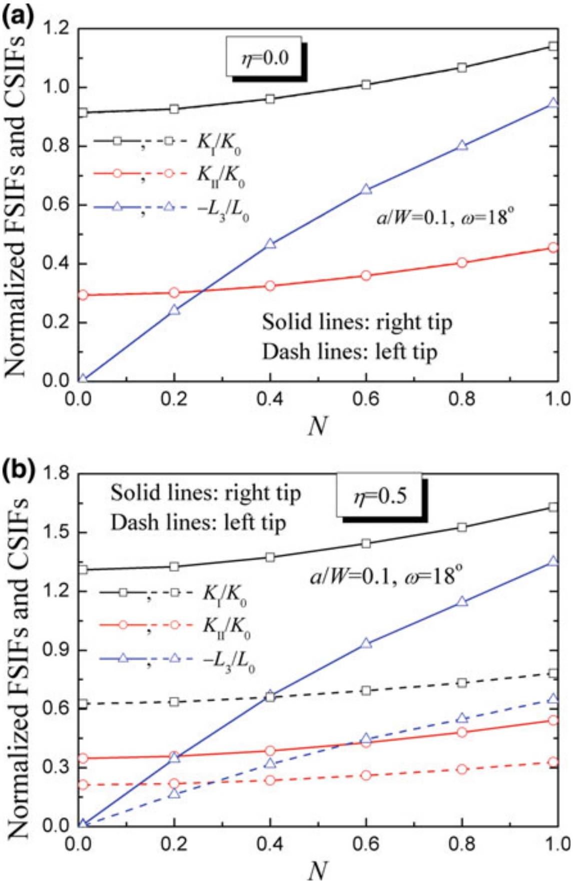

edge crack of length a and angle ω. The finite element mesh consists of 1293 elements and 3997 nodes.

Example 4: A Homogeneous Rectangular Plate with a Horizontal Edge Crack

The geometric and material parameters are set as $a = 1\,\text{mm}$, $\omega = 0$, $E = 100\,\text{GPa}$ and $\nu = 0.3$ to model a horizontal edge crack in a homogeneous plate. A classical elastic plate for which the coupling number is set as $N = 0.01$ and a micropolar plate of $N = 0.85$ are investigated. For a classical elastic plate with such a configuration, the solution of the FSIFs is given in [55] by

$$K_I^{cl} = k\,\sigma_{app}\sqrt{\pi a},\ K_{II}^{cl} = 0 \tag{53}$$

$$k = 1.12 - 0.23\frac{a}{W} + 10.55\left(\frac{a}{W}\right)^2 - 21.72\left(\frac{a}{W}\right)^3 + 30.39\left(\frac{a}{W}\right)^4$$

Fig. 5 Normalized FSIFs and CSIFs versus the gradient parameter η for the coupling number **a** $N = 0.01$ and **b** $N = 0.5$ (Example 3)

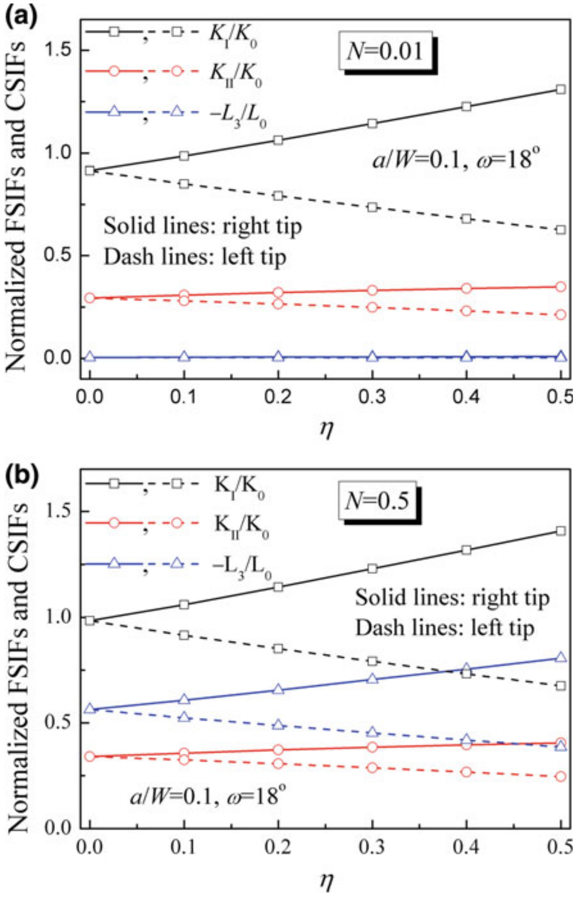

The micropolar plate with such a configuration was investigated by Atroshchenko and Bordas [29]. For both plates, the material parameter l_b is taken to be 0.01, 2.55×10^{-2}, 2.55×10^{-1}, $2.55 \times 10^{-1/2}$ and 2.55, sequentially. The FSIFs and CSIFs are normalized by $K_I^{cl} = 208$ MPa mm$^{1/2}$ and $L_0 = \sigma_{app} a \sqrt{\pi a} = 177$ MPa mm$^{3/2}$, respectively.

Table 5 lists the normalized mode-I FSIFs and in-plane CSIFs for a classical elastic plate ($N = 0.01$). All three formulations generate the same results for a homogeneous plate and thus, the normalized intensity factors are only listed once. When comparing the present results with the reference solution, an agreement within 0.5% is shown. Table 6 lists the normalized mode-I FSIFs and in-plane CSIFs for a micropolar plate ($N = 0.85$). The present results agree within 1.0% with those in Ref. [29]. In addition, the value of l_b affects neither the FSIFs nor the CSIFs when the coupling number N approaches to zero (see Table 5), but affects both the FSIFs and the CSIFs evidently (see Table 6).

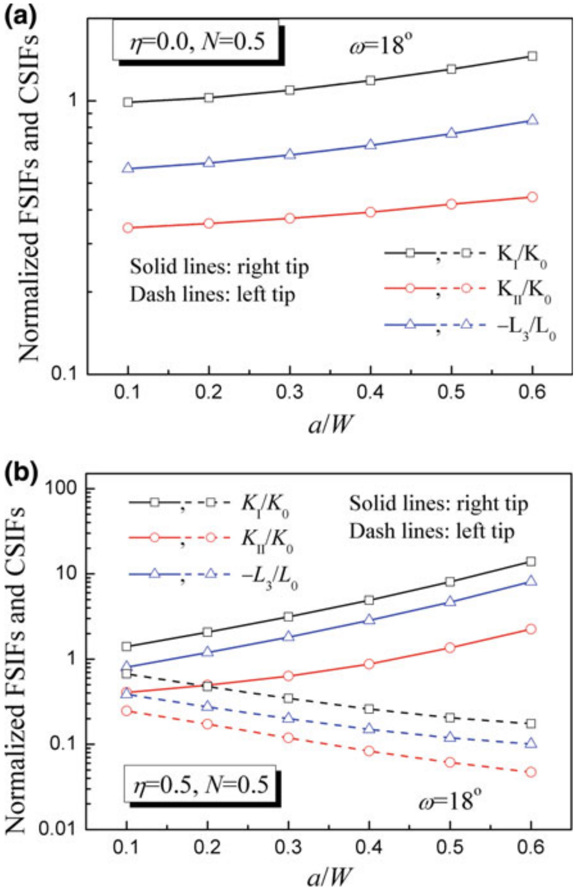

Fig. 6 Normalized FSIFs and CSIFs versus crack length a/W in **a** a homogeneous plate of $\eta = 0$ and **b** a functionally graded plate of $\eta = 0.5$ (Example 3)

Example 5: A Functionally Graded Plate with an Edge Crack

Here, the crack length is taken to be $a = 3\,\text{mm}$, while the crack inclination angle varies from $\omega = 0°$ to $\omega = 72°$. The material parameters are set to $E = E_o(1 + x_1/W)$, $\nu = 0.3$, $l_b = 0.8\,\text{mm}$ and $N = 0.01$, 0.8 and 0.99, where $E_o = 100\,\text{GPa}$. Table 7 lists the FSIFs and CSIFs normalized by $K_0 = \sigma_{app}\sqrt{\pi a}$ and $L_0 = l_b K_0$, respectively. The results show that the normalized FSIFs and CSIFs obtained using all three I-integral formulations agree within 0.1% with each other.

Example 6: A Functionally Graded Plate with a Horizontal Edge Crack

Next, the crack inclination angle is taken to be $\omega = 0°$ and the crack length varies from $a = 1\,\text{mm}$ to $a = 8$ mm. In order to study the influence of the variation of material stiffness on the FSIFs and CSIFs, the following three functions are chosen to define Young's modulus:

Fig. 7 A rectangular plate with an edge crack under tension

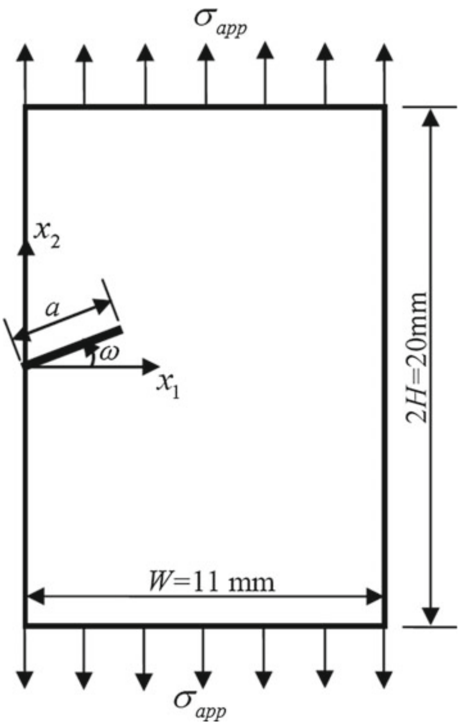

Table 5 Normalized FSIFs and CSIFs of an edge crack in a homogeneous plate (Example 4: $\omega = 0°,\ E = 100\,GPa,\ \nu = 0.3,\ R_I/h_e = 6$)

Present				Ref. [55]	
N	l_b	K_I/K_I^{cl}	$-L_3/L_0$	K_I/K_I^{cl}	$-L_3/L_0$
0.01	0.01	1.0043	0.0001	1.000	0.000
0.01	2.55E-2	1.0042	0.0002	1.000	0.000
0.01	2.55E-1	1.0042	0.0003	1.000	0.000
0.01	2.55E-0.5	1.0042	0.0003	1.000	0.000
0.01	2.55	1.0042	0.0003	1.000	0.000

- Function 1: $E = E_o(1 + 4x_1/W)$
- Function 2: $E = E_o[1 + 4(x_1/W)^2]$
- Function 3: $E = E_o[1 + 8x_1/W - 4(x_1/W)^2]$

As shown in Fig. 8, Young's modulus of all three functions increases from E_o at $x_1 = 0$ to $5E_o$ at $x_1 = W$, but these slopes are ascending (Function 2) or descending (Function 3) or constant (Function 1). The other material parameters are set as $E_o = 100\,\text{GPa}$, $\nu = 0.3$ and $l_b = 0.8\,\text{mm}$. The NE formulation is used to solve the FSIFs and CSIFs. Figure 9a–c show the normalized intensity factors K_I/K_0 and L_3/L_0

Table 6 Normalized FSIFs and CSIFs of an edge crack in a homogeneous micropolar plate (Example 4: $\omega = 0^\circ,\ E = 100\,GPa,\ \nu = 0.3,\ R_I/h_e = 6$)

Present				Ref. [29]	
N	l_b	K_I/K_I^{cl}	$-L_3/L_0$	K_I/K_I^{cl}	$-L_3/L_0$
0.85	0.01	1.1856	0.0107	–	–
0.85	2.55E-2	1.1783	0.0270	1.1819	0.0270
0.85	2.55E-1	1.0792	0.2111	1.0803	0.2120
0.85	2.55E-0.5	0.9580	0.3675	0.9542	0.3689
0.85	2.55	0.8822	0.4630	0.8836	0.4644

Table 7 Normalized FSIFs and CSIFs of a crack in a functionally graded plate (Example 5: $E = E_0(1 + x_1/W),\ E_0 = 100\,GPa,\ \nu = 0.3,\ l_b = 0.8,\ R_I/h_e = 6$)

	CCT formulation			NE formulation			IC formulation		
ω (°)	$\frac{K_I}{K_0}$	$\frac{K_{II}}{K_0}$	$-\frac{L_3}{L_0}$	$\frac{K_I}{K_0}$	$\frac{K_{II}}{K_0}$	$-\frac{L_3}{L_0}$	$\frac{K_I}{K_0}$	$\frac{K_{II}}{K_0}$	$-\frac{L_3}{L_0}$
$N = 0.01$									
0	1.4510	0.0000	0.0023	1.4511	0.0000	0.0023	1.4511	0.0000	0.0023
18	1.3246	0.2392	0.0020	1.3247	0.2392	0.0020	1.3247	0.2392	0.0020
36	1.0018	0.3753	0.0015	1.0020	0.3752	0.0015	1.0020	0.3752	0.0015
54	0.6117	0.3718	0.0009	0.6118	0.3717	0.0009	0.6118	0.3717	0.0009
72	0.2742	0.2459	0.0004	0.2743	0.2458	0.0004	0.2743	0.2458	0.0004
$N = 0.8$									
0	1.3726	0.0000	0.9382	1.3730	0.0000	0.9385	1.3730	0.0000	0.9385
18	1.2458	0.3263	0.8611	1.2461	0.3264	0.8613	1.2461	0.3264	0.8613
36	0.9172	0.5304	0.6578	0.9173	0.5306	0.6580	0.9173	0.5306	0.6580
54	0.5110	0.5486	0.3958	0.5110	0.5487	0.3959	0.5110	0.5487	0.3959
72	0.1644	0.3853	0.1501	0.1644	0.3853	0.1501	0.1644	0.3853	0.1501
$N = 0.99$									
0	1.4124	0.0000	1.0423	1.4129	0.0000	1.0425	1.4129	0.0000	1.0425
18	1.2851	0.3590	0.9560	1.2855	0.3592	0.9562	1.2855	0.3592	0.9562
36	0.9449	0.5847	0.7272	0.9451	0.5849	0.7274	0.9451	0.5849	0.7274
54	0.5263	0.6067	0.4333	0.5263	0.6069	0.4333	0.5263	0.6069	0.4333
72	0.1679	0.4257	0.1608	0.1679	0.4258	0.1608	0.1679	0.4258	0.1608

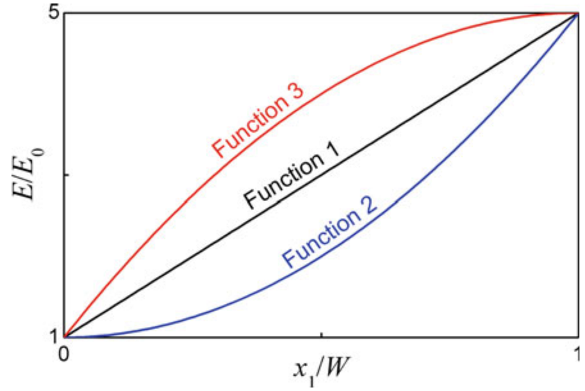

Fig. 8 Young's modulus E/E_0 versus x_1/W (Example 6)

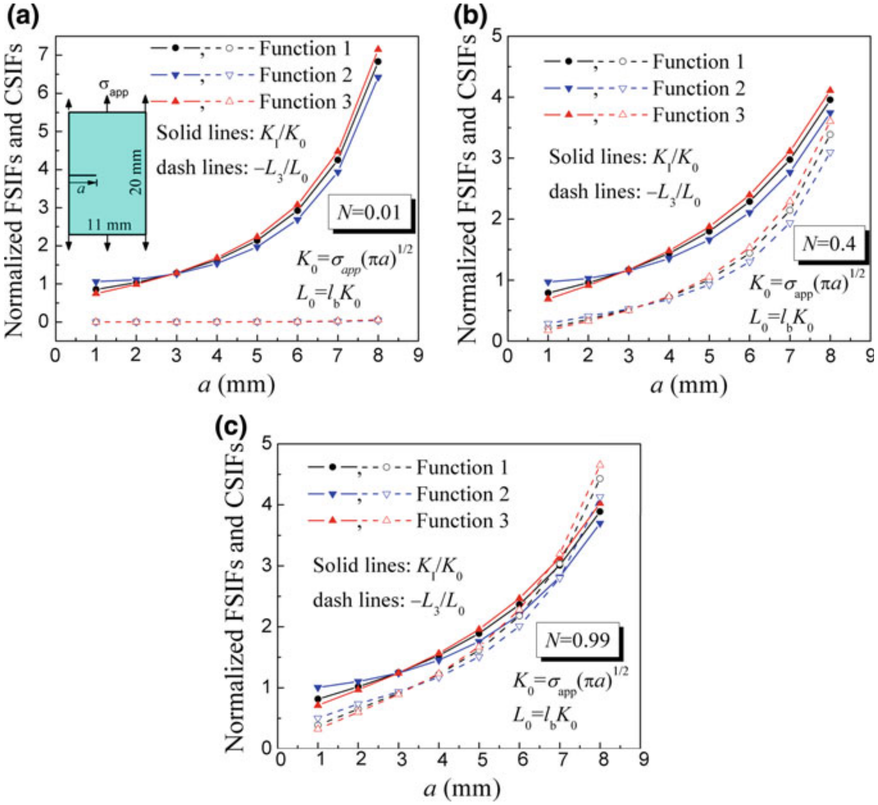

Fig. 9 Normalized FSIFs and CSIFs versus crack length a for the coupling number **a** $N = 0.01$, **b** $N = 0.4$ and **c** $N = 0.99$ (Example 6)

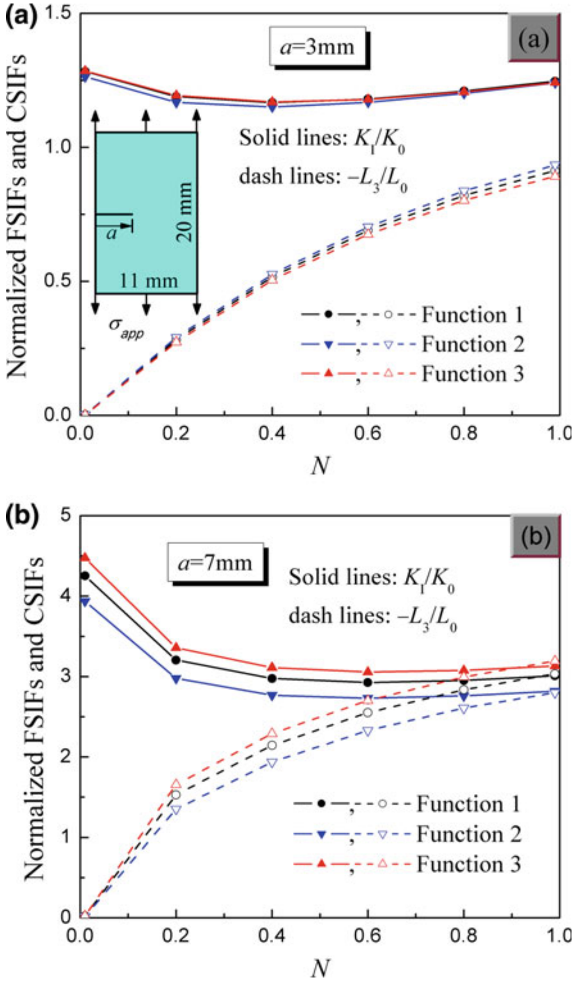

Fig. 10 Normalized FSIFs and CSIFs versus the coupling number N for an edge crack of length **a** $a = 3\,\text{mm}$ and **b** $a = 7\,\text{mm}$ (Example 6)

varying with the crack length for $N = 0.01$, 0.4 and 0.99, respectively, where $K_0 = \sigma_{app}\sqrt{\pi a}$ and $L_0 = l_b K_0$. For all of the above three functions, both the mode-I FSIFs and the CSIFs increase significantly with the increase of the crack length a. The FSIFs and CSIFs in descending order are $K_I|_{\text{Function 2}} > K_I|_{\text{Function 1}} > K_I|_{\text{Function 3}}$ and $L_3|_{\text{Function 2}} > L_3|_{\text{Function 1}} > L_3|_{\text{Function 3}}$ for $a \leq 3\,\text{mm}$, and the inverse order can be observed for $a \geq 3\,\text{mm}$. In other words, Function 3 is better for weakening the crack-tip force stress and couple stress concentration for a small edge crack, while Function 2 is better for a large edge crack. The reason is a different gradient of Young's modulus. The higher the gradient in front of the crack, the more is the crack loading released.

Figure 10a, b show the normalized intensity factors K_I/K_0 and L_3/L_0 varying with the coupling number N for $a = 3\,\text{mm}$ and $a = 7\,\text{mm}$, respectively. The normalized FSIFs and CSIFs have the same trends for all of the above three functions as the coupling number N increases. With increasing coupling number N, the normalized FSIFs K_I/K_0 first decreases and then increases a little for $a = 3\,\text{mm}$, while K_I/K_0 first decreases quickly and then varies slightly for $a = 7\,\text{mm}$, and the normalized CSIF L_3/L_0 increases monotonically for both $a = 3\,\text{mm}$ and $a = 7\,\text{mm}$.

6 Summary and Conclusions

In order to calculate the crack-tip intensity factors for a crack in nonhomogeneous micropolar materials by the I-integral, three applicable formulations are proposed to define the auxiliary field, i.e.,

- CCT formulation (violation of the constitutive equations),
- NE formulation (violation of the equilibrium equations),
- IC formulation (violation of the compatibility equations).

Each of these formulations results in a consistent domain form of the I-integral, in which extra terms naturally appear to compensate for the difference between homogeneous and nonhomogeneous materials. In details,

- The I-integral using the CCT formulation contains strain gradient, curvature gradient and material property gradient. It is not appropriate for nonhomogeneous micropolar materials because the strain gradient and curvature gradient may cause inaccuracy in numerical calculations.
- The I-integral using the NE formulation does not involve any strain gradient or curvature gradient. Therefore, it is reliable for nonhomogeneous micropolar materials with differentiable properties.
- The I-integral using the IC formulation does not involve any material property gradient. It is effective for micropolar material with arbitrary continuous or discontinuous properties.

In order to compute the various I-integrals numerically for arbitrary two-dimensional cracked bodies, the patched-XFEM is applied. The patched-XFEM preserves crack face enrichment functions but renounces crack-tip enrichment functions from the displacement and micro-rotation approximations. Instead, a refined mesh is patched on the main mesh around the crack tip to improve the precision of numerical solution. The I-integral combined with the patched-XFEM is employed to extract the FSIFs and CSIFs for various internal and edge crack configurations in functionally graded micropolar plates. Numerical results show that the NE formulation and the IC formulation give best accuracy for nonhomogeneous micropolar materials, while the CCT formulation generates larger relative errors for nonhomogeneous micropolar materials. For an internal crack, all FSIFs and CSIFs at both crack tips increase monotonically when the coupling number increases, and the differences between the two crack tips are enlarged with increasing gradient parameter. For an edge crack, the increase of coupling number causes a monotonic growth of CSIF, while the mode-I

FSIF first decreases and then varies slightly. All these examples demonstrate that material property functions affect the FSIFs and CSIFs substantially.

Acknowledgements The work was financially supported by the National Natural Science Foundation of China (Grant No. 11772105 and 11472191) and by the Alexander von Humboldt Foundation.

References

1. Eremeyev, V.A., Lebedev, L.P., Altenbach, H.: Foundations of Micropolar Mechanics. Springer, Berlin (2013)
2. Karlis, G.F., Tsinopoulos, S.V., Polyzos, D., Beskos, D.E.: Boundary element analysis of mode I and mixed mode (I and II) crack problems of 2-D gradient elasticity. Comput. Methods Appl. Mech. Eng. **196**, 5092–5103 (2007)
3. Trovalusci, P., Ostoja-Starzewski, M., DeBellis, M.L.: Scale-dependent homogenization of random composites as micropolar continua. Eur. J. Mech. A Solids **49**, 396–407 (2015)
4. Cosserat, E., Cosserat, F.: Theories des Corps Deformables. Hermann et Fils, Paris (1909)
5. Eringen, A.C.: Linear theory of micropolar elasticity. J. Math. Mech. **15**, 909–923 (1966)
6. Eringen, A.C.: In: Liebowitz, H. (ed.) Theory of Micropolar Elasticity (in Fracture). Academic Press, New York (1968)
7. Cowin, S.C.: Stress functions for Cosserat elasticity. Int. J. Solids Struct. **6**, 389–398 (1970)
8. Gauthier, R.D., Jahsman, W.E.: A quest for micropolar elastic constants. J. Appl. Mech. **42**, 369–374 (1975)
9. Yang, J.F.C., Lakes, R.S.: Experimental study of micropolar and couple stress elasticity in compact bone in bending. J. Biomech. **15**, 91–98 (1982)
10. Lakes, R.S.: Size effects and micromechanics of a porous solid. J. Mater. Sci. **18**, 2572–2580 (1983)
11. Lakes, R.S.: Experimental microelasticity of two porous solids. Int. J. Solids Struct. **22**, 55–63 (1986)
12. Lakes, R.S.: Experimental methods for study of Cosserat elastic solids and other generalized elastic continua. Wiley, New York (1995)
13. Lakes, R.S.: On the torsional properties of single osteons. J. Biomech. **28**, 1409–1410 (1995)
14. Sternberg, E., Muki, R.: The effect of couple-stresses on the stress concentration around a crack. Int. J. Solids Struct. **36**(1), 69–95 (1967)
15. Atkinson, C., Leppington, F.G.: Some calculations of the energy-release rate G for cracks in micropolar and couple-stress elastic media. Int. J. Fract. **10**, 599–602 (1974)
16. Paul, H.S., Sridharan, K.: The penny-shaped crack problem in micropolar elasticity. Int. J. Eng. Sci. **18**, 651–664 (1980)
17. Paul, H.S., Sridharan, K.: The problem of a Griffith crack in micropolar elasticity. Int. J. Eng. Sci. **19**, 563–579 (1981)
18. Sridharan, K.: The micropolar thermoelastic problem of uniform heat-flow interrupted by an insulated penny-shaped crack. Int. J. Eng. Sci. **21**, 1459–1469 (1983)
19. Diegele, E., Elsaber, R., Tsakmakis, C.: Linear micropolar elastic crack-tip fields under mixed mode loading conditions. Int. J. Fract. **129**, 309–339 (2004)
20. Yavari, A., Sarkani, S., Moyer, E.T.: On fractal cracks in micropolar elastic solids. J. Appl. Mech. **69**, 45–54 (2002)
21. Midya, G.K., Layek, G.C., De, T.K.: On diffraction of normally incident SH-waves by a line crack in micropolar elastic medium. Int. J. Solids Struct. **44**, 4092–4109 (2007)
22. Warren, W.E., Byskov, E.: A general solution to some plane problems of micropolar elasticity. Eur. J. Mech. A Solids **27**, 18–27 (2008)
23. Li, Y.D., Lee, K.Y.: Fracture analysis in micropolar elasticity: mode-I crack. Int. J. Fract. **156**, 179–184 (2009)

24. Antipov, Y.A.: Weight functions of a crack in a two-dimensional micropolar solid. Q. J. Mech. Appl. Math. **65**, 239–271 (2012)
25. Piccolroaz, A., Mishuris, G., Radi, E.: Mode III interfacial crack in the presence of couple-stress elastic materials. Eng. Fract. Mech. **80**, 60–71 (2012)
26. Kennedy, T.C.: Modeling failure in notched plates with micropolar strain softening. Compos. Struct. **44**, 71–79 (1999)
27. Dillard, T., Forest, S., Ienny, P.: Micromorphic continuum modelling of the deformation and fracture behaviour of nickel foams. Eur. J. Mech. A Solids **25**, 526–549 (2006)
28. Shmoylova, E., Potapenko, S., Rothenburg, L.: Boundary element analysis of stress distribution around a crack in plane micropolar elasticity. Int. J. Eng. Sci. **45**, 199–209 (2007)
29. Atoshchenko, E., Bordas, S.P.A.: Fundamental solutions and dual boundary methods for fracture in plane Cosserat elasticity. Proc. R. Soc. A **471**, 20150216 (2015)
30. Khoei, A.R., Karimi, K.: An enriched-FEM model for simulation of localization phenomenon in Cosserat continuum theory. Comput. Mater. Sci. **44**, 733–749 (2008)
31. Kapiturova, M., Gracie, R., Potapenko, S.: Simulation of cracks in a Cosserat medium using the extended finite element method. Math. Mech. Solids **21**(5), 621–635 (2016)
32. Jaric, J.: The energy release rate and the J-integral in nonlocal micropolar field theory. Int. J. Eng. Sci. **28**, 1303–1313 (1990)
33. Yu, H.J., Sumigawa, T., Kitamura, T.: A domain-independent interaction integral for linear elastic fracture analysis of micropolar materials. Mech. Mater. **74**, 1–13 (2014)
34. Stern, M., Becker, E.B., Dunham, R.S.: A contour integral computation of mixed-mode stress intensity factors. Int. J. Fract. **12**, 359–368 (1976)
35. Kfouri, A.P.: Some evaluations of the elastic T-term using Eshelby's method. Int. J. Fract. **30**, 301–315 (1986)
36. Dolbow, J.E., Gosz, M.: On the computation of mixed-mode stress intensity factors in functionally graded materials. Int. J. Solids Struct. **39**, 2557–2574 (2002)
37. Kim, J.H., Paulino, G.H.: Consistent formulations of the interaction integral method for fracture of functionally graded materials. J. Appl. Mech. T ASME **72**, 351–364 (2005)
38. Guo, L.C., Noda, N.: Modeling method for a crack problem of functionally graded materials with arbitrary properties-piecewise-exponential Model. Int. J. Solids Struct. **44**(21), 6768–6790 (2007)
39. Guo, L.C., Wang, Z.H., Noda, N.: A fracture mechanics model for a crack problem of functionally graded materials with stochastic mechanical properties. Proc. R. Soc. A **468**, 2939–2961 (2012)
40. Yu, H.J., Wu, L.Z., Guo, L.C., Du, S.Y., He, Q.L.: Investigation of mixed-mode stress intensity factors for nonhomogeneous materials using an interaction integral method. Int. J. Solids Struct. **46**, 3710–3724 (2009)
41. Yu, H.J., Wu, L.Z., Guo, L.C., He, Q.L., Du, S.Y.: Interaction integral method for the interfacial fracture problems of two nonhomogeneous materials. Mech. Mater. **42**, 435–450 (2010)
42. Pathak, H., Singh, A., Singh, I.V.: Numerical simulation of bi-material interfacial cracks using EFGM and XFEM. Int. J. Mech. Mater. Des. **8**, 9–36 (2012)
43. Bhattacharya, S., Singh, I.V., Mishra, B.K., Bui, T.Q.: Fatigue crack growth simulations of interfacial cracks in bi-layered FGMs using XFEM. Comput. Mech. **52**, 799–814 (2013)
44. Cahill, L.M.A., Natarajan, S., Bordas, S.P.A., O'Higgins, R.M., McCarthy, C.T.: An experimental/numerical investigation into the main driving force for crack propagation in uni-directional fibre-reinforced composite laminae. Compos. Struct. **107**, 119–130 (2014)
45. Yu, H.J., Sumigawa, T., Wu, L.Z., Kitamura, T.: Generalized domain-independent interaction integral for solving the stress intensity factors of nonhomogeneous materials. Int. J. Solids Struct. **67–68**, 151–168 (2015)
46. Lakes, R.S., Benedict, R.L.: Noncentrosymmetry in micropolar elasticity. Int. J. Eng. Sci. **20**, 1161–1167 (1982)
47. Neff, P., Ghiba, I.D., Madeo, A., Placidi, L., Rosi, G.: A unifying perspective: the relaxed linear micromorphic continuum. Contin. Mech. Thermodyn. **26**, 639–681 (2014)

48. Steinmann, P., Willam, K.: Localization within the framework of micropolar elasto-plasticity. Adv. Contin. Mech. 296–313 (1991)
49. Eischen, J.W.: Fracture of nonhomogeneous materials. Int. J. Fract. **34**, 3–22 (1987)
50. Jin, Z.H., Noda, N.: Crack-tip singular fields in nonhomogeneous materials. J. Appl. Mech. **61**, 738–740 (1994)
51. Lubarda, V.A., Markenscoff, X.: On conservation integrals in micropolar elasticity. Philos. Mag. **83**, 1365–1377 (2003)
52. Rao, B.N., Kuna, M.: Interaction integrals for fracture analysis of functionally graded piezoelectric materials. Int. J. Solids Struct. **45**(20), 5237–5257 (2008)
53. Rao, B.N., Kuna, M.: Interaction integrals for fracture analysis of functionally graded magnetoelectroelastic materials. Int. J. Fract. **153**(1), 15–37 (2008)
54. Moës, N., Dolbow, J., Belytschko, T.: A finite element method for crack growth without remeshing. Int. J. Numer. Methods Eng. **46**, 131–150 (1999)
55. Brown, W.F., Srawley, J.E.: Plane strain crack toughness testing of high strength metallic materials. ASTM STP **410**, 12 (1966)

Analytical Modelling of the Tooth Translational Motions: Comparative Analysis for Different Shapes of Root

Kirill Yurkevich, Sergei Bosiakov and Holm Altenbach

Abstract The orthodontic treatment planning may be carried out based on the finite element and analytical models of periodontal ligament (PDL). For analytical modelling of the PDL behavior the shape of the tooth root mainly was approximated by circular or elliptical paraboloid. Another shape of the tooth root is the elliptical two-sheeted hyperboloid. Semi-axes of the tooth root cross-section in the shape of the elliptical paraboloid and two-sheeted hyperboloid on the alveolar crest level are the same, but the shape of a two-sheeted hyperboloid allows employing the additional parameter for describing the root apex rounding. The aim of this study is the comparative analysis of the hydrostatic stresses patterns during the tooth root translational displacements in the almost incompressible PDL for the root in the shape of the elliptical paraboloid and two-sheeted hyperboloid. As a result, patterns of the hydrostatic stresses in the PDL during translational displacement are nearly identical for the tooth root in the shape of a paraboloid and the tooth root in the shape of a two-sheeted hyperboloid with the rounded apex of the tooth root. The translational movement of the tooth root with a pointed apex leads to the higher hydrostatic stresses in the PDL compared with the tooth root with a rounded apex. The obtained results indicated that the rounding of the tooth root should be considered during planning of orthodontic treatment.

Keywords Orthodontics · Periodontal ligament · Initial translational tooth motion · Idealized shape · Stress patterns · Analytical model

---

K. Yurkevich · S. Bosiakov
Belarusian State University, 4 Nezavisimosti Avenue, 220030 Minsk, Belarus
e-mail: kirill.bsu@gmail.com

S. Bosiakov
e-mail: Belarusemailkirill.bsu@gmail.com

H. Altenbach (✉)
Institute of Mechanics, Faculty of Mechanical Engineering, Otto-von-Guericke-University
Magdeburg, 2 Universitätsplatz, 39106 Magdeburg, Sachsen-Anhalt, Germany
e-mail: holm.altenbach@ovgu.de

© Springer International Publishing AG 2018

H. Altenbach et al. (eds.), *Advances in Mechanics of Materials and Structural Analysis*, Advanced Structured Materials 80,
https://doi.org/10.1007/978-3-319-70563-7_20

1 Introduction

Orthodontic treatment of malocclusion and anomalous dentition is a complex dental procedure and requires careful planning. Various analytical and numerical models are developed for planning of the therapeutic stages [2–5, 7, 10, 11, 16, 20, 22, 25, 26, 28]. In these models, the actual or idealized geometric shape of the teeth are considered and the finite element (FE) method [2–5, 7, 10, 20] or analytical approaches [11, 16, 22, 25, 26, 28] are used.

Initial motions of teeth can be caused by the short-term load, after the load is removed the tooth returns to its previous position; the degenerative and irreversible changes in the periodontal ligament (PDL) are absent [5, 29]. Also, for analytical modelling of tooth motions and behavior of the PDL during tooth displacement, in most cases, the shape of the tooth root is approximated by a paraboloid or a two-sheeted hyperboloid ([1, 18, 25], and others listed therein).

The thickness of the periodontal ligament (PDL) changes within certain limits for each tooth and also varies for different teeth [12, 15, 17, 19, 27]. According to [21], average thickness of the PDL is approximately 0.25 ± 50% mm. The thickness of the PDL can increase near the alveolar crest or near the apex of the tooth root. Also the PDL can take the shape of a hollow chamfer with a minimum thickness in the middle third of the tooth root.

Most of the finite-element models of the PDL were developed for constant thickness cases. Stresses and deformations of the PDL with non-uniform thickness under the tooth root different loading were estimated in several studies. In one of them a two-dimensional finite-element model was developed for the premolar [24]. The thickness of the PDL near the alveolar crest and at the apex of the root was exceeded the thickness of the PDL in the middle third of the tooth root. The finite-element analysis of displacements, principal and equivalent stresses of the PDL under the small intrusive loads demonstrated that the stress distributions for the uniform and non- uniform thickness model were similar [24]. In [8], the finite-element analysis of the maximum principal stresses under vertical loading in the PDL with constant thickness and PDL with thickness increases from the alveolar ridge to the apex of the tooth root was carried out. Geometric models are obtained on the basis of tomographic images of different cross-sections of the tooth root and paradont. The authors concluded that the width of the periodontal cleft affects slightly on the stress distributions in the PDL. Taking into account the conclusions of [8, 24] the constant thickness of the PDL was considered in present research.

A comparative estimation of the tooth root motions in the bilinear elastic PDL for actual shape of the tooth root and for the tooth root in the form of a paraboloid was carried out in [27]. It was concluded in this study, that the more appropriate approximation to the actual shape of canine root is an elliptical paraboloid. According to the [27], the accuracy of the determination of the centre of resistance for the human canine and elliptical paraboloid is within 10 per cent, and the difference between the tipping calculations for actual root and elliptical paraboloid about 2%.

The shape of a circular paraboloid for the maxillary central incisor was employed in [18] to model analytically the initial movement of the tooth root in almost incompressible PDL with Poisson ratio of 0.49. This approach was developed in [25] for the orthodontic treatment planning using the shape of an elliptical paraboloid for the tooth root. Along with this, FE analysis of stresses in the almost incompressible PDL during motions of the tooth root in the shape of a circular and elliptical paraboloid was performed in [18, 25], and an analytical model was validated. The differences between the stresses were detected in small regions of the PDL near the apex, and especially at the alveolar crest region. For other regions of the PDL the stresses predicted on analytical and FE models are practically identical.

At the same time, the model of the tooth root in the shape of a two-sheeted hyperboloid is almost not used for the analytical modelling of the stress patterns in the PDL and displacements of the tooth root, although the feature of this shape is the ability to define the tooth root rounding at the apex region. The aim of this study is the comparative analysis of the stress patterns during the tooth root translational displacements in the almost incompressible PDL for the root in the shape of the elliptical paraboloid and two-sheeted hyperboloid.

2 Methods

2.1 Modelling of the Tooth Root Equilibrium in the PDL

It is assumed that the inner surface of the PDL is defined by one of the equations:

$$F_1(x, y, z) = y - \frac{h}{b^2}\left(x^2(1 - e^2) + z^2\right), \tag{1}$$

$$F_2(x, y, z) = y - \frac{h}{\sqrt{1 + p^2} - p}\left(\sqrt{(1 - e^2)\left(\frac{x}{b}\right)^2 + \left(\frac{z}{b}\right)^2 + p^2} - p\right) = 0, \tag{2}$$

where h is the height of tooth root; $e = \sqrt{1 - (b/a)^2}$, a and b are the eccentricity and semi-axes of the elliptical cross-section of the tooth root at the alveolar crest level, respectively; p is the parameter defining the rounding of the tooth root apex.

Under the force action on the tooth crown, the inner PDL surface $F_k(x, y, z)$ are moved on the distance equal to the displacement of the tooth root. The outer surface of the PDL is rigidly fixed. Moreover, the teeth and the alveolar bone are assumed the rigid bodies [8, 18, 25].

In accordance with [18, 21], it is assumed that the PDL tissue is almost incompressible material with Poisson's ratio equal to 0.49.

After transformations in conformity with [25] the following equilibrium equations of the tooth root were obtained:

$$\begin{aligned} a_{11}^{(k)} u_{0x} + a_{16}^{(k)} \theta_z = f_x, a_{22}^{(k)} u_{0y} = f_y, a_{33}^{(k)} u_{0z} + a_{34}^{(k)} \theta_x = f_z, \\ a_{43}^{(k)} u_{0z} + a_{44}^{(k)} \theta_x = y_f f_z - z_f f_y, a_{55}^{(k)} \theta_y = z_f f_x - x_f f_z, \\ a_{61}^{(k)} u_{0x} + a_{66}^{(k)} \theta_z = x_f f_y - y_f f_x. \end{aligned} \tag{3}$$

where x_f, y_f and z_f are the coordinates of the point where the load is applied; u_x, u_y and u_z are displacements of the tooth root along x-, y- and z-axis; θ_x, θ_y and θ_z are angles of rotations of the tooth root relative to the same axes. The coefficients of the system (3) are presented in Appendix. Indexes $k = 1$ and $k = 2$ correspond to the tooth root in the shape of a paraboloid and a two-sheeted hyperboloid, respectively.

2.2 Hydrostatic Stresses

The regions of largest hydrostatic stresses are primary indicators of the bone remodelling during orthodontic tooth movement [6, 13, 27]. Hydrostatic stress is defined as follows:

$$\sigma_h = \frac{1}{3}(\sigma_{xx} + \sigma_{yy} + \sigma_{zz}) \tag{4}$$

The hydrostatic stresses σ_{hxy} and σ_{hyz} during the tooth root translational displacements in xy-plane and yz-plane are expressed as follows:

$$\sigma_{hxy}^{(k)} = \frac{E\left(a_{22}^{(k)} f_x H_k \sin(\alpha_k) - a_{11}^{(k)} f_y \cos(\alpha_k)\right)}{3\delta\,(2\nu - 1)\, a_{11}^{(k)} a_{22}^{(k)}}, \tag{5}$$

$$\sigma_{hyz}^{(k)} = \frac{E\left(a_{22}^{(k)} f_z G_k \sin(\alpha_k) - a_{33}^{(k)} f_y \cos(\alpha_k)\right)}{3\delta\,(2\nu - 1)\, a_{22}^{(k)} a_{33}^{(k)}}, k = 1, 2, \tag{6}$$

where parameters G_k, H_k and angle α_k are defined in [25].

3 Results

For the calculations the following tooth root geometrical dimensions are assumed $h = 13.0\,\text{mm}$, $b = 3.9\,\text{mm}$ and $e = 0.6$. Elastic properties of the PDL are defined by constants $E = 680$ kPa and $\nu = 0.49$ [23]. Thickness δ of the PDL is 0.229 mm [18].

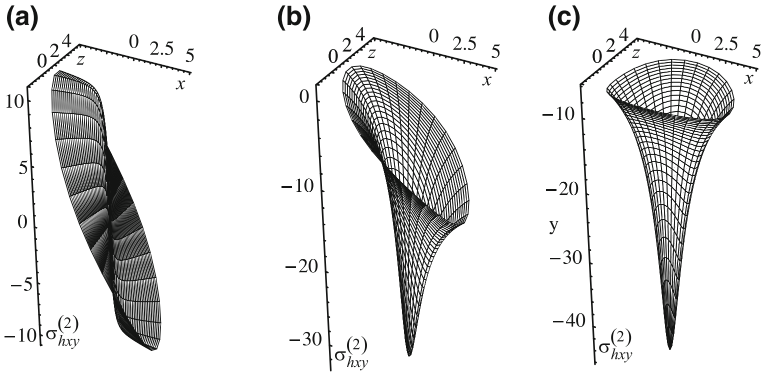

Fig. 1 Patterns of the hydrostatic stresses σ_{hxy} on the inner PDL surface during translational displacement of the tooth root in xy-plane under the load action: **a** $f_x = 1$ N, $f_y = f_z = 0$, **b** $f_x = -f_y = 1/\sqrt{2}$ N, $f_z = 0$, **c** $f_x = f_z = 0$, $f_y = -1$ N

3.1 Hydrostatic Stresses Pattern

Figure 1 depicts the patterns of the hydrostatic stresses σ_{hxy} for the PDL middle surface during translational displacement in the xy-plane. The shape of the tooth root is a two-sheeted hyperboloid with the parameter p of the apex rounding equals to 0.4.

It is seen from Fig. 1a that the highest (in absolute value) hydrostatic stresses σ_{hxy} during translational displacement of the tooth along the x-axis appear in the PDL's region near alveolar crest. If the force component f_x is supplemented by vertical force component f_y directed downwards, then the hydrostatic stresses σ_{hxy} significantly increase in the PDL apical region. During the tooth root vertical displacement downward the hydrostatic stresses σ_{hxy} in the PDL's regions near the alveolar crest are higher near minor semi-axes than near major semi-axes of the tooth root cross-section.

The patterns of the hydrostatic stresses σ_{hyz} after tooth loading by force $f_x = 0$, $f_y = 0$, $f_z = 1$ N or $f_x = 0$, $f_y = -1/\sqrt{2}$ N, $f_z = 1/\sqrt{2}$ N are similar to patterns that depicted in Fig. 1 a, b, respectively. The magnitudes of the hydrostatic stresses σ_{hxy} and σ_{hyz} for PDL's different points $A(\frac{b}{\sqrt{1-e2}}, h, 0)$, $B(b, h, 0)$, $C(-\frac{b}{\sqrt{1-e2}}, h, 0)$ and $D(-b, h, 0)$ for the tooth root with different parameters p are shown in Figs. 2 and 3.

It is may be seen from Figs. 2 and 3 that the parameter p significantly affects the hydrostatic stresses in the PDL. If the parameter p increases, then regardless of the loading type, the hydrostatic stresses are decreased. If the parameter p is equal to 5.0, the hydrostatic stresses in the PDL for the tooth root in the shape of a two-sheeted hyperboloid coincide with the corresponding hydrostatic stresses in the PDL for tooth root in the shape of a paraboloid with an accuracy approximately of 2%.

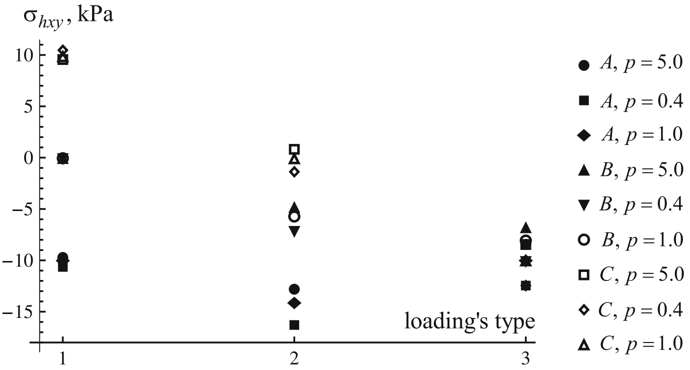

Fig. 2 Hydrostatic stresses at the points $A(a, h, 0)$, $B(b, h, 0)$ and $C(-a, h, 0)$ of PDL during translational displacement of the tooth root in xy-plane under the load action: 1 – $f_x = 1$ N, $f_y = f_z = 0$; 2 – $f_x = -f_y = 1/\sqrt{2}$ N, $f_z = 0$; 3 – $f_x = f_z = 0$, $f_y = 1$ N. Loading's types 1, 2 and 3 are indicated on the horizontal axes

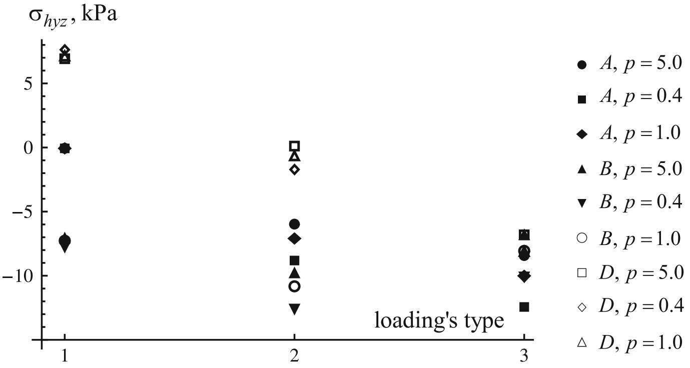

Fig. 3 Hydrostatic stresses at the points $A(a, h, 0)$, $B(b, h, 0)$ and $D(0, h, -b)$ of PDL during translational displacement of the tooth root in yz-plane under the load action (it is indicated on the horizontal axis): 1 – $f_x = 1$ N, $f_y = f_z = 0$; 2 – $f_x = -f_y = 1/\sqrt{2}$ N, $f_z = 0$; 3 – $f_x = f_z = 0$, $f_y = 1$ N. Loading's types 1, 2 and 3 are indicated on the horizontal axes

Parameter p also affects the hydrostatic stresses in the alveolar crest region of the PDL (see Fig. 2, point C and Fig. 3, point D). Under the loading of type 2 in the middle of the PDL for the tooth root with the different rounding of the root apex can occur compressive stresses (Fig. 3, point A, $p = 0.4$) or tensile stresses (Fig. 3, point A, $p = 1.0$, $p = 5.0$). That is, the rounding of the root apex can affect the stresses regime of the PDL. Therefore orthodontic effect under such loading can leads to the bone resorption at the alveolar crest region during the motions of the tooth with the pointed apex and the bone formation in the same region during the motion of the tooth with the rounded root apex under the same loading. It should be noted that the external contours of the patterns σ_{hxy} and σ_{hyz} are bounded almost by plane surface (except of small regions near the apexes and alveolar crest). This indicates that the bone remodelling during the tooth root translational displacement in x- or z-directions will occur uniformly along the root surfaces; below the apex the bone is not reconstructed. If the tooth root moves translationally at an angle to the x- or z-axis, then bone is also remodelled uniformly besides the apical and alveolar crest regions. At this regions, due rather high stresses and bone resorption might occur the negative effects for the patients. Note that in [9, 14] is also mentioned about bone resorption in the apical area during the teeth movement, including the intrusion.

Parameter p has practically no effect on the hydrostatic stresses in the apex region during the vertical downward displacement of the tooth. The difference between the stresses in the PDL during the tooth root translational downward displacement for two considered shapes of the tooth root is not more than 2.5%. It is important that even the addition of a minor vertical load component leads to high stresses in the PDL apex region. In particular, the stresses in the PDL apical region almost twice as many of maximum stress in the alveolar crest region under the tooth loading of type 2 (see Figs. 2 and 3). Also important is the fact that the higher stresses near the alveolar crest region occur during the simultaneous action of horizontal and vertical load components compared with the action only horizontal or vertical force.

The eccentricity of an ellipse in cross-section of the tooth root significantly affect the hydrostatic stresses independently of the parameter p. The hydrostatic stresses at the points A and C (see Fig. 2) during the tooth translation along the x-axis are approximately 24% larger than the hydrostatic stresses in the points B and D (see Fig. 3) during the tooth translational displacement along the z-axis. Conversely, the hydrostatic stresses in the points B and D during the tooth translation along the x-axis are less than the corresponding hydrostatic stresses at the points A and C during tooth translation along the z-axis. This suggests that for any type of loading, and independently of the apex rounding, during the translational displacement of the tooth root in the symmetry plane passing through the minor semi-axes of the elliptical cross-section of the tooth root, the range of hydrostatic stresses in the PDL near the alveolar crest region will be less than during the tooth root translational displacement in the symmetry plane containing the major semi-axes.

3.2 FE Modelling

Foregoing results have shown that the behavior of the PDL during the translational displacement of the tooth root in the shape of a two-sheeted with the large parameters of the apex rounding ($p \geq 5$) and the tooth root in the shape of a paraboloid, are nearly the same. Therefore FE stresses analysis in the PDL is carried out for the tooth root in the shape of a two-sheeted hyperboloid with parameter p of the apex rounding of 0.4. The FE model of the tooth root with the PDL is developed via ANSYS Mechanical APDL 15.0 (ANSYS Inc., USA).

The inner surface of the PDL coincides with the surface of the tooth root, and its displacement is equal to the displacement of the tooth root as a rigid body.

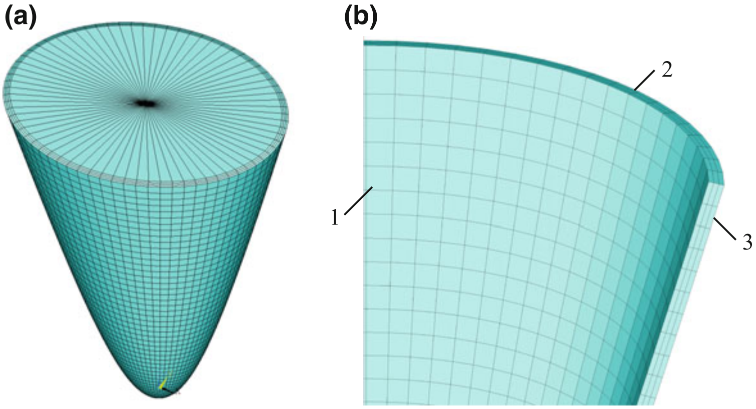

Fig. 4 Details of the FE models of the tooth root and the PDL: **a** the inner and outer PDL surfaces are modelled as a two-sheeted hyperboloid. The nodes on the inner PDL surface 1 is attached to the tooth root; on the nodes of the PDL top surface 2 were no constraints, and the outer surface 3 is fixed; **b** the region of the PDL FE model is divided into elements by using SOLID185 elements. A comparison of the analytical and FE models was carried out for the nodes on the inner PDL surface

Nodes on the outer surface of the PDL in FE model are fixed, that corresponds to the attachment of the PDL to the alveolar bone. Nodes on the top horizontal surface of the PDL are without constraints. The FE mesh of the PDL model and the tooth root model was carried out. The FE model of the PDL is divided into three layers of elements of equal thickness. The result is 4800 elements of SOLID185 type for a model of the tooth root, and 14400 elements of SOLID185 type for the PDL model. The regular hexagonal mesh is used for the FE models of the tooth root and the PDL. The FE model of the tooth root in shape of a two-sheeted hyperboloid and fragment of the PDL FE model is shown in Fig. 4.

Figures 5 and 6 show the normal and shear stress components in the middle of the PDL during translational tooth displacement along x-axis calculated on the basis of analytical and FE models.

The material and geometrical parameters of the analytical and FE models are the same.

It is seen from Figs. 5 and 6 that the largest differences between the stresses components occur in the regions of the alveolar crest and the tooth root apex. This is consistent with the results of similar comparative analysis for the tooth root and the PDL in the shape of a paraboloid [18, 25]. Also note that the coincidence of the magnitudes of the tooth root translational displacement predicted by analytical and FE models is very high; difference between the displacements are not more than 0.5%.

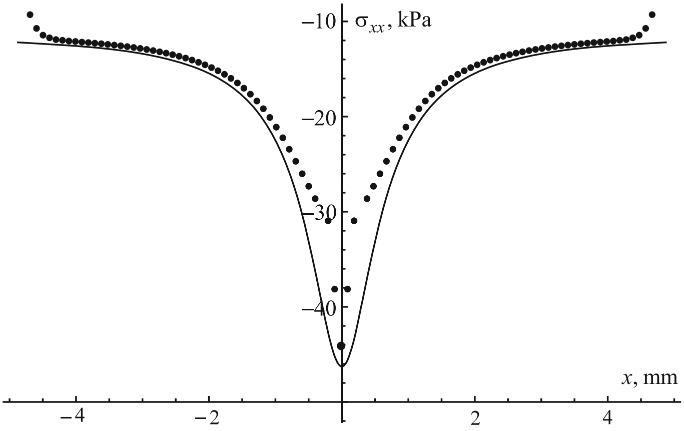

Fig. 5 Normal stress component σ_{xx} in the middle of the PDL during translational tooth root displacement along the positive x-axis. The solid line represents the analytical results, the dots represent the results of the FE modelling

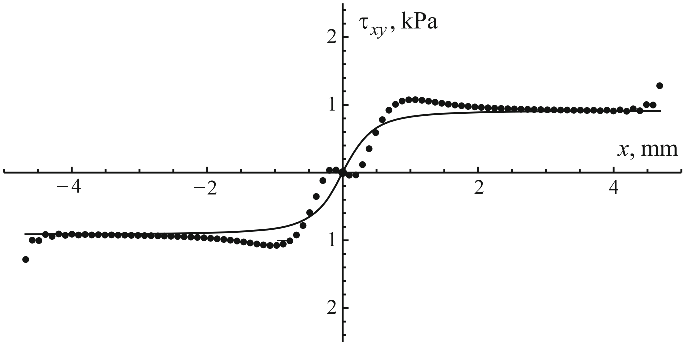

Fig. 6 Shear stress component τ_{xy} in the middle of the PDL during translational tooth root displacement along the positive x-axis. The solid line represents the analytical results, the dots represent the results of the FE modelling

4 Conclusions

The following conclusions can be made:

1. Paraboloid and two-sheeted hyperboloid can be used to describe the shape of the tooth root. For both these cases, the semi-axes of the tooth root cross-section on the alveolar crest level are the same, but for the tooth root in the shape of a two-sheeted hyperboloid need to use the additional parameter for the apex rounding. Patterns of the hydrostatic stresses in the PDL during translational displacement are nearly identical for the tooth root in the shape of a paraboloid and the tooth

root in the shape of a two-sheeted hyperboloid with the parameter of the apex rounding more than 5.0.

2. The translational movement of the tooth root with a pointed apex causes the higher hydrostatic stresses in the PDL compared with the tooth root with a rounded apex. Regardless of parameter of the root apex rounding the hydrostatic stresses in the PDL increase significantly in the apical region, if the line of the force action inclines even at a small angle relative to horizontal. The highest hydrostatic stresses at the PDL region near alveolar crest occur under the inclined position of the force line than under its horizontal or vertical position.
3. Under the same force action on the tooth in the shape of the elliptical two-sheeted hyperboloid the both compressive and tensile stresses in the PDL depending on rounding of the tooth root apex can occur. That is, due to the root apex rounding can change not only stress magnitudes but the stresses regime. This may affect the bone remodelling (resorption or formation) during orthodontic movement of the tooth root.
4. For a more expanded using of the two-sheeted hyperboloid shape for the tooth root and the PDL need to experimentally determine (as possible) the parameter of the apex rounding. It is also necessary to carry out the comparative computations of the PDL behaviour on the basis of actual shape of the tooth root and for the tooth root in the shape of a two-sheeted hyperboloid in the same way as was performed in [27] for the tooth root in the shape of a paraboloid.
5. Comparative analysis of the stress tensor components based on the analytical and FE model of the tooth root in the shape of a two-sheeted hyperboloid revealed sufficiently high agreement between the results except of the PDL regions near the apex and the alveolar crest. This is consistent with similar results [18, 25] for the model of the tooth root in the shape of a paraboloid.

Acknowledgements The authors acknowledge the support of FP7 IRSES Marie Curie grant No 610547 TAMER and DAAD grant No A/12/87820.

Appendix

$$a_{11}^{(k)} = -A \iint\limits_{F_k} (\sin(\alpha_k)(G_k(2\nu-1)n_z^{(k)} + 2H_k(\nu-1)n_x^{(k)}) + \cos(\alpha_k)n_y^{(k)}(1-2\nu))dF_k,$$

$$a_{16}^{(k)} = a_{61}^{(k)} = A \iint\limits_{F_k} (\sin(\alpha_k)(G_k^3(2\nu-1)n_z^{(k)}y + H_k(2G_k^2(\nu-1)n_x^{(k)}y + n_y^{(k)}x(1-2\nu))+$$
$$+G_kH_k^2(2\nu-1)n_z^{(k)}y + 2H_k^3(\nu-1)n_x^{(k)}y) + \cos(\alpha_k)(n_y^{(k)}y - 2\nu(n_x^{(k)}x + n_y^{(k)}y)))dF_k,$$

$$a_{22}^{(k)} = A\iint\limits_{F_k}(2(\nu-1)n_y^{(k)}\cos(\alpha_k) - (2\nu-1)\sin(\alpha_k)(G_k n_z^{(k)} + H_k n_x^{(k)}))dF_k,$$

$$\begin{aligned}
a_{34}^{(k)} = a_{43}^{(k)} = -A\iint\limits_{F_k}(\cos(\alpha_k)(G_k^2(1-2\nu)n_y^{(k)}y+ \\
+H_k^2(1-2\nu)n_y^{(k)}y - 2\nu n_z^{(k)}z) + \sin(\alpha_k)(2G_k^3(\nu-1)n_z^{(k)}y+ \\
+G_k^2H_k(2\nu-1)n_x^{(k)}y + G_k(2H_k^2(\nu-1)n_z^{(k)}y + (1-2\nu)n_y^{(k)}z) + H_k^3(2\nu-1)n_x^{(k)}y))dF_k,
\end{aligned}$$

$$\begin{aligned}
a_{44}^{(k)} = A\iint\limits_{F_k}(\cos(\alpha_k)(G_k^2(2\nu-1)y(n_y^{(k)}y - n_z^{(k)}z)+ \\
+H_k^2(2\nu-1)y(n_y^{(k)}y - n_z^{(k)}z) + 2z(\nu n_y^{(k)}z + \nu n_z^{(k)}y - n_y^{(k)}z))+ \\
+\sin(\alpha_k)(-2G_k^3y(\nu n_y^{(k)}z + (\nu-1)n_z^{(k)}y) + G_k^2H_k(1-2\nu)n_x^{(k)}y^2+ \\
+G_k((2\nu-1)z(n_y^{(k)}y - n_z^{(k)}z) - 2H_k^2y(\nu n_y^{(k)}z + (\nu-1)n_z^{(k)}y))- \\
-H_k(2\nu-1)n_x^{(k)}(H_k^2y^2 + z^2)))dF_k,
\end{aligned}$$

$$\begin{aligned}
a_{55}^{(k)} = -A\iint\limits_{F_k}(\sin(\alpha_k)(G_k(n_z^{(k)}(2(\nu-1)x^2+ \\
+(2\nu-1)z^2) + n_x^{(k)}xz) + H_k(n_x^{(k)}((2\nu-1)x^2+ \\
+2(\nu-1)z^2) + n_z^{(k)}xz)) - (2\nu-1)n_y^{(k)}\cos(\alpha_k)(x^2+z^2))dF_k,
\end{aligned}$$

$$\begin{aligned}
a_{66}^{(k)} = A\iint\limits_{F_k}(\cos(\alpha_k)(n_x^{(k)}xy + n_y^{(k)}(2(\nu-1)x^2 + (2\nu-1)y^2))+ \\
+\sin(\alpha_k)(H_k(n_x^{(k)}((1-2\nu)x^2 - 2G_k^2(\nu-1)y^2)+ \\
+n_y^{(k)}xy(-2(G_k^2-1)\nu - 1)) - G_k(2\nu-1)n_z^{(k)}(G_k^2y^2 + x^2)+ \\
+G_kH_k^2(1-2\nu)n_z^{(k)}y^2 - 2H_k^3y(\nu n_x^{(k)}y + \nu n_y^{(k)}x - n_x^{(k)}y)))dF_k,
\end{aligned}$$

$$A = \frac{E}{2\delta(1+\nu)(1-2\nu)}, G_k = \frac{\partial F_k}{\partial x}, H_k = \frac{\partial F_k}{\partial z}, k = 1, 2.$$

References

1. Bosiakov, S., Mselati, A., Krupoderov, A.: Mathematical modelling of initial displacements of the tooth root in the hyperboloid of two sheets form. Russ. J. Biomech. **19**(2), 161–176 (2015)
2. Bourauel, C., Vollmer, D., Jager, A.: Application of bone remodeling theories in the simulation of orthodontic tooth movements. J. Orofac. Orthop. **61**(4), 266–279 (2000)
3. Cattaneo, P., Dalstra, M., Melsen, B.: The finite element method: a tool to study orthodontic tooth movement. J. Dent. Res. **84**(5), 428–433 (2005)
4. Chang, Y., Shin, S., Baek, S.: Three-dimensional finite element analysis in distal en masse movement of the maxillary dentition with the multiloop edgewise archwire. Eur. J. Orthod. **26**, 339–345 (2004)
5. Clement, R., Schneider, J., Brambs, H., Wunderlich, A., Geiger, M., Sander, F.: Quasi-automatic 3D finite element model generation for individual single-rooted teeth and periodontal ligament. Comp. Meth. Prog. Biomed. **73**(2), 135–144 (2004)
6. De Pauw, G., Dermaut, L., De Bruyn, H.: The value of the centre of rotation in initial and longitudinal tooth and bone displacement. Eur. J. Orthod. **25**, 285–291 (2003)
7. Hayashia, K., Arakib, Y., Uechia, J., Ohnoc, H., Mizoguchi, I.: A novel method for the three-dimensional (3-d) analysis of orthodontic tooth movement calculation of rotation about and translation along the finite helical axis. J. Biomech. **2002**, 45–51 (2002)
8. Hohmann, A., Kober, C., Young, P., Dorow, C., Geiger, M., Boryor, A., Sander, F.M., Sander, C., Sander, F.: Influence of different modeling strategies for the periodontal ligament on finite element simulation results. Am. J. Orthod. Dentofac. Orthop. **139**(6), 775–783 (2011)
9. Jeon, P., Turley, P., Moon, H., Ting, K.: Analysis of stress in the periodontium of the maxillary first molar with a three-dimensional finite element model. Am. J. Orthod. Dentofac. Orthop. **115**(3), 267–274 (1999)
10. Kojima, Y., Fukui, H.: A numerical simulation of tooth movement by wire bending. Am. J. Orthod. Dentofac. Orthop. **130**, 452–459 (2006)
11. Kusy, R., Tulloch, C.: Analysis of moment/force ratios tooth movement. Am. J. Orthod. Dentofac. Orthop. **90**, 127–131 (1986)
12. Maceri, F., Marino, G., Vairo, G.: Mechanical behaviour of endodontic restorations with multiple prefabricated posts: a finite-element approach. J. Biomech. **40**, 2386–2398 (2007)
13. Middleton, J., Jones, M., Wilson, A.: The role of the periodontal ligament in bone modeling: the initial development of a time-dependent finite element model. Am. J. Orthod. Dentofac. Orthop. **109**, 155–162 (1996)
14. Mohandesan, H., Ravanmehr, H., Valaei, N.: A radiographic analysis of external apical root resorption of maxillary incisors during active orthodontic treatment. Eur. J. Orthod. **29**(2), 134–139 (2007)
15. Natali, A.N., Pavan, P.G., Scarpa, C.: Numerical analysis of tooth mobility: formulation of a nonlinear constitutive law for the periodontal ligament. Dent. Mater. **20**, 623–629 (2004)
16. Nikolai, R.: Rigid-body kinematics and single-tooth displacements. Am. J. Orthod. Dentofac. Orthop. **110**, 88–92 (1996)
17. Provatidis, C.G.: A comparative fem-study of tooth mobility using isotropic and anisotropic models of the periodontal ligament. finite element method. Med. Eng. Phys. **22**, 359–370 (2000)
18. Provatidis, C.G.: An analytical model for stress analysis of a tooth in translation. Int. J. Eng. Sci. **39**(12), 1361–1381 (2001)
19. Qian, H., Chen, J., Katona, T.R.: The influence of pdl principal fibers in a 3-dimensional analysis of orthodontic tooth movement. Am. J. Orthod. Dentofac. Orthop. **120**, 272–279 (2001)
20. Qian, Y., Fan, Y., Liu, Z., Zhang, M.: Numerical simulation of tooth movement in a therapy period. Clin. Biomech. **23**, S48–S52 (2008)
21. Rees, J., Jacobsen, P.: Elastic modulus of the periodontal ligament. Biomaterials **18**, 995–999 (1997)
22. Smith, R.J., Burstone, C.J.: Mechanics of tooth movement. Am. J. Orthod. **85**(4), 294–307 (1984)

23. Tanne, K., Nagataki, T., Inoue, Y., Sakuda, M., Burstone, C.J.: Patterns of initial tooth displacement associated with various root lengths and alveolar bone heights. Am. J. Orthod. Dentofac. Orthop. **100**, 66–71 (1991)
24. Toms, S.R., Eberhardt, A.W.: A nonlinear finite element analysis of the periodontal ligament under orthodontic tooth loading. Am. J. Orthod. Dentofac. Orthop. **123**, 657–665 (2003)
25. Van Schepdael, A., Geris, L., Vander Sloten, J.: Analytical determination of stress patterns in the periodontal ligament during orthodontic tooth movement. Med. Eng. Phys. **35**, 403–410 (2013)
26. Van Schepdael, A., Vander Sloten, J., Geris, L.: Mechanobiological modeling can explain orthodontic tooth movement: Three case studies. J. Biomech. **46**, 470–477 (2013)
27. Vollmer, D., Bourauel, C., Maier, K., Jager, A.: Determination of the center of resistance in an upper human canine and idealized tooth model. Eur. J. Orthod. **21**(6), 633–648 (1999)
28. Yashiro, K., Montero, E.D.C., Takada, K.: Simulation of initial tooth displacement by inverse kinematic modeling: Prediction of anchorage-loss for orthodontic tooth movement. Int. Cong. Ser. **1284**, 49–54 (2005)
29. Ziegler, A., Keilig, L., Kawarizadeh, A., Jager, A., Bourauel, C.: Numerical simulation of the biomechanical behaviour of multi-rooted teeth. Eur. J. Orthod. **27**(4), 333–339 (2005)